



FACULTÉ  
DES SCIENCES

UNIVERSITÉ LIBRE DE BRUXELLES



# Towards robust prediction of the dynamics of the Antarctic ice sheet

Uncertainty quantification of sea-level rise projections  
and grounding-line retreat with essential ice-sheet models

## Thesis submitted by Kevin Bulthuis

in fulfilment of the requirements of the PhD Degree in Sciences (ULB - "Docteur en Sciences") and in Applied Sciences (ULiège - "Docteur en Sciences de l'Ingénieur")  
Année académique 2019–2020

Supervisors: Professor Frank Pattyn (Université Libre de Bruxelles)  
Laboratory of Glaciology  
and Professor Maarten Arnst (Université de Liège)  
Computational and Stochastic Modeling

## Thesis jury :

Maarten Arnst (Université de Liège)  
Benjamin Dewals (Université de Liège)  
Frank Pattyn (Université Libre de Bruxelles)  
Catherine Ritz (Université Grenoble Alpes)  
Christian Soize (Université Paris-Est)  
Jean-Louis Tison (Université Libre de Bruxelles)





**Thesis jury:**

The present dissertation has been evaluated by the members of the Jury (sorted by alphabetical order):

Prof. Maarten Arnst	(Supervisor)	Université de Liège;
Prof. Benjamin Dewals		Université de Liège;
Prof. Frank Pattyn	(Co-supervisor)	Université Libre de Bruxelles;
Dr. Catherine Ritz		Université Grenoble Alpes;
Prof. Christian Soize		Université Paris-Est;
Prof. Jean-Louis Tison	(Chair)	Université Libre de Bruxelles.

**Funding:**

The research described in the present dissertation was financially supported by the Fonds de la Recherche Scientifique de Belgique (F.R.S.-FNRS) through an F.R.S.-FNRS Research Fellowship.

Computational resources have been provided by the Consortium des Équipements de Calcul Intensif (CÉCI), funded by the Fonds de la Recherche Scientifique de Belgique (F.R.S-FNRS) under grant no. 2.5020.11.



# **Towards robust prediction of the dynamics of the Antarctic ice sheet:**

## **Uncertainty quantification of sea-level rise projections and grounding-line retreat with essential ice-sheet models**

**Bulthuis Kevin**

### **Abstract**

Recent progress in the modelling of the dynamics of the Antarctic ice sheet has led to a paradigm shift in the perception of the Antarctic ice sheet in a changing climate. New understanding of the dynamics of the Antarctic ice sheet now suggests that the response of the Antarctic ice sheet to climate change will be driven by instability mechanisms in marine sectors. As concerns have grown about the response of the Antarctic ice sheet in a warming climate, interest has grown simultaneously in predicting with quantified uncertainty the evolution of the Antarctic ice sheet and in clarifying the role played by uncertainties in predicting the response of the Antarctic ice sheet to climate change.

Essential ice-sheet models have recently emerged as computationally efficient ice-sheet models for large-scale and long-term simulations of the ice-sheet dynamics and integration into Earth system models. Essential ice-sheet models, such as the fast Elementary Thermomechanical Ice Sheet (f.ETISh) model developed at the Université Libre de Bruxelles, achieve computational tractability by representing essential mechanisms and feedbacks of ice-sheet thermodynamics through reduced-order models and appropriate parameterisations. Given their computational tractability, essential ice-sheet models combined with methods from the field of uncertainty quantification provide opportunities for more comprehensive analyses of the impact of uncertainty in ice-sheet models and for expanding the range of uncertainty quantification methods employed in ice-sheet modelling.

The main contributions of this thesis are twofold. On the one hand, we contribute a new assessment and new understanding of the impact of uncertainties on the multicentennial response of the Antarctic ice sheet. On the other hand, we contribute new methods for uncertainty quantification of geometrical characteristics of the spatial response of physics-based computational models, with, as a motivation in glaciology, a focus on predicting with quantified uncertainty the retreat of the grounded region of the Antarctic ice sheet.

For the first contribution, we carry out new probabilistic projections of the multicentennial response of the Antarctic ice sheet to climate change using the f.ETISh model. We apply methods from the field of uncertainty quantification to the f.ETISh model to investigate the influence of several sources of uncertainty, namely sources of uncertainty in atmospheric forcing, basal sliding, grounding-line flux parameterisation, calving, sub-shelf melting, ice-shelf rheology, and bedrock relation, on the continental response on the Antarctic ice sheet. We provide new probabilistic projections of the contribution of the Antarctic ice sheet to future sea-level rise; we carry out stochastic sensitivity analysis to determine the most influential sources of uncertainty; and

we provide new probabilistic projections of the retreat of the grounded portion of the Antarctic ice sheet.

For the second contribution, we propose to address uncertainty quantification of geometrical characteristics of the spatial response of physics-based computational models within the probabilistic context of the random set theory. We contribute to the development of the concept of confidence sets that either contain or are contained within an excursion set of the spatial response with a specified probability level. We propose a new multifidelity quantile-based method for the estimation of such confidence sets and we demonstrate the performance of the proposed method on an application concerned with predicting with quantified uncertainty the retreat of the Antarctic ice sheet.

In addition to these two main contributions, we contribute to two additional pieces of research pertaining to the computation of Sobol indices in global sensitivity analysis in small-data settings using the recently introduced probabilistic learning on manifolds (PLoM) and to a multi-model comparison of the projections of the contribution of the Antarctic ice sheet to global mean sea-level rise.

**Key-words:** Uncertainty quantification, probabilistic projections, confidence sets, essential ice-sheet models, Antarctic ice sheet.

# **Vers des prédictions robustes de la dynamique de la calotte polaire de l'Antarctique:**

**Quantification de l'incertitude sur les projections de l'augmentation du niveau des mers et du retrait de la ligne d'ancrage à l'aide de modèles glaciologiques essentiels**

**Bulthuis Kevin**

## **Résumé**

Les progrès récents effectués dans la modélisation de la dynamique de la calotte polaire de l'Antarctique ont donné lieu à un changement de paradigme vis-à-vis de la perception de la calotte polaire de l'Antarctique face au changement climatique. Une meilleure compréhension de la dynamique de la calotte polaire de l'Antarctique suggère désormais que la réponse de la calotte polaire de l'Antarctique au changement climatique sera déterminée par des mécanismes d'instabilité dans les régions marines. Tandis qu'un nouvel engouement se porte sur une meilleure compréhension de la réponse de la calotte polaire de l'Antarctique au changement climatique, un intérêt particulier se porte simultanément vers le besoin de quantifier les incertitudes sur l'évolution de la calotte polaire de l'Antarctique ainsi que de clarifier le rôle joué par les incertitudes sur le comportement de la calotte polaire de l'Antarctique en réponse au changement climatique.

D'un point de vue numérique, les modèles glaciologiques dits essentiels ont récemment été développés afin de fournir des modèles numériques efficaces en temps de calcul dans le but de réaliser des simulations à grande échelle et sur le long terme de la dynamique des calottes polaires ainsi que dans l'optique de coupler le comportement des calottes polaires avec des modèles globaux du système terrestre. L'efficacité en temps de calcul de ces modèles glaciologiques essentiels, tels que le modèle f.ETISh (fast Elementary Thermomechanical Ice Sheet) développé à l'Université Libre de Bruxelles, repose sur une modélisation des mécanismes et des rétroactions essentiels gouvernant la thermodynamique des calottes polaires au travers de modèles d'ordre réduit et de paramétrisations. Vu l'efficacité en temps de calcul des modèles glaciologiques essentiels, l'utilisation de ces modèles en complément des méthodes du domaine de la quantification des incertitudes offrent de nombreuses opportunités afin de mener des analyses plus complètes de l'impact des incertitudes dans les modèles glaciologiques ainsi que de développer de nouvelles méthodes du domaine de la quantification des incertitudes dans le cadre de la modélisation glaciologique.

Les contributions de cette thèse sont doubles. D'une part, nous contribuons à une nouvelle estimation et une nouvelle compréhension de l'impact des incertitudes sur la réponse de la calotte polaire de l'Antarctique dans les prochains siècles. D'autre part, nous contribuons au développement de nouvelles méthodes pour la quantification des incertitudes sur les caractéristiques géométriques de la réponse spatiale de modèles physiques numériques avec, comme motivation en glaciologie, un intérêt particulier vers la prédiction sous incertitudes du retrait de

la région de la calotte polaire de l'Antarctique en contact avec le lit rocheux.

Dans le cadre de la première contribution, nous réalisons de nouvelles projections probabilistes de la réponse de la calotte polaire de l'Antarctique au changement climatique au cours des prochains siècles à l'aide du modèle numérique f.ETISh. Nous appliquons des méthodes du domaine de la quantification des incertitudes au modèle numérique f.ETISh afin d'étudier l'impact de différentes sources d'incertitude sur la réponse continentale de la calotte polaire de l'Antarctique. Les sources d'incertitude étudiées sont relatives au forçage atmosphérique, au glissement basal, à la paramétrisation du flux à la ligne d'ancrage, au vêlage, à la fonte sous les barrières de glace, à la rhéologie des barrières de glace et à la relaxation du lit rocheux. Nous réalisons de nouvelles projections probabilistes de la contribution de la calotte polaire de l'Antarctique à l'augmentation future du niveau des mers; nous réalisons une analyse de sensibilité afin de déterminer les sources d'incertitude les plus influentes; et nous réalisons de nouvelles projections probabilistes du retrait de la région de la calotte polaire de l'Antarctique en contact avec le lit rocheux.

Dans le cadre de la seconde contribution, nous étudions la quantification des incertitudes sur les caractéristiques géométriques de la réponse spatiale de modèles physiques numériques dans le cadre de la théorie des ensembles aléatoires. Dans le cadre de la théorie des ensembles aléatoires, nous développons le concept de régions de confiance qui contiennent ou bien sont inclus dans un ensemble d'excursion de la réponse spatiale du modèle numérique avec un niveau donné de probabilité. Afin d'estimer ces régions de confiance, nous proposons de formuler l'estimation de ces régions de confiance dans une famille d'ensembles paramétrés comme un problème d'estimation de quantiles d'une variable aléatoire et nous proposons une nouvelle méthode de type multifidélité pour estimer ces quantiles. Finalement, nous démontrons l'efficacité de cette nouvelle méthode dans le cadre d'une application relative au retrait de la région de la calotte polaire de l'Antarctique en contact avec le lit rocheux.

En plus de ces deux contributions principales, nous contribuons à deux travaux de recherche additionnels. D'une part, nous contribuons à un travail de recherche relatif au calcul des indices de Sobol en analyse de sensibilité dans le cadre de petits ensembles de données à l'aide d'une nouvelle méthode d'apprentissage probabiliste sur des variétés géométriques. D'autre part, nous fournissons une comparaison multimodèle de différentes projections de la contribution de la calotte polaire de l'Antarctique à l'augmentation du niveau des mers.

**Mots-clés:** Quantification des incertitudes, projections probabilistes, régions de confiance, modèles glaciologiques essentiels, calotte polaire de l'Antarctique.

## Acknowledgements

First and foremost, I would like to express my greatest gratitude to my supervisors Maarten Arnst and Frank Pattyn for their help and support throughout these four years. I do think that it was not an easy task to bring engineers and glaciologists together, but they were able to share their respective enthusiasm for stochastic modelling and glaciology with me to achieve this piece of work.

Maarten, dit manuscript is bijna net zo veel je werk als mijn werk. Ik zou graag je hartelijk danken voor je aandacht en je begeleiding tijdens dit doctoraat. Ik dank je om constant dit werk proberen te verbeteren. Als voor mij was glaciologie een nieuw onderwerp van studie voor jou and je hebt constant alle details proberen te verstaan. Dankzij je advies heb ik veel van de wetenschappelijke visie geleerd.

Frank, dat was een groot plezier je te ontmoeten. Ik zou graag je hartelijk danken voor alle je advies met glaciologie and je enthousiasme. Misschien was soms delen van mijn werk een beetje te technisch om alles te verstaan. Sorry! I hoop dat dit manuscript je (een beetje) zal bijlichten! Ik verwacht ook met jou opnieuw te zingen.

I would like to gratefully acknowledge the members of the jury, Benjamin Dewals, Catherine Ritz, Christian Soize, and Jean-Louis Tison, for their interest in this work. I sincerely appreciate the time they spent reviewing and evaluating this thesis. I would like to thank warmly Jean-Louis Tison for being in my thesis committee for this PhD thesis and Christian Soize for giving me the (unique) opportunity to work with him.

I would like to warmly thank all my colleagues from Aerospace and Mechanical Engineering for providing me such a pleasant and enjoyable work place. Thanks to Joffrey and Kim for sharing the same office during these four years (sometimes a bit sad when none of you was there) and Joffrey for being my running partner. Thanks to the Automotive Engineering Research group (Denis, Eduardo, Maxime, Pablo, Simon), the technicians (Antonio, Antoine, Mathieu), and other members of the “billiard club” (Asmaa, Laura, Pilou, . . . ) for the fun we had.

I would also like to thank all my colleagues from the GEMICE group (Elise, Konz, Lars, Sainan, Vio) and more generally from the Laboratory of Glaciology. I did not have much opportunity to collaborate and spend time with you but this was definitely a pleasure to meet you. I wish you good fortune in promoting cryospheric sciences.

Finalement, je tiens à remercier mes amis (avec une dédicace à ceux des mouvements de jeunesse), mes parents, mes frères, mes grands-parents et ma famille pour leur soutien durant cette thèse.



# Contents

<b>I</b>	<b>Modelling ice sheets in the presence of uncertainties</b>	<b>1</b>
<b>1</b>	<b>Introduction</b>	<b>3</b>
1.1	Research Context: Antarctic ice sheet and future sea-level rise . . . . .	3
1.2	Computational ice-sheet models and uncertainty quantification . . . . .	8
1.3	Uncertainty quantification: Methods, challenges, and opportunities . . . . .	9
1.4	Contributions of the thesis . . . . .	10
1.5	Overview of the thesis . . . . .	12
<b>2</b>	<b>Physics of ice sheets</b>	<b>15</b>
2.1	Physics of ice sheets: overview . . . . .	15
2.2	Full-order model . . . . .	17
2.2.1	Mechanical problem . . . . .	17
2.2.2	Thermal problem . . . . .	20
2.2.3	Closure of the system of equations . . . . .	20
2.2.4	Friction laws . . . . .	21
2.3	Reduced-order models . . . . .	23
2.3.1	Shallow-ice approximation . . . . .	26
2.3.2	Shallow-shelf approximation . . . . .	30
2.4	Glacial isostatic adjustment . . . . .	34
2.5	Instability mechanisms in marine ice sheets . . . . .	37
2.5.1	Marine ice-sheet instability . . . . .	37
2.5.2	Marine ice-cliff instability . . . . .	44
2.6	Chapter summary . . . . .	44
<b>3</b>	<b>The Antarctic ice sheet: Present, future, and challenges</b>	<b>47</b>
3.1	The Antarctic ice-sheet in a nutshell . . . . .	47
3.2	Mass balance of the Antarctic ice sheet . . . . .	49
3.3	The future of the Antarctic ice sheet under climate change . . . . .	50
3.3.1	Risk of MISI . . . . .	50
3.3.2	Risk of MICI . . . . .	51
3.3.3	Ice-air interactions . . . . .	52
3.3.4	Ice-ocean interactions . . . . .	52
3.3.5	Bedrock topography and glacial isostatic adjustment . . . . .	53

3.4	Computational ice-sheet models: limitations for sea-level rise projections . . .	54
3.4.1	Ice-sheet model initialisation . . . . .	54
3.4.2	Coupling with other components of the Earth system . . . . .	55
3.4.3	Uncertainties in computational ice-sheet models . . . . .	56
3.5	Conclusion . . . . .	58
<b>II Uncertainty Quantification: Theory and Methods</b>		<b>61</b>
<b>4</b>	<b>Uncertainty quantification methods for computational models</b>	<b>63</b>
4.1	Introduction . . . . .	63
4.2	Characterisation of uncertainties . . . . .	64
4.3	Propagation of uncertainties . . . . .	66
4.3.1	Monte Carlo sampling method . . . . .	67
4.3.2	Surrogate models . . . . .	71
4.3.3	Probabilistic learning on manifolds . . . . .	84
4.4	Global sensitivity analysis . . . . .	85
4.4.1	Pearson correlation coefficients . . . . .	87
4.4.2	Variance-based sensitivity indices . . . . .	87
4.4.3	Generalised sensitivity indices . . . . .	95
4.5	Numerical examples . . . . .	96
4.5.1	Propagation of uncertainties: Branin function . . . . .	96
4.5.2	Sensitivity analysis: Ishigami function . . . . .	101
4.6	Summary . . . . .	107
<b>5</b>	<b>A multifidelity quantile-based approach for confidence sets</b>	<b>109</b>
5.1	Context . . . . .	109
5.2	Literature review . . . . .	111
5.3	Notations . . . . .	112
5.4	Random excursion and contour sets . . . . .	113
5.4.1	Excursion and contour sets . . . . .	113
5.4.2	Capacity functional . . . . .	114
5.4.3	Containment and inclusion functionals . . . . .	114
5.4.4	Coverage function . . . . .	115
5.4.5	Vorob'ev quantiles . . . . .	115
5.5	Confidence sets for random excursion and contour sets . . . . .	116
5.5.1	Optimisation within a parametric family . . . . .	119
5.6	Spatial discretisation . . . . .	122
5.7	Discretisation of the stochastic dimension . . . . .	126
5.7.1	Membership function . . . . .	126
5.7.2	Quantile estimation: Monte Carlo method . . . . .	127
5.7.3	Quantile estimation: spectral method . . . . .	129
5.7.4	Quantile estimation: bifidelity method . . . . .	131
5.8	Numerical example . . . . .	134
5.8.1	Problem set-up . . . . .	134
5.8.2	Sources of uncertainties . . . . .	135

5.8.3	Membership function . . . . .	136
5.8.4	Random variable $\chi^h$ . . . . .	137
5.8.5	Quantile estimation . . . . .	138
5.8.6	Confidence sets . . . . .	141
5.8.7	Spatial discretisation . . . . .	142
5.9	Conclusion . . . . .	143
5.A	Asymptotic properties in Monte Carlo estimation of quantiles . . . . .	143
5.A.1	Monte Carlo quantile estimation based on the distribution function . . .	143
5.A.2	Monte Carlo quantile estimator based on the mid-distribution function .	144
5.B	Proof of Theorem 5.1 . . . . .	145
<b>6</b>	<b>Essential ice-sheet models as an efficient tool for large-scale and long-term simulations and uncertainty quantification</b>	<b>149</b>
6.1	High-fidelity vs essential ice-sheet models . . . . .	149
6.2	Thermomechanical ice-sheet model . . . . .	151
6.2.1	Grounded domain . . . . .	152
6.2.2	Floating domain . . . . .	153
6.3	Interactions with the Earth system . . . . .	156
6.3.1	Ice-air interface . . . . .	156
6.3.2	Ice-bedrock interface . . . . .	156
6.3.3	Ice-ocean interface . . . . .	158
6.3.4	Calving . . . . .	159
6.4	Model initialisation . . . . .	159
6.4.1	Initial conditions . . . . .	159
6.4.2	Input data . . . . .	159
6.4.3	Inversion of the basal sliding coefficient . . . . .	162
6.5	Numerical implementation . . . . .	162
6.5.1	Implementation of grounding-line flux parameterisation . . . . .	163
6.6	Chapter summary . . . . .	165
<b>7</b>	<b>Illustration and performance evaluation of uncertainty quantification methods on ice-sheet model problems</b>	<b>167</b>
7.1	Probabilistic projections of future sea-level rise . . . . .	167
7.1.1	Model problem . . . . .	167
7.1.2	Quantity of interest . . . . .	168
7.1.3	Sources of uncertainty . . . . .	169
7.1.4	Propagation of uncertainties: Monte Carlo method . . . . .	169
7.1.5	Propagation of uncertainties: Surrogate models . . . . .	170
7.1.6	Sea-level rise projections . . . . .	175
7.1.7	Propagation of uncertainty: Discussion . . . . .	176
7.2	Probabilistic assessment of grounded-ice retreat . . . . .	177
7.2.1	Quantity of interest . . . . .	177
7.2.2	Sources of uncertainty . . . . .	177
7.2.3	Membership function . . . . .	180
7.2.4	Quantile estimation: Monte Carlo method . . . . .	181
7.2.5	Quantile estimation: bifidelity method . . . . .	182

7.2.6	Confidence sets . . . . .	185
7.3	Computation of Sobol indices by probabilistic learning on manifolds . . . . .	187
7.3.1	Model problem . . . . .	187
7.3.2	Sources of uncertainty . . . . .	187
7.3.3	Quantity of interest . . . . .	187
7.3.4	Global sensitivity analysis: Monte Carlo method . . . . .	188
7.3.5	Global sensitivity analysis: Spectral method . . . . .	188
7.3.6	Global sensitivity analysis: PLoM method . . . . .	190
7.3.7	Global sensitivity analysis: Comparison of the numerical methods . . . . .	191
7.4	Chapter summary and conclusion . . . . .	192
<b>8</b>	<b>Uncertainty quantification of the multicentennial response of the Antarctic ice sheet to climate change</b>	<b>195</b>
8.1	Introduction . . . . .	196
8.2	Model description and methods . . . . .	198
8.2.1	Ice-sheet model and simulations . . . . .	198
8.2.2	Sources of uncertainty . . . . .	202
8.2.3	Uncertainty quantification methods . . . . .	206
8.3	Results . . . . .	209
8.3.1	Nominal projections . . . . .	209
8.3.2	Parameters-to-projections relationship . . . . .	211
8.3.3	Sea-level rise projections . . . . .	214
8.3.4	Stochastic sensitivity analysis . . . . .	220
8.3.5	Projections of grounded-ice retreat . . . . .	220
8.3.6	Influence of the parameter probability density function . . . . .	224
8.3.7	Projections under a more plastic sliding law . . . . .	224
8.3.8	TGL parameterisation . . . . .	225
8.4	Discussion . . . . .	226
8.4.1	Comparison of the sea-level rise projections with previous work . . . . .	226
8.4.2	Comparison of the impact of parametric uncertainty with previous work . . . . .	228
8.4.3	Comparison of projections of grounded-ice retreat with previous work . . . . .	228
8.4.4	Projections of ice loss and grounding-line retreat under parametric uncertainty . . . . .	228
8.4.5	Structural uncertainty and limitations . . . . .	229
8.5	Conclusion . . . . .	230
8.A	Polynomial chaos expansion . . . . .	231
8.B	Sobol sensitivity indices . . . . .	234
8.C	Confidence regions for grounded ice . . . . .	235
8.D	Supplementary figures . . . . .	236
<b>9</b>	<b>Multi-model comparison of sea-level rise projections</b>	<b>247</b>
9.1	Model description . . . . .	247
9.2	Multi-model comparison . . . . .	250
9.2.1	Short-term sea-level rise projections (2100) . . . . .	250
9.2.2	Medium-term sea-level rise projections (2300) . . . . .	254
9.2.3	Multi-model projections in the SROCC report . . . . .	257

9.3 Chapter summary . . . . .	259
<b>III Conclusion and directions for future work</b>	<b>273</b>
<b>10 Conclusion and perspectives</b>	<b>275</b>
10.1 Summary and general conclusions . . . . .	275
10.2 Directions for future research . . . . .	277
10.2.1 Directions in ice-sheet modelling . . . . .	277
10.2.2 Directions in uncertainty quantification . . . . .	278
<b>IV Appendices</b>	<b>281</b>
<b>A Elements of probability theory</b>	<b>283</b>
A.1 Probability space . . . . .	283
A.1.1 Conditional probability . . . . .	284
A.2 Random variable . . . . .	284
A.3 Random vector . . . . .	285
A.3.1 Gaussian random vector . . . . .	286
A.4 Random field . . . . .	286
A.4.1 Gaussian process . . . . .	287
<b>Bibliography</b>	<b>289</b>
<b>List of Symbols</b>	<b>325</b>



# Acronyms

<b>AIS</b>	Antarctic ice sheet
<b>CDW</b>	Circumpolar Deep Water
<b>EAIS</b>	East Antarctic ice sheet
<b>f.ETISh</b>	fast Elementary Thermomechanical Ice Sheet
<b>GMSL</b>	Global mean sea level
<b>HDMR</b>	High-dimensional model representation
<b>HSIC</b>	Hilbert-Schmidt independence criterion
<b>i.i.d.</b>	independent and identically distributed
<b>NISP</b>	Nonintrusive spectral projection
<b>OLS</b>	Ordinary Least-Squares
<b>PICO</b>	Postdam Ice-shelf Cavity mOdel
<b>RCP</b>	Representative Concentration Pathway
<b>RKHS</b>	Reproducing Kernel Hilbert Space
<b>PLoM</b>	Probabilistic Learning on Manifolds
<b>SIA</b>	Shallow-ice approximation
<b>SMB</b>	Surface mass balance
<b>SSA</b>	Shallow-shelf approximation
<b>UQ</b>	Uncertainty quantification
<b>WAIS</b>	West Antarctic ice sheet



## **Part I**

# **Modelling ice sheets in the presence of uncertainties**



# 1

## Introduction

*“Prediction is very difficult, especially if it’s about the future”*

– Niels Bohr

### 1.1 Research Context: Antarctic ice sheet and future sea-level rise

Coastal areas are home to approximately 28 % of the world’s population, with around 11 % (680 million people) living in so-called low-elevation coastal zones where land elevation is less than 10 metres above sea level (Figure 1.1). Low-elevation coastal zones include megacities, such as Tokyo (~14 million inhabitants), Mumbai (~12.5 million inhabitants), New York City (~8.4 million inhabitants), and Jakarta (~9.8 million inhabitants); heavily populated areas, such as the Bengal Delta, the Nile Delta, and Eastern China; and Small Island Developing States (~65 million inhabitants). Coastal population is expected to grow significantly during the 21st century to exceed one billion people in 2050 [Neumann et al., 2015; Merkens et al., 2016], with Asia expected to experience the highest absolute growth (238–303 million more inhabitants compared to 2000) and Africa to experience the highest relative growth rate (153 % to 218 % increase compared to 2000) [Merkens et al., 2016]. Simultaneously, coastal areas are expected to experience a significant urbanisation growth particularly in Egypt and sub-Saharan countries in Western and Eastern Africa. A study by Kulp and Strauss [2019] has recently highlighted that these estimates may even underestimate the global population at risk from coastal flooding due to biases in the elevation datasets, with the analysis by Kulp and Strauss [2019] suggesting that the global population at risk from coastal flooding might be three times greater than previously estimated. Besides their demographic significance, coastal areas also have an economic significance by providing opportunities for shipping, trade, ports, fisheries, tourism, food and water supply, energy, and exploitation of raw materials (for instance, sand and salt). Low-elevation coastal zones have been estimated to account for 14 % of the global domestic product [Kummu et al., 2016] and are also characterised by the presence of critical infrastructure such as nuclear power plants.

One of the key concerns regarding the future of coastal areas is their vulnerability to the risk of ocean and cryosphere changes (Figure 1.2) as a consequence of natural and anthropogenic

changes in the climate system. Negative impacts and risks for population and infrastructure [Wilby et al., 2011; Hallegatte et al., 2013] resulting from ocean and cryosphere changes include more severe and frequent extreme events associated with high tides, intense storms or marine heat waves; warmer, more acidic and less productive oceans; sea-level rise; flood and inundation risks; changing ocean ecosystems; and declining sea ice. Positive impacts include more opportunities in certain regions for transportation, shipping, tourism, and food supply. The current understanding of ocean and cryosphere changes and their impacts has been recently summarised in the *IPCC Special Report on the Ocean and Cryosphere in a Changing Climate (SROCC)* [IPCC, 2019], a reference to which we refer for a thorough overview on this topic.

In particular, sea-level rise induced by ocean and cryosphere changes and its impact on coastal areas are seen as prominent consequences of natural and anthropogenic changes in the climate system. Future global sea-level change is primarily controlled by thermal expansion of ocean water, mass loss in glaciers, including ice caps, mass loss in ice sheets in Greenland and Antarctica, and changes in land water storage due to groundwater depletion and reservoir impoundment. Thermal expansion of ocean water results from the decrease of the density of ocean water as oceans absorb heat and heat up. Models and observations have suggested that the oceans have absorbed more than 90 % of the increase in energy in the climate system in the last decades. Glaciers outside Greenland and Antarctica have a total volume of  $0.32 \pm 0.08$  m sea-level equivalent [Farinotti et al., 2019]. The mass balance of mountain glaciers is primarily determined by the mass balance between snow accumulation and surface melting. The global trend in glacier recession has been attributed primarily to an increase in surface air temperature. The Greenland and Antarctic ice sheets hold a volume of 7.2 m and 57.2 m of sea-level equivalent, respectively. The mass balance of the Greenland ice sheet is determined primarily by the mass balance between snow accumulation, sublimation, surface melt, and calving. The current observed mass loss in Greenland has been attributed primarily to an increase in surface melt attributed to atmospheric warming. On the other hand, the mass balance of the Antarctic ice sheet is determined primarily by the mass balance between snow accumulation and ice discharge across the grounding line, that is, the transition line between the grounded ice sheet and its floating ice shelves, with subsequent mass loss through sub-shelf melting and calving. The current observed mass loss in Antarctica has been dominated by increased mass loss from marine terminating glaciers in the Amundsen and Bellingshausen Sea sectors [Shepherd et al., 2018; Rignot et al., 2019] as a result of increased flow speeds, which have been attributed to increased sub-shelf melting due to ocean warming and strengthened sub-shelf circulation. Global sea level is also affected by withdrawal of freshwater and storage in reservoirs (mainly during the 20th century) and land water depletion due to domestic, agricultural, and industrial usage.

Human adaptation and mitigation measures to climate change, risk assessment and management, and (long-term) robust decision-making should all be crucially informed by projections of future sea-level rise, ideally in the form of probabilistic projections that provide an assessment of relevant uncertainties. Since the IPCC fifth assessment report (AR5) [Stocker et al., 2013], considerable progress has been made in the observation of sea-level changes and in the assessment of future sea-level changes based on expert assessment and computational models; see, for instance, Kopp et al. [2014, 2017], Le Bars et al. [2017], Bamber et al. [2019], Le Cozannet et al. [2019], IPCC [2019], and Jevrejeva et al. [2019]. In the SROCC report, the IPCC [2019] has concluded that there is limited evidence for major changes since AR5 [Church

et al., 2013] in the projections of the contribution of non-Antarctic components to sea-level rise in the 21st century (Table 1.1). The SROCC report also concluded that up to 2050, uncertainty in climate-change-driven future sea-level rise is relatively small, thus providing a robust basis for short term ( $\leq 30$  years) adaptation planning. Beyond 2050, uncertainty in climate-change-driven future sea-level rise increases substantially due to uncertainties in emission scenarios and associated climate change and the response of the Antarctic ice sheet.

	RCP 2.6	RCP 4.5	RCP 8.5
Thermal expansion	0.14 (0.10–0.18)	0.19 (0.14–0.23)	0.27 (0.21–0.33)
Glaciers	0.10 (0.04–0.16)	0.12 (0.06–0.18)	0.16 (0.09–0.23)
Greenland ice sheet	0.06 (0.04–0.10)	0.08 (0.04–0.13)	0.12 (0.07–0.21)
Land water storage	0.04 (–0.01–0.09)	0.04 (–0.01–0.09)	0.04 (–0.01–0.09)
Total	0.35 (0.23–0.48)	0.43 (0.30–0.57)	0.60 (0.43–0.78)
Antarctic ice sheet	0.05 (–0.03–0.14)	0.05 (–0.04–0.13)	0.04 (–0.06–0.12)

Table 1.1: Median values and “likely” ranges (17–83 % probability intervals) for projections of global mean sea-level rise (in metres) in 2081–2100 relative to 1986–2005 for three RCP scenarios as estimated in the AR5 report [Church et al., 2013]. Total is the total contribution due to thermal expansion, glaciers, the Greenland ice sheet, and land water storage. Estimated projections in the SROCC report [IPCC, 2019] are identical to projections in the AR5 report except for the contribution of the Antarctic ice sheet.

In the AR5 report, Church et al. [2013] provided a first assessment of the contribution of the Antarctic ice sheet to sea-level rise relying mainly on extrapolation of existing observations [Little et al., 2013] and a single limited simulation study [Bindshadler et al., 2013]. This first assessment suggested a limited contribution of the Antarctic ice sheet in the 21st century. In this assessment, the future mass balance of the Antarctic ice sheet is attributed to changes in surface mass balance, which result in a negative contribution to sea-level rise due to a widespread increase in snowfall caused by warmer air temperatures, and to poorly-understood dynamical changes, which result in a positive contribution to sea-level rise due to the inflow of ice into the ocean. The assessment by Church et al. [2013], however, pointed out the potential for the Antarctic ice sheet to contribute significantly to sea-level rise if the collapse of marine basins in Antarctica is initiated and also mentioned challenges in quantifying this contribution. Since AR5, understanding of the dynamics of the Antarctic ice sheet has progressed substantially, owing to new numerical simulations of the dynamic contribution of the Antarctic ice sheet to sea-level rise and new insights into ice-sheet instability mechanisms and processes controlling the thinning of ice shelves. New assessments of the contribution of the Antarctic ice sheet to sea-level rise now suggest that the contribution of the Antarctic ice sheet will be (far) more significant than previously assessed in AR5 and will become the primary contributor to sea-level rise over the next centuries and millennia. However, the evolution of the Antarctic ice sheet beyond the 21st century has also been recognised as a source of *deep uncertainty* [IPCC, 2019].

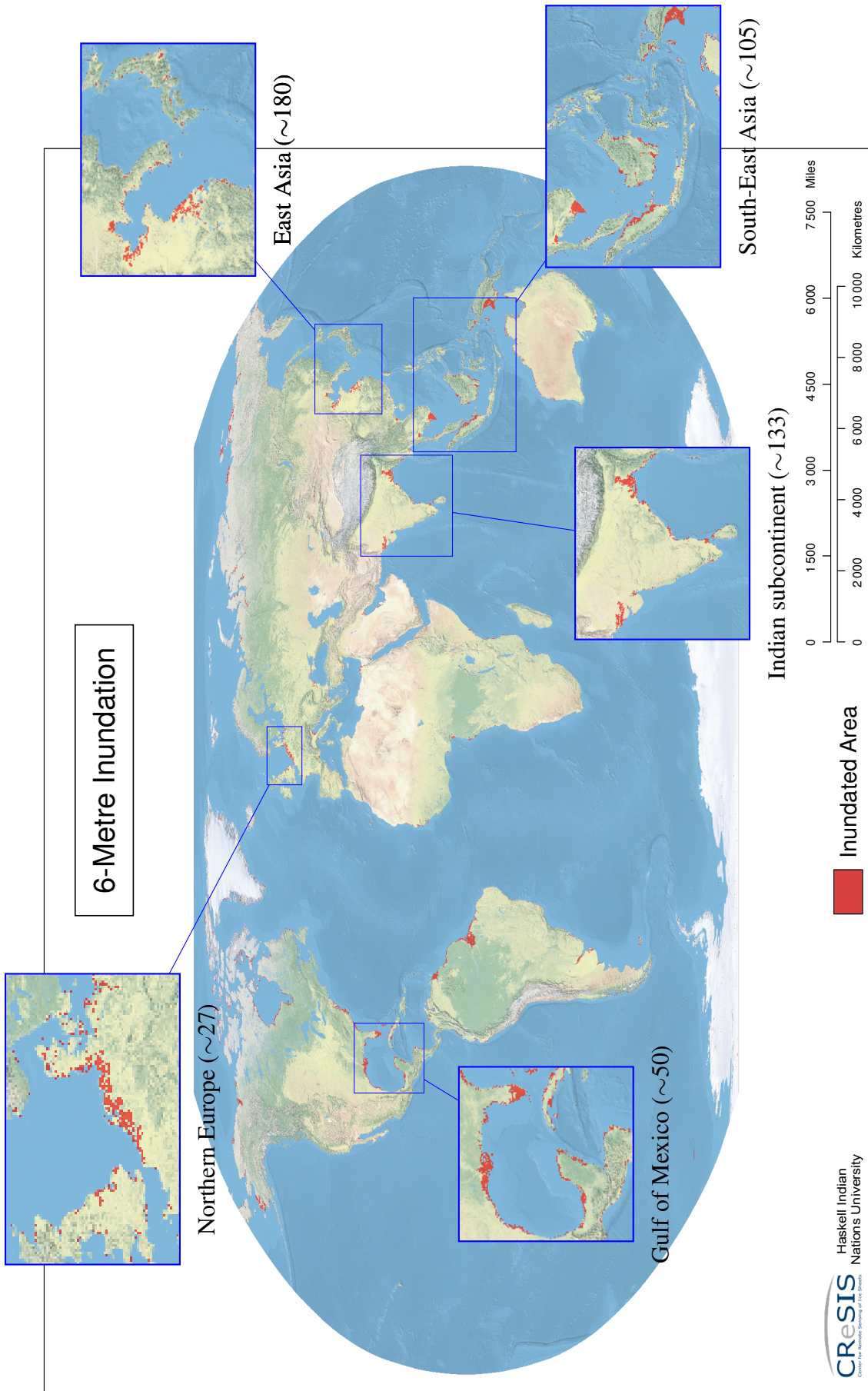


Figure 1.1: Global inundation map for a 6-metre sea-level increase (Credit: [CREsis \[2019\]](#)). Zoom on heavy-populated vulnerable regions: Northern Europe (UK, the Netherlands, Belgium, Germany, Denmark), Gulf of Mexico, Indian subcontinent (India, Pakistan, Sri Lanka, Bangladesh), East Asia (China, North Korea, South Korea, Japan), and South-East Asia (Vietnam, Cambodia, Thailand, Indonesia, Malaysia, the Philippines). In parentheses: Million inhabitants in the low-elevation coastal zone (below 10-metre elevation) in 2000 [[Adams et al., 2004](#); [Vafeidis et al., 2011](#); [Neumann et al., 2015](#)].

### Past and future changes in the ocean and cryosphere

Historical changes (observed and modelled) and projections under RCP2.6 and RCP8.5 for key indicators

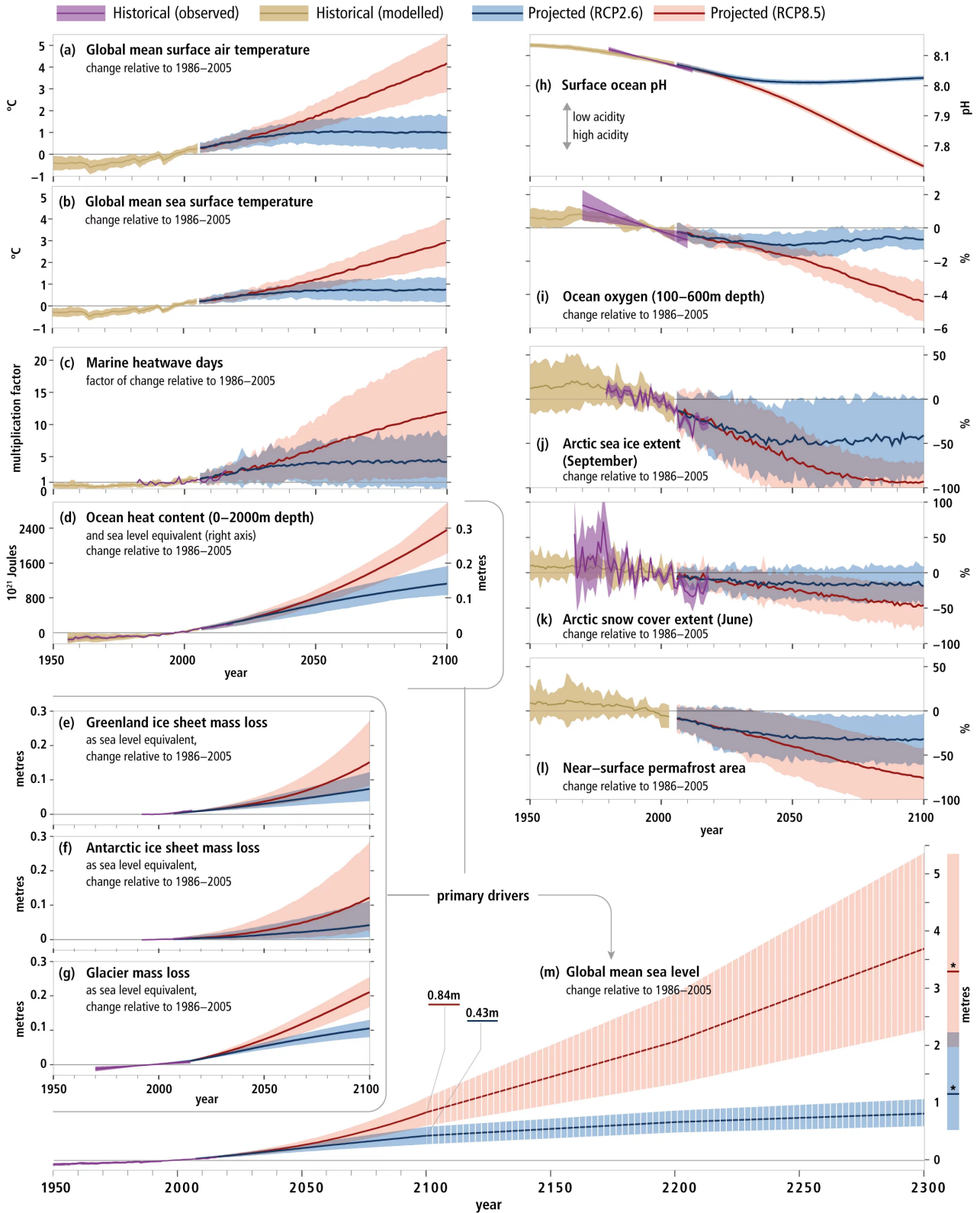


Figure 1.2: Observed and modelled historical changes in the ocean and the cryosphere since 1950 and projected future changes under the RCP 2.6 and RCP 8.5 emission scenarios. Credit: IPCC [2019].

## 1.2 Computational ice-sheet models and uncertainty quantification

Significant progress has been made since AR5 in the understanding and modelling of key processes governing the dynamics of the Antarctic ice sheet [Pattyn et al., 2017; Nowicki and Seroussi, 2018; Pattyn, 2018], including the migration of the grounding line, feedback and instability mechanisms [Schoof, 2007a; Pollard et al., 2015], interactions between the ice sheet and the solid Earth, model initialisation, and sub-shelf melting. Numerical improvements in modelling the dynamics of the Antarctic ice sheet have led to the development of a new generation of computational ice-sheet models that are amenable to continental simulations of the Antarctic ice sheet although for continental and (multi-)centennial simulations these models still continue to rely (heavily) on approximations and parameterisations of the ice-sheet thermodynamics and the interactions between the ice sheet and other components of the Earth system. Despite these limitations, this new generation of computational ice-sheet models has now reached a sufficient degree of maturity and accuracy to provide new sea-level rise projections and new insight into the response of the Antarctic ice sheet to climate change in contrast with the results in AR5; see, for instance, Levermann et al. [2014], Ritz et al. [2015], Golledge et al. [2015], DeConto and Pollard [2016], Schlegel et al. [2018], Bulthuis et al. [2019a], Golledge et al. [2019], and Levermann et al. [2019] for a list of papers published at the beginning and during this thesis.

As the vulnerability of the Antarctic ice sheet to environmental conditions and the sensitivity of computational ice-sheet models to model parameters have become more apparent, interest has grown simultaneously into predicting with quantified uncertainty the evolution of the Antarctic ice sheet in order to provide more robust predictions of sea-level rise. Although uncertainty in computational ice-sheet models had already been highlighted in AR5 as a major limitation for robust predictions of sea-level rise, only a rather limited number of studies had provided insight into the impact of uncertainty on the behaviour of the Antarctic ice sheet [Larour et al., 2012; Pattyn et al., 2013; Bindschadler et al., 2013; Nowicki et al., 2013; Durand and Pattyn, 2015]. At the time of the AR5 report, computational ice-sheet models lacked sufficient maturity and accuracy to lend themselves to being used for uncertainty quantification; by contrast, the new generation of computational ice-sheet models provides new opportunities to predict with quantified uncertainty and sufficient accuracy the evolution of the Antarctic ice sheet.

From the perspectives of large-scale and (multi-)centennial simulations of the response of the Antarctic ice sheet, the computational cost of (high-fidelity) computational ice-sheet models may still be too prohibitive to generate the required number of simulations necessary for uncertainty quantification. Recently, so-called essential ice-sheet models [Winkelmann et al., 2011; Pollard and DeConto, 2012a; Pattyn, 2017; Quiquet et al., 2018] have emerged as computationally efficient ice-sheet models for large-scale and long-term simulations and integration into Earth system models. Essential ice-sheet models, such as the fast Elementary Thermomechanical Ice Sheet (f.ETISh) model [Pattyn, 2017] used in this manuscript, achieve computational tractability by limiting their complexity to the essential interactions and feedback mechanisms of ice-sheet flow, including grounding-line migration, instability mechanisms, glacial isostatic adjustment, and ice-air and ice-ocean interactions. For this reason, essential ice-sheet models combined with methods from the field of uncertainty quantification provide useful opportunities for more comprehensive analyses of the impact of uncertainty in ice-sheet models and for expanding the range of uncertainty quantification methods employed in ice-sheet modelling.

### 1.3 Uncertainty quantification: Methods, challenges, and opportunities

The field of uncertainty quantification (UQ) has recently emerged as an interdisciplinary research area concerned with developing theory, methods, algorithms, and software for investigating the role played by uncertainty in predicting and understanding the behaviour and evolution of complex systems in science and engineering; see, for instance, [Arnst and Ponthot \[2014\]](#), [Smith \[2014\]](#), [Sullivan \[2015\]](#), [Ghanem et al. \[2017\]](#), and [Soize \[2017\]](#). Most of this theory and these methods are based on probability theory, in the context of which uncertain features are represented as random variables, random vectors, random fields, random sets, . . . Theory and methods have been developed or are under development to characterise the sources of uncertainty in a probabilistic framework (characterisation of uncertainty), to deduce the impact of sources of uncertainty on a quantity of interest (propagation of uncertainty), and to ascertain the impact of each source of uncertainty on the uncertainty in the quantity of interest (sensitivity analysis). Methods from uncertainty quantification have been used in various applications in science and engineering and are of interest to be applied to uncertainty quantification of computational ice-sheet models. Conversely, challenges and opportunities remain in developing and applying uncertainty quantification methods to complex physics-based models and for this reason uncertainty quantification in computational ice-sheet models can serve as a motivation to develop new theory and methods for uncertainty quantification. In the following, we discuss some existing UQ methods relevant to ice-sheet modelling and challenges and opportunities for uncertainty quantification motivated by ice-sheet modelling.

Within the probability theory, the characterisation of the uncertain input parameters of a computational model requires the characterisation of their probability distribution, which is typically deduced from available information and by using mathematical statistics methods. Given a probabilistic representation of the uncertain input parameters, a typical model problem in uncertainty quantification is concerned with the propagation and sensitivity analysis of a limited number (low-to-moderate stochastic dimension) of uncertain input parameters of a computational model with a scalar-valued quantity of interest. Within the field of uncertainty quantification, theory and methods are available to estimate various statistical descriptors and the probability distribution of the quantity of interest, for instance, methods based on Monte Carlo sampling and surrogate models. Theory and methods are also available for sensitivity analysis, including variance-based sensitivity indices and their estimation with Monte Carlo sampling or surrogate models. All these existing methods can be readily applied to the quantification of the impact of uncertain input parameters on a (scalar-valued) quantity of interest of a computational ice-sheet model, for instance, the global contribution of an ice sheet to sea-level rise.

Uncertainty quantification methods such as Monte Carlo sampling may lack sufficient accuracy in estimating statistical descriptors of the quantity of interest or sensitivity indices when only a limited number of evaluations of the computational model is available, which typically arises for computational models with a high computational cost, for instance, a computational ice-sheet model. For this reason, opportunities for uncertainty quantification lie in developing new efficient computational methods to improve the accuracy in such small-data settings, including methods based on efficient surrogate models and learning algorithms.

Within the context of ice-sheet modelling, interest is also directed towards projecting with quantified uncertainty the spatial retreat of an ice sheet in response to climate change. More generally, this question raises theoretical and methodological needs for uncertainty quantification of geometrical characteristics of the spatial and temporal response of physics-based computational models. Theoretical issues include the probabilistic characterisation of random excursion sets of (possibly nonstationary) random fields. Methodological issues include the computational cost of the computational model, its spatial discretisation, and the discretisation of the stochastic dimension.

Another limitation for robust projections in glaciology stems from fundamental modelling (structural) uncertainties in computational ice-sheet models. Structural uncertainties encompass discrepancies between computational ice-sheet models and the reality because of imperfect knowledge or representation of physical processes governing the ice-sheet dynamics, as well as numerical errors due to numerical approximations and discretisation errors. To address structural uncertainties in computational models, a typical approach in climate modelling consists in using ensembles of projections from a range of computational models rather than a single model, which leads to so-called multi-model ensembles of projections; see, for instance, [Burnham and Anderson \[2002\]](#) and [Link and Barker \[2006\]](#). Multi-model ensembles represent a challenge for uncertainty quantification, including the assessment of model discrepancies and weighting of multi-model projections.

Other challenges and opportunities for the field of uncertainty quantification relevant to ice-sheet modelling also include uncertainty quantification in large-scale, long-term, multi-scale, or multiphysics simulations; uncertainty quantification in the presence of large datasets that are insufficiently informative and in the presence of partial or missing data; and uncertainty quantification in high stochastic dimension. Challenges and opportunities also exist in clarifying the role of uncertainty in predicting and understanding the response of complex nonlinear dynamical systems, including in predicting and understanding the impact of sources of uncertainty on steady states, instabilities, and bifurcations.

## 1.4 Contributions of the thesis

The main contributions are twofold:

1. New assessment and new understanding of the impact of uncertainties on the multicentennial response of the Antarctic ice sheet.
2. New methods for uncertainty quantification of geometrical characteristics of the spatial response of physics-based computational models, with, as a motivation in glaciology, a focus on predicting with quantified uncertainty the retreat of the grounded region of the Antarctic ice sheet.

During this PhD, we worked first on the first contribution, which led us to identify limitations and further needs in uncertainty quantification, thus motivating the second contribution.

For the first contribution, we carried out uncertainty quantification of sea-level rise projections by using the new fast essential ice-sheet model f.ETISh [Pattyn, 2017]. Based on existing methods from the field of uncertainty quantification, we applied methods for the propagation of uncertainty and sensitivity analysis to provide new probabilistic projections of the contribution of the Antarctic ice sheet to sea-level rise over the next millenium and new assessments of the impact of parametric uncertainties on these projections. The main results and conclusions of this work are summarised in the publication [Bulthuis et al., 2019a].

For the second contribution, we proposed to address uncertainty quantification of geometrical characteristics of the spatial response of physics-based computational models within the probabilistic context of the random set theory, in which we contributed to the development of the concept of confidence sets of random excursion sets. We proposed a new multifidelity quantile-based method for the estimation of such confidence sets and we demonstrated the performance of the proposed method on an application concerned with uncertainty quantification of the retreat of the Antarctic ice sheet. The main results and conclusions of this work are summarised in the manuscript [Bulthuis et al., 2019b], currently under review.

In addition to the two aforementioned main contributions, we contributed during this thesis to two additional pieces of research also presented in this manuscript:

- In the context of uncertainty quantification in small-data settings, Professors Maarten Arnst and Christian Soize proposed to improve the accuracy of Monte Carlo estimates of Sobol indices in global sensitivity analysis using a recently introduced algorithm for probabilistic learning on manifolds (PLoM) [Soize and Ghanem, 2016]. As an illustration of the proposed methodology, we carried out simulations of the response of the Antarctic ice sheet using the f.ETISh model for a set of uncertain parameters. These simulations were then used to demonstrate the efficiency of the PLoM algorithm as compared with methods based on Monte Carlo sampling and stochastic expansions. The main results and conclusions of this work are summarised in the manuscript [Arnst et al., 2019], currently under review.
- With the Expert Group on Ice Sheet Mass Balance (ISMAL), Professor Frank Pattyn carried out a review of the mass balance and glaciers since AR5 [Hanna et al., 2020]. In the context of this review, we provided a multi-model comparison of projections of the contribution of the Antarctic ice sheet to sea-level rise from different models. Following this first multi-model comparison, we decided to carry out in this manuscript a more comprehensive multi-model comparison of projections of the contribution of the Antarctic ice sheet to sea-level rise, including projections by Bulthuis et al. [2019a], as a fairly simple way of assessing the impact of structural uncertainty in inducing uncertainty in sea-level rise projections. This new multi-model comparison is the subject of Chapter 9.

### List of contributed publications

In summary, the main contributions of this thesis are summarised in the following two first-author manuscripts:

- Bulthuis K., Arnst, M., Sun, S., and Pattyn, F. (2019). Uncertainty quantification of the multi-centennial response of the Antarctic ice sheet to climate change. *Cryosphere*, 13(4),1349–1380, <https://doi.org/10.5194/tc-13-1349-2019>.
  - 👁 In this thesis: The manuscript [[Bulthuis et al., 2019a](#)] is reported in its entirety in Chapter 8.
- Bulthuis K., Pattyn, F., and Arnst, M. A multifidelity quantile-based approach for confidence sets of random excursion sets with application to ice-sheet dynamics. Under review.
  - 👁 In this thesis: Sections 2–5 (theory and methods) and Section 6 (application) from [Bulthuis et al. \[2019b\]](#) are reported in Sections 5.4–5.7 and Section 7.2, respectively.

The additional contributions of this thesis are found in the following co-authored manuscripts:

- Hanna, E., Pattyn, F., Francisco Navarro, Vincent Favier, H. G., van den Broeke, M. R., Viczaino, M., Pippa L. Whitehouse, C. R., Bulthuis, K., and Smith, B. (2019). Mass balance of the ice sheets and glaciers – progress since AR5 and challenges. *Earth-Sci. Rev.* <https://doi.org/10.1016/j.earscirev.2019.102976>. In press.
  - 👁 In this thesis: Chapter 9 is built on Figure 5 and Table 1 from [Hanna et al. \[2020\]](#).
- Arnst M., Soize, C., and Bulthuis, K. Computation of Sobol indices in global sensitivity indices from small data sets by probabilistic learning on manifolds. Under review.
  - 👁 In this thesis: Section 5 (illustration) from [Arnst et al. \[2019\]](#) is reported in Section 7.3.

## 1.5 Overview of the thesis

Given its interdisciplinary nature, this thesis has been carried out at the Université de Liège, in the Stochastic and Computational Modelling group of Professor Maarten Arnst, and at the Université Libre de Bruxelles, in the Laboratory of Glaciology of Professor Frank Pattyn. Most chapters of this thesis are written to be “self-contained” so as to enable the reader more interested or less familiar with the field of uncertainty quantification or with cryospheric science to focus on specific chapters without requiring a thorough understanding of other chapters. We structured this manuscript in three consistent parts. It should be noted that the structure of the manuscript does not reflect the chronological order in which this PhD has been carried out. In Part I (Chapters 2–3), we provide a general introduction to ice-sheet modelling and uncertainties in ice-sheet models. In Part II (Chapters 4–5), we discuss and develop theory and methods for uncertainty quantification in computational models. In Part III (Chapters 6–9), we discuss the use of essential ice-sheet models for large-scale and long-term simulations of the Antarctic ice sheet and uncertainty quantification and we apply uncertainty quantification methods discussed in Part II to predict with quantified uncertainty the response of the Antarctic ice sheet to climate change over the next centuries. The detailed structure of this thesis is given below.

Chapter 2 presents a review of the physics of ice sheets from a modelling perspective. We introduce the governing equations for the conservation of mass, momentum, and energy in ice sheets and the equations for the interactions of the ice sheet with its surrounding environment,

namely the atmosphere, the bedrock, and the ocean. We discuss reduced-order models of the ice-sheet dynamics based on the asymptotic behaviour of the full-order model as the aspect ratio of the ice sheet tends to zero, which leads to the shallow-ice and shallow-shelf approximations. We also present other aspects of the physics of ice sheets, namely friction at the ice-bedrock interface, glacial isostatic adjustment, and instability mechanisms in marine ice sheets.

Chapter 3 presents an overview of the present state of the Antarctic ice sheet, its future evolution in a changing climate, and challenges in the numerical modelling of the dynamics of the Antarctic ice sheet. Present-day mass balance of the Antarctic ice sheet is determined by mass gain due to snowfall and mass loss due to ice discharge across the grounding line and subsequent mass loss through sub-shelf melting and calving. The future state of the Antarctic ice sheet will be governed by the risk of instabilities in marine basins, changes in ice-air and ice-ocean interactions, and the potential of the bedrock to provide (de)stabilising conditions for the grounding line. Challenges in the numerical modelling of the dynamics of the Antarctic ice sheet include ice-sheet model initialisation, coupling with other components of the Earth system, and uncertainties in computational ice-sheet models.

Chapter 4 is an introduction to theory and methods for the analysis of computational models subject to uncertain parameters within the field of uncertainty quantification. We discuss methods for the probabilistic characterisation of uncertainty in computational models, the propagation of uncertainty through the computational model to determine a probabilistic characterisation of a quantity of interest predicted by the computational model, and global sensitivity analysis to assess the significance of each source of uncertainty in inducing uncertainty in the quantity of interest. The focus is on nonintrusive methods that do not require any modification of the source code of the computational model.

Chapter 5 addresses uncertainty quantification of physics-based computational models when the quantity of interest concerns geometrical characteristics of their spatial response. Based on the random set theory, we develop the concept of confidence sets that either contain or are contained within an excursion set of the spatial response with a specified probability level. We seek an optimal confidence set in a parametric family of nested sets, a problem equivalent to a problem of quantile estimation of a random variable. We propose an efficient bifidelity method to speed up the computation of confidence sets for computational models with a high computational cost. Theory and methods are based on the manuscript [Bulthuis et al., 2019b].

Chapter 6 provides an introduction to the numerical modelling of the dynamics of the Antarctic ice-sheet based on essential ice-sheet models. With a focus on the fast Elementary Thermomechanical Ice Sheet (f.ETISh) model [Pattyn, 2017], we discuss aspects of the numerical modelling of ice sheets in essential ice-sheet models, including the implementation of reduced-order models for the ice-sheet flow, of a flux condition for the ice flux at the grounding line, of an ocean-model coupler for the ice-ocean interactions, and of an elastic lithosphere-relaxing asthenosphere model for isostatic glacial adjustment.

Chapter 7 addresses the use of theory and methods from the field of uncertainty quantification (Chapters 4–5) to assess the impact of uncertain parameters on the continental response of the Antarctic ice sheet over the next centuries. We demonstrate the interest of uncertainty

quantification methods, including methods for the propagation of uncertainty, the estimation of confidence sets of random excursion sets, and sensitivity analysis, by setting up with the f.ETISh ice-sheet model test problems concerned with the contribution of the Antarctic ice sheet to sea-level rise and the retreat of the grounded portion of the Antarctic ice sheet in response to climate change. The test problems for confidence sets of random excursion sets and sensitivity analysis are presented in the manuscripts [Arnst et al., 2019; Bulthuis et al., 2019b].

Chapter 8 addresses uncertainty quantification of the multicentennial response of the Antarctic ice sheet to climate change. We apply probabilistic methods to the f.ETISh ice-sheet model to investigate the influence of several sources of uncertainty, namely sources of uncertainty in atmospheric forcing, basal sliding, grounding-line flux parameterisation, calving, sub-shelf melting, ice-shelf rheology, and bedrock relaxation. We provide new probabilistic projections of sea-level rise and grounding-line retreat and we carry out a stochastic sensitivity analysis to determine the most influential sources of uncertainty. Chapter 8 is a standalone chapter taken from the publication Bulthuis et al. [2019a].

Chapter 9 provides a qualitative multi-model comparison of sea-level rise projections from studies published after the AR5 report, including new probabilistic projections carried out in this thesis. We provide a comparison with projections from the AR5 report and highlight new advances in the understanding and modelling of the dynamics of the Antarctic ice sheet.

Chapter 10 provides a summary and draws the main conclusions. Some directions for future research in ice-sheet modelling and uncertainty quantification are also addressed.

Appendix A provides an introduction to the theory of probability to the unfamiliar reader.

Finally, Table 1.2 provides a summary of the content of this manuscript. For each chapter, we add a mention “SoA” or “NEW” to specify whether the content is more related to a state-of-the-art review of methods and literature or to novel or original contributions. We also add a mention “P”, “N”, “M”, or “A” to specify whether the chapter provides a more physical, numerical, methodology-oriented, or application-oriented point of view to the objective of clarifying the role played by uncertainties in the response of the Antarctic ice sheet to climate change.

Keywords	Chapter	Content	Point of view
Physics of ice sheets / Reduced-order models	2	SoA	P
AIS / Mass balance / Instabilities	3	SoA	P/N
UQ / Propagation of uncertainty / Sensitivity analysis	4	SoA	M
Random excursion sets / Confidence sets	5	NEW	M
Numerical modelling / Essential ice-sheet models	6	SoA	N
UQ for ice-sheet models / Test problems	7	NEW	A
AIS / Changing climate / Probabilistic projections	8	NEW	A/P
Multi-model comparison / Sea-level rise projections	9	SoA/NEW	P

Table 1.2: Summary of the content of the thesis.

# 2

## Physics of ice sheets

*This chapter is an introduction to the physics of ice sheets, with a focus on physics-based reduced-order models and parameterisations relevant for large-scale and long-term numerical simulations of the Antarctic ice sheet. The dynamics of ice sheets is usually described as the flow of a nonlinear thermo-viscous fluid spreading under its own weight, subject to mass gain and loss due to snowfall and melting, and subject to basal friction on the ice-bedrock interface and water pressure on the ice-ocean interface. In Section 2.2, we first introduce a full-order model of the ice-sheet dynamics. In Section 2.3, we focus on reduced-order models of the ice-sheet dynamics based on the asymptotic behaviour of the full-order model as the aspect ratio of the ice sheet tends to zero. Such reduced-order models lend themselves well to being implemented into efficient large-scale computational models of the Antarctic ice sheet, such as the f.ETISh model (see Chapter 6), and to being used for uncertainty quantification (see Chapters 7–8). In Section 2.4, we present a reduced-order model for the interaction between an ice sheet and the solid Earth. In Section 2.5, we discuss two instability mechanisms in marine ice sheets, namely the marine ice-sheet instability (MISI) and the marine ice-cliff instability (MICI), which have the potential to destabilise and lead to a collapse of marine basins in Antarctica. We introduce an approximate analytical solution for the ice flux at the grounding line, which may serve as a parameterisation for the migration of the grounding line in large-scale computational ice-sheet models (see Chapter 6).*

### 2.1 Physics of ice sheets: overview

Ice sheets are defined as large masses of ice that cover an area greater than 50 000 km<sup>2</sup>. The current ice sheets on Earth are the Greenland and Antarctic ice sheets that cover 1.2% and 8.3% of the global land surface, respectively [Vaughan et al., 2013]. Both ice sheets contain approximately 98% of all freshwater on Earth, with the volume of the Greenland ice sheet and the Antarctic ice sheet equivalent to 7.2 m and 57.2 m sea-level equivalent, respectively.

On the timescales relevant in glaciology (tens to thousands of years), the overall dynamics of ice sheets is that of a gravity-driven viscous fluid flowing towards the coastline. The ice flow is also affected by the thermal state of the ice sheet as the ice softens and becomes less viscous at higher temperatures. As the ice flow approaches the coastline, it speeds up and collects into

(fast-flowing) ice streams. As the ice sheet flows down the coastline, the ice can become afloat and the ice sheet extends in the ocean into floating ice shelves (mainly in Antarctica). This typically arises for so-called marine ice sheets or marine-terminating glaciers whose bedrock is below sea level. The transition line where the ice becomes afloat is referred to as the grounding line. At the ice margins (usually at the edges of floating ice shelves), the ice sheet can lose mass through calving, that is, the breaking of ice chunks from the edge of a glacier.

Ice sheets and ice shelves interact with their surrounding environments, namely the atmosphere, the bedrock, and the ocean. Processes at the interface between the ice and the atmosphere include precipitation (snowfall and rainfall); surface melt and subsequent meltwater runoff, percolation, retention, or refreezing; evaporation and sublimation; and snow erosion. All these processes define the surface mass balance of the ice sheet; see, for instance, [Lenaerts et al. \[2019\]](#). All these processes also contribute to the surface energy balance of the ice sheet. The interaction of the ice and the underlying bedrock leads to friction and basal shear stress that resists ice flow. Processes such as geothermal heat flow, heat dissipation due to basal friction, and melting (or refreezing) also affect the energy balance of the ice sheet at the ice-bedrock interface. Processes at the interface between the ice and the ocean include melting (or refreezing) of the ice-shelf base in contact with the ocean and calving at the ice front; see, for instance, [Depoorter et al. \[2013\]](#), [Rignot et al. \[2013\]](#), and [Liu et al. \[2015\]](#). At large scale, melting underneath ice shelves is driven by heat supply in ice-shelf cavities due to ocean circulation. Processes such as melting (or refreezing) and heat transfer between the ocean and the base of the ice shelf also affect the energy balance of ice shelves at the ice-ocean interface.

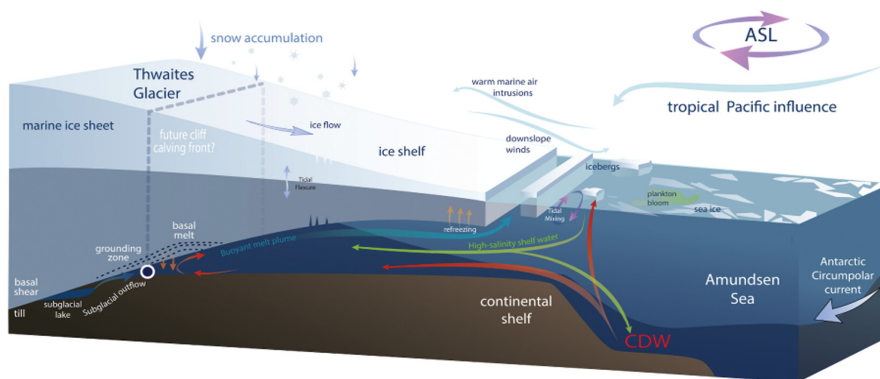


Figure 2.1: Illustration of key drivers of ice-sheet dynamics and their effects on Thwaites Glacier in Antarctica. Credit: [Scambos et al. \[2017\]](#).

In the following, we describe mathematical models for the underlying physics of ice sheets, focusing on fundamental ice-flow models and processes that will serve in the framework of this manuscript. We refer the reader to, for instance, [Cuffey and Paterson \[2010\]](#), [Greve and Blatter \[2009a\]](#), and [van der Veen \[2013\]](#) for textbooks about the physics of ice sheets and [Blatter et al. \[2011\]](#), [Fowler \[2011\]](#), and [Schoof and Hewitt \[2013\]](#) for review papers.

## 2.2 Full-order model

We are interested in the thermomechanical evolution of an ice sheet in a time interval  $]0, \tau[$  with  $\tau > 0$ . At any given time  $t$  in  $]0, \tau[$ , we denote by  $\Omega(t)$  the domain occupied by the ice. We assume that  $\Omega(t)$  is a subset of  $\mathbb{R}^d$ , with  $d = 2$  or  $3$ . We denote by  $\Gamma(t)$  the boundary of the domain  $\Omega(t)$  and we divide  $\Gamma(t)$  into several sections to represent the interfaces of the ice with other media (atmosphere, bedrock, and ocean). We consider in particular a geometrical configuration with  $\Gamma_s(t)$  being the ice-air interface,  $\Gamma_b(t)$  the ice-bedrock interface,  $\Gamma_w(t)$  the ice-ocean interface,  $\Gamma_c(t)$  the vertical calving front (or ice front) in contact with both the air and the ocean, and  $\Gamma_u(t)$  the vertical lateral border of the domain that is not the calving front (here, we assume  $\Gamma_u(t)$  to be an ice divide); see Figure 2.2. This geometrical configuration is representative of a marine ice sheet, that is, an ice sheet that lies on a bedrock below sea level and usually extends in the ocean into a floating ice shelf. Finally, the grounding line  $\gamma(t)$  is given by  $\bar{\Gamma}_b(t) \cap \bar{\Gamma}_w(t)$ .

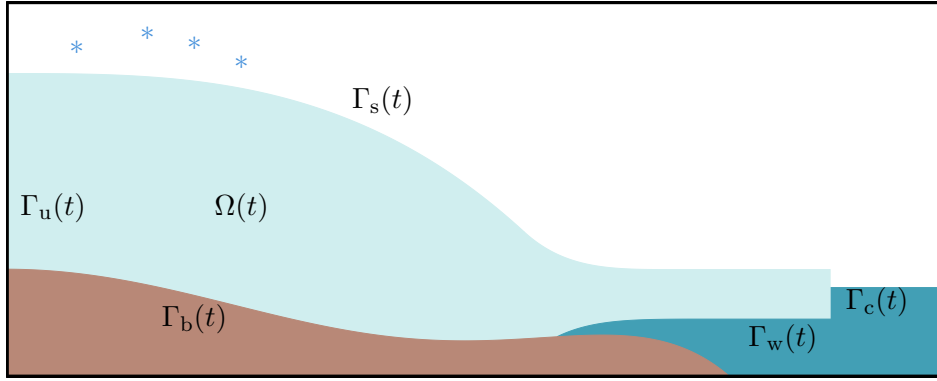


Figure 2.2: Schematic representation of a marine ice sheet (cross-section). At any time  $t$  in  $]0, \tau[$ ,  $\Omega(t)$  denotes the domain occupied by the ice,  $\Gamma_s(t)$  the ice-air interface,  $\Gamma_b(t)$  the ice-bedrock interface,  $\Gamma_w(t)$  the ice-ocean interface,  $\Gamma_c(t)$  the calving front, and  $\Gamma_u(t)$  the ice divide.

In the following, we introduce a system of equations that govern the evolution of the free boundaries  $\Gamma_s(t)$ ,  $\Gamma_b(t)$ ,  $\Gamma_w(t)$ ,  $\Gamma_c(t)$ , and  $\Gamma_u(t)$  and that of the velocity field  $\mathbf{v}$ , the pressure field  $p$ , and the temperature field  $T$ , which are defined in the space-time domain  $\Omega_\tau = \{(\mathbf{x}, t) : \mathbf{x} \in \Omega(t), 0 < t < \tau\}$ . We also refer the reader to [Greve and Blatter \[2009a\]](#) on which is based most of the following material.

### 2.2.1 Mechanical problem

The velocity field  $\mathbf{v}$  and the pressure field  $p$  are governed by the following nonlinear Stokes equations:

$$-\nabla_x p + \operatorname{div}_x(2\eta \mathbf{D}) + \rho \mathbf{g} = \mathbf{0}, \quad \text{in } \Omega(t) \text{ for } 0 < t < \tau, \quad (2.1)$$

$$\operatorname{div}_x \mathbf{v} = 0, \quad \text{in } \Omega(t) \text{ for } 0 < t < \tau. \quad (2.2)$$

Here,  $\mathbf{D} = \frac{1}{2}(\nabla_x \mathbf{v} + \nabla_x \mathbf{v}^T)$  is the strain-rate tensor,  $\eta$  the ice effective viscosity that depends nonlinearly on the temperature and the velocity,  $\rho$  the mass density of the ice, and  $\mathbf{g}$  the grav-

itational acceleration. In Equation (2.1), the stress tensor  $\sigma$  is decomposed into an isotropic stress tensor  $-p\mathbf{I}$ , with  $\mathbf{I}$  being the identity tensor and  $p = -\frac{1}{3}\text{tr}(\sigma)$ , and a deviatoric stress tensor  $\sigma^D = 2\eta\mathbf{D}$ . Equation (2.1) is the Stokes equation for low-Reynolds isotropic flows and expresses the mechanical balance between the pressure gradient, the divergence of the deviatoric stresses, and the gravitational driving force. Equation (2.2) is the incompressibility constraint. Equations (2.1) and (2.1) define a quasi-static model in which the pressure and velocity fields are solved at each time  $t$  on an evolving domain.

In large-scale ice-sheet models, the prevailing rheological law for the ice is Glen's flow law [Glen, 1955]. According to Glen's flow law, the constitutive relation for the ice writes as a power law between the second invariant of the strain-rate tensor and the effective viscosity, that is,

$$\eta = \frac{1}{2}A^{-1/n} \left( \frac{1}{\sqrt{2}}\|\mathbf{D}\|_{\text{F}} \right)^{\frac{1}{n}-1}. \quad (2.3)$$

Here,  $\frac{1}{\sqrt{2}}\|\mathbf{D}\|_{\text{F}}$ , in which  $\|\cdot\|_{\text{F}}$  denotes the Frobenius norm such that  $\|\mathbf{D}\|_{\text{F}}^2 = \text{tr}(\mathbf{D}^2)$ , is the effective strain rate (also denoted by  $d_e$ ),  $A$  the temperature-dependent rheological coefficient, and  $n$  the power-law exponent. The exponent in Equation (2.3) is set to  $n = 3$ , thus corresponding to a shear-thinning fluid whose viscosity decreases when shear increases. The temperature dependence of the rheological coefficient  $A$  is expressed in the form of an Arrhenius-type relationship [Greve and Blatter, 2009a; Cuffey and Paterson, 2010].

The Stokes equations (2.1)–(2.2) are supplemented with boundary conditions that express the interaction of the ice sheet with its surrounding environment at the different interfaces. At any given time  $t$  in  $]0, \tau[$  and any position  $\mathbf{x}$  on the interfaces, we denote by  $\mathbf{n}(\mathbf{x}, t)$  the exterior normal unit vector of the interface pointing outwards of the ice domain and by  $\mathbf{w}(\mathbf{x}, t)$  the rate of change of the position of the interface (“the interface velocity”).

On the ice-air interface, the boundary conditions write as

$$\sigma(\mathbf{n}) = \mathbf{0}, \quad \text{on } \Gamma_s(t) \text{ for } 0 < t < \tau, \quad (2.4)$$

$$(\mathbf{w} - \mathbf{v}) \cdot \mathbf{n} = a_s^\perp, \quad \text{on } \Gamma_s(t) \text{ for } 0 < t < \tau, \quad (2.5)$$

where  $a_s^\perp$  is the surface mass balance perpendicular to the ice-air interface, positive in the case of accumulation and surface refreezing and negative in the case of surface melting and ablation. Here, we use the notation  $\sigma(\mathbf{n})$  to denote the stress vector, also called the traction vector, acting on the interface with exterior unit normal vector  $\mathbf{n}$ . Equation (2.4) expresses mechanical equilibrium at the ice-air interface when this interface is considered to be a free surface (no surface tension and negligible air pressure) and Equation (2.5) expresses mass balance at the ice-air interface.

On the ice-bedrock interface, the boundary conditions write as

$$\boldsymbol{\tau}_b = -f_b(\|\mathbf{v}_b\|, p_e, \mathbf{x})\mathbf{v}_b, \quad \text{on } \Gamma_b(t) \text{ for } 0 < t < \tau, \quad (2.6)$$

$$(\mathbf{w} - \mathbf{v}) \cdot \mathbf{n} = -a_b^\perp, \quad \text{on } \Gamma_b(t) \text{ for } 0 < t < \tau, \quad (2.7)$$

where  $\tau_b$  is the component of the traction vector tangential to the ice-bedrock interface,  $v_b$  the component of the velocity field tangential to the ice-bedrock interface, and  $a_b^\perp$  the mass balance perpendicular to the ice-bedrock interface, taken positive to account for mass loss due to ice melting. Equation (2.6) is a Robin-type boundary condition, expressed as a slip boundary condition, that relates the tangential component of the velocity field to the tangential component of the traction vector and the positive function  $f_b$  is the so-called friction law function that is assumed to depend on the norm of the tangential component of the velocity field, the position  $\boldsymbol{x}$  on the interface, and the effective pressure  $p_e$ , that is, the difference between the normal stress at  $\Gamma_b$  and the water pressure in the subglacial layer underneath  $\Gamma_b$ . We refer the reader to Section 2.2.4 for examples of friction laws commonly used in glaciology. Equation (2.7) expresses mass balance at the ice-bedrock interface.

On the ice-ocean interface, the boundary conditions write as

$$\sigma(\boldsymbol{n}) = -p_w \boldsymbol{n}, \quad \text{on } \Gamma_w(t) \text{ for } 0 < t < \tau, \quad (2.8)$$

$$(\boldsymbol{w} - \boldsymbol{v}) \cdot \boldsymbol{n} = -a_w^\perp, \quad \text{on } \Gamma_w(t) \text{ for } 0 < t < \tau, \quad (2.9)$$

where  $a_w^\perp$  is the mass balance perpendicular to the ice-ocean interface, positive in case of melting underneath ice shelves and negative in case of refreezing, and  $p_w$  is the water pressure. Equation (2.8) expresses mechanical equilibrium at the ice-ocean interface and Equation (2.9) expresses mass balance at the ice-ocean interface.

At the calving front, the boundary conditions write as

$$\sigma(\boldsymbol{n}) = -f_w \boldsymbol{n}, \quad \text{on } \Gamma_c(t) \text{ for } 0 < t < \tau, \quad (2.10)$$

$$(\boldsymbol{w} - \boldsymbol{v}) \cdot \boldsymbol{n} = -c_f^\perp, \quad \text{on } \Gamma_c(t) \text{ for } 0 < t < \tau, \quad (2.11)$$

where  $f_w = p_w$  if the ice is in contact with the ocean and  $f_w = 0$  if the ice is in contact with the air and  $c_f^\perp$  is the calving rate perpendicular to the calving front, positive in case of ice loss by calving.

At the ice divide, the boundary conditions write as

$$\boldsymbol{v} = \mathbf{0}, \quad \text{on } \Gamma_u(t) \text{ for } 0 < t < \tau, \quad (2.12)$$

$$\boldsymbol{w} \cdot \boldsymbol{n} = 0, \quad \text{on } \Gamma_u(t) \text{ for } 0 < t < \tau. \quad (2.13)$$

Equation (2.12) expresses zero velocity at the ice divide and Equation (2.13) expresses that the ice divide is a fixed boundary in the direction of  $\boldsymbol{n}$ .

Finally, a mathematical model must be prescribed for the response of the ice-bedrock interface as a consequence of glacial isostatic adjustment (GIA). We write such a mathematical model in the following abstract form

$$\boldsymbol{w} \cdot \boldsymbol{n} = f^{\text{GIA}}(\{p_{\text{load}}(s), s \leq t\}), \quad \text{on } \Gamma_b(t) \text{ for } 0 < t < \tau, \quad (2.14)$$

where  $p_{\text{load}}$  is the net load exerted on the bedrock, including the ice-sheet loading. Thus, the GIA model in Equation (2.14) provides the normal component of the rate of change of the position of the ice-bedrock interface as a function of the past loading history, including the ice-sheet loading history. We refer the reader to Section 2.4 for an example of such a GIA model.

### 2.2.2 Thermal problem

The temperature field  $T$  is required to satisfy the following conservation-of-energy equation:

$$\rho c \left( \frac{\partial T}{\partial t} + \mathbf{v} \cdot \nabla_x T \right) = \operatorname{div}_x (k \nabla_x T) + 4\eta \|\mathbf{D}\|_{\mathbb{F}}^2, \quad \text{in } \Omega(t) \text{ for } 0 < t < \tau. \quad (2.15)$$

Here,  $c$  and  $k$  are the specific heat capacity and the thermal conductivity of the ice, respectively. Equation (2.15) expresses the energy balance between the rate of change of the internal energy, the advective internal-energy flux, the conduction of heat, and the rate of viscous dissipation.

On the ice-air interface, the boundary condition writes as

$$T = T_s, \quad \text{on } \Gamma_s(t) \text{ for } 0 < t < \tau, \quad (2.16)$$

where  $T_s$  is the surface air temperature.

On the ice-bedrock interface, the boundary condition writes as

$$k \nabla_x T \cdot \mathbf{n} = q_{\text{geo}}^\perp - \boldsymbol{\tau}_b \cdot \mathbf{v}_b - \rho L a_b^\perp, \quad \text{on } \Gamma_b(t) \text{ for } 0 < t < \tau, \quad (2.17)$$

where  $q_{\text{geo}}^\perp$  is the geothermal heat flux perpendicular to the ice-bedrock interface and  $L$  is the specific latent heat of fusion. Equation (2.17) expresses the heat flux at the ice-bedrock interface as a balance between the geothermal heat flux perpendicular to the ice-bedrock interface, the rate of heat production due to basal friction at the ice-bedrock interface, and the rate of heat absorption due to ice melting.

On the ice-ocean interface, the boundary condition writes as

$$T = T_w, \quad \text{on } \Gamma_w(t) \text{ for } 0 < t < \tau, \quad (2.18)$$

where  $T_w$  is the ocean temperature.

At the calving front, we impose the no-flux boundary condition

$$\nabla_x T \cdot \mathbf{n} = 0, \quad \text{on } \Gamma_c(t) \text{ for } 0 < t < \tau. \quad (2.19)$$

At the ice divide, we impose the no-flux boundary condition

$$\nabla_x T \cdot \mathbf{n} = 0, \quad \text{on } \Gamma_u(t) \text{ for } 0 < t < \tau. \quad (2.20)$$

### 2.2.3 Closure of the system of equations

The full-order model provides a system of equations for the pressure field  $p$ , the velocity field  $\mathbf{v}$ , the temperature field  $T$ , and the evolution of the free boundaries  $\Gamma_s$ ,  $\Gamma_b$ ,  $\Gamma_w$ ,  $\Gamma_c$ , and  $\Gamma_u$ . In addition to the prescription of appropriate initial conditions, this system of equations must be closed by providing closure equations for the additional unknowns, which we discuss briefly in the following. The boundary condition (2.6) is closed by prescribing a model for the friction law; see Section 2.2.4 for a discussion. The mass balance  $a_s$  and the temperature  $T_s$  at the ice-air interface are prescribed, for instance, by coupling the ice-sheet model with an atmospheric

circulation model. Similarly, the mass balance  $a_w$  and the temperature  $T_w$  at the ice-ocean interface are prescribed, for instance, by coupling the ice-sheet model with an ocean circulation model that accounts for ocean circulation and heat transfer beneath ice shelves. Approaches to determine the calving rate  $c_f$  include damage and fracture mechanics, which is able to simulate the development of crevasses in the ice and their propagation; see, for instance, [Krug et al. \[2014\]](#) and [Sun et al. \[2017\]](#). A mathematical model must also be prescribed for the response of the ice-bedrock interface; see Section 2.4 for a discussion.

The mechanical problem in Section 2.2.1 must be supplemented with a mathematical model for the position/evolution of the grounding line. Formally, this problem can be addressed as a frictional contact problem in which one seeks to distinguish between a contact zone and a non-contact zone. For a marine ice sheet, the contact zone is the region where the ice is in contact with the bedrock and is subject to basal friction (the grounded region), while the non-contact zone is the region where the ice is not in contact with the bedrock and is subject to water pressure (the floating region). Hence, the (moving) grounding line is associated with the (moving) contact line. A Stokes-flow contact problem for the dynamics of marine ice sheets is studied theoretically in [Schoof \[2011\]](#) and solved numerically in [Durand et al. \[2009\]](#) and [Gagliardini et al. \[2013\]](#). More generally, mathematical models and numerical methods for the movement of the grounding line can be built on theory and methods from applied mathematics and computational mechanics, including variational inequalities, saddle-point problems, and mortar methods; see, for instance, [Kikuchi and Oden \[1988\]](#), [Wriggers \[2006\]](#), [Wohlmuth \[2011\]](#), [Popp \[2012\]](#), and [Capatina \[2014\]](#).

Finally and contrary to the mass balances at the ice-air and ice-ocean interfaces, the mass balance  $a_b$  at the ice-bedrock interface must be determined as part of the solution to the thermal problem in Section 2.2.2. Physically,  $a_b$  corresponds to the basal melting rate and is constrained to be either equal to zero (no melting) or strictly positive (melting). In addition, the basal temperature of the ice is constrained to be equal to or below its pressure melting point. By definition, the basal melting rate can only be different from zero when the ice temperature reaches its pressure melting point. Mathematically, these conditions on the basal temperature and the basal melting rate can be interpreted as the Signori conditions in elastic contact mechanics [[Glowinski et al., 1981](#); [Kikuchi and Oden, 1988](#)] or the Karush-Kuhn-Tucker conditions in optimisation [[Nocedal and Wright, 2006](#)], and thus theory and methods from contact mechanics and optimisation can be used to solve these conditions. We also refer the reader to [Calvo et al. \[2003, 2015\]](#) and [Seroussi \[2012\]](#) for examples of the use of Signorini conditions in glaciology.

## 2.2.4 Friction laws

A friction law in large-scale ice-sheet models usually takes the form

$$\boldsymbol{\tau}_b = -f_b(\|\boldsymbol{v}_b\|, p_e, \boldsymbol{x})\boldsymbol{v}_b, \quad (2.21)$$

where  $\boldsymbol{\tau}_b$  is the component of the traction vector tangential to the ice-bedrock interface, also referred to as the basal stress or the basal traction,  $\boldsymbol{v}_b$  the component of the velocity field tangential to the ice-bedrock interface, also referred to as the basal velocity or sliding velocity, and  $f_b$  the friction law function that is assumed to depend on the basal velocity  $\boldsymbol{v}_b$ , the effective

pressure  $p_e$ , and the position  $\mathbf{x}$  on the interface. Using the same notations as before,  $\tau_b$  and  $\mathbf{v}_b$  can be written as  $\sigma(\mathbf{n}) - (\sigma(\mathbf{n}) \cdot \mathbf{n})\mathbf{n}$  and  $\mathbf{v} - (\mathbf{v} \cdot \mathbf{n})\mathbf{n}$ , respectively. The function  $f_b$  is assumed to be a positive function to indicate that basal friction and basal velocity are always antiparallel and thus basal friction always opposes ice flow. More generally, the function  $f_b$  can be multi-valued to encompass friction laws such as the Coulomb friction law. When Equation (2.21) can be inverted to yield  $\mathbf{v}_b$  as a function of  $\tau_b$ , the resulting equation is often referred to as a sliding law. The choice of the “best” friction law remains an active source of discussion in glaciology. Here, we briefly discuss some common friction laws used in ice-sheet models and we refer the reader to, for instance, [Weertman \[1957\]](#), [Greve and Blatter \[2009a\]](#), [Schoof \[2010\]](#), [Brondex et al. \[2017\]](#), and [Joughin et al. \[2019\]](#) for further discussions about friction laws in ice-sheet models. Please note that other examples of friction laws can be found in the field of computational mechanics for frictional contact problems, including nonlocal friction laws [[Oden and Pires, 1983](#); [Kikuchi and Oden, 1988](#); [Capatina, 2014](#)].

The Coulomb friction law writes as

$$\begin{cases} f_b(\|\mathbf{v}_b\|, p_e, \mathbf{x}) = \frac{\tau_c(p_e, \mathbf{x})}{\|\mathbf{v}_b\|} & \text{if } \|\mathbf{v}_b\| > \mathbf{0} \\ f_b(\|\mathbf{v}_b\|, p_e, \mathbf{x}) \leq \tau_c(p_e, \mathbf{x}) & \text{if } \mathbf{v}_b = \mathbf{0} \end{cases}, \quad (2.22)$$

where  $\tau_c$  is the yield stress. The Coulomb friction law is used to describe sliding over deforming subglacial material such as sand, gravel, or till [[Tulaczyk et al., 2000a,b](#); [Schoof, 2006](#)]. The yield stress represents the maximum stress that a plastic subglacial layer can sustain before deforming plastically and is usually expressed as a linear function of the till cohesion (often assumed to be negligible in ice-sheet models) and the effective pressure based on Mohr–Coulomb theory. The effective pressure on the till depends on the subglacial hydrology. A common assumption is to consider the till to be cohesionless and hydrostatically connected to the ocean, thus leading to the water pressure in the subglacial layer being equal to the hydrostatic water pressure in the ocean. Examples of more sophisticated subglacial hydrology models can be found in [Le Brocq et al. \[2009\]](#), [Werder et al. \[2013\]](#), [Bueler and van Pelt \[2015\]](#), and [De Fleurian et al. \[2018\]](#).

A drawback of the Coulomb friction law is the fact that the relationship between the basal stress and the basal velocity is multivalued at the origin. To avoid computational difficulties associated with the Coulomb friction law, alternatives have been proposed in computational mechanics in the form of regularised Coulomb friction laws that are more suitable for computational purposes; see, for instance, [Campos et al. \[1982\]](#), [Martins and Oden \[1983\]](#), [Kikuchi and Oden \[1988\]](#), and [Lee and Oden \[1993\]](#). In the context of glaciology, [Schoof \[2010\]](#) has proposed regularised Coulomb friction laws in the form

$$f_b(\|\mathbf{v}_b\|, p_e, \mathbf{x}) = f_{b,\text{reg}}(\|\mathbf{v}_b\|, \mathbf{x}) \frac{\tau_c(p_e, \mathbf{x})}{\|\mathbf{v}_b\|}, \quad (2.23)$$

where  $f_{b,\text{reg}} : [0, \infty[ \times \Gamma_b \mapsto [0, \infty[$  is a continuous, non-decreasing function in its first argument with  $f_{b,\text{reg}}(0, \mathbf{x}) = 0$  and  $\lim_{u \rightarrow \infty} f_{b,\text{reg}}(u, \mathbf{x}) = 1$  for  $\mathbf{x}$  on  $\Gamma_b(t)$ . Regularised Coulomb friction laws behave like the Coulomb friction law at high velocities while being single-valued

at low velocities. A particular example of  $f_{b,\text{reg}}$  is given by

$$f_{b,\text{reg}}(\|\mathbf{v}_b\|, \mathbf{x}) = \left( \frac{\|\mathbf{v}_b\|}{\|\mathbf{v}_b\| + \Lambda(\mathbf{x})} \right)^{p-1}, \quad (2.24)$$

where  $p > 1$  is a sliding parameter and  $\Lambda(\mathbf{x}) > 0$  is determined by local properties of the bedrock. Equation (2.24) was originally proposed by Schoof [2005] for glacier sliding on hard bedrock while accounting for the effect of cavitation, that is, the formation of pressurised basal water pockets as the ice slides over the bedrock; since then, Equation (2.24), has been also applied as a regularised Coulomb friction law for sliding over weak till or both hard bedrock and weak till [Schoof, 2010; Joughin et al., 2019]. Other examples for  $f_{b,\text{reg}}$  are given, for instance, in Schoof [2010].

Another common example of friction law in glaciology is the power friction law or Weertman's friction law:

$$f_b(\|\mathbf{v}_b\|, \mathbf{x}) = c_b(\mathbf{x})\|\mathbf{v}_b\|^{p-1}, \quad (2.25)$$

where  $c_b$  is the basal friction coefficient and  $p > 0$  is the friction exponent, also written as  $p = 1/m$ , with  $m$  the sliding exponent. Weertman's friction law was originally developed to describe sliding over hard bedrock [Weertman, 1957]. Weertman's friction law may also be interpreted as a regularisation of the Coulomb friction law because Weertman's friction law tends to the Coulomb friction law as  $m$  approaches infinity. Thus, the sliding exponent  $m$  can be chosen in order to account in some way for till deformation. A drawback of Weertman's friction law is the fact that it does not account for the effective pressure on the till. As an alternative, extensions to Weertman's friction law can be considered in the form of so-called Budd's friction laws [Budd et al., 1984]

$$f_b(\|\mathbf{v}_b\|, p_e, \mathbf{x}) = c_b(\mathbf{x})p_e^q\|\mathbf{v}_b\|^{p-1}, \quad (2.26)$$

where  $q \geq 0$ . Taking  $q = 0$  leads to Weertman's friction law.

Figure 2.3 shows a comparison between different sliding laws, namely the Coulomb friction law, the regularised Coulomb friction law with Equation (2.24), and Weertman's friction law. In the case of the Coulomb friction law, the basal stress is equal to the yield stress whenever the basal velocity is different from zero. Weertman's friction law provides no upper limit on the basal stress for finite  $m$  but approaches the Coulomb friction law as  $m$  approaches infinity. For the regularised Coulomb friction law, the basal stress increases with increasing basal velocity but the maximum basal stress is limited by the yield stress. The sliding parameter  $p$  controls the slope of  $\|\tau_b\|$  at the origin and thus the "level" of regularisation.

## 2.3 Reduced-order models

Computational ice-sheet models based on the full-order model in Section 2.2 still have a prohibitive computational cost for large-scale and long-term projections and uncertainty quantification. As an alternative, reduced-order models of this full-order model have been derived that take advantage of the small aspect ratio of ice sheets, thus leading to the approximation of the ice-sheet flow as a thin-film flow. Examples of such reduced-order models of ice-sheet flow are

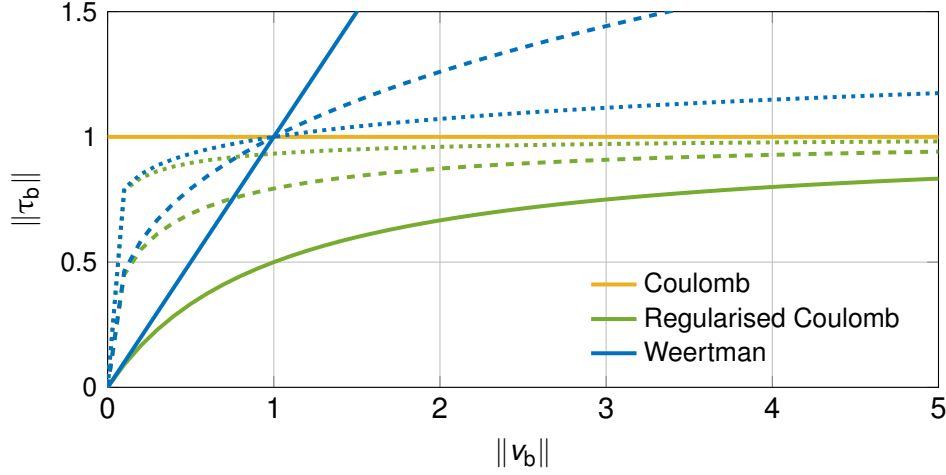


Figure 2.3: Illustration of different sliding laws with no dependence on  $x$  and  $p_e$ . Shown are the Coulomb friction law with  $\tau_c = 1$ ; the regularised Coulomb friction law with  $\tau_c = 1$  and regularisation function given by Equation (2.24) with  $\Lambda = 1$  and sliding parameter  $p = 2$  (solid),  $p = 3/2$  (dashed), and  $p = 11/10$  (dotted); and Weertman’s sliding law with  $c_b = 1$  and sliding exponent  $m = 1$  (solid),  $m = 3$  (dashed), and  $m = 10$  (dotted). Values are in 0.1 MPa for  $\|\tau_b\|$  and in  $\text{m yr}^{-1}$  for  $\|v_b\|$ .

the hydrostatic approximation, the Blatter–Pattyn model, the shallow-ice approximation (SIA), and the shallow-shelf approximation (SSA) [Greve and Blatter, 2009a; Kirchner et al., 2011]. We focus on the last two approximations in the following.

The SIA and SSA reduced-order models can be derived from the asymptotic behaviour of the full-order model as the aspect ratio tends to zero in two different mechanical regimes distinguished by the significance of membrane and vertical shear stresses. In a 3D Cartesian coordinate system with horizontal  $x$ - and  $y$ -axes and vertical  $z$ -axis, the vertical shear stresses refer to the components  $\sigma_{xz}^D$  and  $\sigma_{yz}^D$  of the deviatoric stress tensor and the membrane stresses refer to the components  $\sigma_{xx}^D$ ,  $\sigma_{yy}^D$ , and  $\sigma_{xy}^D$  of the deviatoric stress tensor, with  $\sigma_{xx}^D$  and  $\sigma_{yy}^D$  being also referred to as the longitudinal or extensional stresses and  $\sigma_{xy}^D$  to as the lateral shear stress. In their original derivations, the SIA [Hutter, 1983; Greve and Blatter, 2009a] and SSA [Morland, 1987; MacAyeal, 1989; Weis et al., 1999] reduced-order models are derived from a hydrostatic approximation of the Stokes equations and by neglecting either the membrane stresses or the vertical shear stresses in the conservation-of-momentum equation. Here, we discuss some aspects of the SIA and SSA reduced-order models following the formalism in Gerbeau and Perthame [2001], Fernández-Nieto et al. [2010], and Boutounet et al. [2016] for the asymptotic behaviour of non-Newtonian fluids with small aspect ratio.

Following the formalism in Gerbeau and Perthame [2001], Fernández-Nieto et al. [2010], and Boutounet et al. [2016], the dimensionless form of the nonlinear Stokes equations leads to the identification of three dimensionless numbers, namely an aspect ratio  $\epsilon = H/L$ , which represents the shallowness of the ice sheet, a Reynolds number  $R_e$ , and a Froude number  $F_r$

given by

$$R_e = \frac{\rho U^{2-\frac{1}{n}} H^{\frac{1}{n}} 2^{\frac{1}{n}-1}}{\eta_0}, \quad F_r = \frac{U}{\sqrt{gH}}, \quad (2.27)$$

where  $U$  is a reference horizontal velocity,  $H$  a reference thickness,  $L$  a reference horizontal length, and  $\eta_0(U/(2H))^{\frac{1}{n}-1}$  a reference effective viscosity consistent with the reference strain rate. As an example, we consider the vertical conservation-of-momentum equation in  $\mathbb{R}^2$  for an isothermal ice sheet, that is,

$$\frac{\partial p}{\partial z} = \frac{\partial}{\partial x}(\sigma_{xz}^D) + \frac{\partial}{\partial z}(\sigma_{zz}^D) - \rho g, \quad (2.28)$$

with  $x$  the horizontal coordinate,  $z$  the vertical coordinate, and  $\sigma^D$  the deviatoric stress tensor expressed as

$$\begin{bmatrix} \sigma_{xx}^D & \sigma_{xz}^D \\ \sigma_{xz}^D & \sigma_{zz}^D \end{bmatrix} = 2\eta_0 d_e^{\frac{1}{n}-1} \begin{bmatrix} \frac{\partial v_x}{\partial x} & \frac{1}{2} \left( \frac{\partial v_x}{\partial z} + \frac{\partial v_z}{\partial x} \right) \\ \frac{1}{2} \left( \frac{\partial v_x}{\partial z} + \frac{\partial v_z}{\partial x} \right) & \frac{\partial v_z}{\partial z} \end{bmatrix}, \quad (2.29)$$

with  $\eta_0 = 1/(2A^{1/n})$ ,  $v_x$  the horizontal velocity,  $v_z$  the vertical velocity, and the effective strain rate  $d_e$  given by

$$d_e = \sqrt{\left( \frac{\partial v_x}{\partial x} \right)^2 + \frac{1}{4} \left( \frac{\partial v_x}{\partial z} + \frac{\partial v_z}{\partial x} \right)^2}. \quad (2.30)$$

The horizontal and vertical coordinates are nondimensionalised as

$$\tilde{x} = \frac{x}{L}, \quad \tilde{z} = \frac{z}{H} = \frac{z}{\epsilon L}, \quad (2.31)$$

and the unknowns  $v_x$ ,  $v_z$ , and  $p$  are nondimensionalised as

$$\tilde{v}_x = \frac{v_x}{U}, \quad \tilde{v}_z = \frac{v_z}{\epsilon U}, \quad \tilde{p} = \frac{p}{\rho g H}, \quad (2.32)$$

where tildes are used to indicate dimensionless variables. In dimensionless form, Equation (2.28) writes as

$$\epsilon \frac{\partial}{\partial \tilde{z}} \left( 2(2\tilde{d}_e)^{\frac{1}{n}-1} \frac{\partial \tilde{v}_z}{\partial \tilde{z}} \right) - \frac{R_e}{F_r^2} \frac{\partial \tilde{p}}{\partial \tilde{z}} - \frac{R_e}{F_r^2} = -\epsilon \frac{\partial}{\partial \tilde{x}} \left( (2\tilde{d}_e)^{\frac{1}{n}-1} \left( \frac{\partial \tilde{v}_x}{\partial \tilde{z}} + \epsilon^2 \frac{\partial \tilde{v}_z}{\partial \tilde{x}} \right) \right), \quad (2.33)$$

while the dimensionless deviatoric stress tensor and effective strain rate write as

$$\begin{bmatrix} \tilde{\sigma}_{xx}^D & \tilde{\sigma}_{xz}^D \\ \tilde{\sigma}_{xz}^D & \tilde{\sigma}_{zz}^D \end{bmatrix} = \rho g H \frac{F_r^2}{R_e} (2\tilde{d}_e)^{\frac{1}{n}-1} \begin{bmatrix} 2\epsilon \frac{\partial \tilde{v}_x}{\partial \tilde{x}} & \left( \frac{\partial \tilde{v}_x}{\partial \tilde{z}} + \epsilon^2 \frac{\partial \tilde{v}_z}{\partial \tilde{x}} \right) \\ \left( \frac{\partial \tilde{v}_x}{\partial \tilde{z}} + \epsilon^2 \frac{\partial \tilde{v}_z}{\partial \tilde{x}} \right) & 2\epsilon \frac{\partial \tilde{v}_z}{\partial \tilde{z}} \end{bmatrix}, \quad (2.34)$$

$$\tilde{d}_e = \sqrt{\epsilon^2 \left( \frac{\partial \tilde{v}_x}{\partial \tilde{x}} \right)^2 + \frac{1}{4} \left( \frac{\partial \tilde{v}_x}{\partial \tilde{z}} + \epsilon^2 \frac{\partial \tilde{v}_z}{\partial \tilde{x}} \right)^2}. \quad (2.35)$$

In the dimensionless form of the Stokes equations, the relative size of the aspect ratio  $\epsilon$  as compared with the ratio  $R_e/F_r^2$  fundamentally determines the significance of vertical shear and membrane stresses. This leads to the identification of two scaling regimes. In the first scaling regime, which may be characterised as ‘‘slow’’,  $R_e/F_r^2$  is large as compared with  $\epsilon$

( $\epsilon R_e/F_r^2 = \mathcal{O}(1)$ ) and vertical shear stresses are significant as compared with membrane stresses (see Equation (2.34)). In the second scaling regime, which may be characterised as “rapid”,  $R_e/F_r^2$  is small as compared with  $\epsilon$  ( $\epsilon F_r^2/R_e = \mathcal{O}(1)$ ) and membrane stresses are significant as compared with vertical shear stresses (see Equation (2.34)). In the first scaling regime and at the leading order, the pressure is hydrostatic and vertical shear stresses are dominant in the horizontal conservation-of-momentum equations. This leads to the SIA reduced-order model, which provides an example of a classical lubrication flow in which shearing across the film thickness balances the pressure gradient or the body force in the film. The SIA reduced-order model is thus appropriate in regions where basal sliding is weak and the ice flow is dominated by shearing rather than sliding, that is, the shallow ice approximation is used to represent ice flow in the interior part of large ice sheets. In the second scaling regime and at the leading order, the vertical normal stress is hydrostatic and vertical shear stresses are negligible as compared with membrane stresses in the horizontal conservation-of-momentum equations. This leads to the SSA reduced-order model, also referred to as the shelfy-stream approximation reduced-order model, which provides an example of a “free-flow” model where there is no (or almost no) friction at the base of the fluid film. The SSA reduced-order model is thus appropriate in regions where basal sliding is important and the ice flow is dominated by membrane stresses rather than vertical shear stresses, that is, the shallow-shelf approximation is used to represent ice flow in ice shelves, where basal friction due to the contact with the ocean is negligible, and in fast-flowing ice streams.

Reduced-order models of the thermal problem can also be derived from a dimensional analysis; see, for instance, Vergori [2010], Bernabeu [2015], and Meyer and Minchew [2018] for a discussion of the thermal regime of Stokes flows. The dimensionless form of the thermal problem leads to the identification of three nondimensionless numbers, namely, the aspect ratio  $\epsilon$ , a Péclet number and a Brinkman number given by

$$P_e = \frac{\rho c_0 W H}{k_0}, \quad B_r = \frac{\eta_0 U_n^{\frac{1}{n}+1}}{k_0 \Delta T 2^{\frac{1}{n}+1} H^{\frac{1}{n}-1}}, \quad (2.36)$$

where  $c_0$  is a reference specific heat capacity,  $k_0$  a reference thermal conductivity,  $\Delta T$  a reference temperature change, and  $W = \epsilon U$  a reference vertical velocity. In the dimensionless form of the conservation-of-energy equation, the Péclet number measures the importance of heat advection to heat conduction and the Brinkman number measures the importance of viscous heat dissipation to heat conduction. In the slow mechanical scaling regime (SIA) and at the leading order, vertical heat diffusion is significant as compared to horizontal heat diffusion and viscous heat dissipation is controlled by vertical shearing. In the fast mechanical scaling regime (SSA) and at the leading order, vertical heat diffusion is significant as compared to horizontal heat diffusion and viscous heat dissipation is controlled by longitudinal stresses and lateral shearing.

In the following, we focus on the key aspects of the mathematical formulation of the SIA and SSA reduced-order models.

### 2.3.1 Shallow-ice approximation

We consider a 3D Cartesian coordinate system defined by a horizontal reference plane and a vertical  $z$ -axis as depicted in Figure 2.4. We denote by  $\Omega(t)$  the domain occupied by the ice and

by  $\omega(t)$  the support of the ice sheet in the horizontal reference plane. The position of a point in the ice sheet is denoted by  $(\mathbf{x}, z)$  where  $\mathbf{x} = (x, y)$  is the position in the horizontal reference plane and  $z$  is the vertical coordinate measured from the reference horizontal plane. We denote the velocity field by  $(\mathbf{v}, v_z)$  where  $\mathbf{v} = (v_x, v_y)$  is the horizontal velocity and  $v_z$  the vertical velocity. The boundary  $\Gamma(t)$  of the domain is divided into the ice-air interface  $\Gamma_s(t)$ , the ice-bedrock interface  $\Gamma_b(t)$ , and the ice divide. In the context of the SIA reduced-order model, we do not consider the presence of an ice shelf, that is, we assume no contact of the ice sheet with the ocean. It should be noted that in this section, solution variables represent the leading-order approximations to the solution variables of the full-order problem. For convenience of writing, we do not distinguish in our system of notations the solution variables of the reduced-order model from the solution variables of the full-order problem.

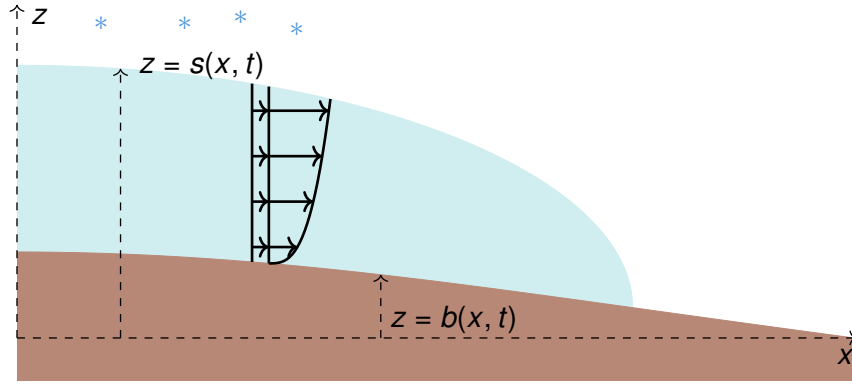


Figure 2.4: Schematic representation of an ice sheet (SIA reduced-order model). At any time  $t$  in  $]0, \tau[$ ,  $z = s(\mathbf{x}, t)$  denotes the elevation of the ice-air interface and  $z = b(\mathbf{x}, t)$  denotes the elevation of the ice-bedrock interface. In the SIA scaling regime, the vertical profile of the horizontal velocity can be decomposed into a constant component due to sliding at the ice-bedrock interface and a non-constant component due to vertical shearing.

In the coordinate system described above, we use the functions  $s$  and  $b$  to track the position of the ice-air and ice-bedrock interfaces, respectively, and we denote by  $h = s - b$  the ice thickness. Thus, at any time  $t$  in  $]0, \tau[$ , the interfaces  $\Gamma_s(t)$  and  $\Gamma_b(t)$  can be expressed as

$$\Gamma_s(t) = \{(\mathbf{x}, z) \in \Omega(t) : z = s(\mathbf{x}, t)\}, \quad (2.37)$$

$$\Gamma_b(t) = \{(\mathbf{x}, z) \in \Omega(t) : z = b(\mathbf{x}, t)\}. \quad (2.38)$$

At the leading order in the SIA scaling regime, Equations (2.1) and (2.2) reduce to

$$\frac{\partial \sigma_{xz}^D}{\partial z} = \frac{\partial p}{\partial x}, \quad \text{in } \Omega(t) \text{ for } 0 < t < \tau, \quad (2.39)$$

$$\frac{\partial \sigma_{yz}^D}{\partial z} = \frac{\partial p}{\partial y}, \quad \text{in } \Omega(t) \text{ for } 0 < t < \tau, \quad (2.40)$$

$$\frac{\partial p}{\partial z} = -\rho g, \quad \text{in } \Omega(t) \text{ for } 0 < t < \tau, \quad (2.41)$$

$$\frac{\partial v_x}{\partial x} + \frac{\partial v_y}{\partial y} + \frac{\partial v_z}{\partial z} = 0, \quad \text{in } \Omega(t) \text{ for } 0 < t < \tau, \quad (2.42)$$

while Glen's flow law reduces to

$$\frac{\partial v_x}{\partial z} = 2A \left( \sqrt{(\sigma_{xz}^D)^2 + (\sigma_{yz}^D)^2} \right)^{n-1} \sigma_{xz}^D, \quad (2.43)$$

$$\frac{\partial v_y}{\partial z} = 2A \left( \sqrt{(\sigma_{xz}^D)^2 + (\sigma_{yz}^D)^2} \right)^{n-1} \sigma_{yz}^D. \quad (2.44)$$

At the leading order, vertical shear stresses in the horizontal plane are dominant as compared with membrane stresses. Thus, the horizontal conservation-of-momentum equation reduces to a balance between the vertical gradient of the vertical shear stresses and the horizontal pressure gradient. Equation (2.41) and the free-surface condition at the ice-air interface indicate that at the leading order the pressure field is hydrostatic. Injecting the expression for the hydrostatic pressure into Equations (2.39) and (2.40) and integrating over the vertical direction with the free-surface condition at the ice-air interface yield analytical expressions for  $\sigma_{xz}^D$  and  $\sigma_{yz}^D$  that can then be injected into Equations (2.43) and (2.44). Integrating the equations thus obtained from the ice base to an arbitrary position  $z$  finally yields an analytical expression for the horizontal velocity. Furthermore, the vertical velocity  $v_z$  can be determined by integrating the incompressibility constraint (2.42) from the ice base to an arbitrary position  $z$ . Consequently, in the SIA regime, the velocity field and the pressure field take the following analytical expressions:

$$\mathbf{v} = \mathbf{v}_b - 2(\rho g)^n \int_b^z A(s - z')^n dz' \|\nabla_{\mathbf{x}s}\|^{n-1} \nabla_{\mathbf{x}s}, \quad \text{in } \Omega(t) \text{ for } 0 < t < \tau, \quad (2.45)$$

$$p = \rho g(s - z), \quad \text{in } \Omega(t) \text{ for } 0 < t < \tau, \quad (2.46)$$

$$v_z = v_z|_{z=b} - \int_b^z \text{div}_{\mathbf{x}} \mathbf{v} dz', \quad \text{in } \Omega(t) \text{ for } 0 < t < \tau, \quad (2.47)$$

where  $\mathbf{v}_b$  is the horizontal sliding velocity and  $v_z|_{z=b}$  the vertical velocity at the ice-bedrock interface determined from the mass balance equation at the ice-bedrock interface.

In the shallow ice approximation, the basal shear stress writes as

$$\boldsymbol{\tau}_b = - \begin{pmatrix} \sigma_{xz}^D|_{z=b} \\ \sigma_{yz}^D|_{z=b} \end{pmatrix} = \rho g h \nabla_{\mathbf{x}s} \equiv -\boldsymbol{\tau}_d, \quad (2.48)$$

where  $\boldsymbol{\tau}_d$  is often called the (gravitational) driving stress. Thus, in the shallow ice approximation, the basal shear stress is completely balanced by the gravitational driving stress. Assuming the friction law to be invertible, the basal velocity  $\mathbf{v}_b$  can then be determined from Equation (2.48). For Weertman's friction law, this yields

$$\mathbf{v}_b = - \frac{1}{c_b^m} \|\boldsymbol{\tau}_d\|^{m-1} \boldsymbol{\tau}_d = - \frac{1}{c_b^m} (\rho g h)^m \|\nabla_{\mathbf{x}s}\|^{m-1} \nabla_{\mathbf{x}s}, \quad \text{in } \omega(t) \text{ for } 0 < t < \tau. \quad (2.49)$$

In the coordinate system described above, one may derive an exact equation for the evolution of the ice thickness from the full-order model. Integrating the incompressibility equation (2.2) over the ice thickness and using Leibniz's rule and the boundary conditions (2.5) and (2.7) yield the following exact conservation-of-height equation:

$$\frac{\partial h}{\partial t} + \text{div}_{\mathbf{x}} \mathbf{q} = \sqrt{1 + \|\nabla_{\mathbf{x}s}\|^2} a_s^\perp - \sqrt{1 + \|\nabla_{\mathbf{x}} b\|^2} a_b^\perp, \quad \text{in } \omega(t) \text{ for } 0 < t < \tau, \quad (2.50)$$

where

$$\mathbf{q} = \int_b^s \mathbf{v} dz \quad (2.51)$$

is the vertically integrated horizontal velocity, that is, the ice flux. At the leading order in the SIA scaling regime, Equation (2.50) reduces to

$$\frac{\partial h}{\partial t} + \operatorname{div}_x \mathbf{q} = a_s - a_b, \quad \text{in } \omega(t) \text{ for } 0 < t < \tau, \quad (2.52)$$

where  $a_s$  is the mass balance at the ice-air interface,  $a_b$  is the mass balance at the ice-bedrock interface, and the ice flux  $\mathbf{q}$  is obtained by integrating Equation (2.45) over the ice thickness, that is,

$$\mathbf{q} = \int_b^s \mathbf{v} dz = \mathbf{v}_b h - 2(\rho g)^n \int_b^s A(s-z)^{n+1} dz \|\nabla_x s\|^{n-1} \nabla_x s. \quad (2.53)$$

At the leading order, the temperature field  $T$  is required to satisfy the following conservation-of-energy equation:

$$\rho c \left( \frac{\partial T}{\partial t} + \mathbf{v} \cdot \nabla_x T + v_z \frac{\partial T}{\partial z} \right) = \frac{\partial}{\partial z} \left( k \frac{\partial T}{\partial z} \right) + 2A\sigma_e^{n+1}, \quad \text{in } \Omega(t) \text{ for } 0 < t < \tau, \quad (2.54)$$

where  $\sigma_e$  is the effective deviatoric stress given by

$$\sigma_e = \rho g (s - z) \|\nabla_x s\|. \quad (2.55)$$

### 2.3.1.1 Discussion

In the SIA reduced-order model, the pressure and velocity fields are determined analytically from Equations (2.45)–(2.47). The horizontal velocity field depends on the local slope of the ice surface elevation. The horizontal velocity field is always antiparallel to the gradient of the ice surface elevation irrespective of the bedrock topography. The computational burden is in the evaluation of the temperature field (Equation (2.54)) and the evolution of the ice thickness (Equation (2.52)). In the SIA reduced-order model, Equation (2.52) for the evolution of the ice thickness can be interpreted as a nonlinear diffusion equation, whose diffusion coefficient is a function of the ice thickness and the gradient of the ice surface elevation. Indeed, Equation (2.52) writes as

$$\frac{\partial s}{\partial t} + \operatorname{div}_x (D \nabla_x s) = a_s - a_b - \frac{\partial b}{\partial t}, \quad \text{in } \omega(t) \text{ for } 0 < t < \tau, \quad (2.56)$$

with the coefficient of diffusion  $D$  given by

$$D = -\frac{1}{c_b^m} (\rho g)^m h^{m+1} \|\nabla_x s\|^{m-1} - 2(\rho g)^n \int_b^s A(s-z)^{n+1} dz \|\nabla_x s\|^{n-1}. \quad (2.57)$$

Thus, in the SIA reduced-order model, the ice flow “diffuses” the ice surface, with the diffusion process that acts more quickly in the presence of large values of the ice thickness or large gradients of the ice surface elevation.

### 2.3.2 Shallow-shelf approximation

We consider a 3D Cartesian coordinate system defined by a horizontal reference plane (for instance, the initial sea-water level) and a vertical  $z$ -axis as depicted in Figure 2.5. We denote by  $\Omega(t)$  the domain occupied by the ice and by  $\omega(t)$  the support of the ice sheet in the horizontal reference plane. To introduce the SSA reduced-order model, we decompose the domain  $\omega(t)$  into a grounded region  $\omega_g(t)$  where the ice is grounded and a floating region  $\omega_f(t)$  covered with the ice shelf and we denote by  $\gamma(t) = \bar{\omega}_g(t) \cap \bar{\omega}_f(t)$  the projection of the grounding line in the horizontal reference plane. Similarly, we decompose  $\Omega(t)$  into a grounded part  $\Omega_g(t)$  and a floating part  $\Omega_f(t)$ . The position of a point in the ice sheet is denoted by  $(\mathbf{x}, z)$  where  $\mathbf{x}$  is the position in the horizontal reference plane and  $z$  is the vertical coordinate measured from the horizontal reference plane. We denote the velocity field by  $(\mathbf{v}, v_z)$  where  $\mathbf{v} = (v_x, v_y)$  is the horizontal velocity and  $v_z$  the vertical velocity. The boundary  $\Gamma(t)$  of the domain is divided into the ice-air interface  $\Gamma_s(t)$ , the ice-bedrock interface  $\Gamma_b(t)$ , the ice-ocean interface  $\Gamma_w(t)$ , the calving front, and the ice divide. As in Section 2.3.1, solution variables represent the leading-order approximations to the solution variables of the full-order problem.

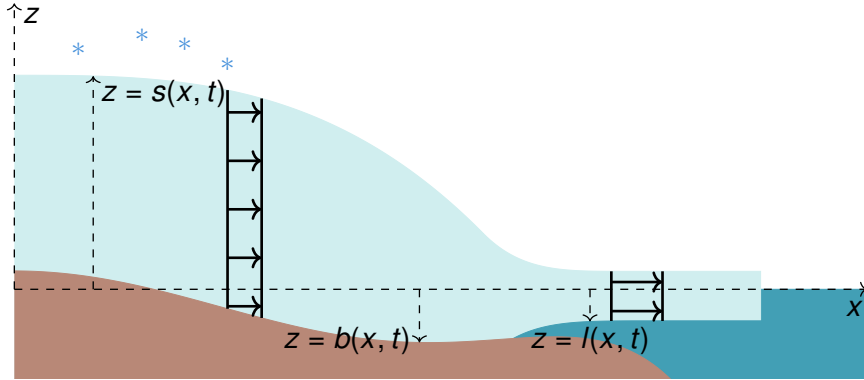


Figure 2.5: Schematic representation of a marine ice sheet (SSA reduced-order model). At any time  $t$  in  $]0, \tau[$ ,  $z = s(\mathbf{x}, t)$  denotes the elevation of the ice-air interface,  $z = b(\mathbf{x}, t)$  the elevation of the ice-bedrock interface, and  $z = l(\mathbf{x}, t)$  the elevation of the ice-ocean interface. In the SSA scaling regime, the horizontal velocity is constant in the vertical direction and equal to the sliding velocity.

In the coordinate system described above, we use the functions  $s$ ,  $b$ , and  $l$  to track the positions of the ice-air interface, the ice-bedrock interface, and the ice-ocean interface, respectively, and we denote by  $h$  the ice thickness. Thus, at any time  $t$  in  $]0, \tau[$ , the interfaces  $\Gamma_s(t)$ ,  $\Gamma_b(t)$ , and  $\Gamma_w(t)$  can be expressed as

$$\Gamma_s(t) = \{(\mathbf{x}, z) \in \Omega(t) : z = s(\mathbf{x}, t)\}, \quad (2.58)$$

$$\Gamma_b(t) = \{(\mathbf{x}, z) \in \Omega(t) : z = b(\mathbf{x}, t)\}, \quad (2.59)$$

$$\Gamma_w(t) = \{(\mathbf{x}, z) \in \Omega(t) : z = l(\mathbf{x}, t)\}. \quad (2.60)$$

In the following, we first discuss aspects of the SSA reduced-order model on the disjoint domains  $\Omega_g(t)$  and  $\Omega_f(t)$  separately and then on the whole domain  $\Omega(t)$ .

### 2.3.2.1 Shallow-shelf approximation in ice streams

At the leading order in the SSA scaling regime, Equations (2.1) and (2.2) reduce to

$$\frac{\partial v_x}{\partial z} = 0, \quad \text{in } \Omega_g(t) \text{ for } 0 < t < \tau, \quad (2.61)$$

$$\frac{\partial v_y}{\partial z} = 0, \quad \text{in } \Omega_g(t) \text{ for } 0 < t < \tau, \quad (2.62)$$

$$\frac{\partial \sigma_{zz}}{\partial z} = \rho g, \quad \text{in } \Omega_g(t) \text{ for } 0 < t < \tau, \quad (2.63)$$

$$\frac{\partial v_x}{\partial x} + \frac{\partial v_y}{\partial y} + \frac{\partial v_z}{\partial z} = 0, \quad \text{in } \Omega_g(t) \text{ for } 0 < t < \tau. \quad (2.64)$$

Equations (2.61) and (2.62) indicate that at the leading order vertical shear stresses vanish, that is, the horizontal velocity is constant in the vertical direction (plug-flow model). Equation (2.63) and the free-surface condition at the ice-air interface indicate that at the leading order the normal stress  $\sigma_{zz}$  is hydrostatic, that is,  $\sigma_{zz} = -\rho g(s - z)$ . It should be mentioned that while the SIA scaling regime leads to only the pressure being hydrostatic, the SSA scaling regime leads to the normal stress being hydrostatic, that is, the deviatoric component of the normal stress is not negligible. Equation (2.64) is the incompressibility constraint that yields the vertical velocity when integrating from the ice base to an arbitrary vertical position  $z$ .

To derive an equation for the horizontal velocity field in the SSA scaling regime, we first derive an exact depth-averaged conservation-of-momentum equation from the full-order model. Integrating the horizontal conservation-of-momentum equation in (2.1) over the ice thickness, then using Leibniz's rule to interchange the partial derivatives with respect to the horizontal coordinates and the integrals over the ice thickness, and finally using the boundary conditions in Equation (2.4), we obtain the exact depth-averaged conservation-of-momentum equations

$$\frac{\partial}{\partial x} \int_b^s p \, dz = \frac{\partial}{\partial x} \int_b^s \sigma_{xx}^D \, dz + \frac{\partial}{\partial y} \int_b^s \sigma_{xy}^D \, dz + \tau_{b,x} - \frac{\partial b}{\partial x} N_b, \quad (2.65)$$

$$\frac{\partial}{\partial y} \int_b^s p \, dz = \frac{\partial}{\partial x} \int_b^s \sigma_{xy}^D \, dz + \frac{\partial}{\partial y} \int_b^s \sigma_{yy}^D \, dz + \tau_{b,y} - \frac{\partial b}{\partial y} N_b, \quad (2.66)$$

where the stress vector at the ice-bedrock interface has been decomposed into a tangential component  $\tau_b$  and a normal component  $-N_b \mathbf{n}$  with  $N_b \geq 0$ . In the SSA scaling regime,  $N_b$  is given by the opposite of  $\sigma_{zz}$  at the ice-bedrock interface, that is,  $N_b = \rho g h$ . By considering the leading-order approximations (2.61)–(2.63) in Equations (2.65) and (2.66) and using Weertman's sliding law with  $\mathbf{v}_b = \mathbf{v}$  (assuming that the bedrock slope is sufficiently small), we obtain the following approximate depth-averaged conservation-of-momentum equations:

$$2 \frac{\partial}{\partial x} \left( 2\bar{\eta} h \frac{\partial v_x}{\partial x} + \bar{\eta} h \frac{\partial v_y}{\partial y} \right) + \frac{\partial}{\partial y} \left( \bar{\eta} h \frac{\partial v_x}{\partial y} + \bar{\eta} h \frac{\partial v_y}{\partial x} \right) - c_b \|\mathbf{v}\|^{p-1} v_x = \rho g h \frac{\partial s}{\partial x}, \quad (2.67a)$$

$$2 \frac{\partial}{\partial y} \left( 2\bar{\eta} h \frac{\partial v_y}{\partial y} + \bar{\eta} h \frac{\partial v_x}{\partial x} \right) + \frac{\partial}{\partial x} \left( \bar{\eta} h \frac{\partial v_x}{\partial y} + \bar{\eta} h \frac{\partial v_y}{\partial x} \right) - c_b \|\mathbf{v}\|^{p-1} v_y = \rho g h \frac{\partial s}{\partial y}, \quad (2.67b)$$

where  $\bar{\eta}$  is the depth-averaged effective viscosity given by

$$\frac{1}{h} \int_b^s \eta \, dz = \frac{1}{2h} \int_b^s A^{-\frac{1}{n}} \, dz \, d_e^{\frac{1}{n}-1}, \quad (2.68)$$

in which the effective strain rate  $d_e$  is given by

$$d_e = \sqrt{\left(\frac{\partial v_x}{\partial x}\right)^2 + \left(\frac{\partial v_y}{\partial y}\right)^2 + \frac{\partial v_x}{\partial x} \frac{\partial v_y}{\partial y} + \frac{1}{4} \left(\frac{\partial v_x}{\partial y} + \frac{\partial v_y}{\partial x}\right)^2}. \quad (2.69)$$

In the SSA scaling regime, the conservation-of-height equation in (2.50) writes as

$$\frac{\partial h}{\partial t} + \operatorname{div}_x(h\mathbf{v}) = a_s - a_b, \quad \text{in } \omega_g(t) \text{ for } 0 < t < \tau. \quad (2.70)$$

Equation (2.70) is an advection equation for the ice thickness, that is, the ice flow “transports” the ice thickness.

At the leading order, the temperature field  $T$  is required to satisfy the following conservation-of-energy equation:

$$\rho c \left( \frac{\partial T}{\partial t} + \mathbf{v} \cdot \nabla_x T + v_z \frac{\partial T}{\partial z} \right) = \frac{\partial}{\partial z} \left( k \frac{\partial T}{\partial z} \right) + 4\eta d_e^2, \quad \text{in } \Omega_g(t) \text{ for } 0 < t < \tau. \quad (2.71)$$

### 2.3.2.2 Shallow-shelf approximation in ice shelves

Leading-order approximations of Equations (2.65) and (2.66) in the SSA scaling regime for ice shelves are obtained in a similar way to Equation (2.67) in Section 2.3.2.1 but in the absence of basal friction. Hence, we have at any time  $t$  in  $]0, \tau[$

$$2 \frac{\partial}{\partial x} \left( 2\bar{\eta}h \frac{\partial v_x}{\partial x} + \bar{\eta}h \frac{\partial v_y}{\partial y} \right) + \frac{\partial}{\partial y} \left( \bar{\eta}h \frac{\partial v_x}{\partial y} + \bar{\eta}h \frac{\partial v_y}{\partial x} \right) = \rho gh \frac{\partial s}{\partial x}, \quad \text{in } \omega_f(t), \quad (2.72)$$

$$2 \frac{\partial}{\partial y} \left( 2\bar{\eta}h \frac{\partial v_y}{\partial y} + \bar{\eta}h \frac{\partial v_x}{\partial x} \right) + \frac{\partial}{\partial x} \left( \bar{\eta}h \frac{\partial v_x}{\partial y} + \bar{\eta}h \frac{\partial v_y}{\partial x} \right) = \rho gh \frac{\partial s}{\partial y}, \quad \text{in } \omega_f(t), \quad (2.73)$$

$$\sigma_{zz} = -\rho g(s - z), \quad \text{in } \Omega_f(t), \quad (2.74)$$

$$v_z = v_z|_{z=b} - \int_b^z \operatorname{div}_x \mathbf{v} dz', \quad \text{in } \Omega_f(t), \quad (2.75)$$

with

$$\bar{\eta} = \frac{1}{h} \int_l^s \eta dz = \frac{1}{2h} \int_l^s A^{-\frac{1}{n}} dz d_e^{\frac{1}{n}-1}. \quad (2.76)$$

In addition, the conservation-of-height and conservation-of-energy equations take the same form as in Equations (2.70) (with  $a_w$  instead of  $a_b$ ) and (2.71), respectively. The temperature field  $T$  in ice shelves is solution to Equation (2.71) with boundary condition  $T = T_s$  at the ice-air interface and boundary condition  $T = T_w$  at the ice-ocean interface.

Besides the absence of friction, differences between the SSA reduced-order model in ice streams and ice shelves lie in the treatment of the boundary conditions. In the coordinate system described above, the boundary condition (2.8) in the vertical direction writes as

$$\sigma_{xz}^D \frac{\partial l}{\partial x} + \sigma_{yz}^D \frac{\partial l}{\partial y} + p - \sigma_{zz}^D = \rho_w g(z_{sl} - l), \quad (2.77)$$

where  $\rho_w$  is the water density and  $z_{sl}$  the sea-water level. Neglecting shear stresses at the leading order and evaluating Equation (2.74) at the ice-shelf base, we obtain

$$p - \sigma_{zz}^D = \rho_w g(z_{sl} - l) \Rightarrow \rho h = \rho_w(z_{sl} - l), \quad (2.78)$$

where the last equation is the so-called floatation condition (Archimedes' principle). Thus, the ice surface elevation in ice shelves is given by  $s = z_{sl} + (1 - \rho/\rho_w)h$ . At the calving front, the boundary condition (2.10) in the horizontal directions writes as

$$-pn_x + \sigma_{xx}^D n_x + \sigma_{xy}^D n_y = -f_w n_x, \quad (2.79a)$$

$$\sigma_{xy}^D n_x - pn_y + \sigma_{yy}^D n_y = -f_w n_y, \quad (2.79b)$$

where  $\mathbf{n} = (n_x, n_y, 0)$  is the exterior normal unit vector to the calving front. Using Equation (2.74) and integrating Equations (2.79a) and (2.79b) over the ice thickness yield the boundary conditions

$$2\bar{\eta}h \left[ \left( 2\frac{\partial v_x}{\partial x} + \frac{\partial v_y}{\partial y} \right) n_x + \frac{1}{2} \left( \frac{\partial v_x}{\partial y} + \frac{\partial v_y}{\partial x} \right) n_y \right] = \frac{1}{2} \rho g h^2 \left( 1 - \frac{\rho}{\rho_w} \right) n_x, \quad (2.80a)$$

$$2\bar{\eta}h \left[ \left( 2\frac{\partial v_y}{\partial y} + \frac{\partial v_x}{\partial x} \right) n_y + \frac{1}{2} \left( \frac{\partial v_x}{\partial y} + \frac{\partial v_y}{\partial x} \right) n_x \right] = \frac{1}{2} \rho g h^2 \left( 1 - \frac{\rho}{\rho_w} \right) n_y. \quad (2.80b)$$

### 2.3.2.3 Multi-domain formulation and transmission conditions

Sections 2.3.2.1 and 2.3.2.2 define a multi-domain formulation [Quarteroni and Valli, 1999; Mathew, 2008] in which the SSA reduced-order model is solved in the disjoint domains  $\omega_g(t)$  and  $\omega_f(t)$ . At each time  $t$  in  $]0, \tau[$ , the floatation condition in Equation (2.78) can be used to distinguish between the grounded and floating regions as

$$\omega_g(t) = \{ \mathbf{x} \in \omega(t) : \rho h(\mathbf{x}, t) > \rho_w(z_{sl} - b(\mathbf{x}, t)) \}, \quad (2.81)$$

$$\omega_f(t) = \{ \mathbf{x} \in \omega(t) : \rho h(\mathbf{x}, t) < \rho_w(z_{sl} - b(\mathbf{x}, t)) \}, \quad (2.82)$$

that is, the ice is grounded if the normal stress at the ice base exceeds sea-water pressure at the bedrock, while the ice is floating if the normal stress at the ice base is inferior to sea-water pressure at the bedrock. It should be noted that Equations (2.81) and (2.82) are equivalent to unilateral contact conditions, with the contact and non-contact zones distinguished based on Archimedes's principle. In addition, the grounding line is determined as

$$\gamma(t) = \{ \mathbf{x} \in \omega(t) : \rho h(\mathbf{x}, t) = \rho_w(z_{sl} - b(\mathbf{x}, t)) \}. \quad (2.83)$$

A multi-domain formulation requires to impose so-called transmission conditions at the interface between both domains. For the SSA reduced-order model, this leads to impose additional conditions at the grounding line. Here, we impose the following transmission conditions

$$\llbracket h \rrbracket = 0, \quad \text{on } \gamma(t) \text{ for } 0 < t < \tau, \quad (2.84)$$

$$\llbracket \mathbf{v} \rrbracket = \mathbf{0}, \quad \text{on } \gamma(t) \text{ for } 0 < t < \tau, \quad (2.85)$$

$$\left[ \left[ 2\bar{\eta}h \left( 2\frac{\partial v_x}{\partial x} + \frac{\partial v_y}{\partial y} \right) n_x + \bar{\eta}h \left( \frac{\partial v_x}{\partial y} + \frac{\partial v_y}{\partial x} \right) n_y \right] \right] = 0, \quad \text{on } \gamma(t) \text{ for } 0 < t < \tau, \quad (2.86)$$

$$\left[ \left[ 2\bar{\eta}h \left( 2\frac{\partial v_y}{\partial y} + \frac{\partial v_x}{\partial x} \right) n_y + \bar{\eta}h \left( \frac{\partial v_x}{\partial y} + \frac{\partial v_y}{\partial x} \right) n_x \right] \right] = 0, \quad \text{on } \gamma(t) \text{ for } 0 < t < \tau, \quad (2.87)$$

where  $\mathbf{n} = (n_x, n_y)$  is the horizontal normal vector the grounding line and we use the notation  $\llbracket \psi \rrbracket$  to denote the jump of the variable  $\psi$  on  $\gamma(t)$ , that is,  $\psi_g - \psi_f$ , where  $\psi_g$  and  $\psi_f$  indicate the

limiting values of  $\psi$  as  $\gamma(t)$  is approached from  $\omega_g(t)$  and  $\omega_f(t)$ , respectively. Equations (2.84) and (2.85) enforce the continuity of the ice thickness and the horizontal velocity field across the grounding line, respectively. Equations (2.86) and (2.87) enforce the continuity of the thickness-integrated stress vector across the grounding line.

### 2.3.2.4 Discussion

The SSA reduced-order model is essentially a two-dimensional model for the horizontal velocity field; see Equations (2.67a) and (2.67b) for the grounded domain and Equations (2.72) and (2.73) for the floating domain. While in the SIA reduced-order model the gravitational driving stress is balanced by shearing within the ice, in the SSA reduced-order model the gravitational driving stress is balanced by the divergence of the membrane stresses and basal friction only for grounded ice. The SSA reduced-order model represents the simplest model in glaciology that incorporates membrane stresses. Contrary to the SIA reduced-order model, membrane models are nonlocal models in which the gravitational driving stress is balanced by connection to distant ice all over the domain. It should be mentioned that Equations (2.67a)–(2.67b) and (2.72)–(2.73) can also be expressed in a vectorial and invariant form. Following Schoof [2006], we write Equations (2.67a)–(2.67b) and (2.72)–(2.73) as

$$\operatorname{div}_x \left( 2\bar{\eta}h[\mathbf{D} + \operatorname{tr}(\mathbf{D})\mathbf{I}] \right) - c_b \|\mathbf{v}\|^{p-1} \mathbf{v} \mathbf{1}_{\omega_g}(\mathbf{x}) = \rho gh \nabla_x s. \quad (2.88)$$

Here,  $\mathbf{D} = \frac{1}{2}(\nabla_x \mathbf{v} + \nabla_x \mathbf{v}^T)$  is the horizontal strain-rate tensor and  $\mathbf{1}_{\omega_g}(\mathbf{x}) = 1$  if  $\mathbf{x}$  is in  $\omega_g$  and 0 otherwise. Here, the tensor  $2\bar{\eta}h[\mathbf{D} + \operatorname{tr}(\mathbf{D})\mathbf{I}]$  represents a thickness-integrated deviatoric membrane stress tensor, whose diagonal components represent the longitudinal or extensional stresses and off-diagonal components represent the lateral shear stress. As mentioned in Bueler and Brown [2009], the trace of this thickness-integrated deviatoric membrane stress tensor is in general different from zero, thus meaning that the membrane flow is “incompressible” in the reference horizontal plane.

## 2.4 Glacial isostatic adjustment

Glacial isostatic adjustment describes the response of the solid Earth, the gravitational field, and the oceans to the growth and decay of ice sheets. In particular, the post-glacial rebound refers to the uplift of the solid Earth following the decay of ice sheets. The field of GIA is an active field of research in glaciology with GIA models of various complexity currently used. Here, we briefly discuss a simple GIA model commonly used in computational ice-sheet models and we refer the reader to, for instance, Le Meur and Huybrechts [1996], Ivins and James [1999], Greve and Blatter [2009b], Whitehouse [2018], and Whitehouse et al. [2019] for further discussions.

Glacial isostatic adjustment models typically represent the lithosphere as a deformable solid plate and the underlying asthenosphere as a highly viscous fluid. Then, the response of the solid Earth is described by using a linear Maxwell viscoelastic rheological model, with an instantaneous elastic response superposed on a longer-term Newtonian viscous relaxation response. For instance, in the elastic lithosphere–relaxing asthenosphere (ELRA) GIA model [Brotchie and Silvester, 1969; Le Meur and Huybrechts, 1996; Huybrechts and de Wolde, 1999;

[Greve and Blatter, 2009b], which we focus on in the following, the lithosphere is described as a thin elastic plate under ice-sheet loading which relaxes towards an equilibrium position.

In the ELRA GIA model, the Earth's surface is modelled as an infinite two-dimensional horizontal plane (flat-Earth approximation) assuming the lithosphere thickness to be much smaller than the Earth's radius and the ice-sheet extent to be much smaller than the Earth's surface. Thus, the ELRA GIA model is defined with respect to a three-dimensional Euclidian space, whose horizontal reference plane is parallel to the Earth's surface. At any time  $t$  in  $]0, \tau[$  and position  $\boldsymbol{x}$  in  $\mathbb{R}^2$ , we denote by  $b(\boldsymbol{x}, t)$  the elevation of the lithosphere, taken positive upward, and by  $w(\boldsymbol{x}, t)$  the vertical displacement of the lithosphere, taken positive downward, with respect to the initial lithosphere elevation  $b_0(\boldsymbol{x})$ , which we identify as the undisturbed elevation of the lithosphere in the absence of any ice loading; see Figure 2.6 for an illustration. Finally, we denote by  $\omega$  the support of the ice sheet in the horizontal reference plane.

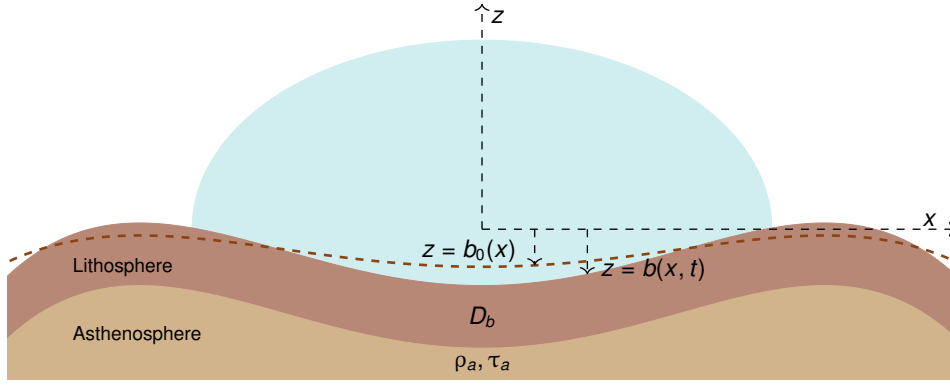


Figure 2.6: Schematic representation of glacial isostatic adjustment. The ice-sheet loading deforms the lithosphere that lies on a viscous asthenosphere. In the figure,  $b(\boldsymbol{x}, t)$  denotes the elevation of the lithosphere at a given time  $t$  in  $]0, \tau[$ ,  $b_0(\boldsymbol{x})$  the initial elevation of the lithosphere,  $D_b$  the flexural rigidity of the lithosphere, and  $\rho_a$  and  $\tau_a$  are the density and the relaxation time of the asthenosphere, respectively.

Assuming the lithosphere to behave like a horizontal elastic thin plate, the equilibrium vertical displacement of the lithosphere  $w^{\text{eq}}$  is required to satisfy the following equation:

$$D_b \Delta_{\boldsymbol{x}}^2 w^{\text{eq}} + \rho_a g w^{\text{eq}} = p_{\text{load}}, \quad \text{in } \mathbb{R}^2, \quad (2.89)$$

where  $D_b$  is the constant flexural rigidity of the lithosphere,  $p_{\text{load}}$  the applied vertical load that exerts on the lithosphere,  $\Delta_{\boldsymbol{x}}^2$  is the bilaplacian operator, and  $\rho_a$  the density of the underlying asthenosphere. Equation (2.89) is the equation for the vertical displacement of an infinite plate supported on a viscous substratum and subject to a vertical load [Hertz, 1884; Nadai, 1963]. Assuming the only applied vertical load on the lithosphere to be the ice-sheet hydrostatic pressure, the vertical load  $p_{\text{load}}$  can be expressed explicitly as

$$p_{\text{load}}(\boldsymbol{x}) = \begin{cases} \rho g h(\boldsymbol{x}), & \text{if } \boldsymbol{x} \in \omega \\ 0, & \text{otherwise} \end{cases}. \quad (2.90)$$

In order to ensure the uniqueness of a solution to Equation (2.89), appropriate boundary conditions must also be prescribed at infinity. Using the concept of Green's functions for linear differential operators, the solution to the linear partial differential equation (2.89) can be established for a general applied load  $p_{\text{load}}$  using a superposition principle. The Green's function for the linear differential operator  $D_b \Delta_x^2 + \rho_a g$  writes as [Hertz, 1884; Nadai, 1963]

$$G(\mathbf{x}) = -\frac{L_r^2}{2\pi D_b} \text{kei}\left(\frac{\|\mathbf{x}\|}{L_r}\right), \quad (2.91)$$

where  $\text{kei}$  denotes the zeroth-order Kelvin function (Figure 2.7) and  $L_r = \sqrt[4]{D_b/(\rho_a g)}$  is the so-called radius of relative stiffness (or flexural length scale), which determines the non-locality of the lithosphere displacement. Using the superposition principle, the solution to the linear partial differential equation (2.89) can be expressed as

$$w^{\text{eq}}(\mathbf{x}) = G(\mathbf{x}) * p_{\text{load}}(\mathbf{x}) = \int_{\mathbb{R}^2} -\frac{L_r^2}{2\pi D_b} \text{kei}\left(\frac{\|\mathbf{x} - \mathbf{x}'\|}{L_r}\right) p_{\text{load}}(\mathbf{x}') d\mathbf{x}'. \quad (2.92)$$

It should be mentioned that in general the flexural rigidity of the lithosphere is not constant. In this case, Equation (2.89) has to be extended to take a spatially flexural rigidity into account; see, for instance, Garcia et al. [2015].

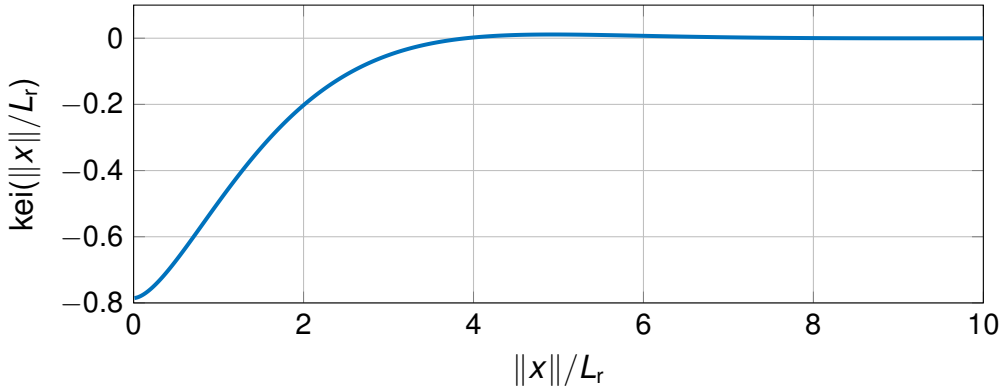


Figure 2.7: Zeroth-order Kelvin function  $\text{kei}$  as a function of the scaled distance  $\|\mathbf{x}\|/L_r$ . The Kelvin function  $\text{kei}$  is derived from the imaginary part of the zeroth-order modified Bessel function of the second kind. The zeroth-order Kelvin function takes the value zero at approximately  $\|\mathbf{x}\| = 4L_r$ , followed by a slight forebulge.

Finally, the evolution of the bedrock elevation is required to satisfy the following equation:

$$\frac{\partial b}{\partial t} = -\frac{1}{\tau_a} (b - b_0 + w^{\text{eq}}), \quad \text{in } \mathbb{R}^2 \text{ for } 0 < t < \tau, \quad (2.93)$$

$$b = b_0, \quad \text{in } \mathbb{R}^2 \text{ at } t = 0, \quad (2.94)$$

where  $\tau_a$  is the relaxation time of the asthenosphere. Thus, the evolution of the bedrock elevation is determined as a relaxation equation in which the rate of vertical displacement of the

lithosphere is related linearly to the deviation of the displacement  $w$  from the equilibrium displacement  $w^{\text{eq}}$ . The solution to Equation (2.93) with initial condition (2.94) writes as

$$b = b_0 - \left[ 1 - \exp\left(-\frac{t}{\tau_a}\right) \right] w^{\text{eq}}, \quad (2.95)$$

that is, the bedrock topography relaxes exponentially towards its equilibrium position.

## 2.5 Instability mechanisms in marine ice sheets

### 2.5.1 Marine ice-sheet instability

The concept of marine ice-sheet instability (MISI) serves as a fundamental mechanism to explain the potential collapse of marine sectors in Antarctica, that is, sectors where the bedrock lies below sea level. This concept was first hypothesised several decades ago by Weertman [1974] and Thomas and Bentley [1978], with further theoretical developments [Schoof, 2007a,b, 2012] and numerical illustrations [Pattyn et al., 2012, 2013] in the recent years. The MISI hypothesis states that marine ice sheets lying on upward sloping beds, or retrograde slopes, are inherently unstable. Figure 2.12 depicts schematically the marine ice-sheet instability. At steady state, the ice discharge (flux) at the grounding line is equal to the surface accumulation of ice upstream of the grounding line due to snow precipitation. Assuming a marine ice sheet initially at steady state on an upward sloping bed, the instability is triggered by a perturbation, for instance, a loss of ice-shelf buttressing due to oceanic melting, that leads to a slight retreat of the grounding-line position. Consequently, the grounding line is grounded deeper on the bed with the ice thickness thicker at the new grounding-line position. Based on a boundary layer theory, Schoof [2007a] showed that the ice flux at the grounding line (at equilibrium) is an increasing function of the ice thickness. Then, as the grounding line gets deeper and the ice flux increases, there is an imbalance between the ice flux at the grounding line and the surface accumulation upstream of the grounding line. This imbalance pushes the grounding line further inland, thus initiating a self-sustained retreat of the grounding line that continues until the grounding line reaches a new stable position, for instance, on a downward sloping bed.

#### 2.5.1.1 Parameterisation of the ice flux at the grounding line

We consider the SSA reduced-order model in 2D in a Cartesian coordinate system with horizontal  $x$ -axis and vertical  $z$ -axis. We denote by  $\omega(t)$  the support of the ice sheet, by  $\omega_g(t)$  its grounded portion, and by  $\omega_f(t)$  its floating portion. We denote by  $u(x, t)$  the horizontal velocity, by  $h(x, t)$  the ice thickness, by  $x_g(t)$  the position of the grounding line, and by  $x_c$  the position of the calving front assumed to be fixed. We assume the marine ice sheet to be isothermal and the bedrock to be fixed (no glacial isostatic adjustment). Based on the floatation condition, the grounded and floating domains are given by

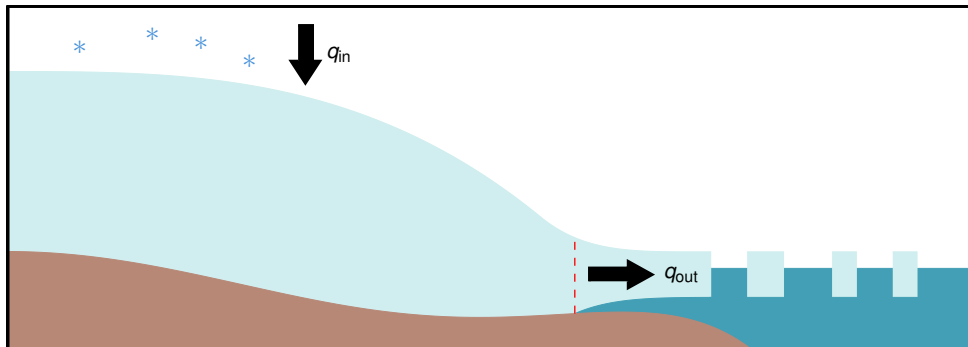
$$\omega_g(t) = \{x \in ]0, x_c[: \rho h(x, t) > \rho_w(z_{\text{sl}} - b(x, t))\}, \quad \text{for } 0 < t < \tau, \quad (2.96)$$

$$\omega_f(t) = \{x \in ]0, x_c[: \rho h(x, t) < \rho_w(z_{\text{sl}} - b(x, t))\}, \quad \text{for } 0 < t < \tau, \quad (2.97)$$

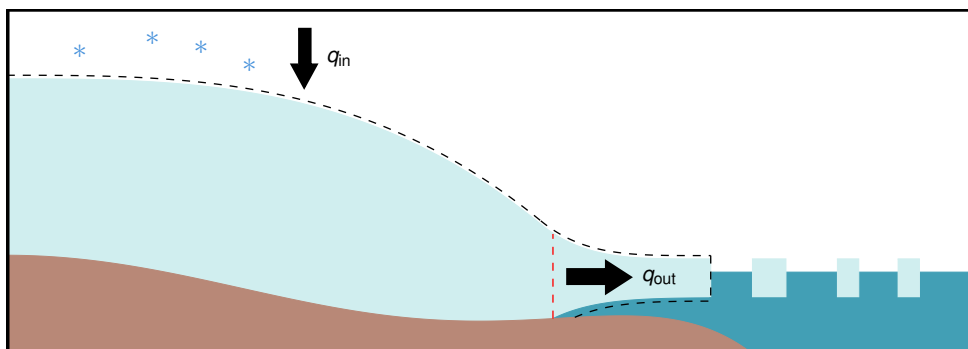
and at the grounding line

$$\rho h(x_g, t) = \rho_w(z_{\text{sl}} - b(x_g, t)), \quad \text{for } 0 < t < \tau. \quad (2.98)$$

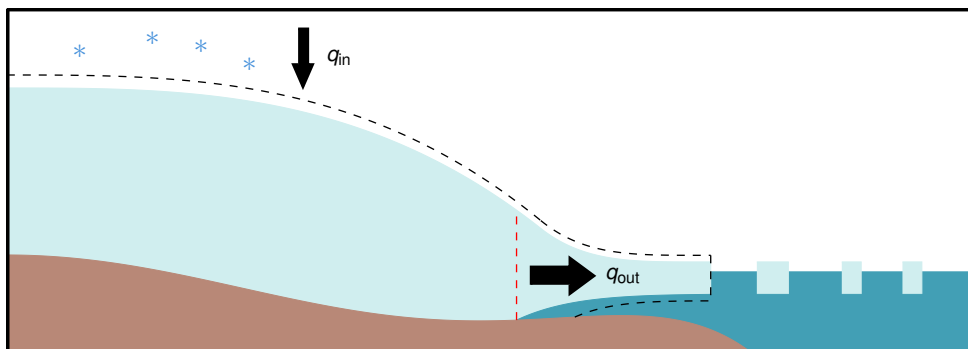
Step 1: Steady state on an upward sloping bed ( $q_{in} = q_{out}$ )



Step 2: Initiation of grounding-line retreat ( $q_{in} < q_{out}$ )



Step 3: Self-sustained grounding-line retreat ( $q_{in} \ll q_{out}$ )



Step 4: New steady state on a downward sloping bed ( $q_{in} = q_{out}$ )

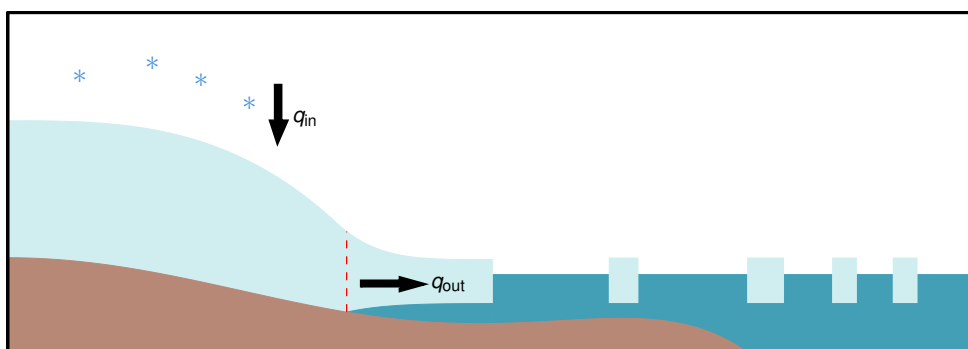


Figure 2.8: Schematic illustration of the marine ice-sheet instability mechanism.

Hence, we consider the following SSA reduced-order model:

$$\begin{cases} \frac{\partial h}{\partial t} + \frac{\partial}{\partial x}(hu) = a_s & \text{in } \omega_g(t) \text{ for } 0 < t < \tau \\ 2 \frac{\partial}{\partial x} \left( A^{-\frac{1}{n}} h \left| \frac{\partial u}{\partial x} \right|^{\frac{1}{n}-1} \frac{\partial u}{\partial x} \right) - c_b |u|^{p-1} u = \rho g h \frac{\partial s}{\partial x} & \text{in } \omega_g(t) \text{ for } 0 < t < \tau, \\ \frac{\partial s}{\partial x} = u = 0 & \text{at } x = 0 \text{ for } 0 < t < \tau \end{cases}, \quad (2.99)$$

$$\begin{cases} \frac{\partial h}{\partial t} + \frac{\partial}{\partial x}(hu) = a_s & \text{in } \omega_f(t) \text{ for } 0 < t < \tau \\ 2 \frac{\partial}{\partial x} \left( A^{-\frac{1}{n}} h \left| \frac{\partial u}{\partial x} \right|^{\frac{1}{n}-1} \frac{\partial u}{\partial x} \right) = \rho g \left( 1 - \frac{\rho}{\rho_w} \right) h \frac{\partial h}{\partial x} & \text{in } \omega_f(t) \text{ for } 0 < t < \tau, \\ 2 A^{-\frac{1}{n}} h \left| \frac{\partial u}{\partial x} \right|^{\frac{1}{n}-1} \frac{\partial u}{\partial x} = \frac{1}{2} \rho \left( 1 - \frac{\rho}{\rho_w} \right) g h^2 & \text{at } x = x_c \text{ for } 0 < t < \tau \end{cases}, \quad (2.100)$$

$$\begin{cases} h_g = h_f & \text{at } x = x_g \text{ for } 0 < t < \tau \\ u_g = u_f & \text{at } x = x_g \text{ for } 0 < t < \tau, \\ 2 A^{-\frac{1}{n}} h_g \left| \frac{\partial u_g}{\partial x} \right|^{\frac{1}{n}-1} \frac{\partial u_g}{\partial x} = 2 A^{-\frac{1}{n}} h_f \left| \frac{\partial u_f}{\partial x} \right|^{\frac{1}{n}-1} \frac{\partial u_f}{\partial x} & \text{at } x = x_g \text{ for } 0 < t < \tau \end{cases}, \quad (2.101)$$

where we have assumed no basal melting and refreezing at the ice-bedrock and ice-ocean interfaces, that is,  $a_b = 0$  and  $a_w = 0$ , and  $c_b$  to be constant on the ice-bedrock interface. Equation (2.99) is the SSA reduced-order model on the grounded domain, Equation (2.100) the SSA reduced-order model on the floating domain, and Equation (2.101) the transmission conditions at the grounding line.

Based on a boundary layer theory at steady state, Schoof [2007b] derived an analytical formula for the ice flux at the grounding line for the SSA reduced-order model defined by Equations (2.99)–(2.101). We can also recover this analytical formula by using an alternative derivation that relies on the transmission conditions at the grounding line without reference to the boundary layer theory. Let us consider the following steady-state approximation of Equations (2.99)–(2.101):

$$\begin{cases} hu = q & \text{in } \omega_g(t) \\ -c_b |u|^{p-1} u - \rho g h \frac{\partial h}{\partial x} = 0 & \text{in } \omega_g \\ \frac{\partial h}{\partial x} = u = 0 & \text{at } x = 0 \end{cases}, \quad (2.102)$$

$$\begin{cases} hu = q & \text{in } \omega_f \\ 2 \frac{\partial}{\partial x} \left( A^{-\frac{1}{n}} h \left| \frac{\partial u}{\partial x} \right|^{\frac{1}{n}-1} \frac{\partial u}{\partial x} \right) - \rho g \left( 1 - \frac{\rho}{\rho_w} \right) h \frac{\partial h}{\partial x} = 0 & \text{in } \omega_f, \\ 2 A^{-\frac{1}{n}} h \left| \frac{\partial u}{\partial x} \right|^{\frac{1}{n}-1} \frac{\partial u}{\partial x} = \frac{1}{2} \rho \left( 1 - \frac{\rho}{\rho_w} \right) g h^2 & \text{at } x = x_c \end{cases}, \quad (2.103)$$

$$\begin{cases} h_g = h_f & \text{at } x = x_g \\ u_g = u_f & \text{at } x = x_g, \\ \frac{\partial u_g}{\partial x} = \frac{\partial u_f}{\partial x} & \text{at } x = x_g \end{cases}, \quad (2.104)$$

where  $q$  is the constant ice flux. Equation (2.102) can be justified formally based on a dimensional analysis of Equation (2.99). Indeed, Schoof [2007b] has shown, that at the leading order and far from the grounding line, the divergence of the extensional stress is small as compared with basal friction and the gravitational driving stress. Physically, extensional stresses become significant only in a narrow transition zone around the grounding line, in which the ice flow transitioned from a shear-dominated ice flow to an ice flow dominated by extensional stresses. In addition, Schoof [2007b] has shown that the spatial variation of the bedrock topography is small as compared with the spatial variation of the ice thickness. Thus, Equation (2.102) represents the leading-order approximation of Equation (2.99) in the main part of the grounded ice sheet or equivalently the leading-order outer problem. In order to match the solution to the outer problem (Equation (2.102)) with the solution in the ice shelf (Equation (2.103)), a matching condition must be prescribed on the ice flux  $q$  at the grounding line. In Schoof [2007b], this condition is determined by first writing Equations (2.99)–(2.101) in a dimensionless form and then by connecting the solution to the outer problem to the solution in the transition zone (inner problem) by matched asymptotics. Here, we determine directly this condition from the dimensional Equations (2.102) and (2.103) and the transmission conditions in Equation (2.104). Starting from Equation (2.102), the spatial derivative of the velocity in the grounded ice sheet can be expressed as

$$-\rho g \frac{q}{u} \left( -\frac{q}{u^2} \right) \frac{\partial u}{\partial x} - c_b |u|^{p-1} u = 0 \Rightarrow \frac{\partial u}{\partial x} = \frac{c_b}{\rho g} \frac{|u|^{p+3}}{q^2}. \quad (2.105)$$

In the ice shelf, the conservation-of-momentum equation and the boundary condition in Equation (2.103) yield for the spatial derivative of the velocity

$$\frac{\partial u}{\partial x} = \left( \frac{1}{4A^{-\frac{1}{n}} \rho} \left( 1 - \frac{\rho}{\rho_w} \right) g \right)^n h^n. \quad (2.106)$$

Imposing the transmission conditions at the grounding line (Equation (2.104)), that is, imposing the continuity of the derivative of the velocity field at the grounding line, leads to the following analytical formula for the ice flux at the grounding line:

$$q(x_g) = \left( \frac{A(\rho g)^{n+1}}{4^n c_b} \left( 1 - \frac{\rho}{\rho_w} \right)^n \right)^{\frac{1}{p+1}} h^{\frac{n+p+3}{p+1}}(x_g). \quad (2.107)$$

Tsai et al. [2015] derived a similar analytical formula for the ice flux at the grounding line under Coulomb friction condition near the grounding line. Assuming the yield stress to be given by  $\tan \phi (\rho g h + \rho_w g \min(0, b))$  with  $\phi$  the till friction angle, the ice flux at the grounding line satisfies the following analytical formula:

$$q(x_g) = Q_0 \frac{8A(\rho g)^n}{4^n \tan \phi} \left( 1 - \frac{\rho}{\rho_w} \right)^{n-1} h^{n+2}(x_g), \quad (2.108)$$

where  $Q_0 \approx 0.61$  is a numerical coefficient determined from the boundary layer theory.

Besides their interest in understanding the dynamical behaviour of marine ice sheets, the analytical flux formulae in Equations (2.107) and (2.108) provide parameterisations of the effect of the narrow transition zone in large-scale ice-sheet models that do not resolve the transition zone; see, for instance, Pollard and DeConto [2009, 2012a] and Section 6.5.1. For this reason, Equations (2.107) and (2.108) are also referred to as Schoof’s and Tsai’s grounding-line flux parameterisations, respectively.

### 2.5.1.2 Stability of marine ice sheets

The results above suggest that the dynamics of the grounded portion of marine ice sheets in one dimension can be described as a nonlinear diffusion problem with a floatation condition and a flux condition at the grounded line. As such, marine ice sheets are driven towards steady-state (equilibrium) profiles under a time-independent accumulation rate  $a_s$ . Schoof [2007a] showed that marine ice sheets only have a discrete set of steady states and the stability of the steady states depends on the slope of the bedrock at the grounding line. More specifically, Schoof [2012] showed that steady states are linearly unstable if an advance of the grounding line away from its steady state leads to a net mass gain or, mathematically,

$$a_s(x_g) - q'(x_g) > 0, \quad (2.109)$$

where  $q'$  denotes the derivative of the ice flux at the grounding line. Consequently, steady-state grounding lines are linearly unstable on upward sloping beds for which  $q'(x_g) < 0$  or beds that have an insufficient downward slope so that  $0 < q'(x_g) \ll a_s(x_g)$ .

A typical illustration for the stability of marine ice sheets is provided by the so-called overdeepened ice-sheet bed [Schoof, 2007a], where the bed has a central part at a higher elevation followed by a deep trough that leads to a shallower bed at the continental shelf edge. Such a configuration leads to the existence of one, two or three equilibrium positions depending on the values of the model parameters as illustrated in Figures 2.9 and 2.10 for different values of the rheological coefficient  $A$ . Values of the parameters in Figures 2.9 and 2.10 are listed in Table 2.1 and the value of  $\tan \phi$  in Equation (2.108) is chosen such that the parameterisations of the ice flux at the grounding line in Equations (2.107) and (2.108) give the same equilibrium position for  $A = 2.48 \text{ s}^{-1} \text{ Pa}^{-3}$ . In addition, Figure 2.11 illustrates that marine ice sheets can also undergo bifurcations and hysteresis under variations in parameters. Figures 2.9, 2.10, and 2.11 also provide a comparison between Schoof’s grounding-line flux parameterisation in Equation (2.107) and Tsai’s grounding-line flux parameterisation in Equation (2.108). Tsai’s grounding-line flux parameterisation ( $q(x_g) \propto h^5(x_g)$ ) exhibits a greater sensitivity to the ice thickness at the grounding line than Schoof’s grounding-line flux parameterisation ( $q(x_g) \propto h^{4.75}(x_g)$ ). As a result, Tsai’s grounding-line flux parameterisation leads to an increased sensitivity of equilibrium positions to parametric forcing, with downward sloping beds being more stable and upward sloping beds being more unstable [Tsai et al., 2015; Pattyn et al., 2017].

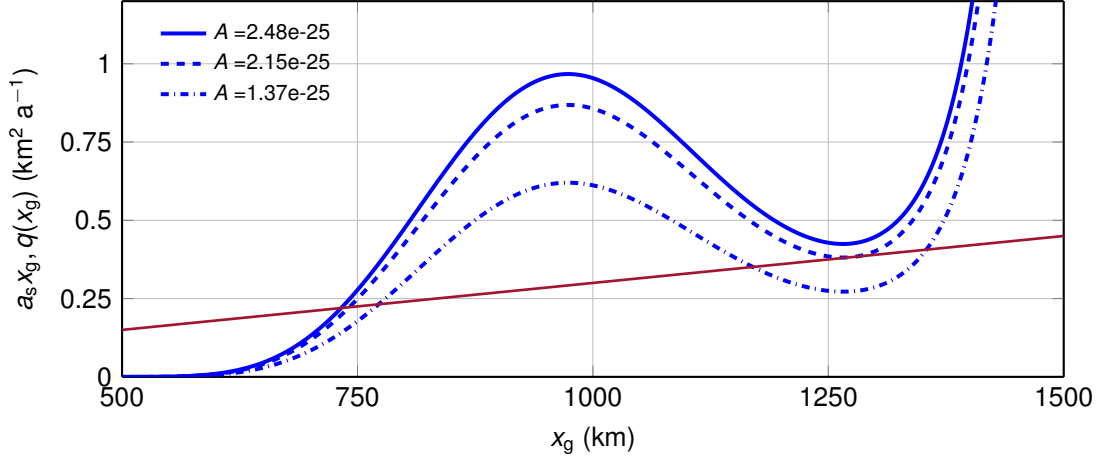


Figure 2.9: Plots of the surface accumulation  $a_s x_g$  and the ice flux  $q(x_g)$  at the grounding line as a function of  $x_g$ . Equilibrium positions of the grounding line are given by the intersection of  $a_s x_g$  with  $q(x_g)$ . Values of the parameter  $A$  ( $\text{s}^{-1} \text{Pa}^{-3}$ ) illustrate the existence of one, two or three equilibrium positions. Results are for Schoof's grounding-line flux parameterisation.

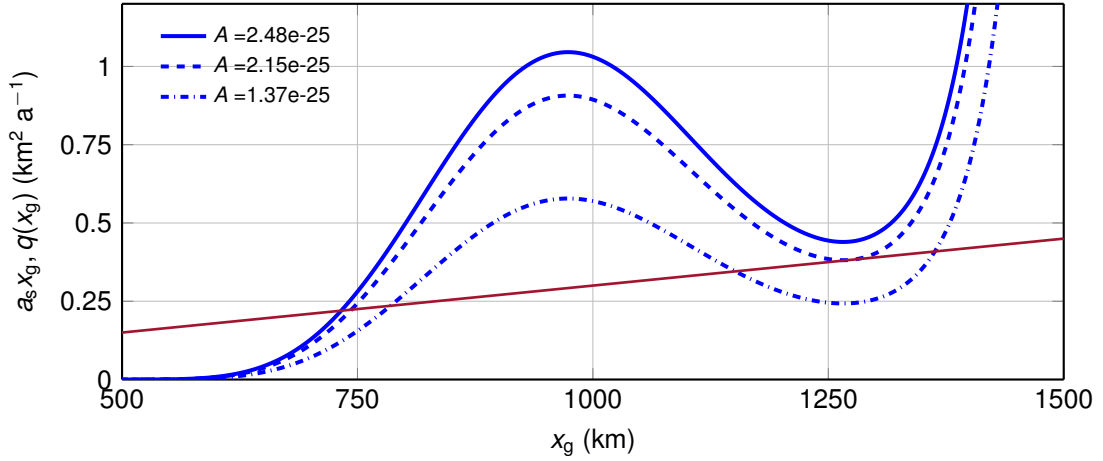


Figure 2.10: Same as Figure 2.9 for Tsai's grounding-line flux parameterisation.

Parameter	Value	Unit
$\rho$	900	$\text{kg m}^{-3}$
$\rho_w$	1000	$\text{kg m}^{-3}$
$g$	9.8	$\text{m s}^{-2}$
$n$	3	
$p$	1/3	
$c_b$	$7.624 \times 10^6$	$\text{Pa m}^{-1/3} \text{s}^{1/3}$
$a_s$	0.3	$\text{m yr}^{-1}$

Table 2.1: List of the parameter values used.

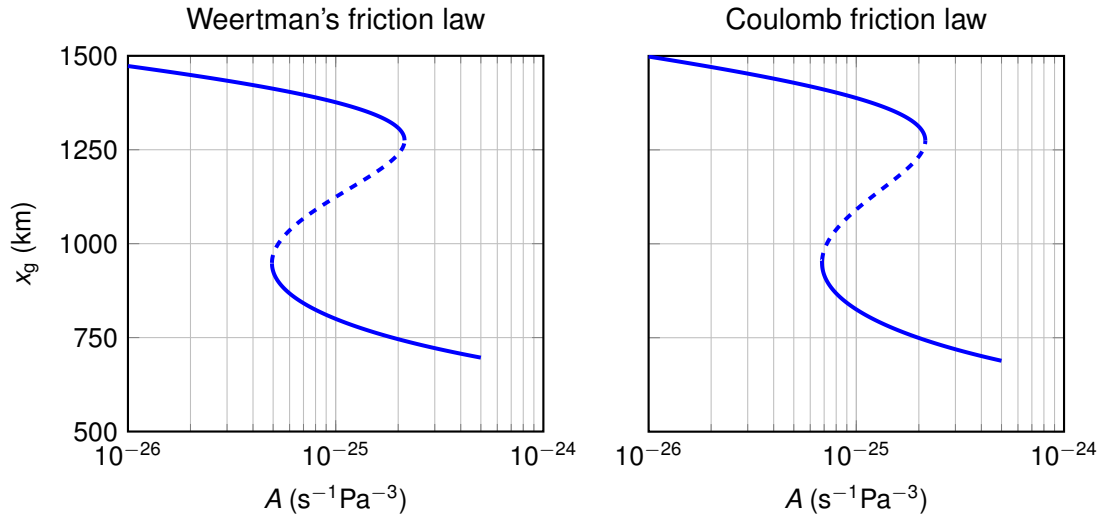


Figure 2.11: Bifurcation diagrams for Weertman’s friction law and Coulomb friction law. Solid lines represent stable equilibrium positions of the grounding line and the dashed line represents unstable equilibrium positions of the grounding line.

### 2.5.1.3 Buttrressing

The ice-sheet model in Equations (2.99)–(2.101) allows to decouple the grounded ice sheet from the ice shelf. Consequently, this model does not account for the impact of ice shelves on the stability of marine ice sheets. However, the lateral confinement of ice shelves in embayments leads to lateral shear stresses that impede the seaward flow of the upstream ice. Bathymetric features on the sea floor, such as ice-shelf pinning points, also provide back stress that impedes the seaward flow of the upstream ice [Favier et al., 2011; Berger et al., 2016; Favier et al., 2016]. The effect of bathymetric features and confined embayments on the ice flow is known as “buttrressing” and can lead to a stabilisation of the ice sheet or a slowdown of grounding-line retreat rates. For this reason, reduction or loss of ice-shelf buttrressing due to the thinning or collapse of ice shelves leads to reduced back stress, thus promoting grounding-line instability or an acceleration in grounding-line retreat.

### 2.5.1.4 Local sea level and glacial isostatic adjustment

The onset and persistence of MISI also depend on the local sea level and glacial isostatic adjustment. Post-glacial rebound leads to a local uplift of the bedrock due to ice-sheet thinning, thus decreasing ice thickness at the grounding line and promoting marine ice-sheet stability. In addition, post-glacial rebound leads to a local drop in sea level near the grounding line as the sea water migrates away from the ice sheet because of reduced gravitational attraction, thus decreasing water depth at the grounding line and promoting marine ice-sheet stability. Both mechanisms thus provide a negative feedback that can mitigate the MISI mechanism. We refer the reader to, for instance, Adhikari et al. [2014] and Gomez et al. [2010, 2013, 2015], for further discussions about the impact of local sea level and glacial isostatic adjustment on the stability of marine ice sheets.

### 2.5.2 Marine ice-cliff instability

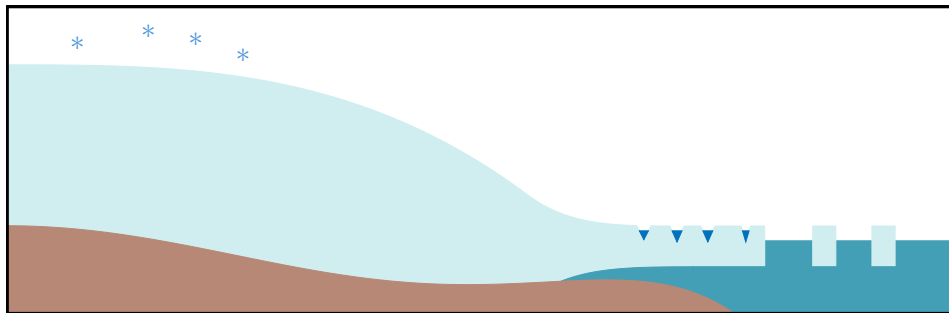
The marine ice-cliff instability mechanism (MICI) has been recently proposed to explain high eustatic sea levels (5 to more than 20 metres higher than today) during the Pliocene epoch (2.5 to 5.2 million years ago) [Pollard et al., 2015]. Previous ice-sheet simulations accounting only for MISI were not able to reproduce high eustatic sea levels over the past million years [Pollard and DeConto, 2009]. In particular, these simulations were not able to initiate the major retreat of marine basins in East Antarctica required to reproduce these high eustatic sea levels. On the contrary, Pollard et al. [2015] showed that MICI had the potential to accelerate the collapse of the West Antarctic ice sheet within a few decades and to trigger a major retreat in major marine basins in East Antarctica within a few thousand years. In a recent study, DeConto and Pollard [2016] carried out simulations of the Antarctic ice sheet over the next centuries based on a computational ice-sheet model that accounts for MICI. They showed that MICI had the potential to trigger substantial ice loss in Antarctica over the next centuries, thus leading to sea-level rise projections much higher than projections that do not account for MICI.

Figure 2.12 depicts schematically the marine ice-cliff instability mechanism. The MICI mechanism hypothesises that ice cliffs higher than approximately 90 m above sea level become unstable because shear stresses at the ice front due to the unbalanced overburden of ice above exceed the yield strength of ice. This causes ice cliffs higher than approximately 90 m above sea level to disintegrate completely or to stabilise in some shape where the ice cliff does not exceed the critical thickness. Contrary to MISI, MICI can occur on downward sloping beds but requires an a priori collapse of ice shelves. Such a collapse of ice shelves can be initiated by sub-shelf melting or hydrofracturing due to surface melt draining into crevasses.

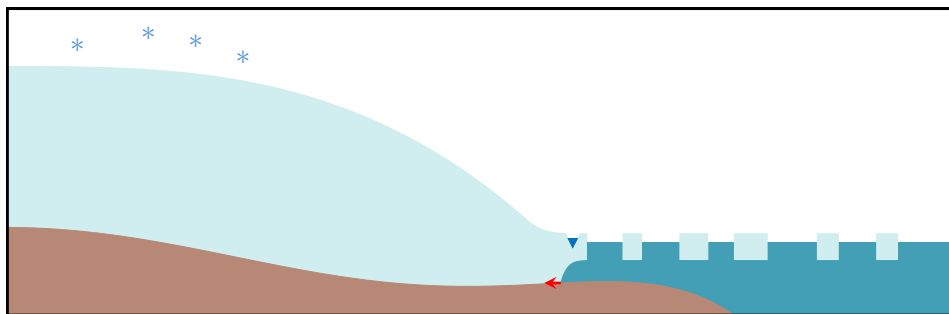
## 2.6 Chapter summary

In this chapter, we presented a brief overview of the physics of ice sheets. We described the evolution of ice sheets as a free-boundary problem for the gravity-driven creep flow of an incompressible, nonlinearly viscous, and heat conducting fluid. Full-order ice-sheet models take the form of a coupled system of conservation-of-mass, conservation-of-momentum, and conservation-of-energy equations supplemented with boundary conditions that take into account the interactions of the ice sheet with its surrounding physical environment, for instance, friction at the ice-bedrock interface, snow accumulation at the ice-air interface, sub-shelf melting at the ice-ocean interface, and calving at the ice front. As a consequence of the shallowness of ice sheets, reduced-order models of the physics of ice sheets can be derived as approximations of full-order ice-sheet models as the aspect ratio of the ice sheet tends to zero. This leads to the shallow-ice approximation (SIA) and the shallow-shelf approximation (SSA) which represent ice-sheet flow in slow and fast mechanical scaling regimes, respectively. For this reason, the SIA reduced-order provides an approximation for the ice flow in interior parts of ice sheets and the SSA reduced-order provides an approximation for the ice flow in (fast-flowing) ice streams and ice shelves. Finally, we reviewed two instability mechanisms, namely the marine ice-sheet instability (MISI) and marine ice-cliff instability (MICI) mechanisms, that could destabilise or accelerate the retreat of the grounding line in marine ice sheets.

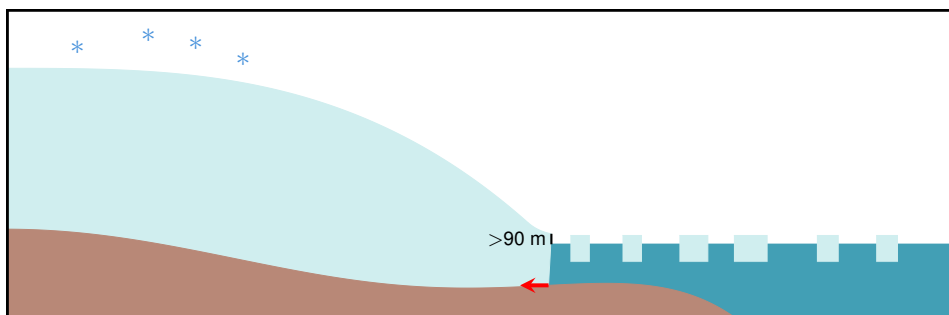
## Step 1: Hydrofracturing weakens ice shelf



## Step 2: Collapse of ice shelf due to hydrofracturing



## Step 3: Unstable ice cliff (structural failure)



## Step 4: Ice-cliff disintegration triggers MICI

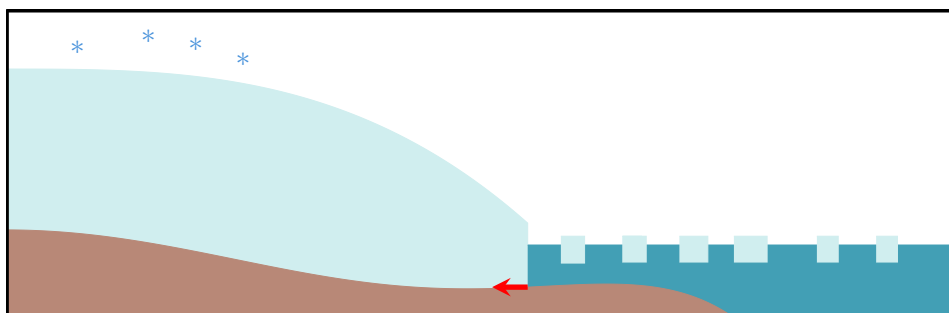


Figure 2.12: Schematic illustration of the marine ice-cliff instability mechanism driven by hydrofracturing.



# 3

## The Antarctic ice sheet: Present, future, and challenges

*This chapter provides an overview about the current state of the Antarctic ice sheet, its future, and the challenges in predicting the contribution of the Antarctic ice sheet to future sea-level rise. After introducing the main geographical characteristics of the Antarctic ice sheet, we discuss its surface mass balance and the mechanisms that drive the ice dynamics in the Antarctic ice sheet. Next, we present an overview of the mass balance of the Antarctic ice sheet over the recent decades. Then, we describe mechanisms that will drive the future response of the Antarctic ice sheet under climate warming. Finally, we discuss challenges associated with the assessment of the future response of the Antarctic ice sheet based on computational ice-sheet models.*

### 3.1 The Antarctic ice-sheet in a nutshell

The Antarctic ice sheet (AIS) covers 8.3% of the global land surface [Vaughan et al., 2013]. It is usually divided geographically into the West Antarctic ice sheet (WAIS), the East Antarctic ice sheet (EAIS), and to a lesser extent the Antarctic Peninsula (AP); see Figure 3.1. West Antarctica is separated from East Antarctica by the Transantarctic Mountains. The topography of the Antarctic ice sheet is characterised by a substantial fraction of the ice sheet that rests on a bedrock hundreds of metres (or more) below sea level, with places where the bedrock slopes down towards the interior of the ice sheet. West Antarctica has its bedrock mostly below sea level while certain major glaciers in East Antarctica, such as glaciers in the Wilkes and Aurora catchment basins, are also grounded below sea level.

The surface mass balance (SMB) of the Antarctic ice sheet is dominated by snow precipitation, which contributes 91% of the sum of the absolute fluxes involved in the surface mass balance [Van Wessem et al., 2014, 2018; Lenaerts et al., 2016]. Snow precipitation varies widely over Antarctica with accumulation rates of a few metres per year in the Antarctic Peninsula, a few tenths of metres per year in West Antarctica, and a few centimetres per year in the interior of the East Antarctic ice sheet. Surface melt is mostly confined to coastal margins of the ice sheet and ice shelves, where it can lead to ice-shelf hydrofracturing. The highest surface melt

rates are found especially in the Antarctic Peninsula. The highest sublimation rates are mostly found in coastal East Antarctica due to strong winds and dry air. The contribution of meltwater runoff to the surface mass balance is negligible even though runoff can be significant locally, for instance, in ice shelves.

Ice dynamics in the Antarctic ice sheet is controlled by the motion of fast-flowing ice streams, which drain about 90 % of the total AIS ice flux [Bennett, 2003] (Figure 3.2). Due to the bedrock topography in Antarctica, most ice streams extend into the ocean as floating ice shelves and subsequently lose ice through sub-shelf melting and calving. Estimates of net mass loss due to iceberg calving is comparable in magnitude to net mass loss due to sub-shelf melting [Depoorter et al., 2013; Rignot et al., 2013; Liu et al., 2015]. Calving is responsible for most of the mass loss of the two largest ice shelves, the Filchner–Ronne and Ross ice shelves, while sub-shelf melting is responsible for most of the mass loss of marine glaciers in the Bellingshausen Sea and Amundsen Sea sectors. The highest basal melt rates are also found in the Bellingshausen Sea and Amundsen Sea sectors, especially underneath the Pine Island and Thwaites Glaciers while the lowest basal melt rates are found underneath the Filchner–Ronne and Ross ice shelves, on which refreezing can also occur.

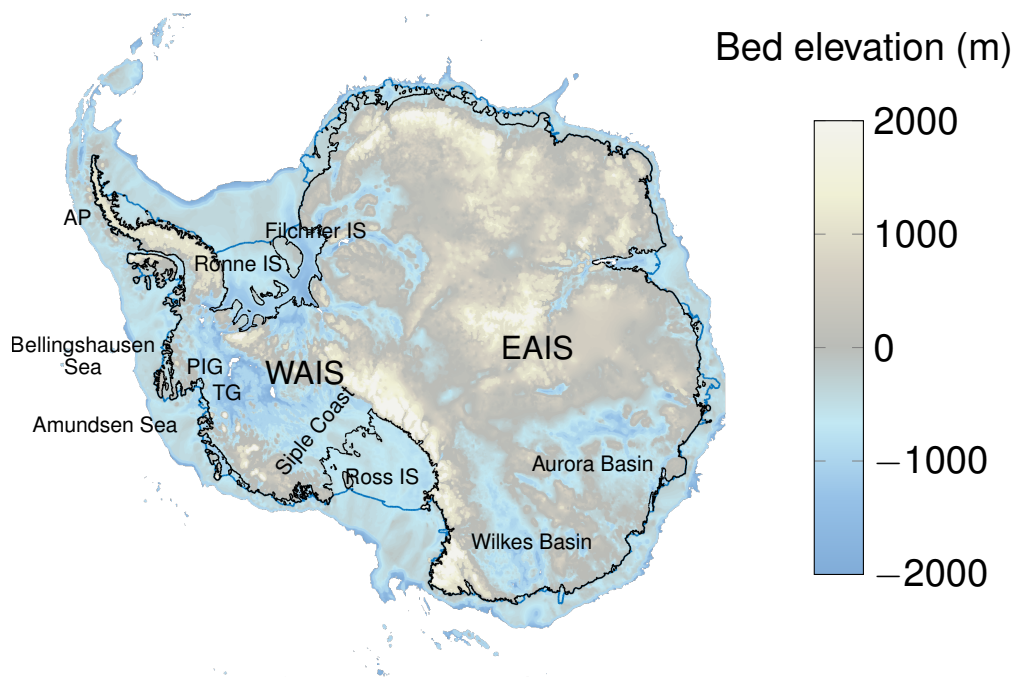


Figure 3.1: Present-day Antarctic bedrock topography [Morlighem et al., 2019] with characteristic geographical regions. WAIS stands for West Antarctic ice sheet, EAIS for East Antarctic ice sheet, AP for Antarctic Peninsula, IS for ice shelf, TG for Thwaites Glacier and PIG for Pine Island Glacier. The grounding line is shown in black and the ice front is shown in blue.

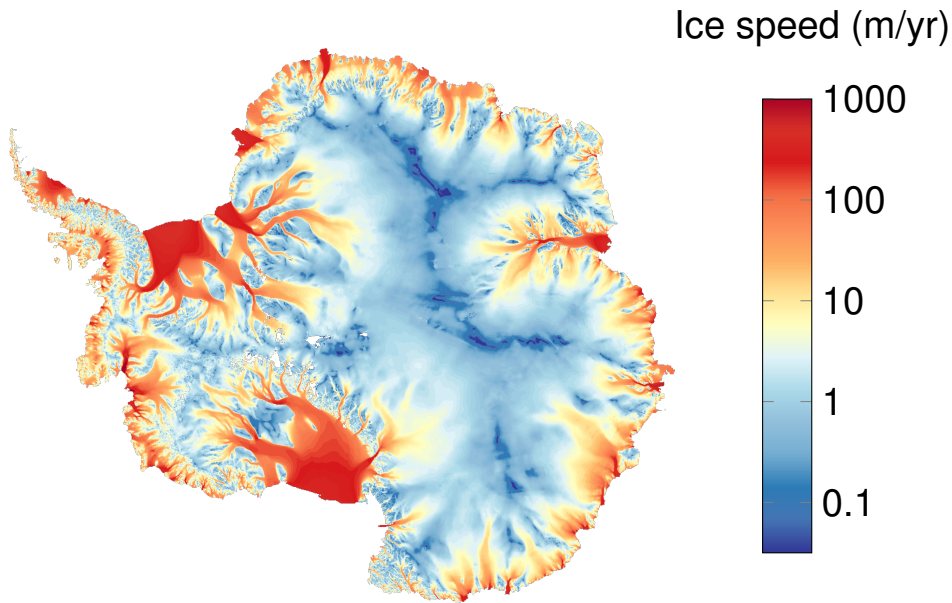


Figure 3.2: Surface ice speed assembled from satellite data acquired between 2007 and 2009 [Rignot et al., 2011].

### 3.2 Mass balance of the Antarctic ice sheet

We provide a short section about the mass balance of the Antarctic ice sheet over the recent decades as an overview of the recent response of the Antarctic ice sheet. We refer the reader to, for instance, Zwally et al. [2015], Martín-Español et al. [2016], Bamber et al. [2018], Gardner et al. [2018], Pattyn et al. [2018], Shepherd et al. [2018], IPCC [2019], Rignot et al. [2019], and Hanna et al. [2020] for additional information and further discussions about the mass balance of the Antarctic ice sheet.

The mass balance of the Antarctic ice sheet is determined by the difference between the surface mass balance and the ice discharge through the grounding line. Because the global surface mass balance of the Antarctic ice sheet is positive (snowfall exceeds surface melt and sublimation), ice discharge through the grounding line and subsequent sub-shelf melting and calving are responsible for the net mass loss of the Antarctic ice sheet. Though sub-shelf melting and calving do not enter directly in the mass balance of the Antarctic ice sheet, both processes modulate the buttressing induced by ice shelves through ice-shelf thinning and break-up. Estimates of the mass balance of the Antarctic ice sheet over the period 1992–2017 indicate continued mass losses from the Antarctic ice sheet over this period, with accelerated mass loss in recent years; see Tables 3.1 and 3.2. Recent work agrees on significant and steadily growing mass losses from the West Antarctic ice sheet and the Antarctic Peninsula over the period 1992–2017, with mass losses from the West Antarctic ice sheet several times larger than mass losses from the East Antarctic ice sheet and the Antarctic Peninsula over the period 2011–2017 [Bamber et al., 2018; Shepherd et al., 2018; Larour et al., 2019]. Estimates of the mass balance of the East Antarctic ice sheet are still subject to high uncertainties. Shepherd et al. [2018] found that the East Antarctic ice sheet was close to balance over the last 25 years, with mass gain over the period 1992–2012 and mass loss over the period 2012–2017. On the other hand, Rignot et al. [2019]

found a significant mass loss of  $57 \pm 2 \text{ Gt yr}^{-1}$  in East Antarctica over the period 1992–2017, while Zwally et al. [2015] found a significant mass gain of  $136 \text{ Gt yr}^{-1}$  in East Antarctica over the period 1992–2008 due to dynamic ice thickening caused by increased snow accumulation since the early Holocene.

The acceleration in the mass loss of the Antarctic ice sheet is primarily caused by increased ice discharge across the grounding lines of marine glaciers in the Bellingshausen and Amundsen Sea sectors, including the Pine Island and Thwaites Glaciers, while observations found no long-term trend in snowfall accumulation [Shepherd et al., 2018]. This increased ice discharge has been attributed to a loss of ice-shelf buttressing caused by increased ice-shelf melt rates due to increased sub-shelf ocean circulation driven by atmospheric and ocean changes.

	1992–1996	1997–2001	2002–2006	2007–2011	2012–2016
EAIS	$28 \pm 76$	$-50 \pm 76$	$52 \pm 37$	$80 \pm 17$	$-19 \pm 20$
WAIS + AP	$-55 \pm 30$	$-53 \pm 30$	$-77 \pm 17$	$-197 \pm 11$	$-172 \pm 27$
AIS	$-27 \pm 82$	$-103 \pm 82$	$-25 \pm 41$	$-117 \pm 20$	$-191 \pm 34$

Table 3.1: Estimates from Bamber et al. [2018] of pentad mass-balance rates ( $\text{Gt yr}^{-1}$ ) for the East Antarctic ice sheet, the West Antarctic ice sheet with the Antarctic Peninsula, and the Antarctic ice sheet over various periods. Errors are  $1\sigma$ .

	1992–1997	1997–2002	2002–2007	2007–2012	2012–2017
EAIS	$11 \pm 58$	$8 \pm 56$	$12 \pm 43$	$23 \pm 38$	$-28 \pm 30$
WAIS	$-53 \pm 29$	$-41 \pm 28$	$-65 \pm 27$	$-148 \pm 27$	$-159 \pm 26$
AP	$-7 \pm 13$	$-6 \pm 13$	$-20 \pm 15$	$-35 \pm 17$	$-33 \pm 16$
AIS	$-49 \pm 67$	$-38 \pm 64$	$-73 \pm 53$	$-160 \pm 50$	$-218 \pm 43$

Table 3.2: Estimates from Shepherd et al. [2018] of pentad mass-balance rates ( $\text{Gt yr}^{-1}$ ) for the East Antarctic ice sheet, the West Antarctic ice sheet, the Antarctic Peninsula, and the Antarctic ice sheet over various periods. Errors are  $1\sigma$ .

### 3.3 The future of the Antarctic ice sheet under climate change

This section reviews key processes that will drive the response of the Antarctic ice sheet under climate change.

#### 3.3.1 Risk of MISI

One of the key concerns about the behaviour of the Antarctic ice sheet is the vulnerability of marine sectors to dramatic and rapid loss of ice due to the onset of an irreversible marine ice sheet instability. The West Antarctic ice sheet, and in particular the Amundsen Sea sector, is particularly at risk for such an instability mechanism given its bedrock topography which is mostly below sea level and slopes downwards towards the interior of the ice sheet. Pine Island Glacier underwent a sustained retreat, which has been attributed to MISI [Favier et al., 2014;

Mouginot et al., 2014], up to 2010 before stabilising since 2010 after reaching an “ice plain” [Park et al., 2013]. Both observations [Rignot et al., 2014; Christianson et al., 2016] and numerical models [Joughin et al., 2014; Seroussi et al., 2017; Yu et al., 2018] suggest that Thwaites Glacier is undergoing a marine ice-sheet instability that could lead to a significant contribution to sea-level rise in the next decades and centuries, thus rendering the estimation of the rate of retreat of Thwaites Glacier and the importance of this retreat a top priority for Antarctic research [Scambos et al., 2017]. Unlike Pine Island Glacier, Thwaites Glacier is not confined to a deep trough with rough basal topography. Observations have shown that its grounding line retreats along clear retrograde pathways [Rignot et al., 2014], with little opportunity for stabilisation from ice-shelf buttressing [Parizek et al., 2013]. Marine basins in East Antarctica are also at risk for MISI even though marine basins in East Antarctica seem more stable than marine basins in West Antarctica due in particular to present-day grounding lines lying on shallower and narrower sills, greater ice-shelf buttressing in narrower embayments, and frozen or stiffer beds.

Marine glaciers in West Antarctica, for instance Thwaites Glacier, subject to MISI have the potential to destabilise adjacent basins and ultimately trigger a dramatic collapse of the West Antarctic ice sheet. This raises concerns about the existence of a tipping point for the West Antarctic ice sheet [Lenton et al., 2008] and the Antarctic ice sheet more generally. The risk of a tipping point suggests the existence of a critical threshold beyond which the Antarctic ice sheet can undergo rapid, abrupt, and irreversible changes. Pattyn et al. [2018] have suggested that a key threshold for the stability of ice shelves, and thus the stability of the ice sheet, lies between 1.5 and 2 °C mean annual air temperature above present while large systems, such as the Ross and Filcher–Ronne drainage basins, might be activated by an increase of mean annual air temperature between 2 and 2.7 °C; see also IPCC [2018] for further discussion about the need to limit climate warming to well below 2 °C to avoid tipping points. It should be mentioned, however, that great challenges remain in representing and detecting tipping points in complex models [Bathiany et al., 2016].

### 3.3.2 Risk of MICI

Hydrofracturing and large ice-cliff failure (MICI) were initially proposed by Pollard et al. [2015] as additional physical processes required to trigger a significant retreat of marine basins in East Antarctica in order to reproduce high eustatic sea levels (5 to more than 20 m above present eustatic sea level) during the Pliocene epoch. DeConto and Pollard [2016] account for both mechanisms in future projections of the AIS contribution to sea-level rise. Hydrofracturing and large ice-cliff failure have the potential to raise sea level faster than MISI and trigger a retreat of marine basins in West Antarctica and, more importantly, East Antarctica under lower atmospheric and oceanic forcings than MISI. Including hydrofracturing and large ice-cliff failure in ice-sheet models thus leads to high-end probabilistic projections [Le Bars et al., 2017; Kopp et al., 2017; Stammer et al., 2019], with differences that can reach several metres when compared with ice-sheet models that do not include these mechanisms.

The validity of MICI is still debated in the scientific community, with only limited observational evidence for MICI in the past [Wise et al., 2017]. Recently, Ma et al. [2017] have provided new insight into bounds on the ice-cliff height of calving glaciers in Greenland and

Parizek et al. [2019] have proposed the so-called retrogressive slumping mechanism that could lead to ice-cliff failure for calving glaciers in Greenland; yet calving glaciers in Greenland may not be representative of marine basins in Antarctica. In addition, Edwards et al. [2019] have recently shown that MICI was not required to reproduce high eustatic sea levels in the past. Thus, MICI is characterised by deep uncertainty and little is known on how mechanisms such as glacial isostatic adjustment or refreezing of meltwater in firn may prevent or mitigate MICI.

### 3.3.3 Ice-air interactions

Atmospheric warming is expected to lead to an increase in surface mass balance driven by increased snowfall, which is partially counteracted by increased surface melt and runoff [Ligtenberg et al., 2013; Frieler et al., 2015; Lenaerts et al., 2016], thus leading to mass gain and mitigation of the AIS net mass loss. Increased precipitation is expected mostly in East Antarctica, while increased surface melt and runoff will take place preferentially in the Antarctic Peninsula, West Antarctica, and ice shelves. The increase in surface mass balance, and in both snowfall and surface melt more specifically, is strongly positively correlated with an increase in AIS mean air surface temperature [Ligtenberg et al., 2013; Trusel et al., 2015; Lenaerts et al., 2016], with the latter being impacted by natural and anthropogenic greenhouse gas emissions. Using only CMIP5 models that best agree with CloudSat-observed Antarctic data, Palerme et al. [2017] assessed on average a 7.4 %/°C precipitation increase with surface temperature warming. Surface melt is expected to double by 2050, independently of the atmospheric forcing scenario, and thereafter to exhibit significant divergence depending on the atmospheric forcing scenario, with surface melt intensities by 2100 under high atmospheric forcing scenarios that may lead to a disintegration of ice shelves [Trusel et al., 2015].

Lenaerts et al. [2016] identified three mechanisms responsible for the future surface mass balance of the Antarctic ice sheet: (1) the increase in evaporation of ocean water intensified by strong sea-ice decline, (2) the increase in the moisture-carrying capacity of the atmosphere, and (3) changes in the characteristics and frequency of Antarctic clouds. Bell et al. [2018] identified three primary modes by which surface melt could impact the mass balance of the Antarctic ice sheet: (1) increased surface runoff leading to ice-sheet thinning, (2) meltwater injection to the bed leading to increased basal sliding and increased melting at calving fronts, and (3) meltwater-induced ice-shelf fracture through hydrofracturing and ice-shelf bending leading to ice-shelf weakening and potential collapse. The activation of each of these modes and their location will control the future contribution of the Antarctic ice sheet to sea-level rise. Nonetheless, refreezing of meltwater in ice shelves [Kuipers Munneke et al., 2014; Hubbard et al., 2016] is expected to delay or prevent meltwater runoff [Ligtenberg et al., 2013], while surface drainage networks on ice shelves might prevent meltwater from destabilising the ice shelves [Bell et al., 2017].

### 3.3.4 Ice-ocean interactions

Changes in ice shelves alter their buttressing capability to restrain the ice discharge across grounding lines. In particular, sub-shelf melting is responsible for ice-shelf thinning, thus increasing the risk of mechanical weakening and fracturing and loss of contact with pinning points. This loss of buttressing may eventually destabilise marine basins due to MISI. The magnitude of

sub-shelf melt rates is determined by the strength of the heat flux entering ice-shelf cavities and the freezing point of seawater, which depends on ocean salinity and water pressure. Large ice shelves, such as the Ross and Filchner–Ronne ice shelves, experience low sub-shelf melt rates due to the intrusion of cold and dense shelf water into ice-shelf cavities. By contrast, ice-shelves in the Bellingshausen and Amundsen Sea sectors and near Totten glacier experience high sub-shelf melt rates driven by the intrusion of relatively warm Circumpolar Deep Water (CDW) into ice-shelf cavities [Schmidtko et al., 2014]. Differences in melting underneath ice shelves around the Antarctic ice sheet are typical of different modes of sub-shelf melting discussed in, for instance, Jacobs et al. [1992], Dinniman et al. [2016], and Silvano et al. [2016].

Climate warming is expected to intensify sub-shelf melting as a result of ocean warming in ice-shelf cavities [Timmermann and Hellmer, 2013; Naughten et al., 2018]. Naughten et al. [2018] identified two main mechanisms leading to ocean warming in ice-shelf cavities: (1) atmospheric warming that leads to a decline in sea-ice cover, which results in a warming of surface water that can subduct beneath ice shelves and (2) increased presence of CDW into ice-shelf cavities. Furthermore, climate variability and wind conditions can also impact sub-shelf melt rates; see, for instance, Dinniman et al. [2012], Dutrieux et al. [2014], and Greene et al. [2017]. Based on the CMIP5 scenarios, Naughten et al. [2018] projected an increase between 41 % and 129 % of the average total sub-shelf mass loss from all Antarctic ice shelves for the period 2091–2099 when compared to the period 1996–2005. The Amundsen Sea sector is expected to experience the largest increase in sub-shelf melting, followed by the Bellingshausen Sea sector, while the Ross ice shelf is expected to experience the lowest increase in sub-shelf melting. Increased melt rates in the Amundsen and Bellingshausen Sea sectors will be driven by a strengthening of the CDW in ice-shelf cavities while increased melt rates in Ross Sea will result from atmospheric warming.

Sub-shelf melting will also modify ocean conditions via the input of freshwater in the ocean. Input of freshwater in the Southern Ocean is expected to result in surface freshening and subsequently to increase the formation of sea ice [Bronse laer et al., 2018; Purich et al., 2018]. In addition, recent studies suggest that the input of freshwater in the ocean will trap warm water below sea surface, thus resulting in ocean warming and increased melt rates near the grounding line [Bronse laer et al., 2018; Silvano et al., 2018; Golledge et al., 2019]. This mechanism may result in a positive feedback that could increase the mass loss from the Antarctic ice sheet [Golledge et al., 2019].

### 3.3.5 Bedrock topography and glacial isostatic adjustment

The risk of MISI in marine basins will be controlled by ice-shelf buttressing and bedrock topography. Topographic features, such as pinning points [Favier et al., 2011, 2016; Berger et al., 2016] and ice rises and rumples [Favier and Pattyn, 2015; Matsuoka et al., 2015], have the potential to stabilise marine basins or at least to slow grounding-line retreat rates. Topographic features, such as cavity shape, bedrock slope, bumps, and hollows, also influence the access of ocean heat to the grounding line and sub-shelf melt rates [Milillo et al., 2019].

The isostatic uplift of the bedrock following the ice-sheet retreat is expected to have a stabilising effect on the grounding line due to a flattening of the reverse bedrock slope and a reduction

of the local sea depth; see, for instance, [Whitehouse et al. \[2019\]](#) for a recent review paper about solid Earth change and the evolution of the Antarctic ice sheet. This negative feedback is expected to mitigate the positive feedback of the marine ice-sheet instability on the migration of the grounding line [[Adhikari et al., 2014](#); [Gomez et al., 2015](#); [Konrad et al., 2015](#); [Pollard et al., 2017](#)] and could even lead to a re-advance of the grounding line in some areas of the Antarctic ice sheet [[Kingslake et al., 2018](#)] even though the impact of isostatic uplift may become significant only on multicentennial and longer time horizons. GPS measurements have shown that the Amundsen Sea sector undergoes a rapid isostatic uplift due to the low viscosity of the underlying mantle and short bedrock relaxation times that could range from tens to hundreds of years [[Barletta et al., 2018](#)]. Short-wavelength (kilometre-scale resolution) uplift in active areas of Antarctica such as Thwaites Glacier could lead to a significant slowdown in Antarctic mass loss over the next centuries [[Larour et al., 2019](#)]. Numerical simulations by [Adhikari et al. \[2014\]](#) further suggest that the Antarctic bedrock may rise from a few metres to a few tens of metres in the next centuries.

In addition, the MICI mechanism is also controlled by bedrock topography and local sea depth [[Pollard et al., 2015](#)], with the instability occurring preferentially in marine basins with sufficiently deep bedrocks while shallow topography provides stabilising conditions. For this reason, the isostatic uplift of the bedrock is also expected to mitigate or prevent the marine ice-cliff instability [[Gasson et al., 2015](#)].

### 3.4 Computational ice-sheet models: limitations for sea-level rise projections

Computational ice-sheet models form the basis for quantitative projections of the response of the Antarctic ice sheet to climate change. Much progress has been made in recent years regarding the comprehension of physical processes involved in the dynamics of the Antarctic ice sheet and their implementation in computational ice-sheet models; see, for instance, [Pattyn et al. \[2017\]](#) and [Nowicki and Seroussi \[2018\]](#) for recent review papers. Yet, there remain large limitations that restrict the accuracy and robustness of these projections. Hereafter, we briefly review some of these limitations, namely the initialisation of the ice-sheet model, limitations in coupling the computational ice-sheet model with other components of the Earth system, and uncertainties in computational ice-sheet models. We refer the reader to, for instance, [Vizcaino \[2014\]](#), [Goelzer et al. \[2017\]](#), [Pattyn et al. \[2017\]](#), and [Nowicki and Seroussi \[2018\]](#) for further discussions about limitations, challenges, and progress in ice-sheet modelling.

#### 3.4.1 Ice-sheet model initialisation

Forward simulations with computational ice-sheet models require an initialisation procedure that precedes their use in predicting climate-change effects. The initial state of an ice sheet at present is typically defined by the ice temperature, the velocity field, the ice-sheet geometry, and the bedrock elevation. Boundary conditions at the ice-bedrock interface and the rheological properties of the ice must also be prescribed as part of the initialisation of the ice-sheet model. Computational ice-sheet models essentially rely on two kinds of initialisation methods, namely the so-called “spin-up” methods and data assimilation methods.

Spin-up methods, originally applied for paleoclimate simulations, aims at defining an initial state in which the state variables, such as the ice temperature, the ice thickness, the velocity field, and the bedrock elevation, are mutually consistent, for instance, the ice temperature is in equilibrium with the stress regime and the bedrock elevation is in equilibrium with the ice-sheet loading. In spin-up approaches, the computational ice-sheet model is run over paleoclimate time periods (typically tens to hundreds of thousands of years) and is forced with a paleoclimate forcing that reproduces the evolution of the climate over this paleoclimate time period; see, for instance, [Aschwanden et al. \[2013\]](#), [Bindshadler et al. \[2013\]](#), and [Saito et al. \[2016\]](#). Spin-up methods yield an ice-sheet configuration at present close to steady state but they generally lead to a simulated ice-sheet configuration far from the present-day ice-sheet configuration and they do not allow to reproduce current trends of mass loss in ice sheets.

Data assimilation methods aims at inferring unknown boundary conditions at the ice-bedrock interface, more specifically the unknown basal friction coefficient, or rheological properties of the ice, typically a flow enhancement factor introduced to account for anisotropy of ice flow. Data assimilation methods usually rely on inverse methods that seek to infer unknown fields through minimisation of the misfit between predicted ice-sheet state variables, usually the velocity field, with observations; see, for instance, [Morlighem et al. \[2010, 2013\]](#), [Petra et al. \[2012\]](#), [Perego et al. \[2014\]](#), and [Isaac et al. \[2015\]](#). Data assimilation methods usually provide a better match between simulated state variables and observations than spin-up methods even though simulated state variables may not be mutually consistent and may not reproduce the past history of the ice sheet.

It should be noted that combinations of spin-up and data assimilation methods exist and that these combined methods can help to alleviate the drawbacks of spin-up and data assimilation methods. An example of a combined method is the fixed-point iteration scheme by [Pollard and DeConto \[2012b\]](#), in which at each iteration the computational method is run over a long period of time until a steady-state configuration is reached and the basal friction coefficient is adjusted so that the thus obtained steady-state configuration matches the present-day ice-sheet configuration.

Despite much progress in recent years [[Goelzer et al., 2017](#); [Pattyn et al., 2017](#)], model initialisation still remains a major limitation for robust predictions of the AIS response to climate change based on computational ice-sheet models. The ISMIP6 intercomparison project has recently provided insight into the impact of model initialisation in computational ice-sheet models and has shown large spreads in projections from different computational ice-sheet models initialised with different methods [[Goelzer et al., 2018](#); [Seroussi et al., 2019](#)].

### 3.4.2 Coupling with other components of the Earth system

Computational ice-sheet models should ideally be coupled with computational models of other components of the Earth system, such as the atmosphere, the ocean, and the bedrock, in order to appropriately represent the interactions and feedbacks between the Antarctic ice sheet and these components. So far, there have been limited attempts to couple computational ice-sheet models with computational models of other components of the Earth system due in particular to the high computational cost of most climate, ocean, and Earth models and differences in spatial

and temporal resolutions between the different components of the Earth system, thus generally requiring asynchronous coupling and appropriate downscaling techniques. We refer the reader to, for instance, [Pollard et al. \[2017\]](#), [Le clec'h et al. \[2019\]](#), [Favier et al. \[2019\]](#), and [Van Kampenhout et al. \[2019\]](#) for recent papers concerned with the coupling of computational ice-sheet models with other components of the Earth system.

Owing to challenges in coupling computational ice-sheet models with computational models of other components of the Earth system, interactions between the Antarctic ice sheet and its environment are often prescribed in a parameterised way. While allowing for a direct representation of the interactions between the ice sheet and its environment, these parameterisations may suffer from limitations in the representation of physical processes and involve a set of free parameters that need to be identified prior to running the computational ice-sheet model.

### 3.4.3 Uncertainties in computational ice-sheet models

In the field of uncertainty quantification, uncertainties in computational models are often classified as either input uncertainties or model uncertainties [[Smith, 2014](#)]. Physics-based computational models result from a mathematical-physical modelling process of a real-world system. Such computational models usually involve the specification of input parameters, external forcings, initial conditions, or boundary conditions, all which can be uncertain. The uncertainties on these quantities then define the input uncertainties. On the other side, modelling errors induced by the modelling process define the model uncertainties, also called structural uncertainties. Computational ice-sheet models, which result from a mathematical-physical modelling process of an ice-sheet system, are also affected by modelling and input uncertainties which limit their ability to provide reliable and robust projections. In the following, we briefly discuss modelling and input uncertainties in computational ice-sheet models.

#### 3.4.3.1 Model uncertainties

Model uncertainties in computational ice-sheet models encompass discrepancies in physics between computational ice-sheet models and the real-world ice-sheet system due to approximate or imprecise mathematical representation and numerical implementation of the underlying physics of ice sheets, and, to a lesser extent, numerical errors due to numerical approximations and discretisation errors. For instance, computational ice-sheet models can implement the Stokes equations or a reduced-order approximation of the ice-sheet flow or they can be discretised using a finite-difference or a finite-element discretisation scheme. Computational ice-sheet models also come with parameterisations that provide a simplified or heuristic representation of complex physical processes that are not resolved by the computational model. For the Antarctic ice sheet, a major source of uncertainty also comes from the numerical representation of the migration of grounding line.

Model uncertainties are generally difficult to quantify. The impact of model uncertainties on the projections is usually assessed by comparing projections from different models on benchmark experiments; see, for instance, [Pattyn et al. \[2012, 2013\]](#), [Bindshadler et al. \[2013\]](#), [Nowicki et al. \[2016\]](#), and [Seroussi et al. \[2019\]](#). These so-called intercomparison (or multi-model comparison) projects give some insight into the impact of model uncertainties although challenges remain in combining the different results [[Knutti et al., 2010](#)].

### 3.4.3.2 Input uncertainties

#### Parametric uncertainties

Parametric uncertainties in computational ice-sheet models are associated with unknown or poorly constrained parameters in the model. Uncertain parameters often come as unknown or poorly constrained free parameters in parameterisations. Uncertain parameters can also reflect uncertainty or variability in ice-sheet characteristics or physical properties and they can be either constant or spatially-varying over the ice sheet.

Given their nature, uncertain parameters are more amenable to quantitative assessments of the impact of uncertainties than model uncertainties. Such assessments are commonly performed by using large ensemble analysis, that is, the model is run for different values of the parameters and the uncertainty in the projections is estimated from the spread in the model runs; see, for instance, [Tarasov and Peltier \[2004\]](#), [Briggs et al. \[2013\]](#), [DeConto and Pollard \[2016\]](#), and [Pollard et al. \[2016\]](#). An alternative but related approach, which will be taken throughout this dissertation, is to assess the impact of parametric uncertainties using methods from the field of uncertainty quantification and the theory of probability.

#### Uncertainties in initial and boundary conditions

Computational ice-sheet models must be prescribed with appropriate initial and boundary conditions (for instance, the AIS present-day geometry and ice thickness, the present-day bedrock topography, the present-day surface accumulation, or the geothermal flux). The prescription of initial and boundary conditions heavily rely on (observational) datasets. Also, the prescription of boundary conditions often requires to infer for unknown fields, typically the basal friction coefficient in computational ice-sheet models. Inference of unknown fields is typically pursued using data assimilation (inverse) methods that also rely on (observational) datasets. In this case, the data assimilation method can also induce uncertainties in the reconstructed field.

Despite increasingly available datasets from satellite and airborne missions, uncertainties remain in datasets due in particular to poorly covered areas, limitations in instrumental resolution, data postprocessing, indirect measurements, . . . . Even when datasets are available with a high level of accuracy and precision at high resolution, uncertainties may arise due to upscaling of available data over computational domains that have a coarser resolution than the datasets. Errors in datasets can have a significant impact on numerical results, in particular, uncertainties in bedrock topography can affect the projections of the stability of marine basins with topographic features that can buttress the flow of ice [[Sun et al., 2014](#); [Gasson et al., 2015](#)]. Assessing the impact of uncertain datasets is generally difficult but insight can be gained by comparing projections with different datasets or by assessing the impact of stochastic perturbations on datasets.

#### Uncertainties in climate forcing

Uncertainties in climate forcing from the atmosphere and the ocean are major sources of uncertainty for accurate and robust projections of future sea-level rise. As discussed in the previous sections, atmospheric and ocean forcings can induce large variations and strong nonlinearities in the response of the Antarctic ice sheet due to their potential to trigger feedback mechanisms,

instabilities, and tipping points; see, for instance, Bakker et al. [2017] and Pattyn et al. [2018]. Uncertainties in climate forcing stem from the natural variability in natural processes, including solar and volcanic activity, natural variability in the climate system, such as changes in wind and ocean circulation, and uncertainty in future emissions of greenhouse gases and aerosols driven by anthropogenic activities; see, for instance, Myhre et al. [2013]. Inherent variability in the climate system represents a source of “irreducible” uncertainty [Hu and Deser, 2013; Marotzke, 2018]. Future emissions of greenhouse gases and aerosols caused by anthropogenic activities are uncertain because they depend on uncertain factors such as demographic patterns, socio-economic development, technological development, energy and land use, and climate change mitigation measures. For all these reasons, climate forcing projections are characterised by a wide range of plausible outcomes. In order to assess the consequences of human-induced climate forcing and its uncertainties, scientists have developed so-called climate change scenarios that represent plausible future changes in climate forcing and can serve as baseline representations of climate forcing across the scientific communities. The scenarios provide future baseline trends for emissions of greenhouse gases and air pollutants that are consistent with various scenarios for economic and environmental developments. Examples of climate change scenarios are the SRES (Special Report on Emissions Scenarios) scenarios [Nakićenović et al., 2000] and the RCP (Representative Concentration Pathways) scenarios [Van Vuuren et al., 2011]. Such climate change scenarios can then be used to force climate models to provide atmospheric and oceanic forcings that can be coupled to computational ice-sheet models. Forcing the computational ice-sheet model with (different) atmospheric and oceanic forcings consistent with the climate change scenarios then provides insight into the impact of uncertainties in climate forcing on the response of the ice sheet.

### 3.5 Conclusion

In this chapter, we provided an overview of the current state of the Antarctic ice sheet, its future in a warming world, and the limitations and uncertainties in the use of computational ice-sheet models to predict the response of the Antarctic ice sheet to climate change. So far, the Antarctic ice sheet has been only a limited contributor to sea-level rise, with, for instance, the Greenland ice sheet currently losing twice as much ice as the Antarctic ice sheet. Yet, the contribution of the Antarctic ice sheet to sea-level rise is expected to exceed other contributions to sea-level rise and become the dominant contributor to sea-level rise in the next centuries. However, predicting the AIS contribution to sea-level rise is challenged by the wide range and importance of processes that can affect the AIS response to climate change and the limitations and uncertainties in computational ice-sheet models. In its Special Report on the Ocean and Cryosphere in a Changing Climate [IPCC, 2019], the IPCC has described this situation as a situation of *deep uncertainty*. Following IPCC [2019] (adapted from Lempert et al. [2003] and Marchau et al. [2019]), a situation of deep uncertainty exists when experts or stakeholders do not know or cannot agree on: (1) appropriate conceptual models that describe relationships among key driving forces in a system; (2) the probability distributions used to represent uncertainty about key variables and parameters; and/or, (3) how to weigh and value desirable alternative outcomes. A situation of deep uncertainty thus involves many plausible futures, many alternative physics-based models, a wide range of outcomes (or quantities) of interest, and a wide range of weights that experts or stakeholders can prescribe to the outcomes of interest. For this reason, projections of the AIS response to climate change should incorporate in some way uncertainties in the

system, including uncertainties in computational models, physics, and key variables and parameters, and quantify the uncertainty in the desirable outcomes in order to increase confidence in the projections.



## **Part II**

# **Uncertainty Quantification: Theory and Methods**



# 4

## Uncertainty quantification methods for computational models

*This chapter is an introduction to theory and methods for the analysis of computational models subject to uncertain input parameters within the field of uncertainty quantification. Within the probability theory, we discuss theory and methods for the characterisation of uncertainties in computational models, the propagation of uncertainties through the computational model to characterise the uncertainty in the quantity of interest, and the assessment of the impact of sources of uncertainty in inducing uncertainty in the quantity of interest. The focus is on non-intrusive methods that do not require any modification of the source code of the computational model, including methods based on Monte Carlo sampling, surrogate models (polynomial chaos expansion and Gaussian-process regression), and probabilistic learning.*

### 4.1 Introduction

In applications in computational physics and engineering, the prediction of the behaviour and the evolution of physical and engineering systems relies on (physics-based) computational models. Examples include global climate models in climatology, ice-sheet models in glaciology, and finite-element models for real-world engineering problems (mechanics and aerospace). These computational models, also referred to as simulators, which result from a mathematical-physical modelling process of real-world physical and engineering systems, usually exhibit uncertain features. These uncertain features are associated with model uncertainties induced by modelling errors and parametric uncertainties due to uncertain input parameters, which we focus on in this chapter. For this reason, robust prediction of the behaviour and the evolution of physical and engineering systems based on computational models needs to consider and quantify the impact of uncertain input parameters and modelling errors on the response of the computational model.

In this context, the field of uncertainty quantification (UQ) has emerged as a general framework to handle uncertainties associated with predictions based on computational models. The field of uncertainty quantification develops theory and methods to describe quantitatively the origin, propagation, and interplay of sources of uncertainty in the analysis and projection of the behaviour of complex systems in physics and engineering; see, for instance, [Smith \[2014\]](#),

Sullivan [2015], Ghanem et al. [2017], and Soize [2017] for recent textbooks and Arnst and Ponthot [2014] for a recent review paper. Most of this theory and these methods are based on probability theory, in the context of which uncertain parameters and projections are represented as random quantities characterised by their probability distribution; we refer the reader to Appendix A for an introduction to the theory of probability. Within the probability theory, the field of uncertainty quantification, as depicted schematically in Figure 4.1, develops theory and methods to characterise sources of uncertainty by distribution functions inferred from observational data and expert assessment (*characterisation of uncertainty*), to deduce the impact of sources of uncertainty on the projections (*propagation of uncertainty*), and to ascertain the impact of each source of uncertainty on the projection uncertainty and rank them in order of significance (*stochastic sensitivity analysis*).

In this chapter, we represent a computational model as a mapping of a set of input parameters of the computational model into a quantity of interest. For this reason, we consider the following (nonlinear) mapping

$$y = f(\mathbf{x}), \quad (4.1)$$

where  $\mathbf{x} = (x_1, \dots, x_n)$  is a vector of input parameters of the computational model and  $y$  is the *quantity of interest*. In the context of a computational model, the quantity of interest may represent a real-valued scalar, vector, or field. In the context of ice-sheet modelling, the reader may think of the computational model  $f$  as an abstract representation of the computational ice-sheet model, the input parameters as physical parameters such as the relaxation time of the bedrock, the exponent in Weertman's sliding law, or the atmospheric temperature, and the quantity of interest as the change in volume above floatation for the whole Antarctic ice sheet (scalar quantity of interest), the change in volume above floatation for both the West and East Antarctic ice sheets (vector-valued quantity of interest), or the change in ice thickness (field-valued quantity of interest). In the following, we will focus (mostly) on scalar quantities of interest and we will discuss vector-valued and field-valued quantities of interest when appropriate.

Based on theory and methods from uncertainty quantification and the theory of probability, this chapter provides an overview of theory and methods to characterise the uncertainty in the input parameters (Section 4.2), to propagate the uncertainty in the input parameters through the computational model (Section 4.3), and to carry out a stochastic sensitivity analysis to ascertain the impact of each source of uncertainty on the quantity of interest (Section 4.4). We refer the reader to Arnst and Ponthot [2014], Ghanem et al. [2017], and Soize [2017] for the main references on which this chapter is based.

## 4.2 Characterisation of uncertainties

The first step in a UQ analysis is the identification and characterisation of the sources of uncertainty in the computational model. Here, we represent the sources of uncertainty as a set of uncertain input parameters  $\mathbf{x} = (x_1, \dots, x_n)$  of the computational model and we adopt an approach based on the theory of probability to model these uncertain input parameters. A probabilistic approach to modelling uncertainties begins by defining a probability space, which provides the mathematical foundation on which the probability theory and its concepts, such that the probability of an event or the concept of a random variable, can be defined rigorously

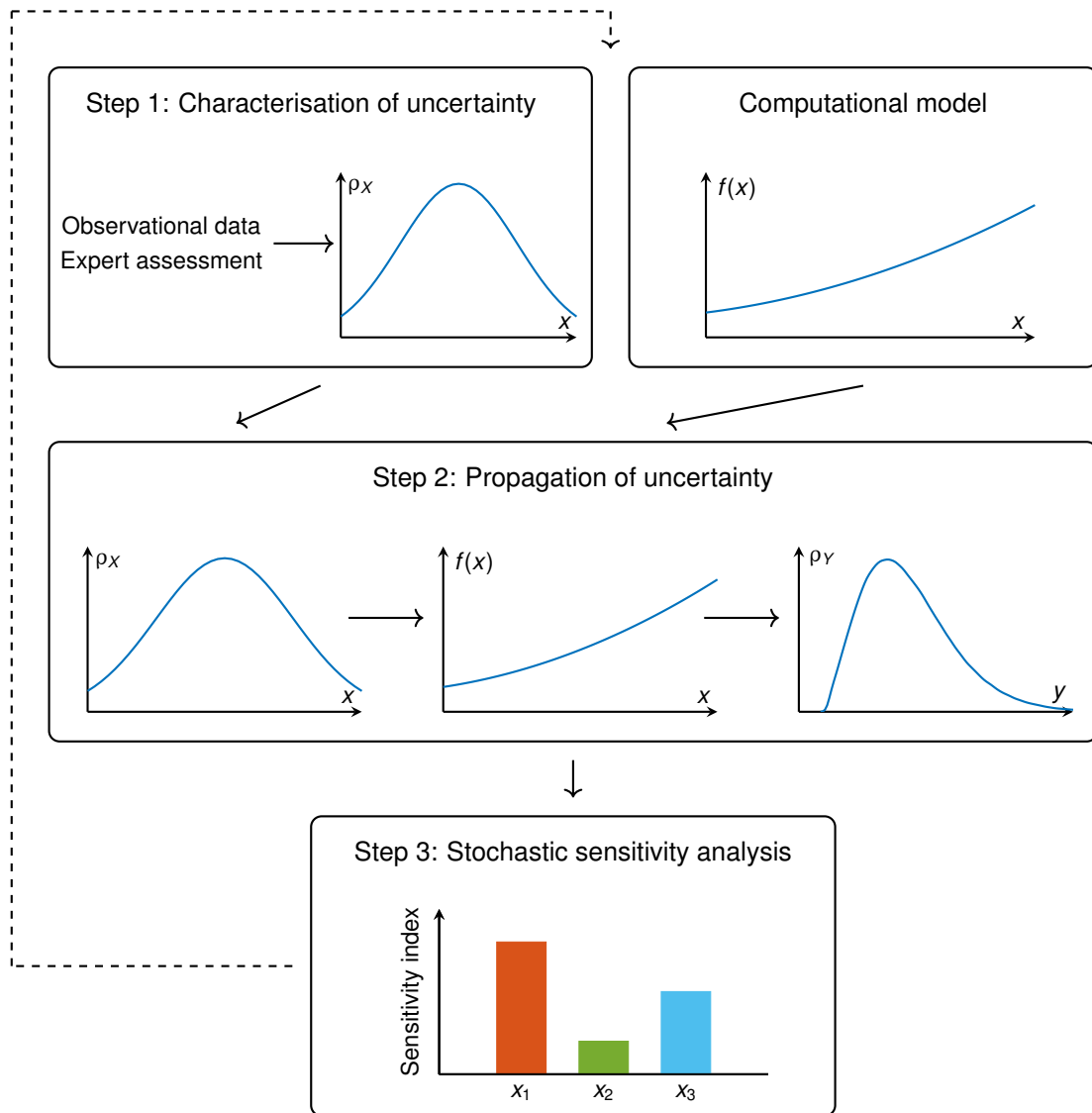


Figure 4.1: Schematic illustration of a UQ analysis of a computational model with uncertain input parameters.

within the framework of measure theory [Billingsley, 2012]. Within the framework of probability theory, we represent the set of uncertain input parameters as an  $\mathbb{R}^n$ -valued random vector  $\mathbf{X} = (X_1, \dots, X_n)$  defined on a complete probability space  $(\Theta, \mathfrak{B}, \mathbb{P})$ . The probabilistic characterisation of the sources of uncertainty involves the characterisation of the probability distribution  $\mathbb{P}_{\mathbf{X}}$  of the random vector  $\mathbf{X}$  or equivalently its probability density function  $\rho_{\mathbf{X}}$  if  $\mathbf{X}$  is a continuous random vector. Such a characterisation of the sources of uncertainty usually relies on expert assessment, observational data, physical constraints, and statistical methods. In the following, we assume that such a probabilistic characterisation with a probability distribution  $\mathbb{P}_{\mathbf{X}}$  is available and we briefly mention two popular approaches to characterise the probability distribution  $\mathbb{P}_{\mathbf{X}}$ .

A first approach is to assign a “labelled” probability distribution from a list of probability distributions. These “labelled” probability distributions are common probability distributions that depend on a small number of parameters, which can be inferred from expert assessment or statistical methods, such as maximum likelihood estimation [Fisher, 1912]. Examples of univariate “labelled” probability distributions are the uniform, exponential, Gaussian, Gamma, and Beta probability distributions. The choice of a specific “labelled” probability distribution is usually based on expert assessment and must be consistent with physical constraints. For instance, a uniform probability distribution can be used to represent random variables whose support is the only available information, a Gaussian probability distribution to represent observations with measurement errors, and a Gamma distribution to represent positive random variables. For random vectors, a common assumption is to consider the components of the random vector to be mutually independent random variables and to characterise the marginal probability distribution of each component separately. Then, the probability distribution  $\mathbb{P}_{\mathbf{X}}$  writes as

$$\mathbb{P}_{\mathbf{X}} = \mathbb{P}_{X_1} \times \dots \times \mathbb{P}_{X_n}, \quad (4.2)$$

where  $\mathbb{P}_{X_i}$ ,  $1 \leq i \leq n$ , denotes the marginal probability distribution of the random variable  $X_i$ . When the components of  $\mathbf{X}$  cannot be assumed independent, the random vector  $\mathbf{X}$  can still be represented as a random vector of independent components by using an isoprobabilistic transformation such as the Rosenblatt [Rosenblatt, 1952] and Nataf [Nataf, 1962; Lebrun and Dutfoy, 2009], transformations, or the statistical dependence between random variables can be accounted for by using the copula formalism [Nelsen, 2006; Torre et al., 2019].

A second approach is to adopt a Bayesian inference framework to infer the probability distribution of the uncertain parameters; see, for instance, Tarantola [2005] and Bernardo and Smith [2000]. In a Bayesian inference framework, a prior probability distribution, which encodes prior information about the uncertain input parameters such as physical constraints, is updated by accounting for newly available data according to Bayes’ theorem to obtain a posterior probability distribution, which encodes all available information.

### 4.3 Propagation of uncertainties

Given uncertainty in the input parameters, the quantity of interest of the computational model becomes uncertain. In a probabilistic setting, the quantity of interest is represented as a random variable  $Y$  defined on the probability space  $(\Theta, \mathfrak{B}, \mathbb{P})$ . The random variable  $Y$  represents the transformation of the random vector  $\mathbf{X}$  through the computational model  $f$ , which writes formally as

$$Y = f(\mathbf{X}). \quad (4.3)$$

Thus, the probability distribution of  $Y$  is the image of the probability distribution of  $\mathbf{X}$  under  $f$ . It should be noted that when the quantity of interest is a vector or a field, it can be similarly represented as a random vector or a random field.

Given a probabilistic characterisation of the uncertain input parameters in terms of the probability distribution  $\mathbb{P}_{\mathbf{X}}$ , propagating the uncertainty through the computational model aims at determining a probabilistic characterisation of the uncertain quantity of interest in terms of its

probability distribution  $\mathbb{P}_Y$ , from which can be deduced various statistical descriptors of  $Y$ , for instance, its mean and its variance (if they exist) are given by

$$\mathbb{E}[Y] = \int_{\mathbb{R}} y \mathbb{P}_Y(dy) \equiv m_Y, \quad (4.4)$$

$$\mathbb{V}[Y] = \int_{\mathbb{R}} (y - m_Y)^2 \mathbb{P}_Y(dy) \equiv \sigma_Y^2. \quad (4.5)$$

Formally, the probability distribution  $\mathbb{P}_Y$  can be deduced as the image of the probability distribution  $\mathbb{P}_X$  of  $\mathbf{X}$  under  $f$ , that is,

$$\mathbb{P}_Y(B) = \mathbb{P}_X(\{\mathbf{x} \in \mathbb{R}^n : f(\mathbf{x}) \in B\}) \quad (4.6)$$

for all meaningful subsets  $B$  of  $\mathbb{R}$ ; see Figure 4.2 for an illustration. Using the change-of-variables theorem [Dudley, 2002] in the context of probability theory, the statistical descriptors of  $Y$  can be computed equivalently as

$$m_Y = \int_{\mathbb{R}^n} f(\mathbf{x}) \mathbb{P}_X(d\mathbf{x}), \quad (4.7)$$

$$\sigma_Y^2 = \int_{\mathbb{R}^n} (f(\mathbf{x}) - m_Y)^2 \mathbb{P}_X(d\mathbf{x}). \quad (4.8)$$

When  $f$  is a strictly monotone and differentiable function of a single variable, there exists a closed-form expression between  $\rho_Y$  and  $\rho_X$  involving the Jacobian of the transformation. However, except for a few specific cases such as the example above, there exists no such closed-form expression for  $\mathbb{P}_Y$  as a function of  $\mathbb{P}_X$  and  $f$ . Similarly, there exist in general no closed-form expressions for the statistical descriptors of  $Y$  as a function of the statistical descriptors of  $\mathbf{X}$ . For instance, the  $m_Y$  of  $Y$  is in general not equal to  $f(m_X)$ , with  $m_X$  the mean of  $\mathbf{X}$  (the equality is satisfied only when  $f$  is an affine function), and the computation of  $m_Y$  requires the knowledge of  $\mathbb{P}_X$ . For this reason, the propagation of uncertainties is often implemented using computational and mathematical methods developed in the field of uncertainty quantification. Methods in uncertainty quantification are often classified as either “nonintrusive” or “intrusive”. Nonintrusive methods only require the evaluation of the computational model without any modification of the source code of the computational model; hence, the computational model may be seen as a *black-box*. Unlike nonintrusive methods, intrusive methods, see, for instance, Le Maître and Knio [2010], require a modification of the source code of the computational model, which can be hardly affordable for complex computational models such as climate or ice-sheet models. Thus, in the following, we do not discuss intrusive methods and only consider nonintrusive methods for uncertainty quantification. We will focus mainly on methods to estimate the probability distribution of  $Y$  and some of its statistical descriptors but it should be mentioned that the methods introduced in the following can also be applied to, for instance, sensitivity analysis, optimisation under uncertainty, and estimation of extreme value statistics.

### 4.3.1 Monte Carlo sampling method

Monte Carlo sampling methods encompass a broad class of computational methods based on random sampling. A typical implementation of the Monte Carlo sampling method begins by generating from the probability distribution  $\mathbb{P}_X$  an ensemble of independent and identically distributed (i.i.d) samples  $\{\mathbf{x}^{(k)}, 1 \leq k \leq \nu\}$  of the uncertain input parameters. Then, an ensemble

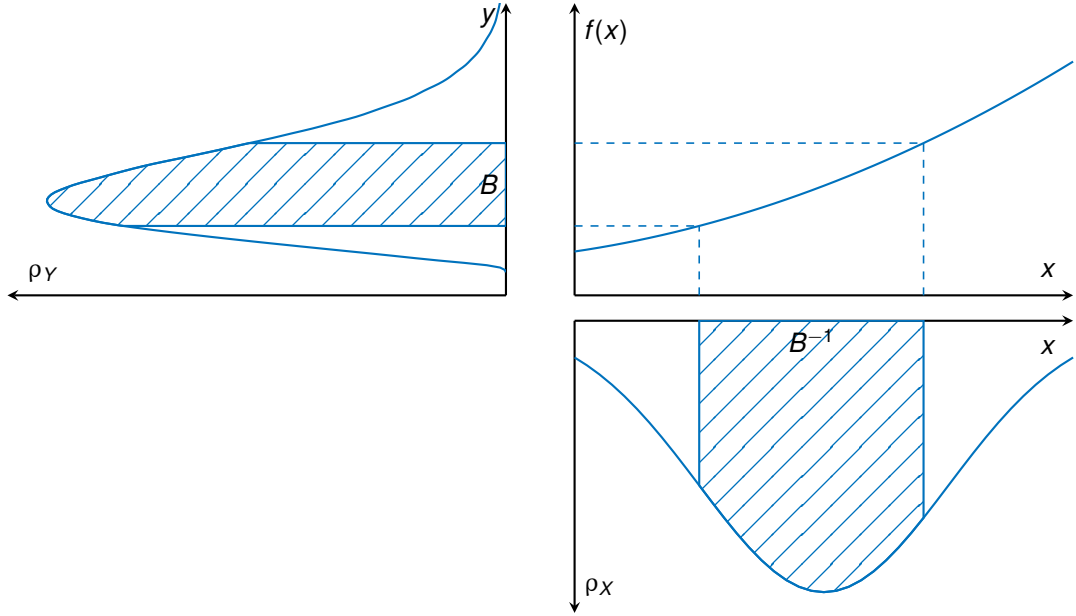


Figure 4.2: Schematic illustration of the propagation of uncertainties. The uncertain parameter  $x$  is mapped to the quantity of interest  $y$  through the computational model  $f$ . The probability that  $y$  lies within the interval  $B$ , represented as the blue dashed area under  $\rho_Y$ , is equivalent to the probability of  $X$  being in  $B^{-1}$ , represented as the blue dashed area under  $\rho_X$ , with  $B^{-1} = \{x \in \mathbb{R} : f(x) \in B\}$ . In this illustration,  $f$  is a strictly increasing and differentiable function of a single variable. Thus,  $\rho_Y$  admits a closed-form expression as a function of  $\rho_X$  and the Jacobian of the transformation.

of solutions to the computational model is generated in the form of the corresponding ensemble  $\{y^{(k)} = f(\mathbf{x}^{(k)}), 1 \leq k \leq \nu\}$  of i.i.d samples of the quantity of interest. From these samples, various statistical descriptors of the probability distribution  $\mathbb{P}_Y$  can be estimated with statistical methods. For instance, the mean and the variance of  $Y$  (if they exist) are estimated as the sample (empirical) mean and variance, that is,

$$m_Y \approx m_Y^\nu = \frac{1}{\nu} \sum_{k=1}^{\nu} y^{(k)}, \quad (4.9)$$

$$\sigma_Y^2 \approx (\sigma_Y^\nu)^2 = \frac{1}{\nu} \sum_{k=1}^{\nu} (y^{(k)} - m_Y^\nu)^2, \quad (4.10)$$

where the superscript  $\nu$  is used to indicate that the quantity of interest is estimated from a finite number of samples. The probability density function  $\rho_Y$  (if it exists) can be estimated using kernel density estimation [Scott, 2015]. A kernel density estimate of  $\rho_Y$  writes as

$$\rho_Y(y) \approx \rho_Y^{\nu,h}(y) = \frac{1}{\nu h} \sum_{k=1}^{\nu} K\left(\frac{y - y^{(k)}}{h}\right), \quad (4.11)$$

where  $K$  is a non-negative function called the kernel,  $h$  is a smoothing parameter called the bandwidth, and the superscripts  $\nu$  and  $h$  are used to indicate that the kernel density estimate

depends on a finite number of samples and the choice of the bandwidth. See Figure 4.3 for an illustration.

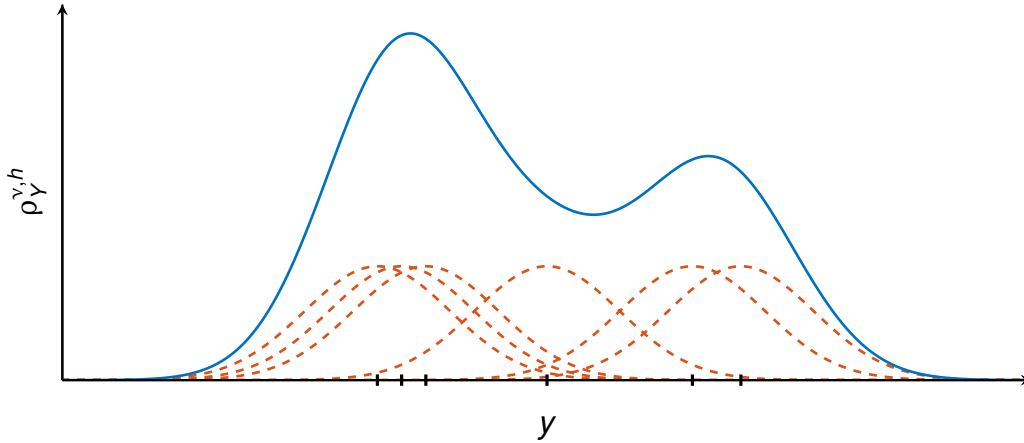


Figure 4.3: Illustration of the estimation of the probability density function  $\rho_Y$  using kernel density estimation. Ticks represent the samples. Orange curves represent Gaussian kernels centred at each sample and the blue curve is the reconstructed probability density function.

From a theoretical point of view, the convergence of Monte Carlo estimators can be analysed using the law of large numbers and the central limit theorem; see, for instance, [Dudley \[2002\]](#) and [Robert and Casella \[2013\]](#). The law of large numbers ensures that for a  $\mathbb{P}_Y$ -integrable random variable  $Y$ , the Monte Carlo estimator of the mean converges towards the exact value  $m_Y$  while the central limit theorem ensures that for a  $\mathbb{P}_Y$ -square-integrable random variable  $Y$ , the standard deviation of the Monte Carlo estimator decreases as the square root of the number of samples for sufficiently large  $\nu$ , irrespectively of the stochastic dimension  $n$  of the random vector  $\mathbf{X}$ .

From an application-oriented point of view, two main issues may limit the applicability of the Monte Carlo method:

1. The Monte Carlo sampling method assumes the ability to generate random samples from the probability distribution of the uncertain input parameters. Although pseudorandom number generators have been implemented to sample from common probability distributions, more sophisticated algorithms are necessary to sample from more general probability distributions. These algorithms include rejection sampling, importance sampling, and Markov chain Monte Carlo sampling; see, for instance, [Robert and Casella \[2013\]](#).
2. The Monte Carlo method requires to solve the computational model for each i.i.d sample from  $\mathbb{P}_X$ . For this reason, the total computational cost of the Monte Carlo method scales with the number of samples  $\nu$ . As the accuracy of the Monte Carlo estimate decreases with the square root of  $\nu$ , attaining sufficient accuracy may become intractable for computational models with a high computational cost. For this reason, much research has been dedicated in the field of uncertainty quantification to develop methods that seek

to alleviate the computational cost of the Monte Carlo sampling method. These methods include advanced Monte Carlo sampling methods (Section 4.3.1.1), surrogate models (Section 4.3.2), and learning algorithms (Section 4.3.3).

### 4.3.1.1 Advanced sampling methods

Variants of the Monte Carlo sampling method based on improved sampling strategies have been proposed to achieve a lower variance of the Monte Carlo estimator. These improved sampling strategies include stratified sampling [McKay et al., 1979; Shields and Sundar, 2015], Latin hypercube sampling [McKay et al., 1979; Stein, 1987], partial stratified sampling [Shields et al., 2015; Shields and Zhang, 2016], and quasi-Monte Carlo sampling [Niederreiter, 1992; Caffisch, 1998]; see Figure 4.4 for an illustration. Stratified sampling is based on a partition of the sample space into disjoint subsets (strata) and samples are drawn randomly within each stratum. Latin hypercube sampling is based on dividing the range of each vector component  $X_i$ ,  $1 \leq i \leq n$ , into  $\nu$  disjoint intervals (strata) of equal probability and samples of each vector component are drawn within each interval. The samples of the random vector  $\mathbf{X}$  are assembled by randomly grouping (without replacement) the generated samples for each vector component. Thus, there are  $(\nu!)^{n-1}$  possible grouping combinations of the component samples for a Latin hypercube design of  $\nu$  samples in  $n$  dimensions. Quasi-Monte Carlo sampling methods are a class of sampling methods based on deterministic sequences of points that seek to maximise the uniformity of the samples as quantified in terms of discrepancy. In this context, sequences with low discrepancy achieve a high uniformity of the samples. Examples of common low-discrepancy sequences of points are the Halton and Sobol sequences.

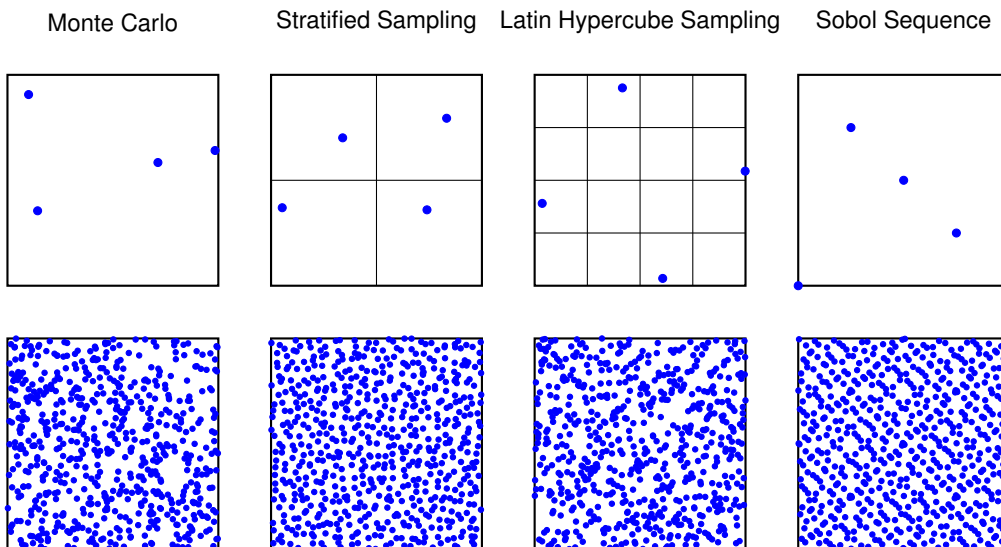


Figure 4.4: Illustration of (pseudo-)random samples over the unit square with  $\nu = 4$  (top row) and  $\nu = 625$  (bottom row) samples, using Monte Carlo sampling, stratified sampling, Latin hypercube sampling, and quasi-Monte Carlo sampling (Sobol sequence). Generally, stratified sampling, Latin hypercube sampling, and quasi-Monte Carlo sampling methods achieve a better space filling than the Monte Carlo sampling method.

Similarly to Monte Carlo sampling, the accuracy of the Monte Carlo estimate based on either stratified sampling or Latin hypercube sampling decreases with the square root of  $\nu$ ; yet, both sampling methods can achieve a reduced variance of the estimator when compared to Monte Carlo sampling. McKay et al. [1979] showed that stratified sampling achieves a reduced variance of the estimator for a balanced sampling scheme, that is, for each stratum the percentage of samples in the stratum is equal to the probability of belonging to the stratum. Stein [1987] showed that Latin hypercube sampling achieves a reduced variance of the estimator for  $\nu$  sufficiently large as compared to  $n$ . In particular, the reduction in variance is more important when the function  $f$  is well approximated by an additive function, that is, a function that is the sum of terms that are each a function of only one of the uncertain input parameters. For certain low-discrepancy sequences, the accuracy of the Monte Carlo estimate based on quasi-Monte Carlo sampling decreases as  $(\log \nu)^n / \nu$  [Niederreiter, 1992; Morokoff and Caflisch, 1995], which is an asymptotically better convergence rate than the Monte Carlo sampling method with respect to the number of samples although it increases with the stochastic dimension  $n$ . Similarly to the Monte Carlo sampling method, the convergence rates of Monte Carlo estimates based on advanced sampling methods may be prohibitive for computational models with a high computational cost.

### 4.3.2 Surrogate models

Conceptually, a *surrogate model* is an approximation of the original computational model. Formally, a surrogate model can be defined as the mapping

$$\mathbf{x} \mapsto \tilde{f}(\mathbf{x}), \quad (4.12)$$

from  $\mathbb{R}^n$  into  $\mathbb{R}$ , such that, in some sense,  $\tilde{f}$  is close to  $f$ . In the context of uncertainty quantification, surrogate models, also known as surface response models, metamodels, or emulators, often serve as fast-to-evaluate models that mimic the mapping between the uncertain input parameters and the quantity of interest, as provided by the computational model, in order to gain a computational speedup. For this reason, surrogate models are usually determined from a limited number of evaluations of the computational model at a selected set of points in the parameter space, the so-called experimental design or training set  $\{\mathbf{x}_\lambda^{(k)}, 1 \leq k \leq \lambda\}$ , with  $\lambda$  small as compared to  $\nu$ .

Once a surrogate model is available, it can be used as a computationally efficient substitute for the computational model to estimate statistical descriptors of the quantity of interest using, for instance, Monte Carlo sampling; see Figure 4.5 for an illustration. Considering an ensemble of i.i.d. samples  $\{\mathbf{x}^{(k)}, 1 \leq k \leq \nu\}$  of the uncertain parameters and the corresponding ensemble of solutions to the surrogate model, that is,  $\{\tilde{y}^{(k)} = \tilde{f}(\mathbf{x}^{(k)}), 1 \leq k \leq \nu\}$ , then the mean and the variance of  $Y$  are estimated as the sample mean and variance of the surrogate model, that is,

$$m_Y \approx m_{\tilde{Y}}^\nu = \frac{1}{\nu} \sum_{k=1}^{\nu} \tilde{y}^{(k)}, \quad (4.13)$$

$$\sigma_Y^2 \approx (\sigma_{\tilde{Y}}^2)^\nu = \frac{1}{\nu} \sum_{k=1}^{\nu} (\tilde{y}^{(k)} - m_{\tilde{Y}}^\nu)^2, \quad (4.14)$$

where  $\tilde{Y}$  denotes the random variable  $\tilde{f}(\mathbf{X})$  with mean  $m_{\tilde{Y}}$  and variance  $\sigma_{\tilde{Y}}^2$ .

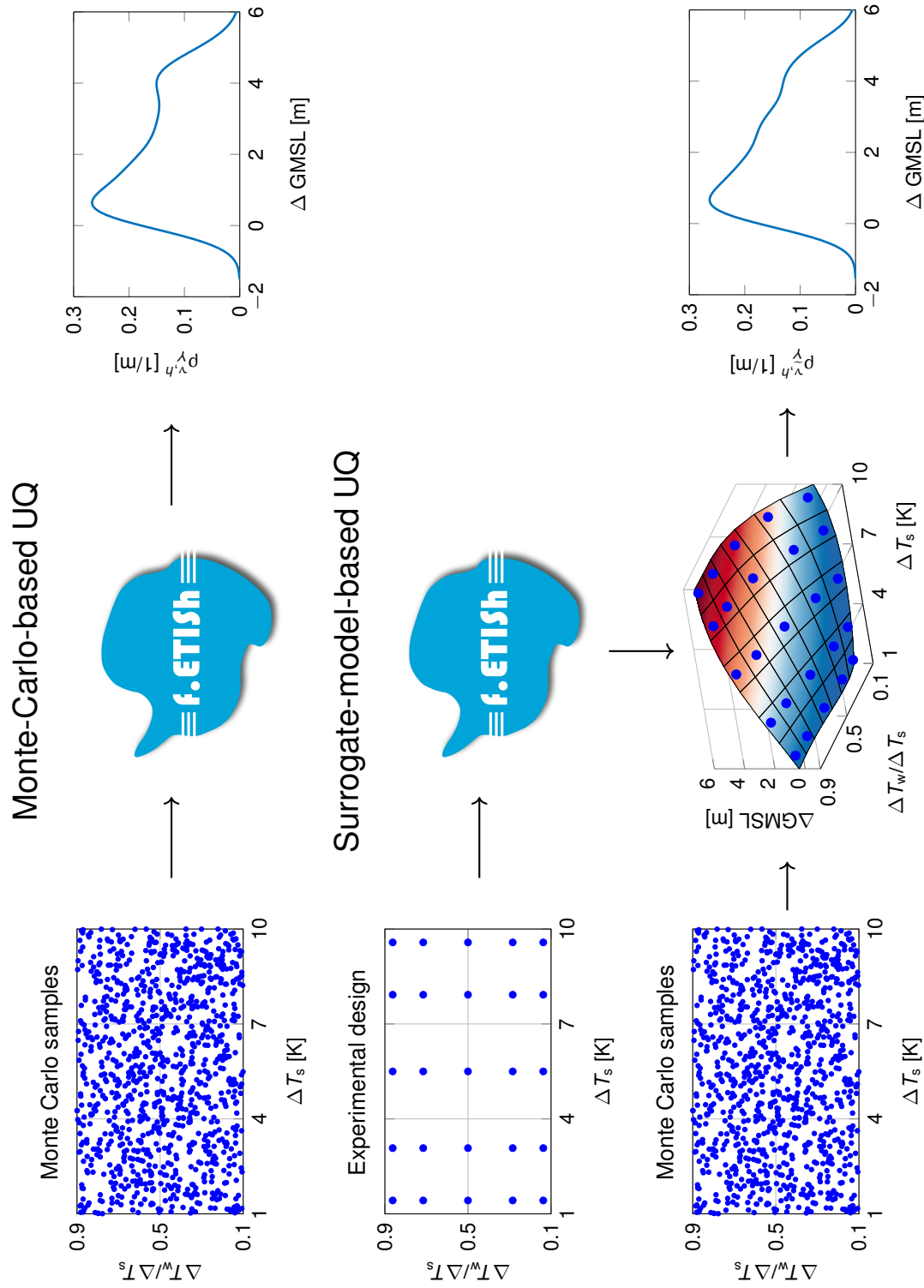


Figure 4.5: Schematic illustration of the propagation of uncertainties for the application in Section 7.1. For the propagation of uncertainties based on Monte Carlo sampling, Monte Carlo samples are propagated through the computational model (here illustrated by the f.ETISH ice-sheet model). For the propagation of uncertainties based on a surrogate model, a surrogate model for the computational model is built from an experimental design and Monte Carlo samples are propagated through the surrogate model.

Various surrogate models have been proposed over the years, including surrogate models based on polynomial chaos expansions [Ghanem and Spanos, 2003; Soize and Ghanem, 2004; Le Maître and Knio, 2010], Gaussian-process regression (kriging) [Santner et al., 2003; Rasmussen and Williams, 2006; Dubourg, 2011], support vector machine [Vapnik, 2000; Smola and Schölkopf, 2004; Bourinet, 2018], and artificial neural networks [Haykin, 2009]. It should be noted that any type of surrogate models relies on an underlying set of assumptions regarding the form of the approximation. These assumptions are expected to be consistent with the properties of the computational model (for instance, continuity and smoothness) to yield an appropriate approximation. In the following, we discuss two classes of surrogate models commonly used in uncertainty quantification, namely surrogate models based on polynomial chaos expansions and Gaussian-process regression.

### 4.3.2.1 Polynomial chaos expansions

#### Polynomial chaos expansion of a second-order random variable

Let  $\mathbf{X}$  be an  $\mathbb{R}^n$ -valued random vector that admits a probability density function  $\rho_{\mathbf{X}}$  and possess finite moments of all orders ( $\mathbb{E}[\|\mathbf{X}\|^q] < \infty$  for all  $q$  in  $\mathbb{N}$ ). Let the random variable  $Y$  be a deterministic (nonlinear) transformation  $f$  of the random vector  $\mathbf{X}$ , with  $Y$  being of the second order. Then, the polynomial chaos expansion of  $Y = f(\mathbf{X})$  writes as

$$\sum_{|\alpha|=0}^{\infty} y_{\alpha} \Psi_{\alpha}(\mathbf{X}). \quad (4.15)$$

Here,  $\alpha = (\alpha_1, \dots, \alpha_n)$  is a multi-index of  $\mathbb{N}^n$  with  $|\alpha| = \alpha_1 + \dots + \alpha_n$  and  $\{\Psi_{\alpha}(\mathbf{X}), \alpha \in \mathbb{N}^n\}$  is a basis of polynomials of order  $|\alpha|$  from  $\mathbb{R}^n$  into  $\mathbb{R}$ , the so-called multivariate polynomial chaos, and the scalars  $y_{\alpha}$  are the polynomial chaos coordinates. It is desirable that the series in Equation (4.15) converges in some sense, typically in a mean-square sense, towards  $Y$  as the order of the expansion increases. The convergence of the series typically depends on the probability distribution of  $\mathbf{X}$  as well as the function  $f$ ; see, for instance, Ernst et al. [2012] for a more detailed discussion about conditions under which the series converges. As examples of sufficient conditions, we mention that the convergence property holds if the probability distribution of  $\mathbf{X}$  has a compact support or the random vector is exponentially integrable, that is, there exists  $a > 0$  such that  $\int_{\mathbb{R}^n} \exp(a\|\mathbf{x}\|) \mathbb{P}_{\mathbf{X}}(d\mathbf{x}) < \infty$ , where  $\|\cdot\|$  denotes any norm on  $\mathbb{R}^n$  [Ernst et al., 2012]. For instance, the first condition holds if  $\mathbb{P}_{\mathbf{X}}$  is a uniform distribution and the second condition holds if  $\mathbb{P}_{\mathbf{X}}$  is a Gaussian distribution.

In general, the basis  $\{\Psi_{\alpha}(\mathbf{X}), \alpha \in \mathbb{N}^n\}$  is an orthonormal basis in  $\mathbb{L}^2(\Theta, \mathbb{R}^n)$  with respect to the probability distribution  $\mathbb{P}_{\mathbf{X}}$ , that is,

$$\mathbb{E}[\Psi_{\alpha} \Psi_{\beta}] = \int_{\mathbb{R}^n} \Psi_{\alpha}(\mathbf{x}) \Psi_{\beta}(\mathbf{x}) \rho_{\mathbf{X}}(\mathbf{x}) d\mathbf{x} = \delta_{\alpha\beta}, \quad \forall \alpha, \beta \in \mathbb{N}^n, \quad (4.16)$$

where  $\delta_{\alpha\beta} = 1$  for  $\alpha = \beta$  and 0 otherwise. Thanks to the orthonormality of the basis functions, the polynomial chaos coordinates write as

$$y_{\alpha} = \mathbb{E}[\Psi_{\alpha} Y] = \int_{\mathbb{R}^n} \Psi_{\alpha}(\mathbf{x}) f(\mathbf{x}) \rho_{\mathbf{X}}(\mathbf{x}) d\mathbf{x}, \quad \forall \alpha \in \mathbb{N}^n. \quad (4.17)$$

When the random vector  $\mathbf{X}$  has independent components, its probability density function writes as the product of the marginal probability density functions and the orthonormal basis functions  $\{\Psi_{\alpha}(\mathbf{X}), \alpha \in \mathbb{N}^n\}$  are built as

$$\Psi_{\alpha}(\mathbf{X}) = \psi_{\alpha_1}^{(1)}(X_1) \times \dots \times \psi_{\alpha_n}^{(n)}(X_n), \quad (4.18)$$

such that, for all  $i = 1, \dots, n$ ,  $\{\psi_m^{(i)}(x_i), m \in \mathbb{N}\}$  is a family of univariate orthonormal polynomials, that is,

$$\int_{\mathbb{R}} \psi_m^{(i)}(x_i) \psi_{m'}^{(i)}(x_i) \rho_{X_i}(x_i) dx_i = \delta_{mm'}, \quad \forall m, m' \in \mathbb{N}. \quad (4.19)$$

The family of univariate orthonormal polynomials is typically chosen of increasing order, with the index  $m$  corresponding to the order of the polynomial and the constant polynomial being equal to 1. Univariate orthonormal polynomials can be determined from the Askey scheme for “labelled” probability distributions [Xiu and Karniadakis, 2002; Xiu et al., 2002], for instance, the Legendre polynomials for uniform probability distributions and the Hermite polynomials for Gaussian probability distributions (see Figure 4.6), or from the Stieltjes and Gram-Schmidt orthonormalisation procedures for arbitrary probability distributions [Gautschi, 1982; Witteveen and Bijl, 2006; Wan and Karniadakis, 2006; Arnst et al., 2012].

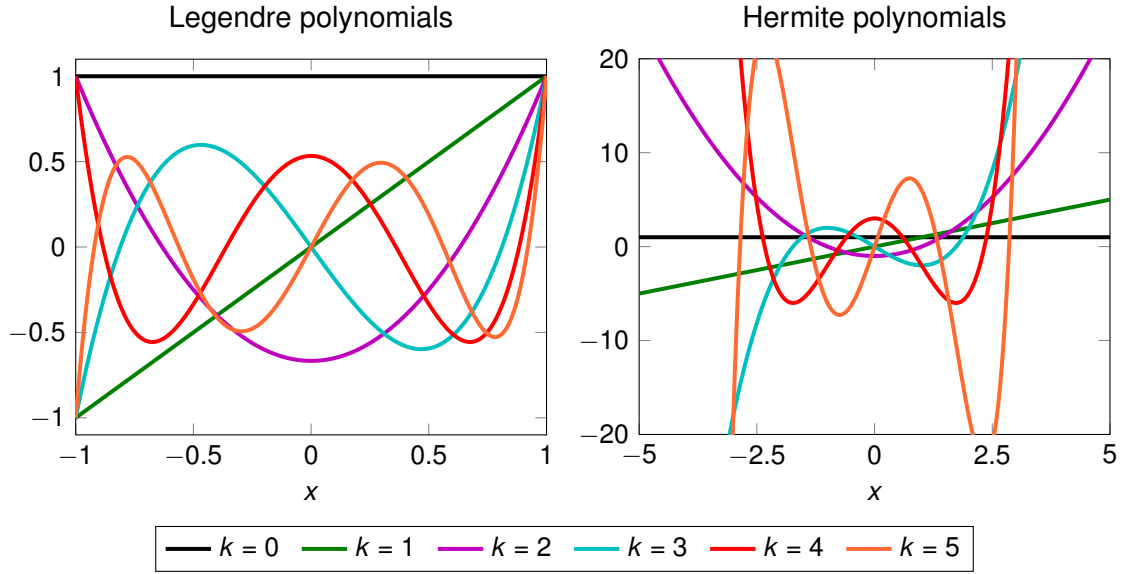


Figure 4.6: Univariate (non-normalised) Legendre and Hermite polynomials of order  $k = 0, \dots, 5$ . Legendre polynomials are orthogonal for the uniform probability distribution and Hermite polynomials are orthogonal for the Gaussian probability distribution.

In applications, the series in Equation (4.15) is usually limited to a subset of multi-indices  $\mathcal{A}$  in  $\mathbb{N}^n$  by using a truncation scheme. The standard truncation scheme, which we will consider in this dissertation, retains all polynomials whose degree is less than or equal to  $p$ , that is, the multi-index  $\alpha$  takes values in the set  $\mathcal{A}^p = \{\alpha \in \mathbb{N}^n : |\alpha| \leq p\}$ . Hence, the truncated polynomial chaos expansion of order  $p$  of the random variable  $Y$  writes as

$$\sum_{|\alpha|=0}^p y_{\alpha} \Psi_{\alpha}(\mathbf{X}) \equiv Y^p. \quad (4.20)$$

When the series in Equation (4.15) converges, then  $Y^p$  converges to  $Y$  in a mean-square sense as the order  $p$  tends to  $\infty$ . In this case, the convergence of the series is usually fast when the mapping  $f$  is sufficiently smooth. The number of polynomial chaos coordinates in Equation (4.20) is given by

$$\text{card}(\mathcal{A}^p) = \frac{(n+p)!}{n!p!} \equiv K_p, \quad (4.21)$$

thus the number of polynomial chaos coordinates grows rapidly with the number  $n$  of uncertain input parameters and the total polynomial order  $p$ . For this reason, other truncation schemes have been developed, such as the maximum interaction and the hyperbolic truncation schemes; see Figure 4.7 for an illustration and Blatman [2009] for a reference.

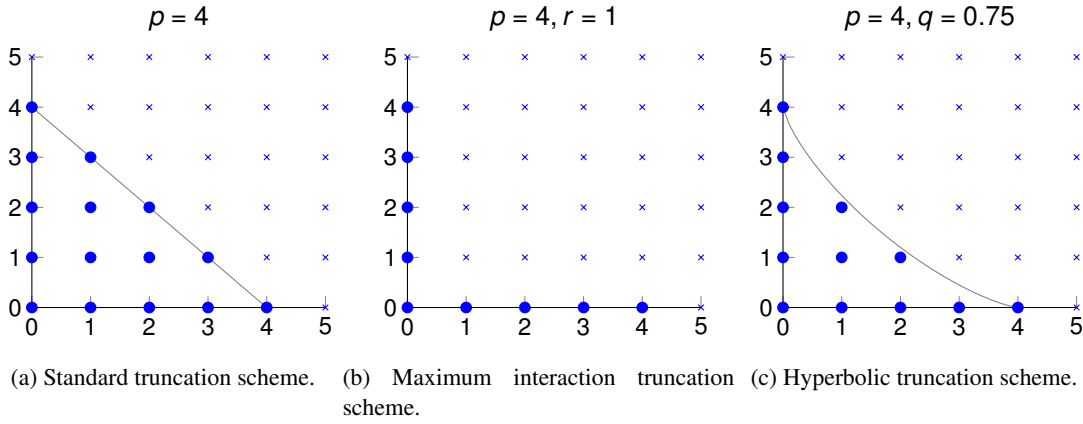


Figure 4.7: Comparison of different truncation schemes in the two-dimensional parameter space. The blue dots represents the multi-indices retained in the truncation scheme. (a) Standard truncation scheme: the multi-index  $\alpha$  takes values in the set  $\mathcal{A}^p = \{\alpha \in \mathbb{N}^n : |\alpha| \leq p\}$ . (b) Maximum iteration truncation scheme: the multi-index  $\alpha$  takes values in the set  $\mathcal{A}^{p,r} = \{\alpha \in \mathcal{A}^p : \sum_{i=1}^n \mathbf{1}(\alpha_i > 0) \leq r\}$ . (c) Hyperbolic truncation scheme: the multi-index  $\alpha$  takes values in the set  $\mathcal{A}^{p,q} = \{\alpha \in \mathcal{A}^p : (\sum_{i=1}^n \alpha_i^q)^{1/q} \leq p\}$ .

### Surrogate model based on polynomial chaos expansion

A surrogate model based on a polynomial chaos expansion of order  $p$  of the computational model writes as the mapping

$$\mathbf{x} \mapsto f^p(\mathbf{x}) = \sum_{|\alpha|=0}^p y_\alpha \Psi_\alpha(\mathbf{x}), \quad (4.22)$$

where the  $\Psi_\alpha(\mathbf{x})$  are an orthonormal basis with respect to  $\mathbb{P}_X$  and the scalars  $y_\alpha$  are the polynomial chaos coordinates. The main task in building such a surrogate model lies in the evaluation of these polynomial chaos coordinates from an experimental design. Here, we discuss two approaches, namely *spectral projection* and (weighted) *least-squares regression*. See also Figure 4.8 for an illustration.

In a spectral projection approach, also called nonintrusive spectral projection (NISP) approach, the polynomial chaos coordinates are determined as the projection of the response of computational model on each basis function; see Equation (4.17). The integral in Equation (4.17) can be evaluated numerically by using numerical integration algorithms, for instance, quadrature rules. A quadrature rule consists of a set  $\{(\mathbf{x}_\lambda^{(k)}, w_\lambda^{(k)}), 1 \leq k \leq \lambda\}$  of nodes  $\mathbf{x}_\lambda^{(k)}$  and weights  $w_\lambda^{(k)}$  that allows to approximate an integral as a weighted sum of integrand evaluations; thus, the polynomial chaos coordinates are estimated as

$$y_\alpha = \int_{\mathbb{R}^n} \Psi_\alpha(\mathbf{x}) f(\mathbf{x}) \rho_{\mathbf{X}}(\mathbf{x}) d\mathbf{x} \approx \sum_{k=1}^{\lambda} w_\lambda^{(k)} \Psi_\alpha(\mathbf{x}_\lambda^{(k)}) f(\mathbf{x}_\lambda^{(k)}). \quad (4.23)$$

When the random vector  $\mathbf{X}$  has  $n$  independent components, the quadrature nodes and weights are based on the tensor product of the quadrature rules for each individual component. Examples of quadrature rules for one-dimensional integration are the Gauss quadrature rules for “labelled” probability distributions, for instance the Gauss–Legendre and Gauss–Hermite quadrature rules for the uniform and Gaussian probability distributions, respectively; see, for instance, Abramowitz and Stegun [1970] and Golub and Meurant [2010] for a list of quadrature rules and tables of quadrature nodes and weights. The number of quadrature nodes usually depends on the degree of the polynomial  $\Psi_\alpha$  and the smoothness of the mapping  $f$ , with Gauss quadrature rules in one dimension that can integrate exactly polynomials of degree less than or equal to  $2\lambda - 1$  with  $\lambda$  quadrature nodes. For this reason, the polynomials orthonormal up to degree  $p$  with respect to the probability density function of  $\mathbf{X}$  are also orthonormal with respect to the corresponding Gauss quadrature rule with  $\lambda = p + 1$  nodes.

In a (weighted) least-squares regression approach, the polynomial chaos coordinates are determined as the solution of a minimisation problem for the weighted squared error between the computational model and the surrogate model evaluated at the experimental design, that is,

$$\sum_{k=1}^{\lambda} w_\lambda^{(k)} \left[ f(\mathbf{x}_\lambda^{(k)}) - f^p(\mathbf{x}_\lambda^{(k)}) \right]^2 = \sum_{k=1}^{\lambda} w_\lambda^{(k)} \left[ f(\mathbf{x}_\lambda^{(k)}) - \sum_{|\alpha|=0}^p y_\alpha \Psi_\alpha(\mathbf{x}_\lambda^{(k)}) \right]^2, \quad (4.24)$$

with  $\{\mathbf{x}_\lambda^{(k)}, 1 \leq k \leq \lambda\}$  the experimental design and  $\{w_\lambda^{(k)}, 1 \leq k \leq \lambda\}$  the associated ensemble of (positive) weights. The solution to the minimisation problem writes in a matrix form as

$$\hat{\mathbf{y}} = \arg \min_{\mathbf{d} \in \mathbb{R}^{K_p}} \frac{1}{2} (\mathbf{y} - [\Psi] \mathbf{d})^T [W] (\mathbf{y} - [\Psi] \mathbf{d}), \quad (4.25)$$

where  $\hat{\mathbf{y}}$  is the  $K_p$ -dimensional vector whose entries are the least-squares estimates of the polynomial chaos coordinates,  $\mathbf{y}$  is the  $\lambda$ -dimensional vector with entries  $y_k = f(\mathbf{x}_\lambda^{(k)})$ ,  $[\Psi]$  is the  $(\lambda \times K_p)$ -dimensional matrix whose columns are the polynomials indexed by the multi-indices in  $\mathcal{A}^p$  evaluated at the experimental design, and  $[W]$  is the  $\lambda$ -dimensional diagonal positive-definite weight matrix that collects the weights  $w_\lambda^{(k)}$  along its diagonal. The solution  $\hat{\mathbf{y}}$  in Equation (4.25) can be computed from the normal equations

$$([\Psi]^T [W] [\Psi]) \hat{\mathbf{y}} = [\Psi]^T [W] \mathbf{y}, \quad (4.26)$$

or more explicitly

$$\sum_{|\beta|=0}^p \hat{y}_\beta \left( \sum_{k=1}^{\lambda} w_\lambda^{(k)} \Psi_\alpha(\mathbf{x}_\lambda^{(k)}) \Psi_\beta(\mathbf{x}_\lambda^{(k)}) \right) = \sum_{k=1}^{\lambda} w_\lambda^{(k)} y_k \Psi_\alpha(\mathbf{x}_\lambda^{(k)}), \quad \forall \alpha \in \mathcal{A}^p. \quad (4.27)$$

Contrary to the spectral projection approach, the least-squares approach allows more freedom in the selection of the experimental design. However, the accuracy, the efficiency, as measured in terms of the number of evaluations of the computational model, and the numerical stability of the least-squares problem depend on the experimental design. For this reason, different sampling methods have been investigated in the context of the design-of-experiments field, including space-filling designs and optimal designs of experiments; see, for instance, [Fajraoui et al. \[2017\]](#) and [Hadigol and Doostan \[2018\]](#) for references. As a rule of thumb, the number of samples in the experimental design is usually chosen to be approximately two to three times the number of polynomial chaos coordinates.

It should be noted that solving the normal equations in Equation (4.26) is identical to approximating the polynomial chaos coordinates using a quadrature rule (Equation (4.23)) when the experimental design and the weights are chosen as the quadrature nodes and weights and the polynomials up to a total degree of  $p$  are also orthonormal with respect to the quadrature rule; see, for instance, [Le Maître and Knio \[2010\]](#) and [Arnst and Ponthot \[2014\]](#). Indeed, for weights and nodes satisfying

$$\sum_{k=1}^{\lambda} w_\lambda^{(k)} \Psi_\alpha(\mathbf{x}_\lambda^{(k)}) \Psi_\beta(\mathbf{x}_\lambda^{(k)}) = \delta_{\alpha\beta}, \quad \forall \alpha, \beta \in \mathcal{A}^p, \quad (4.28)$$

Equation (4.27) reduces to

$$\hat{y}_\alpha = \sum_{k=1}^{\lambda} w_\lambda^{(k)} y_k \Psi_\alpha(\mathbf{x}_\lambda^{(k)}), \quad \forall \alpha \in \mathcal{A}^p, \quad (4.29)$$

which is identical to the approximation using a quadrature rule in Equation (4.23). In general, the polynomial exactness of the quadrature rule plays a role in the differences between the two approaches. [Iskandarani et al. \[2016\]](#) discussed differences between the spectral projection and least-squares approaches in the presence of noise data due to, for instance, algorithmic errors. In this context, the least-square approach has been shown to accommodate noise more efficiently than the spectral projection approach.

Once a surrogate model based on a polynomial chaos expansion is available, it can serve as a substitute for the computational model to estimate the probability distribution of  $Y$  and its statistical descriptors. Thanks to the orthonormality of the polynomials, some of the statistical descriptors of  $Y$  can be estimated directly from the polynomial chaos coordinates. For instance, the mean and the variance of the random variable  $Y^p$  are given by

$$m_{Y^p} = y_0, \quad (4.30)$$

$$\sigma_{Y^p}^2 = \sum_{|\alpha|=1}^p y_\alpha^2, \quad (4.31)$$

and  $m_Y$  and  $\sigma_Y^2$  are estimated as  $m_{Y^p}$  and  $\sigma_{Y^p}^2$ , respectively.

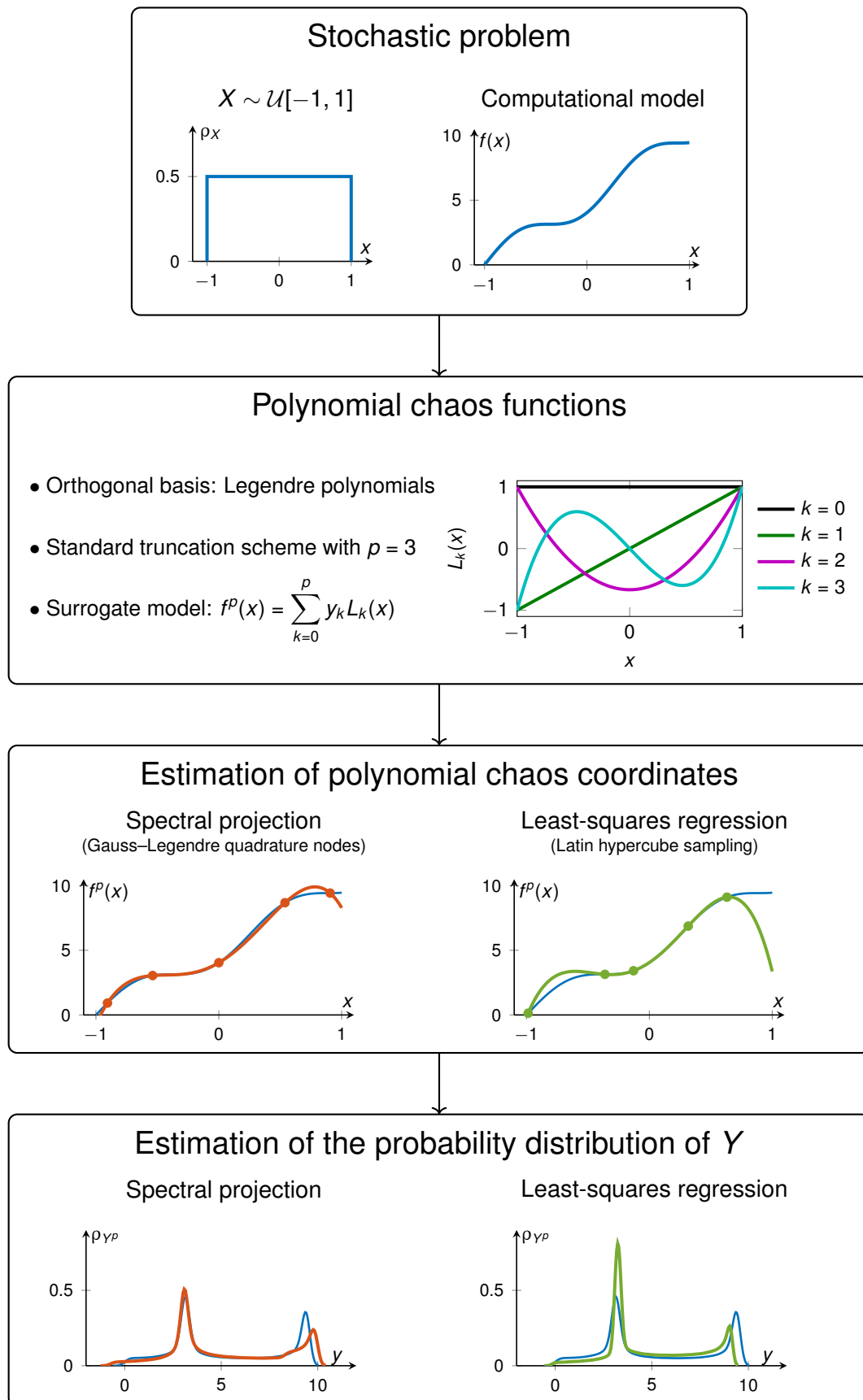


Figure 4.8: Flowchart of the propagation of uncertainties using a surrogate model based on a polynomial chaos expansion (using either spectral projection or least-squares regression).

### Computational cost

The computational cost of constructing a surrogate model based on a polynomial chaos expansion depends on the number of evaluations of the computational model. Using a standard truncation scheme for the polynomial chaos expansion yields a number of polynomial chaos coordinates that grows rapidly with both  $p$  and  $n$ . Consequently, the number of training points required in the experimental design to estimate these polynomial chaos coordinates with sufficient accuracy grows rapidly with both  $p$  and  $n$ . For instance, the computation of the polynomial chaos coordinates using a quadrature rule exhibits an exponential increase in the number of quadrature points with the stochastic dimension. For this reason, surrogate models based on polynomial chaos expansion suffer from the so-called ‘‘curse of dimensionality’’; the number of evaluations of the computational model increases exponentially with the stochastic dimension  $n$ . Methods have been developed to mitigate the curse of dimensionality, including maximum interaction and hyperbolic truncation schemes, (adaptive) sparse polynomial chaos expansions [Blatman and Sudret, 2010, 2011], or (adaptive) sparse-grid quadrature rules [Smolyak, 1963; Gerstner and Griebel, 1998, 2003]. Despite these improved methods, surrogate models based on polynomial chaos expansions remains only a viable option for UQ analysis with a low ( $\mathcal{O}(1-10)$ ) or moderate ( $\mathcal{O}(10-10^2)$ ) stochastic dimension.

#### 4.3.2.2 Gaussian-process regression model

##### Conditional expectation and variance of a Gaussian process

Let  $\{Y(\mathbf{x}), \mathbf{x} \in \mathbb{R}^n\}$  be a Gaussian process  $\text{GP}(\mu(\mathbf{x}), C(\mathbf{x}, \mathbf{x}'))$  with mean function  $\mu(\mathbf{x})$  and covariance function  $C(\mathbf{x}, \mathbf{x}')$  (Section A.4.1). Here, we use the same notation  $\mathbf{x}$  to denote both the index of the Gaussian process and the uncertain input parameters and we use the same notation  $y$  to denote both the value taken by the Gaussian process and the uncertain quantity of interest. Let  $\{\mathbf{x}_1, \dots, \mathbf{x}_\lambda\}$  be a set of locations in  $\mathbb{R}^n$  where the Gaussian process is observed and let  $\{y_1, \dots, y_\lambda\}$  be the observed values of the Gaussian process at the aforementioned locations. Then, for any location  $\mathbf{x}^*$  in  $\mathbb{R}^n$ , the conditional probability distribution of the random variable  $Y(\mathbf{x}^*)$  is a Gaussian probability distribution with mean  $\hat{\mu}(\mathbf{x}^*)$  and variance  $\hat{\sigma}^2(\mathbf{x}^*)$  given by

$$\hat{\mu}(\mathbf{x}^*) = \mu(\mathbf{x}^*) + \Sigma^T(\mathbf{x}^*)[\Sigma]^{-1}(\mathbf{y} - \boldsymbol{\mu}), \quad (4.32)$$

$$\hat{\sigma}^2(\mathbf{x}^*) = \sigma^2(\mathbf{x}^*) - \Sigma^T(\mathbf{x}^*)[\Sigma]^{-1}\Sigma(\mathbf{x}^*), \quad (4.33)$$

with  $\mu(\mathbf{x}^*)$  and  $\sigma^2(\mathbf{x}^*)$  the mean and the variance of the Gaussian process at location  $\mathbf{x}^*$ , respectively,  $\mathbf{y}$  the  $\lambda$ -dimensional vector with entries  $y_i$ ,  $\boldsymbol{\mu}(\mathbf{x}^*)$  the  $\lambda$ -dimensional mean vector with entries  $\mu_i = \mu(\mathbf{x}_i)$ ,  $[\Sigma]$  the  $(\lambda \times \lambda)$ -dimensional covariance matrix with entries  $\Sigma_{ij} = C(\mathbf{x}_i, \mathbf{x}_j)$ , and  $\Sigma(\mathbf{x}^*)$  the  $\lambda$ -dimensional covariance vector with entries  $\Sigma_i(\mathbf{x}^*) = C(\mathbf{x}^*, \mathbf{x}_i)$ . More generally, the conditional field is the Gaussian process  $\text{GP}(\hat{\mu}(\mathbf{x}), \hat{C}(\mathbf{x}, \mathbf{x}'))$  with mean  $\hat{\mu}(\mathbf{x})$  and covariance function  $\hat{C}(\mathbf{x}, \mathbf{x}')$  given by

$$\hat{C}(\mathbf{x}, \mathbf{x}') = C(\mathbf{x}, \mathbf{x}') - \Sigma^T(\mathbf{x})[\Sigma]^{-1}\Sigma(\mathbf{x}'). \quad (4.34)$$

As an illustration, Figure 4.9 shows realisations of a Gaussian process and of the corresponding conditional Gaussian process for a set of observation locations.

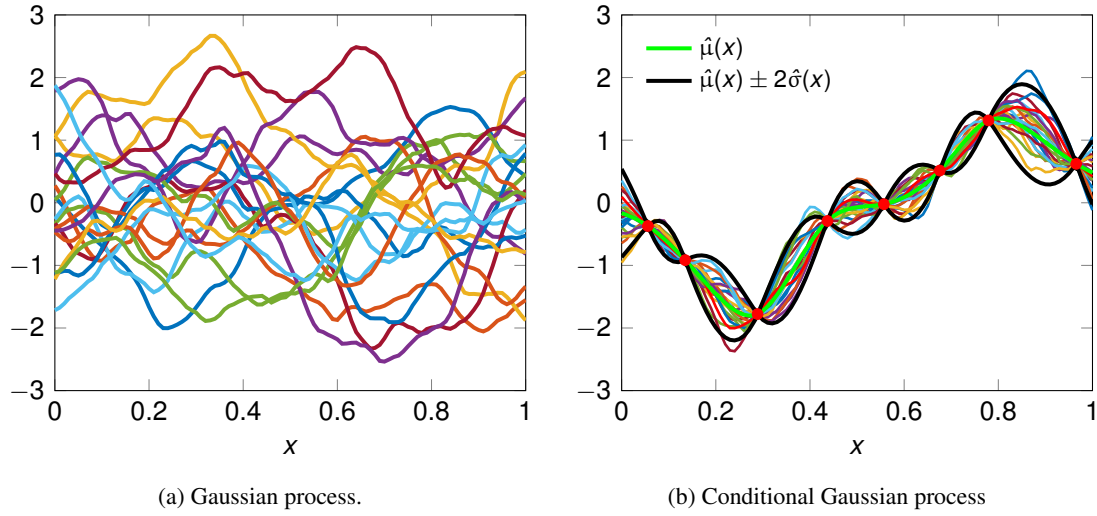


Figure 4.9: (a) Illustration of a Gaussian process with mean zero and Matérn 3/2 covariance function. The curves show realisations of the Gaussian process. (b) Illustration of the associated conditional Gaussian process given the observations at the red dots. The green curve is the conditional mean and the black curves are the conditional mean  $\pm$  two times the conditional standard deviation. Other curves are realisations of the conditional Gaussian process.

### Surrogate model based on Gaussian-process regression

The principle behind the construction of a Gaussian-process (or kriging) surrogate model is to consider the mapping  $\mathbf{x} \mapsto f(\mathbf{x})$  as a realisation of a Gaussian process  $\text{GP}(\mu(\mathbf{x}), C(\mathbf{x}, \mathbf{x}'))$  with mean  $\mu(\mathbf{x})$  and covariance function  $C(\mathbf{x}, \mathbf{x}')$ . Usually, the mean and the covariance function are written as

$$\mu(\mathbf{x}) = \mathbf{g}(\mathbf{x})^T \boldsymbol{\beta}, \quad (4.35)$$

$$C(\mathbf{x}, \mathbf{x}') = \sigma^2 R(\mathbf{x}, \mathbf{x}'; \boldsymbol{\theta}), \quad (4.36)$$

where  $\mathbf{g}(\mathbf{x}) = (g_1(\mathbf{x}), \dots, g_p(\mathbf{x}))$  is a vector of  $p$  basis functions,  $\boldsymbol{\beta}$  a vector of  $p$  coefficients,  $\sigma^2$  the constant variance of the Gaussian process, and  $R(\mathbf{x}, \mathbf{x}'; \boldsymbol{\theta})$  the correlation function of the Gaussian process. We assume the correlation function to be stationary that is  $R(\mathbf{x}, \mathbf{x}'; \boldsymbol{\theta}) = R(\mathbf{x} + \mathbf{h}, \mathbf{x}' + \mathbf{h}; \boldsymbol{\theta})$  for all  $\mathbf{h}$  in  $\mathbb{R}^n$ . We also assume that the correlation function depends on a vector  $\boldsymbol{\theta} = (\theta_1, \dots, \theta_n)$  of hyperparameters, referred to as the correlation lengths, which control the strength of the correlation in each direction of the parameter space.

In this context, the experimental design  $\{\mathbf{x}_\lambda^{(k)}, 1 \leq k \leq \lambda\}$  is interpreted as the set of locations where the Gaussian process  $\text{GP}(\mu(\mathbf{x}), C(\mathbf{x}, \mathbf{x}'))$  is observed and the corresponding solutions to the computation model  $\{y^{(k)} = f(\mathbf{x}_\lambda^{(k)}), 1 \leq k \leq \lambda\}$  are interpreted as the observed values of the Gaussian process at these locations. Then, a Gaussian-process surrogate model is defined as the conditional mean of the Gaussian process  $\text{GP}(\mu(\mathbf{x}), C(\mathbf{x}, \mathbf{x}'))$  given the observations  $\{y^{(k)} = f(\mathbf{x}_\lambda^{(k)}), 1 \leq k \leq \lambda\}$ , that is, the mapping

$$\mathbf{x} \mapsto f^{\text{GP}}(\mathbf{x}) = \mathbb{E} \left[ Y(\mathbf{x}) \mid \left\{ Y(\mathbf{x}_\lambda^{(k)}) = f(\mathbf{x}_\lambda^{(k)}), 1 \leq k \leq \lambda \right\} \right] \equiv \hat{\mu}(\mathbf{x}), \quad (4.37)$$

with

$$\hat{\mu}(\mathbf{x}) = \mathbf{g}(\mathbf{x})^T \boldsymbol{\beta} + \boldsymbol{\Sigma}^T(\mathbf{x})[\boldsymbol{\Sigma}]^{-1}(\mathbf{y} - \boldsymbol{\mu}), \quad (4.38)$$

where we use the same notations as before. It can be shown that the conditional mean of the Gaussian process is actually the best linear unbiased predictor of  $f$  [Santner et al., 2003]. An estimation of the approximation error is provided by the conditional variance of the Gaussian process  $\text{GP}(\mu(\mathbf{x}), C(\mathbf{x}, \mathbf{x}'))$  given the observations  $\{y^{(k)} = f(\mathbf{x}_\lambda^{(k)}), 1 \leq k \leq \lambda\}$ , that is,

$$\mathbb{V} \left[ Y(\mathbf{x}) \mid \left\{ Y(\mathbf{x}_\lambda^{(k)}) = f(\mathbf{x}_\lambda^{(k)}), 1 \leq k \leq \lambda \right\} \right] \equiv \hat{\sigma}^2(\mathbf{x}), \quad (4.39)$$

with

$$\hat{\sigma}^2(\mathbf{x}) = \sigma^2 - \boldsymbol{\Sigma}^T(\mathbf{x})[\boldsymbol{\Sigma}]^{-1}\boldsymbol{\Sigma}(\mathbf{x}). \quad (4.40)$$

More generally, the conditional Gaussian process  $\text{GP}(\hat{\mu}(\mathbf{x}), \hat{C}(\mathbf{x}, \mathbf{x}'))$  with mean  $\hat{\mu}(\mathbf{x})$  and covariance function

$$\hat{C}(\mathbf{x}, \mathbf{x}') = \sigma^2 - \boldsymbol{\Sigma}^T(\mathbf{x})[\boldsymbol{\Sigma}]^{-1}\boldsymbol{\Sigma}(\mathbf{x}') \quad (4.41)$$

defines a stochastic surrogate model, denoted by  $F^{\text{fGP}}(\mathbf{x})$ , also referred to as the full-Gaussian-process surrogate model [De Lozzo and Marrel, 2016; Marrel, 2017]. Here, we use a capital letter to denote the full-Gaussian-process surrogate model to highlight that this surrogate model is stochastic.

Usually,  $\boldsymbol{\beta}$ ,  $\sigma^2$ , and  $\boldsymbol{\theta}$  have to be estimated. The vector of hyperparameters  $\boldsymbol{\theta}$  is usually determined by solving an optimisation problem; see, for instance, Santner et al. [2003] and Dubourg [2011]. For  $\boldsymbol{\theta}$  fixed, the vector  $\boldsymbol{\beta}$  and the variance  $\sigma^2$  can be estimated as the following generalised least-square estimates:

$$\hat{\boldsymbol{\beta}} = ([G]^T[R]^{-1}[G])^{-1}[G]^T[R]^{-1}\mathbf{y}, \quad (4.42)$$

$$\hat{\sigma}^2 = \frac{1}{\lambda}(\mathbf{y} - [G]\hat{\boldsymbol{\beta}})^T[R]^{-1}(\mathbf{y} - [G]\hat{\boldsymbol{\beta}}), \quad (4.43)$$

with  $[R]$  the  $(\lambda \times \lambda)$ -dimensional covariance matrix with entries  $R_{ij} = R(\mathbf{x}_i, \mathbf{x}_j; \boldsymbol{\theta})$  and  $[G]$  the  $(\lambda \times p)$ -dimensional matrix with entries  $G_{ij} = g_j(\mathbf{x}_i)$ . Thus, the conditional mean and the conditional variance of the Gaussian process write as

$$\hat{\mu}(\mathbf{x}) = \mathbf{g}(\mathbf{x})^T \hat{\boldsymbol{\beta}} + \mathbf{r}^T(\mathbf{x})[R]^{-1}(\mathbf{y} - [G]\hat{\boldsymbol{\beta}}), \quad (4.44)$$

$$\hat{\sigma}^2(\mathbf{x}) = \hat{\sigma}^2(1 - \mathbf{r}^T(\mathbf{x})[R]^{-1}\mathbf{r}(\mathbf{x}) + \mathbf{u}^T(\mathbf{x})([G]^T[R]^{-1}[G])^{-1}\mathbf{u}(\mathbf{x})), \quad (4.45)$$

where the vector  $\mathbf{u}(\mathbf{x})$  is given by

$$\mathbf{u}(\mathbf{x}) = [G]^T[R]^{-1}\mathbf{r}(\mathbf{x}) - \mathbf{g}(\mathbf{x}), \quad (4.46)$$

and  $\mathbf{r}(\mathbf{x})$  is the  $\lambda$ -dimensional correlation vector with entries  $r_i(\mathbf{x}) = R(\mathbf{x}, \mathbf{x}_i; \boldsymbol{\theta})$ .

The basis functions in  $\mathbf{g}(\mathbf{x})$  are usually taken to be low-order polynomials, that is, the mean function is often assumed to be a constant, linear, or quadratic function. In one dimension, the stationary correlation function depends on the distance  $h$  between  $x$  and  $x'$  and is in general selected in a standard family of correlation functions including the linear, exponential, Gaussian, and Matérn correlation functions (Figure 4.10). In higher dimensions, correlation functions can

be built from one-dimensional correlation functions; see, for instance, [Rasmussen and Williams \[2006\]](#) and [Dubourg \[2011\]](#). The choice of the covariance function depends on the properties of the computational model; for instance, Gaussian processes with a Gaussian correlation function have infinitely differentiable realisations while Gaussian processes with an exponential correlation function have only continuous realisations. Finally, we refer the reader to [Figure 4.11](#) for an illustration of the propagation of uncertainties using a Gaussian-process surrogate model.

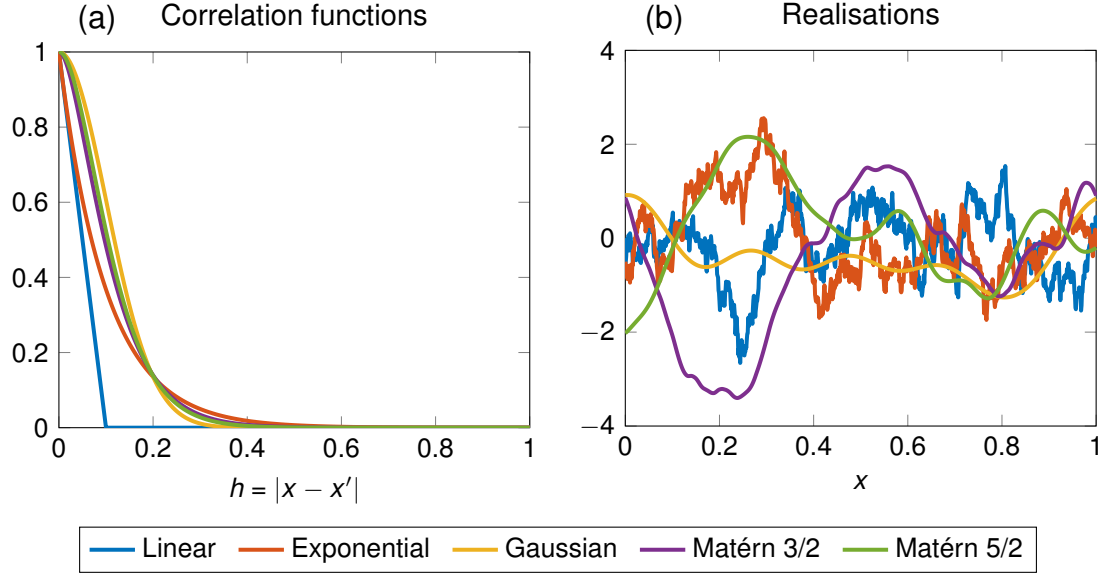


Figure 4.10: (a) Examples of correlation functions and (b) a realisation of the Gaussian process for each example of correlation function. The correlation length is  $\theta = 1$ .

### 4.3.2.3 Error estimation

Once a surrogate model of the computational model is built, its predictive accuracy can be assessed by evaluating the relative mean-square error between both models:

$$\frac{\mathbb{E}[(Y - \tilde{Y})^2]}{\mathbb{E}[Y^2]} = \frac{\mathbb{E}[(f(\mathbf{X}) - \tilde{f}(\mathbf{X}))^2]}{\mathbb{E}[f^2(\mathbf{X})]}. \quad (4.47)$$

When a new ensemble  $\left\{(\mathbf{x}^{(k)}, y^{(k)} = f(\mathbf{x}^{(k)})), 1 \leq k \leq \nu\right\}$  of samples can be generated from the computational model, this error can be estimated as

$$\frac{\frac{1}{\nu} \sum_{k=1}^{\nu} \left(f(\mathbf{x}^{(k)}) - \tilde{f}(\mathbf{x}^{(k)})\right)^2}{\frac{1}{\nu} \sum_{k=1}^{\nu} f^2(\mathbf{x}^{(k)})}. \quad (4.48)$$

This new ensemble of samples is sometimes referred to as the test set in opposition with the training set that is used to train the surrogate model. When such a test set cannot be generated due to the computational cost of the computational model, the predictive accuracy of the surrogate model can be assessed using  $K$ -fold cross-validation on the training set. The idea is to split

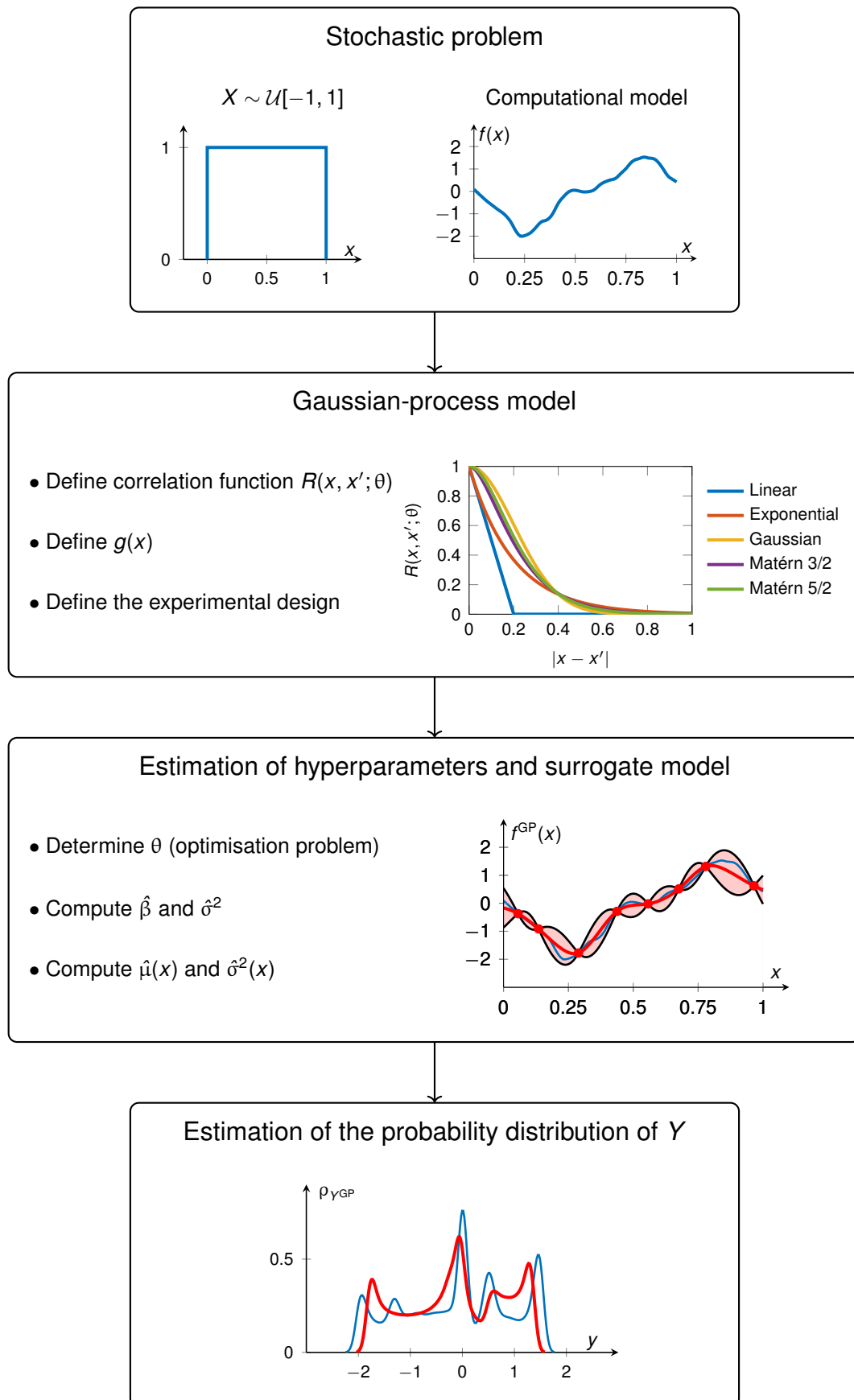


Figure 4.11: Flowchart of the propagation of uncertainties using a surrogate model based on Gaussian-process regression.

the experimental design into  $K$  equally sized disjoint subsets. One of these subsets is used as a test set and the other  $K - 1$  subsets are used to train the surrogate model. The procedure is repeated  $K$  times, each time with a different subset of the training set as test set and the predictive accuracy of the surrogate model is estimated as the mean predictive error on all test sets. A special case is obtained for  $K = \lambda$ , thus leading to the so-called leave-one-out cross-validation error. Considering the experimental design  $\{\mathbf{x}_\lambda^{(k)}, 1 \leq k \leq \lambda\}$  and denoting by  $\tilde{f}_{\lambda \setminus i}$  the surrogate model built on the set of samples  $\{\mathbf{x}_\lambda^{(1)}, \dots, \mathbf{x}_\lambda^{(i-1)}, \mathbf{x}_\lambda^{(i+1)}, \dots, \mathbf{x}_\lambda^{(\lambda)}\}$ , the leave-one-out cross-validation error writes as

$$\frac{\sum_{k=1}^{\lambda} \left( f(\mathbf{x}_\lambda^{(k)}) - \tilde{f}_{\lambda \setminus i}(\mathbf{x}_\lambda^{(k)}) \right)^2}{\sum_{k=1}^{\lambda} f^2(\mathbf{x}_\lambda^{(k)})}. \quad (4.49)$$

For surrogate models based on a polynomial chaos expansion, this error can be computed from a single polynomial chaos expansion of the full experimental design; see, for instance, [Blatman \[2009\]](#).

### 4.3.3 Probabilistic learning on manifolds

When the computational model is computationally expensive, only a limited number of evaluations of this computational model may be carried out at a reasonable computational cost. Such a limited number of evaluations may not be sufficient to obtain sufficient accuracy in estimating the probability distribution or statistical descriptors of the quantity of interest and more generally may be challenging in other applications such as sensitivity analysis, optimisation under uncertainty, extreme value analysis, . . . As a means of improving the accuracy in such so-called small-data settings, we briefly address in this section the use of the probabilistic learning on manifolds (PLOM) method that has been recently introduced by [Soize and Ghanem \[2016\]](#).

We assume that i.i.d. samples  $\mathbf{x}^{(1)}, \dots, \mathbf{x}^{(\nu_{\text{ir}})}$  of the uncertain input parameters have been generated and the corresponding samples  $y^{(1)} = f(\mathbf{x}^{(1)}), \dots, y^{(\nu_{\text{ir}})} = f(\mathbf{x}^{(\nu_{\text{ir}})})$  of the quantity of interest have been obtained by evaluating the computational model. The ensemble

$$\{\mathbf{w}^{(k)} = (\mathbf{x}^{(k)}, y^{(k)}), 1 \leq k \leq \nu_{\text{ir}}\} \quad (4.50)$$

defines the so-called initial dataset that collects the available information about the uncertain input parameters and the corresponding values of the quantity of interest. Here, the subscript “ir” stands for initial realisations and  $\nu_{\text{ir}}$  is the length of the initial dataset and is assumed to be a small number because only a limited number of evaluations of the computational model is computationally affordable. In a probabilistic setting, the initial dataset is interpreted as an ensemble of i.i.d. samples of the  $\mathbb{R}^{n+1}$ -valued random vector  $\mathbf{W} = (\mathbf{X}, Y)$ . Here, we assume that the initial dataset represents the only available information about the random vector  $\mathbf{W}$ . As a means of improving the accuracy of the Monte Carlo method in small-data settings, we are interested in generating additional realisations of  $\mathbf{W}$  to obtain the so-called learned dataset

$$\{\mathbf{w}^{(k)} = (\mathbf{x}^{(k)}, y^{(k)}), 1 \leq k \leq \nu_{\text{ar}}\}, \quad (4.51)$$

where the subscript “ar” stands for additional realisations and  $\nu_{\text{ar}}$  is the length of the learned dataset and is assumed to be much larger than  $\nu_{\text{ir}}$ . It should be noted that the learned dataset is

generated without resort to the computational model and the additional realisations are generated to be statistically consistent with the initial dataset so that these additional realisations can be considered as being sampled from the same probability distribution as  $\mathbf{W}$ .

As an effective way to build a learned dataset, we discuss in the following the PLoM method. The PLoM method has been recently introduced in [Soize and Ghanem \[2016\]](#) with complementary developments in [Soize and Ghanem \[2017, 2020\]](#), [Ghanem and Soize \[2018\]](#), and [Soize et al. \[2019\]](#). Hereafter, we briefly review key aspects of this method and we refer the interested reader to the aforementioned references for further details about the theoretical framework and applications. The central idea underlying manifold learning and the PLoM method is that a dataset in a Euclidean space is often concentrated near a lower-dimensional subset, also called a manifold, of this Euclidean space; see [Figure 4.12](#) for an illustration. Thus, through the identification of this underlying manifold, one can obtain a reduced-dimensional representation of the initial dataset that captures its geometric structure. In the PLoM method, the identification of this underlying manifold is performed by means of the diffusion-map method, a nonlinear dimension-reduction method that seeks to learn the structure of the manifold by computing the so-called diffusion maps from a diffusion operator [[Coifman et al., 2005](#); [Coifman and Lafon, 2006](#)]. In the first step of the PLoM method, the initial dataset is normalised by means of a principal component analysis. Then, a probabilistic representation of the random vector  $\mathbf{W}$  is built from the normalised initial dataset by using multi-dimensional Gaussian kernel-density estimation in combination with a reduced-order representation of the normalised initial dataset using the eigenvectors involved in the construction of the nonlinear diffusion map in order to preserve the concentration of the samples near the manifold. Finally, this probabilistic representation is used to generate additional realisations of the random vector  $\mathbf{W}$  with a Markov chain Monte Carlo algorithm based on a reduced-order Itô stochastic differential equation [[Soize, 2008, 2015](#)]. As an illustration, [Figure 4.13](#) shows the additional realisations generated with the PLoM method for the initial datasets in [Figure 4.12](#). We can observe that the PLoM method has preserved the concentration of the additional realisations near the manifold near which the initial realisations are concentrated.

## 4.4 Global sensitivity analysis

Sensitivity analysis can be broadly viewed as the study of how different sources of uncertainty in the computational model contribute to the uncertainty in the quantity of interest. Thus, sensitivity analysis can serve to ascertain the impact of each source of uncertainty on the uncertainty in the quantity of interest and rank them in order of significance, to identify non-influential sources of uncertainty in order to fix them to nominal values, to identify regimes in the parameter space that impact significantly the model response, and to identify sources of uncertainty that could be calibrated in order to reduce the uncertainty in the quantity of interest.

Methods for sensitivity analysis are usually classified as either local or global. In the context of local sensitivity analysis, the impact of small perturbations in the input parameters on the quantity of interest is investigated. Local sensitivity analysis is typically performed by evaluating the derivatives of the quantity of interest with respect to the input parameters at specific points in the parameter space or by using adjoint-based methods for a large number of input parameters. In contrast to local sensitivity analysis, global sensitivity analysis, which we focus

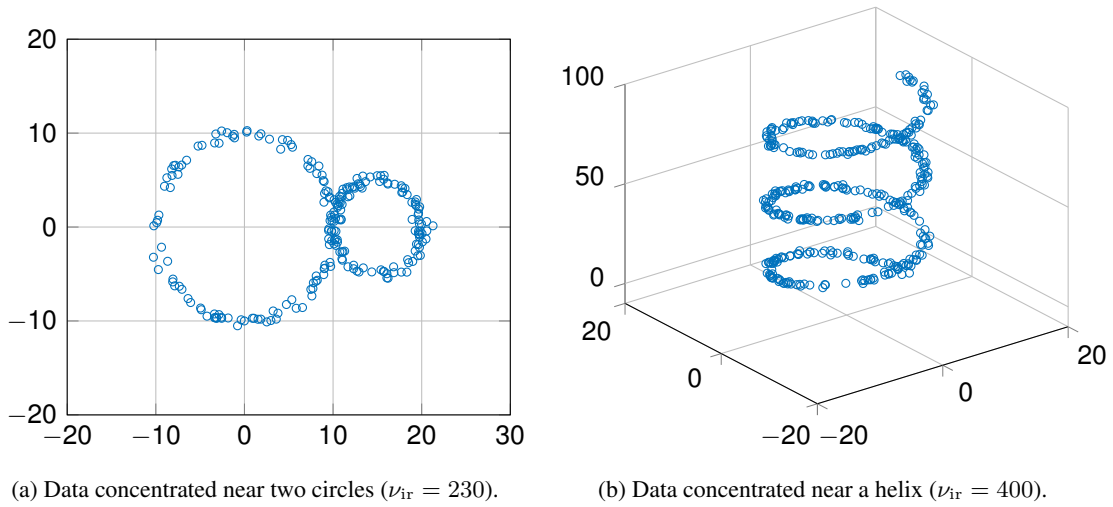


Figure 4.12: Examples of noisy data concentrated near a manifold [Soize and Ghanem, 2016]. (a) Data in  $\mathbb{R}^2$  concentrated near two circles and (b) data in  $\mathbb{R}^3$  concentrated near a helix.

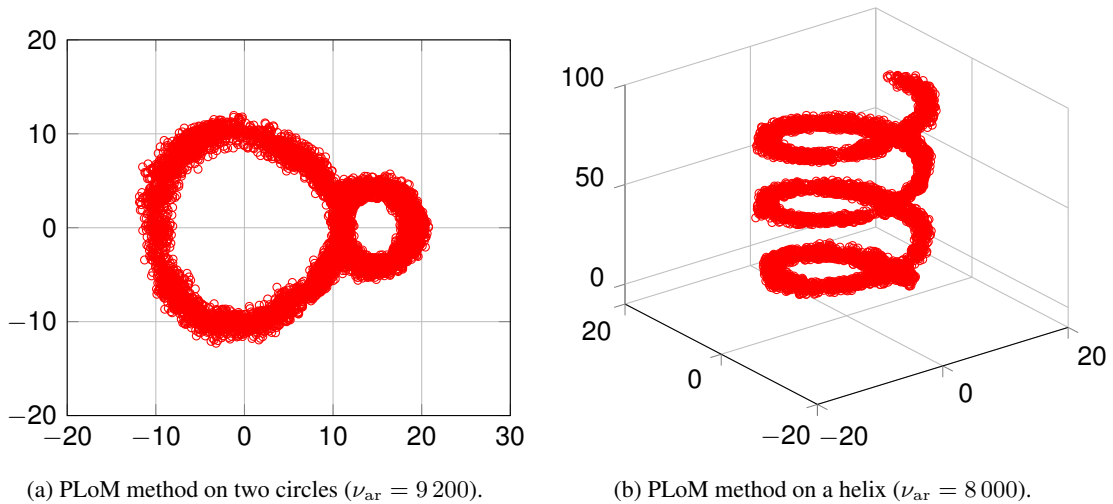


Figure 4.13: Examples of additional realisations using the PLoM algorithm for the initial datasets in Figure 4.12. (a) Additional realisations concentrated near two circles and (b) additional realisations concentrated near a helix. Parameters of the PLoM algorithm are taken from Soize and Ghanem [2016].

on in the following, aims at assessing how the whole uncertainty in the quantity of interest can be apportioned to each source or each combination of sources of uncertainty when considering the whole range of variation of the sources of uncertainty.

Several methods have been proposed in the literature for global sensitivity analysis; see, for instance, Saltelli et al. [2008] and Ghanem et al. [2017] for textbooks and Iooss and Lemaitre [2015] for a review paper. In the following, we focus on methods based on importance mea-

asures, also referred to as quantitative sensitivity indices, including essentially variance-based sensitivity indices, but also Pearson correlation coefficients and sensitivity indices based on the Hilbert-Schmidt independence criterion.

#### 4.4.1 Pearson correlation coefficients

The Pearson correlation coefficient is a measure of the linear correlation between two random variables. The Pearson correlation coefficient between the random variable  $X_i$ ,  $1 \leq i \leq n$ , and the random variable  $Y$  is defined by

$$\rho(X_i, Y) = \frac{\text{Cov}(X_i, Y)}{\sqrt{\mathbb{V}[X_i]\mathbb{V}[Y]}} = \frac{\mathbb{E}[X_i - \mathbb{E}[X_i]]\mathbb{E}[Y - \mathbb{E}[Y]]}{\sqrt{\mathbb{V}[X_i]\mathbb{V}[Y]}}. \quad (4.52)$$

The Pearson correlation coefficient equals 1 or  $-1$  if there exists a perfect positive or negative linear relationship between  $X_i$  and  $Y$  and is equal to 0 for independent random variables. Thus, the Pearson correlation coefficient is usually inappropriate when dealing with nonlinear and non-monotonic relationships and interactions between the input parameters.

Given an ensemble of i.i.d. samples  $\{\mathbf{x}^{(k)}, 1 \leq k \leq \nu\}$  of the uncertain input parameters and the corresponding ensemble  $\{y^{(k)} = f(\mathbf{x}^{(k)}), 1 \leq k \leq \nu\}$  of solutions to the computational model, Monte Carlo estimates of the Pearson correlation coefficients are obtained as

$$\rho^\nu(X_i, Y) = \frac{\sum_{k=1}^{\nu} (x_i^{(k)} - m_{X_i}^\nu)(y^{(k)} - m_Y^\nu)}{\sqrt{\sum_{k=1}^{\nu} (x_i^{(k)} - m_{X_i}^\nu)^2 \sum_{k=1}^{\nu} (y^{(k)} - m_Y^\nu)^2}}, \quad 1 \leq i \leq n, \quad (4.53)$$

with

$$m_{X_i}^\nu = \frac{1}{\nu} \sum_{k=1}^{\nu} x_i^{(k)}, \quad (4.54)$$

$$m_Y^\nu = \frac{1}{\nu} \sum_{k=1}^{\nu} y^{(k)}. \quad (4.55)$$

When the computational model has a high computational cost that prohibits the use of the Monte Carlo sampling method, a surrogate model, or a learning algorithm can be used instead of the computational model.

#### 4.4.2 Variance-based sensitivity indices

Variance-based sensitivity indices, also called Sobol indices, provide for each uncertain parameter or group of uncertain parameters a sensitivity index that quantifies the relative contribution of the uncertainty in this uncertain parameter or group of uncertain parameters to the variance of the quantity of interest. Variance-based sensitivity indices are often defined based on a decomposition of the mapping  $f$  between the uncertain input parameters and the quantity of interest into component functions. In this section, we follow this approach to define the Sobol indices and we discuss methods to estimate these sensitivity indices. We refer the reader to, for instance, Owen [2013], Sobol [2001], Saltelli [2002], and Oakley and O'Hagan [2004] for complementary details about Sobol indices and to a recent co-authored manuscript by Arnst et al. [2019] about the computation of Sobol indices using the PLoM algorithm.

#### 4.4.2.1 HDMR decomposition

Let us assume that the random vector  $\mathbf{X}$  has independent components and the random variable  $Y = f(\mathbf{X})$  is of the second order. The high-dimensional model representation (HDMR) of  $f$  writes as

$$\begin{aligned} f(\mathbf{x}) &= f_\emptyset + \sum_{i=1}^n f_{\{i\}}(x_i) + \sum_{i=1}^n \sum_{i < j}^n f_{\{i,j\}}(x_i, x_j) + \dots + f_{\{1,\dots,n\}}(x_1, \dots, x_n) \\ &= \sum_{\mathbf{u} \in \mathcal{P}(\{1,\dots,n\})} f_{\mathbf{u}}(\mathbf{x}_{\mathbf{u}}), \end{aligned} \quad (4.56)$$

with

$$\int_{\mathbb{R}} f_{\mathbf{u}}(\mathbf{x}_{\mathbf{u}}) \mathbb{P}_{X_i}(dx_i) = 0, \quad \forall i \in \mathbf{u}, \quad \forall \mathbf{u} \in \mathcal{P}(\{1, \dots, n\}). \quad (4.57)$$

Here,  $\mathcal{P}(\{1, \dots, n\})$  denotes the collection of all subsets of  $\{1, \dots, n\}$  and  $\mathbf{u} = (i_1, \dots, i_{|\mathbf{u}|})$  denotes a set in  $\mathcal{P}(\{1, \dots, n\})$  of cardinality  $|\mathbf{u}|$ . The notation  $\mathbf{x}_{\mathbf{u}} = (x_{i_1}, \dots, x_{i_{|\mathbf{u}|}})$  denotes the subvector of the input parameters whose components are indexed by the indices in  $\mathbf{u}$ ; by convention  $\mathbf{x}_\emptyset = 1$  for  $\mathbf{u} = \emptyset$  and we use the shorthand  $i$  to denote the singleton  $\mathbf{u} = \{i\}$ . In the following, we also denote by  $\sim \mathbf{u}$  the complement of  $\mathbf{u}$  in  $\{1, \dots, n\}$ . For two subvectors  $\mathbf{u}$  and  $\mathbf{v}$ , we denote by  $\mathbf{u} \subseteq \mathbf{v}$  that  $\mathbf{u}$  is a subset of  $\mathbf{v}$  and by  $\mathbf{u} \subsetneq \mathbf{v}$  that  $\mathbf{u}$  is a proper subset of  $\mathbf{v}$ .

The conditions in Equation (4.57) define orthogonality constraints on the summands of Equation (4.56) that ensure the existence and uniqueness of the HDMR. It follows from Equation (4.57) that all non-constant summands in Equation (4.56) have zero mean. Another consequence of Equation (4.57) is that

$$\mathbb{E}[Y] = \int_{\mathbb{R}^n} f(\mathbf{x}) \mathbb{P}_{\mathbf{X}}(d\mathbf{x}) = f_\emptyset, \quad (4.58)$$

$$\mathbb{E}[f_{\mathbf{u}}(\mathbf{X}_{\mathbf{u}}) f_{\mathbf{v}}(\mathbf{X}_{\mathbf{v}})] = \int_{\mathbb{R}^n} f_{\mathbf{u}}(\mathbf{x}_{\mathbf{u}}) f_{\mathbf{v}}(\mathbf{x}_{\mathbf{v}}) \mathbb{P}_{\mathbf{X}}(d\mathbf{x}) = 0, \quad \forall \mathbf{u} \neq \mathbf{v} \in \mathcal{P}(\{1, \dots, n\}), \quad (4.59)$$

that is,  $f_\emptyset$  is the mean value of  $Y$  and the summands in Equation (4.56) are orthogonal in pairs with respect to the probability distribution  $\mathbb{P}_{\mathbf{X}}$ . Thus, the HDMR provides a decomposition of a function of a random vector as a sum of uncorrelated terms, also called factors, where the sum is made up of a constant function, univariate functions  $\{f_i(x_i), 1 \leq i \leq n\}$ , bivariate functions,  $\dots$ , and an  $n$ -variate function  $f_{\{1,\dots,n\}}(x_1, \dots, x_n)$ . The univariate factor  $f_i(x_i)$  is the so-called main effect associated with the uncertain parameter  $x_i$  and the factors for subvectors  $\mathbf{u}$  of cardinality larger than one are the so-called interaction effects. The total interaction effect is given by

$$f_I(\mathbf{x}) = f(\mathbf{x}) - f_\emptyset - \sum_{i=1}^n f_i(x_i) = \sum_{\mathbf{u} \in \mathcal{P}(\{1,\dots,n\}), |\mathbf{u}| > 1} f_{\mathbf{u}}(\mathbf{x}_{\mathbf{u}}). \quad (4.60)$$

The factor  $f_{\mathbf{u}}$  in Equation (4.56) can be determined either from the solution of a regression problem or from the conditional expectation of  $Y$  given the random vector  $\mathbf{X}_{\mathbf{u}}$ ; see, for instance, [Oakley and O'Hagan \[2004\]](#) and [Owen \[2013\]](#). The second approach leads to the following recursive manner to compute the factors in Equation (4.56):

$$f_\emptyset = \mathbb{E}[f(\mathbf{X})] = \int_{\mathbb{R}^n} f(\mathbf{x}) \mathbb{P}_{\mathbf{X}}(d\mathbf{x}), \quad (4.61)$$

$$f_i(x_i) = \mathbb{E}[f(\mathbf{X})|X_i = x_i] - f_\emptyset = \int_{\mathbb{R}^{n-1}} f(\mathbf{x}) \mathbb{P}_{\mathbf{X}_{\sim i}}(d\mathbf{x}_{\sim i}) - f_\emptyset, \quad (4.62)$$

$$\begin{aligned} f_u(\mathbf{x}_u) &= \mathbb{E}[f(\mathbf{X})|\mathbf{X}_u = \mathbf{x}_u] - \sum_{v \subsetneq u} f_v(\mathbf{x}_v) \\ &= \int_{\mathbb{R}^{n-|u|}} f(\mathbf{x}) \mathbb{P}_{\mathbf{X}_{\sim u}}(d\mathbf{x}_{\sim u}) - \sum_{v \subsetneq u} f_v(\mathbf{x}_v). \end{aligned} \quad (4.63)$$

It should be mentioned that under certain assumptions, the HDMR can be extended to dependent uncertain input parameters, from which can be deduced generalised variance-based sensitivity indices; see, for instance, [Chastaing \[2013\]](#) and [Chastaing et al. \[2012, 2015\]](#). Yet, these generalised variance-based sensitivity indices may lack interpretability and for the sake of simplicity, we do not discuss them in this manuscript.

#### 4.4.2.2 Sobol indices

Thanks to the orthogonality of the summands in Equation (4.56), the variance of  $Y$  can be decomposed as

$$\begin{aligned} \mathbb{V}[Y] &= \mathbb{V}[f(\mathbf{X})] \\ &= \sum_{i=1}^n \mathbb{V}[f_i(X_i)] + \sum_{i=1}^n \sum_{i < j}^n \mathbb{V}[f_{\{i,j\}}(X_i, X_j)] + \dots + \mathbb{V}[f_{\{1,\dots,n\}}(X_1, \dots, X_n)] \\ &= \sum_{u \in \mathcal{P}(\{1,\dots,n\})} \mathbb{V}[f_u(\mathbf{X}_u)]. \end{aligned} \quad (4.64)$$

This decomposition leads to the definition of the Sobol indices.

**Definition 4.1 (Sobol index).** The Sobol index  $S_u$  of order  $|u|$  measuring the contribution of the variable  $\mathbf{X}_u$  in the model  $Y = f(\mathbf{X})$  is given by

$$S_u = \frac{\mathbb{V}[f_u(\mathbf{X}_u)]}{\mathbb{V}[Y]} = \frac{\mathbb{V}[\mathbb{E}(Y|\mathbf{X}_u)] + \sum_{v \subsetneq u} (-1)^{|u|-|v|} \mathbb{V}[\mathbb{E}(Y|\mathbf{X}_v)]}{\mathbb{V}[Y]}. \quad (4.65)$$

In particular, the Sobol index of order 1 measuring the contribution of the variable  $X_i$  writes as

$$S_i = \frac{\mathbb{V}[f_i(X_i)]}{\mathbb{V}[Y]} = \frac{\mathbb{V}[\mathbb{E}(Y|X_i)]}{\mathbb{V}[Y]}. \quad (4.66)$$

Thus, the Sobol index  $S_u$  represents the relative portion of the variance of  $Y$  that is explained by the factor  $f_u(\mathbf{X}_u)$  in the HDMR. In particular, the Sobol index  $S_i$ , also called the first-order sensitivity index or main effect index for the random variable  $X_i$ , represents the relative portion of the variance of  $Y$  that is explained by the random variable  $X_i$  independently of the other random variables. Hence, the random variable  $X_i$  has a significant impact on the variability of the quantity of interest, as measured by its variance, when  $S_i$  is close to 1, whereas it has a negligible impact when  $S_i$  is close to 0. In addition, the model is “free” of interactions if  $\sum_{i=1}^n S_i$  is close to 1.

The Sobol index  $S_u$  measures the contribution of the random subvector  $\mathbf{X}_u$  to the variance of  $Y$  while neglecting the interactions with other subvectors. Another way to describe the impact of the random variables indexed by the indices in  $\mathbf{u}$  is to consider the closed Sobol index.

**Definition 4.2 (Closed Sobol index).** The closed Sobol index  $S_u$  of order  $|\mathbf{u}|$  measuring the contribution of the variables  $\mathbf{X}_{i_1}, \dots, \mathbf{X}_{i_{|\mathbf{u}|}}$  in the model  $Y = f(\mathbf{X})$  is given by

$$S_u^{\text{clo}} = \sum_{v \subseteq u} S_v. \quad (4.67)$$

Thus, the closed Sobol index  $S_u$  can be interpreted as the portion of the variance of the uncertain quantity of interest that is explained as stemming from the uncertain input parameters indexed by the indices  $i_1, \dots, i_{|\mathbf{u}|}$ . Please note that the closed Sobol indices of order 1 are equivalent to the first-order Sobol indices.

In practice, the computation of Sobol indices is often limited to the first-order sensitivity indices, which we focus on in the following. Please note that the estimation methods presented hereafter can be readily extended to the estimation of any closed Sobol index  $S_u$ .

#### 4.4.2.3 Estimation of Sobol indices using Monte Carlo sampling

The Sobol index in Equation (4.66) can be rewritten as

$$S_i = \frac{\text{Cov}(f(X_i, \mathbf{X}_{\sim i}), f(X_i, \mathbf{X}'_{\sim i}))}{\mathbb{V}[f(X_i, \mathbf{X}_{\sim i})]}, \quad (4.68)$$

where  $\mathbf{X}_{\sim i} = (X_1, \dots, X_{i-1}, X_{i+1}, \dots, X_n)$  and  $\mathbf{X}'_{\sim i}$  denotes an independent copy of  $\mathbf{X}_{\sim i}$ ; see, for instance, [Janon et al. \[2014\]](#) for a proof of Equation (4.68). Then, Monte Carlo estimates of Equation (4.68) yield Monte Carlo estimates of the Sobol index  $S_i$ .

A typical implementation of the Monte Carlo sampling method for Sobol indices goes as follows. Let

$$\left\{ (x_i^{(k)}, \mathbf{x}_{\sim i}^{(k)}, y^{(k)}), 1 \leq k \leq \nu \right\}, \quad \text{in which } y^{(k)} = f(x_i^{(k)}, \mathbf{x}_{\sim i}^{(k)}), \quad (4.69)$$

$$\left\{ (x_i^{(k)}, \mathbf{x}'_{\sim i}^{(k)}, y'^{(k)}), 1 \leq k \leq \nu \right\}, \quad \text{in which } y'^{(k)} = f(x_i^{(k)}, \mathbf{x}'_{\sim i}^{(k)}) \quad (4.70)$$

be two ensembles of sample values of the uncertain input parameters that share the same i.i.d. samples for  $X_i$  but have different i.i.d. samples for the other random variables along with the corresponding sample values of the quantity of interest evaluated by using the computational model. A Monte Carlo estimate  $S_i^\nu$  of  $S_i$ , described in reference [\[Homma and Saltelli, 1996\]](#), is then obtained as

$$S_i^{\nu, \text{Hom}} = \frac{\frac{1}{\nu} \sum_{k=1}^{\nu} y^{(k)} y'^{(k)} - \left( \frac{1}{\nu} \sum_{k=1}^{\nu} y^{(k)} \right) \left( \frac{1}{\nu} \sum_{k=1}^{\nu} y'^{(k)} \right)}{\frac{1}{\nu} \sum_{k=1}^{\nu} (y^{(k)})^2 - \left( \frac{1}{\nu} \sum_{k=1}^{\nu} y^{(k)} \right)^2}, \quad (4.71)$$

or by noting that  $\mathbb{E}[f(X_i, \mathbf{X}_{\sim i})] = \mathbb{E}[f(X_i, \mathbf{X}'_{\sim i})]$ , we obtain the following Monte Carlo estimate due initially to [Sobol \[1993\]](#):

$$S_i^{\nu, \text{Sob}} = \frac{\frac{1}{\nu} \sum_{k=1}^{\nu} y^{(k)} y'^{(k)} - \left( \frac{1}{\nu} \sum_{k=1}^{\nu} y^{(k)} \right)^2}{\frac{1}{\nu} \sum_{k=1}^{\nu} (y^{(k)})^2 - \left( \frac{1}{\nu} \sum_{k=1}^{\nu} y^{(k)} \right)^2}. \quad (4.72)$$

Another Monte Carlo estimate of  $S_i$  described by Janon et al. [2014] writes as

$$S_i^{\nu, \text{Jan}} = \frac{\frac{1}{\nu} \sum_{k=1}^{\nu} y^{(k)} y'^{(k)} - \left( \frac{1}{\nu} \sum_{k=1}^{\nu} \left[ \frac{y^{(k)} + y'^{(k)}}{2} \right] \right)^2}{\frac{1}{\nu} \sum_{k=1}^{\nu} \left[ \frac{(y^{(k)})^2 + (y'^{(k)})^2}{2} \right] - \left( \frac{1}{\nu} \sum_{k=1}^{\nu} \left[ \frac{y^{(k)} + y'^{(k)}}{2} \right] \right)^2}. \quad (4.73)$$

Thus evaluating the first-order sensitivity indices for the  $n$  components of  $\mathbf{X}$  using Equations (4.71), Equation (4.72), or Equation (4.73) requires a total of  $\nu \times (n + 1)$  evaluations of the computational model. In addition, the accuracy of these estimates improves as the square root of the number  $\nu$  of samples, with the estimate in Equation (4.73) that performs better than the estimates in Equations (4.71) and (4.72); see, for instance, Janon et al. [2014]. For these reasons, the evaluations of Sobol indices with Monte Carlo sampling can become prohibitive for computational models with a high computational cost or a high stochastic dimension  $n$ . As for the propagation of uncertainties, much research has thus been dedicated in the field of uncertainty quantification to develop methods that seek to alleviate the computational cost of estimating Sobol indices with Monte Carlo sampling. These methods include methods based on surrogate models (Section 4.4.2.5) or learning algorithms (Section 4.4.2.6).

#### 4.4.2.4 Estimation of Sobol indices using nonparametric kernel methods

The principle of nonparametric kernel methods for the estimation of Sobol indices is to approximate the main effects in Equation (4.62) using nonparametric kernel regression; see, for instance, Luo et al. [2014]. These methods rely on the following equivalent formulation of the main effect  $f_i(x_i)$ :

$$f_i(x_i) = \mathbb{E}[Y | X_i = x_i] = \int_{\mathbb{R}} y \rho_{Y|X_i}(y | x_i) dy = \frac{\int_{\mathbb{R}} y \rho_{(Y, X_i)}(y, x_i) dy}{\int_{\mathbb{R}} \rho_{(Y, X_i)}(y, x_i) dy}, \quad (4.74)$$

where, if they exist,  $\rho_{Y|X_i}$  is the conditional probability density function of  $Y$  given  $X_i$  and  $\rho_{(Y, X_i)}$  is the joint probability density function of the random vector  $(Y, X_i)$ . The joint probability density function  $\rho_{(Y, X_i)}$  can then be estimated using kernel density estimation as

$$\rho_{(Y, X_i)} \approx \rho_{(Y, X_i)}^{\nu} = \frac{1}{\nu} \sum_{k=1}^{\nu} K_Y(y - y^{(k)}) K_{X_i}(x - x_i^{(k)}). \quad (4.75)$$

Here,  $K_Y$  is a univariate kernel for the uncertain quantity of interest,  $K_{X_i}$  is a univariate kernel for the uncertain input parameter  $x_i$ , and

$$\left\{ (x_i^{(k)}, \mathbf{x}_{\sim i}^{(k)}, y^{(k)}), 1 \leq k \leq \nu \right\}, \quad \text{in which } y^{(k)} = f(x_i^{(k)}, \mathbf{x}_{\sim i}^{(k)}), \quad (4.76)$$

is an ensemble of i.i.d. sample values of the uncertain input parameters along with the corresponding values of the quantity of interest evaluated by using the computational model. Please note that both kernels depend on a bandwidth parameter that has to be appropriately chosen. Provided that  $K_Y$  satisfies the moment conditions

$$\int_{\mathbb{R}} K_Y(y - y^{(k)}) dy = 1, \quad \int_{\mathbb{R}} y K_Y(y - y^{(k)}) dy = y^{(k)}, \quad (4.77)$$

the numerator and denominator in Equation (4.74) can be estimated as

$$\begin{aligned} \int_{\mathbb{R}} y \rho_{(Y, X_i)}(y, x_i) dy &\approx \int_{\mathbb{R}} y \rho_{(Y, X_i)}^{\nu}(y, x_i) dy \\ &= \frac{1}{\nu} \sum_{k=1}^{\nu} \underbrace{\int_{\mathbb{R}} y K_Y(y - y^{(k)}) dy}_{=y^{(k)}} K_{X_i}(x - x_i^{(k)}) \\ &= \frac{1}{\nu} \sum_{k=1}^{\nu} y^{(k)} K_{X_i}(x - x_i^{(k)}), \end{aligned} \quad (4.78)$$

$$\begin{aligned} \int_{\mathbb{R}} \rho_{(Y, X_i)}(y, x_i) dy &\approx \int_{\mathbb{R}} \rho_{(Y, X_i)}^{\nu}(y, x_i) dy \\ &= \frac{1}{\nu} \sum_{k=1}^{\nu} \underbrace{\int_{\mathbb{R}} K_Y(y - y^{(k)}) dy}_{=1} K_{X_i}(x - x_i^{(k)}) \\ &= \frac{1}{\nu} \sum_{k=1}^{\nu} K_{X_i}(x - x_i^{(k)}), \end{aligned} \quad (4.79)$$

thus leading to the following kernel-based estimate of  $f_i(x_i)$ :

$$f_i^{\text{KDE}}(x_i) = \frac{\frac{1}{\nu} \sum_{k=1}^{\nu} y^{(k)} K_{X_i}(x - x_i^{(k)})}{\frac{1}{\nu} \sum_{k=1}^{\nu} K_{X_i}(x - x_i^{(k)})}. \quad (4.80)$$

The Sobol index  $S_i$  is then approximated as

$$S_i^{\text{KDE}} = \frac{\mathbb{V}[f_i^{\text{KDE}}(X_i)]}{\mathbb{V}[Y]}, \quad (4.81)$$

where  $\mathbb{V}[f_i^{\text{KDE}}(X_i)]$  and  $\mathbb{V}[Y]$  can be estimated using a numerical integration scheme such as trapezoidal quadrature rules, Gaussian quadrature rules, or Monte Carlo integration; see [Luo et al. \[2014\]](#) for a discussion.

Evaluating the first-order sensitivity indices for the  $n$  components of  $\mathbf{X}$  using nonparametric kernel methods requires a total of  $\nu$  evaluations of the computational model as the same ensemble of samples of the uncertain input parameters can be used to evaluate each sensitivity index. Yet, similarly to Monte Carlo sampling methods, nonparametric kernel methods may require a large number of samples to obtain sufficient accuracy of the Sobol estimates. Thus, the evaluation of Sobol indices with nonparametric kernel methods can also be prohibitive for computational models with a high computational cost.

#### 4.4.2.5 Estimation of Sobol indices using surrogate models

##### Surrogate model based on a polynomial chaos expansion

Let us consider a truncated polynomial chaos expansion of order  $p$  of the second-order random variable  $Y = f(\mathbf{X})$ , that is,

$$Y \approx Y^p = \sum_{|\alpha|=0}^p y_{\alpha} \Psi_{\alpha}(\mathbf{X}), \quad (4.82)$$

where  $\mathbf{X}$  has independent components, the  $\Psi_\alpha$  are orthonormal polynomials with respect to  $\mathbb{P}_\mathbf{X}$ ,  $|\alpha|$  is the polynomial order, and the scalars  $y_\alpha$  are the polynomial chaos coordinates.

The truncated polynomial chaos expansion of a random variable lends itself to a practical estimation of Sobol sensitivity indices; see, for instance, [Sudret \[2008\]](#) and [Crestaux et al. \[2009\]](#). By defining  $\mathcal{A}_i^p$  as the set of multi-indices in  $\mathcal{A}^p$  with non-zero cardinality whose only non-zero component is  $\alpha_i$ , that is,

$$\mathcal{A}_i^p = \{\alpha \in \mathcal{A}^p : \alpha_i > 0, \alpha_j = 0 \forall j \neq i\}, \quad (4.83)$$

the polynomial

$$\sum_{\alpha \in \mathcal{A}_i^p} y_\alpha \Psi_\alpha(\mathbf{X}) \quad (4.84)$$

is in fact the main effect associated with the uncertain input parameter  $x_i$  for the random variable  $Y^p$ . In addition, the variance of  $Y$  can be approximated as

$$\mathbb{V}[Y] \approx \mathbb{V}[Y^p] = \sum_{|\alpha|=1}^p y_\alpha^2. \quad (4.85)$$

Thus, the first-order sensitivity index  $S_i$  can be approximated as

$$S_i^{\text{PCE}} = \frac{\mathbb{V}[\mathbb{E}(Y^p | X_i)]}{\mathbb{V}[Y^p]} = \frac{\sum_{\alpha \in \mathcal{A}_i^p} y_\alpha^2}{\sum_{|\alpha|=1}^p y_\alpha^2}. \quad (4.86)$$

#### Surrogate model based on Gaussian-process regression

Let the mapping  $\mathbf{x} \mapsto f(\mathbf{x})$  be a realisation of a Gaussian process  $\text{GP}(\mu(\mathbf{x}), C(\mathbf{x}, \mathbf{x}'))$  indexed by  $\mathbb{R}^n$  and defined on  $\Theta^{\text{GP}}$  with mean  $\mu(\mathbf{x})$  and covariance function  $C(\mathbf{x}, \mathbf{x}') = \sigma^2 R(\mathbf{x}, \mathbf{x}')$ . In this context, two approaches can be considered for the evaluation of Sobol indices; see, for instance, [Marrel et al. \[2009\]](#).

In the first approach, Sobol indices are estimated by substituting the conditional mean for the computational model, that is, we consider the following Gaussian-process surrogate model

$$\mathbf{x} \mapsto f^{\text{GP}}(\mathbf{x}) = \hat{\mu}(\mathbf{x}), \quad (4.87)$$

where the conditional mean  $\hat{\mu}(\mathbf{x})$  is given by Equation (4.38). Thus, the first-order sensitivity index  $S_i$  can be approximated as

$$S_i^{\text{GP}} = \frac{\mathbb{V}[\mathbb{E}(f^{\text{GP}}(\mathbf{X}) | X_i)]}{\mathbb{V}[f^{\text{GP}}(\mathbf{X})]}. \quad (4.88)$$

Equation (4.88) can be estimated using Monte Carlo sampling and the formulas in Equation (4.71), Equation (4.72), or Equation (4.73).

In the second approach, Sobol indices are estimated by substituting the conditional Gaussian process for the computational model, that is, we consider the full-Gaussian-process surrogate model (see Section 4.3.2.2)

$$\mathbf{x} \mapsto F^{\text{fGP}}(\mathbf{x}) = \text{GP}(\hat{\mu}(\mathbf{x}), \hat{C}(\mathbf{x}, \mathbf{x}')), \quad (4.89)$$

where the conditional mean  $\hat{\mu}(\boldsymbol{x})$  is given by Equation (4.38) and the conditional covariance function by Equation (4.41). Thus, the Sobol indices obtained when substituting the computational model with the full-Gaussian-process surrogate model write as

$$S_i^{\text{fGP}} = \frac{\mathbb{V}[\mathbb{E}(F^{\text{fGP}}(\mathbf{X})|X_i)]}{\mathbb{V}[F^{\text{fGP}}(\mathbf{X})]}, \quad 1 \leq i \leq n. \quad (4.90)$$

Here, the mathematical expectation and the variance are taken with respect to the random vector  $\mathbf{X}$ . Thus,  $S_i^{\text{fGP}}$  is a random variable defined on the sample space  $\Theta^{\text{fGP}}$ . In this context, the expectation  $\mathbb{E}_{\Theta^{\text{fGP}}}[S_i^{\text{fGP}}]$  of  $S_i^{\text{fGP}}$  can serve as an approximation of  $S_i$  and its variance  $\mathbb{V}_{\Theta^{\text{fGP}}}[S_i^{\text{fGP}}]$  as an indicator of the uncertainty in approximating  $S_i$  with  $\mathbb{E}_{\Theta^{\text{fGP}}}[S_i^{\text{fGP}}]$  due to the representation of the computational model with the full-Gaussian-process surrogate model. Here, the notations  $\mathbb{E}_{\Theta^{\text{fGP}}}$  and  $\mathbb{V}_{\Theta^{\text{fGP}}}$  are used to indicate that the mathematical expectation and the variance are taken in the sample space  $\Theta^{\text{fGP}}$ .

[Le Gratiet et al. \[2014\]](#) proposed a Monte Carlo sampling method to estimate  $\mathbb{E}_{\Theta^{\text{fGP}}}[S_i^{\text{fGP}}]$  and  $\mathbb{V}_{\Theta^{\text{fGP}}}[S_i^{\text{fGP}}]$ . Let  $f^{\text{fGP}}(\boldsymbol{x}; \theta)$ ,  $\theta$  in  $\Theta^{\text{GP}}$ , denote a realisation of  $F^{\text{fGP}}(\boldsymbol{x})$ . Let

$$\left\{ (x_i^{(k)}, \boldsymbol{x}_{\sim i}^{(k)}), 1 \leq k \leq \nu \right\}, \quad (4.91)$$

$$\left\{ (x_i'^{(k)}, \boldsymbol{x}_{\sim i}'^{(k)}), 1 \leq k \leq \nu \right\}, \quad (4.92)$$

be two ensembles of samples of the uncertain input parameters that share the same i.i.d. samples for  $X_i$  but have different i.i.d. samples for the other random variables and

$$\left\{ y^{(k)} = f^{\text{fGP}}(x_i^{(k)}, \boldsymbol{x}_{\sim i}^{(k)}; \theta), 1 \leq k \leq \nu \right\}, \quad (4.93)$$

$$\left\{ y'^{(k)} = f^{\text{fGP}}(x_i'^{(k)}, \boldsymbol{x}_{\sim i}'^{(k)}; \theta), 1 \leq k \leq \nu \right\} \quad (4.94)$$

be the two corresponding ensembles of solutions to the surrogate model  $f^{\text{fGP}}(\boldsymbol{x}; \theta)$ . Using Equation (4.73),  $S_i^{\text{fGP}}(\theta)$  can be estimated as

$$S_i^{\text{fGP}}(\theta) \approx \frac{\frac{1}{\nu} \sum_{k=1}^{\nu} y^{(k)} y'^{(k)} - \left( \frac{1}{\nu} \sum_{k=1}^{\nu} \left[ \frac{y^{(k)} + y'^{(k)}}{2} \right] \right)^2}{\frac{1}{\nu} \sum_{k=1}^{\nu} \left[ \frac{(y^{(k)})^2 + (y'^{(k)})^2}{2} \right] - \left( \frac{1}{\nu} \sum_{k=1}^{\nu} \left[ \frac{y^{(k)} + y'^{(k)}}{2} \right] \right)^2}. \quad (4.95)$$

Then, for an ensemble  $\left\{ \theta^{(k)}, 1 \leq k \leq \kappa \right\}$  of i.i.d. samples in  $\Theta^{\text{GP}}$ , the Sobol index  $S_i$  is estimated as

$$\mathbb{E}_{\Theta^{\text{GP}}}[S_i^{\text{fGP}}] \approx \frac{1}{\kappa} \sum_{k=1}^{\kappa} S_i^{\text{fGP}}(\theta^{(k)}) \equiv m_{S_i^{\text{fGP}}}^{\kappa}, \quad (4.96)$$

and its variance is estimated as

$$\mathbb{V}_{\Theta^{\text{GP}}}[S_i^{\text{fGP}}] \approx \frac{1}{\kappa} \sum_{k=1}^{\kappa} (S_i^{\text{fGP}}(\theta^{(k)}) - m_{S_i^{\text{fGP}}}^{\kappa})^2. \quad (4.97)$$

In practice, realisations of the Gaussian process can be generated by using a Cholesky decomposition or by using a conditional simulation algorithm when  $n$  is large; see, for instance, [Emery \[2007\]](#), [Chilès and Delfiner \[2012\]](#), and [Emery et al. \[2014\]](#).

#### 4.4.2.6 Estimation of Sobol indices using probabilistic learning on manifolds

The PLoM algorithm discussed in Section 4.3.3 can provide an alternative to Monte Carlo methods for the computation of Sobol indices in small-data settings. This topic has been recently explored by [Arnst et al. \[2019\]](#), a reference to which we refer for further details. In [Arnst et al. \[2019\]](#), additional realisations of the random vector  $(\mathbf{X}, Y)$  generated with the PLoM algorithm are used to estimate the Sobol indices with a nonparametric kernel method (Section 4.4.2.4). [Arnst et al. \[2019\]](#) have demonstrated the interest of the PLoM method for global sensitivity analysis when the initial dataset encapsulates sufficient information to allow the learning method to build a consistent probabilistic representation of the data; see Section 7.3 where the numerical illustration in [Arnst et al. \[2019\]](#) is reported.

#### 4.4.3 Generalised sensitivity indices

Sobol indices measure the impact of each uncertain input parameter on  $Y$  through their contribution to the variance of  $Y$ . For this reason, they provide only limited insight into the impact of each uncertain input parameter on the probability distribution of  $Y$ . In addition, Sobol indices do not generalise readily to multivariate quantities of interest. Recent work has thus been dedicated to introducing new sensitivity indices that go beyond the Sobol indices; see, for instance, [Owen \[2014\]](#), [Da Veiga \[2015\]](#), and [Rahman \[2016\]](#). In this subsection, we review briefly some of these generalised sensitivity indices.

From a broad perspective, [Da Veiga \[2015\]](#) proposed to use the concept of dissimilarity measure between the probability distribution  $\mathbb{P}_Y$  and the conditional probability distribution  $\mathbb{P}_{Y|X_i}$  to quantify the impact of  $X_i$  on  $Y$ . Formally, [Da Veiga \[2015\]](#) defined the following family of sensitivity indices:

$$\mathbb{E}(d(\mathbb{P}_Y, \mathbb{P}_{Y|X_i})), \quad (4.98)$$

where  $d(\cdot, \cdot)$  denotes a dissimilarity measure between two probability distributions and the expectation is with respect to  $X_i$ . The idea behind the family of sensitivity indices in Equation (4.98) is that if  $\mathbb{P}_Y$  and  $\mathbb{P}_{Y|X_i}$  are similar in some sense, then  $X_i$  has little impact on  $Y$ , while if  $\mathbb{P}_Y$  and  $\mathbb{P}_{Y|X_i}$  are dissimilar in some sense, then  $X_i$  has a significant impact on  $Y$ . [Da Veiga \[2015\]](#) discussed different dissimilarity measures based on the Csiszár- $f$ -divergences, including the Kullback-Leibler divergence. It should be mentioned that the unnormalised Sobol index is a special case of Equation (4.98) for the dissimilarity measure

$$d(\mathbb{P}_Y, \mathbb{P}_{Y|X_i}) = (\mathbb{E}[Y] - \mathbb{E}[Y|X_i])^2, \quad (4.99)$$

that is, the dissimilarity between  $\mathbb{P}_Y$  and  $\mathbb{P}_{Y|X_i}$  is measured as the square of the difference between their mean values.

Alternatively, [Da Veiga \[2015\]](#) proposed to build sensitivity indices using the concept of dependence measure between  $X_i$  and  $Y$ , where a dependence measure compares in some way the joint probability distribution of  $X_i$  and  $Y$  and the product of their marginal probability distributions. The idea is that if  $X_i$  and  $Y$  are weakly dependent, then  $X_i$  has little impact on  $Y$  while if  $X_i$  and  $Y$  are strongly dependent in some sense, then  $X_i$  has a significant impact on  $Y$ . An example of such a dependence measure is based on the Hilbert–Schmidt independence criterion (HSIC) [[Gretton et al., 2005](#)]. This criterion builds upon kernel-based methods in reproducing

kernel Hilbert spaces (RKHSs) [Aronszajn, 1950; Rasmussen and Williams, 2006] and cross-covariance operators for detecting dependence between random variables. More formally, let us consider a first RKHS  $\mathcal{F}$  of functions from  $\mathcal{X} = \mathbb{R}$  into  $\mathbb{R}$  with kernel  $k_{\mathcal{X}}$  and inner product  $\langle \cdot, \cdot \rangle_{\mathcal{F}}$  and a second RKHS  $\mathcal{G}$  of functions from  $\mathcal{Y} = \mathbb{R}$  to  $\mathbb{R}$  with kernel  $k_{\mathcal{Y}}$  and inner product  $\langle \cdot, \cdot \rangle_{\mathcal{G}}$ . By definition, the cross-covariance operator  $C_{X_i Y}$  associated with the joint probability distribution of  $X_i$  and  $Y$  is the linear operator from  $\mathcal{G}$  into  $\mathcal{F}$  defined for every  $f$  in  $\mathcal{F}$  and  $g$  in  $\mathcal{G}$  by

$$\langle f, C_{X_i Y} g \rangle_{\mathcal{F}} = \text{Cov}(f(X_i), g(Y)), \quad (4.100)$$

that is, the cross-covariance operator provides a generalisation of the covariance function between  $X_i$  and  $Y$  by allowing to represent nonlinear correlations between  $X_i$  and  $Y$  through the use of nonlinear kernels. Then, the HSIC between  $X_i$  and  $Y$  is defined as the square Hilbert-Schmidt norm of the cross-covariance operator, that is,

$$\text{HSIC}(X_i, Y) = \|C_{X_i Y}\|_{\text{HS}}^2 = \sum_{k, l \in \mathbb{N}} \text{Cov}(f_k(X_i), g_l(Y)), \quad (4.101)$$

where the  $f_k$  and the  $g_l$  are orthonormal basis functions of  $\mathcal{F}$  and  $\mathcal{G}$ , respectively. Gretton et al. [2005] showed that  $\text{HSIC}(X_i, Y)$  can be written equivalently as

$$\begin{aligned} \text{HSIC}(X_i, Y) &= \mathbb{E}_{(X_i, X'_i, Y, Y')} [k_{\mathcal{X}}(X_i, X'_i) k_{\mathcal{Y}}(Y, Y')] \\ &\quad + \mathbb{E}_{(X_i, X'_i)} [k_{\mathcal{X}}(X_i, X'_i)] \mathbb{E}_{(Y, Y')} [k_{\mathcal{Y}}(Y, Y')] \\ &\quad - 2 \mathbb{E}_{(X_i, Y)} [\mathbb{E}_{X'_i} [k_{\mathcal{X}}(X_i, X'_i)] \mathbb{E}_{Y'} [k_{\mathcal{Y}}(Y, Y')]]. \end{aligned} \quad (4.102)$$

where  $X'_i$  and  $Y'$  are independent copies of  $X_i$  and  $Y$ , respectively. The HSIC between  $X_i$  and  $Y$  is zero if  $X_i$  and  $Y$  are independent. Finally, Da Veiga [2015] introduced the following HSIC sensitivity index

$$S_i^{\text{HSIC}} = \frac{\text{HSIC}(X_i, Y)}{\sqrt{\text{HSIC}(X_i, X_i) \text{HSIC}(Y, Y)}}. \quad (4.103)$$

Assuming  $\{(x_i^{(k)}, \mathbf{x}_{\sim i}^{(k)}), 1 \leq k \leq \nu\}$  to be an ensemble of i.i.d samples of the uncertain input parameters and  $\{y^{(k)} = f(x_i^{(k)}, \mathbf{x}_{\sim i}^{(k)}), 1 \leq k \leq \nu\}$  to be the corresponding ensemble of samples of the quantity of interest evaluated by using the computational model, Gretton et al. [2005] proposed the following consistent estimate of  $\text{HSIC}(X_i, Y)$ :

$$\text{HSIC}^{\nu}(X_i, Y) = \frac{1}{\nu^2} \text{Tr}([K_{\mathcal{X}}][H][K_{\mathcal{Y}}][H]), \quad (4.104)$$

with  $[K_{\mathcal{X}}]$  and  $[K_{\mathcal{Y}}]$  the  $(\nu \times \nu)$ -dimensional matrices with entries  $K_{\mathcal{X}kl} = k_{\mathcal{X}}(x_i^{(k)}, x_i^{(l)})$  and  $K_{\mathcal{Y}kl} = k_{\mathcal{Y}}(y^{(k)}, y^{(l)})$  and  $[H]$  is the  $\nu$ -dimensional diagonal matrix with entries  $H_{kl} = \delta_{kl} - 1/\nu$ . The evaluation of the estimate (4.104) can be sped-up with a surrogate model.

## 4.5 Numerical examples

### 4.5.1 Propagation of uncertainties: Branin function

To illustrate UQ methods for the propagation of uncertainties, we consider the Branin function (Figure 4.14), which is used as a benchmark function for surrogate modelling [Forrester et al.,

2008; Picheny et al., 2013]:

$$y = f(\mathbf{x}) = \left( x_2 - \frac{5.1}{(2\pi)^2} x_1^2 + \frac{5}{\pi} x_1 - 6 \right)^2 + 10 \left( 1 - \frac{1}{8\pi} \right) \cos x_1 + 10. \quad (4.105)$$

The uncertain input variables  $x_1$  and  $x_2$  are modelled as two independent uniform random variables  $X_1 \sim \mathcal{U}[-5, 10]$  and  $X_2 \sim \mathcal{U}[0, 15]$  and the uncertain quantity of interest  $y$  is modelled as the random variable  $Y = f(\mathbf{X})$ .

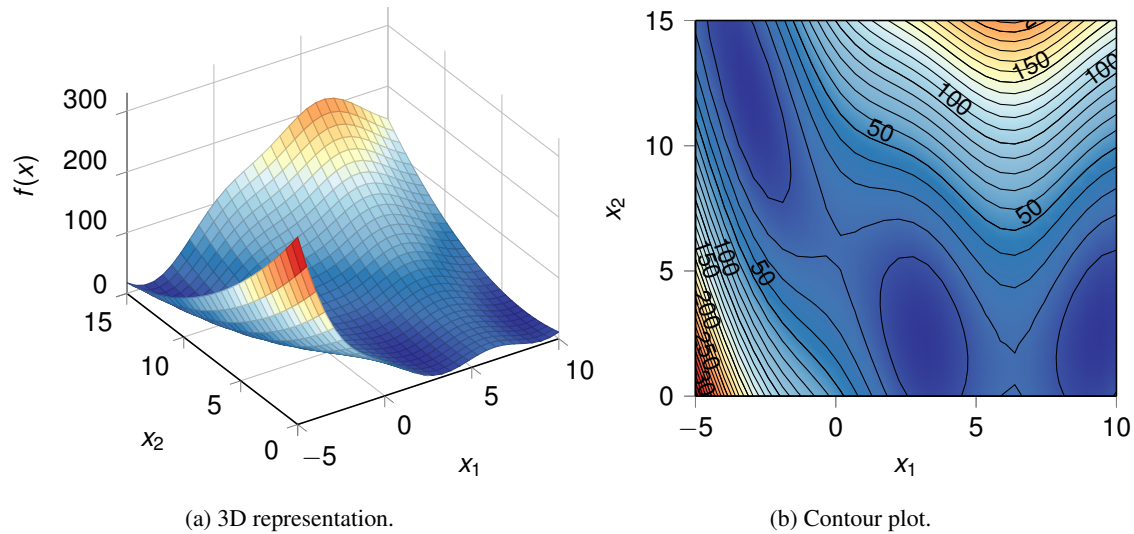


Figure 4.14: Representation of the Branin function.

#### 4.5.1.1 Monte Carlo sampling

We used the Monte Carlo sampling method as described in Section 4.3.1 to estimate the mean and the standard deviation of the uncertain quantity of interest. We used for  $\nu$  values up to 10 000. Figures 4.15 and 4.16 show the convergence of the Monte Carlo estimates for the mean and the standard deviation, respectively. We carried out the computation ten times to provide an overview of the dispersion of the estimates. The dispersion in the Monte Carlo estimates for  $\nu = 10\,000$  for the ten experiments indicates that the results are not (sufficiently) converged even with 10 000 samples. Using the central limit theorem for the Monte Carlo estimator [Dudley, 2002; Robert and Casella, 2013], we determined a 95%-confidence interval of  $54.2886 \pm 1.0642$  for the Monte Carlo estimates of the mean and of  $51.2414 \pm 0.9444$  for the Monte Carlo estimates of the standard deviation obtained with  $\nu = 10\,000$  samples.

#### 4.5.1.2 Surrogate models

To reduce the number of evaluations of the computational model in estimating statistical descriptors of  $Y$ , we built surrogate models of the computational model as discussed in Section 4.3.2. Here, we considered four different kinds of surrogate models:

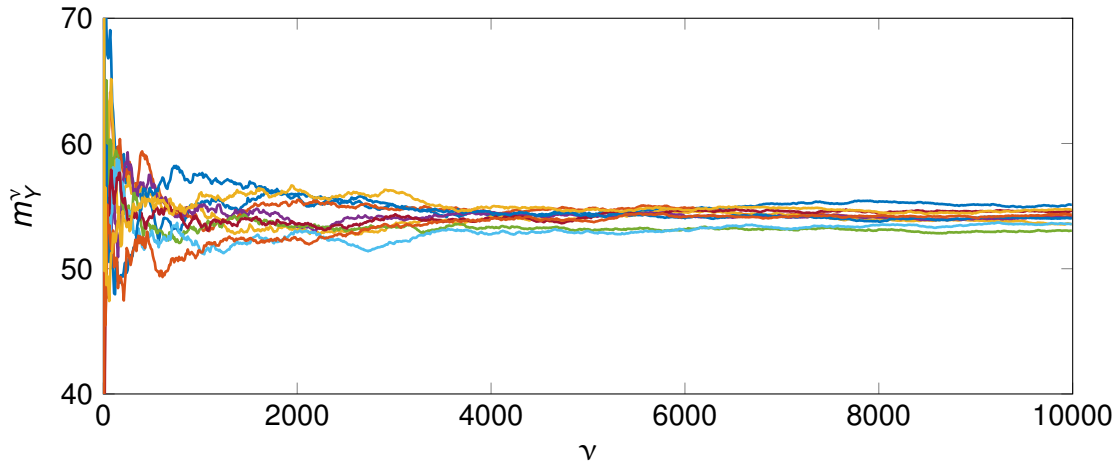


Figure 4.15: Convergence analysis: convergence of Monte Carlo estimates of the mean of the uncertain quantity of interest as a function of the number of samples  $\nu$ .

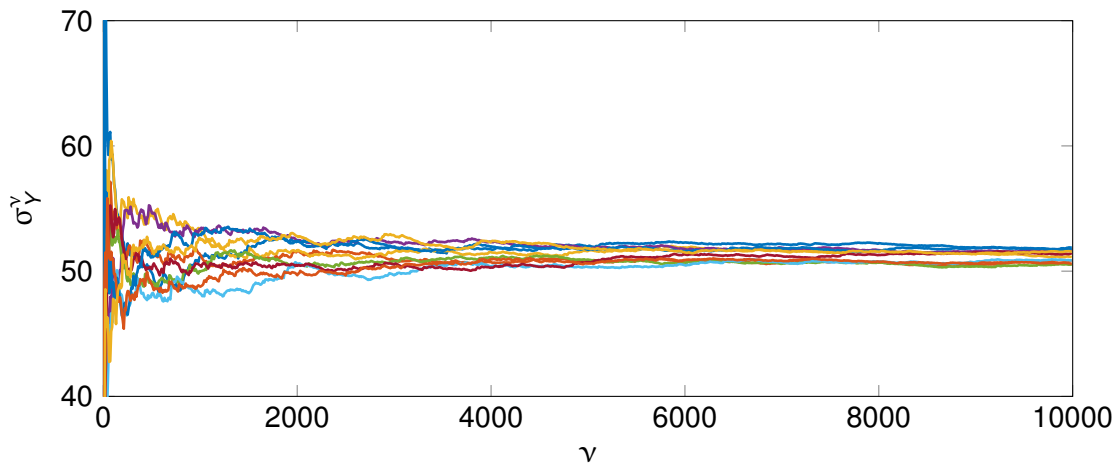


Figure 4.16: Convergence analysis: convergence of Monte Carlo estimates of the standard deviation of the uncertain quantity of interest as a function of the number of samples  $\nu$ .

1. For the first kind of surrogate models, we considered surrogate models based on polynomial chaos expansions for which we determined the polynomial chaos coordinates using nonintrusive spectral projection (NISP). We used multivariate polynomials set up as the products of scaled Gauss–Legendre polynomials. We built the experimental designs from the nodes of fully tensorised scaled Gauss–Legendre quadrature integration rules, with the size of the experimental equal to  $(p + 1)^2$  for a polynomial chaos expansion of order  $p$ .
2. For the second kind of surrogate models, we considered surrogate models based on polynomial chaos expansions for which we determined the polynomial chaos coordinates using least-squares regression. We used multivariate polynomials set up as the products of scaled Gauss–Legendre polynomials. We generated the experimental designs using a

Latin hypercube sampling scheme, with the size of the experimental equal to  $(p + 1)^2$  for a polynomial chaos expansion of order  $p$ . As we constructed the training points by using a Latin hypercube sampling design, we used least-squares regression with a diagonal weight matrix  $[W]$  with equal weights  $W_{ii} = 1/\lambda$  ( $1 \leq i \leq \lambda$ ). We refer to this regression method as ordinary least squares (OLS) in the following.

3. For the third kind of surrogate models, we considered surrogate models based on Gaussian-process regression with constant mean and Gaussian covariance function. We generated the experimental designs using a Latin hypercube sampling scheme.
4. For the fourth kind of surrogate models, we considered surrogate models based on Gaussian-process regression with constant mean and Matérn-5/2 covariance function. We generated the experimental designs using a Latin hypercube sampling scheme.

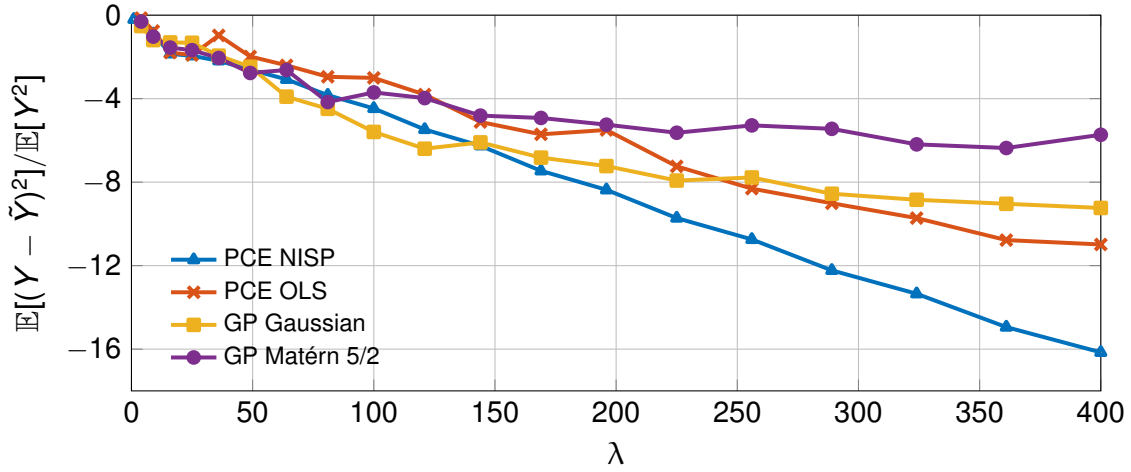


Figure 4.17: Relative mean-square error between the Branin function and its approximation with a surrogate model as a function of the number of samples  $\lambda$  in the experimental design.

Figure 4.17 shows the relative mean-square error (see Equation (4.47)) between the Branin function and the four surrogate models as a function of the size of the experimental design. We can observe that the relative mean-square error decreases reasonably for all surrogate models, with surrogate models based on a polynomial chaos expansion that achieve in general a lower relative mean-square error than surrogate models based on Gaussian-process regression, especially for larger experimental designs. Surrogate models based on a polynomial chaos expansion using NISP achieve a lower relative mean-square error than surrogate models based on a polynomial chaos expansion using OLS. Indeed, in the absence of noise in the data, spectral projection leads to the optimal surrogate model based on a polynomial chaos expansion of order  $p$  in terms of the mean-square error. In addition, surrogate models based on Gaussian-process regression with Gaussian covariance function achieve a lower relative mean-square error than surrogate models based on Gaussian-process regression with Matérn-5/2 covariance function. This results from the Branin function being infinitely differentiable and sample paths of Gaussian process with Gaussian covariance function being infinitely differentiable. We also represented in Figure 4.20 surrogate models based on polynomial chaos expansions of different orders and

in Figure 4.21 surrogate models based on Gaussian-process regression for various sizes of the experimental design.

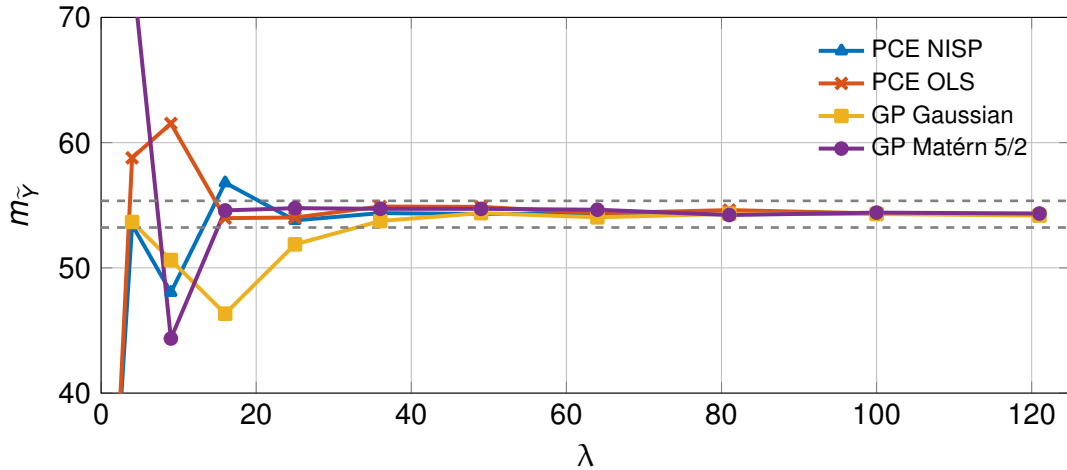


Figure 4.18: Convergence analysis: convergence of surrogate-based estimates of the mean of the uncertain quantity of interest as a function of the size  $\lambda$  of the experimental design. The dashed lines represent the 95%-confidence interval for the Monte Carlo estimates based on  $\nu = 10\,000$  samples.

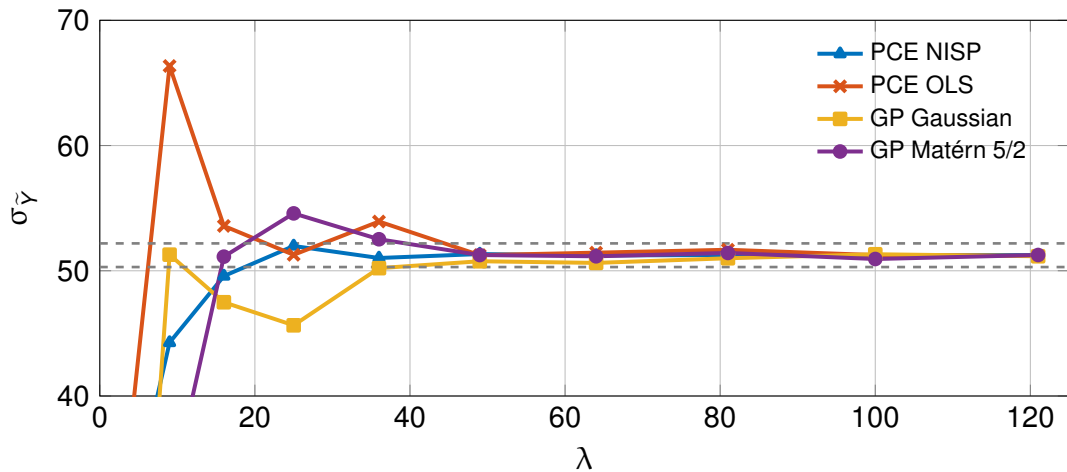


Figure 4.19: Idem as in Figure 4.15 but for the standard deviation of the uncertain quantity of interest.

We used the surrogate models to estimate the mean and the variance of the uncertain quantity of interest either directly from the polynomial chaos coordinates (Equations (4.30) and (4.31)) or using Monte Carlo sampling for surrogate models based on Gaussian-process regression with  $\nu = 10^6$ . Figures 4.18 and 4.19 show the convergence of the surrogate-based estimates for the mean and the standard deviation, respectively, as a function of the number of samples  $\lambda$  in

the experimental design. We can observe that reasonable convergence is already achieved after a few tens of samples ( $\lambda > 60$ ) in the experimental design, thus suggesting that the use of a surrogate model can effectively reduce the number of evaluations of the computational model to estimate the statistical descriptors. Figure 4.22 compares the kernel density estimate of the probability density function of  $Y$  obtained by using Monte Carlo sampling ( $\nu = 10^6$ ) with the kernel density estimates obtained with the surrogate models. The probability density function of the uncertain quantity of interest is bimodal and thus can be difficult to estimate. We can observe that surrogate models provide a poor estimation of the probability density function for small experimental designs but the estimation improves for larger experimental designs ( $\lambda \geq 25$ ).

### 4.5.2 Sensitivity analysis: Ishigami function

To illustrate UQ methods for sensitivity analysis, we consider the so-called Ishigami function, which is used as a benchmark function for sensitivity analysis [Saltelli et al., 2008; Sudret, 2008; Crestaux et al., 2009]:

$$y = f(\mathbf{x}) = \sin x_1 + a \sin^2 x_2 + b x_3^4 \sin x_1, \quad (4.106)$$

with  $a = 7$  and  $b = 0.1$ . The uncertain input variables  $x_1$ ,  $x_2$ , and  $x_3$  are modelled as three independent uniform random variables  $X_1 \sim \mathcal{U}[-\pi, \pi]$ ,  $X_2 \sim \mathcal{U}[-\pi, \pi]$ , and  $X_3 \sim \mathcal{U}[-\pi, \pi]$  and the uncertain quantity of interest  $y$  is modelled as the random variable  $Y = f(\mathbf{X})$ . In the following, we will focus mainly on the first-order Sobol indices as sensitivity indices.

First-order Sobol indices of the Ishigami function can be evaluated analytically. Indeed, the HDMR of the Ishigami function writes as

$$f(\mathbf{x}) = f_\emptyset + f_{X_1}(x_1) + f_{X_2}(x_2) + f_{X_3}(x_3) + f_I(\mathbf{x}), \quad (4.107)$$

with

$$f_\emptyset = \frac{1}{8\pi^3} \int_{-\pi}^{\pi} \int_{-\pi}^{\pi} \int_{-\pi}^{\pi} f(\mathbf{x}) dx_1 dx_2 dx_3 = \frac{a}{2}, \quad (4.108)$$

$$f_{X_1}(x_1) = \frac{1}{4\pi^2} \int_{-\pi}^{\pi} \int_{-\pi}^{\pi} f(\mathbf{x}) dx_2 dx_3 - f_\emptyset = \left(1 + \frac{\pi^4}{5} b\right) \sin x_1, \quad (4.109)$$

$$f_{X_2}(x_2) = \frac{1}{4\pi^2} \int_{-\pi}^{\pi} \int_{-\pi}^{\pi} f(\mathbf{x}) dx_1 dx_3 - f_\emptyset = -\frac{a}{2} \cos(2x_2), \quad (4.110)$$

$$f_{X_3}(x_3) = \frac{1}{4\pi^2} \int_{-\pi}^{\pi} \int_{-\pi}^{\pi} f(\mathbf{x}) dx_1 dx_2 - f_\emptyset = 0, \quad (4.111)$$

$$\begin{aligned} f_I(\mathbf{x}) &= f(\mathbf{x}) - f_\emptyset - f_{X_1}(x_1) - f_{X_2}(x_2) - f_{X_3}(x_3) \\ &= -\frac{\pi^4}{5} b \sin x_1 + b x_3^4 \sin x_1. \end{aligned} \quad (4.112)$$

The variance of the factors are given by

$$\mathbb{V}[f_{X_1}(X_1)] = \frac{1}{2\pi} \int_{-\pi}^{\pi} f_{X_1}^2(x_1) dx_1 = \frac{1}{2} + \frac{b\pi^4}{5} + \frac{b^2\pi^8}{50}, \quad (4.113)$$

$$\mathbb{V}[f_{X_2}(X_2)] = \frac{1}{2\pi} \int_{-\pi}^{\pi} f_{X_2}^2(x_2) dx_2 = \frac{a^2}{8}, \quad (4.114)$$

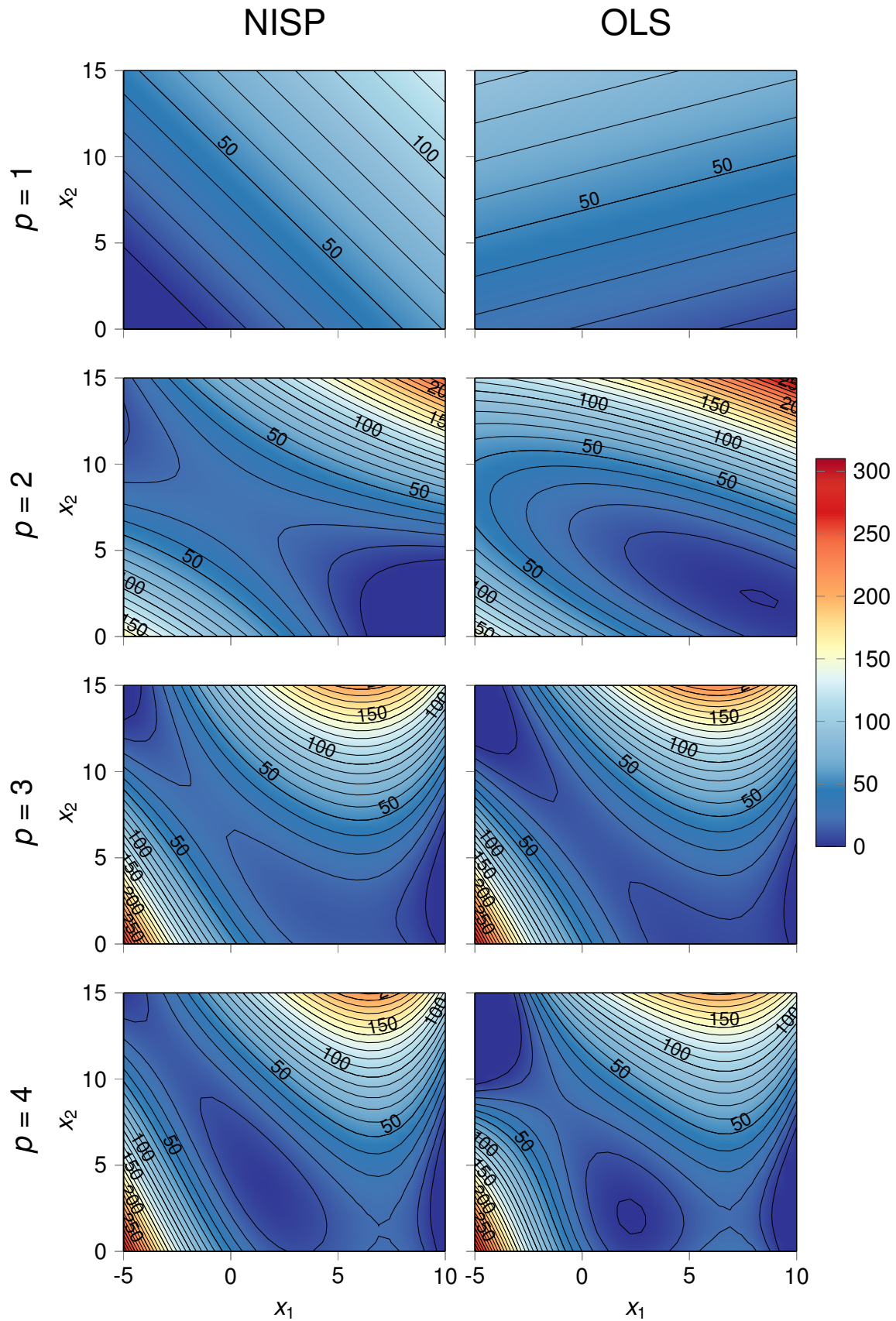


Figure 4.20: Illustrations of surrogate models of the Branin function based on polynomial chaos expansions. Polynomial chaos coordinates are evaluated using either nonintrusive spectral projection (NISP) or ordinary least-squares regression (OLS). The rows correspond to different polynomial orders  $p$  and the number of points in the experimental design is  $\lambda = (p + 1)^2$ .

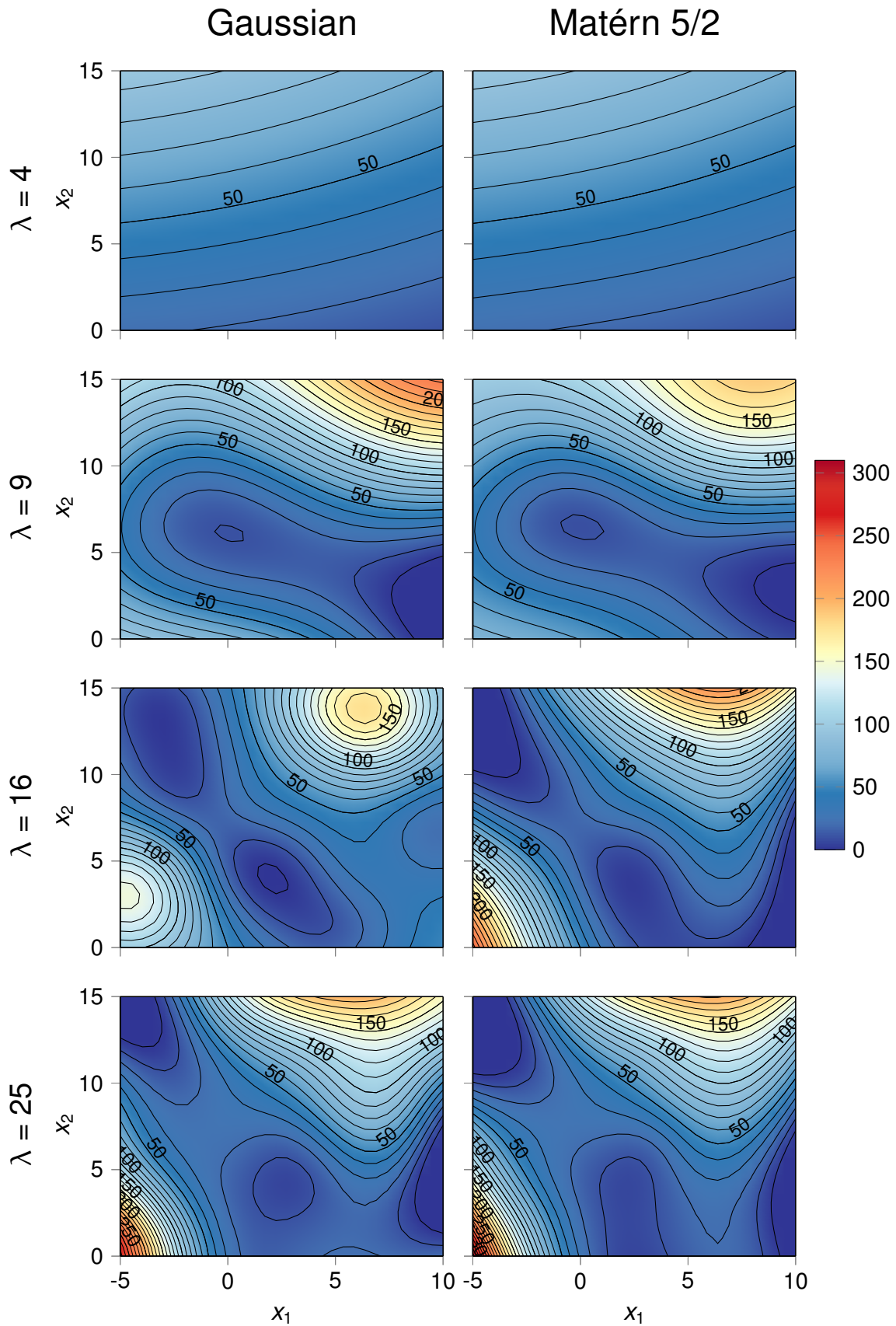


Figure 4.21: Illustrations of surrogate models of the Branin function based on Gaussian-process regression. The Gaussian process has a constant mean and either a Gaussian covariance function or a Matérn-5/2 covariance function. The rows correspond to the size  $\lambda$  of the experimental design.

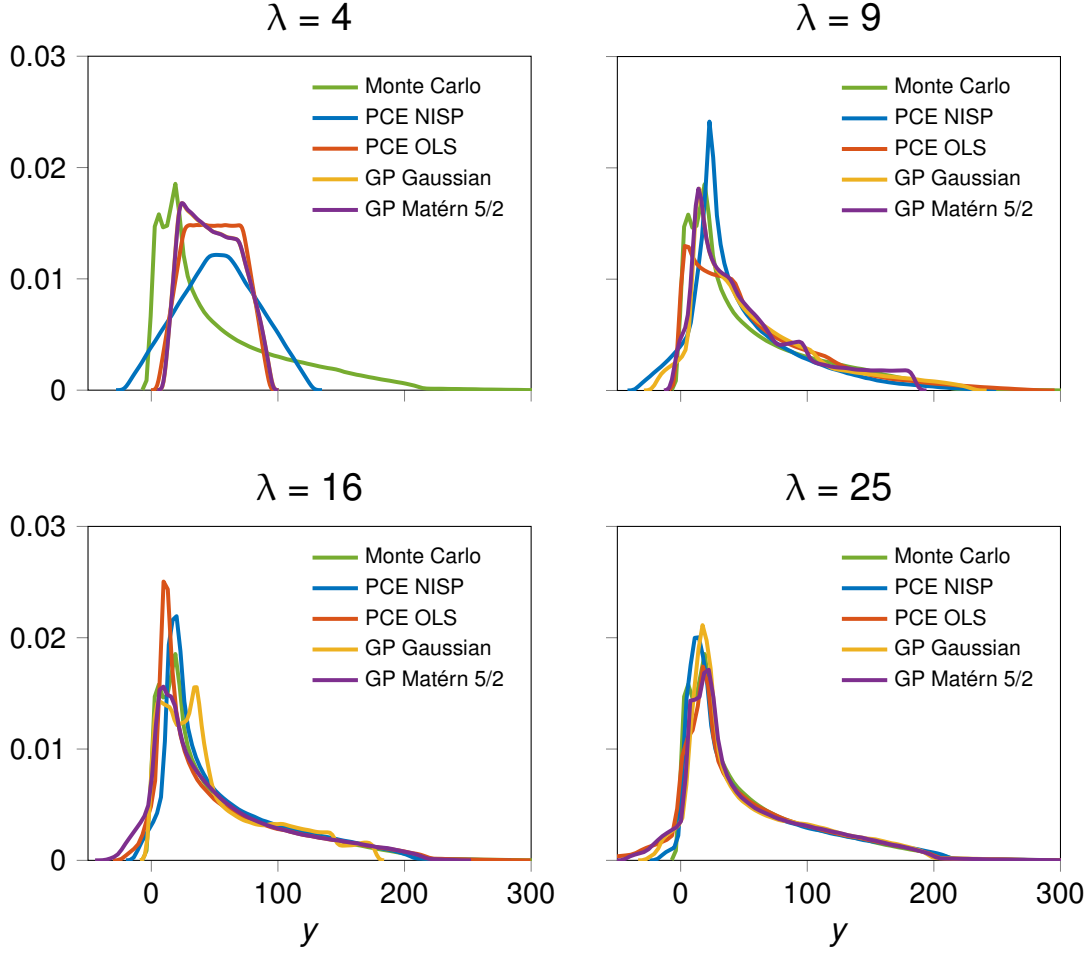


Figure 4.22: Surrogate-based kernel density estimates of the probability density function of the uncertain quantity of interest for different numbers of samples  $\lambda$  in the experimental design.

$$\mathbb{V}[f_{X_3}(X_3)] = \frac{1}{2\pi} \int_{-\pi}^{\pi} f_{X_3}^2(x_3) dx_3 = 0, \quad (4.115)$$

$$\mathbb{V}[f_1(\mathbf{X})] = \frac{1}{8\pi^3} \int_{-\pi}^{\pi} \int_{-\pi}^{\pi} \int_{-\pi}^{\pi} f_1^2(\mathbf{x}) dx_1 dx_2 dx_3 = \frac{8b^2\pi^8}{225}. \quad (4.116)$$

Then, the Sobol indices are given by

$$S_1 = \frac{\mathbb{V}[f_{X_1}(X_1)]}{\mathbb{V}[Y]} \approx 0.3129, S_2 = \frac{\mathbb{V}[f_{X_2}(X_2)]}{\mathbb{V}[Y]} \approx 0.4424, S_3 = \frac{\mathbb{V}[f_{X_3}(X_3)]}{\mathbb{V}[Y]} = 0. \quad (4.117)$$

Thus, the random variable  $X_2$  has the most significant individual impact in inducing uncertainty in the random variable  $Y$ , accounting for 44% of the variance of  $Y$ , the random variable  $X_1$  has the second most significant individual impact in inducing uncertainty in the random variable  $Y$ , accounting for 31% of the variance of  $Y$ , and the random variable  $X_3$  has no individual impact in inducing uncertainty in the random variable  $Y$ . The random variable  $X_3$  only induces uncertainty in the random variable  $Y$  through its interaction with the random variable  $X_1$ , with the interaction between both random variables accounting for 24% of the variance of  $Y$ .

### 4.5.2.1 Estimation of Sobol indices using Monte Carlo sampling

We used the Monte Carlo sampling method as described in Section 4.4.2.3 to estimate the Sobol indices using Equation (4.73). We use for  $\nu$  values up to 10 000. Figure 4.23 shows the convergence of the Monte Carlo estimates for the three first-order sensitivity indices. We can observe that the estimates have reasonably converged for  $\nu$  of about 6000 for the first and second uncertain parameters and for  $\nu$  of about 8000 for the third uncertain parameter. We can observe that Monte Carlo estimates using Equation (4.73) can lead to negative values of the Sobol indices, thus making more challenging the estimation of small sensitivity indices with sufficient accuracy.

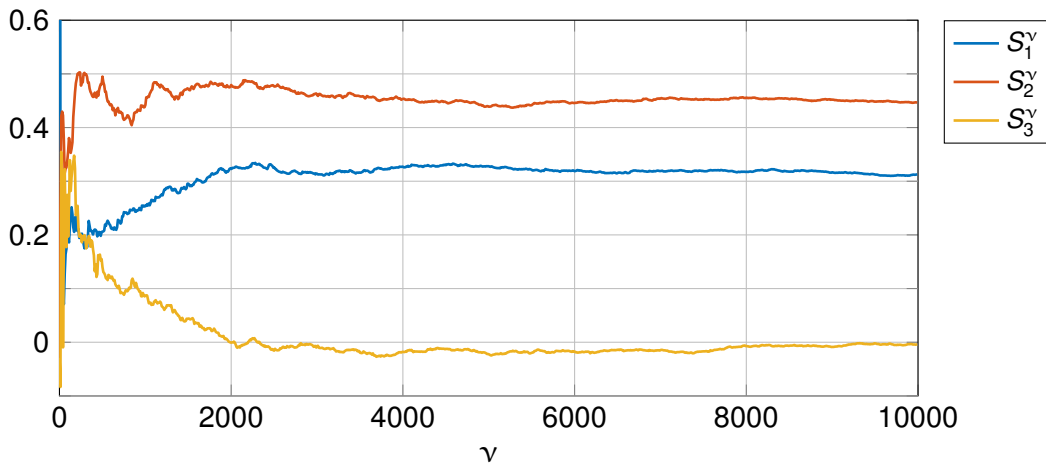


Figure 4.23: Convergence analysis: Estimates of the Sobol indices for the three uncertain input variables of the Ishigami function by using Monte Carlo estimation (Equation (4.73)) as a function of the number of samples  $\nu$ .

### 4.5.2.2 Estimation of Sobol indices using surrogate models

We consider the estimation of Sobol indices using surrogate models (see Section 4.4.2.5). We considered the same kinds of surrogate models as in Section 4.5.1.2 to build the surrogate models. We used the surrogate models to estimate the Sobol indices of the Ishigami function either directly from the polynomial chaos coordinates (Equation (4.86)) or using Monte Carlo sampling for surrogate models based on Gaussian-process regression. For surrogate models based on Gaussian-process regression, we estimated the Sobol indices using the conditional mean of the Gaussian process (Equation (4.88)) with  $\nu = 10^5$  Monte Carlo samples and the full-Gaussian-process surrogate model (Equation (4.90)) with  $\nu = 10^4$  Monte Carlo samples and  $\kappa = 100$  realisations of the conditional Gaussian process. Figure 4.24 shows the convergence of the surrogate-based estimates of the Sobol indices as a function of the number of samples  $\lambda$  in the experimental design. For the full-Gaussian-process approach, we represented the mean of the Monte Carlo estimates of  $S_i^{\text{fGP}}$  and the error bars represent the 95%-confidence interval. We can observe that after a value for  $\lambda$  of about 300, reasonable convergence of the estimates is achieved for all surrogate models.

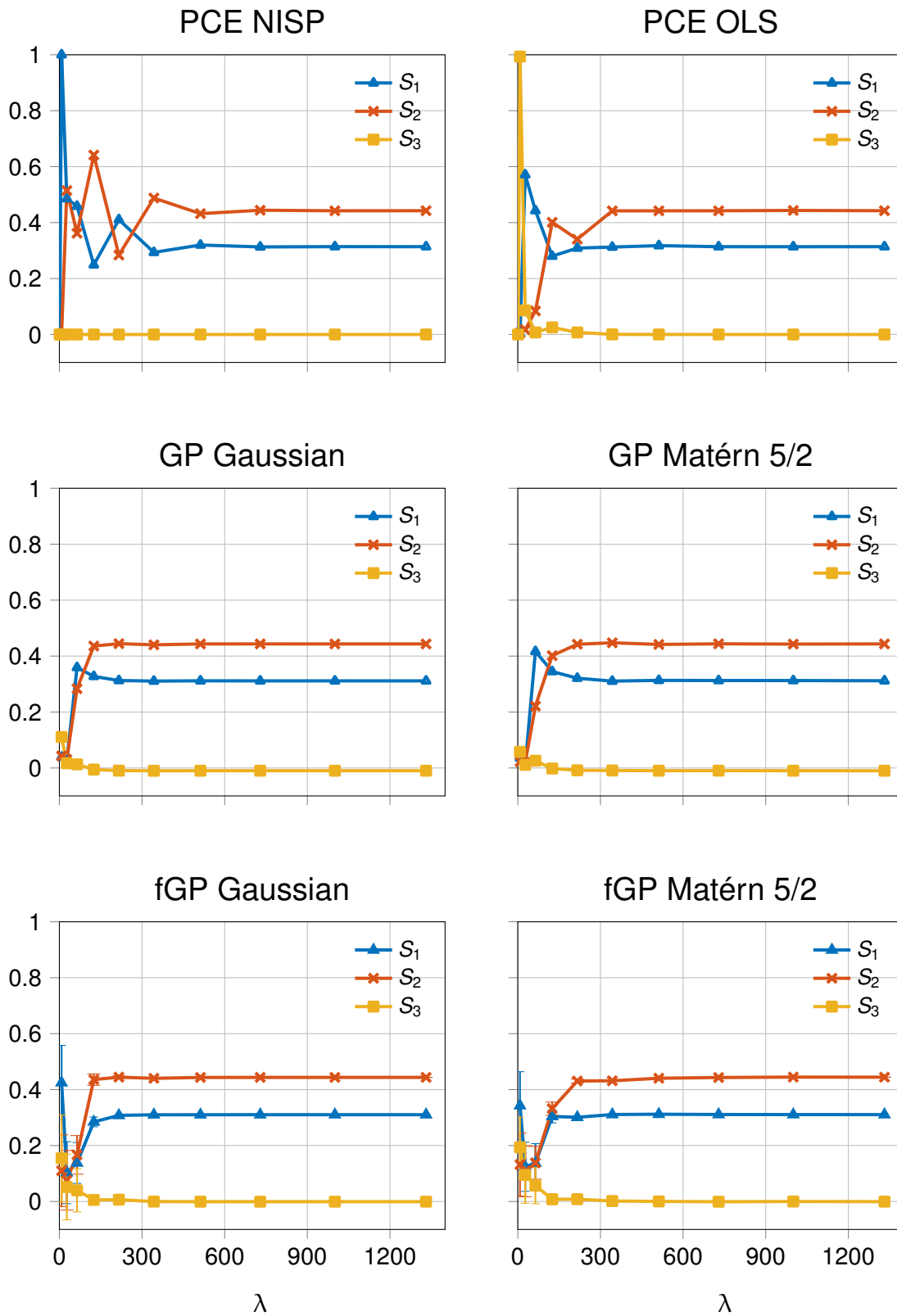


Figure 4.24: Convergence analysis: Surrogate-based estimates of the Sobol indices for the three uncertain input variables of the Ishigami function. For the full-Gaussian-process approach, we represented the mean of the Monte Carlo estimate of  $S_i^{\text{fGP}}$  and the error bars represent the 95%-confidence intervals. Please note that for large experimental designs, these error bars are too small to be visible on the figure.

## 4.6 Summary

In this chapter, we reported theory and existing methods for the analysis of computational models subject to uncertain input parameters within the field of uncertainty quantification. We discussed methods for the propagation of uncertainties and global sensitivity analysis, including Monte Carlo methods, surrogate models, and, to a lesser extent, probabilistic learning on manifolds. Most of these methods have been applied successfully to uncertainty quantification in science and engineering and are of interest to be applied for uncertainty quantification in glaciology; see Chapters 7 and 8.



# 5

## A multifidelity quantile-based approach for confidence sets of random excursion sets

*In this chapter, we address uncertainty quantification of physics-based computational models when the quantity of interest concerns geometrical characteristics of their spatial response. Within the probabilistic context of the random set theory, we develop the concept of confidence sets that either contain or are contained within an excursion set of the spatial response with a specified probability level. We seek such confidence sets in a parametric family of nested candidate sets defined as a parametric family of sublevel or superlevel sets of a membership function. We show that the problem of identifying a confidence set with a given probability level in such a parametric family is equivalent to a problem of estimating a quantile of a random variable obtained as a global extremum of the membership function over the complement of the excursion set. To construct such confidence sets, we propose a computationally efficient bifidelity method that exploits a spectral representation of this random variable to reduce the required number of evaluations of the computational model. We show the interest of this concept of confidence sets and the efficiency gain of the proposed bifidelity method in a test case concerned with excursion sets of a Gaussian function with an uncertain input parameter. Theory and methods presented in Sections 5.4–5.7 are part of the manuscript [Bulthuis et al., 2019b], currently under review.*

### 5.1 Context

In the previous chapter, we provided a review of theory and methods to quantify the uncertainty in the quantity of interest of a (physics-based) computational model with uncertain input parameters. We assumed this quantity of interest to represent a scalar-valued, vector-valued, or field-valued characteristic of the spatial response of the computational model. The subject of this chapter is in uncertainty quantification of (physics-based) computational models when the quantity of interest concerns geometrical characteristics of their spatial response. This issue may typically arise in applications in which interest is directed towards determining within a spatial domain a subregion where the spatial response of a computational model exceeds a specified threshold. This task may serve to determine, for instance, a critical level of safety or help distin-

guish between different characteristics of the spatial response. Examples include applications in chemical contamination, geophysics (volcanic hazards [Bayarri et al., 2009]), and climatology (heat-wave detection [French et al., 2019]). In the context of ice-sheet modelling, the reader may think of the problem of assessing the retreat of the grounded portion of the Antarctic ice sheet in response to climate forcing as a motivating example for this chapter. Hence, understanding and quantifying the impact of the input uncertainties on geometrical characteristics of the spatial response of a computational model is an interesting problem relevant for ice-sheet modelling and more generally for uncertainty quantification.

Here, we seek to quantify uncertainty in excursion sets of spatial responses of computational models using the concept of confidence sets that either contain an excursion set of the spatial response or are contained within an excursion set of the spatial response with a specified confidence level. Such confidence sets were first introduced in French and Sain [2013], French [2014], Bolin and Lindgren [2015], and French and Hoeting [2015], in a context of Bayesian inference under a stationary Gaussian spatial process prior and further extended to non-stationary and non-Gaussian spatial processes in Sommerfeld et al. [2018]. From a theoretical point of view, excursion sets of random fields can be studied by using the random set theory [Azzimonti, 2016; Azzimonti et al., 2016; Molchanov, 2017] or the geometry theory of random fields [Adler and Taylor, 2007; Adler, 2008]. In French [2014], Bolin and Lindgren [2015], French and Hoeting [2015], and Azzimonti [2016], confidence sets are computed by seeking the optimal confidence set in a parametric family of nested candidate sets by solving either an optimisation problem or an equivalent problem of quantile estimation. These references have addressed the numerical solution of these optimisation and quantile estimation problems in specific contexts in which the random field is obtained by Bayesian inference under a Gaussian spatial process prior, including kriging methods. In such contexts, the random field can be evaluated everywhere in the spatial domain by using the Gaussian-process or kriging interpolants, and numerous samples of the random field can be simulated at low computational cost.

In this chapter, we address the computation of confidence sets of excursion sets of random fields obtained as solution quantities of stochastic computational models with a high computational cost. In this context, the definition and computation of excursion sets and confidence sets must be based on the spatial discretisation of the computational model obtained, for instance, with a finite-difference or a finite-element discretisation scheme. Based on the random set theory, we propose a spatial discretisation of excursion sets and confidence sets that relies on a partitioning of the domain into subsets and testing the exceedance constraints in representative points in these subsets. Such a spatial discretisation is shown to have an impact on the stochastic dimension of the problem and the accuracy one may achieve in computing confidence sets.

The computation of confidence sets for computational models with a high computational cost requires computationally efficient methods for the discretisation of the stochastic dimension. Monte Carlo methods may lead to a slow decrease of the estimation error as a function of the number of samples, which may be intractable for computational models with a high computational cost or high confidence levels. The use of surrogate models, such as stochastic expansions, may reduce the computational cost but may lead to an additional approximation error. Here, we propose a bifidelity method in which a surrogate model is used further away from the quantile to be estimated and the computational model is used closer to the quantile to

be estimated.

In this chapter, the proposed methodology is applied in an illustration in which we build confidence sets for superlevel sets of a Gaussian function with an uncertain input parameter. We illustrate how the proposed bifidelity method may help reduce the computational cost of computing confidence sets. We refer the reader to Chapter 7 for an illustration relevant to the retreat of the grounded portion of the Antarctic ice sheet and we show in Chapters 7 and 8 how confidence sets may help assess with quantified uncertainty the vulnerability of the Antarctic ice sheet to climate change.

This chapter is organised as follows. In Section 5.2, we provide a literature review of various methods to quantify uncertainty in excursion and contour sets in a context of Bayesian inference. In Sections 5.4 and 5.5, we review the concepts of excursion sets, contour sets, and confidence sets of a random field based on the random set theory [Molchanov, 2017], and we discuss the identification of an optimal confidence set in a parametric family of nested candidate sets. Then, Section 5.6 addresses the spatial discretisation, Section 5.7 is concerned with the discretisation of the stochastic dimension, and Section 5.8 provides the illustration.

## 5.2 Literature review

This section provides a non-exhaustive review of methods to quantify the uncertainty in excursion and contour sets in the context of Bayesian inference. In the undermentioned references, interest is in quantifying the uncertainty in the estimation of contour sets (or level sets) and excursion sets (or superlevel sets) of an unknown real-valued function considered as a realisation of a random field that is observed at a set of locations in the domain. In this context, confidence sets quantify the uncertainty in the estimated contour and excursion sets. Please note that in the undermentioned references, confidence sets are also referred to as confidence bands, confidence regions, or conservative estimates. In this section, we use the same terminology as in the quoted references but in the next sections, we will adopt the terminology of confidence sets to make connections with the set theory.

Lindgren and Rychlik [1995] addressed the problem of quantifying the uncertainty in level sets in the context of Bayesian inference under a Gaussian process prior. They proposed a method to quantify the uncertainty in the estimation of the level set of a realisation of a Gaussian random field observed at a set of regularly or irregularly spaced observation points. From a technical perspective, the level set for the level  $u$  is interpreted as the union of all crossings of the level  $u$  when one follows straight lines in the spatial domain. This interpretation of the level set also allows to take into account both continuous and discontinuous crossings of the level  $u$ . Lindgren and Rychlik [1995] proposed to construct for each point on the estimated level set a symmetric confidence interval perpendicular to the estimated level set that intersects the true level set with calculable probability. The union of these symmetric confidence intervals for all points along the estimated level set then defines a confidence band that represents the uncertainty in assessing level sets.

Polfeldt [1999] proposed an alternative approach to assess the accuracy of a contour map by calculating the probability that the true response at a location lies between the values of the two

closest estimated contour sets. Under a Gaussian process prior, this probability can be evaluated readily. The higher the probability, the higher the confidence that the true response lies between the values of the two closest estimated contour sets.

Wameling and Saborowski [2001] extended the approach in Lindgren and Rychlik [1995] to construct asymmetric confidence bands for non-Gaussian random fields using a conditional simulation algorithm. Wameling [2003a] applied this approach to quantify the accuracy of geostatistical predictions of yearly precipitation in Lower Saxony. Wameling [2003b] further derived an approximate relation between spatial horizontal uncertainty in geostatistical prediction, as described with confidence bands, and spatial vertical uncertainty in geostatistical prediction, as estimated with the kriging variance, for transects having a small horizontal uncertainty.

In the context of risk assessment and catastrophic events, Bayarri et al. [2009] approximated the contour set separating catastrophic events from benign events in the parameter space as the median of a Gaussian posterior distribution. The uncertainty in the approximation is reflected with confidence bands constructed from the quantiles of the posterior distribution.

Confidence bands for excursion sets and contour sets as proposed in references [Lindgren and Rychlik, 1995; Bayarri et al., 2009; Wameling and Saborowski, 2001] are all constructed locally without providing any control over the simultaneous coverage probability of these confidence bands. A first approach to control the simultaneous coverage probability of confidence bands was proposed in Bolin [2012] and Bolin and Lindgren [2015]. Bolin and Lindgren [2015] proposed to construct confidence regions that are contained within the true excursion set with a certain level of probability. An approximation of the largest confidence region is obtained by seeking in a parametric family of nested candidate sets the largest set satisfying the desired level of inclusion. The inclusion probability is evaluated using an importance sampling method in the context of latent Gaussian random fields. Azzimonti [2016] revisited the approach by Bolin and Lindgren [2015] with the random set theory and evaluated the inclusion probability with an asymmetric nested Monte Carlo method.

French and Hoeting [2015] proposed a complementary approach to Bolin and Lindgren [2015] that relies on multiple-hypothesis testing. For each location  $\boldsymbol{x}$  in a spatial domain  $D$ , French and Hoeting [2015] considered a pointwise test statistic  $T(\boldsymbol{x})$  for the hypothesis test  $y(\boldsymbol{x}) \geq u$ , where  $y$  is the true response of the model. The decision rule of this hypothesis test is  $\mathbf{1}(T(\boldsymbol{x}) > \rho)$ , with  $\rho$  a threshold that controls the Type I error rate and  $\mathbf{1}(T(\boldsymbol{x}) > \rho) = 1$  for  $T(\boldsymbol{x}) > \rho$  and 0 otherwise. French and Hoeting [2015] then built a confidence region for the true excursion set by controlling the Type I error rate of all hypothesis tests simultaneously, that is, the family-wise error rate. French and Hoeting [2015] showed that this problem is equivalent to the estimation of a quantile of a random variable. A similar approach was used in French and Sain [2013] and French [2014] to construct confidence regions for level sets.

### 5.3 Notations

We denote a deterministic set by a Latin or a Greek upper case letter such as  $D$  or  $\Omega$ , a random set by a calligraphic upper case letter such as  $\mathcal{E}$ , and a family of subsets of a topological space or a  $\sigma$ -algebra by a Fraktur upper case letter such as  $\mathfrak{F}$ . Throughout this chapter, we denote by  $D$

a compact subset of the  $d$ -dimensional Euclidean space  $\mathbb{R}^d$ . We use the symbol  $\subset$  to denote the strict and non-strict inclusion relations. For a subset  $E \subset D$ , we denote by  $E^c$ ,  $\text{cl}(E)$ ,  $\text{int}(E)$ ,  $\text{ext}(E)$ ,  $\partial E$ , and  $|E|$  the complement in  $D$ , the closure, the interior, the exterior, the boundary, and the Lebesgue measure of  $E$ , respectively. Finally, we denote by  $\mathfrak{F}$  the family of all closed subsets of  $D$  and by  $\mathfrak{L}$  the family of all open subsets of  $D$ .

## 5.4 Random excursion and contour sets

Let  $\{Y(\mathbf{x}), \mathbf{x} \in D\}$  be a random field defined on a complete probability space  $(\Theta, \mathfrak{B}, \mathbb{P})$ , indexed by  $D$ , with values in  $\mathbb{R}$ , and with continuous sample paths almost surely. Please note that we do not consider vector-valued random fields; yet, we mention that vector-valued random fields can be handled through operations of vector reduction, for instance, norm computation.

### 5.4.1 Excursion and contour sets

The positive and negative excursion sets of  $\{Y(\mathbf{x}), \mathbf{x} \in D\}$  for the threshold  $u$  in  $\mathbb{R}$  (Figure 5.1) are defined by

$$\mathcal{E}_u^+ = \{\mathbf{x} \in D : Y(\mathbf{x}) \geq u\}, \quad (5.1)$$

$$\mathcal{E}_u^- = \{\mathbf{x} \in D : Y(\mathbf{x}) \leq u\}. \quad (5.2)$$

Similarly, the contour set of  $\{Y(\mathbf{x}), \mathbf{x} \in D\}$  for the threshold  $u$  is defined by

$$\mathcal{E}_u^0 = \{\mathbf{x} \in D : Y(\mathbf{x}) = u\}. \quad (5.3)$$

Because  $\{Y(\mathbf{x}), \mathbf{x} \in D\}$  has continuous sample paths almost surely,  $\mathcal{E}_u^+$ ,  $\mathcal{E}_u^-$ , and  $\mathcal{E}_u^0$  are closed subsets of  $D$  almost surely.

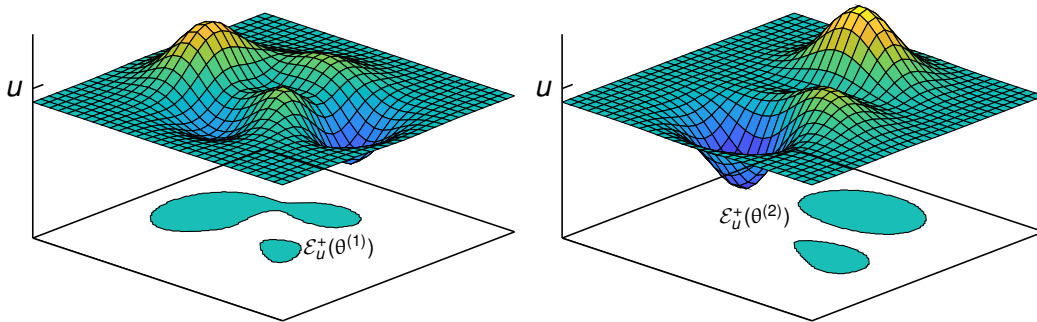


Figure 5.1: Two realisations of a random field with the corresponding positive excursion set.

The random set theory, see, for instance, [Molchanov \[2017\]](#), provides a rigorous framework for the definition and description of such excursion and contour sets as set-valued random variables, which requires to be more specific about measurability. Within the random set theory,  $\mathcal{E}_u^+$ ,  $\mathcal{E}_u^-$ , and  $\mathcal{E}_u^0$  are defined as measurable mappings from  $(\Theta, \mathfrak{B}, \mathbb{P})$  into  $(\mathfrak{F}, \mathfrak{S}(\mathfrak{F}))$ , with  $\mathfrak{S}(\mathfrak{F})$  the

$\sigma$ -algebra generated by the sets  $\{K \in \mathfrak{F} : K \cap F \neq \emptyset\}$  for  $F$  running through the family  $\mathfrak{F}$  of closed subsets of  $D$  (Figure 5.2). The random set theory provides several descriptors for random closed sets, such as the capacity, the containment, and the inclusion functionals, the coverage function, and the Vorob'ev quantiles, which are described next.

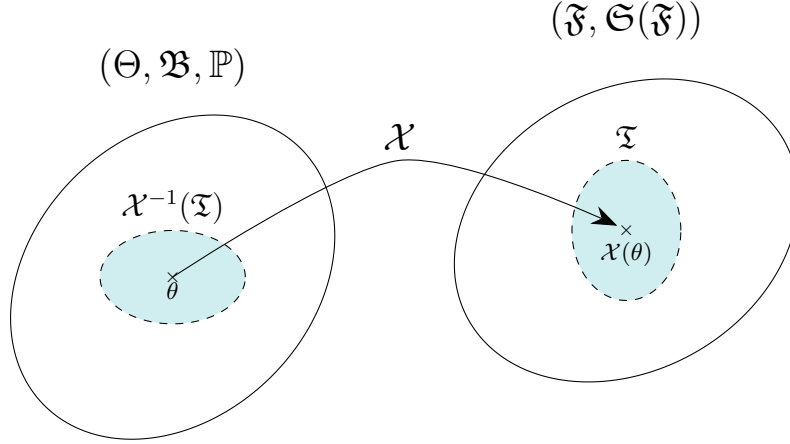


Figure 5.2: A random closed set  $\mathcal{X}$  is a set-valued measurable mapping from  $(\Theta, \mathfrak{B}, \mathbb{P})$  into  $(\mathfrak{F}, \mathfrak{S}(\mathfrak{F}))$ . This means that, for each  $\mathfrak{T}$  in  $\mathfrak{S}(\mathfrak{F})$ ,  $\mathcal{X}^{-1}(\mathfrak{T}) = \{\theta \in \Theta : \mathcal{X}(\theta) \in \mathfrak{T}\}$  is in  $\mathfrak{B}$ .

### 5.4.2 Capacity functional

The capacity functional of  $\mathcal{E}_u^+$  is defined by

$$T_{\mathcal{E}_u^+} : \mathfrak{F} \rightarrow [0, 1]; F \mapsto T_{\mathcal{E}_u^+}(F) = \mathbb{P}(\mathcal{E}_u^+ \cap F \neq \emptyset). \quad (5.4)$$

The capacity functional is in general not a probability measure because it is subadditive and not additive, that is,

$$T_{\mathcal{E}_u^+}(F_1 \cup F_2) \leq T_{\mathcal{E}_u^+}(F_1) + T_{\mathcal{E}_u^+}(F_2), \quad F_1, F_2 \in \mathfrak{F}, F_1 \cap F_2 = \emptyset. \quad (5.5)$$

The capacity functional of a random closed set is a probability measure if and only if the random closed set is a random singleton. The capacity functional uniquely determines the probability distribution of a random closed set.

Please note that the capacity functional can be defined similarly for  $\mathcal{E}_u^-$  and  $\mathcal{E}_u^0$ .

### 5.4.3 Containment and inclusion functionals

The random set theory also defines further functionals associated with the random closed set  $\mathcal{E}_u^+$ , namely the containment and inclusion functionals. The containment functional of  $\mathcal{E}_u^+$  is defined by

$$C_{\mathcal{E}_u^+} : \mathfrak{F} \rightarrow [0, 1]; F \mapsto C_{\mathcal{E}_u^+}(F) = \mathbb{P}(\mathcal{E}_u^+ \subset F), \quad (5.6)$$

and the inclusion functional of  $\mathcal{E}_u^+$  is defined by

$$I_{\mathcal{E}_u^+} : \mathfrak{F} \rightarrow [0, 1]; F \mapsto I_{\mathcal{E}_u^+}(F) = \mathbb{P}(F \subset \mathcal{E}_u^+). \quad (5.7)$$

Containment and inclusion functionals can be defined similarly for  $\mathcal{E}_u^-$ . Although, the containment functional may be defined similarly for  $\mathcal{E}_u^0$ , the definition of the inclusion functional is less meaningful for  $\mathcal{E}_u^0$  because  $\mathcal{E}_u^0$  is generally of lower dimension than  $D$  and its inclusion functional vanishes for all  $F$  in  $\mathfrak{F}$  of the same dimension as  $D$ . Please note that, as for the capacity functional, neither the containment functional nor the inclusion functional is a probability measure, except for the case of random singletons. The containment functional, and the inclusion functional for random closed sets that coincide with the closure of their interior almost surely, uniquely determines the probability distribution of a random closed set.

In the following, we will focus (mostly) on the containment and inclusion functionals rather than the capacity functional because they provide a natural choice to define confidence sets.

#### 5.4.4 Coverage function

By limiting  $F = \{\mathbf{x}\}$  to be a singleton, the capacity functional

$$T_{\mathcal{E}_u^+}(F) = I_{\mathcal{E}_u^+}(\mathbf{x}) = \mathbb{P}(\mathbf{x} \in \mathcal{E}_u^+) = \mathbb{P}(Y(\mathbf{x}) \geq u) \equiv p_{\mathcal{E}_u^+}(\mathbf{x}) \quad (5.8)$$

reduces to the so-called (one-point) coverage function of  $\mathcal{E}_u^+$ , which provides the pointwise (marginal) probability of exceeding the threshold  $u$ . The set of points  $\mathbf{x}$  in the domain  $D$  such that  $p_{\mathcal{E}_u^+}(\mathbf{x}) = 1$  is called the set of fixed points of  $\mathcal{E}_u^+$ . Thus, the set of fixed points is the set of locations that belong to  $\mathcal{E}_u^+$  almost surely, that is, the set of locations that exceed the threshold  $u$  almost surely. Please note that the coverage function can be defined similarly for  $\mathcal{E}_u^-$ , which provides the pointwise (marginal) probability of being lower than the threshold  $u$ .

#### 5.4.5 Vorob'ev quantiles

As a generalisation of quantiles of scalar-valued random variables, the random set theory defines the so-called Vorob'ev  $\rho$ -quantile

$$Q_\rho^V = \{\mathbf{x} \in D : p_{\mathcal{E}_u^+}(\mathbf{x}) \geq \rho\} \quad (5.9)$$

as the superlevel set of the coverage function for the level  $\rho$ . Thus, the Vorob'ev  $\rho$ -quantile is the set of locations where the pointwise (marginal) probability of exceeding the threshold  $u$  is at least  $\rho$ . The Vorob'ev quantiles are of particular interest because they are used in the random set theory to define a notion of expectation for random closed sets [Azzimonti et al., 2016; Azzimonti, 2016; Molchanov, 2017]; the so-called Vorob'ev expectation is the Vorob'ev quantile whose Lebesgue measure is equal or closest to the expected Lebesgue measure of the random closed set. The Vorob'ev quantiles are also minimisers of an expected distance in Lebesgue measure among sets with the same Lebesgue measure [Azzimonti, 2016]. Please note that the Vorob'ev quantiles can be defined similarly for  $\mathcal{E}_u^-$ , with the Vorob'ev  $\rho$ -quantile of  $\mathcal{E}_u^-$  being the set of locations where the pointwise (marginal) probability of being lower than the threshold  $u$  is at least  $\rho$ .

## 5.5 Confidence sets for random excursion and contour sets

In a context of Bayesian inference under a Gaussian process prior, French and Sain [2013], French [2014], Bolin and Lindgren [2015], French and Hoeting [2015], and Azzimonti [2016] defined alternative descriptors of excursion and contour sets, namely, confidence sets, which we focus on in this chapter. In French and Sain [2013], French [2014], Bolin and Lindgren [2015], and French and Hoeting [2015], these confidence sets were defined without reference to the aforementioned descriptors of the random set theory. Azzimonti [2016] first revisited confidence sets based on the random set theory. Here, we follow this approach and introduce these confidence sets equivalently with the help of the containment and inclusion functionals of the random set theory.

A closed subset  $C_{u^+, \alpha}^{\text{out}}$  of  $D$  is an outer confidence set for  $\mathcal{E}_u^+$  with a probability of at least  $\alpha$  if

$$C_{\mathcal{E}_u^+}(C_{u^+, \alpha}^{\text{out}}) \geq \alpha, \quad (5.10)$$

and an open subset  $C_{u^+, \alpha}^{\text{in}}$  of  $D$  is an inner confidence set for  $\mathcal{E}_u^+$  with a probability of at least  $\alpha$  if

$$I_{\mathcal{E}_u^+}(\text{cl}(C_{u^+, \alpha}^{\text{in}})) \geq \alpha. \quad (5.11)$$

Thus, an outer confidence set  $C_{u^+, \alpha}^{\text{out}}$  is such that with a (joint) probability of at least  $\alpha$ , it contains all locations where  $u$  is exceeded simultaneously. And, an inner confidence set  $C_{u^+, \alpha}^{\text{in}}$  is such that with a (joint) probability of at least  $\alpha$ , all locations in  $C_{u^+, \alpha}^{\text{in}}$  exceed  $u$  simultaneously. An outer confidence set  $C_{u^-, \alpha}^{\text{out}}$  and an inner confidence set  $C_{u^-, \alpha}^{\text{in}}$  can be defined similarly for  $\mathcal{E}_u^-$ . A closed subset  $C_{u^0, \alpha}$  of  $D$  is a confidence set for  $\mathcal{E}_u^0$  with a probability of at least  $\alpha$  if

$$C_{\mathcal{E}_u^0}(C_{u^0, \alpha}) \geq \alpha. \quad (5.12)$$

Thus, a confidence set  $C_{u^0, \alpha}$  for  $\mathcal{E}_u^0$  is such that with a (joint) probability of at least  $\alpha$ , it contains all locations where  $u$  is attained simultaneously. Figure 5.3 provides a schematic illustration of an outer confidence set  $C_{u^+, \alpha}^{\text{out}}$  and an inner confidence set  $C_{u^+, \alpha}^{\text{in}}$  for the random closed set  $\mathcal{E}_u^+$ .

Proposition 5.1 by French and Hoeting [2015] shows that if  $C_{u^+, \alpha}^{\text{out}}$  and  $C_{u^-, \alpha}^{\text{out}}$  are outer confidence sets for  $\mathcal{E}_u^+$  and  $\mathcal{E}_u^-$ , respectively, with a probability of at least  $\alpha$ , then their exteriors in  $D$  are inner confidence sets for  $\mathcal{E}_u^-$  and  $\mathcal{E}_u^+$ , respectively, with a probability of at least  $\alpha$ .

**Proposition 5.1.** *Let  $C_{u^+, \alpha}^{\text{out}}$  and  $C_{u^-, \alpha}^{\text{out}}$  be outer confidence sets for  $\mathcal{E}_u^+$  and  $\mathcal{E}_u^-$ , respectively, with a probability of at least  $\alpha$ . Then  $\text{ext}(C_{u^-, \alpha}^{\text{out}})$  and  $\text{ext}(C_{u^+, \alpha}^{\text{out}})$  are inner confidence sets for  $\mathcal{E}_u^-$  and  $\mathcal{E}_u^+$ , respectively, with a probability of at least  $\alpha$ .*

*Proof.* As  $C_{u^+, \alpha}^{\text{out}}$  is an outer confidence set for  $\mathcal{E}_u^+$ , we have

$$\begin{aligned} \alpha &\leq \mathbb{P}\left(\mathcal{E}_u^+ \subset C_{u^+, \alpha}^{\text{out}}\right) \\ &= \mathbb{P}\left(\left(C_{u^+, \alpha}^{\text{out}}\right)^c \subset \left(\mathcal{E}_u^+\right)^c\right) \\ &\leq \mathbb{P}\left(\left(C_{u^+, \alpha}^{\text{out}}\right)^c \subset \mathcal{E}_u^-\right) \\ &\leq \mathbb{P}\left(\text{ext}(C_{u^+, \alpha}^{\text{out}}) \subset \mathcal{E}_u^-\right). \end{aligned} \quad (5.13)$$

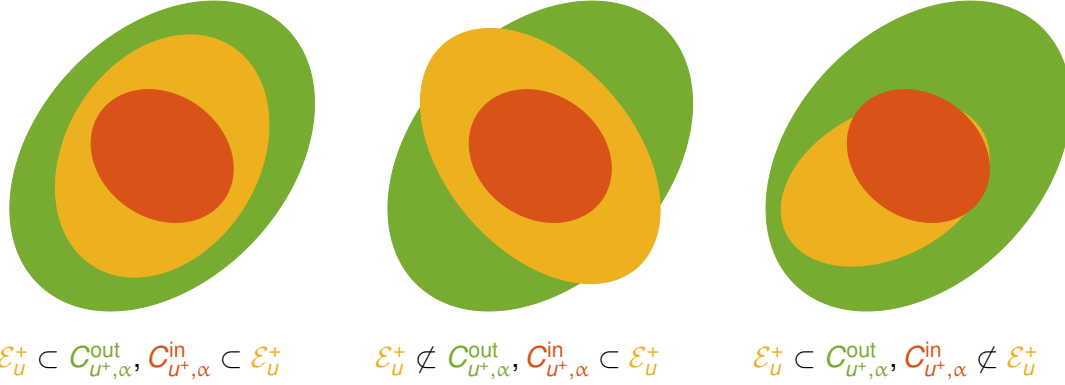


Figure 5.3: Schematic illustration of an outer confidence set  $C_{u^+, \alpha}^{out}$  and an inner confidence set  $C_{u^+, \alpha}^{in}$  for the random closed set  $\mathcal{E}_u^+$ .

The third line is obtained by noticing that  $(\mathcal{E}_u^+)^c = \{\mathbf{x} \in D : Y(\mathbf{x}) < u\}$  is a subset of  $\mathcal{E}_u^- = \{\mathbf{x} \in D : Y(\mathbf{x}) \leq u\}$ . Similarly, one can show that  $\mathbb{P}(\text{ext}(C_{u^-, \alpha}^{out}) \subset \mathcal{E}_u^+) \geq \alpha$ .  $\square$

When  $\mathcal{E}_u^0 \subset \partial \mathcal{E}_u^+$ , confidence sets for contour sets can be determined from confidence sets of related excursion sets. For instance, the set

$$C_{u^+, \beta}^{out} \cap (C_{u^+, \beta}^{in})^c, \quad \beta \geq \frac{1}{2}(\alpha + 1), \quad (5.14)$$

and the set

$$(N_{u^+, \alpha}^{in} \cup N_{u^-, \alpha}^{in})^c, \quad (5.15)$$

with  $N_{u^+, \alpha}^{in}$  and  $N_{u^-, \alpha}^{in}$  in  $\mathfrak{L}$  that satisfy  $\mathbb{P}(\text{cl}(N_{u^+, \alpha}^{in}) \subset \mathcal{E}_u^+, \text{cl}(N_{u^-, \alpha}^{in}) \subset \mathcal{E}_u^-) \geq \alpha$ , are both confidence sets for  $\mathcal{E}_u^0$  with a probability of at least  $\alpha$ .

*Proof.* We first prove Equation (5.14). We start from the following inequalities:

$$\beta \leq \mathbb{P}(\text{cl}(C_{u^+, \beta}^{in}) \subset \mathcal{E}_u^+) \quad (5.16a)$$

$$= \mathbb{P}(\partial \mathcal{E}_u^+ \subset (C_{u^+, \beta}^{in})^c) \quad (5.16b)$$

$$= \mathbb{P}(\mathcal{E}_u^0 \subset (C_{u^+, \beta}^{in})^c) \quad (5.16c)$$

$$= \mathbb{P}(\mathcal{E}_u^0 \subset C_{u^+, \beta}^{out}, \mathcal{E}_u^0 \subset (C_{u^+, \beta}^{in})^c) + \mathbb{P}(\mathcal{E}_u^0 \not\subset C_{u^+, \beta}^{out}, \mathcal{E}_u^0 \subset (C_{u^+, \beta}^{in})^c). \quad (5.16d)$$

In going from Equation (5.16a) to Equation (5.16b), we use the fact that  $C_{u^+, \beta}^{in}$  is an open set. In going from Equation (5.16b) to Equation (5.16c), we use the assumption that  $\mathcal{E}_u^0 \subset \partial \mathcal{E}_u^+$ . Finally, Equation (5.16d) is obtained by decomposing Equation (5.16c) into the sum of the probabilities of two disjoint events. Similarly, we have the following inequalities:

$$\beta \leq \mathbb{P}(\mathcal{E}_u^+ \subset C_{u^+, \beta}^{out}) \quad (5.17a)$$

$$= \mathbb{P}\left(\mathcal{E}_u^0 \subset C_{u^+,\beta}^{\text{out}}\right) \quad (5.17b)$$

$$= \mathbb{P}\left(\mathcal{E}_u^0 \subset C_{u^+,\beta}^{\text{out}}, \mathcal{E}_u^0 \subset (C_{u^+,\beta}^{\text{in}})^c\right) + \mathbb{P}\left(\mathcal{E}_u^0 \subset C_{u^+,\beta}^{\text{out}}, \mathcal{E}_u^0 \not\subset (C_{u^+,\beta}^{\text{in}})^c\right), \quad (5.17c)$$

In going from Equation (5.17a) to Equation (5.17b), we use the fact that  $\mathcal{E}_u^0 \subset \mathcal{E}_u^+$ . Equation (5.17c) is obtained by decomposing Equation (5.17b) into the sum of the probabilities of two disjoint events. By adding inequalities (5.16) and (5.17), we obtain

$$2\mathbb{P}\left(\mathcal{E}_u^0 \subset C_{u^+,\beta}^{\text{out}}, \mathcal{E}_u^0 \subset (C_{u^+,\beta}^{\text{in}})^c\right) + \mathbb{P}\left(\mathcal{E}_u^0 \not\subset C_{u^+,\beta}^{\text{out}}, \mathcal{E}_u^0 \subset (C_{u^+,\beta}^{\text{in}})^c\right) + \mathbb{P}\left(\mathcal{E}_u^0 \subset C_{u^+,\beta}^{\text{out}}, \mathcal{E}_u^0 \not\subset (C_{u^+,\beta}^{\text{in}})^c\right) \geq 2\beta. \quad (5.18)$$

Moreover, we have the following inequality

$$\begin{aligned} & \mathbb{P}\left(\mathcal{E}_u^0 \subset C_{u^+,\beta}^{\text{out}}, \mathcal{E}_u^0 \subset (C_{u^+,\beta}^{\text{in}})^c\right) + \mathbb{P}\left(\mathcal{E}_u^0 \not\subset C_{u^+,\beta}^{\text{out}}, \mathcal{E}_u^0 \subset (C_{u^+,\beta}^{\text{in}})^c\right) \\ & + \mathbb{P}\left(\mathcal{E}_u^0 \subset C_{u^+,\beta}^{\text{out}}, \mathcal{E}_u^0 \not\subset (C_{u^+,\beta}^{\text{in}})^c\right) \\ & = \mathbb{P}\left(\mathcal{E}_u^0 \subset C_{u^+,\beta}^{\text{out}}\right) + \mathbb{P}\left(\mathcal{E}_u^0 \not\subset C_{u^+,\beta}^{\text{out}}, \mathcal{E}_u^0 \subset (C_{u^+,\beta}^{\text{in}})^c\right) \\ & \leq \mathbb{P}\left(\mathcal{E}_u^0 \subset C_{u^+,\beta}^{\text{out}}\right) + \mathbb{P}\left(\mathcal{E}_u^0 \not\subset C_{u^+,\beta}^{\text{out}}\right) \\ & = 1. \end{aligned} \quad (5.19)$$

By subtracting Equation (5.19) from Equation (5.18), we get

$$\mathbb{P}\left(\mathcal{E}_u^0 \subset C_{u^+,\beta}^{\text{out}}, \mathcal{E}_u^0 \subset (C_{u^+,\beta}^{\text{in}})^c\right) \geq 2\beta - 1. \quad (5.20)$$

Thus,  $C_{u^+,\beta}^{\text{out}} \cap (C_{u^+,\beta}^{\text{in}})^c$  is a confidence set for  $\mathcal{E}_u^0$  with a probability of at least  $\alpha$  if  $\beta \geq \frac{1}{2}(1+\alpha)$ .

We now prove Equation (5.15). We have the following equalities

$$\mathbb{P}\left(\text{cl}(N_{u^+,\alpha}^{\text{in}}) \subset \mathcal{E}_u^+, \text{cl}(N_{u^-, \alpha}^{\text{in}}) \subset \mathcal{E}_u^-\right) = \mathbb{P}\left(\partial\mathcal{E}_u^+ \subset (N_{u^+,\alpha}^{\text{in}})^c, \partial\mathcal{E}_u^- \subset (N_{u^-, \alpha}^{\text{in}})^c\right) \quad (5.21a)$$

$$= \mathbb{P}\left(\mathcal{E}_u^0 \subset (N_{u^+,\alpha}^{\text{in}})^c, \mathcal{E}_u^0 \subset (N_{u^-, \alpha}^{\text{in}})^c\right) \quad (5.21b)$$

$$= \mathbb{P}\left(\mathcal{E}_u^0 \subset (N_{u^+,\alpha}^{\text{in}} \cup N_{u^-, \alpha}^{\text{in}})^c\right). \quad (5.21c)$$

In Equation (5.21a), we use the fact that  $N_{u^+,\alpha}^{\text{in}}$  and  $N_{u^-, \alpha}^{\text{in}}$  are both open sets. In going from Equation (5.21a) to Equation (5.21b), we use the assumption that  $\mathcal{E}_u^0 \subset \partial\mathcal{E}_u^+$  and thus  $\mathcal{E}_u^0 \subset \partial\mathcal{E}_u^-$ . Equation (5.21c) results from De Morgan's laws. Thus,  $(N_{u^+,\alpha}^{\text{in}} \cup N_{u^-, \alpha}^{\text{in}})^c$  is a confidence set for  $\mathcal{E}_u^0$  with a probability of at least  $\alpha$  if  $\mathbb{P}\left(\text{cl}(N_{u^+,\alpha}^{\text{in}}) \subset \mathcal{E}_u^+, (N_{u^-, \alpha}^{\text{in}}) \subset \mathcal{E}_u^-\right) \geq \alpha$ .  $\square$

For the sake of brevity and without loss of generality, we will focus the discussion to follow (mostly) on the construction of an inner confidence set for the positive excursion set.

### 5.5.1 Optimisation within a parametric family

The confidence sets defined above are in general not unique. To determine such confidence sets uniquely, additional restrictions must be imposed. In French [2014], Bolin and Lindgren [2015], French and Hoeting [2015], and Azzimonti [2016], uniqueness is obtained by first defining a parametric family of candidate sets and then seeking in this family the largest or the smallest set satisfying the joint probability of exceedance constraint. In French [2014], Bolin and Lindgren [2015], French and Hoeting [2015], and Azzimonti [2016], the family of candidate sets is taken as a parametric family of sets  $T_\rho$  indexed by a real number  $\rho$  in  $(0, 1)$  such that

$$T_\rho = \{\mathbf{x} \in \text{int}(D) : T(\mathbf{x}) > \rho\}, \quad (5.22)$$

where  $T$  is a function from  $D$  into  $[0, 1]$ , also referred to as the membership function by analogy with fuzzy theory. The membership function is assumed to be continuous in  $\text{int}(D)$  so as to ensure that the sets  $T_\rho$  belong to  $\mathfrak{L}$ . Clearly, such a parametric family is nested, that is,  $T_\rho \subseteq T_\sigma$  for  $\sigma \leq \rho$ . Seeking in this parametric family the largest set satisfying the required joint probability of exceedance constraint amounts to the optimisation problem

$$\rho^* = \inf_{\rho \in (0,1)} \rho \text{ subject to } I_{\mathcal{E}_u^+}(\text{cl}(T_\rho)) \geq \alpha, \quad (5.23)$$

with the optimal threshold  $\rho^*$  leading to the identification of  $T_{\rho^*}$  as the largest inner confidence set with a probability of a least  $\alpha$  in the parametric family. For outer confidence sets, one may seek similarly the smallest set in a parametric family of nested candidate sets.

#### 5.5.1.1 Choice of the membership function

The definition in Equation (5.22) uses a generic membership function  $T$ . For the purpose of constructing confidence sets for the positive excursion set, Azzimonti [2016], Bolin and Lindgren [2015], and French and Hoeting [2015] suggested and used the following membership functions:

$$T_1(\mathbf{x}) = \mathbb{P}(Y(\mathbf{x}) \geq u), \quad (5.24)$$

$$T_2(\mathbf{x}) = \frac{1}{2} \left( 1 + \text{erf} \left( \frac{\mathbb{E}[Y(\mathbf{x})] - u}{\sqrt{2\mathbb{V}[Y(\mathbf{x})]}} \right) \right), \quad (5.25)$$

$$T_3(\mathbf{x}) = \frac{1}{2} \left( 1 + \frac{\mathbb{E}[Y(\mathbf{x})] - u}{\sqrt{\mathbb{E}[(Y(\mathbf{x}) - u)^2]}} \right), \quad (5.26)$$

where  $\mathbb{E}$  denotes the mathematical expectation,  $\mathbb{V}$  the variance, and  $\text{erf}$  the error function. French and Hoeting [2015] argued that the functions in Equations (5.24)–(5.26) are suitable choices for the membership function because they quantify the difference between the value taken by the random field at a location and the threshold level  $u$  and they account for the associated measure of uncertainty for this difference. The membership function  $T_1$  is the coverage function defined in Equation (5.8) so that the corresponding sets in the parametric family are open Vorob'ev quantiles. The membership functions  $T_2$  and  $T_3$ , whose use requires the random field to be of the second order, are transformations of the pointwise difference between the expectation of the random field and the threshold  $u$  rescaled respectively by the standard deviation

of the random field and the square root of the expected squared deviation of the random field about the threshold  $u$ . If the pointwise (marginal) probability distribution of the random field is Gaussian, then  $T_1$  and  $T_2$  are equal. In addition, when  $u$  is zero, as considered in Section 7.2,  $T_2$  and  $T_3$  may be expressed only as a function of the pointwise coefficient of variation  $\delta_Y(\mathbf{x})$  of the random field:

$$T_2(\mathbf{x}) = \frac{1}{2} \left( 1 + \operatorname{erf} \left( \frac{1}{\sqrt{2}\delta_Y(\mathbf{x})} \right) \right), \quad (5.27)$$

$$T_3(\mathbf{x}) = \frac{1}{2} \left( 1 + \frac{\operatorname{sgn}(\delta_Y(\mathbf{x}))}{\sqrt{\delta_Y^2(\mathbf{x}) + 1}} \right), \quad (5.28)$$

where  $\operatorname{sgn}$  is the sign function, equal to 1 if  $\delta_Y(\mathbf{x}) \geq 0$  and  $-1$  otherwise. See Figure 5.4 for a comparison between  $T_2$  and  $T_3$  as a function of the pointwise coefficient of variation.

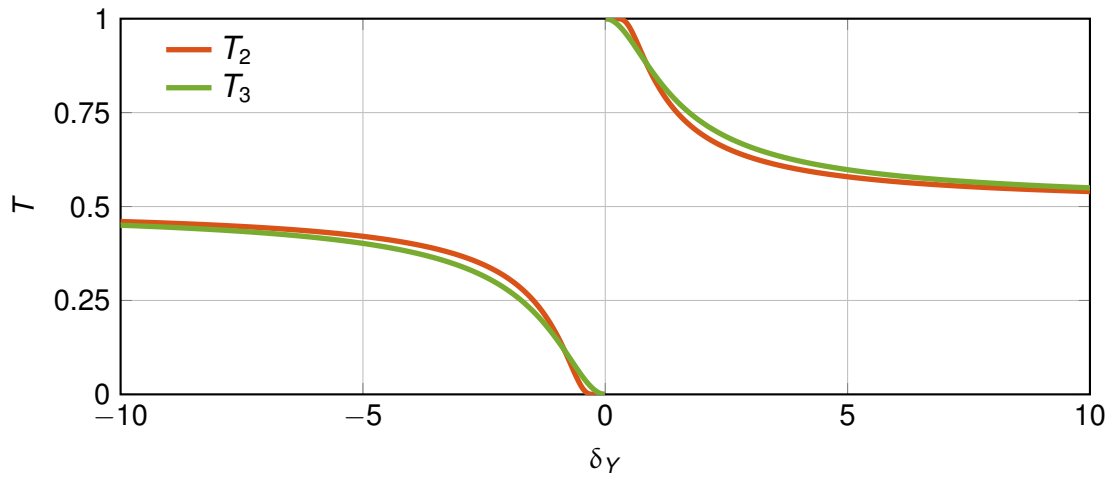


Figure 5.4: Representation of the membership functions  $T_2$  and  $T_3$  as a function of the pointwise (marginal) coefficient of variation  $\delta_Y$ . The maximum difference in absolute value between both functions is about 0.03.

### 5.5.1.2 Interpretation

The membership functions in Equations (5.24)–(5.26) are based on pointwise statistical descriptors of the random field. As such, they quantify in some way the pointwise probability of exceeding  $u$  at all locations in  $D$  but do not quantify the joint probability of exceeding  $u$  simultaneously at all locations in  $T_\rho$ . For instance, the probability of exceeding  $u$  simultaneously at all locations in the Vorob'ev  $\rho$ -quantile is at most  $\rho$ , with a probability of  $\rho$  that is achieved when the description of the random field reduces to the description of a single random variable. To achieve the desired confidence level, the threshold  $\rho^*$  is determined following the optimisation problem (5.23).

The membership function can also be interpreted in the context of the fuzzy set theory [Goodman and Nguyen, 2002; Nguyen and Walker, 2006]. In the fuzzy set theory, any continuous

membership function  $T$  can be written as  $T(\mathbf{x}) = \mu(\mathbf{x} \in \mathcal{E}_u^+)$ , where  $\mu$  is a fuzzy measure defined on  $(\Theta, \mathfrak{B})$ . The fuzzy measure  $\mu$  may be interpreted as a subjective degree of belief about the inclusion of a point  $\mathbf{x}$  in  $D$  in the confidence set. The higher the value of  $T$  at a point, the higher the probability of being a member of the confidence set whatever the confidence level. Taking the probability measure  $\mathbb{P}$  as a fuzzy measure gives the coverage function of the random set  $\mathcal{E}_u^+$ .

### 5.5.1.3 Equivalent problem of quantile estimation

Following the approach by French [2014] and French and Hoeting [2015], the solution of the optimisation problem (5.23) can be recast equivalently as a problem of quantile estimation. Indeed:

$$I_{\mathcal{E}_u^+}(\text{cl}(T_\rho)) = \mathbb{P}(\text{cl}(T_\rho) \subset \mathcal{E}_u^+) \quad (5.29a)$$

$$= \mathbb{P}(T_\rho \subset \mathcal{E}_u^+) \quad (5.29b)$$

$$= \mathbb{P}((\mathcal{E}_u^+)^c \subset T_\rho^c) \quad (5.29c)$$

$$= \mathbb{P}\left(T(\mathbf{x}) \leq \rho, \mathbf{x} \in (\mathcal{E}_u^+)^c\right) \quad (5.29d)$$

$$= \mathbb{P}\left(\sup_{\mathbf{x} \in (\mathcal{E}_u^+)^c} T(\mathbf{x}) \leq \rho\right). \quad (5.29e)$$

In going from Equation (5.29c) to Equation (5.29d), care should be taken about the behaviour of  $T$  on  $\partial D$ , because there is no guarantee that  $T(\mathbf{x}) \leq \rho$  for all  $\mathbf{x}$  in  $\partial D$  (this is a consequence of  $T_\rho$  being defined on  $\text{int}(D)$  rather than  $D$ ). Thus, the behaviour of  $T$  on  $\partial D$  must be excluded in Equation (5.29). This can be achieved, for instance, by assuming either that  $T$  achieves its supremum in  $\text{ext}(\mathcal{E}_u^+)$  or that  $T$  vanishes on  $\partial D$ . With these considerations, the optimisation problem in (5.23) is equivalent to

$$\rho^* = \inf_{\rho \in (0,1)} \rho \text{ subject to } \mathbb{P}\left(\sup_{\mathbf{x} \in (\mathcal{E}_u^+)^c} T(\mathbf{x}) \leq \rho\right) \geq \alpha, \quad (5.30)$$

that is, the problem of quantile estimation

$$\rho^* = \inf \{\rho \in (0, 1) : F_\chi(\rho) \geq \alpha\} \equiv q_\chi(\alpha), \quad (5.31)$$

where  $F_\chi$  and  $q_\chi$  are respectively the distribution function and the generalised quantile function of the random variable

$$\chi = \sup_{\mathbf{x} \in (\mathcal{E}_u^+)^c} T(\mathbf{x}). \quad (5.32)$$

Please note that the randomness of  $\chi$  stems from the random closed set  $\mathcal{E}_u^+$ , hence the set over which the supremum of  $T$  is evaluated. Here,  $q_\chi$  is a generalised quantile function because, in general,  $F_\chi$  is not necessarily strictly monotone, for instance, when  $\chi$  is a discrete random variable (see also Section 5.6). If  $\chi$  is a continuous random variable, then  $F_\chi$  is strictly monotone and the quantile function is the inverse function of  $F_\chi$ , that is,  $q_\chi(\alpha) = F_\chi^{-1}(\alpha)$ .

#### 5.5.1.4 Equivalent problem of reliability-based design optimisation

Besides the formalisms (5.23) and (5.31) for the estimation of confidence sets in a parametric family of nested candidate sets, we mention, as a side note, the existence of a third formalism. Indeed, the optimisation problem (5.23) can be recast as

$$\begin{aligned} I_{\mathcal{E}_u^+}(\text{cl}(T_\rho)) &= \mathbb{P}(\text{cl}(T_\rho) \subset \mathcal{E}_u^+) \\ &= \mathbb{P}(Y(\mathbf{x}) \geq u, \mathbf{x} \in \text{cl}(T_\rho)) \\ &= \mathbb{P}\left(\inf_{\mathbf{x} \in \text{cl}(T_\rho)} Y(\mathbf{x}) \geq u\right). \end{aligned} \quad (5.33)$$

Thus, the optimisation problem in (5.23) is equivalent to

$$\rho^* = \inf_{\rho \in (0,1)} \rho \text{ subject to } \mathbb{P}\left(\inf_{\mathbf{x} \in \text{cl}(T_\rho)} Y(\mathbf{x}) \geq u\right) \geq \alpha, \quad (5.34)$$

where the probability in the optimisation problem in (5.34) is known as the excursion probability of the random field over  $\text{cl}(T_\rho)$ ; see, for instance, Adler and Taylor [2007] and Adler [2008]. The optimisation problem in (5.34) can be written as

$$\rho^* = \inf_{\rho \in (0,1)} \rho \text{ subject to } \mathbb{P}(\zeta_\rho \geq u) \geq \alpha, \quad (5.35)$$

with the random variable  $\zeta_\rho$  given by

$$\zeta_\rho = \inf_{\mathbf{x} \in \text{cl}(T_\rho)} Y(\mathbf{x}). \quad (5.36)$$

We mention that the optimisation problem in (5.35) can be solved by using methods from reliability-based design optimisation; see, for instance, Valdebenito and Schuëller [2010], Dubourg et al. [2011], and Moustapha et al. [2016]. Please note that, although all three problems (5.23), (5.30), and (5.34) are equivalent, we will focus (mostly) on the quantile estimation problem in (5.30) to compute confidence sets in a parametric family of nested candidate sets in a computationally efficient way.

## 5.6 Spatial discretisation

To be able to compute confidence sets in practice, a discretisation is required. In this section, we describe a discretisation of the spatial dimension and discuss its impact on the stochastic dimension. Specifically, we describe a spatial discretisation that relies on partitioning the spatial domain into subsets and testing the exceedance constraints in representative points in these subsets. The discrete closed sets thus obtained are random closed sets that the theory of random sets [Molchanov, 2017] refers to as simple random closed sets by the virtue of them taking only a finite number of values. Please note that alternative spatial discretisations could also be considered, such as spatial discretisations based on computational geometry or computational shape optimisation, but we do not consider such alternative spatial discretisations here. We will continue to focus the discussion (mostly) on the positive excursion set and related confidence

sets, but please note that the extensions to other confidence sets for negative excursion and contour sets can be obtained analogously.

Let  $D^h = \{D_i^h\}_{1 \leq i \leq N_h}$  be a partition of  $D$  into  $N_h$  pairwise disjoint nonempty closed subsets of  $D$ , with  $h$  a positive number that describes the characteristic size of the subsets. If the random field is a solution quantity of a stochastic computational model that is discretised in space by means of a finite-difference scheme, this partition may be taken as a tessellation based on the grid points; if the stochastic computational model is discretised in space by means of a finite-element scheme, this partition may be taken as the mesh.

Let each subset  $D_i^h$  be associated with a representative point  $\mathbf{x}_i^h$  in  $D_i^h$  where we test the exceedance constraint and evaluate the membership function. If the random field is a solution quantity of a stochastic computational model that is discretised in space by means of a finite-difference scheme, these representative points may be taken as the grid points; if the stochastic computational model is discretised in space by means of a finite-element scheme, these representative points may be taken as characteristic points of the elements of the mesh, for instance, the centroids of the elements.

With reference to the partitioning, we approximate  $\mathcal{E}_u^+$  with  $\mathcal{E}_u^{+h}$  (see Figure 5.5 for an illustration) described by the binary random vector  $\mathbf{E}^h = (E_1^h, \dots, E_{N_h}^h)$  with values in  $\{0, 1\}^{N_h}$  such that

$$\mathcal{E}_u^{+h} = \bigcup_{E_i^h=1} D_i^h = \bigcup_{i \in \mathcal{I}_u^{+h}} D_i^h, \quad (5.37)$$

where  $\mathcal{I}_u^{+h} = \{i : E_i^h = 1\}$  is the random active index set, with

$$E_i^h = \mathbf{1}(Y(\mathbf{x}_i^h) \geq u), \quad i = 1, \dots, N_h; \quad (5.38)$$

here,  $\mathbf{1}(Y(\mathbf{x}_i^h) \geq u)$  is equal to 1 if  $Y(\mathbf{x}_i^h) \geq u$  and 0 otherwise.

With reference to the partitioning, we seek inner confidence sets of the form of sets described by a binary vector  $\mathbf{c}^h = (c_1^h, \dots, c_{N_h}^h)$  in  $\{0, 1\}^{N_h}$  such that

$$C_{u^+, \alpha}^{\text{in}, h} = \text{int} \left( \bigcup_{c_i^h=1} D_i^h \right) = \text{int} \left( \bigcup_{i \in I_{u^+, \alpha}^{\text{in}, h}} D_i^h \right), \quad (5.39)$$

where  $I_{u^+, \alpha}^{\text{in}, h} = \{i : c_i^h = 1\}$  is the active index set. As in the continuous case, we seek such an inner confidence set in a parametric family described by a binary vector  $\mathbf{T}_\rho^h = (T_{\rho, 1}^h, \dots, T_{\rho, N_h}^h) = (\mathbf{1}(T_1^h > \rho), \dots, \mathbf{1}(T_{N_h}^h > \rho))$  in  $\{0, 1\}^{N_h}$  such that

$$T_\rho^h = \text{int} \left( \bigcup_{T_{\rho, i}^h=1} D_i^h \right) = \text{int} \left( \bigcup_{i \in I_\rho^h} D_i^h \right), \quad (5.40)$$

where  $I_\rho^h = \{i : T_i^h > \rho\}$  is the parametric index set and  $\mathbf{T}^h = (T_1^h, \dots, T_{N_h}^h)$  is the membership vector, with  $T_i^h = T(\mathbf{x}_i^h)$ ,  $i = 1, \dots, N_h$ .

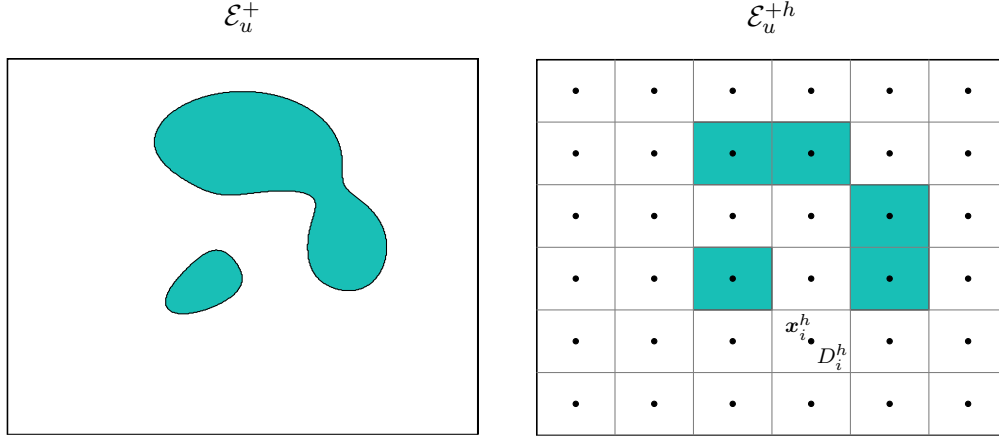


Figure 5.5: Approximation of the random set  $\mathcal{E}_u^+$  as a simple random set  $\mathcal{E}_u^{+h}$  based on a structured partitioning of  $D$ . The representative points are chosen as the centroids of the elements.

Seeking the largest set in this parametric family satisfying the joint probability of exceedance constraint associated with the representative points leads to

$$\rho^{*h} = \inf_{\rho \in (0,1)} \rho \text{ subject to } \mathbb{P}\left(\max_{i \in (\mathcal{I}_u^{+h})^c} T_i^h \leq \rho\right) \geq \alpha, \quad (5.41)$$

thus leading to the equivalent problem of quantile estimation

$$\rho^{*h} = \inf \left\{ \rho \in (0, 1) : F_{\chi^h}(\rho) \geq \alpha \right\} \equiv q_{\chi^h}(\alpha), \quad (5.42)$$

where  $F_{\chi^h}$  and  $q_{\chi^h}$  are respectively the distribution function and the generalised quantile function of the random variable

$$\chi^h = \max_{i \in (\mathcal{I}_u^{+h})^c} T_i^h. \quad (5.43)$$

Due to the approximation of the random closed set as a simple random set,  $\chi^h$  is a discrete random variable with distinct discrete values  $\chi_1^h < \chi_2^h < \dots < \chi_{L_h}^h$  ( $L_h \leq N_h$ ). In general,  $L_h$  is smaller than  $N_h$  because there may be locations  $x_i^h$  in  $D$  where  $T$  does not attain its maximum for any realisation of  $(\mathcal{E}_u^{+h})^c$ .

The distribution function  $F_{\chi^h}$  may be written in terms of the probability masses  $p_l = \mathbb{P}(\chi^h = \chi_l^h)$ ,  $1 \leq l \leq L_h$ , as

$$F_{\chi^h}(\rho) = \mathbb{P}(\chi^h \leq \rho) = \sum_{\chi_l^h \leq \rho} \mathbb{P}(\chi^h = \chi_l^h) = \sum_{\chi_l^h \leq \rho} p_l. \quad (5.44)$$

Then, the problem of quantile estimation reads as

$$\rho^{*h} = \min \chi_l^h \text{ subject to } \sum_{k=1, \dots, l} p_k \geq \alpha. \quad (5.45)$$

Thus, the impact of the discretisation of the spatial dimension on the stochastic dimension is that both  $F_{\chi^h}$  and  $q_{\chi^h}$  are piecewise-constant functions with discontinuities whose number

and magnitude depend on the spatial resolution of the computational model. Consequently, the accuracy one may achieve in estimating confidence sets for a spatial discretisation of the domain is influenced by the spatial resolution of the computational model. Specifically, the solution  $\rho^*$  of Equation (5.31) is always larger than or equal to the solution  $\rho^{*h}$  of Equation (5.42), with the difference between both solutions depending on the magnitude of the discontinuities around  $\rho^*$ .

*Proof.* We consider the following implications:

$$\max_{i \in (\mathcal{T}_u^{+h})^c} T_i^h \leq \sup_{\mathbf{x} \in (\mathcal{E}_u^+)^c} T(\mathbf{x}) \implies \chi^h \leq \chi \implies F_{\chi^h}(\rho) \geq F_\chi(\rho), \quad \forall \rho \in (0, 1). \quad (5.46)$$

Hence,

$$\inf \{ \rho \in (0, 1) : F_{\chi^h}(\rho) \geq \alpha \} \leq \inf \{ \rho \in (0, 1) : F_\chi(\rho) \geq \alpha \}, \quad (5.47)$$

that is,  $\rho^{*h} \leq \rho^*$ .  $\square$

Please note that a similar spatial discretisation had already been used in reference [French and Hoeting, 2015], which provided a consistency result:

**Proposition 5.2.** *Suppose that*

(a)  $\exists \epsilon > 0$  such that

$$\mathbb{P} \left[ \inf \{ \|\mathbf{x} - \mathbf{x}'\| : \mathbf{x} \in \partial T_{\rho^*}, \mathbf{x}' \in \partial \mathcal{E}_u^+ \} \geq \epsilon \mid \text{cl}(T_{\rho^*}) \subset \mathcal{E}_u^+ \right] = 1, \quad (5.48)$$

where  $\|\cdot\|$  is the Euclidean norm and  $\partial$  the boundary of the set;

(b) the partitions satisfy the following conditions:

- 1)  $\forall N_h, N_{h'} \in \mathbb{N}_0$  with  $N_{h'} > N_h$ ,  $D^{h'}$  is a refinement of  $D^h$  in the particular sense that each subset of  $D^{h'}$  is a subset of some subset of  $D^h$ ;
- 2)  $\forall \eta > 0, \exists M_\eta \in \mathbb{N}_0 : D_i^h \subset B_\eta(\mathbf{x}_i^h)$  for  $i = 1, \dots, M_\eta$ , where  $B_\eta(\mathbf{x})$  is a ball of radius  $\eta$  centered at  $\mathbf{x}$ .

Then,  $\forall N_h \geq M_{\epsilon/2}, I_{\mathcal{E}_u^+}(\text{cl}(T_{\rho^{*h}}^h)) \geq \alpha$ .

Condition (a) states that there is at least a small "buffer" between the boundary of  $\mathcal{E}_u^+$  and  $T_{\rho^*}$ . Condition (b.1) means that finer partitions are built by dividing the subsets of the coarser partitions. Condition (b.2) means that all subsets in the partition become arbitrarily small for large enough  $N_h$ . Proposition 5.2 ensures that for  $N_h$  sufficiently large, an inner confidence set  $T_{\rho^{*h}}^h$  for the simple random set  $\mathcal{E}_u^{+h}$  in Equation (5.37) for a confidence level  $\alpha$  is an inner confidence set for the random closed set  $\mathcal{E}_u^+$  for the same confidence level.

*Proof.* We note that for all  $N_h \in \mathbb{N}_0$ , we have  $T_{\rho^{*h}}^h = T_{\rho^*}^h$ . We will show that  $\exists M \in \mathbb{N}_0$  such that for all  $N_h \leq M$  the inclusion relation  $\text{cl}(T_{\rho^*}) \subset \mathcal{E}_u^+$  implies  $\text{cl}(T_{\rho^{*h}}^h) \subset \mathcal{E}_u^+$ . Hence, for all  $N_h \geq M, I_{\mathcal{E}_u^+}(\text{cl}(T_{\rho^*})) \geq \alpha$  implies  $I_{\mathcal{E}_u^+}(\text{cl}(T_{\rho^{*h}}^h)) \geq \alpha$ .

We assume that  $\text{cl}(T_{\rho^*}) \subset \mathcal{E}_u^+$  for a give  $\theta \in \Theta$ . By condition (b.2), there exists  $M_{\epsilon/2} \in \mathbb{N}_0$  such that,  $D_i^h \subset B_{\epsilon/2}(\mathbf{x}_i^h)$  for  $i = 1, \dots, M_{\epsilon/2}$  and  $\epsilon$  given by condition (a).

We have  $\mathbf{x}_i^h$  in  $T_{\rho^*}$  for all  $i$  in  $I_{\rho}^h$ . By condition (a), the distance between  $\mathbf{x}$  on  $\partial\mathcal{E}_u^+$  and  $\mathbf{x}_k$  must be more than  $\epsilon$  for all  $i$  in  $I_{\rho}^h$ . Since  $D_i^h \subseteq B_{\epsilon/2}(\mathbf{x}_i^h)$  for  $i = 1, \dots, M_{\epsilon/2}$ , the distance between  $\mathbf{x}$  on  $\partial T_{\rho^*}^h$  and  $\mathbf{x}$  on  $\partial\mathcal{E}_u^+$  must be more than  $\epsilon/2$ . Therefore,  $\text{cl}(T_{\rho^*}^h) \subset \mathcal{E}_u^+$ . By the condition (b.1), it is also true for all  $N_h \geq M_{\epsilon/2}$ .  $\square$

## 5.7 Discretisation of the stochastic dimension

The identification of a confidence set in a parametric family of candidate sets leads to a two-step problem. The first step involves the determination of the membership function, and the second step involves the determination of the appropriate threshold by solving an optimisation problem that may be recast equivalently as a quantile estimation problem. The first step requires the approximation of pointwise (marginal) statistical descriptors of the random field, and the second step requires the approximation of joint probabilities of exceedance at all considered locations simultaneously. Because the second step requires the approximation of joint probabilities, it can be expected to be more computationally challenging, and especially so when evaluating whether inclusion relationships hold with high probability levels, which raises the issue of rare events. Hence, while we will provide some details regarding the estimation of pointwise statistical descriptors, we will focus (most of) the discussion to follow on the quantile estimation problem.

By writing the distribution function  $F_{\chi}$  (Equation (5.31)) of the random variable  $\chi$  (Equation (5.32)) as

$$F_{\chi}(\rho) = \mathbb{P}(\chi \leq \rho) = \int_{\Theta_{\rho}} d\mathbb{P}(\theta) = \int_{\Theta} \mathbf{1}_{\Theta_{\rho}}(\theta) d\mathbb{P}(\theta), \quad (5.49)$$

it can be seen that the solution of the quantile estimation problem is related to the fundamental problem of reliability engineering of evaluating the probability of an event  $\Theta_{\rho} = \{\theta \in \Theta : \chi(\theta) - \rho \leq 0\}$  defined by a limit state function, also called performance function, here,  $\chi - \rho$ . In reliability engineering, methods have been developed for the efficient approximation of such probabilities, such as methods using surrogate models, subset simulation, and other methods. Hence, we will draw from reliability engineering methods that can reduce the number of samples of the stochastic computational model that must be solved.

In the following, we assume  $\{Y(\mathbf{x}), \mathbf{x} \in D\}$  to be a solution quantity of a stochastic computational model that depends on a finite number of uncertain input parameters  $\xi_1, \dots, \xi_n$ , modelled as an  $\mathbb{R}^n$ -valued random vector  $\boldsymbol{\xi} = (\xi_1, \dots, \xi_n)$  defined on  $(\Theta, \mathfrak{B}, \mathbb{P})$ . We use the symbol  $\chi$  as a generic notation for both the continuous random variable  $\chi$  and its stochastic discretisation  $\chi^h$  following Section 5.6, and we discuss the impact of the spatial discretisation when appropriate.

### 5.7.1 Membership function

The membership functions defined in Equations (5.24)–(5.26) involve pointwise (marginal) statistical descriptors of  $\{Y(\mathbf{x}), \mathbf{x} \in D\}$ . For each  $\mathbf{x}$  in  $D$ , an approximation of  $T(\mathbf{x})$  may be obtained by using standard nonintrusive methods for uncertainty quantification. In Section 7.2.3,

we compute the required approximations to the pointwise (marginal) statistical descriptors of the random field by applying a kernel density estimation method to an ensemble of independent and identically distributed (i.i.d.) samples of the random field, from which we deduce a Monte Carlo approximation of  $T$  by using a Monte Carlo sampling of the kernel density estimates. Please note that although the choice of a different membership function or errors entailed by its numerical approximation may change the parametric family of candidate sets, a set satisfying the joint probability of exceedance constraint may still be sought within this parametric family.

## 5.7.2 Quantile estimation: Monte Carlo method

### 5.7.2.1 Use of distribution function

An implementation of the Monte Carlo method begins by generating an ensemble of i.i.d. samples  $\{\xi(\theta^{(k)}), 1 \leq k \leq \nu\}$  of the uncertain input parameters. Then, an ensemble of solutions to the computational model is generated in the form of the ensemble of the corresponding i.i.d. samples of the random field, from which is deduced the ensemble of the corresponding i.i.d. samples  $\{\mathcal{E}_u^+(\theta^{(k)}), 1 \leq k \leq \nu\}$  of the excursion set and the ensemble of the corresponding i.i.d. samples  $\{\chi(\theta^{(k)}), 1 \leq k \leq \nu\}$  of  $\chi$ . Then, the sample (empirical) distribution function evaluated at  $\rho$  in  $(0, 1)$  writes as

$$F_\chi^\nu(\rho) = \frac{1}{\nu} \sum_{k=1}^{\nu} \mathbf{1}(\chi(\theta^{(k)}) \leq \rho), \quad (5.50)$$

where the superscript  $\nu$  is used to indicate that the quantity is estimated from a finite number of samples. The corresponding sample quantile  $q_\chi^\nu(\alpha)$  is then given by

$$q_\chi^\nu(\alpha) = \inf \left\{ \rho \in (0, 1) : F_\chi^\nu(\rho) \geq \alpha \right\}. \quad (5.51)$$

Equivalently, this Monte Carlo estimate may be obtained by ordering the i.i.d. samples as  $\chi_{1:\nu} \leq \chi_{2:\nu} \leq \dots \leq \chi_{\nu:\nu}$ , where  $\chi_{k:\nu}$  denotes the  $k$ -th order statistic of the samples [Arnold et al., 1992], that is,  $\chi_{1:\nu}$  denotes the smallest sample,  $\chi_{2:\nu}$  the second smallest sample,  $\dots$ , and  $\chi_{\nu:\nu}$  the largest sample. Then  $q_\chi^\nu(\alpha)$  is given by  $\chi_{k:\nu}$ , where  $(k-1)/\nu < \alpha \leq k/\nu$ .

If  $\chi$  is a continuous random variable with a probability density function,  $q_\chi^\nu(\alpha)$  is associated with a consistent estimator of  $q_\chi(\alpha)$  that satisfies a central limit theorem [Arnold et al., 1992] (see Section 5.A.1). However, if  $\chi$  is a discrete random variable, then the Monte Carlo estimator is not guaranteed to satisfy a central limit theorem or to be a consistent estimator. The lack of consistency mainly results from the discontinuities of the distribution function, if any, which may cause the problem of quantile estimation to be ill-conditioned because small perturbations in  $\alpha$  or  $F_\chi^\nu$  may cause large perturbations in  $q_\chi^\nu(\alpha)$ . Feldman and Tucker [1966] showed that, for an arbitrary distribution function, a sequence of Monte Carlo estimates  $\{q_\chi^\nu(\alpha)\}$  may oscillate between  $\inf \{\rho \in (0, 1) : F_\chi(\rho) \geq \alpha\}$  and  $\sup \{\rho \in (0, 1) : F_\chi(\rho) \leq \alpha\}$ . We refer the interested reader to Section 5.A.1 for complementary information regarding Monte Carlo estimation based on the distribution function.

### 5.7.2.2 Use of mid-distribution function

If  $\chi$  is a discrete random variable, an alternative method is to rely on a regularisation of the problem of quantile estimation based on the mid-distribution function [Parzen, 2004; Ma et al., 2011]. Let  $\chi_1 < \dots < \chi_L$  denote the discrete values that  $\chi$  may take; then the mid-distribution function  $F_\chi^{\text{mid}}$  is the following continuous, piecewise linear modification of the distribution function

$$F_\chi^{\text{mid}}(\rho) = \begin{cases} 0 & \text{if } \rho < \chi_1 \\ \frac{F_\chi^{\text{mid}}(\chi_{l+1}) - F_\chi^{\text{mid}}(\chi_l)}{\chi_{l+1} - \chi_l}(\rho - \chi_l) + F_\chi^{\text{mid}}(\chi_l) & \text{if } \chi_l \leq \rho \leq \chi_{l+1}, \\ 1 & \text{if } \rho > \chi_L \end{cases} \quad (5.52)$$

where  $F_\chi^{\text{mid}}(\chi_l) = F_\chi(\chi_l) - \frac{1}{2}p_\chi(\chi_l)$  for  $1 \leq l \leq L$ , with  $p_\chi(\rho) = \mathbb{P}(\chi = \rho)$  the probability mass function; see Figure 5.6(a) for an illustration. The corresponding mid-quantile function is then a continuous, piecewise linear modification of the quantile function given by

$$q_\chi^{\text{mid}}(\alpha) = \inf \left\{ \rho \in (0, 1) : F_\chi^{\text{mid}}(\rho) \geq \alpha \right\}; \quad (5.53)$$

see Figure 5.6(b) for an illustration.

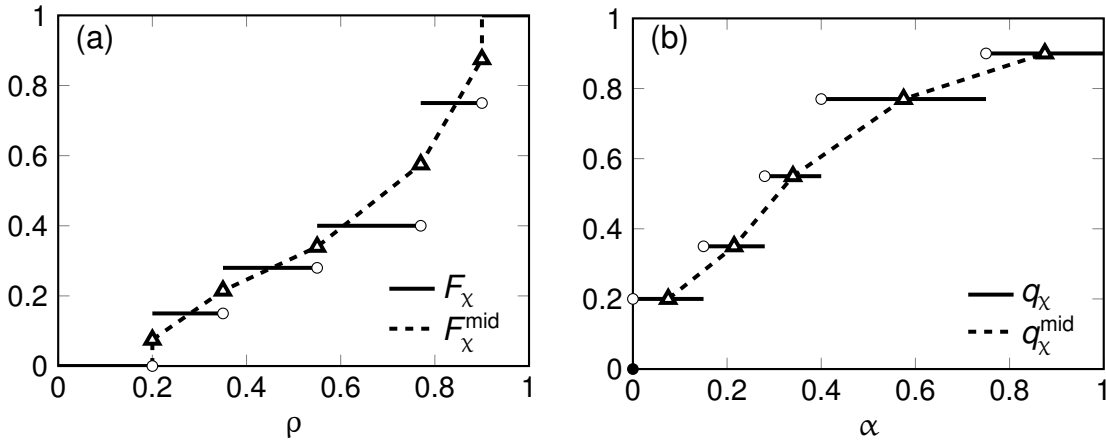


Figure 5.6: (a) An illustration of the distribution function (solid horizontal lines) and mid-distribution function (dashed line). The circles are the jumps in the distribution function and the triangles are the values of the mid-distribution function at the supporting points. (b) An illustration of the corresponding quantile function (solid horizontal lines) and mid-quantile function (dashed line). The circles are the jumps in the quantile function and the triangles are the values of the mid-quantiles.

The Monte Carlo estimate  $q_\chi^{\text{mid},\nu}(\alpha)$  of  $q_\chi^{\text{mid}}(\alpha)$  is given by

$$q_\chi^{\text{mid},\nu}(\alpha) = \inf \left\{ \rho \in (0, 1) : F_\chi^{\text{mid},\nu}(\rho) \geq \alpha \right\}, \quad (5.54)$$

where the sample mid-distribution function is given by

$$F_{\chi}^{\text{mid},\nu}(\rho) = \begin{cases} 0 & \text{if } \rho < \chi_1 \\ \frac{F_{\chi}^{\text{mid},\nu}(\chi_{l+1}) - F_{\chi}^{\text{mid},\nu}(\chi_l)}{\chi_{l+1} - \chi_l}(\rho - \chi_l) + F_{\chi}^{\text{mid},\nu}(\chi_l) & \text{if } \chi_l \leq \rho \leq \chi_{l+1}, \\ 1 & \text{if } \rho > \chi_L \end{cases} \quad (5.55)$$

with

$$F_{\chi}^{\text{mid},\nu}(\chi_l) = \frac{1}{\nu} \sum_{k=1}^{\nu} \mathbf{1}(\chi(\theta^{(k)}) \leq \chi_l) - \frac{1}{2\nu} \sum_{k=1}^{\nu} \mathbf{1}(\chi(\theta^{(k)}) = \chi_l), \quad 1 \leq l \leq L. \quad (5.56)$$

[Ma et al. \[2011\]](#) have shown that  $q_{\chi}^{\text{mid},\nu}(\alpha)$  is associated with a consistent estimator of  $q_{\chi}^{\text{mid}}(\alpha)$  that satisfies a generalised central limit theorem. However,  $q_{\chi}^{\text{mid},\nu}(\alpha)$  is not guaranteed to be associated with a consistent estimator of  $q_{\chi}(\alpha)$  because  $q_{\chi}^{\text{mid}}(\alpha)$  may be different from  $q_{\chi}(\alpha)$ . Yet, the difference between  $q_{\chi}(\alpha)$  and  $q_{\chi}^{\text{mid}}(\alpha)$  may be expected to tend to zero as the set of discrete values taken by  $\chi$  becomes denser and denser as  $L$  tends to infinity. We refer the interested reader to [Section 5.A.1](#) for complementary information regarding Monte Carlo estimation based on the distribution function.

### 5.7.2.3 Computational cost

The Monte Carlo estimator based on the distribution function for continuous  $\chi$  entails an approximation error that decreases with the square root of the number of samples  $\nu$  and increases with the ratio of the square root of  $\alpha(1 - \alpha)$  and the value taken by the probability density function of  $\chi$  at the quantile to be estimated [[Arnold et al., 1992](#); [Ma et al., 2011](#)]; for the Monte Carlo estimator based on the mid-distribution function for discrete  $\chi$ , there exists an analogous result that involves a generalised notion of probability density function [[Ma et al., 2011](#)]. Thus, attaining sufficient accuracy may become intractable for computational models with a high computational cost and for quantiles associated with low and high levels of probability (rare events).

## 5.7.3 Quantile estimation: spectral method

We propose two methods that seek to alleviate the computational cost via the construction of a surrogate model.

### 5.7.3.1 Spectral representation of the random field

The first method involves building a polynomial chaos expansion of  $\{Y(\mathbf{x}), \mathbf{x} \in D\}$  and then using this polynomial chaos expansion as a substitute for evaluations of the computational model when solving the quantile estimation problem. A truncated polynomial chaos expansion of order  $p$  of the random field, assumed to be of the second order, writes as

$$Y^p(\mathbf{x}) = \sum_{|\alpha|=0}^p y_{\alpha}^p(\mathbf{x}) \psi_{\alpha}(\boldsymbol{\xi}). \quad (5.57)$$

Here,  $\boldsymbol{\alpha} = (\alpha_1, \dots, \alpha_n)$  is a multi-index with  $|\boldsymbol{\alpha}| = \alpha_1 + \dots + \alpha_n$  and  $\{\psi_{\alpha}, \boldsymbol{\alpha} \in \mathbb{N}^n\}$  is a suitable basis of orthogonal polynomials from  $\mathbb{R}^n$  into  $\mathbb{R}$ . The functions  $y_{\alpha}^p$  from  $D$  into  $\mathbb{R}$

are the polynomial chaos coordinates. In practice, these polynomial chaos coordinates may be determined by using nonintrusive methods from solutions of the computational model for an experimental design of the uncertain input parameters denoted by  $\{\boldsymbol{\xi}(\theta_\lambda^{(k)}), 1 \leq k \leq \lambda\}$ .

The random set  $\mathcal{E}_u^+$  is then approximated with the corresponding excursion set determined with the polynomial chaos expansion, that is,

$$\mathcal{E}_u^{+,p} = \{\mathbf{x} \in D : Y^p(\mathbf{x}) \geq 0\}, \quad (5.58)$$

and  $\chi$  is approximated with

$$\sup_{\mathbf{x} \in (\mathcal{E}_u^{+,p})^c} T(\mathbf{x}). \quad (5.59)$$

This first method amounts to approximating a confidence set for the excursion set of the random field  $\{Y(\mathbf{x}), \mathbf{x} \in D\}$  with the corresponding confidence set for the excursion set of  $\{Y^p(\mathbf{x}), \mathbf{x} \in D\}$ . The confidence set can then be evaluated by using either formalism (5.23), with  $\mathcal{E}_u^+$  approximated with  $\mathcal{E}_u^{+,p}$ , or formalism (5.31), with  $F_\chi$  approximated with a Monte Carlo estimate as

$$\frac{1}{\nu} \sum_{k=1}^{\nu} \mathbf{1} \left( \sup_{\mathbf{x} \in (\mathcal{E}_u^{+,p}(\theta^{(k)}))^c} T(\mathbf{x}) \leq \rho \right). \quad (5.60)$$

### 5.7.3.2 Spectral representation of the random variable $\chi$

The second method, enabled by the reformulation of the optimisation problem in Equation (5.23) as the quantile estimation problem in Equation (5.31), involves building a polynomial chaos expansion directly of  $\chi$ . A truncated polynomial chaos expansion of order  $p$  of  $\chi$ , assumed to be of the second order, writes as

$$\chi^p = \sum_{|\alpha|=0}^p \chi_\alpha^p \psi_\alpha(\boldsymbol{\xi}), \quad (5.61)$$

where the scalars  $\chi_\alpha^p$  are the polynomial chaos coordinates. In practice, these polynomial chaos coordinates may be determined by using nonintrusive methods from solutions of the computational model for an experimental design of the uncertain input parameters denoted by  $\{\boldsymbol{\xi}(\theta_\lambda^{(k)}), 1 \leq k \leq \lambda\}$ . The confidence set can then be evaluated using formalism (5.31), with  $F_\chi$  approximated with a Monte Carlo estimate as

$$\frac{1}{\nu} \sum_{k=1}^{\nu} \mathbf{1}(\chi^p(\theta^{(k)}) \leq \rho). \quad (5.62)$$

Whereas the accuracy of the spectral representation depended in the previous section on how well  $\{Y(\mathbf{x}), \mathbf{x} \in D\}$  lends itself to being approximated with a truncated polynomial chaos expansion, the accuracy of the spectral representation depends here on how well  $\chi$  lends itself to being approximated with a truncated polynomial chaos expansion. The choice of the membership function plays a role in this issue, which we will study numerically later in the illustrations in Sections 5.8 and 7.2.

### 5.7.3.3 Surrogate-based quantile estimation

The use of a truncated polynomial chaos expansion as in Equation (5.57) or in Equation (5.61) as an approximation to  $\{Y(\boldsymbol{x}), \boldsymbol{x} \in D\}$  or  $\chi$  in the quantile estimation may lead to an approximation error, which obeys the following result in Enss et al. [2016] and Krzyżak [2016]:

**Theorem 5.1.** Let  $\chi$  and  $\tilde{\chi}$  be random variables with values in  $\mathbb{R}$  and  $\alpha$  a scalar in  $(0, 1)$ . Let  $\delta > 0$  be such that

$$|\tilde{\chi} - \chi| \leq \frac{\delta}{2} + \frac{1}{2}|q_\chi(\alpha) - \chi|, \quad (5.63)$$

almost surely. Then, the error in approximating  $q_\chi(\alpha)$  with  $q_{\tilde{\chi}}(\alpha)$  satisfies

$$|q_{\tilde{\chi}}(\alpha) - q_\chi(\alpha)| \leq \delta. \quad (5.64)$$

Here, we use the notation  $\tilde{\chi}$  to denote a generic surrogate model that could be obtained based on Equation (5.57) or Equation (5.61), and we will continue to use this notation throughout the remainder of this section. Please note that a similar result may be obtained for quantile estimation using the mid-distribution function. Theorem 5.1 provides for the error between  $q_{\tilde{\chi}}(\alpha)$  and  $q_\chi(\alpha)$  an error bound  $\delta$  that depends on the local approximation error  $|\tilde{\chi} - \chi|$  between  $\chi$  and its surrogate model and on the distance  $|q_\chi(\alpha) - \chi|$  between the quantile to be estimated and  $\chi$ . Hence, one may seek to reduce the value of  $\delta$  by lowering the local approximation error where  $\chi$  is close to  $q_\chi(\alpha)$ , while the surrogate model does not need to be a good approximation to  $\chi$  further away from the quantile to be estimated.

*Proof.* The proof, which is given in Section 5.B, follows the proof of Lemma 1 in Enss et al. [2016].  $\square$

### 5.7.3.4 Computational cost

The computational cost of constructing a truncated polynomial chaos expansion as in Equation (5.57) or Equation (5.61) depends on the order  $p$ ; the higher the order  $p$  must be to attain sufficient accuracy, the higher the number of training points must be in the experimental design. This computational cost also scales with the number of uncertain input parameters (the stochastic dimension  $n$ ); the higher the stochastic dimension  $n$ , the higher the number of required training points may be expected to be in the experimental design.

## 5.7.4 Quantile estimation: bifidelity method

Based on the relationship in Equation (5.49) between the fundamental problem of reliability engineering and the quantile estimation problem, we will build on a hybrid method introduced in Li and Xiu [2010] in reliability engineering to develop a new bifidelity method for the efficient solution of the quantile estimation problem.

### 5.7.4.1 Method

Conceptually, this method relies on a bifidelity model that combines a surrogate model, such as one of those discussed in Section 5.7.3, with the computational model. The surrogate model is

used further away from the quantile to be estimated, and the computational model is used closer to the quantile to be estimated:

$$\tilde{\chi}^\gamma = \tilde{\chi} \mathbf{1}(|\tilde{\chi} - q_\chi(\alpha)| > \gamma) + \chi \mathbf{1}(|\tilde{\chi} - q_\chi(\alpha)| \leq \gamma), \quad (5.65)$$

where  $\tilde{\chi}$  is the surrogate model of  $\chi$  and  $\gamma > 0$  is a threshold parameter that controls the size of the region in the parameter space where  $\chi$  is used. From Equation (5.65), we see that the local approximation error  $|\tilde{\chi}^\gamma - \chi|$  vanishes where  $|\tilde{\chi} - q_\chi(\alpha)| \leq \gamma$ . Therefore, the error bound  $\delta$  in the inequality (5.63) may be expected to decrease with an increase in  $\gamma$ .

By adapting Theorem 4.1 stated in Li and Xiu [2010] for the computation of failure probabilities, the following result is obtained as an error estimate for the quantile estimation problem:

**Theorem 5.2.** Let  $\chi$  and  $\tilde{\chi}$  be random variables with values in  $\mathbb{R}$ , and let  $\tilde{\chi}^\gamma$  be defined as in Equation (5.65) with  $\gamma$  that satisfies

$$\mathbb{P}(|\tilde{\chi} - \chi| > \gamma) \leq \epsilon \quad (5.66)$$

for some  $\epsilon \geq 0$ . Then, the quantile function  $q_{\tilde{\chi}^\gamma}$  satisfies

$$q_{\tilde{\chi}^\gamma}(\alpha - \epsilon) \leq q_\chi(\alpha) \leq q_{\tilde{\chi}^\gamma}(\alpha + \epsilon). \quad (5.67)$$

*Proof.* We consider the following inequality

$$\mathbb{P}(\tilde{\chi}^\gamma \leq q_\chi(\alpha)) \geq \mathbb{P}(\chi \leq q_\chi(\alpha)) - \mathbb{P}(\tilde{\chi}^\gamma > q_\chi(\alpha), \chi \leq q_\chi(\alpha)). \quad (5.68)$$

The last event is possible only if  $|\tilde{\chi}^\gamma - q_\chi(\alpha)| > \gamma$ . Then, we have

$$\begin{aligned} \mathbb{P}(\tilde{\chi}^\gamma > q_\chi(\alpha), \chi \leq q_\chi(\alpha)) &= \mathbb{P}(\tilde{\chi} - q_\chi(\alpha) > \gamma, \chi \leq q_\chi(\alpha)) \\ &\leq \mathbb{P}(\tilde{\chi} - \chi > \gamma) \\ &\leq \epsilon. \end{aligned} \quad (5.69)$$

Therefore, inequality (5.68) becomes

$$F_{\tilde{\chi}^\gamma}(q_\chi(\alpha)) \geq F_\chi(q_\chi(\alpha)) - \epsilon = \alpha - \epsilon, \quad (5.70)$$

that is, the infimum of  $\tilde{\chi}^\gamma$  for which  $F_{\tilde{\chi}^\gamma}$  is equal to or exceeds  $\alpha - \epsilon$  is at most  $q_\chi(\alpha)$ . Hence,

$$q_{\tilde{\chi}^\gamma}(\alpha - \epsilon) = \inf \left\{ \rho \in (0, 1) : F_{\tilde{\chi}^\gamma}(\rho) \geq \alpha - \epsilon \right\} \leq q_\chi(\alpha). \quad (5.71)$$

Similarly, we can show that

$$F_{\tilde{\chi}^\gamma}(q_\chi(\alpha)) \leq F_\chi(q_\chi(\alpha)) + \epsilon = \alpha + \epsilon, \quad (5.72)$$

that is, the infimum of  $\tilde{\chi}^\gamma$  for which  $F_{\tilde{\chi}^\gamma}$  is equal to or exceeds  $\alpha + \epsilon$  is at least  $q_\chi(\alpha)$ . Hence,

$$q_{\tilde{\chi}^\gamma}(\alpha + \epsilon) = \inf \left\{ \rho \in (0, 1) : F_{\tilde{\chi}^\gamma}(\rho) \geq \alpha + \epsilon \right\} \geq q_\chi(\alpha). \quad (5.73)$$

□

The value of the threshold  $\gamma$  required to achieve a level of accuracy  $\epsilon$  depends on the approximation error between  $\chi$  and its surrogate model  $\tilde{\chi}$ . Proposition 5.3 by Li and Xiu [2010] gives a lower bound on the threshold parameter  $\gamma$  when the  $\mathbb{L}^q$ -error between  $\chi$  and  $\tilde{\chi}$  is bounded:

**Proposition 5.3.** *Let  $\chi$  and  $\tilde{\chi}$  be random variables with values in  $\mathbb{R}$  and  $q$  a scalar with  $q \geq 1$  such that*

$$\|\chi - \tilde{\chi}\|_{\mathbb{L}^q} = (\mathbb{E}(|\chi - \tilde{\chi}|^q))^{1/q} < \infty. \quad (5.74)$$

*Then for all  $\epsilon > 0$ , there exists  $\gamma^* > 0$  such that for all  $\gamma \geq \gamma^*$ :*

$$\mathbb{P}(|\tilde{\chi} - \chi| > \gamma) \leq \epsilon; \quad (5.75)$$

*more precisely,*

$$\gamma^* = \frac{1}{\epsilon^{1/q}} \|\chi - \tilde{\chi}\|_{\mathbb{L}^q}. \quad (5.76)$$

*Proof.* The proof follows the proof of Theorem 4.1 in Li and Xiu [2010]. We have

$$\begin{aligned} \|\chi - \tilde{\chi}\|_{\mathbb{L}^q}^q &= \int_{\Theta} |\chi(\theta) - \tilde{\chi}(\theta)|^q d\mathbb{P}(\theta) \\ &= \int_{\Theta} \mathbf{1}(|\chi(\theta) - \tilde{\chi}(\theta)| > \gamma) |\chi(\theta) - \tilde{\chi}(\theta)|^q d\mathbb{P}(\theta) \\ &\quad + \int_{\Theta} \mathbf{1}(|\chi(\theta) - \tilde{\chi}(\theta)| \leq \gamma) |\chi(\theta) - \tilde{\chi}(\theta)|^q d\mathbb{P}(\theta) \\ &\geq \gamma^q \int_{\Theta} \mathbf{1}(|\chi(\theta) - \tilde{\chi}(\theta)| > \gamma) d\mathbb{P}(\theta) \\ &= \gamma^q \mathbb{P}(|\tilde{\chi} - \chi| > \gamma). \end{aligned} \quad (5.77)$$

Thus, we have

$$\mathbb{P}(|\tilde{\chi} - \chi| > \gamma) \leq \frac{1}{\gamma^q} \|\chi - \tilde{\chi}\|_{\mathbb{L}^q}^q. \quad (5.78)$$

Thus, for any given  $\epsilon > 0$  and  $\gamma > \gamma^*$ , with  $\gamma^*$  defined in Equation (5.76), we have

$$\mathbb{P}(|\tilde{\chi} - \chi| > \gamma) \leq \epsilon. \quad (5.79)$$

□

### 5.7.4.2 Implementation

The construction of the bifidelity model (5.65) requires knowing the quantile  $q_\chi(\alpha)$  and the threshold parameter  $\gamma$ , which depends on the  $\mathbb{L}^q$ -error between  $\chi$  and  $\tilde{\chi}$ . The quantile  $q_\chi(\alpha)$  and the approximation error are in general not known *a priori*. Following Li and Xiu [2010], one can use a constructive iterative algorithm that does not require the *a priori* choice of  $\gamma$  (Algorithm 1). To initialize this algorithm, a number  $\nu$  of i.i.d. samples of the uncertain input parameters is simulated, a surrogate model  $\tilde{\chi}$  is built, and a small positive parameter  $\eta$  is chosen for setting a stopping criterion. At each iteration  $j$ , the sample set  $S$  is divided into a set  $\tilde{S}^{(j)}$  of samples for which  $\tilde{\chi}$  is evaluated and a set  $S \setminus \tilde{S}^{(j)}$  for which  $\chi$  is evaluated. In the initialisation step,  $\tilde{S}^{(0)} = S$  and an initial estimate of the quantile is determined by using only  $\tilde{\chi}$ . At each iteration  $j$ , the set  $S \setminus \tilde{S}^{(j)}$  is determined by enriching the set  $S \setminus \tilde{S}^{(j-1)}$  with the  $\Delta\nu$  samples in  $\tilde{S}^{(j-1)}$  that are closest to the current quantile estimate and a new quantile estimate is evaluated by using the updated bifidelity model

$$\tilde{\chi}^\gamma(\theta^{(k)}) = \tilde{\chi}(\theta^{(k)}) \mathbf{1}(\xi(\theta^{(k)}) \in \tilde{S}^{(j)}) + \chi(\theta^{(k)}) \mathbf{1}(\xi(\theta^{(k)}) \in (S \setminus \tilde{S}^{(j)})), \quad 1 \leq k \leq \nu. \quad (5.80)$$

**Algorithm 1** Iterative algorithm for the bifidelity method**Initialisation:**

1. Build a surrogate model  $\tilde{\chi}$  of  $\chi$ .
2. Draw  $\nu$  i.i.d. samples to obtain  $S = \{\xi(\theta^{(k)}), 1 \leq k \leq \nu\}$ .
3. Set  $k = 0$ ,  $\tilde{S}^{(0)} = S$ ,  $\Delta\nu \ll \nu$  (step size), and  $\eta \geq 0$  (small number).
4. Evaluate  $\{\tilde{\chi}(\theta^{(k)}), 1 \leq k \leq \nu\}$ .
5. Set  $q^{(0)}(\alpha)$  as the  $\alpha$ -quantile of  $\{\tilde{\chi}(\theta^{(k)}), 1 \leq k \leq \nu\}$ .

**Iteration:** at the  $j$ -th iteration ( $j \geq 1$ ), **do:**

1. Sort  $\{|\tilde{\chi}(\theta^{(k)}) - q^{(j-1)}(\alpha)|, \theta^{(k)} \in \tilde{S}^{(j-1)}\}$  in ascending order.  
Let  $\Delta\tilde{S}^{(j)}$  collect the  $\Delta\nu$  smallest elements and  $\tilde{S}^{(j)} = \tilde{S}^{(j-1)} \setminus \Delta\tilde{S}^{(j)}$ .
2. Evaluate  $\chi(\theta^{(k)})$  and replace  $\tilde{\chi}(\theta^{(k)})$  with  $\chi(\theta^{(k)})$ ,  $\forall \theta^{(k)} \in \Delta\tilde{S}^{(j)}$ .
3. Set  $q^{(j)}(\alpha)$  as the  $\alpha$ -quantile of  $\{\tilde{\chi}(\theta^{(k)}), 1 \leq k \leq \nu\}$ .
4. If  $|q^{(j)}(\alpha) - q^{(j-1)}(\alpha)| \leq \eta$  or  $\tilde{S}^{(j)} = \emptyset$ , exit; otherwise increment  $j$  by 1.

**Return**  $q^{(j)}(\alpha)$  as an estimate of  $q_\chi(\alpha)$ .

**5.7.4.3 Computational cost**

In addition to the computational cost of constructing a truncated polynomial chaos expansion as in Equation (5.57) or Equation (5.61), the accuracy and efficiency of Algorithm 1 depend on the stopping criterion and the step size  $\Delta\nu$ . In principle, the algorithm will converge to the Monte Carlo estimate once all the samples are evaluated with the computational model. In practice, it is desirable to stop the algorithm before this point to reduce the number of evaluations of the computational model. Nevertheless, while a stopping criterion implies the numerical convergence of the quantile estimate, it may not guarantee the convergence towards the quantile to be estimated. Thus, the accuracy of the surrogate model may be expected to have a direct impact on the efficiency of the algorithm. A small step size may be expected to be more optimal in terms of the total number of evaluations of the computational model but to converge in more iterations, while a higher step size may be expected to be less optimal in terms of the total number of evaluations of the computational model but to converge in less iterations. At each iteration, the  $\Delta\nu$  new evaluations of the computational model may be performed in parallel depending on the available computational resources.

**5.8 Numerical example****5.8.1 Problem set-up**

We provide in this section a numerical example using a test function to illustrate aspects of the proposed methodology and we postpone to Chapter 7 an illustration relevant to the retreat of the grounded portion of the Antarctic ice sheet. In addition, we do not seek to provide physical interpretations of excursion sets and confidence sets and we postpone to Chapters 7 and 8 these interpretations.

Let  $D = [-2, 2] \times [-2, 2]$  be a compact subset of  $\mathbb{R}^2$ . We consider the Gaussian function

$$y(\mathbf{x}) = y_0 \exp\left(-\left[k_1(x_1 \cos \theta + x_2 \sin \theta)^2 + k_2(x_1 \sin \theta - x_2 \cos \theta)^2\right]\right), \quad \mathbf{x} \in D, \quad (5.81)$$

to be the solution quantity. Here,  $y_0$ ,  $k_1$ ,  $k_2$  and  $\theta$  are input parameters. The solution quantity given by Equation (5.81) may be interpreted as the solution at a given time to a diffusion equation, with  $y$  that may be interpreted as a concentration level,  $\theta$  that may be associated with a preferential direction of diffusion, and  $k_1$  and  $k_2$  that may be associated with the diffusion coefficients in the direction parallel to  $\theta$  and orthogonal to  $\theta$ , respectively.

Here, we are interested in the subset of  $D$  where the spatial response  $y$  exceeds half of its value at the origin, that is, we consider the superlevel set

$$\left\{ \mathbf{x} \in D : y(\mathbf{x}) \geq \frac{y_0}{2} \right\}. \quad (5.82)$$

Figure 5.7 illustrates the Gaussian function in Equation (5.81) for the parameters  $y_0 = 100$ ,  $k_1 = 1$ ,  $k_2 = 0.5$ ,  $\theta = \pi/4$ . Levels sets of a Gaussian function are ellipses and thus its superlevel sets are contained inside ellipses. Hence,  $\theta$  defines the direction of the ellipses and the parameters  $k_1$  and  $k_2$  are associated with the lengths of the semi-axes of the ellipses.

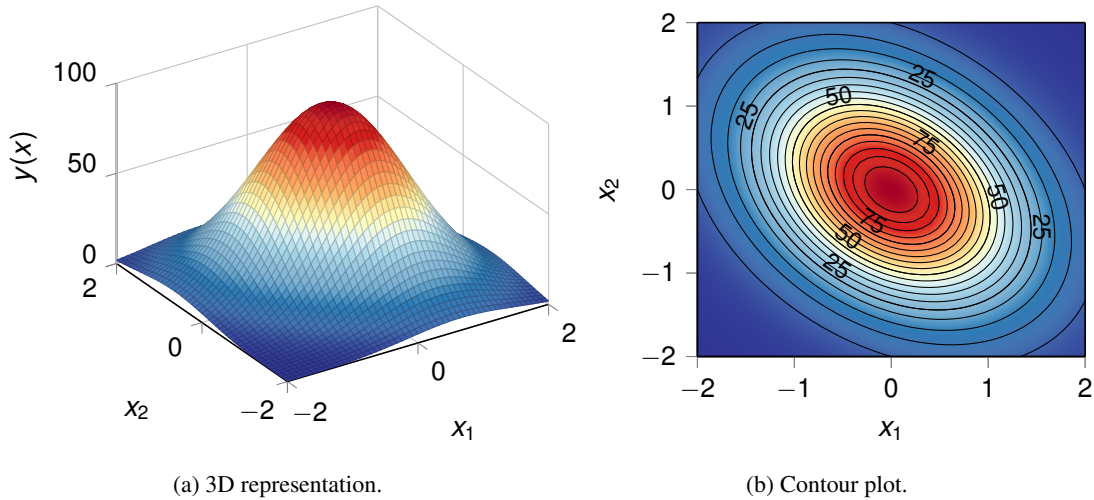


Figure 5.7: Representation of the Gaussian function in Equation (5.81) ( $y_0 = 100$ ,  $k_1 = 1$ ,  $k_2 = 0.5$ ,  $\theta = \pi/4$ ).

### 5.8.2 Sources of uncertainties

We consider the parameter  $k_1$  to be uncertain and we consider the parameters  $k_2$ ,  $\theta$ , and  $y_0$  to be fixed with values of 0.5,  $\pi/4$ , and 100, respectively. We represent the uncertain parameter  $k_1$  as a uniform random variable  $\xi$  with values in  $[0.5, 5]$ . Hence, we consider the length of the minor axis of the level sets of the Gaussian function in Equation (5.81) to be uncertain. Figure 5.8 shows representations of the Gaussian function for the minimum and maximum values of the

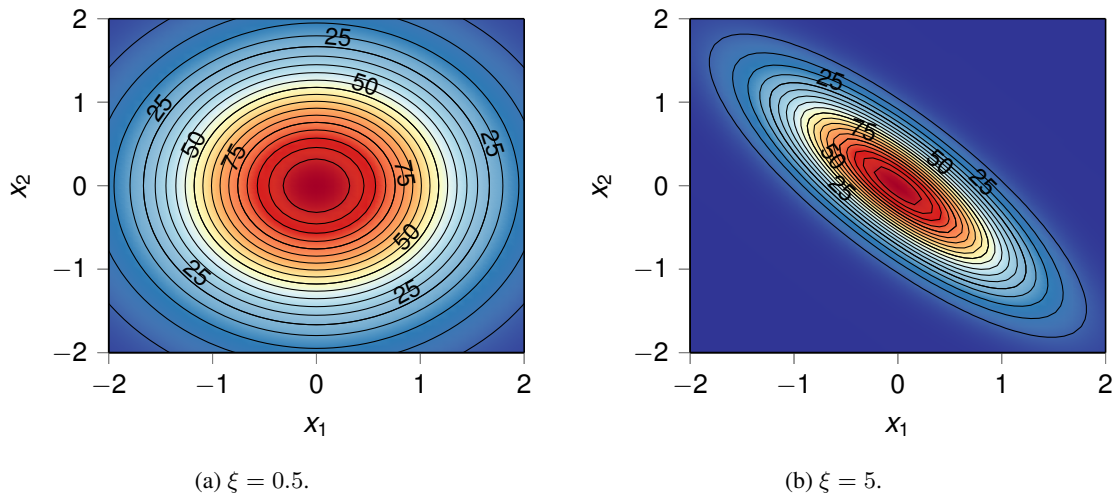


Figure 5.8: Examples of realisations of the Gaussian function in Equation (5.81) and its level sets for the minimum and maximum values of the uncertain input parameter.

input parameter.

Upon representing the uncertain input parameter  $k_1$  with the aforementioned random variable, the solution quantity becomes the random field  $\{Y(\mathbf{x}), \mathbf{x} \in D\}$ . We are interested in its positive excursion set

$$\mathcal{E}_u^+ = \{\mathbf{x} \in D : Y(\mathbf{x}) \geq u\}, \quad (5.83)$$

for the level  $u = y_0/2 = 50$ . In the following, we will seek an inner confidence set  $C_{u^+, \alpha}^{\text{in}}$  for  $\mathcal{E}_u^+$  for different confidence levels  $\alpha$ . Following the approach in Section 5.6, we consider a partitioning of the domain and define the excursion sets and confidence sets with reference to this partitioning. Here, we evaluate the Gaussian function on a square grid with 1 001 grid points in each direction and the partitioning is taken as a square tessellation based on the grid points and the representative points are the grid points. This spatial discretisation leads to a partitioning into 1 002 001 subsets. Owing to the partitioning of the domain,  $\chi$  is a discrete variable, denoted here explicitly by  $\chi^h$ .

### 5.8.3 Membership function

We estimated the membership functions defined in Equations (5.24)–(5.26) for the random Gaussian function using Monte Carlo sampling. We first generated an ensemble of 5 000 i.i.d. samples of the uncertain input parameter, from which we deduced the corresponding realisations of the random Gaussian function. Then, we estimated the statistical descriptors of the random field from these realisations using Monte Carlo estimation. Finally, we evaluated the membership functions defined in Equations (5.24)–(5.26) using the statistical descriptors thus obtained. Figure 5.9 illustrates these membership functions.

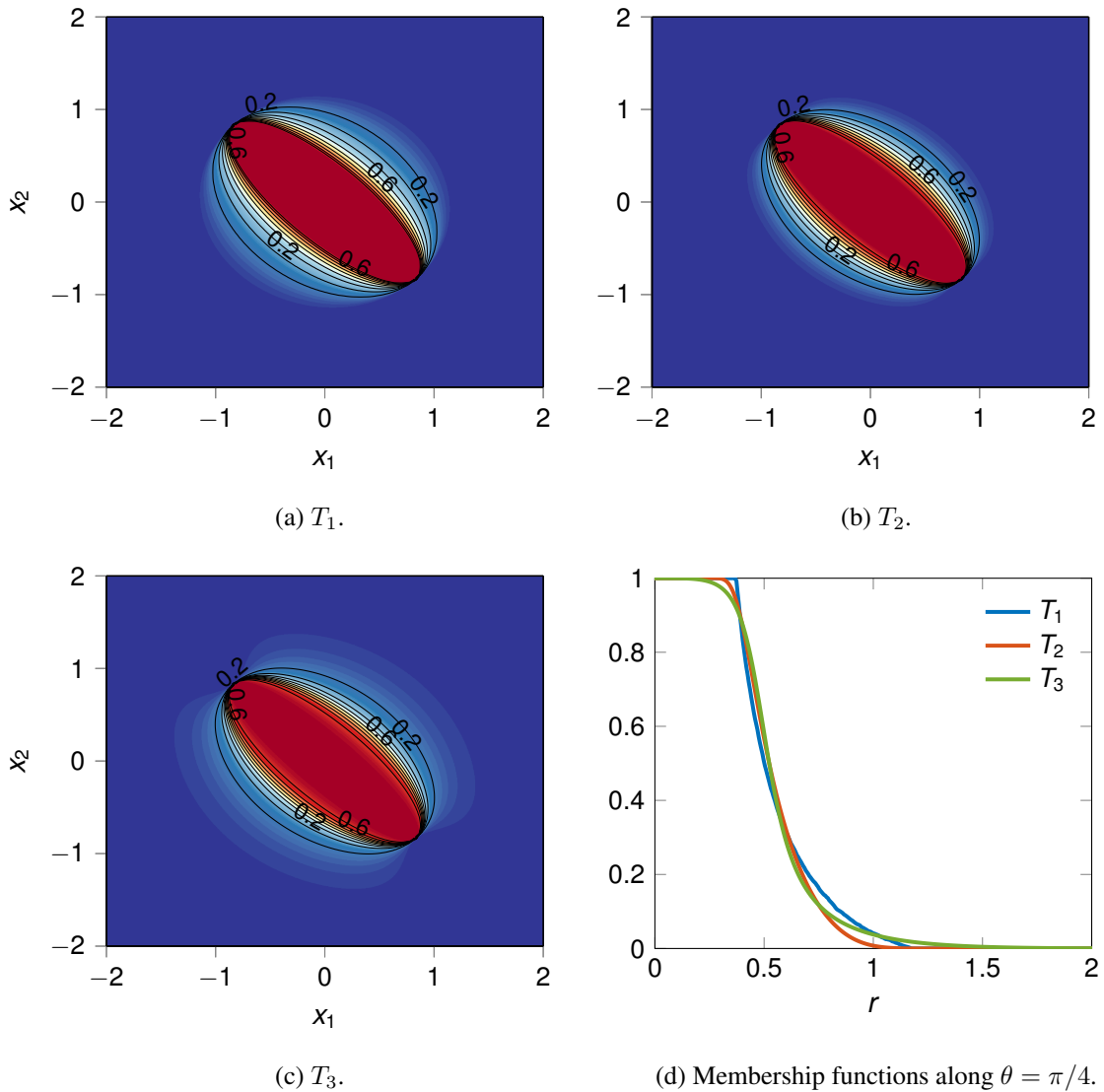


Figure 5.9: Illustrations of membership functions for the Gaussian function: (a)  $T_1$ , (b)  $T_2$ , (c)  $T_3$ , and (d) representation of the membership function along the direction  $\theta = \pi/4$  with  $r$  the distance to the centre.

### 5.8.4 Random variable $\chi^h$

Figure 5.10 shows, as a function of the values taken by the uncertain input parameter, the corresponding value taken by  $\chi^h$  for the membership functions defined in Equations (5.24)–(5.26). For small values of  $\xi$ , the superlevel sets of  $y$  are ellipses whose minor axis is of similar length as the major axis, and the supremum of  $T$  in  $(\mathcal{E}_u^+)^c$  is small. On the other hand, for large values of  $\xi$ , the superlevel sets of  $y$  are ellipses whose minor axis is much smaller than the major axis, and the supremum of  $T$  in  $(\mathcal{E}_u^+)^c$  is large. We can observe that the mapping from the values taken by the uncertain input parameters to the value by the random variable  $\chi^h$  is almost linear for the membership function  $T_1$  and exhibits a similar behaviour for  $T_2$  and  $T_3$ .

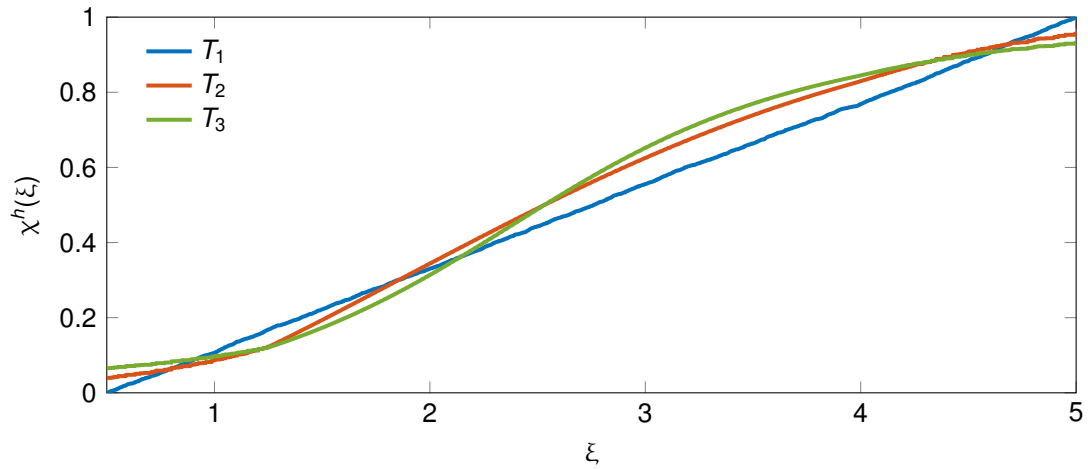


Figure 5.10: Value taken by the random variable as a function of the values taken by the uncertain input parameter for the membership functions defined in Equations (5.24)–(5.26).

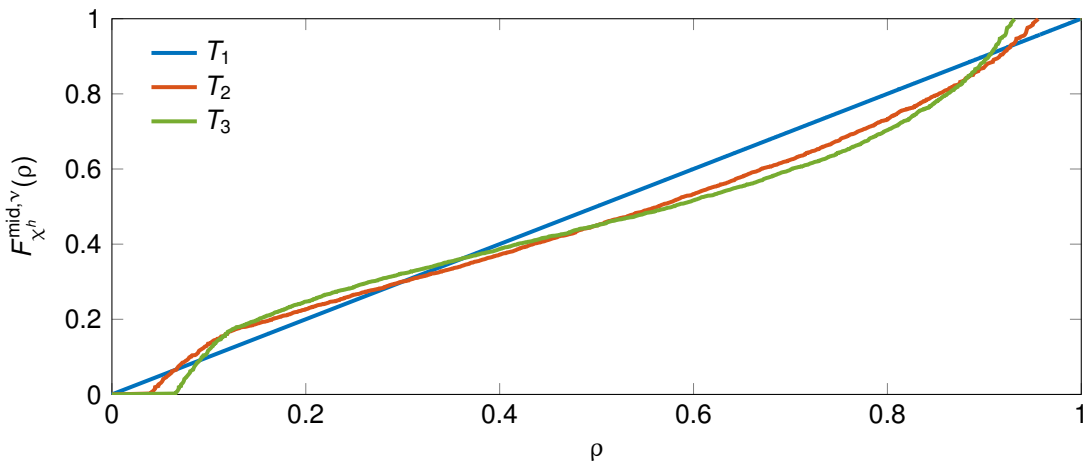


Figure 5.11: Sample mid-distribution functions ( $\nu = 5\,000$ ).

## 5.8.5 Quantile estimation

### 5.8.5.1 Monte Carlo method

We determined the value of the optimal threshold  $\rho^*$  with an ensemble of 5 000 i.i.d. samples. Figure 5.11 shows the sample mid-distribution function for the three membership functions, from which we estimated the corresponding mid-quantiles for the confidence levels 0.5, 0.9, and 0.99. In Figure 5.12, we conducted a numerical convergence analysis to examine the convergence of the Monte Carlo estimates of the mid-quantiles with respect to the number of samples. Figure 5.12 suggests that using 5 000 samples is sufficient to ensure a reasonable convergence of the Monte Carlo estimates, with reasonable convergence achieved after a value for  $\nu$  of about 2 000.

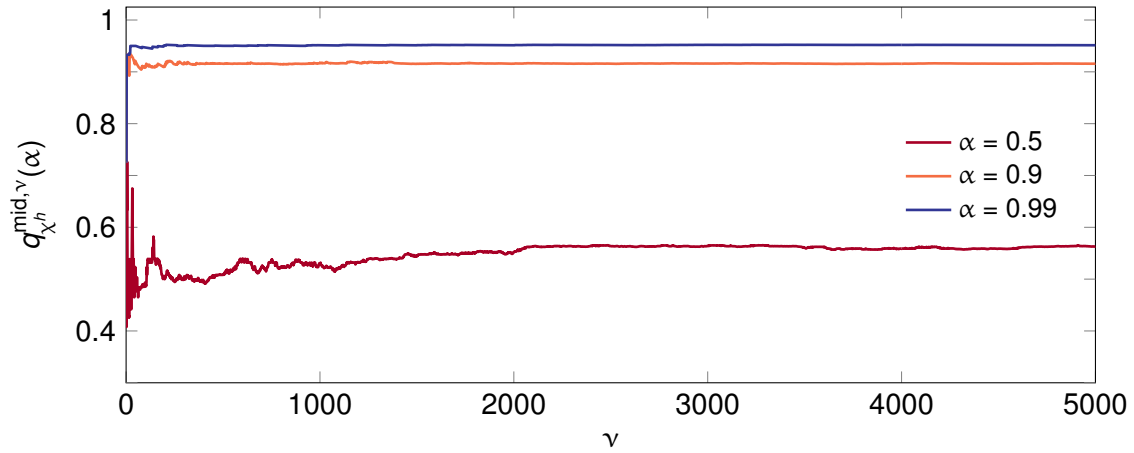


Figure 5.12: Convergence analysis of the Monte Carlo estimates as a function of the number of samples  $\nu$  for  $T_2$ .

### 5.8.5.2 Bifidelity method

We implemented the bifidelity method by reusing the ensemble of 5000 i.i.d samples that we had used in the Monte Carlo method in Section 5.8.5.1 so as to allow the solution given by the bifidelity method to be compared with the Monte Carlo solution. We built polynomial chaos expansions for several choices of the order  $p$  using scaled Legendre polynomials whereby we determined the polynomial chaos coordinates from an experimental design made up of the nodes of a fully tensorised scaled Gauss–Legendre quadrature integration rule with  $(p + 1)$  nodes. In Algorithm 1, we used a step size of  $\Delta\nu = 50$  and we set  $\eta = 0$ .

In this numerical illustration, we found that Algorithm 1 stops when the mid-quantile estimate based on the bifidelity method is equal to the Monte Carlo estimate. For this reason, we measure the efficiency of the bifidelity method as the number of iterations before exiting Algorithm 1, with the maximum number of iterations equal to 100. Figure 5.13 gives the efficiency of the bifidelity method for a surrogate model based on a polynomial chaos expansion either of the random field or of  $\chi^h$  as a function of the order  $p$ . The number of iterations is high for low orders but drops significantly for higher orders, with only one or two iterations necessary to exit Algorithm 1 for higher orders. Hence, the mid-quantile can be estimated with only a reduced number of samples compared to the Monte Carlo sampling method. In addition, the bifidelity method based on a polynomial chaos expansion of  $\chi$  generally achieves a higher efficiency than the bifidelity method based on a polynomial chaos expansion of  $\chi^h$  for a given order  $p$ . Regarding differences between the membership functions defined in Equations (5.24)–(5.26), the bifidelity method based on a polynomial chaos expansion of  $\chi^h$  achieves a higher efficiency for the membership function  $T_1$  than  $T_2$  and  $T_3$ , which results from  $\chi^h$  being almost linear for  $T_1$ .

### 5.8.5.3 Discussion: efficiency of the bifidelity approach

In this illustration, the bifidelity method based on a polynomial chaos expansion of the random field achieves in general a higher efficiency than the bifidelity method based on a polynomial

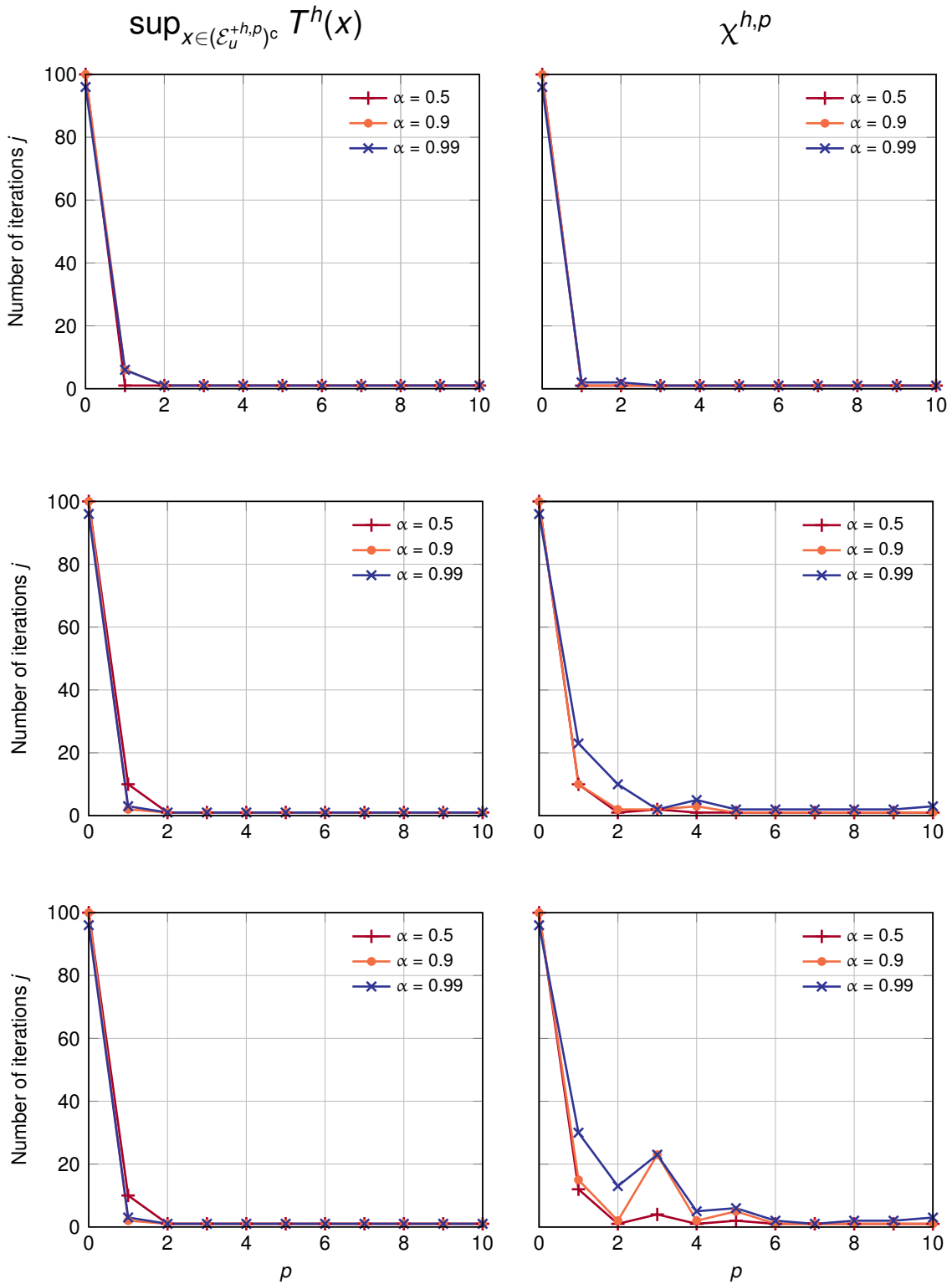


Figure 5.13: Efficiency of the hybrid sampling method: number of iterations before exiting Algorithm 1 as a function of the polynomial order  $p$ . Surrogate models are based on a polynomial chaos expansion either of the random field (first column) or of  $\chi^h$  (second column). Results are for  $T_1$  (top row),  $T_2$  (middle row), and  $T_3$  (bottom row).

chaos expansion of  $\chi^h$ . To understand these observations, we looked at how well the random variable  $\chi^h$  lends itself to being approximated with surrogate models based on a polynomial chaos expansion of either the random field or the random variable  $\chi^h$ . Figure 5.14 shows, as a function of the polynomial order  $p$ , the relative mean-square error between the random variable  $\chi^h$  and a surrogate model  $\tilde{\chi}$  based on a polynomial chaos expansion of either the random field (Figure 5.14(a)) or the random variable  $\chi^h$  (Figure 5.14(b)). While the approximation error decreases as a function the polynomial order  $p$  for both kinds of surrogate model, the convergence is in general faster for a surrogate model based on a polynomial chaos expansion of the random field than one of the random variable  $\chi^h$ . Thus, the random variable  $\chi^h$  lends itself better to being approximated with surrogate models based on a polynomial chaos expansion of the random field than one of the random variable  $\chi^h$ , which leads to the observed higher efficiency for the bifidelity method based on a polynomial chaos expansion of the random field. It should be noted that for the membership function  $T_1$ , the relative mean-square error between the random variable  $\chi^h$  and a surrogate model  $\tilde{\chi}$  based on a polynomial chaos expansion of  $\chi^h$  exhibits initially a very fast convergence rate because  $\chi^h$  is almost linear (see Figure (5.10)). For the Gaussian function in Equation (5.81) with an uncertain input parameter, the random field  $\{Y(\mathbf{x}), \mathbf{x} \in D\}$  is sufficiently smooth to lend itself well to being approximated with a polynomial chaos expansion of low order.

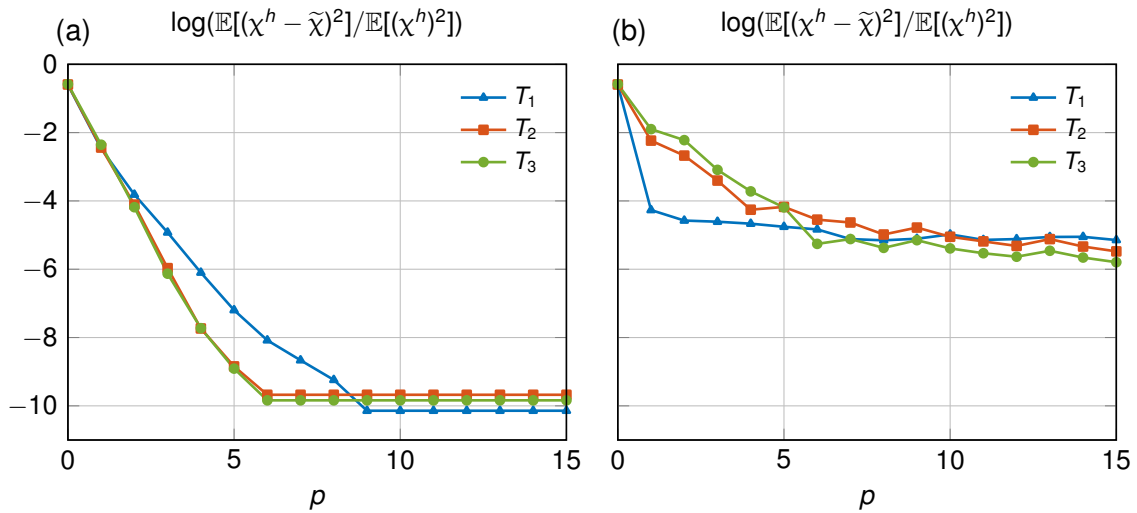


Figure 5.14: Relative mean-square error between the random variable  $\chi^h$  and a surrogate model  $\tilde{\chi}$  based on a polynomial chaos expansion either (a) of the random field or (b) of  $\chi^h$ .

### 5.8.6 Confidence sets

Figure 5.15 represents confidence sets for various confidence levels. We built this figure by superimposing these confidence sets for increasing confidence levels.

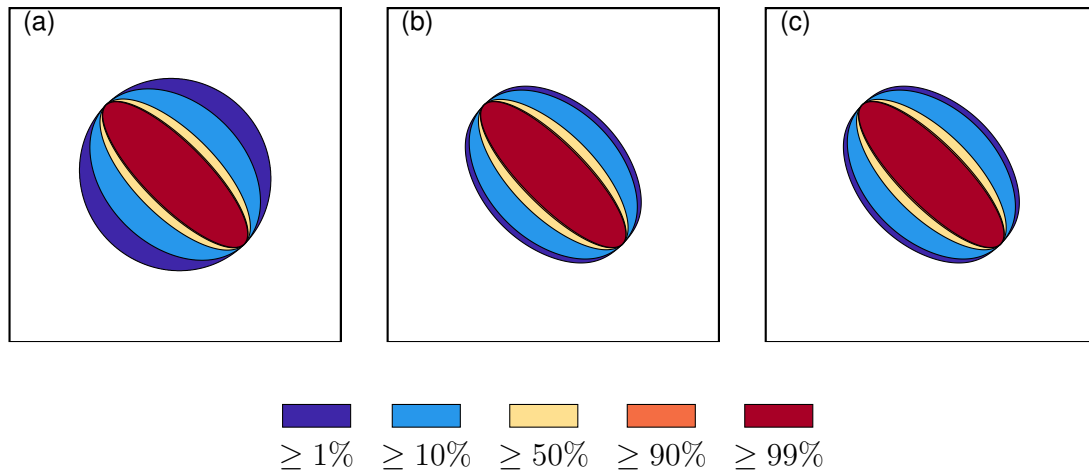


Figure 5.15: Superimposition of confidence sets for various confidence levels. Membership function: (a)  $T_1$ , (b)  $T_2$ , and (c)  $T_3$ .

### 5.8.7 Spatial discretisation

Figure 5.16 provides insight into the impact of the spatial discretisation on the accuracy one may achieve in computing confidence sets. Figure 5.16 shows the convergence of the mid-quantile estimates obtained using Monte Carlo sampling as a function of the number of grid points  $N_h$ . We can observe that reasonably converged estimates of the mid-quantiles are obtained after a value for  $N_h$  of about 123 201 (351 grid points in each dimension of the domain). Figure 5.16 also shows that  $q_{\chi^h}^{\text{mid}}(\alpha)$  essentially increases as a function of the number of grid points.

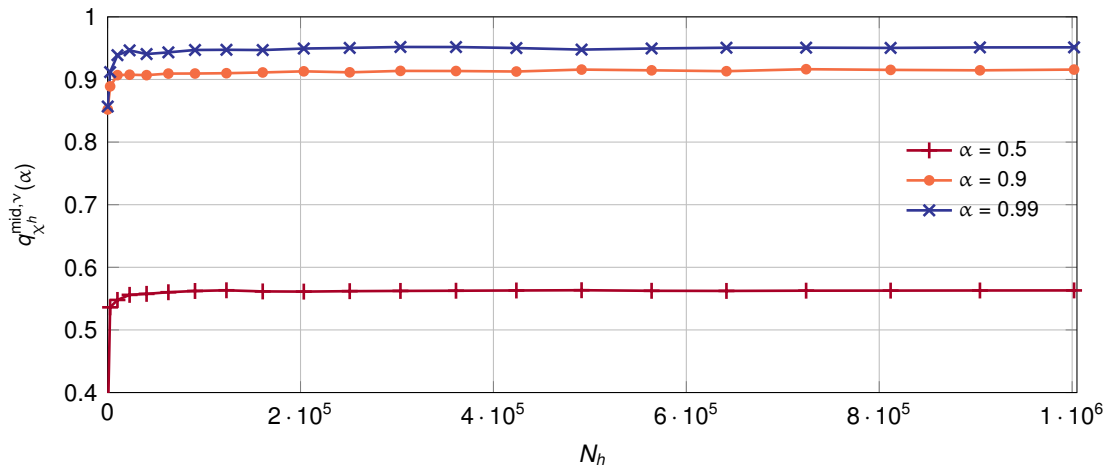


Figure 5.16: Convergence analysis of the mid-quantile estimates obtained using Monte Carlo sampling ( $\nu = 5\,000$ ) as a function of the number of grid points  $N_h$ . Results are for  $T_2$ .

## 5.9 Conclusion

We investigated confidence sets of random excursion sets in the context of stochastic computational models with a high computational cost. We proposed to recast the problem of estimating an optimal confidence set in a parametric family of candidate sets as an equivalent quantile estimation problem of a random variable. We proposed to solve the quantile estimation problem using a surrogate model either of the random field or of the random variable  $\chi$ , and we introduced a bifidelity method that aims at reducing the approximation error by using the computational model close to the quantile to be estimated. We illustrated this method on a simple model problem and we showed that only a small number of evaluations of the computational model was necessary to achieve an accurate estimate of the quantile.

The bifidelity method relies on the construction of a surrogate model based on a polynomial chaos expansion, which is especially well suited for low or moderate stochastic dimension. With a methodology-oriented point of view, future work could investigate the stochastic discretisation of the quantile estimation problem for computational models with a high stochastic dimension by using, for instance, other methods from reliability engineering such as subset simulation or adaptive methods. With an application-oriented point of view, future work could apply the proposed method to provide probabilistic projections and insight into the evolution of complex physics-based models. For an example of such an application, we refer the reader to Chapter 8, in which we used the proposed method to provide new probabilistic projections and insight into the evolution of Antarctic ice sheet based on realistic forcings and suitable probabilistic characterisations of uncertain input parameters.

## 5.A Asymptotic properties in Monte Carlo estimation of quantiles

In this appendix, we provide the interested reader with theoretical results regarding asymptotic properties in Monte Carlo estimation of quantiles.

### 5.A.1 Monte Carlo quantile estimation based on the distribution function

When the random variable  $\chi$  is a continuous random variable with a probability density function, Theorem 5.3 [Arnold et al., 1992] shows that the Monte Carlo estimate  $q_\chi^\nu(\alpha)$  is associated with a consistent estimator of  $q_\chi(\alpha)$  that satisfies a central limit theorem.

**Theorem 5.3.** Let  $\{\chi^{(1)}, \dots, \chi^{(\nu)}\}$  be a sequence of independent and identically distributed random variables with distribution function  $F_\chi$  and let  $\chi_{k:\nu}$  denotes the corresponding  $k$ -th order statistics. For  $0 < \alpha < 1$ , let  $F_\chi$  be absolutely continuous with probability density function  $f_\chi$  which is positive at  $F_\chi^{-1}(\alpha)$  and is continuous at that point. For  $k = [\nu\alpha] + 1$ , where  $[\nu\alpha]$  represents the integer part of  $\nu\alpha$ , as  $\nu \rightarrow \infty$ ,

$$\sqrt{\nu} f_\chi(F_\chi^{-1}(\alpha)) \frac{(\chi_{k:\nu} - F_\chi^{-1}(\alpha))}{\sqrt{\alpha(1-\alpha)}} \xrightarrow{d} \mathcal{N}(0, 1). \quad (5.84)$$

When  $\chi$  is a discrete random variable, then the Monte Carlo estimate  $q_\chi^\nu(\alpha)$  is not guaranteed to be associated with a consistent estimator of  $q_\chi(\alpha)$  or to satisfy a central limit theorem.

Theorem 5.4 by Feldman and Tucker [1966] indicates that the Monte Carlo estimate  $q_\chi^\nu(\alpha)$  satisfies the so-called oscillatory effect with respect to the interval  $[q_\chi^{\text{inf}}(\alpha), q_\chi^{\text{sup}}(\alpha)]$  where  $q_\chi^{\text{inf}}$  and  $q_\chi^{\text{sup}}$  are respectively the lower and upper  $\alpha$ -quantiles of  $\chi$ , that is,

$$q_\chi^{\text{inf}}(\alpha) = \inf \{ \rho \in \mathbb{R} : F_\chi(\rho) \geq \alpha \}, \quad (5.85)$$

$$q_\chi^{\text{sup}}(\alpha) = \sup \{ \rho \in \mathbb{R} : F_\chi(\rho) \leq \alpha \}. \quad (5.86)$$

It should be noted that the lower quantile  $q_\chi^{\text{inf}}(\alpha)$  is actually equivalent to our definition of  $q_\chi(\alpha)$  and that  $q_\chi^{\text{inf}}(\alpha)$  is equivalent to  $q_\chi^{\text{sup}}(\alpha)$  when  $\chi$  is a continuous random variable. As explained in Elfverson et al. [2014], the problem of estimating  $q_\chi(\alpha)$  is actually ill-conditioned since small perturbations in  $\alpha$  or in the distribution function  $F_\chi$  cause large variations in  $q_\chi(\alpha)$ . This results in  $q_\chi^\nu(\alpha)$  converging to either  $q_\chi^{\text{inf}}(\alpha)$  or  $q_\chi^{\text{sup}}(\alpha)$  or to cycle between them.

**Theorem 5.4.** Let  $\{\chi^{(1)}, \dots, \chi^{(\nu)}\}$  be a sequence of independent and identically distributed random variables with distribution function  $F_\chi$  and let  $\chi_{k:\nu}$  denotes the corresponding  $k$ -th order statistics. For  $0 < \alpha < 1$ , the sequence  $\{\chi^{(1)}, \dots, \chi^{(\nu)}\}$  obeys the oscillatory effect with respect to the interval  $[a, b]$ , i.e.,  $\mathbb{P}[\chi_{k:\nu} \leq a, i.o.] = \mathbb{P}[\chi_{k:\nu} \geq a, i.o.] = 1$  (i.o. means “infinitely often”).

### 5.A.2 Monte Carlo quantile estimator based on the mid-distribution function

Theorem 5.5 [Ma et al., 2011] shows that the Monte Carlo estimate  $q_\chi^{\text{mid},\nu}(\alpha)$  is associated with a consistent estimator of  $q_\chi^{\text{mid}}(\alpha)$  that satisfies a generalised central limit theorem. In Theorem 5.5, Ma et al. [2011] distinguish four different cases depending on the value of  $\alpha$ . In cases 1 ( $\alpha < p_1/2$ ) and 2 ( $\alpha > F_\chi^{\text{mid}}(\chi_L)$ ), the Monte Carlo estimates based on the mid-distribution function are associated with an estimator that converges in probability towards the minimum and maximum values of the random variable, respectively. Case 3 corresponds to a value of  $\alpha$  being strictly between two distinct discrete values of the mid-distribution function. In case 3, the Monte Carlo estimates based on the mid-distribution function are associated with an estimator that satisfies a central limit theorem in accordance with Theorem 5.3. The term  $(1 - (\lambda - 1)^2)^{\frac{p_L+1}{4}} + (1 - \lambda^2)^{\frac{p_L+2}{4}}$  can be viewed as an efficiency gain due to the fact that the estimates are more concentrated in the discrete case than in the continuous case. This term vanishes in the continuous case because the probability mass function is zero. Case 4 corresponds to a value of  $\alpha$  being equal to one of the distinct discrete values of the mid-distribution function. In case 4, the Monte Carlo estimates based on the mid-distribution function are associated with an estimator that converges in distribution towards a joined half-Gaussian (or two-piece normal) distribution. In a similar way to case 3, the term  $\frac{p_L+1}{4}$  can be viewed as an efficiency gain.

**Theorem 5.5.** Let  $\{\chi^{(1)}, \dots, \chi^{(\nu)}\}$  be a sequence of independent and identically distributed random variables with distribution function  $F_\chi$  and mid-distribution function  $F_\chi^{\text{mid}}$ . Let the support of the distribution function be  $\chi_1 < \dots < \chi_L$  and denote the corresponding probability masses by  $p_1 = p_\chi(\chi_1), \dots, p_L = p_\chi(\chi_L)$ . Further define  $p_0 = 0, p_{L+1} = 0, \chi_0 = \chi_1$ , and  $\chi_{L+1} = \chi_L$ . For  $0 < \alpha < 1$ , let  $\chi^{\text{mid},\nu}(\alpha)$  be the random variable defined by

$$\chi^{\text{mid},\nu}(\alpha) = \inf \left\{ \rho \in (0, 1) : F^{\text{mid},\nu}(\rho) \geq \alpha \right\}, \quad (5.87)$$

where  $F^{\text{mid},\nu}(\rho)$  is given by

$$F^{\text{mid},\nu}(\rho) = \begin{cases} 0 & \text{if } \rho < \chi_1 \\ \frac{F^{\text{mid},\nu}(\chi_{k+1}) - F^{\text{mid},\nu}(\chi_k)}{\chi_{k+1} - \chi_k}(\rho - \chi_k) + F^{\text{mid},\nu}(\chi_k) & \text{if } \chi_k \leq \rho \leq \chi_{k+1}, \\ 1 & \text{if } \rho > \chi_L \end{cases} \quad (5.88)$$

with

$$F^{\text{mid},\nu}(\chi_k) = \frac{1}{\nu} \sum_{l=1}^{\nu} \mathbf{1}(\chi^{(l)} \leq \chi_k) - \frac{1}{2\nu} \sum_{l=1}^{\nu} \mathbf{1}(\chi^{(l)} = \chi_k), \quad 1 \leq k \leq L. \quad (5.89)$$

Then, as  $\nu \rightarrow \infty$

1.  $\chi^{\text{mid},\nu}(\alpha) \xrightarrow{p} \chi_1$  if  $\alpha < F_{\chi}^{\text{mid}}(\chi_1) = p_1/2$ .
2.  $\chi^{\text{mid},\nu}(\alpha) \xrightarrow{p} \chi_L$  if  $\alpha > F_{\chi}^{\text{mid}}(\chi_L)$ .
- 3.

$$\sqrt{\nu} f_{\chi}(q_{\chi}^{\text{mid}}(\alpha)) (\chi^{\text{mid},\nu}(\alpha) - q_{\chi}^{\text{mid}}(\alpha)) \xrightarrow{d} \mathcal{N} \left[ 0, \alpha(1 - \alpha) - (1 - (\lambda - 1)^2) \frac{p_{l+1}}{4} - (1 - \lambda^2) \frac{p_{l+2}}{4} \right]. \quad (5.90)$$

if  $\alpha = \lambda F_{\chi}^{\text{mid}}(\chi_{l+1}) + (1 - \lambda) F_{\chi}^{\text{mid}}(\chi_{l+2})$  for  $0 < \lambda < 1$  and  $l = 0, \dots, L - 2$ .

4.  $\sqrt{\nu} f_{\chi}(\chi^{\text{mid},\nu}(\alpha), \chi_{l+1}) (\chi^{\text{mid},\nu}(\alpha) - \chi_{l+1}) \xrightarrow{d} \mathcal{N}(0, \alpha(1 - \alpha) - \frac{p_{l+1}}{4})$ . (5.91)

if  $\alpha = F_{\chi}^{\text{mid}}(\chi_{l+1})$  for  $l = 0, \dots, L - 1$ . Here,  $f_{\chi}(\hat{\chi}, \chi)$  denotes the right derivative of  $F_{\chi}^{\text{mid}}$  at  $\chi$  if  $\hat{\chi} > \chi$  and the left derivative of  $F_{\chi}^{\text{mid}}$  at  $\chi$  if  $\hat{\chi} < \chi$ .

## 5.B Proof of Theorem 5.1

The quantiles  $q_{\chi}(\alpha)$  and  $q_{\tilde{\chi}}(\alpha)$  are given by

$$q_{\chi}(\alpha) = \inf \{ \rho \in (0, 1) : F_{\chi}(\rho) \geq \alpha \}, \quad (5.92)$$

$$q_{\tilde{\chi}}(\alpha) = \inf \{ \rho \in (0, 1) : F_{\tilde{\chi}}(\rho) \geq \alpha \}. \quad (5.93)$$

We first assume that the following inequalities hold

$$F_{\tilde{\chi}}(q_{\chi}(\alpha) + \delta) = \mathbb{P}(\tilde{\chi} \leq q_{\chi}(\alpha) + \delta) \geq \alpha, \quad (5.94)$$

$$F_{\tilde{\chi}}(q_{\chi}(\alpha) - \delta - \epsilon) = \mathbb{P}(\tilde{\chi} \leq q_{\chi}(\alpha) - \delta - \epsilon) < \alpha, \quad \forall 0 < \epsilon < \delta. \quad (5.95)$$

From (5.94), we can deduce

$$q_{\tilde{\chi}}(\alpha) = \inf \{ \rho \in (0, 1) : F_{\tilde{\chi}}(\rho) \geq \alpha \} \leq q_{\chi}(\alpha) + \delta. \quad (5.96)$$

Moreover, as cumulative distribution functions are monotone functions, we have

$$F_{\tilde{\chi}}(\rho_1) = \mathbb{P}(\tilde{\chi} \leq \rho_1) \leq F_{\tilde{\chi}}(\rho_2) = \mathbb{P}(\tilde{\chi} \leq \rho_2), \forall \rho_1 \leq \rho_2. \quad (5.97)$$

From (5.95), we have  $\{\rho \in (0, 1) : \mathbb{P}(\tilde{\chi} \leq \rho) \geq \alpha\} \subset [q_{\chi}(\alpha) - \delta, \infty[$ . Then

$$q_{\tilde{\chi}}(\alpha) = \inf \left\{ \rho \in (0, 1) : F_{\tilde{\chi}}(\rho) \geq \alpha \right\} \geq q_{\chi}(\alpha) - \delta. \quad (5.98)$$

From (5.96) and (5.98), we have

$$|q_{\tilde{\chi}}(\alpha) - q_{\chi}(\alpha)| \leq \delta_{\lambda}. \quad (5.99)$$

To prove (5.94), we have to show that

$$\tilde{\chi} \leq q_{\chi}(\alpha) \Rightarrow \tilde{\chi} \leq q_{\chi}(\alpha) + \delta \text{ almost surely.} \quad (5.100)$$

Indeed, if (5.B) holds, then

$$F_{\tilde{\chi}}(q_{\chi}(\alpha) + \delta) = \mathbb{P}(\tilde{\chi} \leq q_{\chi}(\alpha) + \delta) \geq \mathbb{P}(\tilde{\chi} \leq q_{\chi}(\alpha)) \geq \alpha. \quad (5.101)$$

Assuming that (5.63) and  $\tilde{\chi} \leq q_{\chi}(\alpha)$  hold, we have almost surely

$$\begin{aligned} \tilde{\chi} &\leq \chi + |\tilde{\chi} - \chi| \quad (|\tilde{\chi} - \chi| \geq \tilde{\chi} - \chi) \\ &\leq \chi + \frac{\delta}{2} + \frac{1}{2}|q_{\chi}(\alpha) - \chi| \quad (\text{given (5.63)}) \\ &= \chi + \frac{\delta}{2} + \frac{1}{2}q_{\chi}(\alpha) - \frac{1}{2}\chi \quad (q_{\chi}(\alpha) \geq \chi) \\ &= \frac{1}{2}\chi + \frac{\delta}{2} + \frac{1}{2}q_{\chi}(\alpha) \\ &\leq q_{\chi}(\alpha) + \frac{\delta}{2} \quad (q_{\chi}(\alpha) \geq \chi) \\ &\leq q_{\chi}(\alpha) + \delta. \end{aligned} \quad (5.102)$$

To prove (5.95), we have to show that

$$\tilde{\chi} \leq q_{\chi}(\alpha) - \delta - \epsilon \Rightarrow \chi \leq q_{\chi}(\alpha) - \epsilon \text{ almost surely.} \quad (5.103)$$

Indeed, if (5.103) holds, then

$$F_{\tilde{\chi}}(q_{\chi}(\alpha) - \delta - \epsilon) = \mathbb{P}(\tilde{\chi} \leq q_{\chi}(\alpha) - \delta - \epsilon) \leq \mathbb{P}(\tilde{\chi} \leq q_{\chi}(\alpha) - \epsilon) < \alpha \quad \forall 0 < \epsilon < \delta. \quad (5.104)$$

Equation (5.103) is equivalent to

$$\chi > q_{\chi}(\alpha) - \epsilon \Rightarrow \tilde{\chi} > q_{\chi}(\alpha) - \delta - \epsilon \text{ almost surely } \forall 0 < \epsilon < \delta. \quad (5.105)$$

Assuming that (5.63) and  $\chi > q_\chi(\alpha) - \epsilon$  hold, we have almost surely

$$\begin{aligned}
\tilde{\chi} &\geq \chi - |\tilde{\chi} - \chi| \quad (|\tilde{\chi} - \chi| \geq \chi - \tilde{\chi}) \\
&\geq \chi - \frac{\delta}{2} - \frac{1}{2}|q_\chi(\alpha) - \chi| \quad (\text{given (5.63)}) \\
&= \chi - \frac{\delta}{2} - \frac{1}{2}|\chi - q_\chi(\alpha)| \\
&= \chi - \frac{\delta}{2} - \frac{1}{2}|(\chi - q_\chi(\alpha) + \epsilon) - \epsilon| \\
&\geq \chi - \frac{\delta}{2} - \frac{1}{2}|\chi - q_\chi(\alpha) + \epsilon| - \frac{1}{2}|\epsilon| \quad (|a - b| \leq |a| + |b|) \\
&= \chi - \frac{\delta}{2} - \frac{1}{2}(\chi - q_\chi(\alpha) + \epsilon) - \frac{1}{2}\epsilon \quad (\chi - q_\chi(\alpha) + \epsilon > 0) \\
&= \frac{1}{2}\chi - \frac{\delta}{2} + \frac{1}{2}(q_\chi(\alpha) - \epsilon) - \frac{1}{2}\epsilon \\
&> \frac{1}{2}(q_\chi(\alpha) - \epsilon) - \frac{\delta}{2} + \frac{1}{2}(q_\chi(\alpha) - \epsilon) - \frac{1}{2}\epsilon \quad (\chi - q_\chi(\alpha) + \epsilon > 0) \\
&= (q_\chi(\alpha) - \epsilon) - \frac{\delta}{2} - \frac{1}{2}\epsilon \\
&= q_\chi(\alpha) - \frac{\delta}{2} - \frac{3}{2}\epsilon \\
&> q_\chi(\alpha) - \delta - \epsilon \quad (0 < \epsilon < \delta).
\end{aligned} \tag{5.106}$$

□

partUncertainty Quantification: Application to ice-sheet modelling



# 6

## Essential ice-sheet models as an efficient tool for large-scale and long-term simulations and uncertainty quantification

*In this chapter, we discuss the use of so-called essential ice-sheet models for simulations of the Antarctic ice sheet. Essential ice-sheet models are computational models that rely on reduced-order models and appropriate parameterisations in order to capture the overall dynamics of ice sheets at a reduced computational cost. For this reason, such models are amenable to large-scale and long-term simulations of the Antarctic ice sheet and uncertainty quantification. We discuss aspects of essential ice-sheet models with a particular focus on the fast Elementary Thermomechanical Ice Sheet (f.ETISh) model. In particular, we discuss reduced-order models and parameterisations for the thermodynamics of ice sheets and ice shelves, the interactions between an ice sheet and the Earth system, and the dynamics of the grounding line.*

### 6.1 High-fidelity vs essential ice-sheet models

Computational (or numerical) ice-sheet models differ by their discretisation of the governing equations but also by the physical processes included in the ice-sheet models and their numerical representations. This defines a hierarchy of computational ice-sheet models with the end members corresponding to computational ice-sheet models based on a discretisation of the full-order model discussed in Section 2.2 and minimal (or conceptual) ice-sheet models with no spatial extent [Shaffer, 2014; Robel et al., 2019]. In this dissertation, we distinguish within this hierarchy of ice-sheet models two classes of computational models to simulate the spatial response of ice sheets, namely *high-fidelity* and *essential* ice-sheet models. We call a high-fidelity ice-sheet model a computational model that solves a full-order model as in Section 2.2 or high-order approximations such as the Blatter–Pattyn higher-order model. These models are able to simulate the ice flow with high accuracy at high spatial resolution ( $\sim 100$  m) but with a high computational cost, thus lending themselves well to simulating ice sheets on regional scales and multidecadal periods. Examples of high-fidelity ice-sheet models are BISICLES [Cornford et al., 2013], ELMER-ICE [Gagliardini et al., 2013], Albany/FELIX [Tezaur et al., 2015a,b], MALI [Hoffman et al., 2018], and NCAR-CISM [Lipscomb et al., 2019]. On the other hand,

we call an essential ice-sheet model a computational model that solves reduced-order models of the full-order model discussed in Section 2.2 such as the SIA and SSA reduced-order models while representing essential mechanisms and feedbacks of ice-sheet flow using parameterisations. These models lend themselves well to simulating large ice sheets at low spatial resolution ( $\sim 10$  km) on multicentennial-to-millennial time horizons and are computationally tractable for large ensemble analysis and integration into (large-scale) Earth system models. Examples of essential ice-sheet models are PISM [Winkelmann et al., 2011], PSUICE3-D [Pollard and DeConto, 2012a], GRISLI [Quiquet et al., 2018], and f.ETISH [Pattyn, 2017].

Coupling computational ice-sheet models with computational models of other components of the Earth system is generally intractable for simulations on multicentennial-to-millennial time horizons and uncertainty quantification. Thus, to avoid the need for computational models of other components of the Earth system, the interactions between the ice sheet and other components of the Earth system can be computed by using parameterisations or reduced-order models.

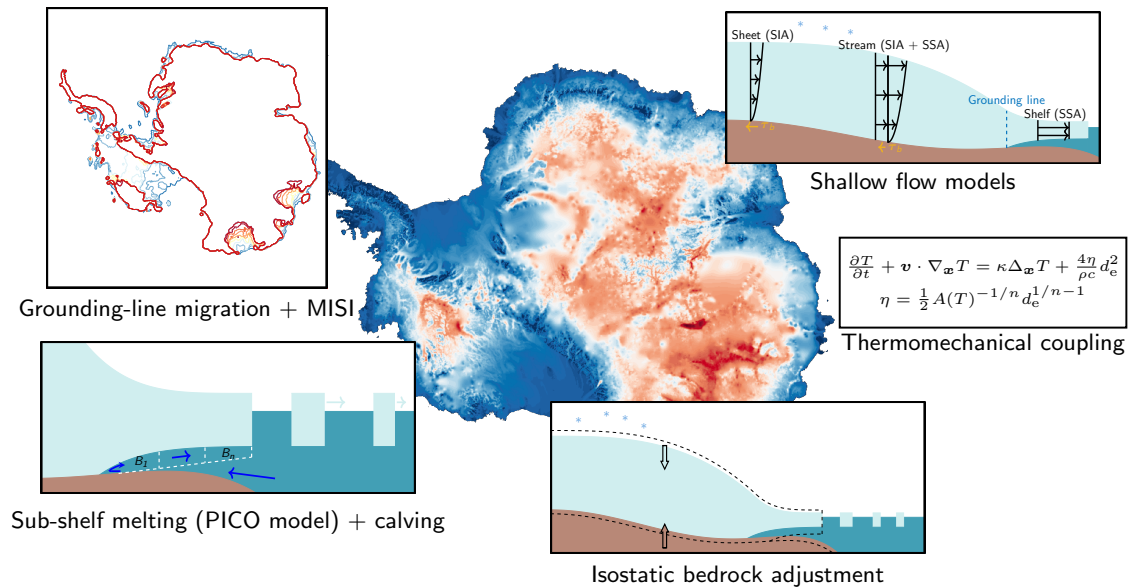


Figure 6.1: Illustration of the f.ETISH essential ice-sheet model [Pattyn, 2017]. Boxes around the map of Antarctica represent essential mechanisms and interactions implemented in the f.ETISH model.

With the aim of demonstrating methods from uncertainty quantification in ice-sheet modelling as well as providing probabilistic projections for the response of the Antarctic ice sheet on multicentennial-to-millennial time horizons, we will focus in the following on essential ice-sheet models. In this chapter, we will describe in particular the governing equations implemented in the f.ETISH ice-sheet model. The fast Elementary Thermomechanical Ice Sheet (f.ETISH) model [Pattyn, 2017], developed at the Université Libre de Bruxelles, is a hybrid ice-sheet model that captures the essential characteristics of ice flow and allows large-scale and long-term projections at a reasonable computational cost; see Figure 6.1 for an illustration. We describe in Section 6.2 the thermomechanical ice-sheet model implemented in the f.ETISH model and we describe in

Section 6.3 aspects regarding the representation of the interactions between the ice sheet and other components of the Earth system in the f.ETISh model. We discuss in Section 6.4 the initialisation of the f.ETISh model, including the inversion of the basal sliding coefficient and input datasets used to perform simulations in Chapters 7 and 8, and finally we discuss in Section 6.5 aspects regarding the numerical implementation of the governing equations, including the migration of the grounding line. It should be noted that we do not aim at providing a thorough description of the f.ETISh model but we rather aim at providing insight into the numerical modelling of ice sheets with essential ice-sheet models to the unfamiliar reader. We refer to Pattyn [2017] for further details about the f.ETISh model, its numerical implementation, and the values of the model parameters.

## 6.2 Thermomechanical ice-sheet model

The f.ETISh model is essentially a two-dimensional computational model. The computational domain is a two-dimensional rectangular domain representing both the ice sheet and surrounding ocean. Here, the computational domain is represented by the open set  $\omega$  and its boundary by  $\partial\omega$  (Figure 6.2). The computational domain is divided into a grounded portion  $\omega_g(t)$  and a floating portion  $\omega_f(t)$ , so that  $\bar{\omega} = \bar{\omega}_g(t) \cup \bar{\omega}_f(t)$ , and the grounding line is given by  $\gamma(t) = \bar{\omega}_g(t) \cap \bar{\omega}_f(t)$ . It should be mentioned that in the f.ETISh model the floating portion  $\omega_f(t)$  not only represents the ice shelves but also an artificial extension of the ice shelves in the open ocean. This artificial extension is represented numerically as a thin layer of sea ice with a thickness  $h_{si}$  of a few metres. As will be discussed in the following, this approach simplifies the treatment of the calving front but results in a discontinuity of the ice thickness and viscosity at the calving front.

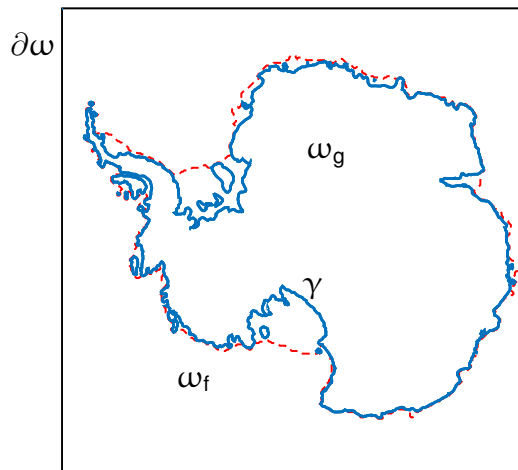


Figure 6.2: Representation of the computational domain  $\omega$ . At any time  $t$ , the ice is grounded in  $\omega_g(t)$  and floating in  $\omega_f(t)$ . The transition line  $\gamma$  (blue line) between  $\omega_g$  and  $\omega_f$  is the grounding line. The calving front (red dashed line) is not tracked explicitly in the f.ETISh model but rather represents a discontinuity line in the floating portion  $\omega_f$ .

The f.ETISh model implements a thermomechanical ice-sheet model derived from the SIA and SSA reduced-order models (see Sections 2.3.1 and 2.3.2). The f.ETISh model solves

essentially for the depth-averaged horizontal velocity field  $\mathbf{v}$  of the ice flow, the evolution of the ice thickness  $h$ , and the evolution of the bedrock elevation  $b$ . Unless otherwise stated, we use the same notations as in Sections 2.3.1 and 2.3.2. In the following, we describe the thermo-mechanical ice-sheet model implemented in the f.ETISH model with a multi-domain formulation in the domains  $\omega_g(t)$  and  $\omega_f(t)$ . Based on the floatation condition, the grounded and floating domains can be expressed as

$$\omega_g(t) = \{\mathbf{x} \in \omega : \rho h(\mathbf{x}, t) > \rho_w(z_{sl} - b(\mathbf{x}, t))\}, \quad \text{for } 0 < t < \tau, \quad (6.1)$$

$$\omega_f(t) = \{\mathbf{x} \in \omega : \rho h(\mathbf{x}, t) < \rho_w(z_{sl} - b(\mathbf{x}, t))\}, \quad \text{for } 0 < t < \tau, \quad (6.2)$$

and the grounding line is expressed as

$$\gamma(t) = \{\mathbf{x} \in \omega : \rho h(\mathbf{x}, t) = \rho_w(z_{sl} - b(\mathbf{x}, t))\}, \quad \text{for } 0 < t < \tau. \quad (6.3)$$

### 6.2.1 Grounded domain

The f.ETISH model determines the depth-averaged horizontal velocity  $\mathbf{v}$  in the grounded domain by using a combination of the SIA and SSA reduced-order models. First, the depth-averaged horizontal velocity  $\mathbf{v}$  is determined by averaging the SIA equation (2.45) over the ice thickness. Considering a depth-independent rheological coefficient  $\bar{A}$ , the depth-averaged horizontal velocity  $\mathbf{v}$  then writes as

$$\mathbf{v} = \mathbf{v}_b - \frac{2\bar{A}}{n+2} (\rho g)^n h^{n+1} \|\nabla_{\mathbf{x}s}\|^{n-1} \nabla_{\mathbf{x}s}, \quad \text{in } \omega_g(t) \text{ for } 0 < t < \tau. \quad (6.4)$$

In the f.ETISH model, the depth-independent rheological coefficient  $\bar{A}$  is given by  $A(\bar{T})$ , where the temperature  $\bar{T}$  is the depth-averaged temperature field. Second, the basal sliding velocity  $\mathbf{v}_b$  in Equation (6.4) is determined from the horizontal conservation-of-momentum equations (2.67a) and (2.67b) in the SSA reduced-order model, that is,

$$2 \frac{\partial}{\partial x} \left( 2\bar{\eta}h \frac{\partial v_x}{\partial x} + \bar{\eta}h \frac{\partial v_y}{\partial y} \right) + \frac{\partial}{\partial y} \left( \bar{\eta}h \frac{\partial v_x}{\partial y} + \bar{\eta}h \frac{\partial v_y}{\partial x} \right) - c_b \|\mathbf{v}\|^{p-1} v_x = \rho g h \frac{\partial s}{\partial x}, \quad (6.5a)$$

$$2 \frac{\partial}{\partial y} \left( 2\bar{\eta}h \frac{\partial v_y}{\partial y} + \bar{\eta}h \frac{\partial v_x}{\partial x} \right) + \frac{\partial}{\partial x} \left( \bar{\eta}h \frac{\partial v_x}{\partial y} + \bar{\eta}h \frac{\partial v_y}{\partial x} \right) - c_b \|\mathbf{v}\|^{p-1} v_y = \rho g h \frac{\partial s}{\partial y}. \quad (6.5b)$$

Thus, the f.ETISH model represents the velocity field in the grounded ice sheet as a linear combination of the depth-averaged horizontal velocity field according to the shallow-ice approximation and the horizontal velocity field according to the shallow-shelf approximation. This kind of model is an example of a so-called hybrid SIA/SSA reduced-order model in which the velocity field writes as a weighted linear combination of the velocity fields according to the SIA and SSA reduced-order models, with more weight given to the SSA reduced-order model for large values of the norm of the SSA velocity field; see, for instance, [Bueler and Brown \[2009\]](#) and [Winkelmann et al. \[2011\]](#). Hybrid SIA/SSA reduced-order models provide the most straightforward way to include both vertical shearing and membrane stresses in the ice-sheet dynamics. In the f.ETISH model, the velocity field is simply expressed as the sum of the SIA and SSA velocity fields, without any need to choose for a weighting function, as proposed in [Winkelmann et al. \[2011\]](#).

The evolution of the ice thickness is determined from the following conservation-of-height equation:

$$\frac{\partial h}{\partial t} + \operatorname{div}_{\mathbf{x}}(h\mathbf{v}) = a_s(T_s), \quad \text{in } \omega_g(t) \text{ for } 0 < t < \tau, \quad (6.6)$$

where the mass balance  $a_b$  at the ice-bedrock is neglected. In the f.ETISH model, the mass balance  $a_s$  at the ice-air interface is expressed as a function of the surface air temperature  $T_s$  (also referred to as the atmospheric temperature in Chapters 7 and 8). Given the expression of the velocity field  $\mathbf{v}$  as a linear combination of the velocity fields according to the SIA and SSA reduced-order models, Equation (6.6) can be interpreted as a nonlinear diffusion-advection equation that is expected to be dominated by diffusion in the interior of the ice sheet and by advection in (fast-flowing) ice streams.

In the f.ETISH model, the thermal model for the temperature field in the grounded ice sheet is derived from Equation (2.54) in the SIA reduced-order model. For  $0 < t < \tau$  and  $\mathbf{x} \in \omega_g(t)$ , the temperature field is determined as the solution to

$$\frac{\partial T}{\partial t} + (\mathbf{v}_d + \mathbf{v}_s) \cdot \nabla_{\mathbf{x}} T + v_z \frac{\partial T}{\partial z} = \kappa \frac{\partial^2 T}{\partial z^2} - \frac{\rho g}{\rho c} (s - z) \nabla_{\mathbf{x}} s \cdot \frac{\partial \mathbf{v}_d}{\partial z}, \quad \text{for } 0 < z < s, \quad (6.7)$$

$$T = T_s, \quad \text{for } z = s, \quad (6.8)$$

$$-k \frac{\partial T}{\partial z} = q_{\text{geo}} - \rho g h \nabla_{\mathbf{x}} s \cdot \mathbf{v}_s, \quad \text{for } z = b, \quad (6.9)$$

where the thermal diffusivity  $\kappa = k/(\rho c)$  and the heat capacity  $c$  of the ice are fixed at a constant value and the surface mass balance at the ice-bedrock interface is neglected. Here,  $\mathbf{v}_d$  is the horizontal component of the velocity field due to vertical shearing solely (deformational velocity),  $\mathbf{v}_s$  the basal sliding velocity, and  $v_z$  the vertical velocity. All three velocities are determined following the SIA reduced-order model; see Equation (2.45) for  $\mathbf{v}_d$ , Equation (2.49) for  $\mathbf{v}_s$ , and Equation (2.47) for  $v_z$ . Introducing the scaled vertical coordinate  $\zeta = (s - z)/h$ ,  $\mathbf{v}_d$  and  $\mathbf{v}_s$  can be expressed as

$$\mathbf{v}_d = -\frac{2}{n+1} \bar{A} (\rho g)^n h^{n+1} (1 - \zeta^{n+1}) \|\nabla_{\mathbf{x}} s\|^{n-1} \nabla_{\mathbf{x}} s, \quad (6.10)$$

$$\mathbf{v}_s = -\frac{1}{c_b^m} (\rho g h)^m \|\nabla_{\mathbf{x}} s\|^{m-1} \nabla_{\mathbf{x}} s, \quad (6.11)$$

while the vertical velocity is approximated as [Hindmarsh, 1999; Pattyn, 2010]

$$v_z = -a_s \left[ \frac{\zeta^{n+2} - 1 + (n+2)(1-\zeta)}{n+1} \right] + (\mathbf{v}_d + \mathbf{v}_s) \cdot \nabla_{\mathbf{x}} b + (1-\zeta) \nabla_{\mathbf{x}} h. \quad (6.12)$$

## 6.2.2 Floating domain

The f.ETISH model determines the depth-averaged horizontal velocity field  $\mathbf{v}$  in the floating domain from the SSA reduction-order model (see Equations (2.72) and (2.73)), that is, at any time  $t$  in  $]0, \tau[$ , the depth-averaged horizontal velocity  $\mathbf{v}$  is determined as the solution to

$$2 \frac{\partial}{\partial x} \left( 2\bar{\eta} h \frac{\partial v_x}{\partial x} + \bar{\eta} h \frac{\partial v_y}{\partial y} \right) + \frac{\partial}{\partial y} \left( \bar{\eta} h \frac{\partial v_x}{\partial y} + \bar{\eta} h \frac{\partial v_y}{\partial x} \right) = \rho g h \frac{\partial s}{\partial x}, \quad \text{in } \omega_f(t), \quad (6.13a)$$

$$2 \frac{\partial}{\partial y} \left( 2\bar{\eta} h \frac{\partial v_y}{\partial y} + \bar{\eta} h \frac{\partial v_x}{\partial x} \right) + \frac{\partial}{\partial x} \left( \bar{\eta} h \frac{\partial v_x}{\partial y} + \bar{\eta} h \frac{\partial v_y}{\partial x} \right) = \rho g h \frac{\partial s}{\partial y}, \quad \text{in } \omega_f(t), \quad (6.13b)$$

with the stress boundary conditions (see Equations (2.80a) and (2.80b))

$$2\bar{\eta}h \left[ \left( 2\frac{\partial v_x}{\partial x} + \frac{\partial v_y}{\partial y} \right) n_x + \frac{1}{2} \left( \frac{\partial v_x}{\partial y} + \frac{\partial v_y}{\partial x} \right) n_y \right] = \frac{1}{2}\rho gh^2 \left( 1 - \frac{\rho}{\rho_w} \right) n_x, \quad \text{on } \partial\omega, \quad (6.14a)$$

$$2\bar{\eta}h \left[ \left( 2\frac{\partial v_y}{\partial y} + \frac{\partial v_x}{\partial x} \right) n_y + \frac{1}{2} \left( \frac{\partial v_x}{\partial y} + \frac{\partial v_y}{\partial x} \right) n_x \right] = \frac{1}{2}\rho gh^2 \left( 1 - \frac{\rho}{\rho_w} \right) n_y, \quad \text{on } \partial\omega. \quad (6.14b)$$

It should be noted that the f.ETISh model implements the stress boundary conditions in Equations (6.14a) and (6.14b) at the edges of the computational domain rather than at the calving front. This approach enables a more readily implementation of these boundary conditions but is expected to generate a less-accurate back stress on the ice sheet as compared to approaches that implement these boundary conditions at the calving front; see, for instance, Winkelmann et al. [2011] for a discussion. Also, this approach raises mathematical and computational issues about the discontinuity of the ice thickness and viscosity in  $\omega_f(t)$ .

The evolution of the ice thickness is determined from the following conservation-of-height equation:

$$\frac{\partial h}{\partial t} + \text{div}_x(h\mathbf{v}) = a_s(T_s) - a_w(T_w) - c_f, \quad \text{in } \omega_f(t) \text{ for } 0 < t < \tau. \quad (6.15)$$

The mass balance at the ice-air interface and the mass balance at the ice-ocean interface are only applied to ice shelves, that is, where the ice thickness exceeds the thickness  $h_{\text{si}}$  of sea ice. In the f.ETISh model, the mass balance  $a_s$  at the ice-air interface and the mass balance  $a_w$  at the ice-ocean interface are expressed as functions of the surface air temperature  $T_s$  and the ocean temperature  $T_w$ , respectively. Given the definition of the floating domain  $\omega_f(t)$  that includes both the ice shelves and their artificial extension in the open ocean, the calving rate  $c_f$  is introduced as a sink term in the conservation-of-height equation and is applied only at the calving front or in the vicinity of the calving front. It should be mentioned that the f.ETISh model does not track the position of the calving front explicitly but rather determines its position based on the ice thickness in the floating domain.

In the f.ETISh model, the temperature field  $T$  in the ice shelf is expressed as an analytical approximate solution to Equation (2.71) with boundary condition  $T = T_s$  at the ice-air interface and boundary condition  $T = T_w$  at the ice-ocean interface. The analytical temperature profile is determined assuming the ice shelf to be at steady state, the absence of horizontal advection and viscous dissipation of heat, constant thermal properties  $c$  and  $k$ , and the vertical velocity to be equal to the surface mass balance  $a_s$ ; see, for instance, Holland and Jenkins [1999] and Pattyn [2010]. Under these assumptions, an analytical expression of the vertical temperature profile is obtained as

$$T(\zeta) = \frac{(T_s - T_w)e^{\beta\zeta} + T_w - T_s e^\beta}{1 - e^\beta}, \quad \text{in } \omega_f(t) \text{ for } 0 < t < \tau, \quad (6.16)$$

where  $\beta = a_s h / \kappa$ ,  $\zeta = (s - z) / h$  is the scaled vertical coordinate, and the temperature  $T_w$  at the ice-ocean interface is expressed as  $T_w = T_{\text{oc}} - 0.12 \times 10^{-3} \rho / \rho_w h$ , with  $T_{\text{oc}}$  the temperature of the ocean at depth of the continental shelf [Maris et al., 2014].

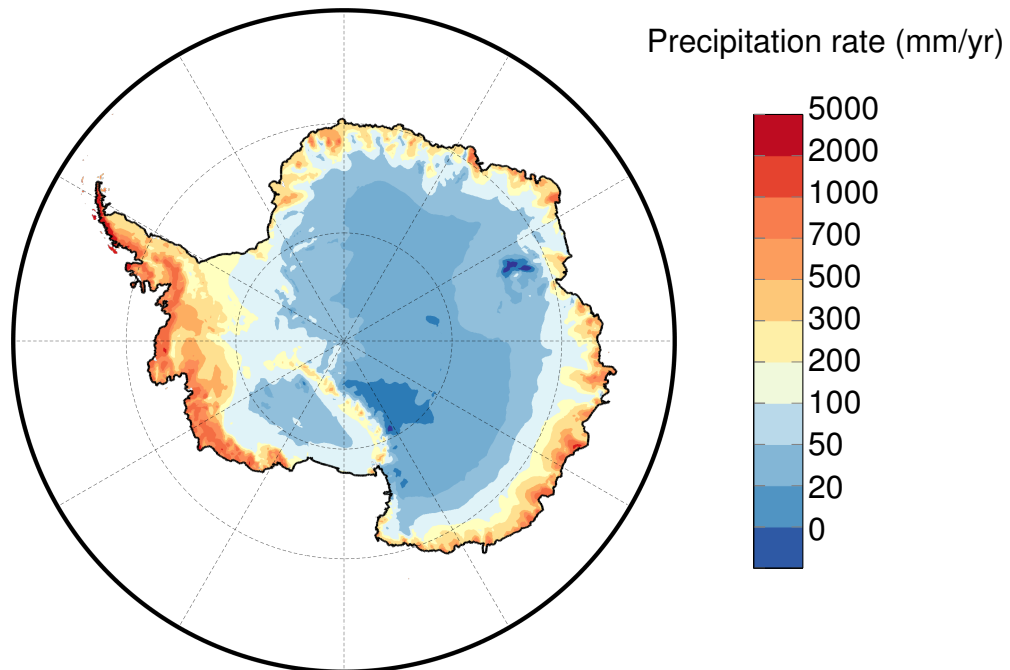


Figure 6.3: Present-day annual precipitation rates from [Van Wessem et al. \[2014\]](#), based on the regional atmospheric climate model RACMO2.

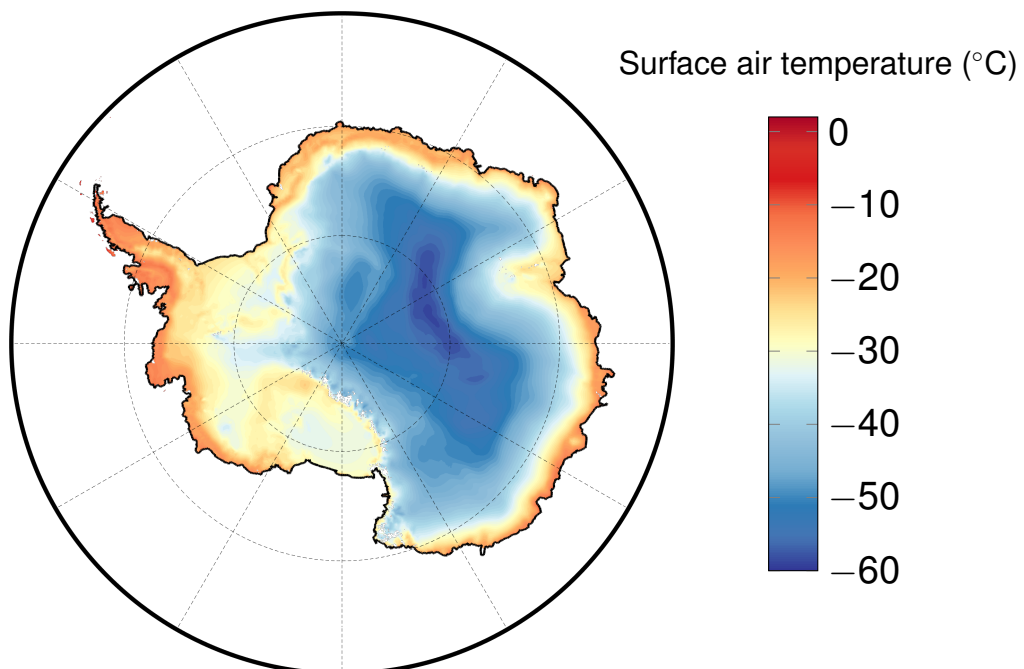


Figure 6.4: Present-day mean annual surface air temperature from [Van Wessem et al. \[2014\]](#), based on the regional atmospheric climate model RACMO2.

## 6.3 Interactions with the Earth system

### 6.3.1 Ice-air interface

The f.ETISH model determines the surface mass balance  $a_s$  and the surface air temperature  $T_s$  by considering changes in the present-day observed precipitation rates (Figure 6.3) and surface air temperature (Figure 6.4). Changes in surface mass balance and surface air temperature are applied in a parameterised way. The parameterisation for changes in surface mass balance accounts for the increase in precipitation with temperature increase [Huybrechts et al., 1998; Pollard and DeConto, 2012a], surface melt via a positive degree-day model [Janssens and Huybrechts, 2000], and surface meltwater percolation and refreezing [Huybrechts and de Wolde, 1999]. The parameterisation for changes in surface air temperature accounts for elevation changes (ice-elevation feedback) and a change in background atmospheric temperature  $\Delta T$  [Huybrechts et al., 1998; Pollard and DeConto, 2012a].

### 6.3.2 Ice-bedrock interface

The f.ETISH model implements the ELRA GIA model (Section 2.4) to determine the evolution of the bedrock in response to glacial isostatic adjustment. Given the initial elevation  $b_0$  of the lithosphere, assumed to be at equilibrium with present-day ice and water loadings, the ELRA GIA model writes as

$$\frac{\partial b}{\partial t} = -\frac{1}{\tau_a}(b - b_0 + w^{\text{eq}}), \quad \text{in } \omega \text{ for } 0 < t < \tau, \quad (6.17)$$

$$b = b_0, \quad \text{in } \omega \text{ at } t = 0, \quad (6.18)$$

where the equilibrium vertical displacement of the lithosphere  $w^{\text{eq}}$  is solution to

$$D_b \Delta_x^2 w^{\text{eq}} + \rho_a g w^{\text{eq}} = p_{\text{load}}, \quad \text{in } \omega, \quad (6.19)$$

with appropriate boundary conditions describing the behaviour of the solution at infinity. Here, the notation  $p_{\text{load}}$  denotes the change in ice and water loadings from the initial configuration and can be expressed as

$$p_{\text{load}} = \rho g (h - h_0) + \rho_w g (h_w - h_{w,0}), \quad (6.20)$$

where  $h_w$  denotes the ocean column thickness and  $h_0$  and  $h_{w,0}$  are the ice thickness and the ocean column thickness at the initial time, respectively. The f.ETISH implements the ELRA GIA model with a spatially-varying flexural rigidity  $D_b$  [Chen et al., 2018] (Figure 6.5) under the assumption that Equation (6.19) holds for a spatially-varying flexural rigidity as a first approximation.

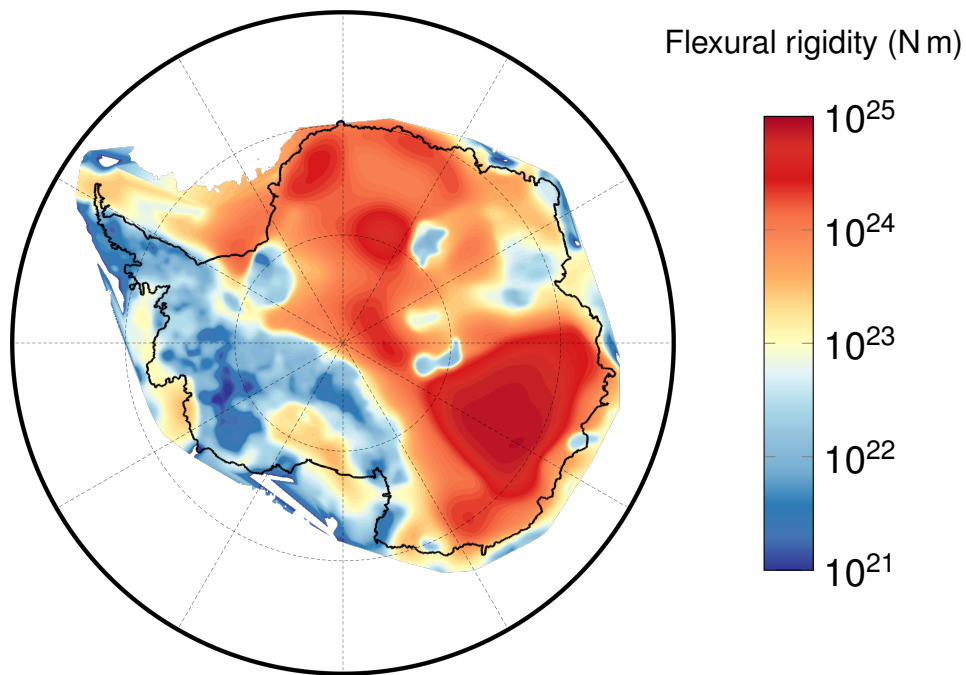


Figure 6.5: Flexural rigidity  $D_b$  of the lithosphere in Antarctica reconstructed from ice thickness, bedrock topography, and terrestrial gravity data [Chen et al., 2018].

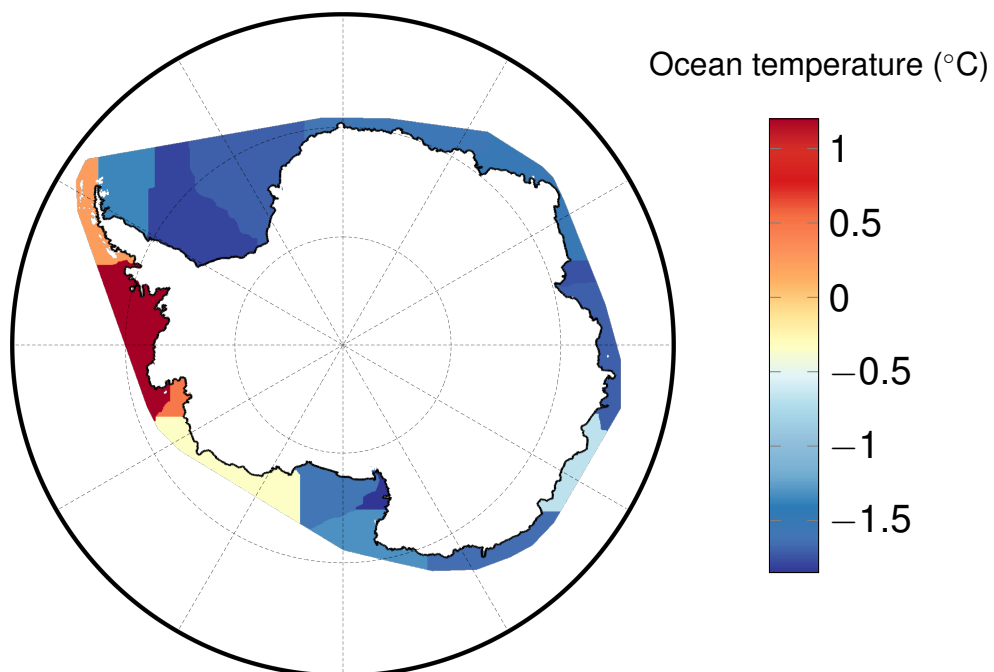


Figure 6.6: Temperature of the ocean water in front of the ice-shelf cavities at depth of the continental shelf [Schmidtke et al., 2014]. The ice sheet, the ice shelves, and the surrounding Southern Ocean are split into drainage basins as defined in Zwally et al. [2012].

### 6.3.3 Ice-ocean interface

In the f.ETISH model, the ocean temperature  $T_{oc}$  on the continental shelf is computed using the following parameterisation:

$$T_{oc} = T_{oc,0} + F_{melt}\Delta T, \quad (6.21)$$

where  $F_{melt}$  is the so-called ocean melt factor that represents the ratio between oceanic and atmospheric temperature changes [Maris et al., 2014; Golledge et al., 2015] and  $T_{oc,0}$  the present-day ocean temperature on the continental shelf determined from observations or numerical simulations [Schmidtko et al., 2014] (Figure 6.6).

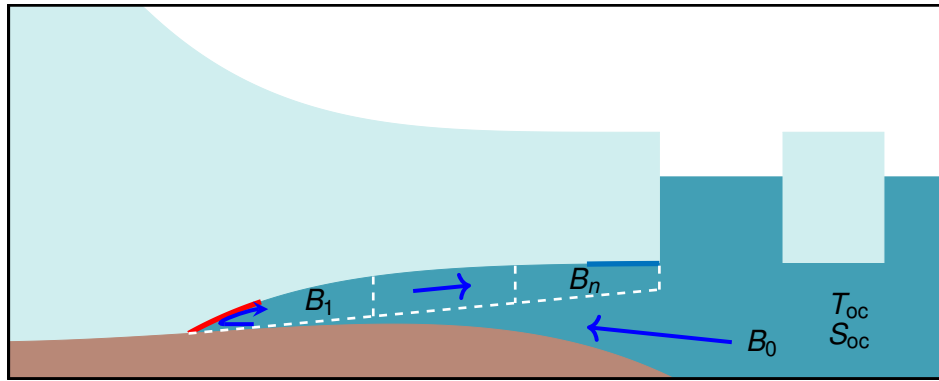


Figure 6.7: Schematic representation of a box model of the ocean circulation in an ice-shelf cavity (based on Reese et al. [2018a]). The ice-shelf cavity is split into  $n$  boxes  $B_1, \dots, B_n$  and box  $B_0$  represents the ocean extended from the ice-shelf cavity to the continental shelf. The box model solves for the transport of heat and salt between the ocean boxes. The overturning flux is driven by density changes through sub-shelf melting. Freshwater influx from melting at the ice-shelf base makes the water buoyant, causing it to rise along the upward slope of the ice shelf. Temperature differences between the ocean temperature in a box and the freezing point at the ice-ocean interface causes the ice shelf to melt (or refreeze). The highest melt rates are generally found near the grounding line and the lowest melt rates or refreezing are generally found near the calving front.

Reliable estimates of the mass balance  $a_w$  at the ice-ocean interface with three-dimensional ocean circulation computational models remain too computationally expensive for simulations of the Antarctic ice sheet on multicentennial-to-millennial time horizons. As an alternative, the mass balance  $a_w$  at the ice-ocean interface can be determined from simple parameterisations based on the ice-shelf depth [Beckmann and Goosse, 2003; Holland et al., 2008; Pollard and DeConto, 2012a; de Boer et al., 2015; Cornford et al., 2016] or from more sophisticated ocean-model couplers that link the ocean temperature at the continental shelf to the mass-balance  $a_w$  at the ice-ocean interface by using box models of the circulation in ice-shelf cavities [Olbers and Hellmer, 2010; Lazeroms et al., 2018; Reese et al., 2018a; Pelle et al., 2019]. In the f.ETISH model, the mass balance  $a_w$  is determined with an ocean-model coupler based on the Postdam Ice-shelf Cavity mOdel (PICO) ocean-model coupler [Reese et al., 2018a]. The PICO ocean-model coupler captures the basic overturning circulation within ice-shelf cavities driven by the “ice pump” mechanism [Lewis and Perkin, 1986]. The intrusion of warm ocean water in the

ice-shelf cavity melts the ice shelf near the grounding line and reduces the water salinity. Since the ocean temperatures are generally close to the local freezing point, changes in sea-water density are primarily controlled by salinity. For this reason, freshwater influx into the ocean makes sea water buoyant. Buoyant water then rises along the upward slope of the ice shelf and progressively cools down. The strength of this overturning circulation depends on the heat content of water masses on the continental shelf: the warmer these masses, the stronger the overturning circulation and the resulting melting. Figure 6.7 illustrates the mechanism of the overturning circulation within ice-shelf cavities based on a box-model representation.

### 6.3.4 Calving

A common approach to modelling calving in ice-sheet models is to rely on parameterisations based on continuum damage mechanics. In this framework, the calving rate  $c_f$  is usually obtained from the large-scale ice flow based on the horizontal strain-rate tensor  $D$ , which measures the overall expansion of the ice flow. Levermann et al. [2012] suggested that the first-order large-scale kinematic contribution to calving is proportional to the product of the eigenvalues of  $D$ , for both eigenvalues being positive; see also Martin et al. [2011] and Winkelmann et al. [2011]. Both eigenvalues coincide approximatively with the strain rates in directions along and transversal to the ice flow and positive eigenvalues denote expansion in these directions, which tend to promote ice-shelf weakening and thereby calving. Pollard and DeConto [2012a] proposed a similar representation of the calving rate  $c_f$ , in which the overall expansion of the ice flow is measured as a function of the divergence of the ice flow rather than the eigenvalues of the tensor  $D$ . The f.ETISH model implements the approach in Pollard and DeConto [2012a] to compute the calving rate; see also Pattyn [2017] and Section 8.2.2.4 for further discussions.

## 6.4 Model initialisation

### 6.4.1 Initial conditions

The initial state of the ice sheet is defined by present-day ice-sheet geometry, bedrock topography, velocity field, and temperature field. Present-day ice-sheet geometry and bedrock topography are given by datasets such as Bedmap2 [Fretwell et al., 2013] or Bedmachine [Morlighem et al., 2019]; see Figures 3.1 and 6.8. The velocity field is given by datasets such as Rignot et al. [2011]; see Figure 3.2. The initial ice-sheet temperature field is estimated as either the steady-state temperature field at the initial time or the temperature field at the end of the inversion procedure for the basal sliding coefficient (see Section 6.4.3).

### 6.4.2 Input data

Input data include the geothermal heat flux  $q_{\text{geo}}$ , present-day surface mass balance  $a_{\text{s},0}$  and mean annual surface air temperature  $T_{\text{s},0}$ , present-day ocean temperature  $T_{\text{oc},0}$  at the continental shelf, ocean salinity  $S_{\text{oc}}$  at the continental shelf, and the flexural rigidity  $D_{\text{b}}$  of the lithosphere. Datasets include Shapiro and Ritzwoller [2004], Purucker [2013], An et al. [2015] (Figure 6.9), and Martos et al. [2017] for the geothermal heat flux; Van Wessem et al. [2014, 2018], Agosta et al. [2019], and Souverijns et al. [2019] for present-day surface mass balance and mean annual surface air temperature; Schmidtke et al. [2014] for present-day ocean temperature and salinity; and Chen et al. [2018] for the flexural rigidity of the lithosphere.

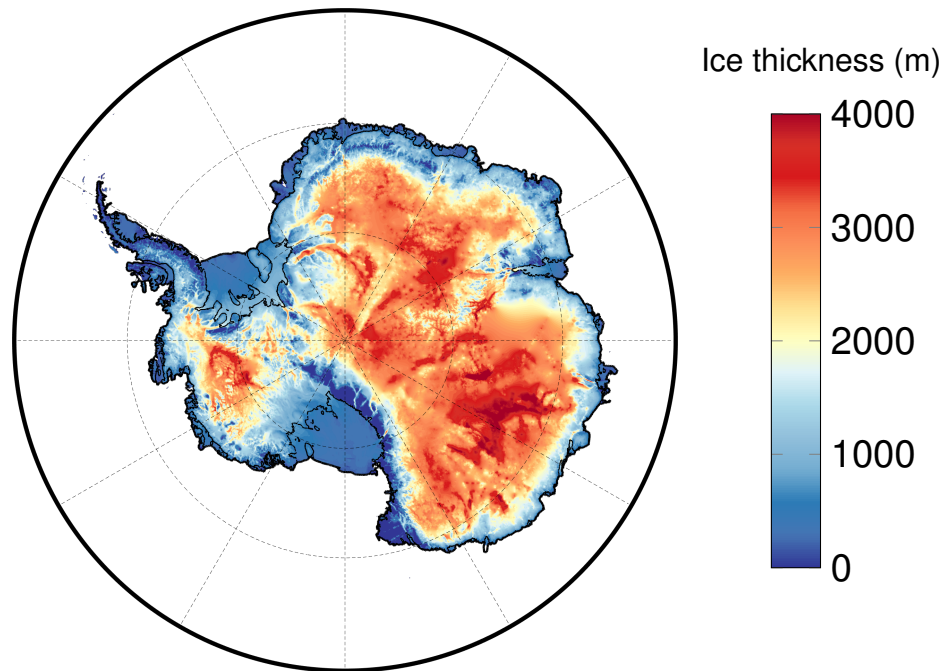


Figure 6.8: Present-day ice thickness [Fretwell et al., 2013].

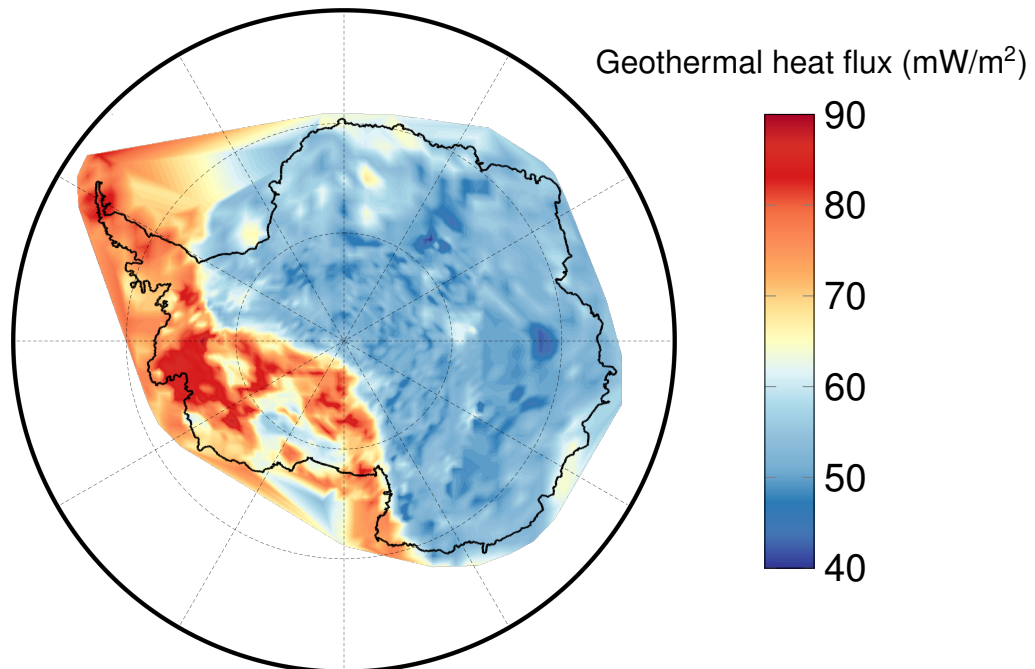


Figure 6.9: Geothermal heat flux from An et al. [2015], based on the 3D shear velocity model AN1-S.

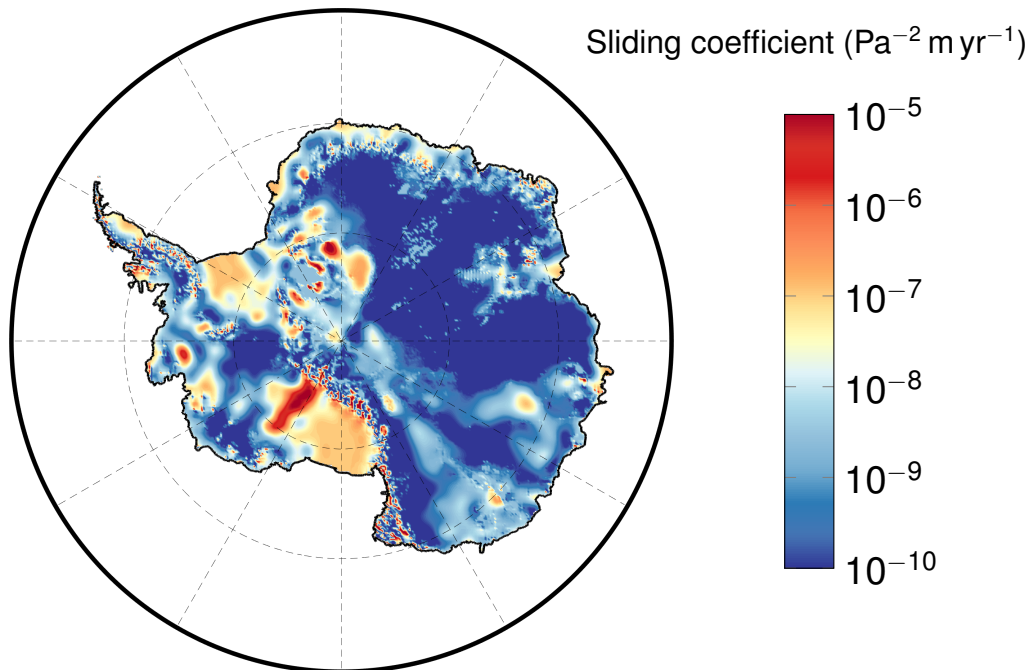


Figure 6.10: Optimised basal sliding coefficient  $A_b$  using the fixed-point iteration scheme by [Pollard and DeConto \[2012b\]](#). The friction law is Weertman's friction law with  $m = 2$  and the ice-flow dynamics is solved using only the SIA reduced-order model.

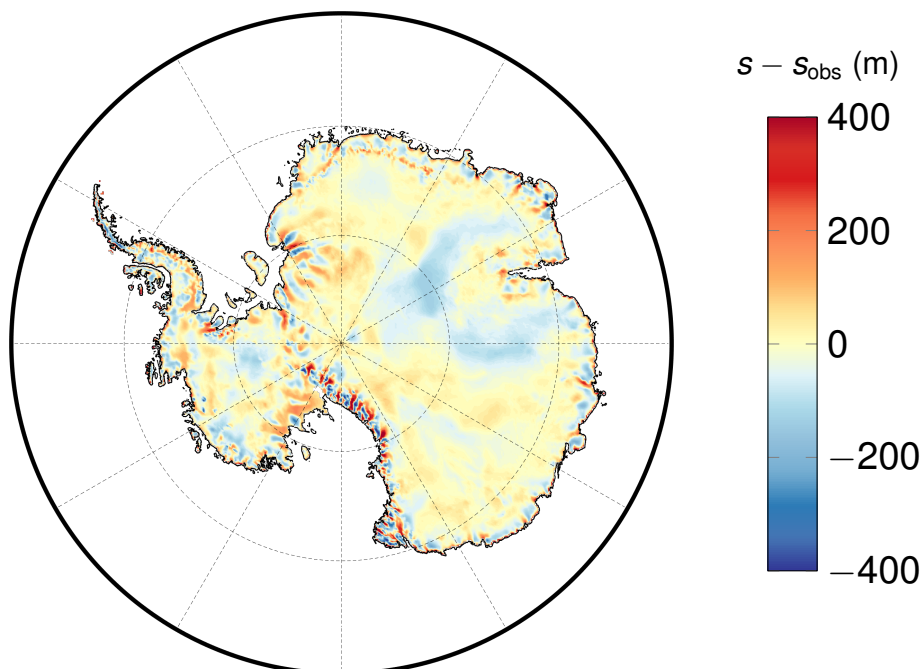


Figure 6.11: Difference between predicted and observed surface elevations.

### 6.4.3 Inversion of the basal sliding coefficient

The basal sliding coefficient  $A_b = c_b^{-m}$  is obtained by solving an inverse problem that seeks to match the observed present-day ice-sheet surface while assuming that the ice sheet is in steady state. The f.ETISH model implements this inverse problem based on the fixed-point iteration scheme by [Pollard and DeConto \[2012b\]](#). At each iteration of the algorithm, the ice-sheet model is run forward in time (with fixed grounding line) until a new steady state is reached. Then, the predicted basal sliding coefficient  $A_b^{(i)}$  at iteration  $i$  is adjusted as

$$A_b^{(i+1)} = A_b^{(i)} \times 10^{f^{\text{misfit}}(s^{(i)} - s_{\text{obs}})}, \quad (6.22)$$

where  $s_{\text{obs}}$  is the observed surface elevation of the ice sheet and  $f^{\text{misfit}}$  is a “misfit” function chosen such that the iteration corrects the predicted basal sliding coefficient in order to match the simulated steady-state surface elevation  $s^{(i)}$  with observations. Intuitively, Equation (6.22) increases sliding where the predicted surface elevation is higher than the observed surface elevation so as to increase the velocity field locally and make the surface elevation at steady state lower, and conversely, decreases sliding where the predicted surface elevation is lower than the observed surface elevation so as to decrease the velocity field locally and make the surface elevation at steady state higher. The algorithm stops when there are no more significant differences between the predicted surface elevations at two successive iterations. Figure 6.10 shows the value of the optimised basal sliding coefficient after a forward integration of 100 000 years. The misfit function is taken as  $(s^{(i)} - s_{\text{obs}})/h_{\text{inv}}$ , with  $h_{\text{inv}} = 2000$  m a scaling constant, and the basal sliding coefficient is updated every  $\Delta t_{\text{inv}} = 1000$  years. At the end of the algorithm, the misfit between the predicted and observed surface elevations is small in the interior of the ice sheet where small values of the basal sliding coefficient are found and the misfit is generally the highest around the coastline where the highest values of the basal sliding coefficient are found (Figure 6.11). We refer the reader to [Pollard and DeConto \[2012b\]](#) and [Pattyn \[2017\]](#) for further discussions about the efficiency of this fixed-point iteration scheme for the inversion of the basal sliding coefficient and to [Bernales et al. \[2017\]](#) for possible improvements.

## 6.5 Numerical implementation

In the f.ETISH model, the discretisation of space is based on a finite-difference discretisation scheme on two-dimensional rectangular finite-difference grids and the discretisation of time is implicit. The heat equation, the conservation-of-momentum equations, the conservation-of-height equation, and the GIA model are solved independently at each time step (weak coupling), as depicted in Figure 6.13. The f.ETISH model introduces a (binary) mask array to distinguish between the grounded domain and the floating domain. This mask is used to specify that an operation must be performed only at the grid points that are either grounded or floating (masked array assignment), for instance, basal friction is applied only at the grid points that are grounded. The mask array is updated at each time step based on the floatation criterion. The conservation-of-momentum equations of the SSA reduced-order model are discretised on two different staggered Arakawa C grids [[Arakawa and Lamb, 1977](#)] (Figure 6.12) and a fixed-point iteration method is used to solve the nonlinearity in the equations. The solution to Equation (6.19) in the GIA model is expressed as an integral superposition by means of the Green’s function of Equation (6.19), which can be written in terms of the Kelvin function of zeroth order; see discussion

in Section 2.4. The heat equation (6.7) is discretised vertically using irregularly spaced layers, with a minimum layer thickness at the bottom, because the highest variability in the vertical temperature occurs close to the bed. The deformational velocity  $v_d$ , its vertical gradient, and the vertical velocity  $v_z$  in the heat equation in the grounded domain are approximated using shape functions [Hindmarsh, 1999; Pattyn, 2017]. Finally, we discuss in the next section the numerical treatment of the migration of the grounding line in the f.ETISh model.

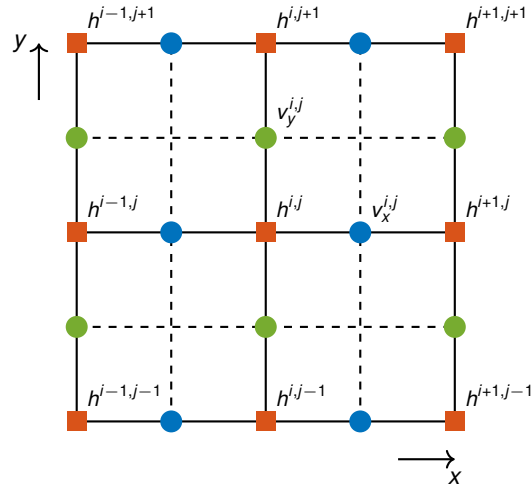


Figure 6.12: Staggered finite-difference grids used in the f.ETISh model. The basic grid is the grid for the ice thickness (shown with orange squares). The velocity field is discretised on two different staggered Arakawa C grids (shown with blue circles for  $v_x$  and green circles for  $v_y$ ).

### 6.5.1 Implementation of grounding-line flux parameterisation

Reduced-order ice-sheet models (based on the SSA and hybrid SSA/SIA reduced-order models) that implement the transmission conditions (2.101) are generally unable to capture the migration of the grounding line properly unless they resolve the transition zone around the grounding line at sufficiently fine resolution [Docquier et al., 2011; Pattyn et al., 2012]. Such resolutions are generally not feasible for large-scale and long-term simulations of the Antarctic ice sheet. As an alternative, Pollard and DeConto [2009] proposed to account for the migration of the grounding line at coarse resolution by applying the grounding-line flux condition in Equation (2.107) as an internal boundary condition following a heuristic rule. For a one-dimensional computational domain, this heuristic rule goes as follows (see Figure 6.14): if the ice flux  $q_g$  at the grounding line derived from Equation (2.107) is greater than the modelled ice flux  $q_i$  at the last grounded point  $x_i$  on the finite-difference grid, then  $q_g$  is imposed at  $x_i$ ; otherwise  $q_g$  is imposed at the first floating point  $x_{i+1}$ . The subgrid position  $x_g$  of the grounding line is determined by interpolating linearly the quantity  $h + \rho_w/\rho(z_{sl} - b)$  between  $x_i$  and  $x_{i+1}$  and setting it to zero. Then, the ice thickness  $h_g$  at the grounding line is also determined by interpolating linearly the ice thickness between  $x_i$  and  $x_{i+1}$ . Benchmark experiments [Docquier et al., 2011; Pattyn et al., 2012, 2013] showed that the implementation of this heuristic rule allowed to reproduce the migration of the grounding line and its steady-state behaviour [Schoof, 2007b] at coarse resolution for the SSA and hybrid SSA/SIA reduced-order models.

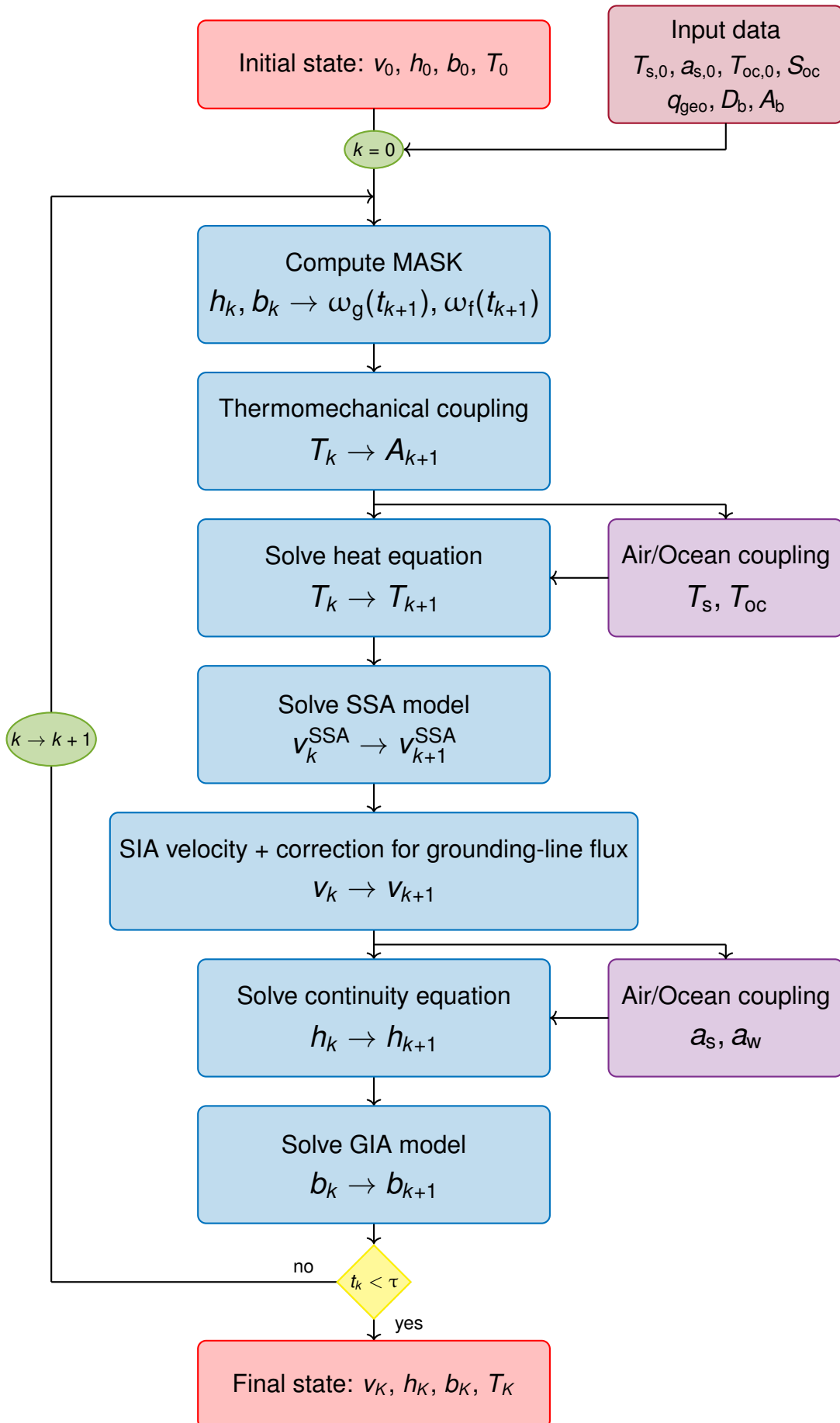


Figure 6.13: Algorithm flowchart of the f.ETISH model.

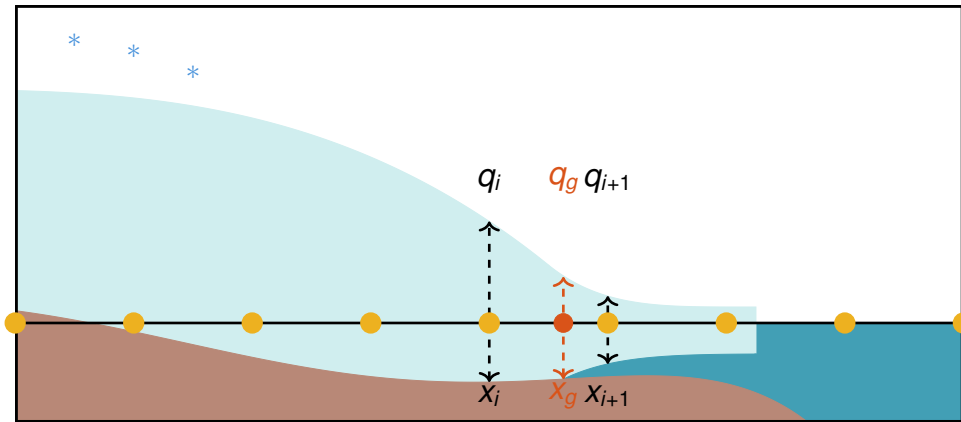


Figure 6.14: Illustration of the fixed-grid heuristic rule (adapted from Pollard and DeConto [2009]). The SSA reduced-order model is solved on the whole computational domain at the grid points. The velocity field is then corrected following a heuristic rule: if the ice flux  $q_g$  at the grounding line derived from Equation (2.107) is greater than the modelled ice flux  $q_i$  at the last grounded point  $x_i$  on the grid, then  $q_g$  is imposed at  $x_i$ ; otherwise  $q_g$  is imposed at the first floating point  $x_{i+1}$ .

The f.ETISH model implements an extension of the heuristic rule by Pollard and DeConto [2009] to two-dimensional computational domains [Pollard and DeConto, 2009, 2012b], even though the implications of such an extension are not fully understood. For two-dimensional computational domains, the ice flux  $\mathbf{q}$  is decomposed into a component  $q_x$  in the  $x$ -direction and a component  $q_y$  in the  $y$ -direction. The heuristic rule by Pollard and DeConto [2009] is applied equally in the  $x$ - and  $y$ -directions on the two Arakawa C grids for  $v_x$  and  $v_y$ , respectively.

Finally, the implementation in the f.ETISH model of the grounding-line flux parametrisation in Equation (2.107) involves a so-called buttressing factor [Pollard and DeConto, 2012a; Patyn, 2017] that accounts for back stress at the grounding line due to pinning points and lateral shearing. For a flowline ice-sheet model, this buttressing factor is determined by evaluating the longitudinal stress just downstream of the grounding line. For two-dimensional computational domains, the buttressing factor for the  $x$ - and  $y$ -directions is determined by evaluating the longitudinal stress along the  $x$ - and  $y$ -directions, respectively.

## 6.6 Chapter summary

In this chapter, we discussed the use of essential ice-sheet models for large-scale and long-term simulations of the Antarctic ice sheet. Essential ice-sheet models reduce the complex physics of ice-sheet dynamics to essential (or characteristics) mechanisms through the use of reduced-order models and appropriate parameterisations. For this reason, essential ice-sheet models are particularly attractive for large-scale and long-term simulations of the Antarctic sheet and uncertainty quantification; see Chapters 7 and 8.



# Illustration and performance evaluation of uncertainty quantification methods on ice-sheet model problems

*Throughout this thesis, we seek on the one hand to apply existing uncertainty quantification methods to problems in glaciology and on the other hand, motivated by problems in glaciology, to develop new methods for uncertainty quantification. With this perspective, this chapter aims at illustrating and evaluating the performance of both the existing and the newly developed uncertainty quantification methods discussed in Chapters 4 and 5 on model problems in glaciology using the f.ETISh model. In Section 7.1, with the aim of providing probabilistic projections of the AIS contribution to sea-level rise, we illustrate and evaluate the performance of existing methods for the propagation of uncertainties discussed in Section 4.3. In Section 7.2, with the aim of providing probabilistic projections of the retreat of the grounded portion of the Antarctic ice sheet, we illustrate and evaluate the performance of the multifidelity method for the estimation of confidence regions for random excursion sets proposed in Chapter 5. In Section 7.3, with the aim of assessing the most significant sources of uncertainty in inducing uncertainty in the projections of the AIS contribution to sea-level rise, we illustrate and evaluate the performance of existing and newly developed methods for global sensitivity analysis discussed in Section 4.4.2. Results in Section 7.2 and Section 7.3 are based respectively on illustrations in the manuscript [Bulthuis et al., 2019b] and the co-authored manuscript [Arnst et al., 2019], both currently under review.*

## 7.1 Probabilistic projections of future sea-level rise

### 7.1.1 Model problem

In order to illustrate the UQ framework with the purpose of predicting the AIS contribution to sea-level rise, we set up a model problem using the f.ETISh model. In this model problem, we simulate the response of the AIS over the next 700 years, starting from its present-day configuration, under a simplified forcing scenario in which the atmospheric and ocean temperatures increase linearly in the first 300 years and then remain constant in the next 400 years. The use of

such a simplified forcing scenario is justified by the fact that we do not seek here to provide new probabilistic projections and insight into the evolution of the AIS but seek only to demonstrate our proposed methodology. An increase in atmospheric temperature has an impact on the surface mass balance through an increase in precipitation and surface melting, as represented by the dependence of the surface mass balance  $a_s$  at the ice-air interface on the surface air temperature, or simply the atmospheric temperature  $T_s$  in Equations (6.6) and (6.15). In our model problem, as we set it up using the f.ETISh model, an increase in ocean temperature has an impact on the mass balance underneath the ice shelves through an increase in the strength of the overturning ocean circulation in ice shelf cavities, as represented by the dependence of the surface mass balance  $a_w$  at the ice-ocean interface on the ocean temperature  $T_w$  in Equation (6.15). We let the forcing scenario be defined as a function of two input parameters. The first input parameter is the change in atmospheric temperature  $\Delta T_s$  after 300 years, for which we will consider values in the range between 1 and 10 K. To allow the reader to appreciate this range of values, the lower and upper bounds are respectively in the range of values for the projected atmospheric temperature increase after 300 years for the strongly mitigated RCP 2.6 scenario and the warm RCP 8.5 scenario [Collins et al., 2013]. The second input parameter is the ratio between the change in ocean temperature and the change in atmospheric temperature, that is, the ocean melt factor in Equation (6.21), for which we will consider values in the range between 0.1 and 0.9; the lower and upper bound account respectively for a slowdown or an amplification of the overturning ocean circulation in ice shelf cavities. Please note that our choice of a wide range of values for the atmospheric and oceanic forcings was also motivated by a desire to trigger significant variability in the retreat of the grounded portion of the AIS and thus obtain a challenging model problem for the proposed methodology. Except for the forcing scenario, the setup of our model problem is similar to the setup of the nominal simulation in Bulthuis et al. [2019a] (reported in Chapter 8), and we also refer the reader to Bulthuis et al. [2019b] where this setup is used as an illustration for the construction of confidence sets for the retreat of the grounded portion of the Antarctic ice sheet (see also Section 7.2 where this illustration is reported).

We use a square grid with a length of 5 600 km in each direction with a spatial resolution of 16 km and we use a time step of 0.05 year. The computing time of a single simulation on two threads of a SkyLake 2.3 GHz CPU of the Lemaitre 3 cluster (CÉCI clusters, F.R.S-FNRS & Walloon Region, Belgium) is approximately 8 hours.

### 7.1.2 Quantity of interest

As the predicted quantity of interest, we consider the contribution of the Antarctic ice sheet to global mean sea level over the next 700 years. Let the quantity

$$\text{VAF}(t) = \int_{D_g(t)} h(\mathbf{x}, t) + \frac{\rho_w}{\rho} \min(0, z_{sl} - b(\mathbf{x}, t)) d\mathbf{x} \quad (7.1)$$

be the so-called volume above floatation [Bindenschadler et al., 2013; Nowicki et al., 2013]. The volume above floatation represents the potential total volume of ice that might contribute to global sea-level change. Equation (7.1) considers that mass loss from floating ice shelves does not contribute to global sea-level change owing to Archimedes' principle. When the ice is grounded above sea level ( $b(\mathbf{x}) \geq z_{sl}$ ), all the ice column has the potential to contribute to global sea-level change. On the contrary, when the ice is grounded below sea level ( $b(\mathbf{x}) < z_{sl}$ ),

only the ice thickness in excess of the maximum floating ice thickness has the potential to contribute to global sea-level change. In Equation (7.1), the ice thickness in excess of the maximum floating ice thickness is determined from Archimedes' principle, assuming the ice sheet to be in vertical hydrostatic equilibrium.

The AIS contribution to global mean sea level at any time  $0 < t < \tau$  is computed by converting the change in volume above floatation into global sea-level equivalent (SLE) as follows:

$$\frac{\rho}{\rho_w A_{oc}} (\text{VAF}(t) - \text{VAF}(0)) \equiv \Delta\text{GMSL}(t), \quad (7.2)$$

where  $A_{oc}$  is the ocean area ( $A_{oc} \approx 3.62 \cdot 10^8 \text{ km}^2$ ) and  $\Delta\text{GMSL}$  is the change in global mean sea level (GMSL) stemming from the evolution of the Antarctic ice sheet.

### 7.1.3 Sources of uncertainty

In our model problem, we consider the two aforementioned input parameters to be uncertain. We represent the change in atmospheric temperature after 300 years with a uniform random variable  $W_1$  with values in  $[1, 10]$  K. And we represent the ratio between the ocean and atmospheric temperature changes with a uniform random variable  $W_2$  with values in  $[0.1, 0.9]$ . We let  $W_1$  and  $W_2$  be statistically independent and for the sake of convenience, unless explicitly noted, we rescale the random variables such that  $W_1$  and  $W_2$  are uniformly distributed in the interval  $[0, 1]$ . Similarly to our use of a simplified forcing scenario, our use of such a simplified representation of input uncertainty is justified by the fact that we do not seek to provide new probabilistic projections and insight into the contribution of the Antarctic ice sheet to sea-level rise but we seek only to demonstrate the UQ methodology.

Figure 7.1 shows the mapping from the uncertain input parameters to  $\Delta\text{GMSL}$ , also referred to as the parameters-to-projection relationship in this manuscript. Large values of the uncertain input parameters leads essentially to an increased contribution of the Antarctic ice sheet to sea level as a result of increased ocean temperature and subsequent enhanced sub-shelf melting, which is only partially compensated by increased snowfall. Both uncertain input parameters display strong interaction effects on  $\Delta\text{GMSL}$  because the increase in ocean temperature in Equation (6.21) depends on the product of  $w_1$  and  $w_2$ . Figure 7.1 also suggests that the mapping from the uncertain input parameters to  $\Delta\text{GMSL}$  is polluted by the presence of small noise in the output of the computational ice-sheet model. We attribute this computational noise in particular to discretisation errors, algorithmic errors, and iterative procedures in the model. In general, the signal-to-noise ratio only represents of a few percents; see the discussion in Section 7.1.5.

### 7.1.4 Propagation of uncertainties: Monte Carlo method

We use the Monte Carlo sampling method as described in Section 4.3.1 to estimate the mean and the standard deviation of the uncertain quantity of interest. We use for  $\nu$  values up to 5 000. Figure 7.2 shows the convergence of the Monte Carlo estimates for the mean and the standard deviation. We can observe that reasonably converged estimates are obtained after a value for  $\nu$  of about 3 000 for the mean and of about 4 000 for the standard deviation although more than

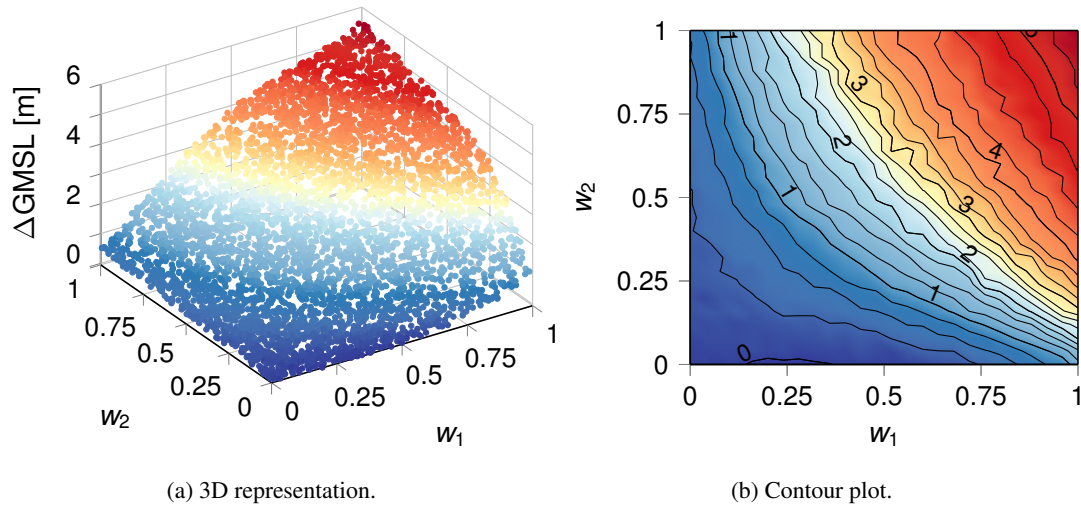


Figure 7.1: Representation of the mapping from the uncertain input parameters to  $\Delta\text{GMSL}$ .

5 000 samples would be necessary to further increase the accuracy of the estimates. The results obtained with  $\nu = 5\,000$  are  $m^\nu = 2.0980$  m and  $\sigma^\nu = 1.5693$  m.

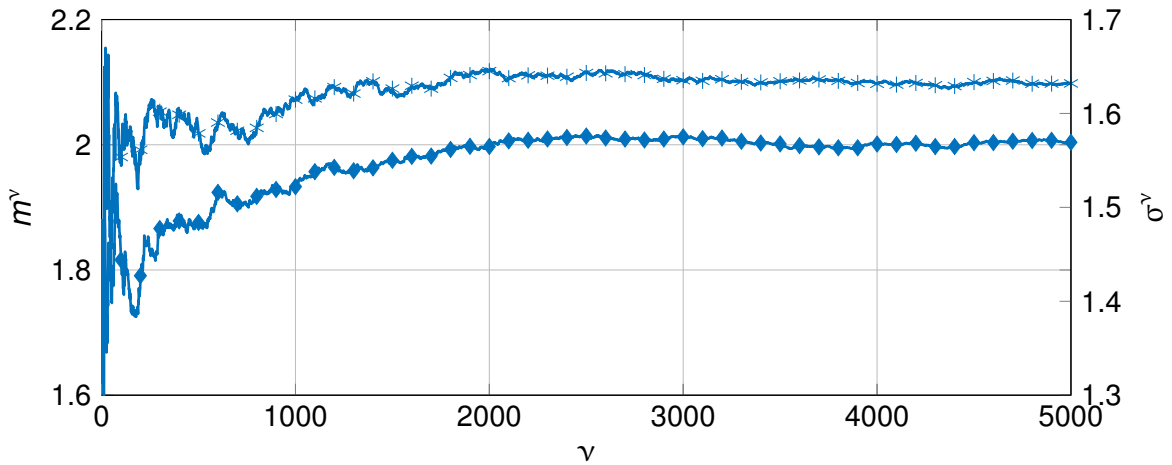


Figure 7.2: Convergence analysis: convergence of Monte Carlo estimate of the mean (asterisk) and standard deviation (diamond) for  $\Delta\text{GMSL}$  (m) after 700 years as a function of  $\nu$ . The aggregate computing time for the 5 000 evaluations of the computation model was 40 000 hours.

### 7.1.5 Propagation of uncertainties: Surrogate models

As for the numerical example in Section 4.5.1.2, we consider four different kinds of surrogate model in order to reduce the number of evaluations of the computational model to estimate the statistical descriptors of  $\Delta\text{GMSL}$ . We consider surrogate models based on polynomial chaos expansions whose polynomial chaos coordinates are computed using either spectral pro-

jection with fully tensorised scaled Gauss–Legendre quadrature integration rules or ordinary least-squares regression (Section 4.3.2.1), and surrogate models based on Gaussian-process regression with either Gaussian covariance or Matérn 5/2 covariance function (Section 4.3.2.2).

The existence of noisy data precludes a traditional convergence analysis of the approximation error as carried out in Section 4.5.1.2. In particular, surrogate models based on high-order polynomial chaos expansions may tend to overfit the data. In addition, the accuracy of the surrogate model may be very sensitive to the experimental design. Figures 7.3 and 7.4 show a convergence analysis of the surrogate-based estimates of the mean and the standard deviation of  $\Delta\text{GMSL}$  as a function of the number of samples  $\lambda$  in the experimental design. We considered surrogate models based on polynomial chaos expansions of order 3. Except for surrogate models based on a polynomial chaos expansion using spectral projection, we generated the experimental design by sampling without replacement  $\lambda$  samples from the  $\nu = 5\,000$  Monte Carlo samples and we replicated the experiment 200 times to assess the effect of stochastic variations in the generation of the experimental design. To account for the estimation error in Monte Carlo estimation, we also represented a 95%-confidence interval for the Monte Carlo estimate with  $\nu = 5\,000$  samples by using a bootstrap sampling method [Efron and Tibshirani, 1993], in which we resampled with replacement the  $\nu = 5\,000$  Monte Carlo samples in order to generate new estimates of the mean and the standard deviation to obtain estimates of the statistical descriptors of the Monte Carlo estimator. The mean value over the 200 experiments of the surrogate-based estimates falls within the bootstrap 95%-confidence interval for each size  $\lambda$  of the experimental design, except for the estimates for the standard deviation based on Gaussian-process regression with a Gaussian covariance function and small size of the experimental design. Globally, Figures 7.3 and 7.4 suggest that surrogate models can provide sufficiently accurate estimates of the mean and the standard deviation of  $\Delta\text{GMSL}$  for sufficiently large experimental designs.

Figure 7.5 represents the mapping from the uncertain input parameters to the quantity of interest as determined with the surrogate models. We use a Latin hypercube sampling scheme to generate the same experimental design for the surrogate model based on a polynomial chaos expansion using ordinary least-squares regression and the surrogate models based on Gaussian-process regression. These surrogate models provide a sufficiently accurate representation of the response of the computational model (Figure 7.1(b)), while fitting the noise in the data. By contrast the aggregate computing time of 40 000 hours for the evaluation of the 5 000 Monte Carlo samples, the aggregate computing time is only of 288 hours and 512 hours for an experimental design of size  $\lambda = 36$  and  $\lambda = 64$ , respectively.

To measure of the accuracy of a surrogate model in the presence of noisy data, we follow the approach in Iskandarani et al. [2016] and we consider the relative local error as

$$e(\mathbf{w}^{(k)}) = \frac{|\tilde{f}(\mathbf{w}^{(k)}) - f(\mathbf{w}^{(k)})|}{\max(f(\mathbf{w}^{(k)})) - \min(f(\mathbf{w}^{(k)}))}, \quad 1 \leq k \leq \nu, \quad (7.3)$$

where  $\mathbf{w}^{(k)}$  refers to a Monte Carlo sample in the parameter space and  $f$  and  $\tilde{f}$  denote the computational model and the surrogate model, respectively. Figure shows the relative local error between the values of the quantity of interest determined with the computational ice-sheet model and its approximation with a surrogate model for the 5 000 Monte Carlo samples used in Section 7.1.4. Results are shown for two sizes of the experimental design ( $\lambda = 36$  and  $\lambda = 64$ ).

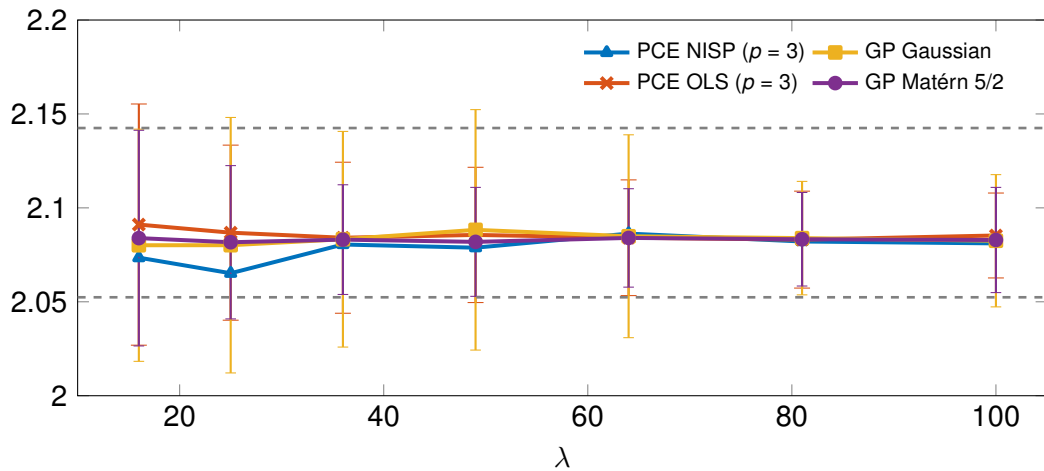


Figure 7.3: Convergence analysis: convergence of surrogate-based estimates of the mean of  $\Delta\text{GMSL}$  as a function of the number of samples  $\lambda$  in the experimental design. The points represent the mean estimate over the 200 experiments and the error bars are the 95%-confidence intervals. The dashed lines represent the bootstrap 95%-confidence interval based on Monte Carlo sampling with  $\nu = 5000$  samples.

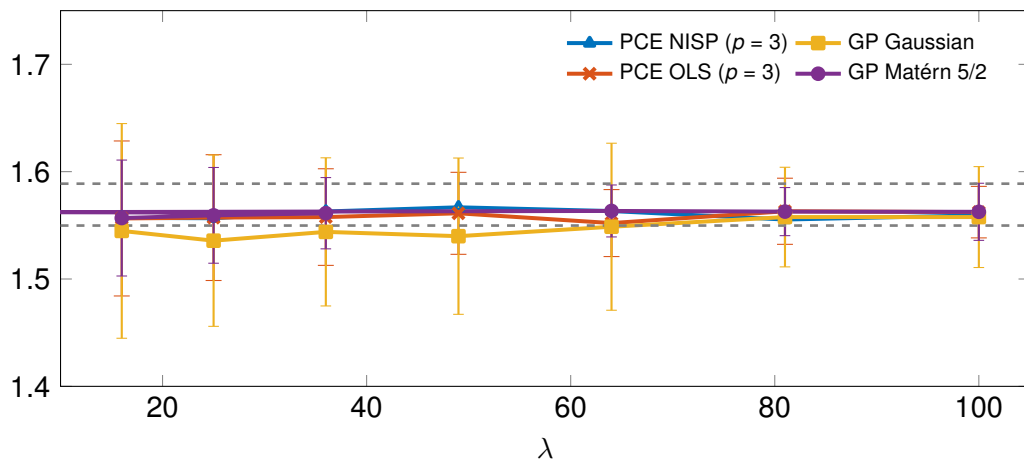


Figure 7.4: Same as Figure (7.3) but for the standard deviation of  $\Delta\text{GMSL}$ .

Red lines indicate the 95%-percentile relative local error in order to judge the magnitudes of the 5% largest errors. For each surrogate model in Figure 7.6, the 95%-percentile relative local error is less than 5%, which suggests that the signal-to-noise ratio is of a few percents. The 95%-percentile relative local error is generally lower for the largest experimental design. In this illustration, Figure 7.6 suggests that surrogate models based on Gaussian-process regression handle noise more efficiently than surrogate models based on polynomial chaos expansions although the lowest 95%-percentile relative local error is observed for a surrogate model based on a polynomial chaos expansion of order 5 with spectral projection.

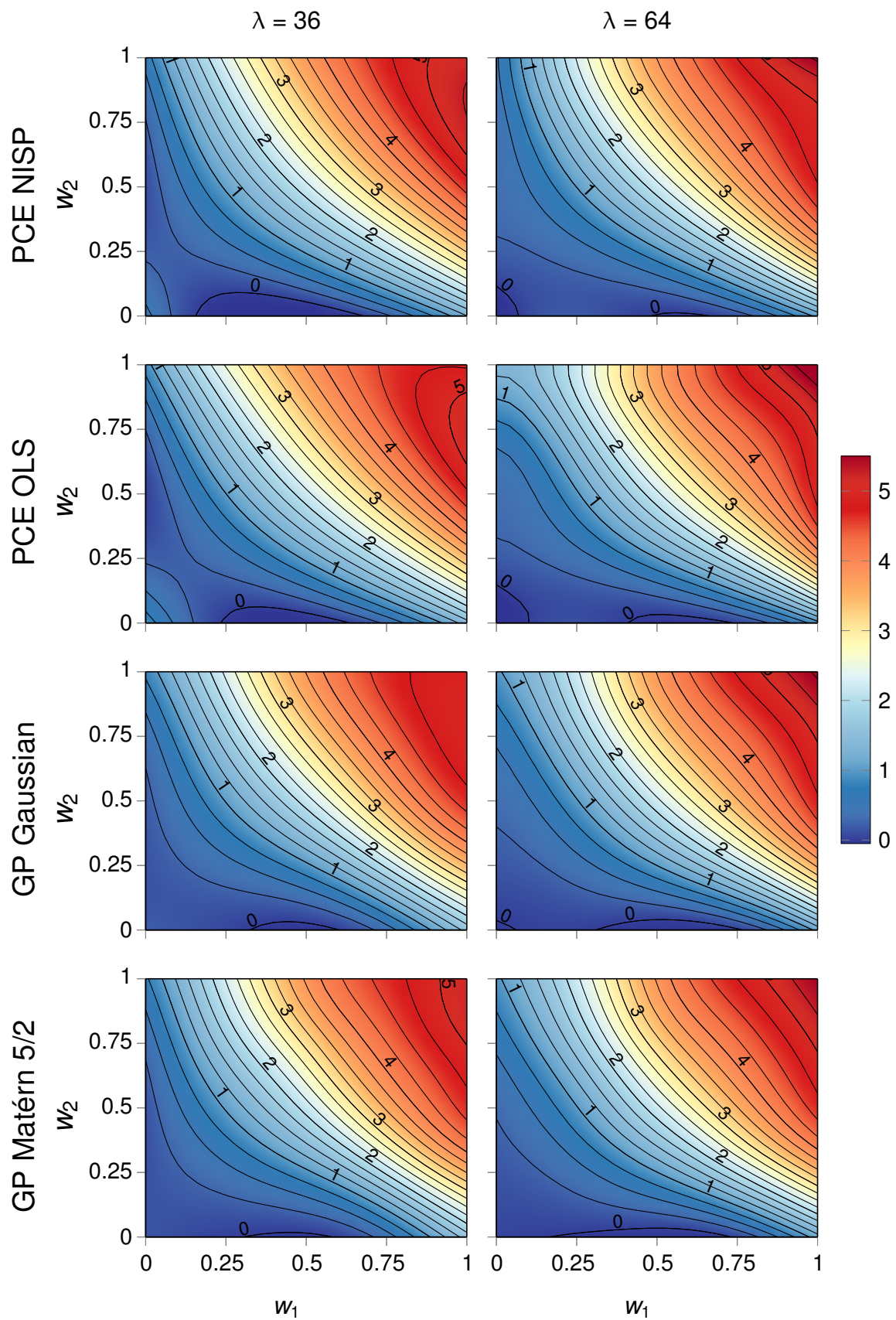


Figure 7.5: Comparison of surrogate models of the mapping between the uncertain input parameters and  $\Delta\text{GMSL}$ . The columns correspond to different sizes of the experimental design. Polynomial chaos expansions are of order 3 for  $\lambda = 36$  and of order 5 for  $\lambda = 64$ .

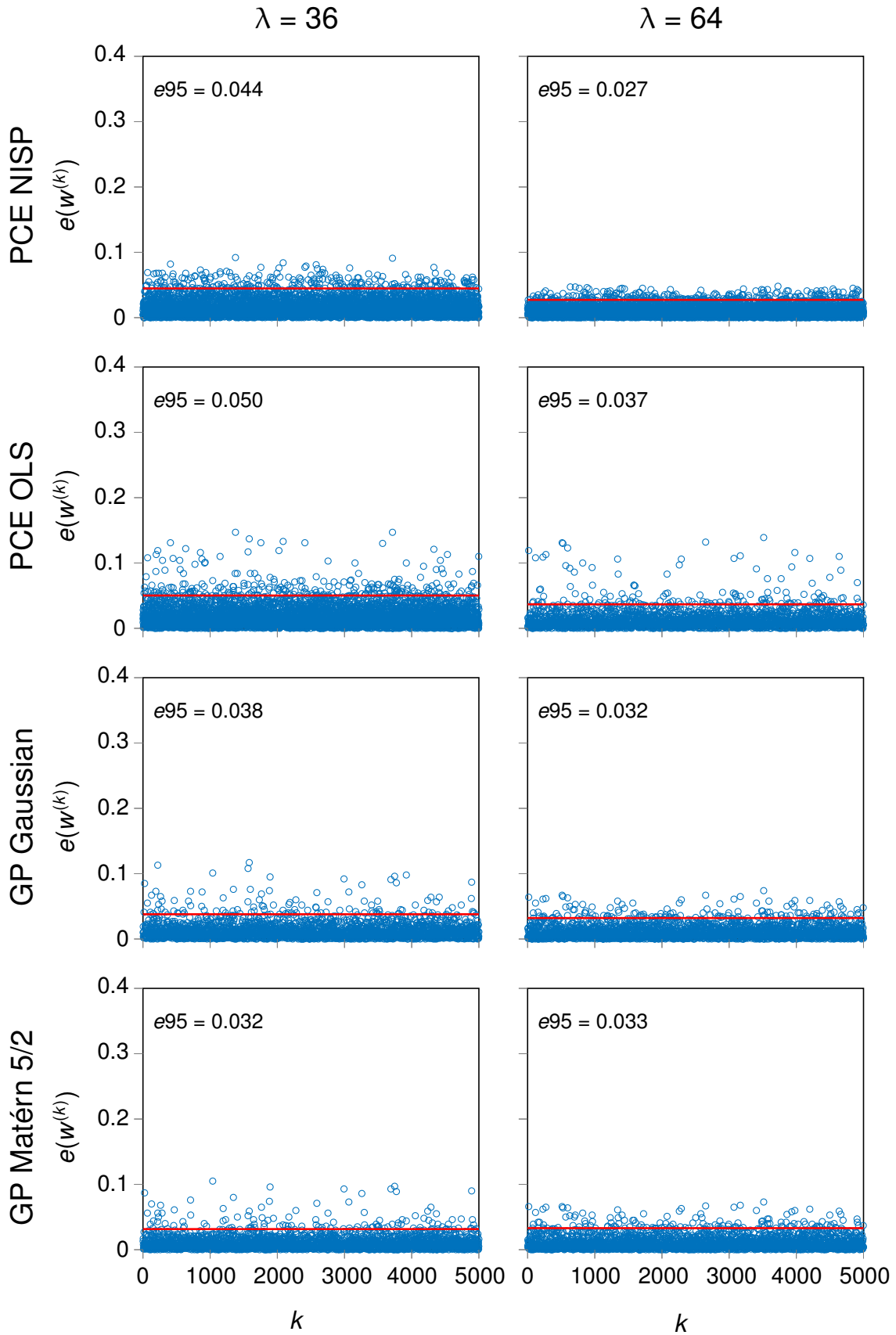


Figure 7.6: Blue points indicate for each Monte Carlo sample the relative local error between the values of the quantity of interest determined with the computational ice-sheet model and its approximation with a surrogate model. The horizontal red lines indicate the 95%-percentile error  $e_{95}$ . Polynomial chaos expansions are of order 3 for  $\lambda = 36$  and of order 5 for  $\lambda = 64$ .

Figure 7.7 compares the kernel density estimate of the probability density function of the change in global mean sea level obtained by using Monte Carlo sampling ( $\nu = 5\,000$ ) with the kernel density estimates obtained with the surrogate models. We observe that the probability density function of the uncertain quantity of interest is bimodal. This bimodality in the probability density function is determined by the behaviour of the West Antarctic ice sheet, with values of the uncertain input parameters that can trigger a limited retreat of the West Antarctic ice sheet or a complete collapse of the West Antarctic ice sheet ( $\sim 3\text{--}3.5$  m sea-level equivalent) in addition to a partial retreat of the Wilkes basin (Figure 7.9) in East Antarctica ( $\sim 0.5\text{--}1$  m sea-level equivalent). High-end estimates ( $5\text{--}6$  m sea-level equivalent) are due to a more significant retreat of the Wilkes basin that can only be triggered for the highest values of the uncertain input parameters. For an experimental design of size  $\lambda = 36$ , the surrogate model based on a polynomial chaos expansion using spectral projection faces difficulties in detecting the largest mode. For an experimental design of size  $\lambda = 64$ , the kernel density estimates obtained with the surrogate models are all bimodal and of similar accuracy.

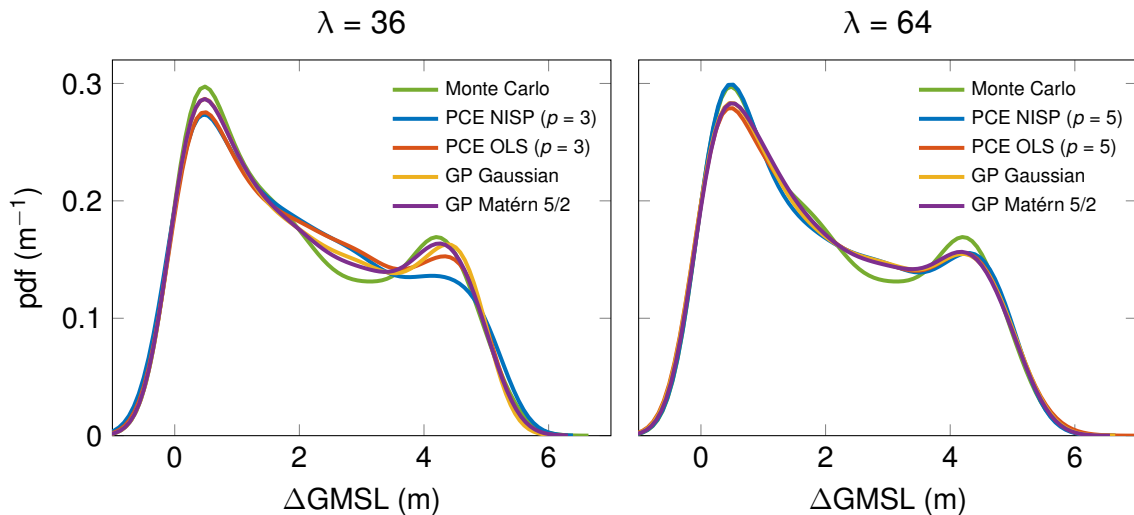


Figure 7.7: Comparison of surrogate-based kernel density estimates of the probability density function of the uncertain quantity of interest. Results are for experimental designs of size  $\lambda = 36$  and  $\lambda = 64$ .

### 7.1.6 Sea-level rise projections

Propagation of uncertainty can serve to determine time series for the projected contribution of the Antarctic ice sheet to sea level with uncertainty ranges. In Figure 7.8(a), we estimated the median AIS contribution to sea-level rise over the period 2000–2700 as well as the 33–66% and 5–95% probability intervals using Monte Carlo estimation with  $\nu = 5\,000$  samples.

In order to reduce the computational time of Monte Carlo simulation, we also determined the median AIS contribution to sea-level rise and the probability intervals using surrogate models. For each instant of analysis, we fitted to the experimental design a surrogate model, which we then used to evaluate the quantiles of  $\Delta\text{GMSL}$  by running the surrogate model with an ensemble

of  $10^6$  independent and identically distributed samples from the parameter space. The experimental design is of size  $\lambda = 36$  and was built by using a Latin hypercube sampling scheme. Figures 7.8(b)–(d) show the resulting probabilistic projections for a surrogate model based on a polynomial chaos expansion of order 3 using ordinary least-squares regression and two surrogate models based on Gaussian-process regression. Comparison between Figure 7.8(a) and Figures 7.8(b)–(d) suggest that surrogate models can provide accurate probabilistic projections at only a small fraction of the computing time of the Monte Carlo sampling method.

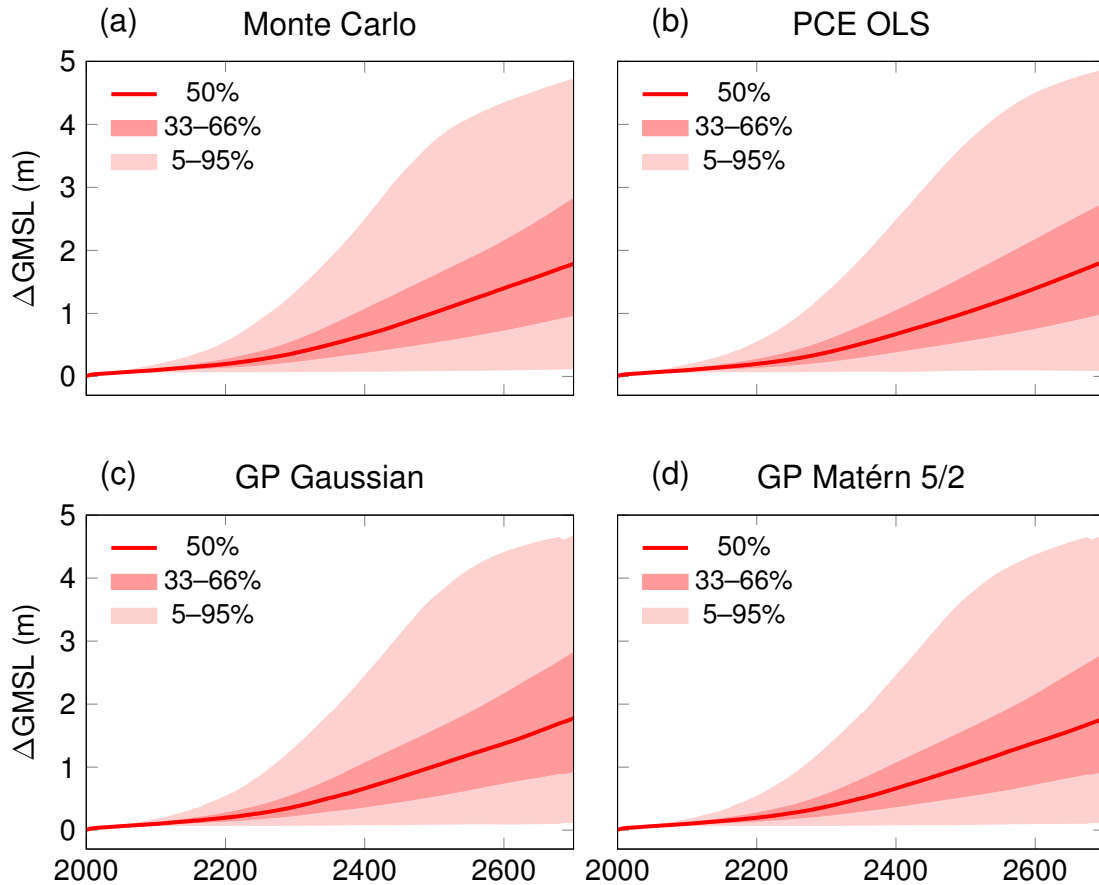


Figure 7.8: Comparison of probabilistic assessment of the AIS contribution to sea level from 2000 to 2700 using different UQ methods (Monte Carlo, PCE of order 3 with OLS, GP with Gaussian covariance function, and GP with Matérn 5/2 covariance function).

### 7.1.7 Propagation of uncertainty: Discussion

Propagation of uncertainty using surrogate models provides an efficient way to alleviate the computing time of computational ice-sheet models for Monte Carlo sampling. We pointed out that the presence of noise in the data stemming from numerical noise and errors precludes a traditional analysis of the approximation error via a convergence analysis. We refer to [Iskandarani et al. \[2016\]](#) for a discussion about surrogate modelling in the presence of noisy data. In general, polynomial chaos expansions using ordinary least-squares regression and surrogate models

based on Gaussian-process regression handle numerical noise more efficiently than polynomial chaos expansions using spectral projections. Moreover, high-order polynomial chaos expansions may suffer from overfitting and may not be adequate in the presence of noise. We also showed that surrogate-based estimates could be very sensitive to the size and choice of the experimental design. Small experimental designs may lead to large stochastic variations in surrogate-based estimates. Given a sufficiently large experimental design, we showed that all kinds of surrogate model provide estimates of similar accuracy.

## 7.2 Probabilistic assessment of grounded-ice retreat

The results in this section are presented in the manuscript [Bulthuis et al. \[2019b\]](#). We use the same model problem and the same uncertain parameters as in Section 7.1.1.

### 7.2.1 Quantity of interest

As the predicted quantity of interest, we consider the grounded portion of the Antarctic ice sheet at time  $\tau = 700$  yr. Let the so-called height above floatation

$$y(\mathbf{x}, t) = h(\mathbf{x}, t) + \frac{\rho_w}{\rho}(z_{sl} - b(\mathbf{x}, t)) \quad (7.4)$$

be the solution quantity of the computational ice-sheet model. When the bedrock is below sea level, the height above floatation represents the ice thickness in excess of floatation; thus, the height above floatation is positive for grounded ice and negative for floating ice. The grounded portion of the Antarctic ice sheet at time  $\tau = 700$  yr writes in terms of the height above floatation as

$$D_g = \left\{ \mathbf{x} \in D : y(\mathbf{x}) = h(\mathbf{x}) + \frac{\rho_w}{\rho}(z_{sl} - b(\mathbf{x})) \geq 0 \right\} \text{ for } t = \tau. \quad (7.5)$$

Thus, the grounded portion of  $D$  is determined as the superlevel set of the height above floatation for the threshold 0. Please note that similarly, we may define the floating portion  $D_f$  of the Antarctica ice sheet as the sublevel set of the height above floatation for the threshold 0 and the grounding line  $\Gamma$  as the level set of the height above floatation for the threshold 0. Figure 7.9 illustrates these grounded and floating portions for the present-day configuration of the Antarctic ice sheet.

Figure 7.10 illustrates the evolution of the grounded portion and the grounding line as a function of time for  $\Delta T_a = 8.5$  K and  $\Delta T_o/\Delta T_a = 0.84$ . We observe a limited retreat of the grounding line in the first 200 years, followed by a retreat of the grounding line in the WAIS, especially in the Amundsen Sea sector and in Siple Coast, in the next 200 years. After 700 years, the WAIS has almost completely collapsed as a consequence of a MISI, while vulnerable marine sectors, such as the Wilkes sector, in East Antarctica are undergoing a significant retreat.

### 7.2.2 Sources of uncertainty

We adopt the same probabilistic characterisation of the uncertain parameters as in Section 7.1.3. Figure 7.11 shows the grounded portion for the minimum, mean, and maximum values of the uncertain input parameters (see also Figure 7.12). We observe a very limited retreat of the grounding line for the minimum values, an ongoing retreat of the grounding line in the Amundsen Sea

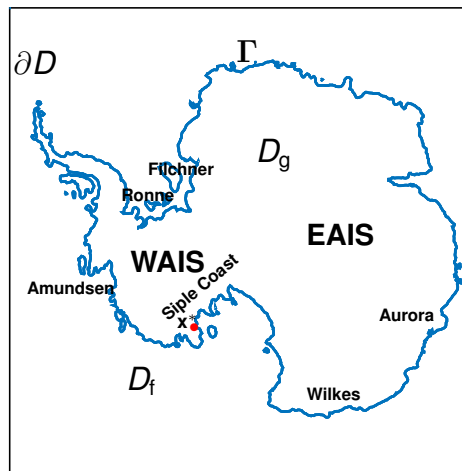


Figure 7.9: Present-day configuration of the Antarctic ice sheet with key geographic sectors in bold type. The ice is grounded on the bedrock in  $D_g$  and floating in  $D_f$ . The separation line  $\Gamma$  between  $D_g$  and  $D_f$  is the grounding line. **WAIS** is the West Antarctic ice sheet and **EAIS** is the East Antarctic ice sheet.

(a)  $t = 200$  yr

(b)  $t = 400$  yr

(c)  $t = 700$  yr

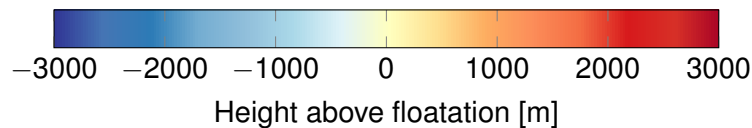
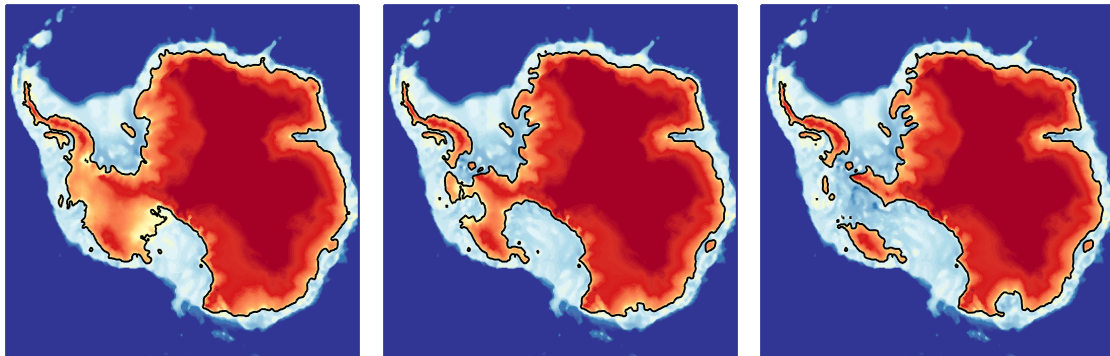


Figure 7.10: Illustration of a simulation with  $\Delta T_a = 8.5$  K and  $\Delta T_o/\Delta T_a = 0.84$ . Height above floatation at time (a)  $t = 200$  yr, (b)  $t = 400$  yr, and (c)  $t = 700$  yr. The grounded domain is the set of locations where the height above floatation is larger than 0. The black line is the grounding line.

and Ronne sectors and in Siple Coast for the mean values, and an almost complete collapse of the WAIS and a retreat of the Wilkes sector for the maximum values.

Upon representing the two uncertain input parameters of the computational model with the

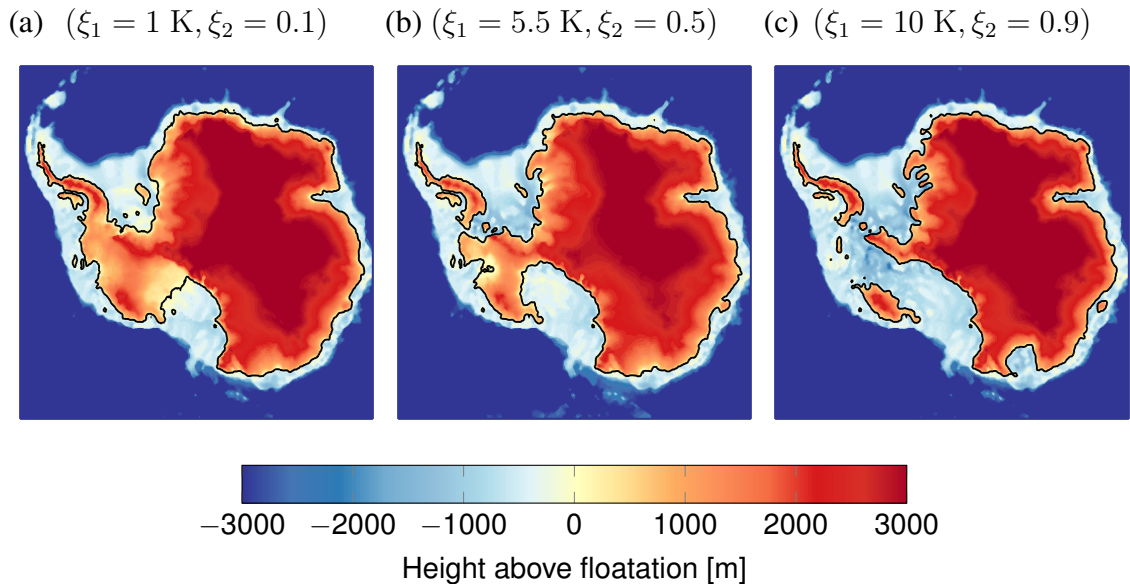


Figure 7.11: Height above floatation for the (a) minimum, (b) mean, and (c) maximum values of the uncertain input parameters at time  $\tau = 700$  yr. The grounded domain is the set of locations where the height above floatation is larger than 0. The black line is the grounding line.

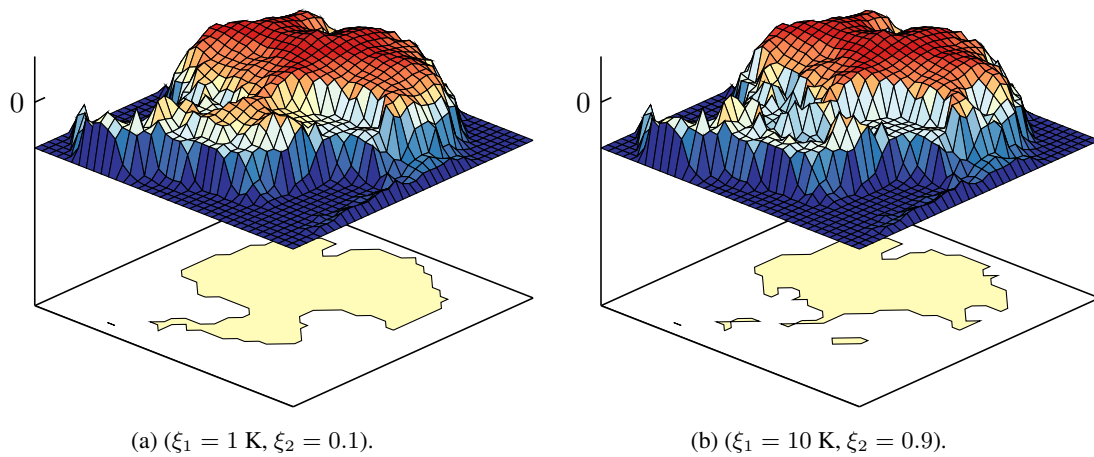


Figure 7.12: Three-dimensional representation (on a coarser grid) of the height above floatation for the (a) minimum and (b) maximum values of the uncertain input parameters at time  $\tau = 700$  yr. The grounded domain is the set of locations where the height above floatation is larger than 0.

aforementioned random variables, the predicted height above floatation becomes the random field  $\{Y(\mathbf{x}), \mathbf{x} \in D\}$ . We are interested in its positive excursion set

$$\mathcal{E}_0^+ = \{\mathbf{x} \in D : Y(\mathbf{x}) \geq 0\}. \quad (7.6)$$

For several confidence levels  $\alpha$ , we will seek an inner confidence set  $C_{0^+, \alpha}^{\text{in}}$  for  $\mathcal{E}_0^+$ . This inner confidence set  $C_{0^+, \alpha}^{\text{in}}$  may be interpreted as the set in which, with a probability of at least  $\alpha$ , all locations remain covered with grounded ice. It may also be interpreted as the set to within which, with a probability of at least  $\alpha$ , the grounded portion does not retreat with a probability of at least  $\alpha$ .

Following the approach of Section 5.6, we consider a partitioning of the computational domain and define the excursion sets and confidence sets with reference to this partitioning. Here, the partitioning is taken as a square tessellation of the finite-difference grid points and the representative points are the grid points. The spatial discretisation used in the simulations leads to a partitioning into 123 201 subsets.

### 7.2.3 Membership function

We first generated an ensemble of 500 i.i.d. samples of the uncertain input parameters, from which we deduced the corresponding ensemble of samples of the height above floatation using the computational model. Then, we approximated the pointwise probability density functions of the random field using the kernel density estimation method. Subsequently, we determined the statistical descriptors of the random field from the kernel density estimates. Finally, we evaluated the membership functions defined in (5.24)–(5.26) using the statistical descriptors thus obtained. Figure 7.13 illustrates these membership functions. We present results for all three membership functions to allow us to comment on the impact of the choice of the membership function on the methodology, for instance, the impact of the membership function on  $\chi$ . In Figure 7.13, both membership functions  $T_2$  and  $T_3$  exhibit a similar behavior, which may be explained by a similar dependence of (5.27) and (5.28) on the coefficient of variation of the random field. The larger difference between  $T_1$  and the two other membership functions may be explained by the non-Gaussianity and bimodality of the random field in regions vulnerable to instabilities as will be shown in Section 7.2.5.1.

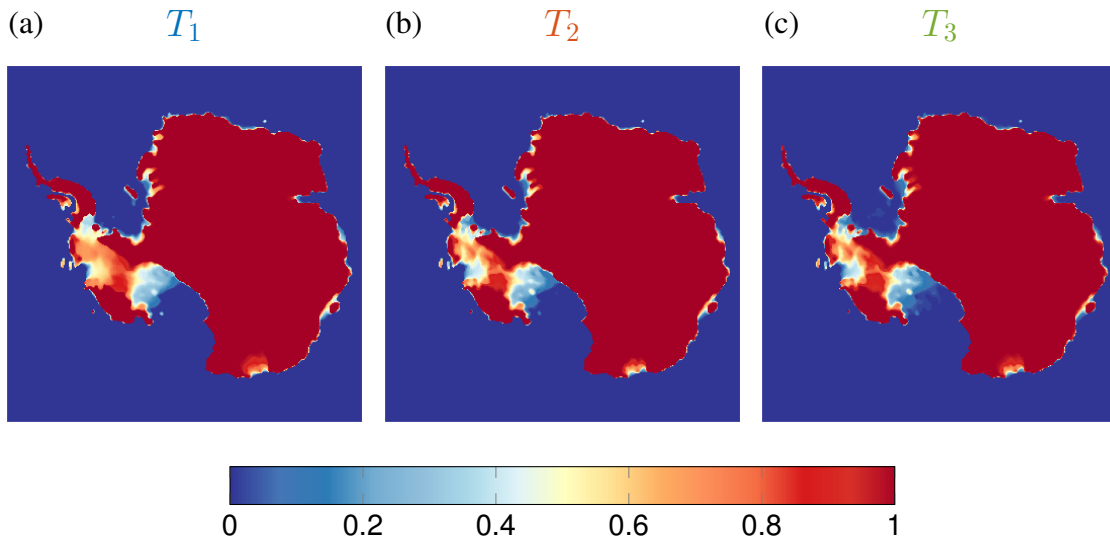


Figure 7.13: Membership function: (a)  $T_1$ , (b)  $T_2$ , and (c)  $T_3$ .

### 7.2.4 Quantile estimation: Monte Carlo method

As discussed in Section 5.7, we may expect the quantile estimation problem to be more computationally challenging than the estimation of the membership function and we require a higher accuracy of the estimate. Hence, we determined the value of the optimal threshold  $\rho^*$  with a larger ensemble of 5000 i.i.d. samples. Owing to the partitioning,  $\chi$  is a discrete random variable, denoted here explicitly by  $\chi^h$ , with values in a set with a cardinality of 2815 for  $T_1$ , of 2407 for  $T_2$ , and of 2440 for  $T_3$ . The number of values that  $\chi^h$  takes is two orders of magnitude smaller than the number of representative points because most representative points are either inside the excursion set or outside the excursion set almost surely and a significant retreat of the grounding line only happens in vulnerable marine sectors. As a consequence of the number of values that  $\chi^h$  takes being sufficiently large and these values being sufficiently dense, the difference between the distribution function and the mid-distribution function is small, with the magnitude of the discontinuities of the distribution function of the order of  $10^{-4}$  to  $10^{-3}$ . However, both the spatial and the stochastic discretization limit the accuracy in determining confidence sets.

Figure 7.14 shows the sample mid-distribution function for the three membership functions, from which we estimated the corresponding mid-quantiles for the confidence levels 0.5, 0.9, and 0.99. In Figure 7.15, we conducted a numerical convergence analysis to examine the convergence of the Monte Carlo estimates of the mid-quantiles with respect to the number of samples. Figure 7.15 suggests that using 5 000 samples is sufficient to ensure a reasonable convergence of the Monte Carlo estimates. Figure 7.15 also suggests that reasonable convergence of the Monte Carlo estimates is reached for a number of samples larger than 2 500.

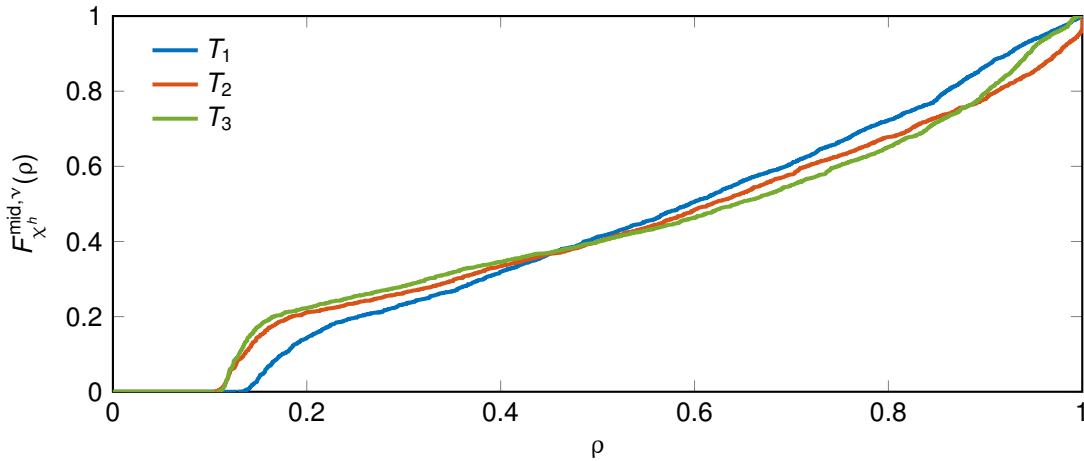


Figure 7.14: Sample mid-distribution functions ( $\nu = 5\,000$ ).

Table 7.1 shows the Monte Carlo estimates of the optimal threshold  $\rho^*$  for the confidence levels 0.5, 0.9, and 0.99. We also determined the area of the resulting confidence sets. Table 7.1 suggests that using  $T_1$  leads to larger (more optimal) confidence sets than the two other membership functions. For each confidence level  $\alpha$ , the inner confidence set for  $T_1$  is smaller than

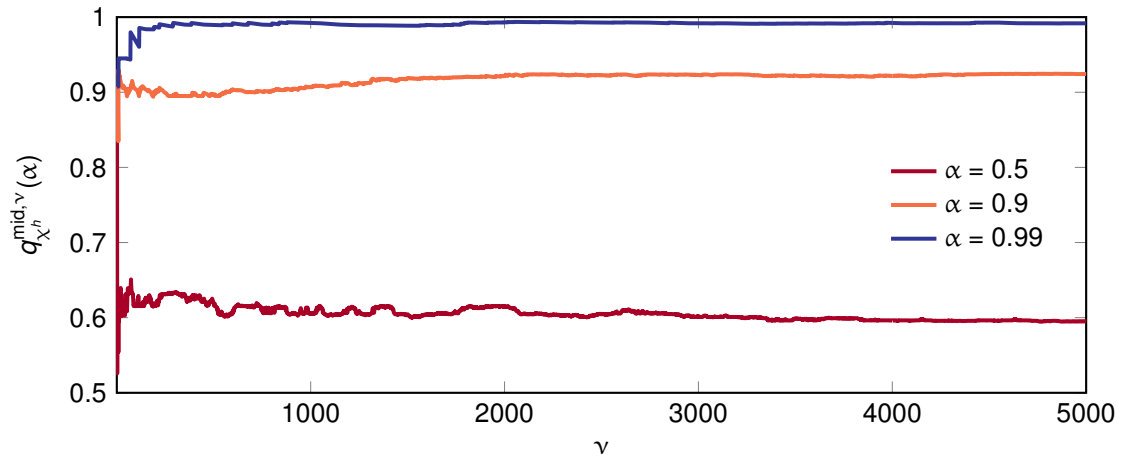


Figure 7.15: Convergence analysis of the Monte Carlo estimates as a function of the number of samples  $\nu$  for  $T_1$ .

the corresponding Vorob'ev  $\alpha$ -quantile. The use of  $T_2$  and  $T_3$  yields confidence sets of similar size, which is consistent with the similarity that we observed between them.

	$T_1$		$T_2$		$T_3$	
$\alpha$	$q_{\chi^h}^{\text{mid}, \nu}(\alpha)$	Area	$q_{\chi^h}^{\text{mid}, \nu}(\alpha)$	Area	$q_{\chi^h}^{\text{mid}, \nu}(\alpha)$	Area
0.5	0.5949	11.03	0.6183	10.92	0.6440	10.92
0.90	0.9243	10.28	0.9734	10.20	0.9442	10.20
0.99	0.9917	10.09	1.0000	9.83	0.9895	9.83

Table 7.1: Monte Carlo estimates of the mid-quantiles and area (millions of  $\text{km}^2$ ) of the resulting confidence sets.

### 7.2.5 Quantile estimation: bifidelity method

We will now use the bifidelity method of Section 5.7.4, and we will investigate the extent to which it can reduce the computational cost of evaluating the mid-quantiles for the membership function  $T_1$  as compared with the Monte Carlo method used in Section 7.2.4. We will investigate the use of the two methods for obtaining the surrogate model required for the bifidelity method, namely, the method based on the spectral representation of the random field (Section 5.7.3.1) and the method based on the spectral representation of  $\chi^h$  (Section 5.7.3.2). We built polynomial chaos expansions for several choices of the order  $p$  using scaled Legendre polynomials whereby we determined the polynomial chaos coordinates from an experimental design made up of the nodes of a fully tensorised scaled Gauss–Legendre quadrature integration rule with  $(p + 1)^2$  nodes. We implemented the bifidelity method by reusing the ensemble of 5000 i.i.d samples that we had used in the Monte Carlo method in Section 7.2.4 so as to allow the solution given by the bifidelity method to be compared with the Monte Carlo solution. We used a step size of  $\Delta\nu = 50$  and we set  $\eta = 0$ .

Figure 7.16 shows a numerical convergence analysis of the mid-quantile estimate as a function of the number of iterations in Algorithm 1 using a stochastic expansion of order  $p = 5$  either of the random field or of  $\chi^h$ . In our illustration, we found that Algorithm 1 stops when the mid-quantile estimate based on the bifidelity method is equal to the Monte Carlo estimate in Table 7.1. When  $j = 0$ , the estimate corresponds to the mid-quantile estimate based on only the surrogate model (see Section 5.7.3). We observe that the mid-quantile estimate based on only the surrogate model already provides an accurate estimate of the Monte Carlo mid-quantile. When we apply the bifidelity method, the mid-quantile converges quickly towards the Monte Carlo mid-quantile, thus suggesting that only a small percentage of evaluations of the computational model is required. We can observe that the bifidelity method converges in fewer iterations for a surrogate model based on a stochastic expansion of  $\chi^h$  (Figure 7.16(a)) than when using one of the random field (Figure 7.16(b)).

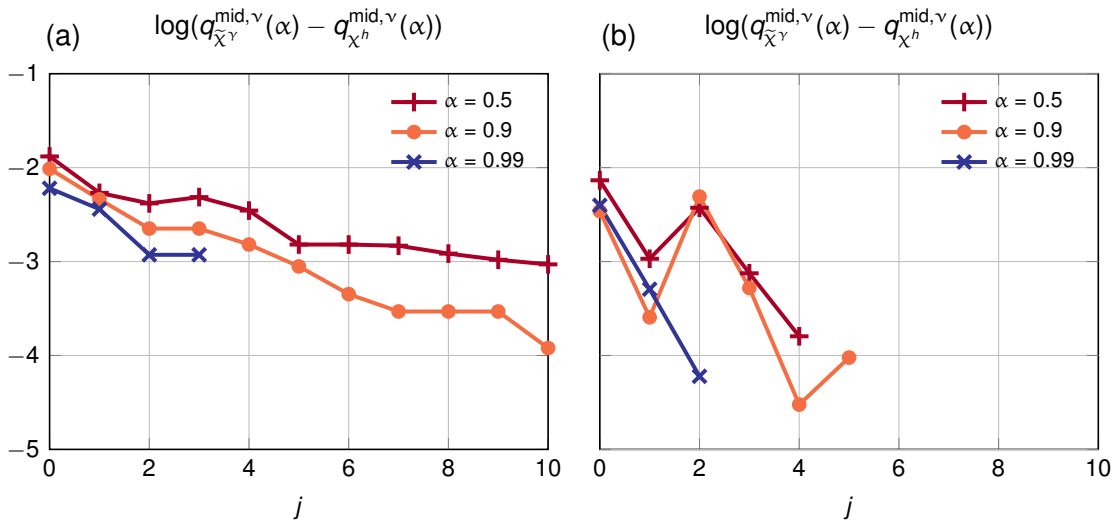


Figure 7.16: Convergence analysis of the mid-quantile estimate based on the bifidelity method based on a polynomial chaos expansion either (a) of the random field or (b) of  $\chi^h$  as a function of the number of iterations in Algorithm 1. The absence of data indicates that the mid-quantile estimate based on the bifidelity method is equal to the Monte Carlo estimate. Results are for  $T_1$ , order  $p = 5$ ,  $\Delta\nu = 50$ , and  $\nu = 5000$ . The equivalent total CPU time, determined from the number of samples of the computational model required to construct the polynomial chaos expansion and to achieve convergence of Algorithm 1, is provided as a means of comparison with the Monte Carlo solution (total CPU time of 40 000h).

Figure 7.17 gives the efficiency of the bifidelity method for a surrogate model based on a polynomial chaos expansion either of the random field (Figure 7.17(a)) or of  $\chi^h$  (Figure 7.17(b)) as a function of the order  $p$ . We measure the efficiency of the bifidelity method as the number of iterations before exiting Algorithm 1, with the maximum number of iterations equal to 100. The number of iterations is high for low orders but drops significantly for higher orders and the 0.99-quantile. Hence, the mid-quantile can be estimated with only a reduced number of

samples compared to the Monte Carlo sampling method. In addition, the bifidelity method based on a polynomial chaos expansion of  $\chi$  achieves a higher efficiency than the bifidelity method based on a polynomial chaos expansion of the random field. Please note that an analysis of the efficiency of the bifidelity method should also take into account the computational cost of constructing the polynomial chaos expansions.

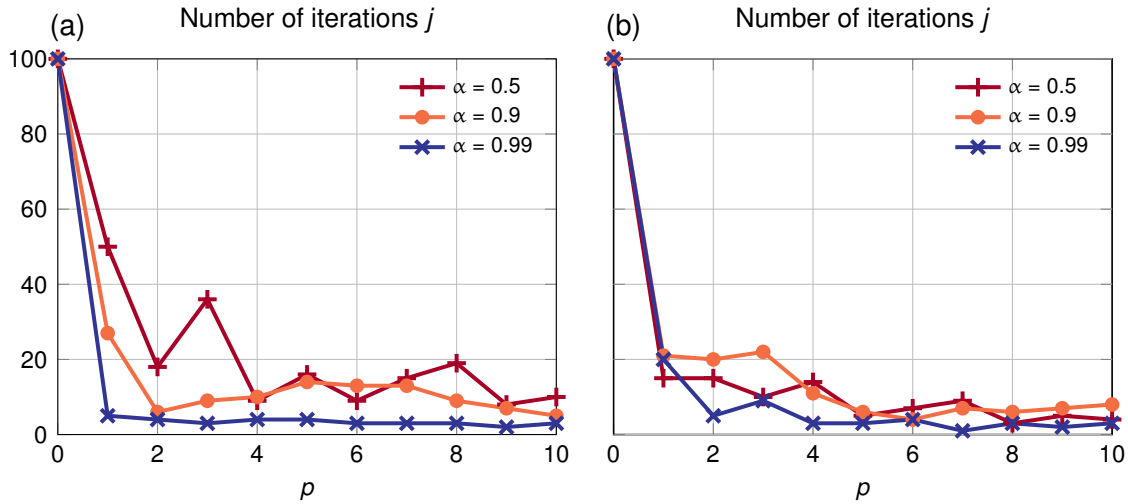


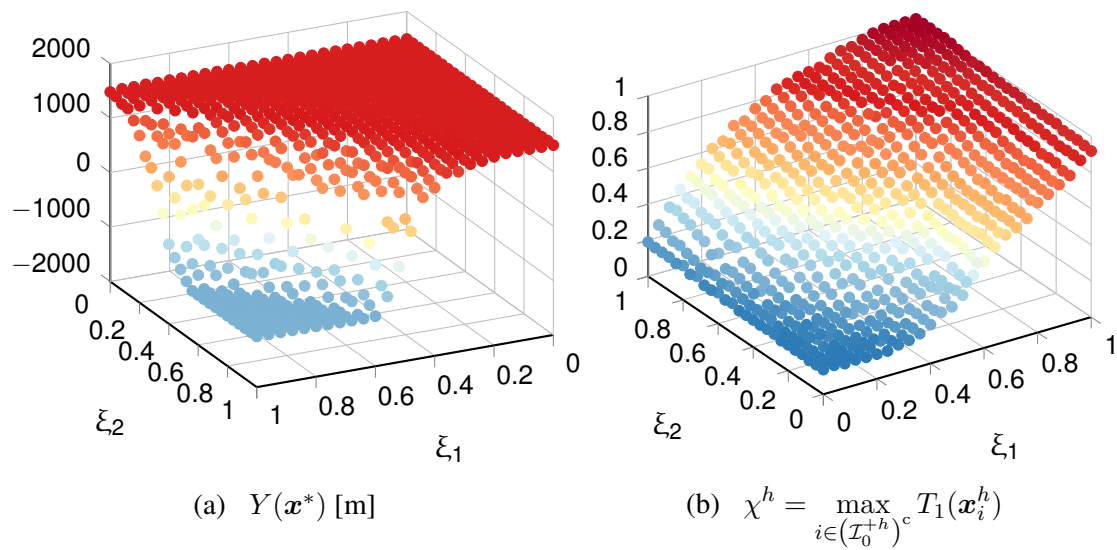
Figure 7.17: Efficiency of the hybrid sampling method: number of iterations before exiting Algorithm 1 as a function of the polynomial order  $p$ . Surrogate models are based on a polynomial chaos expansion either (a) of the random field or (b) of  $\chi^h$ . Results are for  $T_1$ .

### 7.2.5.1 Efficiency of the bifidelity method

We obtained similar convergence and efficiency rates for the other two membership functions. In general, the bifidelity method based on a polynomial chaos expansion of  $\chi^h$  achieved a higher efficiency than the bifidelity method based on a polynomial chaos expansion of the random field. Also, the bifidelity method based on a polynomial chaos expansion of  $\chi^h$  showed a higher efficiency for  $T_1$  than  $T_2$  and  $T_3$ .

To understand the observations mentioned in the previous paragraphs, we looked at how well the random field and the random variable  $\chi^h$  lend themselves to being approximated with polynomial chaos expansions. Figure 7.17(a) shows, as a function of the values taken by the uncertain input parameters, the corresponding value taken by the height above floatation at the location  $\mathbf{x}^*$  in Siple Coast (see Figure 7.9). The random variable  $Y(\mathbf{x}^*)$  has a bimodal distribution with well-separated modes, which suggests the occurrence of a MISI in Siple Coast. The higher mode corresponds to small values (low forcing) of the uncertain input parameters and a limited retreat of the grounding line, while the lower mode corresponds to large values (high forcing) of the uncertain input parameters and an important retreat of the grounding line. This suggests that the random field lends itself less well to being approximated with low-order polynomial chaos expansions, especially at locations where a MISI takes place. By contrast, Figures 7.17(b)–(d) show, as a function of the values taken by the uncertain input parameters,

the corresponding value taken by  $\chi^h$  for  $T_1$ ,  $T_2$  and  $T_3$ , respectively. For small values of the uncertain input parameters, the retreat of the grounding line is limited and the supremum of  $T$  in  $(\mathcal{E}_0^{+h})^c$  is small, while, for large values of the uncertain input parameters, the retreat of the grounding line is important and the supremum of  $T$  in  $(\mathcal{E}_0^{+h})^c$  is large. We can observe that the mapping from the values taken by the uncertain input parameters to the value taken by the random variable  $\chi^h$  based on  $T_1$ ,  $T_2$  or  $T_3$  is sufficiently smooth to lend  $\chi^h$  to better being approximated well with low-order polynomial chaos expansions. In addition, a surrogate model based on a polynomial chaos expansion converges more rapidly towards  $\chi^h$  for  $\chi^h$  based on  $T_1$  than on  $T_2$  or  $T_3$ , as may be expected from the mapping from the values taken by the uncertain input parameters to the value taken by random variable  $\chi^h$  for small values of the uncertain input parameters



### 7.2.6 Confidence sets

In Figure 7.18, we represented the confidence sets for the confidence levels 0.5, 0.9, and 0.99. We superimposed these confidence sets to represent risk-assessment maps. We interpret the confidence sets with confidence levels 0.5, 0.9, and 0.99 as the sets to within which, with medium, low, and very low probability, respectively, the grounded domain does not retreat. Thus, Figure 7.18 suggests that, within the context of the model problem as we set it up, there is a medium risk that about half of the WAIS may disappear over the next 700 years and a low risk that the whole WAIS may collapse over the next 700 years. All three membership functions lead to similar interpretations although the confidence set with confidence level 0.5 for  $T_2$  and  $T_3$  suggests that the WAIS (especially in the Amundsen Sea and Filchner sectors) is more vulnerable than the corresponding confidence set for  $T_1$ . Also, the confidence sets for  $T_3$  display the highest vulnerability for the WAIS but the least vulnerability in the Wilkes sector. More generally, such risk-assessment maps may benefit both observational missions and ice-sheet modelling initiatives by indicating critical regions in Antarctica whose evolution has to be tracked and understood in more details.

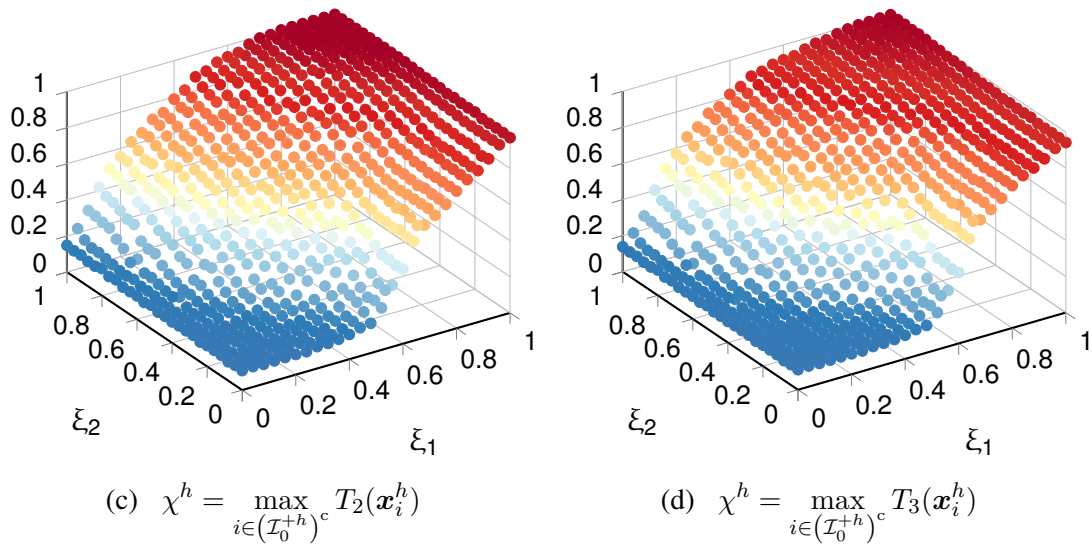


Figure 7.17: a) Height above flotation at the location  $\mathbf{x}^*$  in Siple Coast as a function of the values taken by the uncertain input parameters. Value taken by the random variable  $\chi^h$  as a function of the values taken by the uncertain input parameters for (b)  $T_1$ , (c)  $T_2$  and (d)  $T_3$ .

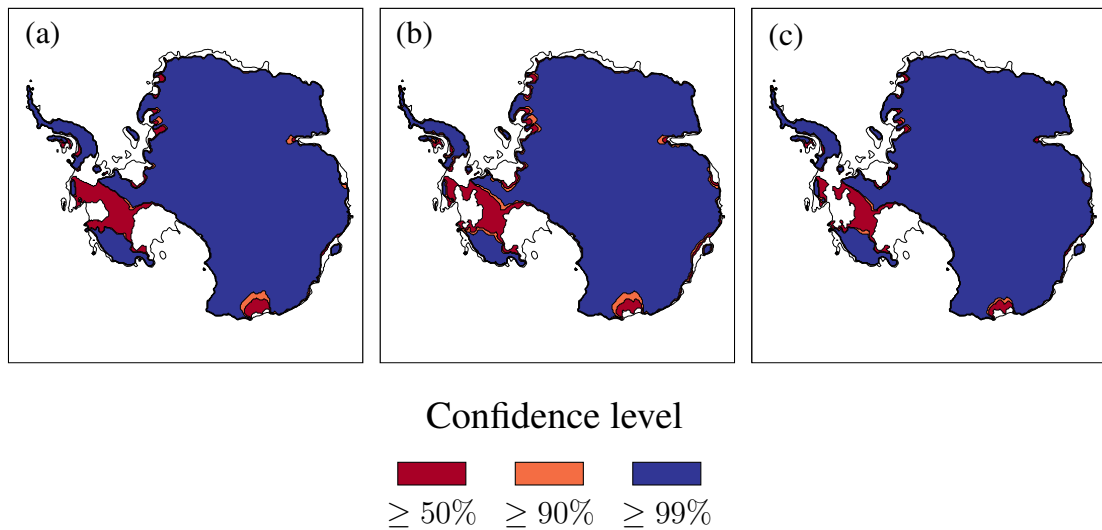


Figure 7.18: Risk-assessment maps of the AIS retreat. The blue set, the union of the blue and orange sets, and the union of the blue, orange, and red sets are respectively the confidence set for the confidence levels 0.99, 0.9, and 0.5. Membership function: (a)  $T_1$ , (b)  $T_2$ , and (c)  $T_3$ . The black line is the present-day grounding line.

## 7.3 Computation of Sobol indices by probabilistic learning on manifolds

The results in this section are presented in the manuscript [Arnst et al., 2019]. In Arnst et al. [2019], the model problem has been used as a means to assess the efficiency of the probabilistic learning on manifolds to compute Sobol indices in so-called small-data settings.

### 7.3.1 Model problem

In order to illustrate UQ methods for the evaluation of Sobol sensitivity indices with the purpose of identifying the most significant sources of uncertainty in inducing uncertainty in the AIS contribution to sea-level rise, we set up a second model problem using the f.ETISh model. The model problem is similar to the model problem in Section 7.1.1 except for the uncertain parameters (see Section 7.3.2), the spatial resolution (20 km instead of 16 km), the time period of the simulation (1 000 years instead of 700 years), and the atmospheric temperature, which is determined under the atmospheric forcing scenario RCP 4.5 defined for the next hundred years by the IPCC and extended in time as reported in Golledge et al. [2015] (see Figure 8.2). The computing time of a single model evaluation on two threads of a SkyLake 2.3 GHz CPU of the Lemaitre 3 cluster is similar to the computing time of a single model evaluation in Section 7.1.1, that is, approximately 8 hours.

### 7.3.2 Sources of uncertainty

In this model problem, we considered five input parameters to be uncertain (Table 7.2). We chose parameters that have different impacts on the response of the Antarctic ice sheet and whose uncertainty may have a more or less significant impact in inducing uncertainty in the projections. We briefly discuss the input parameters in the following and we refer the reader to Section 8.2.2 for additional information about their definition and their physical interpretation. The first uncertain input parameter, the calving multiplier factor, controls the magnitude of the calving rate at the edges of ice shelves. The second uncertain input parameter, the ocean melt factor, controls the magnitude of the change in the ocean temperature on the continental shelf as a function of the change in the background atmospheric temperature under the atmospheric forcing scenario. The third uncertain input parameter, the shelf anisotropy factor, controls the magnitude of the change in ice viscosity as shear-dominated stress behaviour of grounded ice transitions to extension-dominated stress behaviour of floating ice. The fourth and fifth uncertain input parameter, the East and West Antarctic bedrock relaxation times, control the characteristic timescales of the bedrock uplift due to deglaciation in East and West Antarctica. We represented these uncertain input variables as independent uniform random variables with ranges of values determined by the minimum and maximum values in Table 7.2. Similarly to Section 8.2.2, we chose the representation of the input uncertain parameters with an illustrative purpose and we do seek to provide new insights into the impact of uncertain parameters in inducing uncertainty in sea-level rise projections.

### 7.3.3 Quantity of interest

As the predicted quantity of interest, we consider the contribution of the Antarctic ice sheet to global mean sea level after 1 000 years as defined in Section 7.1.2. Under the aforementioned

Uncertain input parameter	Symbol	Nominal	Min	Max	Units
Calving multiplier factor	$w_1$	1	0	2.0	
Ocean melt factor	$w_2$	0.3	0.1	0.5	
Shelf anisotropy factor	$w_3$	0.5	0.2	1	
East Antarctic bedrock relaxation time	$w_4$	3000	1000	5000	yr
West Antarctic bedrock relaxation time	$w_5$	3000	1000	5000	yr
Uncertain input parameter	Symbol	Nominal	Min	Max	Units
Contribution to global mean sea level	$\Delta\text{GMSL}$				m

Table 7.2: List of uncertain input parameters (with uncertainty ranges) and quantity of interest.

probabilistic description of the uncertain input parameter, we found using Monte Carlo estimation with 3 000 samples for this quantity of interest a mean value of 0.46 m, a standard deviation of 0.49 m, and thus a variance of 0.24 m<sup>2</sup> and a coefficient of variation of 108%.

### 7.3.4 Global sensitivity analysis: Monte Carlo method

We used the Monte Carlo method as in Equation (4.72) as described in Section 4.4.2.3 to estimate the main-effect global sensitivity indices for the first, third, and fifth uncertain input parameters. We used for  $\nu$  values up to 3 000, so that the Monte Carlo estimation of these three main-effect global sensitivity indices required  $3\,000 \times (3 + 1) = 12\,000$  evaluations of the computational model. Figure 7.19 shows the convergence of the estimates as a function of  $\nu$ . We can observe that the uncertainties introduced in the calving factor and the shelf anisotropy factor are more significant in inducing uncertainty in the contribution to global mean sea level than the uncertainty introduced in the West Antarctic relaxation time. We can observe that reasonably converged estimates of the main-effect global sensitivity indices for the first and third uncertain input parameters are obtained after a value for  $\nu$  of about 1 000 and that reasonably converged estimates of the main-effect global sensitivity index for the fifth uncertain input parameter are obtained after a value for  $\nu$  of about 2 000. The results obtained with  $\nu = 3\,000$  are  $S_1^\nu = 0.3869$ ,  $S_3^\nu = 0.2322$ ,  $S_5^\nu = 0.0026$ . Please note that we did not compute the main-effect global sensitivity indices for the second and fourth uncertain input parameters because we preferred to avoid the high computational cost of the additionally required  $3\,000 \times 2 = 6\,000$  evaluations of the computational model.

### 7.3.5 Global sensitivity analysis: Spectral method

We used the spectral method as in Equation (4.86) as described in Section 4.4.2.5. Especially to facilitate a comparison of the performance of the spectral method with the performance of the probabilistic learning method to be presented next, we used for the size of the experimental design  $\nu_{\text{ir}}$  values up to only 224. We used independent samples to form the experimental design of values of the uncertain input parameters for which the computational model is evaluated. We used multivariate polynomials set up as products of univariate normalised Legendre polynomials up to a total degree of 4; a polynomial chaos expansion of dimension  $n = 5$  and a total degree of  $p = 4$  as described in Section 4.3.2.1 involves  $(4+5)!/4!/5! = 126$  terms (see Equation (4.21)). We used a regression method to determine the polynomial chaos coefficients. Figure 7.20 shows the convergence of the estimates as a function of the size of the experimental design  $\lambda$ . We can

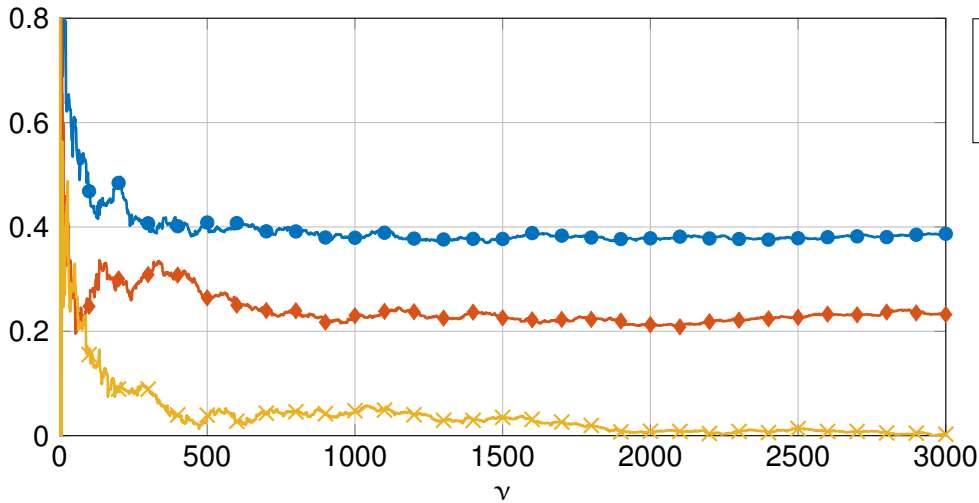


Figure 7.19: Estimates of the main-effect global sensitivity indices for the first (circle), third (diamond), and fifth (x-mark) uncertain input parameters obtained by using the Monte Carlo method as a function of  $\nu$ .

observe that especially for the main-effect global sensitivity index for the first uncertain input variable, the estimate obtained with the spectral method after  $\nu_{\text{ir}} = 224$  evaluations of the computational model in Figure 7.20 is not yet converged to the reasonably converged value obtained with the Monte Carlo method after  $\nu = 3000$  evaluations of the computational model in Figure 7.19. The results obtained with  $\nu_{\text{ir}} = 224$  and  $p = 4$  are  $S_1^{\text{PCE}} = 0.4294$ ,  $S_2^{\text{PCE}} = 0.2945$ ,  $S_3^{\text{PCE}} = 0.2192$ ,  $S_4^{\text{PCE}} = 0.0003$ ,  $S_5^{\text{PCE}} = 0.0009$ .

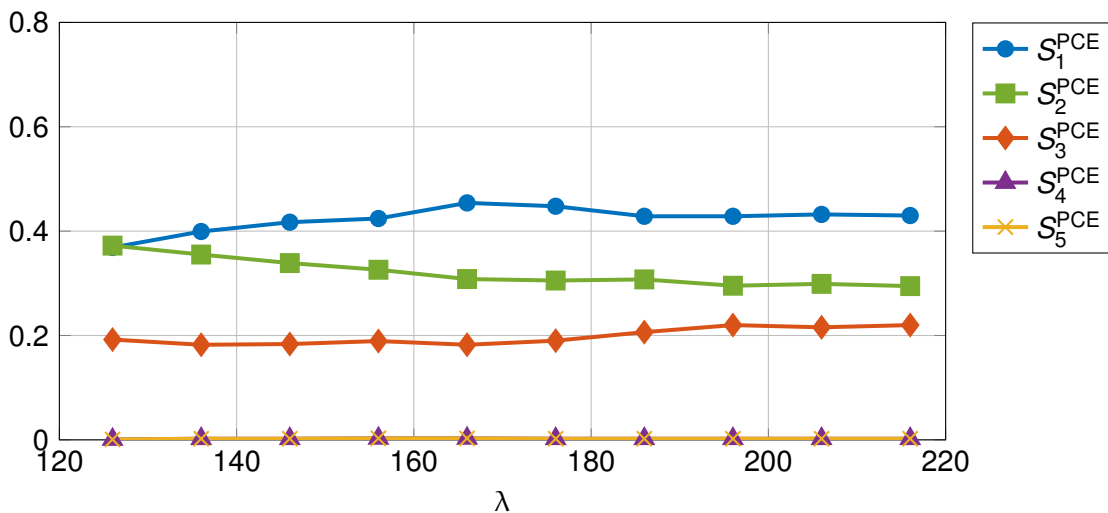


Figure 7.20: Estimates of the main-effect global sensitivity indices for the first (circle), second (square), third (diamond), fourth (triangle), and fifth (x-mark) uncertain input parameters obtained by using the spectral method as a function of  $\lambda$ .

### 7.3.6 Global sensitivity analysis: PLoM method

We used the PLoM method as briefly discussed in Section 4.3.3 to estimate the main-effect global sensitivity indices for the uncertain input variables. We refer the reader to [Arnst et al. \[2019\]](#) for further details about the implementation of the PLoM method and the choice of the parameters in the algorithm.

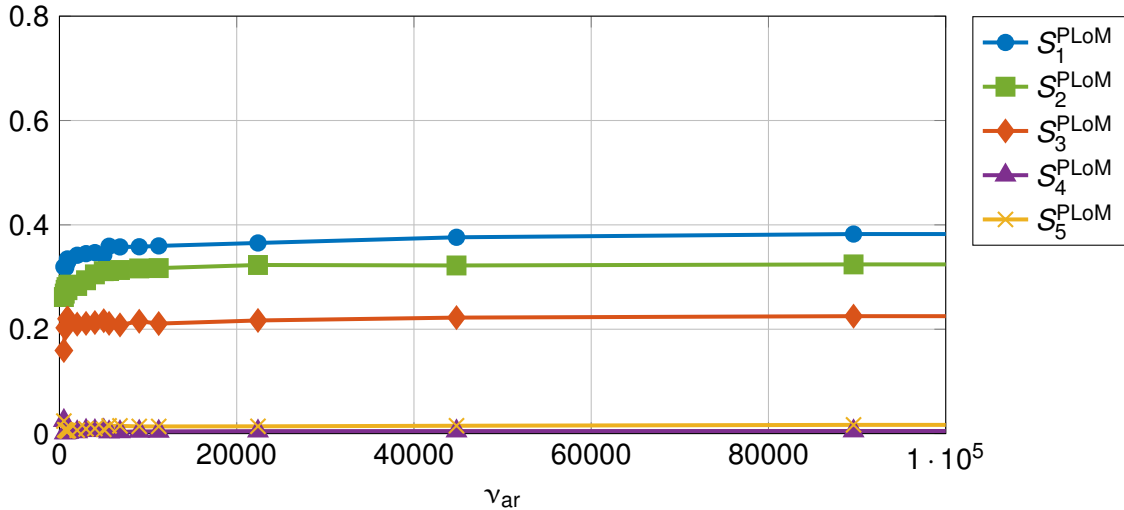


Figure 7.21: Estimates of the main-effect global sensitivity indices for the first (circle), second (square), third (diamond), fourth (triangle), and fifth (x-mark) uncertain input parameters obtained by using the PLoM method as a function of the number  $\nu_{ar}$  of additional realisations of initial realisations for  $\nu_{ir} = 224$  of initial realisations.

We set the maximum value considered for the length  $\nu_{ir}$  of the initial data set to 224. Figure 7.21 shows the convergence of the estimates as a function of a function of the number  $\nu_{ar}$  of additional realisations of initial realisations for  $\nu_{ir} = 224$  of initial realisations. The PLoM method was computationally expedient, and we could readily take  $\nu_{ar}$  sufficiently large for estimates to be converged with respect to  $\nu_{ar}$  without accruing a significant contribution to the total computational cost. Figure 7.22 shows the convergence of the estimates as a function of the number  $\nu_{ir}$  of initial realisations for  $\nu_{ar} = 89\,600$  additional realisations. We can observe that the estimates obtained with the PLoM method are well converged with respect to the length  $\nu_{ir}$  of the initial data set even for small initial data sets with lengths of only  $\nu_{ir} = 190$  or only  $\nu_{ir} = 224$ . We can also observe that the estimates obtained with the PLoM method even for small initial data sets with lengths of only  $\nu_{ir} = 190$  or only  $\nu_{ir} = 224$  in Figure 7.22 correspond well with the converged values obtained with the Monte Carlo method in Figure 7.19. Notably, we can observe that for the main-effect global sensitivity index for the first uncertain input parameter, the estimate obtained with the PLoM method even for the small initial data set with a length of only  $\nu_{ir} = 224$  in Figure 7.22 corresponds better with the reasonably converged value obtained with the Monte Carlo method with  $\nu = 3\,000$  in Figure 7.19 than the estimate obtained with the spectral method with  $\lambda = 224$  in Figure 7.20. We carried out a final computation with the PLoM method with  $\nu_{ar} = 1\,000\,000$  for  $\nu_{ir} = 224$ . The results obtained with

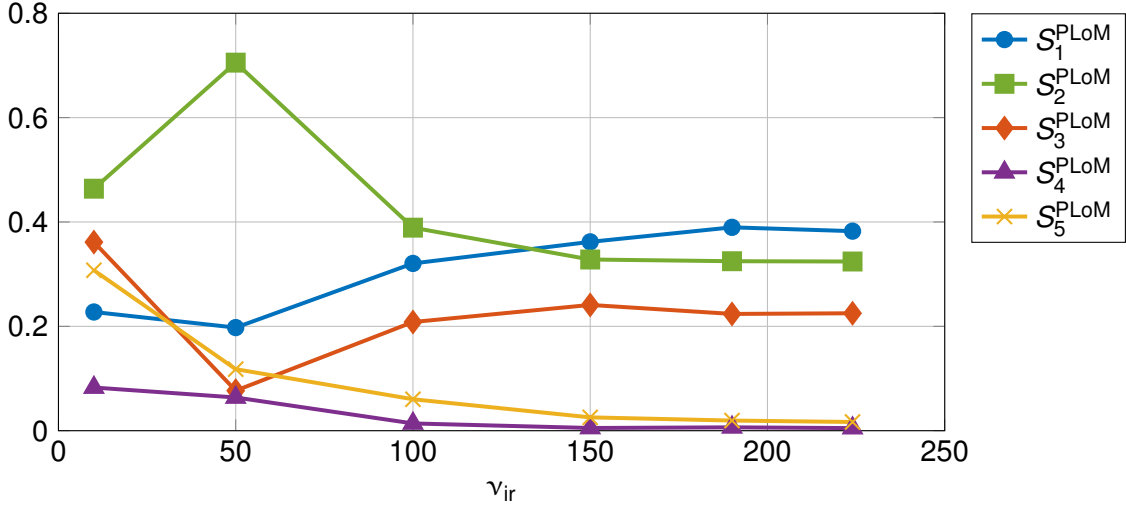


Figure 7.22: Estimates of the main-effect global sensitivity indices for the first (circle), second (square), third (diamond), fourth (triangle), and fifth (x-mark) uncertain input parameters obtained by using the PLoM method as a function of the number  $\nu_{ir}$  of initial realisations for  $\nu_{ar} = 89\,600$  additional realisations.

$\nu_{ir} = 224$  and  $\nu_{ar} = 1\,000\,000$  are  $S_1^{PLoM} = 0.3963$ ,  $S_2^{PLoM} = 0.3353$ ,  $S_3^{PLoM} = 0.2361$ ,  $S_4^{PLoM} = 0.0066$ , and  $S_5^{PLoM} = 0.0182$

### 7.3.7 Global sensitivity analysis: Comparison of the numerical methods

Parameter	$D_i^{MC}$ [m <sup>2</sup> ]	$S_i^{PCE}$	$D_i^{PCE}$ [m <sup>2</sup> ]	$S_i^{PCE}$	$D_i^{PLoM}$ [m <sup>2</sup> ]	$S_i^{PLoM}$
$w_1$	$0.0956 \pm 0.0100$	0.3869	0.1040	0.4294	0.0960	0.3963
$w_2$			0.0714	0.2945	0.0812	0.3353
$w_3$	$0.0578 \pm 0.0093$	0.2322	0.0531	0.2192	0.0572	0.2361
$w_4$			$7.2687E-5$	0.0003	0.0016	0.0066
$w_5$	$6.6151E-4 \pm 0.0094$	0.0026	$2.1806E-4$	0.0009	0.0044	0.0182

Table 7.3: Unnormalised (denoted  $D_i$  for the  $i$ -th uncertain input parameter) and normalised global sensitivity indices with the Monte Carlo method with  $\nu = 3\,000$ , the spectral method with  $\lambda = 224$  and  $p = 4$ , and the PLoM method with  $\nu_{ir} = 224$  for  $\nu_{ar} = 100\,000$ .

Table 7.3 lists the unnormalised and normalised global sensitivity indices obtained with the Monte Carlo, spectral, and PLoM methods. In addition, Table 7.3 provides 95%-confidence intervals for the Monte Carlo estimates of the unnormalised global sensitivity indices obtained by using the central limit theorem for the Monte Carlo estimator. These 95%-confidence intervals quantify the error that may be present in the Monte Carlo estimates of the unnormalised global sensitivity indices owing to their estimation from only the finite number of  $N = 3\,000$  samples. We can observe that the estimates of the unnormalised global sensitivity indices obtained with the spectral and PLoM methods fall within the 95%-confidence intervals for the corresponding

estimates obtained with the Monte Carlo method. We can also observe that for the first and third uncertain input variables, the estimates obtained with the PLoM method correspond better with the estimates obtained with the Monte Carlo method than the estimates obtained with the spectral method. This is not the case for the fifth uncertain input variable, but the global sensitivity index for the fifth uncertain input variable is very small, and the 95%-confidence interval for its Monte Carlo estimate indicates that this estimate may be subject to a large relative error due to its estimation from only  $N = 3\,000$  samples.

Since a single evaluation of the computational model on two threads of a SkyLake 2.3 GHz CPU of the employed cluster takes about 8 hours, the aggregate computing time for the  $3\,000 \times (3 + 1) = 12\,000$  evaluations of the computational model to obtain the Monte Carlo estimates was 96 000 hours. By contrast, the aggregate computing time for the 224 evaluations of the computational model to obtain the spectral and PLoM estimates was only 1 792 hours.

## 7.4 Chapter summary and conclusion

In this chapter, we illustrated and evaluated the performance of existing and newly developed uncertainty quantification methods on model problems concerned with uncertainty quantification of the response of the Antarctic ice sheet to climate change.

In Section 7.1, we illustrated and evaluated the performance of existing methods for the propagation of uncertainties. We illustrated these methods on a stochastic problem concerned with assessing with quantified uncertainty the AIS contribution to sea-level rise. In this illustration, a usual Monte Carlo method required a data set of several thousands of samples to attain a reasonable convergence of the estimates of the statistical descriptors of the quantity of interest, but the use of surrogate models allowed to attain converged estimates based on only a small data set of only a few tens of samples. We also pointed out the need to handle the presence of noise in the data appropriately in order to avoid data overfitting.

In Section 7.2, we investigated confidence sets of random excursion sets in the context of stochastic computational models with a high computational cost. We illustrated this method on a stochastic problem concerned with assessing with quantified uncertainty the retreat of the grounded portion of the Antarctic ice sheet and we showed that, using the bifidelity method proposed in Chapter 5, only a small number of evaluations of the computational model was necessary to achieve an accurate estimate of the quantile. We discussed the impact of the membership function on the efficiency of the bifidelity method, and we concluded that, in the context of our model problem, the bifidelity method based on a polynomial chaos expansion of the random variable can be more efficient than the bifidelity method based on a surrogate model of the random field.

In Section 7.3, we have proposed to use the PLoM method for the computation of global sensitivity indices in small-data settings in which the computational model can be evaluated only a small number of times. The probabilistic learning on manifolds serves to learn from the available samples a probabilistic representation that is used to generate statistically consistent additional samples, on the basis of which estimates of the global sensitivity indices are then computed. We provided an illustration concerned with assessing the impact of uncertain in-

put parameters in inducing uncertainty in sea-level rise projections of a computational ice-sheet model. In this illustration, a usual Monte Carlo method required a data set of several thousands of samples to attain a reasonable convergence of the estimates, but the proposed PLoM method was able to attain converged estimates based on only a small data set of only a few hundred samples. In this illustration, these results indicated that the small data set encapsulated information that the PLoM method was able to exploit to accelerate the convergence of the estimates of the global sensitivity indices with respect to the number of samples.



## Uncertainty quantification of the multicentennial response of the Antarctic ice sheet to climate change

*Ice loss from the Antarctic ice sheet (AIS) is expected to become the major contributor to sea level in the next centuries. Projections of the AIS response to climate change based on numerical ice-sheet models remain challenging due to the complexity of physical processes involved in ice-sheet dynamics, including instability mechanisms that can destabilise marine basins with retrograde slopes. Moreover, uncertainties in ice-sheet models limit the ability to provide accurate sea-level rise projections. Here, we apply probabilistic methods to a hybrid ice-sheet model to investigate the influence of several sources of uncertainty, namely sources of uncertainty in atmospheric forcing, basal sliding, grounding-line flux parameterisation, calving, sub-shelf melting, ice-shelf rheology, and bedrock relaxation, on the continental response of the Antarctic ice sheet to climate change over the next millennium. We provide probabilistic projections of sea-level rise and grounding-line retreat and we carry out stochastic sensitivity analysis to determine the most influential sources of uncertainty. We find that all investigated sources of uncertainty, except bedrock relaxation time, contribute to the uncertainty in the projections. We show that the sensitivity of the projections to uncertainties increases and the contribution of the uncertainty in sub-shelf melting to the uncertainty in the projections becomes more and more dominant as atmospheric and oceanic temperatures rise, with a contribution to the uncertainty in sea-level rise projections that goes from 5% to 25% in RCP 2.6 to more than 90% in RCP 8.5. We show that the significance of the AIS contribution to sea level is controlled by the marine ice-sheet instability (MISI) in marine basins, with the biggest contribution stemming from the more vulnerable West Antarctic ice sheet. We find that, irrespective of parametric uncertainty, the strongly mitigated RCP 2.6 scenario prevents the collapse of the West Antarctic ice sheet, that in both the RCP 4.5 and RCP 6.0 scenarios the occurrence of MISI in marine basins is more sensitive to parametric uncertainty and that, almost irrespective of parametric uncertainty, RCP 8.5 triggers the collapse of the West Antarctic ice sheet.*

## 8.1 Introduction

The Antarctic ice sheet (AIS) is the largest reservoir of freshwater on Earth ( $\sim 60$  m sea-level equivalent [Fretwell et al., 2013; Vaughan et al., 2013]) and has the potential to become one of the largest contributors to sea level in the next centuries. Yet, studies such as the IPCC Fifth Assessment Report (AR5) [Stocker et al., 2013] and Kopp et al. [2014] have identified the magnitude of the AIS response as the largest source of uncertainty in projecting sea-level rise, when compared with other contributors, such as thermal expansion, glaciers, and the Greenland ice sheet. Recent observations [Shepherd et al., 2018] have shown an acceleration in the rate of ice loss from the Antarctic ice sheet, especially in West Antarctica, where an irreversible retreat may be underway in the Amundsen Sea Embayment as a consequence of a marine ice-sheet instability (MISI) [Favier et al., 2014; Joughin et al., 2014; Rignot et al., 2014].

Assessing the future response of the Antarctic ice sheet requires numerical ice-sheet models amenable to large-scale and long-term simulations and quantification of the impact of modelling hypotheses and parametric uncertainty. So far, there exist only a limited number of projections [Golledge et al., 2015; Ritz et al., 2015; DeConto and Pollard, 2016; Schlegel et al., 2018] for the whole Antarctic ice sheet on a (multi-)centennial timescale. These projections show similar trends for the next centuries, but they differ in the magnitude of the mass loss they predict, with differences and uncertainty ranges that can reach several metres for eustatic sea level. Using a numerical ice-sheet model supplemented with a statistical approach for the probability of MISI onset, Ritz et al. [2015] have projected a contribution to sea level around 0.1 m by 2100, with a very low probability of exceeding 0.5 m in the A1B scenario. Running their simulations with and without sub-grid melt interpolation at the grounding line, Golledge et al. [2015] have projected that sea-level rise could range from 0.01 m to 0.38 m by 2100 and from 0.21 m to more than 5 m by 2500 considering all RCP scenarios. Including the marine ice-cliff instability mechanism [Pollard et al., 2015] in a numerical ice-sheet model, DeConto and Pollard [2016] have projected that sea level could rise much more significantly, with projections exceeding 1 m by 2100 and 15 m by 2500 in the RCP 8.5 scenario. Synthesising recent results for the expected response of the Antarctic ice sheet to climate change, Pattyn et al. [2018] have highlighted that the projected contribution to sea level of the Antarctic ice sheet is limited to well below 1 m by 2500 in the RCP 2.6 scenario while a key threshold for the stability of the Antarctic ice sheet is expected to lie between 1.5 and 2 °C. mean annual air temperature above present and the activation of larger ice systems, such as the Ross and Ronne–Filchner drainage basins, could be triggered by global warming between 2 and 2.7 °C. Emulating the numerical ice-sheet model by DeConto and Pollard [2016] with a Gaussian process emulator, Edwards et al. [2019] have established new probabilistic projections for the AIS contribution to sea level by 2100, with the probability of exceeding 0.5 m that reaches 4 % in RCP 2.6 and 71 % in RCP 8.5 when considering the marine ice-cliff instability mechanism. Coupling an ice-sheet model with a climate model, Golledge et al. [2019] have shown that freshwater released by the Antarctic ice sheet can trap warm waters below the sea surface, thus leading to higher projections by 2100, with a contribution to sea level that could reach 0.05 m in RCP 4.5 and 0.14 m in RCP 8.5.

Despite recent progress in the numerical modelling of ice-sheet dynamics [Pattyn et al., 2017], differences in modelling hypotheses between ice-sheet models remain a major source of uncertainty for sea-level rise projections. Intercomparison projects such as the SeaRise project

[Bindschadler et al., 2013] and the ongoing ISMIP6 project [Nowicki et al., 2016; Goelzer et al., 2018] aim at quantifying the impact of such so-called structural uncertainty in ice-sheet models by comparing projections from multiple numerical models. Such multimodel ensembles give some insight into the impact of the structural uncertainty, although challenges remain in combining the different results [Knutti et al., 2010].

Uncertainties in the ice-sheet initial state, climate forcing, and parameters in numerical ice-sheet models are another major limitation for accurate projections. To date, the impact of such parametric uncertainty is assessed most often by using large ensemble analysis; that is, the model is run for different values of the parameters and the uncertainty in the projections is estimated from the spread in the model runs. For example, Golledge et al. [2015] ran their model with simplified sensitivity experiments to evaluate qualitatively the sensitivity of the Antarctic ice sheet to temperature, precipitation, and sea-surface temperature individually, while DeConto and Pollard [2016] assessed the sensitivity of their model to parametric uncertainty by evaluating the model response at a few samples in the parameter space. By contrast, Ritz et al. [2015] adopted a probabilistic approach and estimated the uncertainty in sea-level rise projections by running an ice-sheet model with samples of parameters drawn randomly from probability density functions for the parameters and subsequently deducing probability density functions for sea-level rise projections.

The field of uncertainty quantification (UQ) develops theory and methods to describe quantitatively the origin, propagation, and interplay of sources of uncertainty in the analysis and projection of the behaviour of complex systems in science and engineering; see, for instance, Ghanem et al. [2017] for a recent handbook and Arnst and Ponthot [2014] for a recent review paper. Most of this theory and these methods are based on probability theory, in the context of which uncertain parameters and projections are represented as random variables characterised by their probability density function. Theory and methods are under development to characterise sources of uncertainty by probability density functions inferred from observational data and expert assessment (characterisation of uncertainty), to deduce the impact of sources of uncertainty on projections (propagation of uncertainty), and to ascertain the impact of each source of uncertainty on the projection uncertainty and rank them in order of significance (stochastic sensitivity analysis). These developments have led to new theories and new methods that are of interest to be applied to uncertainty quantification of ice-sheet models, beyond the theory and methods that Golledge et al. [2015], Ritz et al. [2015], DeConto and Pollard [2016], and Schlegel et al. [2018] have already applied.

In this chapter, we apply probabilistic methods to assess the impact of uncertainties on the continental AIS response over the next millennium. We use the fast Elementary Thermomechanical Ice Sheet (f.ETISh) model [Pattyn, 2017], a hybrid ice-sheet model that captures the essential characteristics of ice flow and allows large-scale and long-term projections at a reasonable computational cost. To reduce the computational cost of assessing the impact of uncertainties on the change in global mean sea level (GMSL), we draw from UQ methods based on the construction of an emulator [Le Maître and Knio, 2010; Ghanem et al., 2017], also known as a surrogate model, that is, a computational model that mimics the response of the original ice-sheet model at a reduced computational cost. To assess the significance of each individual source of uncertainty in inducing uncertainty in the change in GMSL, we draw from UQ

methods for stochastic sensitivity analysis [Saltelli et al., 2008]. To express the uncertainty in projections of the retreat of grounded ice, we draw from UQ methods for constructing confidence regions for excursion sets [Bolin and Lindgren, 2015; French and Hoeting, 2015], with a confidence region for grounded ice interpreted as a region of Antarctica that remains covered everywhere with grounded ice for a given level of probability.

On the one hand, our study adds to previous studies [Golledge et al., 2015; Ritz et al., 2015; DeConto and Pollard, 2016] that also provided projections for the multicentennial response of the whole Antarctic ice sheet: whereas these previous studies provided projections by running the ice-sheet model with samples of parameters from the parameter space, our study differs by the adoption of additional methods from UQ and the analysis of a broader set of parameters that includes uncertainty in climate forcing, basal sliding, grounding-line flux parameterisation, calving, sub-shelf melting, ice-shelf rheology, and bedrock relaxation. On the other hand, our study also adds to previous studies [Pollard et al., 2016; Schlegel et al., 2018; Edwards et al., 2019] that also applied methods from UQ for uncertainty propagation in ice-sheet models: whereas these previous studies analysed AIS paleoclimatic responses with Gaussian process (kriging) emulators [Pollard et al., 2016] and multi-decadal forecasts with Latin hypercube sampling [Schlegel et al., 2018], our study differs by its focus on the analysis of the multicentennial response of the whole Antarctic ice sheet with polynomial emulators; and in addition to uncertainty propagation, we complement our uncertainty analysis with stochastic sensitivity analysis and confidence regions.

This chapter is organised as follows. First, Section 8.2 describes the f.ETISH model, the uncertain processes and parameters and the UQ methods, including the use of an emulator, stochastic sensitivity analysis, and the construction of confidence regions. Subsequently, Section 8.3 shows and interprets the results for the multicentennial response of the Antarctic ice sheet as well as the advantages of the adopted UQ methods. Finally, Section 8.4 provides an overall discussion of the results.

## 8.2 Model description and methods

### 8.2.1 Ice-sheet model and simulations

We perform simulations of the response of the Antarctic ice sheet (Figure 8.1(a)) to environmental and parametric perturbations over the period 2000–3000 CE with the fast Elementary Thermomechanical Ice Sheet (f.ETISH) model [Pattyn, 2017] version 1.2. The f.ETISH model is a vertically integrated, thermomechanical, hybrid ice-sheet/ice-shelf model that incorporates essential characteristics of ice-sheet thermomechanics and ice-stream flow, such as the mass-balance feedback, bedrock deformation, sub-shelf melting, and calving. The ice flow is represented as a combination of the shallow-ice (SIA) [Hutter, 1983; Greve and Blatter, 2009a] and shallow-shelf (SSA) [Morland, 1987; MacAyeal, 1989; Weis et al., 1999] approximations for grounded ice [Bueler and Brown, 2009], while only the shallow-shelf approximation is applied for floating ice shelves. Bedrock deformation is represented as a combined time-lagged asthenospheric relaxation and elastic lithospheric response [Greve and Blatter, 2009b; Pollard and DeConto, 2012a], in which the lithosphere relaxes towards isostatic equilibrium due to the viscous properties of the underlying asthenosphere. Calving at the ice front is parameterised

based on the large-scale stress field, represented by the horizontal divergence of the ice-shelf velocity field [Pollard and DeConto, 2012a]. Prescribed input data include the present-day ice-sheet geometry and bedrock topography from the Bedmap2 dataset [Fretwell et al., 2013], the basal sliding coefficient, and the geothermal heat flux by An et al. [2015].

We perform simulations at a spatial resolution of 20 km while accounting for grounding-line migration at coarse resolution with a flux condition derived from a boundary layer theory at steady state based on either a Weertman (or power) friction law [Schoof, 2007b] or a Coulomb friction law [Tsai et al., 2015] at the grounding line. This flux condition at the grounding line is imposed as an internal boundary condition following the implementation by Pollard and DeConto [2009, 2012a]. This implementation has been shown to reproduce the migration of the grounding line and its steady-state behaviour [Schoof, 2007a] at coarse resolution for the SSA and hybrid SSA/SIA models, while these models can only reproduce the migration of the grounding line and its steady-state behaviour at sufficiently fine resolution in the absence of a flux condition [Docquier et al., 2011; Pattyn et al., 2012]. Numerical simulations [Pollard and DeConto, 2012a; DeConto and Pollard, 2016] of the Antarctic ice sheet using a flux condition have also been able to reproduce MISI in large-scale ice-sheet simulations. In addition, Pattyn [2017] has shown that a flux condition makes the f.ETISh model rather independent of the resolution for a spatial resolution of the order of 20 km. While the implementation of a flux condition at the grounding line has been shown to reproduce qualitatively ice-sheet dynamics as determined with other ice-sheet models, it cannot reproduce quantitatively changes in ice-sheet mass and the contribution to sea level as determined from models with a higher level of complexity, such as the Blatter–Pattyn [Blatter, 1995; Pattyn, 2003] and full Stokes [Greve and Blatter, 2009a] models that include vertical shearing at the grounding line, especially for short transients (decadal timescales) as these flux conditions have been derived at steady state [Drouet et al., 2013; Pattyn et al., 2013; Pattyn and Durand, 2013]. A proper representation of grounding-line migration without the need for a flux condition would require a very fine grid resolution (possibly less than 200 metres). In addition, the flux condition has been derived for unbuttressed ice shelves [Schoof, 2007b] and may fail to appropriately represent grounding-line migration for buttressed ice shelves [Reese et al., 2018b] as found mostly around Antarctica even when the flux condition is corrected for buttressing with a buttressing factor accounting for back stress at the grounding line. In particular, Pattyn et al. [2013] have shown that models that implement the flux condition cannot reproduce compressional stresses that may apply in the presence of buttressing. Moreover, using a spatial resolution of 20 km does not allow us to capture properly certain mechanisms that control grounding-line migration such as bedrock irregularities and ice-shelf pinning points even with sub-grid parameterisations of these mechanisms. Therefore, we may expect discrepancies between our results and results at higher spatial resolutions (<5 km), especially for important small ice streams such as Pine Island and Thwaites Glaciers, which represent only a few grid points with a 20-km resolution. Despite the limitations of the flux condition and our coarse grid resolution, we have adopted these modelling assumptions as an efficient way to capture the essential mechanisms of grounding-line migration in large-scale, long-term and large-ensemble ice-sheet simulations while keeping the computational cost tractable. The computational cost of a single forward simulation with a time step of 0.05 years on the CÉCI clusters (F.R.S-FNRS & Walloon Region) on two threads is approximately 8 h. To investigate the impact of the spatial resolution on the results, we performed additional runs at a spatial resolution of 16 km (Figure 8.15). We found that the uncertainty in the projections due

to the spatial resolution is (far) less important than the uncertainty due to the uncertainty in the parameters.

The main changes in f.ETISh version 1.2 as compared to version 1.0 [Pattyn, 2017] consist of the computation of sub-shelf melt rates with an ocean-model coupler based on the Potsdam Ice-shelf Cavity mOdel (PICO) ocean-model coupler [Reese et al., 2018a] rather than simpler parameterisations of sub-shelf melt rates [Beckmann and Goosse, 2003; Holland et al., 2008; Pollard and DeConto, 2012a; de Boer et al., 2015; Cornford et al., 2016], the inclusion of a laterally varying flexural rigidity for the lithosphere [Chen et al., 2018] to compute glacial isostatic adjustment more realistically with an elastic lithosphere/relaxed asthenosphere model, an improvement of the SSA numerical scheme based on the implementation by Rommelaere and Ritz [1996], and a description of atmospheric forcing based on a parameterisation of the changes in atmospheric temperature and precipitation rate [Huybrechts et al., 1998; Pollard and DeConto, 2012a], a parameterisation of surface melt with a positive degree-day model [Janssens and Huybrechts, 2000], and the inclusion of meltwater percolation and refreezing [Huybrechts and de Wolde, 1999].

We drive our simulations with both atmospheric and oceanic forcings. Present-day mean surface air temperature and precipitation are obtained from Van Wessem et al. [2014], based on the regional atmospheric climate model RACMO2. Changes in atmospheric temperature and precipitation rate induced by a forcing temperature change  $\Delta T$  are applied in a parameterised way that accounts for elevation changes [Huybrechts et al., 1998; Pattyn, 2017]. We use a positive degree-day (PDD) model to calculate surface melt [Janssens and Huybrechts, 2000], assuming a PDD factor of  $3 \text{ mm } ^\circ\text{C}^{-1} \text{ day}^{-1}$  and  $8 \text{ mm } ^\circ\text{C}^{-1} \text{ day}^{-1}$  for snow and ice, respectively. The PDD model also includes meltwater percolation and refreezing [Huybrechts and de Wolde, 1999].

Basal melting underneath ice shelves is determined from the PICO ocean-model coupler [Reese et al., 2018a], which evaluates sub-shelf melting from the ocean temperature  $T_{\text{oc}}$  and salinity fields on the continental shelf via an ocean box model that captures the basic overturning circulation within ice-shelf cavities. We employ data by Schmidt et al. [2014] for present-day ocean temperature  $T_{\text{oc}}^{\text{obs}}$  and salinity on the continental shelf. For a change in background atmospheric temperature  $\Delta T$ , we assume that the ocean temperature  $T_{\text{oc}}$  on the continental shelf changes as

$$T_{\text{oc}} = T_{\text{oc}}^{\text{obs}} + F_{\text{melt}}\Delta T, \quad (8.1)$$

where  $F_{\text{melt}}$  is an ocean melt factor that represents the ratio between oceanic and atmospheric temperature changes [Maris et al., 2014; Golledge et al., 2015]. Equation (8.1) with  $F_{\text{melt}} = 0.25$  has been shown to reproduce trends in ocean temperatures following an analysis of the Climate Model Intercomparison Project phase 5 (CMIP5) data set [Taylor et al., 2012] for changes in atmospheric and ocean temperatures [Golledge et al., 2015]. Figure 8.1(b) shows the initial sub-shelf melt rate as computed with the PICO model. The PICO model is able to reproduce the general pattern of sub-shelf melting with higher melt rates near the grounding line and lower melt rates near the calving front. Sub-shelf melt rates are also higher in the Amundsen Sea sector and lower underneath the large Ross and Filchner–Ronne ice shelves.

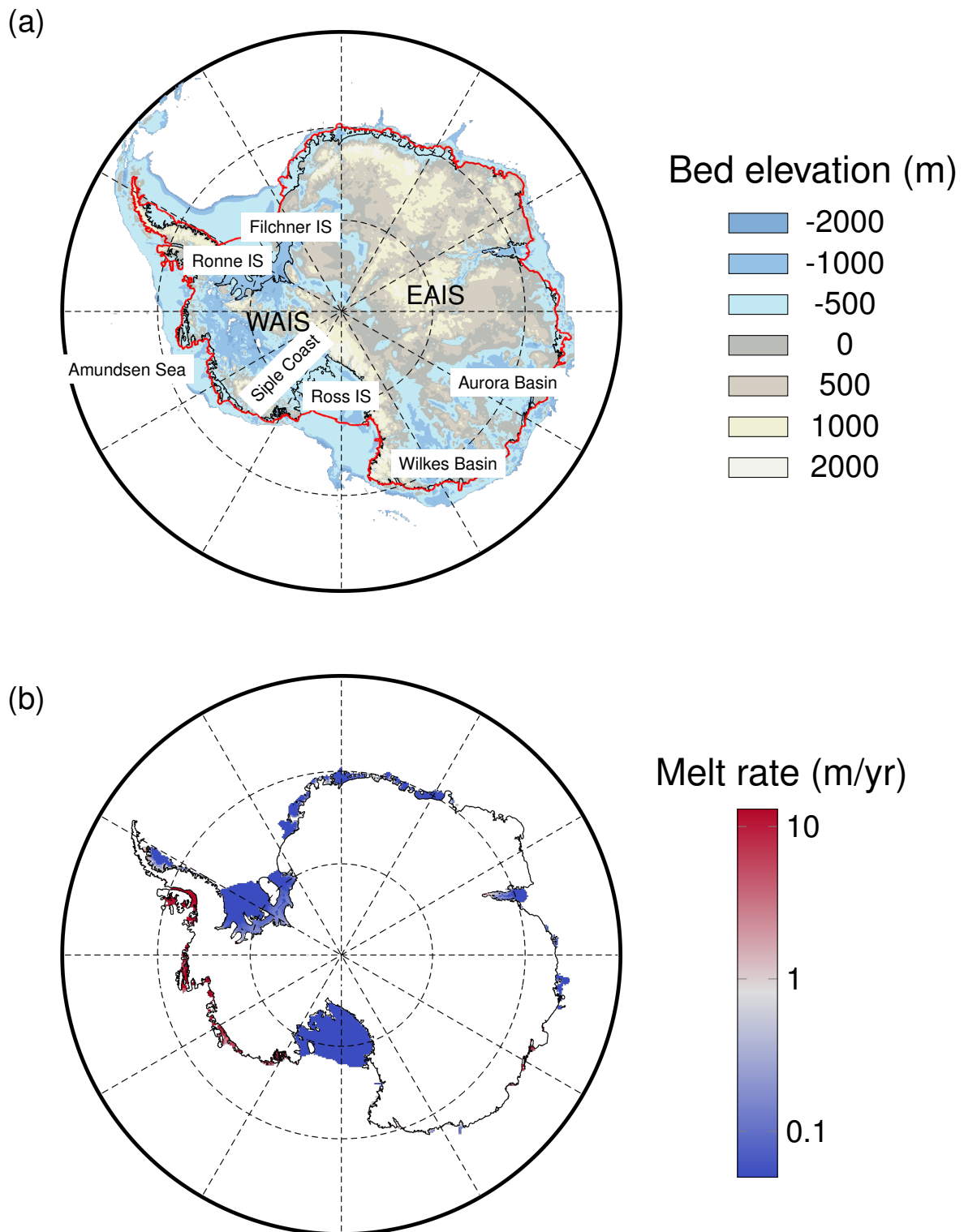


Figure 8.1: Antarctic bedrock topography and sub-shelf melting. **(a)** Bedrock topography (m above sea level) [Fretwell et al., 2013] of the present-day Antarctic ice sheet and geographic features. WAIS is the West Antarctic ice sheet, EAIS is the East Antarctic ice sheet, and IS is ice shelf. Grounding line is shown in black and ice front is shown in red. **(b)** Sub-shelf melt rate for the present-day Antarctic ice sheet computed with the PICO ocean-model coupler [Reese et al., 2018a]. Refreezing under ice shelves is not allowed.

The calibration of the basal sliding coefficient follows the data assimilation method of ice-sheet geometry by [Pollard and DeConto \[2012b\]](#). This approach is based on a fixed-point iteration scheme that adjusts the basal sliding coefficient iteratively so as to match the present-day ice-sheet configuration while assuming that the present-day configuration is in steady state. After applying this approach, we further adjust the basal sliding coefficient in ice streams with a sliding multiplier factor similar to [Bindschadler et al. \[2013\]](#) to reduce the initial drift. We carry out the calibration step independently for the different sliding and grounding-line flux conditions investigated in this chapter. For the nominal values of the model parameters and without forcing anomaly, the initial drifts (reference runs) range from 0.1 to 0.2 metre of sea-level rise by 3000. To make our analysis insensitive to model initialisation, we correct all our results for this initial bias by subtracting the reference runs from the results. Therefore, after corrections for present-day dynamical changes, our results reflect the model response to perturbations. These corrections have in general little impact on medium-term and long-term projections as the initial drift is small compared to the projections but leads to a more significant bias for short-term projections.

## 8.2.2 Sources of uncertainty

We aim at quantifying the response of the Antarctic ice sheet to climate change while accounting for uncertainty in atmospheric forcing, basal sliding, grounding-line flux parameterisation, calving, sub-shelf melting, ice-shelf rheology, and bedrock relaxation. We account for uncertainty in these physical processes by introducing uncertainty in parameters in the f.ETISh model (see [Table 8.1](#)). Here, we choose the uncertainty ranges for the parameters sufficiently large so as to encompass extreme conditions. The effect of choosing narrower uncertainty ranges for the parameters is discussed in [Section 8.3.6](#). We assume the parameters to take the same value everywhere over the whole Antarctic ice sheet. This approach is likely to be conservative as the parameters may vary at least regionally. We refer to [Schlegel et al. \[2018\]](#) for a discussion about uncertainty quantification based on a partitioning of the ice-sheet domain. In the remainder of this section, we list the uncertain parameters and briefly discuss their influence on the AIS response.

Definition	Parameter	Nominal	Min	Max	Units
Sliding exponent	$m$	2	1	5	
Calving multiplier factor	$F_{\text{calv}}$	1	0.5	1.5	
Ocean melt factor	$F_{\text{melt}}$	0.3	0.1	0.8	
Shelf anisotropy factor	$E_{\text{shelf}}$	0.5	0.2	1	
East Antarctic bedrock relaxation time	$\tau_e$	3000	2500	5000	year
West Antarctic bedrock relaxation time	$\tau_w$	3000	1000	3500	year

Table 8.1: List of parameters and parameter ranges used in the uncertainty analysis.

### 8.2.2.1 Atmospheric forcing

Alongside oceanic forcing, atmospheric forcing is generally considered to be the primary driver of future changes in the AIS mass balance [[Lenaerts et al., 2016](#); [Pattyn et al., 2018](#)]. Sim-

ulating atmospheric forcing over several centuries with regional climate models is computationally prohibitive. In addition, the accuracy of the climate models is limited by uncertainties such as the possible trajectories of anthropogenic greenhouse gas emissions. Therefore, we adopt here the four schematic extended representative concentration pathway (RCP) scenarios RCP 2.6, RCP 4.5, RCP 6.0, and RCP 8.5 introduced by [Golledge et al. \[2015\]](#) for temperature changes  $\Delta T$  in the atmosphere (Figure 8.2) as a means of representing different atmospheric forcings relevant for policymakers.

The scenario plays a significant role in the amplitude and speed of the AIS retreat. Recent studies [[Golledge et al., 2015](#); [DeConto and Pollard, 2016](#)] have shown no substantial retreat of the grounding-line position in the strongly mitigated RCP 2.6 scenario. The other scenarios lead to a reduction in the extent of the major ice shelves (Ross, Filchner–Ronne and Amery ice shelves) within 100–300 years, leading to accelerated grounding-line recession due to reduced buttressing. [DeConto and Pollard \[2016\]](#) have also highlighted that the hydrofracturing and ice-cliff failure mechanisms (not included in f.ETISH version 1.2) driven by increased surface melt and sub-shelf melting could potentially lead to an accelerated collapse of the West Antarctic ice sheet and a deeper grounding-line retreat in the East Antarctic subglacial marine basins.

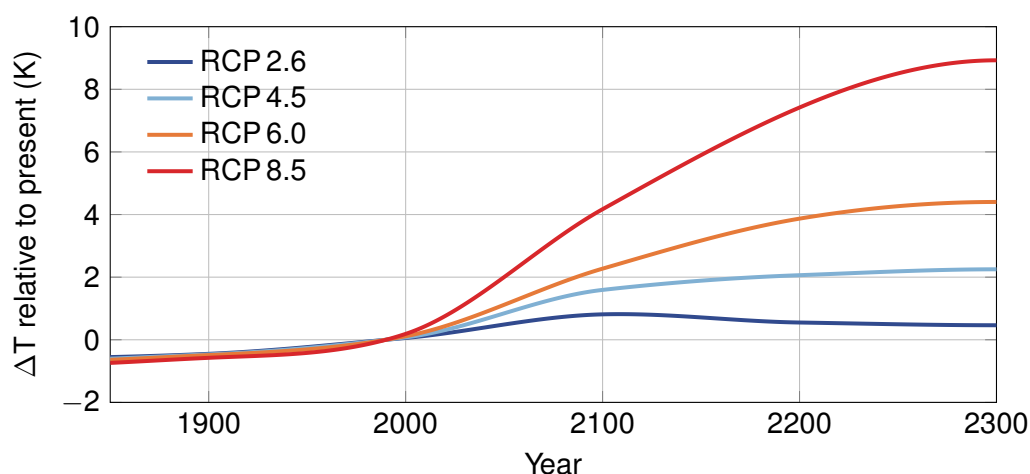


Figure 8.2: Long-term RCP temperature scenarios [[Golledge et al., 2015](#)] for Antarctica (60°–90° S) based on the CMIP5 data [[Taylor et al., 2012](#)] and extended to 2300. Temperatures are held constant after 2300.

### 8.2.2.2 Basal sliding

Basal sliding controls the motion of fast-flowing ice streams, which drain about 90% of the total Antarctic ice flux [[Bennett, 2003](#)]. Several studies have shown the importance of basal sliding for the behaviour of ice streams and stressed the need for the understanding of physical processes at play at the ice–bedrock interface [[Joughin et al., 2009, 2010](#); [Ritz et al., 2015](#); [Brondex et al., 2017, 2019](#)]. In particular, [Ritz et al. \[2015\]](#) have shown that, under a power-law rheology for basal sliding, the contribution to future sea level is an increasing function of the sliding exponent.

We introduce basal sliding as a Weertman sliding law, that is,

$$v_b = -A_b \|\tau_b\|^{m-1} \tau_b, \quad (8.2)$$

where  $\tau_b$  is the basal shear stress,  $v_b$  the basal velocity,  $A_b$  the basal sliding coefficient, and  $m$  a sliding exponent. The sliding exponent is often related to Glen's flow law exponent  $n$  as  $m = n$  for sliding over hard bedrock [Weertman, 1957]. The value  $m = 3$ , related to the usual value  $n = 3$  for Glen's flow law exponent, has been applied in a number of studies [Schoof, 2007a; Pattyn et al., 2012, 2013; Brondex et al., 2017; Gladstone et al., 2017] but the value  $m = 1$  has also been commonly used in ice-flow models [Larour et al., 2012; Schäfer et al., 2012; Gladstone et al., 2014; Yu et al., 2018].

In addition to the usual exponents  $m = 1$  and  $m = 3$ , we consider for the sliding exponent a nominal value of 2 as an intermediate sliding condition between the two usual exponents used in ice-flow models. Hereafter, we refer to the exponents  $m = 1, 2$ , and 3 as the viscous (or linear), the weakly non-linear, and the strongly non-linear sliding law, respectively. We consider the discrete values  $m = 1, 2$ , and 3 as representative of the most common values in large-scale ice-sheet modelling and discuss in Section 8.3.7 the impact of a more plastic sliding law ( $m = 5$ ) to represent a quasi-plastic deformation of the till in ice streams [Gillet-Chaulet et al., 2016].

### 8.2.2.3 Grounding-line flux parameterisation

The f.ETISH model employs a parameterisation of the grounding-line flux based on a boundary layer theory at steady state by either Schoof [2007b] (SGL) or Tsai et al. [2015] (TGL). For the TGL parameterisation, Pattyn [2017] has shown an increased AIS contribution to sea level and a more significant retreat of the grounding line. We consider SGL parameterisation as the reference parameterisation for most of the simulations and discuss the impact of TGL parameterisation in Section 8.3.8.

We applied the TGL parameterisation under the weakly non-linear sliding law. There is no consensus on the compatibility between the TGL parameterisation and the Weertman sliding law, as the TGL parameterisation was derived from the Coulomb friction law near the grounding line [Tsai et al., 2015]. Yet, the Coulomb friction law is applicable in a narrow transition region in the vicinity of the grounding line not resolved on our coarse mesh, which lends validity to the combination of the TGL parameterisation and Weertman's sliding law.

### 8.2.2.4 Calving

Ice loss due to ice calving at the edges of ice shelves is responsible for almost half of the present-day ice mass loss of the Antarctic ice sheet [Depoorter et al., 2013; Rignot et al., 2013]. Iceberg calving can have strong feedback effects as it affects ice-shelf buttressing [Fürst et al., 2016] and therefore ice flux at the grounding line and the stability of marine ice sheets [Schoof et al., 2017]. It can also lead to a total disintegration of ice shelves followed by a potential marine ice-cliff instability [Pollard et al., 2015].

The nominal calving rate  $c_f$  (in  $\text{m yr}^{-1}$ ) in the f.ETISH model is evaluated with the following parameterisation [Pollard and DeConto, 2012a; Pattyn, 2017]

$$c_f = 30 (1 - w_c) + 3 \times 10^5 \max(\text{div } \mathbf{v}, 0) \frac{w_c h_e}{\Delta x}, \quad (8.3)$$

where  $\mathbf{v}$  is the vertical mean of the horizontal velocity,  $h_e$  is the sub-grid ice thickness within a fraction of the ice-edge grid cell that is occupied by ice [Pollard and DeConto, 2012a],  $\Delta x$  is the spatial resolution, and  $w_c = \min(1, h_e/200)$  is a weight factor.

We introduce uncertainty in sub-shelf melting by controlling the magnitude of the calving rate with a scalar multiplier factor  $F_{\text{calv}}$ . This approach is similar to Briggs et al. [2013] and Pollard et al. [2016]. Here, we consider for  $F_{\text{calv}}$  a nominal value of 1.0 and an uncertainty range from 0.5 to 1.5, that is, we consider the calving rate to vary between 50 %–150 % of the nominal calving rate  $c_f$ .

### 8.2.2.5 Oceanic forcing

Sub-shelf melting is mainly controlled by sub-shelf ocean circulation, which can be affected by atmospheric changes. Ice-shelf thinning caused by increased sub-shelf melting leads to a reduction in ice-shelf buttressing. West Antarctica, where the bedrock lies mainly below sea level, is particularly vulnerable, as suggested by observational [Rignot et al., 2014] and modelling [Favier et al., 2014; Joughin et al., 2014] studies.

High melt rates at the base of ice shelves result from the inflow of relatively warm Circumpolar Deep Water in ice-shelf cavities [Hellmer et al., 2012; Schmidtko et al., 2014]. Changes in ocean circulation resulting in stronger sub-ice-shelf circulation are expected to increase basal melt rates at the base of ice shelves [Jacobs et al., 2011; Hellmer et al., 2017]. Increase in atmospheric temperature leading to the presence of warmer deep water on the continental shelf is expected to strengthen sub-ice-shelf circulation, thus leading to an increase in sub-shelf melting. Yet, the link between global climate change and changes in sub-shelf melting is not always clear: it has been suggested that future climate change could lead to an increase in sub-shelf melting [Hellmer et al., 2012; Timmermann and Hellmer, 2013], a positive meltwater feedback that enhances sub-ice-shelf circulation and can trigger a climate tipping point [Hellmer et al., 2017], and even to a decrease in sub-shelf melting [Dinniman et al., 2012]. Golledge et al. [2019] have also highlighted the need to couple ice-sheet models to climate models as the increased discharge of freshwater from the Antarctic ice sheet could trap warm waters of the Southern Ocean below the sea surface.

Here, we capture the basic overturning circulation in ice-shelf cavities with the PICO box model. In the PICO model, the strength of the overturning flux is represented by a single parameter that depends on the density difference, or equivalently on both the salinity and temperature differences, between the incoming water masses on the continental shelf and the water masses near the deep grounding line of the ice shelf. An increase in the ocean temperature on the continental shelf leads to a stronger overturning flux and higher melt rates at the base of ice shelves. The ocean temperature on the continental shelf is determined from the present-day ocean temperature  $T_{\text{oc}}^{\text{obs}}$  and the change in background atmospheric temperature  $\Delta T$  via the lin-

ear relationship in Equation (8.1).

We introduce uncertainty in sub-shelf melting by controlling the strength of the overturning flux through uncertainty in the ocean temperature on the continental shelf. Hence, we consider the ocean melt factor  $F_{\text{melt}}$  as an uncertain parameter with a nominal value of 0.3 [Maris et al., 2014; Golledge et al., 2015] and an uncertainty range from 0.1 to 0.8.

### 8.2.2.6 Ice-shelf rheology

Ice rheology in large-scale ice-sheet models is usually described as an isotropic material obeying Glen's flow law [Greve and Blatter, 2009a]. However, ice is known to be an anisotropic material whose fabric is dependent on the temperature field, the strain-rate history, and the stress history [Ma et al., 2010; Calonne et al., 2017]. For a given fabric, the anisotropic response depends on the stress regime, which explains the ice stiffening when moving from a shear-dominated stress regime for grounded ice to an extension-dominated stress regime for floating ice.

We introduce an ice-shelf tune parameter  $E_{\text{shelf}}$  that accounts for anisotropy between grounded and floating ice. A lower value makes ice shelves more viscous [Briggs et al., 2013; Maris et al., 2014]. We consider for  $E_{\text{shelf}}$  a nominal value of 0.5 and an uncertainty range from 0.2 to 1, where a value of 0.5 means that the ice in the ice shelves is 2 times more viscous than without shelf tuning.

### 8.2.2.7 Bedrock relaxation

Bedrock relaxation due to deglaciation may induce a negative feedback that promotes stability in marine portions and mitigates the effect of a marine ice-sheet instability [Gomez et al., 2010, 2013; Adhikari et al., 2014]. The amplitude of the glacial isostatic uplift is determined by the flexural rigidity of the lithosphere and the viscous relaxation time of the asthenosphere. Recent studies [Van der Wal et al., 2015; Chen et al., 2018] have shown significant differences in the properties of the lithosphere and the asthenosphere between West and East Antarctica. Van der Wal et al. [2015] have found a lower viscosity and therefore a lower relaxation time for Earth's mantle underneath West Antarctica, making the glacial isostatic uplift in this region more sensitive to changes in ice thickness.

We account for the differences between East and West Antarctica by introducing two characteristic relaxation times  $\tau_e$  and  $\tau_w$  that we consider to both have a nominal value of 3000 years. We consider that  $\tau_e$  has an uncertainty range from 2500 to 5000 years and that  $\tau_w$  has an uncertainty range from 1000 to 3500 years.

## 8.2.3 Uncertainty quantification methods

### 8.2.3.1 Characterisation of uncertainty

To quantify the impact of uncertainties on the AIS response, we adopt a probabilistic framework. Here, we assume, in the absence of any prior information other than the aforementioned nominal values and minimal and maximal values of the uncertainty ranges, that the parameters  $F_{\text{calv}}$ ,  $F_{\text{melt}}$ ,  $E_{\text{shelf}}$ ,  $\tau_e$ , and  $\tau_w$  are uniform independent random variables with bounds given

by the minimal and maximal values of their uncertainty ranges. We explore the uncertainty in the sliding exponent  $m$  by considering its nominal and extremal values separately, thus allowing us to reduce the dimension of the parameter space while being consistent with other studies [Ritz et al., 2015]. We explore the uncertainty in the atmospheric forcing  $\Delta T$  by considering the four RCP scenarios. We limit the probabilistic characterisation to assuming uniform probability density functions, and we do not address how this probabilistic characterisation could be refined by using expert assessment, data, and statistical methods such as Bayesian inference. Yet, we provide results that give some insight into the impact of the choice of this probabilistic characterisation later in Section 8.3.6. We refer the reader to Petra et al. [2014], Isaac et al. [2015], Ruckert et al. [2017], Gopalan et al. [2018], and Conrad et al. [2018] for applications of Bayesian inference in glaciology and to Aschwanden et al. [2016] and Gillet-Chaulet et al. [2016] for examples of a calibration of the sliding exponent based on a comparison between simulated and observed surface velocities that can be used to prescribe a probabilistic characterisation of the sliding exponent.

### 8.2.3.2 Propagation of uncertainty

Given the probabilistic characterisation of the uncertainty in the parameters, the propagation of uncertainty serves to assess the impact of the uncertainty on the global mean sea-level change. In particular, its intent is to estimate the probability density functions for the change in GMSL as well as some of its statistical descriptors such as its mean, variance, and quantiles. Various methods have been developed in UQ to estimate these statistical descriptors in a nonintrusive manner treating the ice-sheet model as a black box. Here, we use emulation methods based on a polynomial chaos (PC) expansion.

An emulator, also known as a surrogate model, is a computational model that mimics the ice-sheet model at low computational cost. Although emulators can also be obtained by Gaussian process regression [Rasmussen and Williams, 2006], we use polynomial chaos (PC) expansions [Ghanem and Spanos, 2003; Le Maître and Knio, 2010], which involve approximating the parameters-to-projection relationship as a polynomial in the parameters. We write this polynomial as a linear combination of polynomial basis functions and use least-squares regression (Appendix 8.A) to evaluate the coefficients from a limited number of ice-sheet model runs at an ensemble of training points in the parameter space. The training points must be adequately chosen in the parameter space [Hadigol and Doostan, 2018] and the convergence of the PC expansion must be assessed to ensure accuracy. PC expansion may suffer from limitations: PC expansions require the parameters-to-projection relationship to be sufficiently smooth (no discontinuity or highly non-linear behaviour) to allow an efficient approximation as a low-degree polynomial and PC expansions may be inefficient in high-dimensional problems.

The emulator of the relationship between the parameters and the projection is then used as a substitute for the ice-sheet model in a Monte Carlo method [Robert and Casella, 2013], in which samples of the parameters are drawn randomly from their probability density function and mapped through the emulator into corresponding samples of the projections. Approximations to the probability density function of the projection and its statistical descriptors are then obtained from these samples of the projections by using statistical estimation methods: for instance, the mean and quantiles are approximated with the sample mean and quantiles.

The use of an emulator has the following advantages: (i) it provides an inexpensive approximation of the ice-sheet model that accelerates UQ; (ii) it provides an explicit view of the relationship between the parameters and the projection, highlighting potential linear or non-linear dependences and interactions between the parameters; (iii) it allows efficient interpolation of the projections in the parameter space; (iv) it can be used to carry out stochastic sensitivity analysis to assess the influence of each parameter on the projections; (v) under certain conditions, the same emulator can be reused between UQ analyses with different probability density functions for the parameters; and (vi) it can be used for Bayesian calibration [Ruckert et al., 2017].

We consider an ensemble of 20 distinct model configurations given by each combination of RCP scenario with a sliding law ( $m = 1, 2, 3$ , or 5) and each combination of RCP scenario with the TGL parameterisation under the weakly non-linear sliding law ( $m = 2$ ). For each model configuration, we built a separate PC expansion to investigate the impact of uncertainty in the five parameters  $F_{\text{calv}}$ ,  $F_{\text{melt}}$ ,  $E_{\text{shelf}}$ ,  $\tau_e$ , and  $\tau_w$  on the uncertainty in  $\Delta\text{GMSL}$ . Here, we assume the continental response of the Antarctic ice sheet, as measured through  $\Delta\text{GMSL}$ , to be sufficiently smooth to be represented with a PC expansion. For each model configuration, we generated an ensemble of 500 training points in the parameter space with a maximin Latin hypercube sampling design [Stein, 1987] and performed 500 forward simulations at these training points. In total, we carried out 10 000 forward simulations of the f.ETISH model. For each model configuration and time instant of analysis, we fitted to the corresponding ensemble of 500 training points and forward simulations a polynomial chaos expansion of degree 3, which we then used as an emulator to evaluate the statistical descriptors, either directly from the coefficients of the PC expansion or by running the emulator with an ensemble of  $10^6$  independent and identically distributed samples from the parameter space. We present a convergence study and cross-validation for the PC expansion in Appendix 8.A. Finally, the confidence regions for each model configuration are determined directly from the corresponding ensemble of 500 training points and forward simulations without the need for an emulator.

### 8.2.3.3 Stochastic sensitivity analysis

Stochastic sensitivity analysis serves to identify which uncertain parameters and their associated physical phenomenon are most influential in inducing uncertainty in the ice-sheet response. Here, we adopt the variance-based sensitivity indices [Saltelli et al., 2008], also called Sobol indices, described in more detail in Appendix 8.B. Variance-based sensitivity indices rely on the decomposition of the variance of the projections as a sum of contributions from each uncertain parameter taken individually and an interaction term. Then, the Sobol index of a given uncertain parameter represents the fraction of the variance of the projections explained as stemming from this sole uncertain parameter. A Sobol index takes values between 0 and 1, whereby a value of 1 indicates that the entire variance of the projections is explained by this sole uncertain parameter and a value of 0 indicates that the uncertain parameter has no impact on the projection uncertainty.

We compute the Sobol indices directly from the PC coefficients [Crestaux et al., 2009; Le Gratiet et al., 2017].

### 8.2.3.4 Confidence regions for grounded-ice retreat

To gain insight into the impact of the uncertainty in determining which regions of Antarctica are most at risk of ungrounding, we construct confidence regions for grounded ice for several probability levels. We define a confidence region for grounded ice for a given probability level as a region of Antarctica that remains covered everywhere with grounded ice with a probability of at least the given probability level under the uncertainty introduced in the ice-sheet model (see Appendix 8.C for the mathematical definition). The differences between these confidence regions for grounded ice for different probability levels provide insight into the risk of ungrounding (see Section 8.3.5). Such confidence regions are useful because confidence regions with boundaries far from the initial grounding line may indicate an important MISI and large differences between confidence regions for different probability levels indicate a significant impact of the uncertainty on the ice-sheet ungrounding. We construct these confidence regions for grounded ice based on an extension of previous work by Bolin and Lindgren [2015] for Gaussian random fields to our glaciological context.

## 8.3 Results

We present nominal and probabilistic projections (relative to 2000 CE) for short-term (2100), medium-term (2300), and long-term (3000) timescales under different RCP scenarios and sliding laws.

### 8.3.1 Nominal projections

We first present nominal projections obtained using the nominal values of the parameters given in Table 8.1. We first present results under nominal conditions in order to assess subsequently the impact of uncertainties on AIS sea-level rise projections. Under nominal conditions, we find (Table 8.2) in RCP 2.6 an AIS contribution to sea level of 0.02 m by 2100, 0.07 m by 2300, and 0.20 m by 3000 and in RCP 8.5 an AIS contribution to sea level of 0.05 m by 2100, 0.59 m by 2300, and 3.90 m by 3000. In Figure 8.3(a), we represented the nominal projections as a function of time in all RCP scenarios. We find that the nominal AIS contribution to sea level is rather small in the first decades and starts to increase more significantly around 2100 with a rather constant growth rate. In Figures 8.3(b)–(e), we represented the nominal grounded ice region by 3000 for all RCP scenarios. We find that there is little ungrounding by 3000 in RCP 2.6 and RCP 4.5, while we observe a more significant ungrounding in Siple Coast and the Ronne basin in RCP 6.0 and a much more significant ungrounding in Siple Coast and the Amundsen Sea sector in RCP 8.5.

Year	RCP 2.6	RCP 4.5	RCP 6.0	RCP 8.5
2100	0.02	0.01	0.03	0.05
2300	0.07	0.10	0.22	0.59
3000	0.20	0.39	0.86	3.90

Table 8.2: Nominal projections (in metres) of AIS contribution to sea level on short-term (2100), medium-term (2300), and long-term (3000) timescales in different RCP scenarios.

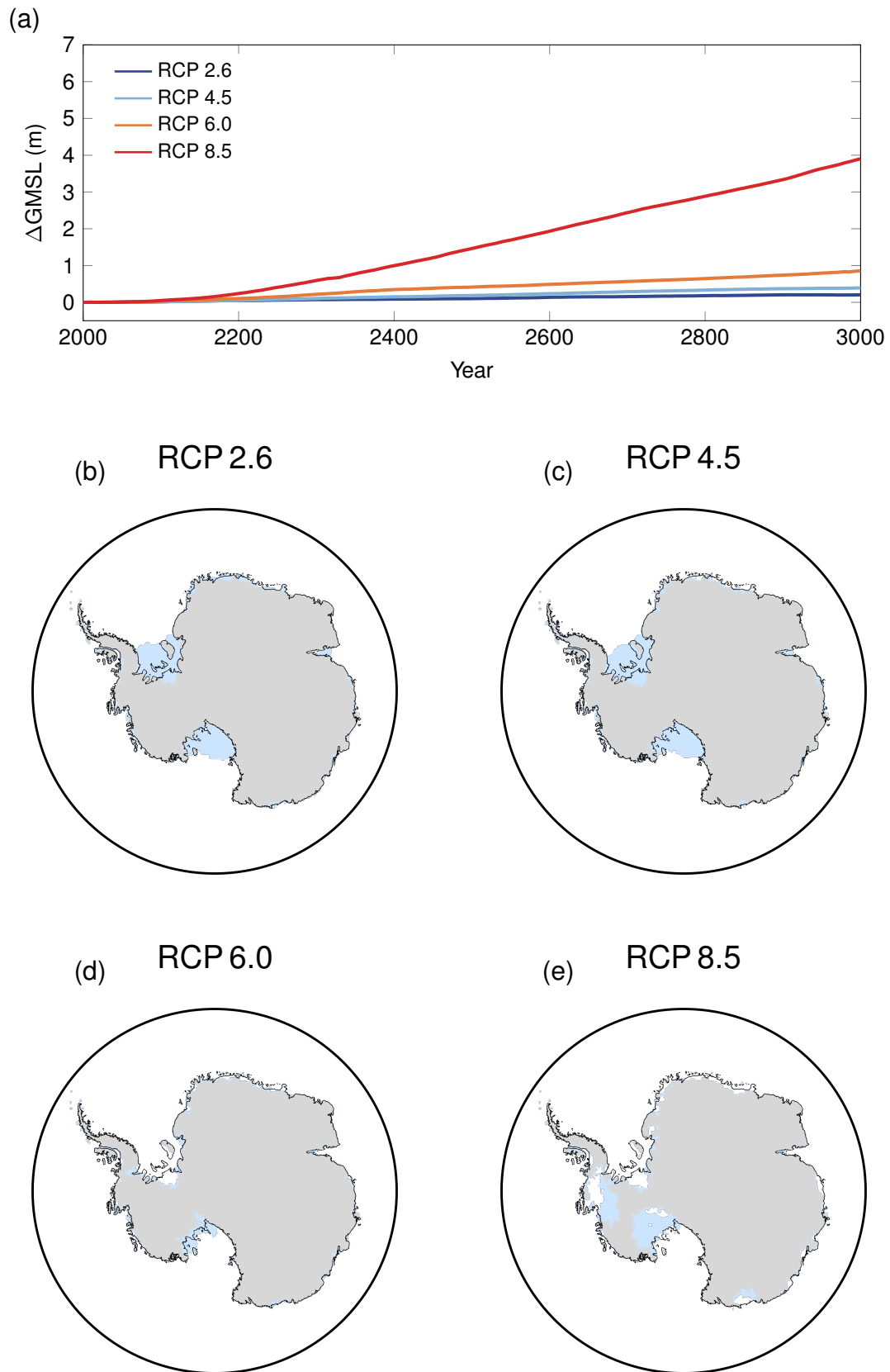


Figure 8.3: (a) Nominal AIS contribution to sea level. Grounded ice (grey area) and ice shelves (light blue area) by 3000 in (b) RCP 2.6, (c) RCP 4.5, (d) RCP 6.0, and (e) RCP 8.5 for the nominal values of the parameters. The present-day grounding line is shown in black.

### 8.3.2 Parameters-to-projections relationship

One of the advantages of a polynomial chaos expansion is that it provides an explicit approximation to the parameters-to-projections relationship, which can be visualised to gain insight into the relationship between the parameters and the projections.

In Figures 8.4 and 8.5, we used the PC expansions to visualise how the projections depend on each parameter individually (one-at-a-time) while keeping the other parameters fixed at their nominal value under the weakly non-linear sliding law in RCP 2.6 and RCP 8.5, respectively.

Figures 8.4(a)–(c) show that in RCP 2.6  $\Delta\text{GMSL}$  increases with an increase in the calving factor non-linearly. The slope is steeper for small values of this parameter, thus suggesting that  $\Delta\text{GMSL}$  is more sensitive to small changes about small values than about higher values. Figures 8.4(d)–(f) indicate that  $\Delta\text{GMSL}$  increases rather linearly with an increase in the melt factor. Figures 8.4(g)–(i) indicate a rather quadratic dependence on the shelf anisotropy factor for short-term and medium-term projections, with small and large values of this factor leading to more significant ice loss than the nominal value. This quadratic dependence can be explained by the influence of  $E_{\text{shelf}}$  on two competing processes: a higher value of  $E_{\text{shelf}}$  softens the ice, thus leading to faster ice flow in the ice shelves; but a higher value of  $E_{\text{shelf}}$  also leads to ice-shelf thinning, thus reducing ice flux at the grounding line. In addition, we find that  $\Delta\text{GMSL}$  depends only little on the bedrock relaxation times (Figures 8.4(j)–(o)). In fact, lower bedrock relaxation times do tend to stabilise the ice sheet and lower sea-level rise but this impact is weak compared to the influence of the other parameters. This result may be explained by our orders of magnitude of the bedrock relaxation times being of the order of a few millennia, thus preventing any significant uplift in the next few centuries. Yet, a recent study by Barletta et al. [2018] has suggested a bedrock relaxation timescale of the order of decades to a century in the Amundsen Sea sector, thus making glacial isostatic adjustment significant in the next decades and centuries in this region. To assess the influence of shorter relaxation times, we performed additional numerical experiments, albeit not reported in this chapter, with a relaxation time for the whole West Antarctic ice sheet that varies widely from a few decades to a few millennia. For this range of values, we found that bedrock relaxation has a more significant influence on the AIS response, with a contribution to the uncertainty in  $\Delta\text{GMSL}$  that can reach 10% in RCP 2.6 when  $\tau_w$  is allowed to vary widely between 50 years and 3500 years.

We find in RCP 8.5 similar trends. However, whereas  $F_{\text{calv}}$ ,  $F_{\text{melt}}$ , and  $E_{\text{shelf}}$  influence  $\Delta\text{GMSL}$  equally in RCP 2.6, the melt factor influences  $\Delta\text{GMSL}$  most significantly in RCP 8.5. Whereas Figures 8.5(d)–(e) show that  $\Delta\text{GMSL}$  increases rather linearly with an increase in the melt factor, Figure 8.5(f) shows that  $\Delta\text{GMSL}$  rather levels off at a plateau for large values of  $F_{\text{melt}}$  for long-term projections in RCP 8.5.

Additionally, Figure 8.16 shows the emulators for several pairs of parameters with the other parameters fixed at their nominal values in RCP 2.6 and RCP 8.5. These figures show essentially the same trends as those identified in Figures 8.4 and 8.5, in addition to interaction effects between the parameters. In particular, we find that smaller values of the calving and melt factors lead to mass gain (Figure 8.16(c)), while larger values of the shelf anisotropy and melt factors lead to an important mass loss (Figure 8.16(d)).

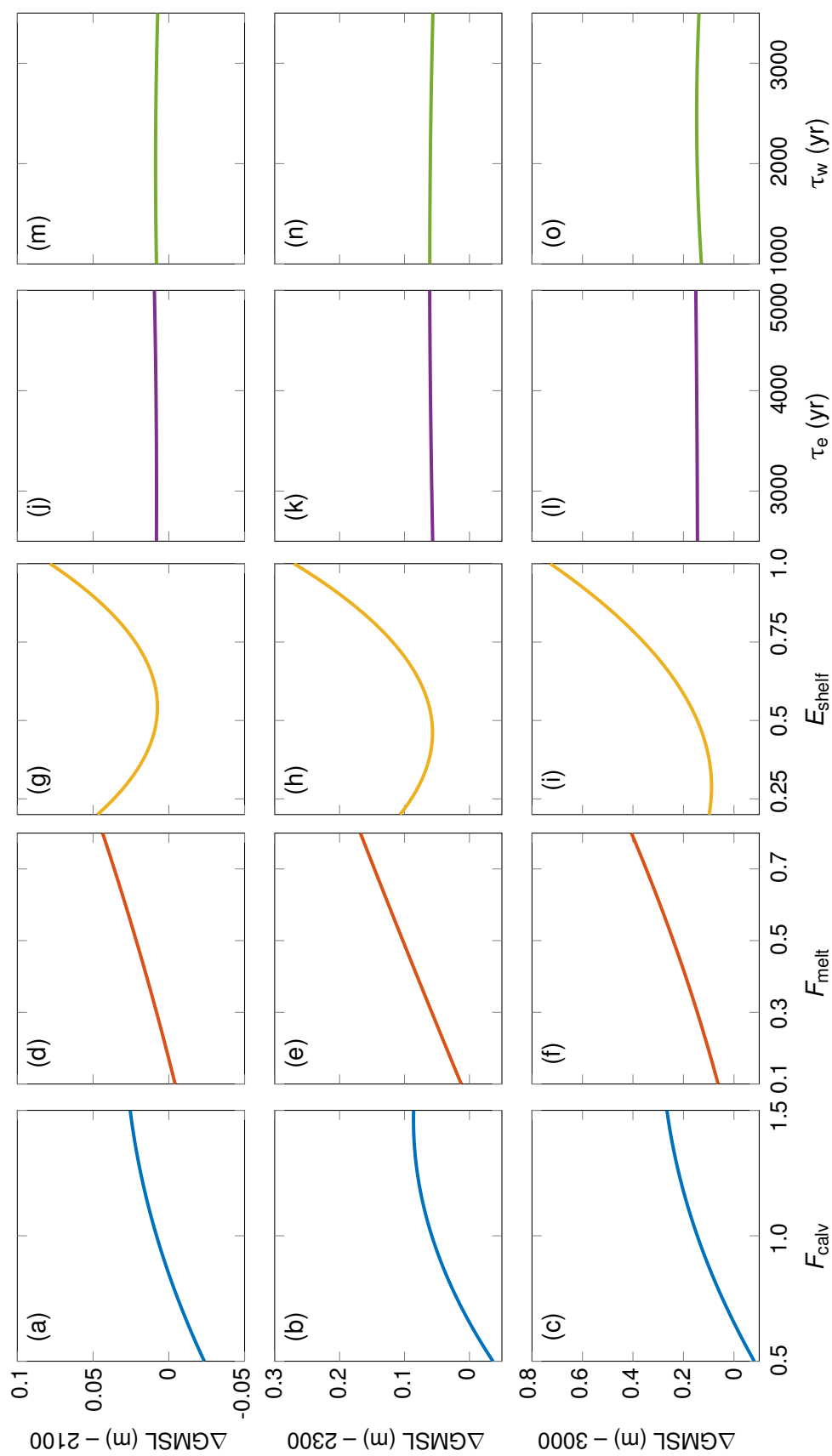


Figure 8.4: Representation of the parameters-to-projection relationships in RCP 2.6 under the weakly non-linear sliding law as given by a PC expansion. The PC expansion is shown for each parameter individually, with the other parameters fixed at their nominal value. PC expansions at (a, d, g, j, m) 2100, (b, e, h, k, n) 2300, and (c, f, i, l, o) 3000.

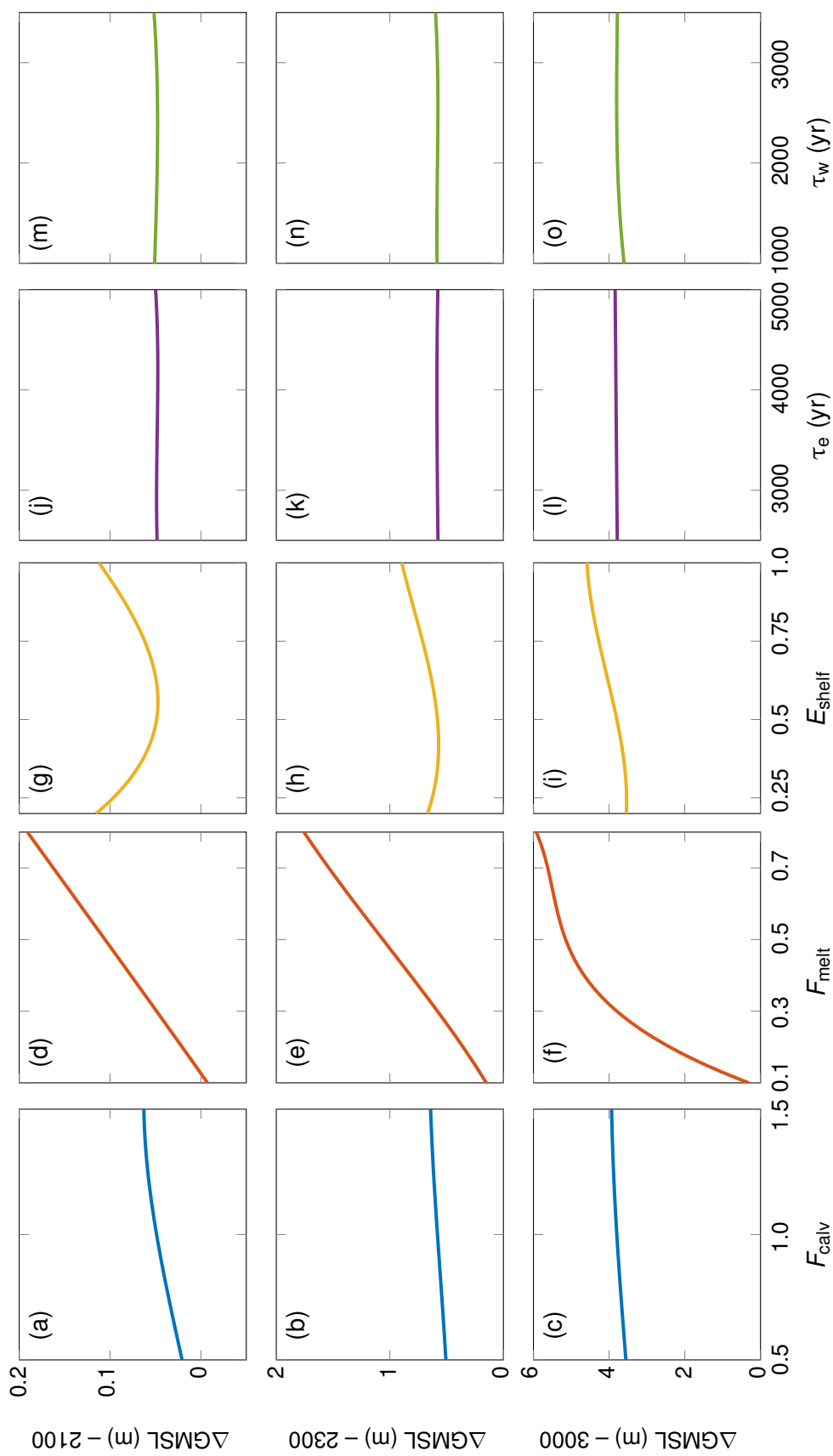


Figure 8.5: Same as Figure 8.4 but in RCP 8.5.

### 8.3.3 Sea-level rise projections

Under parametric uncertainties, we find (Table 8.3, Figure 8.6) in RCP 2.6 a median AIS contribution to sea level that ranges from 0.02 to 0.03 m by 2100, from 0.07 to 0.13 m by 2300, and from 0.18 to 0.30 m by 3000 for the three sliding laws, as compared with the nominal projections of 0.02 m by 2100, 0.07 m by 2300, and 0.20 m by 3000; and we find in RCP 8.5 a median AIS contribution to sea level that ranges from 0.09 to 0.11 m by 2100, from 0.78 to 1.15 m by 2300, and from 3.18 to 6.12 m by 3000, as compared with the nominal projection of 0.05 m by 2100, 0.59 m by 2300, and 3.90 m by 3000. The median AIS sea-level rise projections are higher than the nominal projections, except for certain cases under the viscous sliding law. The nominal projections are not equal to the median projections because the ice-sheet model exhibits non-linearities, as illustrated in Figures 8.4 and 8.5, and the probability density functions for the parameters are not symmetric about their nominal value. As in the nominal projections, we find that in all RCP scenarios and under all sliding laws, the median AIS contribution to sea level is rather small in the first decades and starts to increase around 2100. As in the nominal projections, the median AIS contribution to sea level shows a rather constant growth rate in RCP 2.6, RCP 4.5, and RCP 6.0; contrary to the nominal projection, the median AIS contribution to sea level exhibits initially an acceleration before subsequently exhibiting a deceleration in RCP 8.5 under both non-linear sliding laws (Figure 8.6). This behaviour in the median projections in RCP 8.5 is a consequence of the initial rapid collapse of the West Antarctic ice sheet, which contributes 3–3.5 m to sea level, followed by a slower retreat in the East Antarctic ice sheet. By contrast, the nominal projections, which involve a melt factor of 0.3, indicate that the West Antarctic ice sheet does not completely collapse by the year 3000.

In RCP 2.6, we find (Table 8.3) 5–95 % probability intervals for sea-level rise projections that range from  $-0.06$  to  $0.10$  m by 2100, from  $-0.14$  to  $0.31$  m by 2300, and from  $-0.36$  to  $0.91$  m by 3000. In RCP 8.5, these probability intervals range from  $-0.03$  to  $0.23$  m by 2100,  $0.17$  to  $2.01$  m by 2300, and  $0.82$  to  $7.68$  m by 3000. The nominal projections are inside the 5–95 % probability intervals. We see that the 5–95 % probability intervals indicate an increase in sea level, though a decrease cannot be ruled out for the viscous sliding law and cooler atmospheric conditions. Figure 8.6 highlights that the 33–66 % probability intervals become wider under warmer atmospheric conditions and, to a lesser extent, more non-linear sliding conditions. The uncertainty in the projections due to parametric uncertainty is rather significant, with possible overlaps between the 5–95 % probability intervals for different RCP scenarios. For instance, Figure 8.4(i) shows that a contribution to sea level of about 0.7 m can be reached by 3000 in RCP 2.6 for the extreme value  $E_{\text{shelf}} = 1$ , while Figure 8.5(f) shows that this value is reached in RCP 8.5 for very limited sub-shelf melting ( $F_{\text{melt}}$  of about 0.12). This suggests that projections with similar contributions to sea level can arise in different RCP scenarios with different combinations of parameter values. Measuring the relative dispersion in  $\Delta\text{GMSL}$  via the coefficients of variation, that is, the ratio between the standard deviation and the mean value, we find a coefficient of variation of 0.74 in RCP 2.6, 0.67 in RCP 4.5, 0.59 in RCP 6.0, and 0.33 in RCP 8.5 by 3000 under the weakly non-linear sliding law. This demonstrates that the relative uncertainty in  $\Delta\text{GSLM}$  projections is higher in cooler RCP scenarios. This results from a much larger increase in the values of  $\Delta\text{GSLM}$  projections compared to the increase in their dispersion when the RCP scenario gets warmer.

Year	Sliding ( $m$ )	RCP 2.6	RCP 4.5	RCP 6.0	RCP 8.5
2100	1	0.02 (−0.06, 0.10)	0.04 (−0.05, 0.12)	0.05 (−0.04, 0.13)	0.09 (−0.03, 0.20)
	2	0.03 (−0.01, 0.09)	0.05 (0.00, 0.11)	0.06 (0.00, 0.14)	0.11 (0.01, 0.22)
	3	0.03 (−0.03, 0.09)	0.04 (−0.02, 0.11)	0.06 (−0.01, 0.14)	0.11 (0.00, 0.23)
2300	1	0.07 (−0.14, 0.31)	0.20 (−0.09, 0.48)	0.36 (−0.04, 0.72)	0.78 (0.17, 1.35)
	2	0.13 (0.01, 0.30)	0.26 (0.03, 0.54)	0.45 (0.06, 0.88)	1.04 (0.27, 1.81)
	3	0.09 (−0.09, 0.29)	0.28 (−0.03, 0.58)	0.50 (0.02, 0.96)	1.15 (0.31, 2.01)
3000	1	0.18 (−0.36, 0.82)	0.77 (−0.14, 1.82)	1.60 (−0.01, 2.71)	3.18 (0.82, 4.25)
	2	0.30 (−0.01, 0.82)	0.93 (0.08, 2.24)	2.16 (0.15, 4.06)	5.08 (1.36, 6.00)
	3	0.30 (−0.25, 0.91)	1.15 (0.08, 2.56)	2.50 (0.34, 5.17)	6.12 (1.65, 7.68)

Table 8.3: Probabilistic projections (in metres) of the AIS contribution to sea level on short-term (2100), medium-term (2300), and long-term (3000) timescales in different RCP scenarios and under different sliding conditions with Schoof’s grounding-line parameterisation.  $\Delta$ GMSL projections are the median projections with their 5–95 % probability intervals between parentheses.

Figure 8.7 shows the probability density functions for the change in GMSL at different timescales. The results display essentially unimodal probability density functions with wider tails for warmer scenarios and longer timescales. In RCP 2.6, the probability density functions resemble Gaussian probability density functions. In RCP 8.5 and at the short and medium timescales, the probability density functions are rather flat, which can be explained by the dependence of  $\Delta$ GMSL on  $F_{\text{melt}}$  being rather linear (Figures 8.5(d) and (e)). In RCP 8.5 and at the long timescale, the probability density functions exhibit a more localised mode at higher values of  $\Delta$ GMSL, which can be explained by the collapse of the West Antarctic ice sheet and thus the presence of the plateau for higher values of the melt factor (Figure 8.5(f)).

Figure 8.8 gives the probability of exceeding the threshold values of 0.5 m, 1.0 m, and 1.5 m as a function of time. We find that the probability of exceeding 0.5 m by 2100 is negligible (probability of less than 1 %) in all RCP scenarios and under all sliding conditions. In RCP 2.6, the AIS contribution to sea level in the next centuries is strongly limited, with a probability of exceeding 0.5 m by 3000 reaching at most 30 %. In RCP 4.5 and RCP 6.0, we found nominal sea-level rise projections well below 1.5 m, while in RCP 8.5 this threshold is exceeded. In the presence of uncertainties, we find that the probability of exceeding 1.5 m of sea-level rise by 3000 can reach about 35 % in RCP 4.5, about 70 % in RCP 6.0, and about 95 % in RCP 8.5. The last result can be seen from Figure 8.5, which indicates that  $\Delta$ GMSL is below 1.5 m only in a small region of the parameter space associated with small values of the melt factor. Furthermore, the shape of the exceedance curves in Figure 8.8 provides some insight into the uncertainty in the time when a certain threshold value is exceeded. The time when  $\Delta$ GMSL exceeds 0.5 m with a probability of 33 % under the weakly non-linear sliding law is 2415 in RCP 4.5, 2270 in RCP 6.0, and 2185 in RCP 8.5, while this value is exceeded with a probability of 66 % at 2790 in RCP 4.5, 2430 in RCP 6.0, and 2245 in RCP 8.5. We find that nominal projections overestimate the time when  $\Delta$ GMSL exceeds 0.5 m, with the exceedance time being beyond 3000 in RCP 4.5, around 2620 in RCP 6.0, and around 2280 in RCP 8.5.

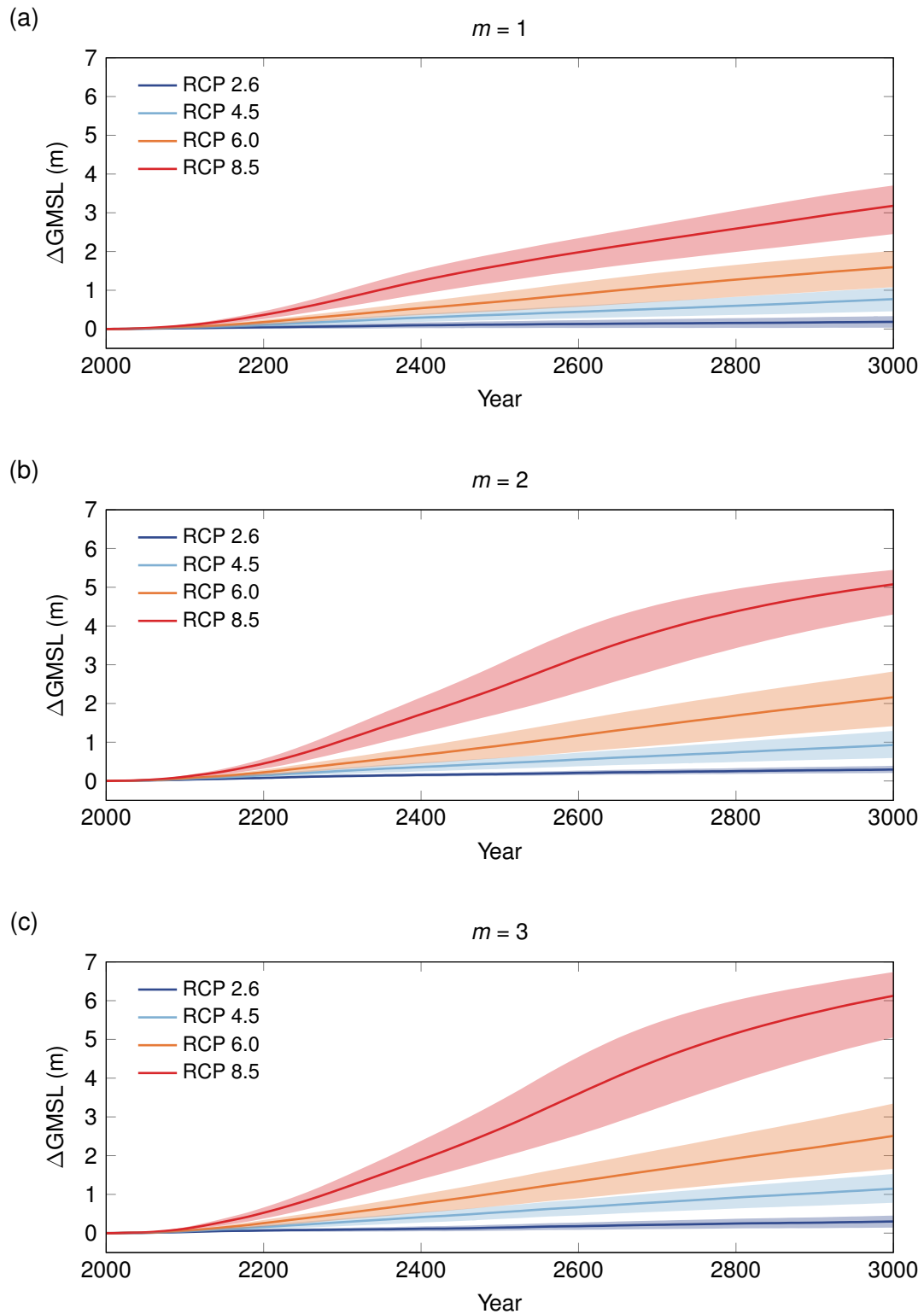


Figure 8.6: AIS contribution to sea level. (a) Viscous sliding law, (b) weakly nonlinear sliding law, and (c) strongly nonlinear sliding law. Solid lines are the median projections and the shaded areas are the 33–66% probability intervals that represent the parametric uncertainty in the model.

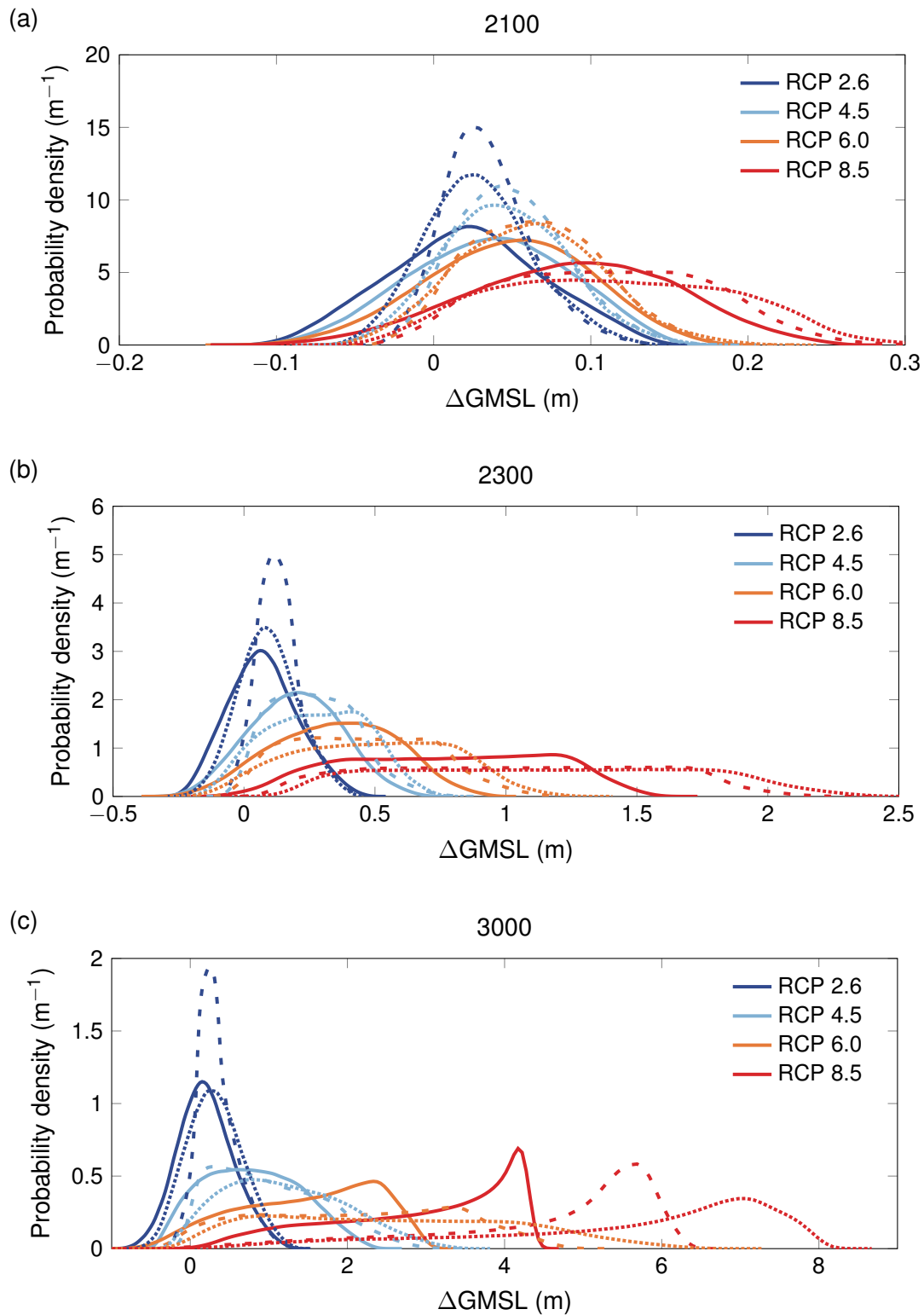


Figure 8.7: Probability density functions for the AIS contribution to sea level at (a) 2100, (b) 2300, and (c) 3000 under the viscous sliding law (solid lines), the weakly non-linear sliding law (dashed lines), and the strongly non-linear sliding law (dotted lines).

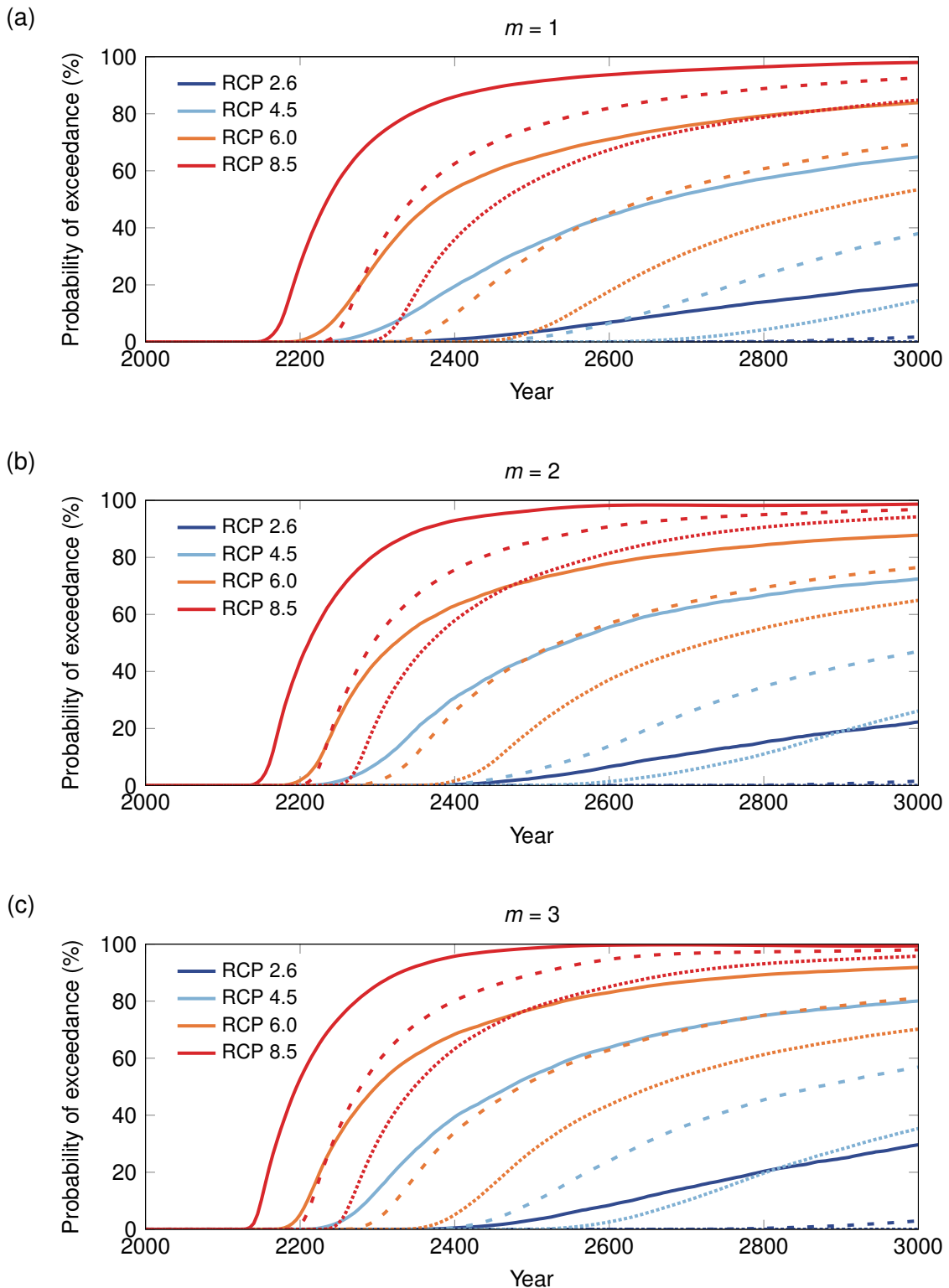


Figure 8.8: Probability of exceeding some characteristic threshold sea-level rise values as a function of time, evaluated from the complementary cumulative distribution functions of the probability density functions for  $\Delta\text{GMSL}$ . Probability of exceedance under (a) the viscous sliding law, (b) the weakly non-linear sliding law, and (c) the strongly non-linear sliding law. Solid lines correspond to a threshold value of 0.5 m, dashed lines to a threshold value of 1 m, and dotted lines to a threshold value of 1.5 m.

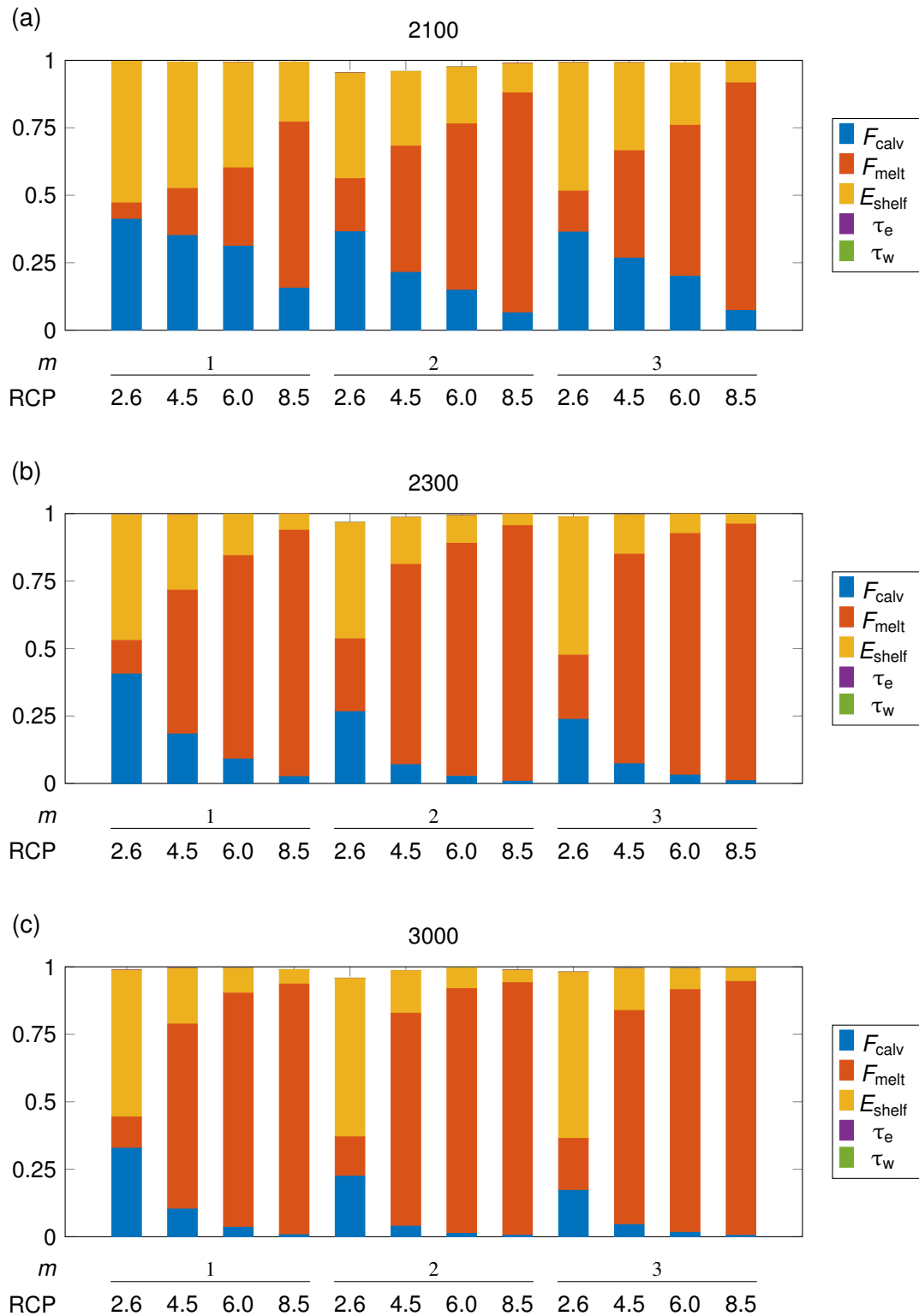


Figure 8.9: Sobol sensitivity indices for the AIS contribution to sea level in different RCP scenarios and for different values of the sliding exponent  $m$  in Weertman's sliding law. Sobol indices at (a) 2100, (b) 2300, and (c) 3000. The gap between the height of a bar and the unit value represents the interaction index.

### 8.3.4 Stochastic sensitivity analysis

Figure 8.9 provides the Sobol sensitivity indices for the change in GMSL on short-term, medium-term and long-term timescales in different RCP scenarios and under different sliding laws. We find that in RCP 2.6, the largest contribution to the uncertainty in  $\Delta\text{GMSL}$  stems from the uncertainty in the ice-shelf rheology (Sobol indices ranging from 40 % to 60 %) followed by the uncertainty in the calving rate (Sobol indices ranging from 20 % to 40 %) and sub-shelf melting (Sobol indices ranging from 5 % to 25 %). Indeed, in RCP 2.6, sub-shelf melting plays only a limited role because ocean conditions remain essentially unchanged. Therefore, in RCP 2.6, the dispersion in  $\Delta\text{GMSL}$  is mainly controlled by the ice-shelf rheology, which controls ice flow and buttressing in ice shelves, as well as calving, which reduces the extent of ice shelves and their buttressing.

By contrast, in warmer RCP scenarios and for longer timescales, the dominant source of uncertainty becomes the uncertainty in sub-shelf melting, which accounts in RCP 8.5 for more than 90 % of the uncertainty in sea-level rise projections. As shown in Figure 8.5, in RCP 8.5 at 3000  $\Delta\text{GMSL}$  varies by several metres over the range of values of  $F_{\text{melt}}$ , while  $\Delta\text{GMSL}$  varies only by a few tens of centimetres over the range of values of the other parameters. Hence, the dominant influence of the uncertainty in the melting factor is also a consequence of the rather wide uncertainty range that we chose for this parameter.

Finally, we find that, in all RCP scenarios and under all sliding laws, the uncertainty in the bedrock relaxation times for West and East Antarctica has a limited impact (Sobol index smaller than 1 %), which is a direct consequence of the very limited dependence of the projections on the bedrock relaxation times. Moreover, the interactions between the parameters have a negligible impact as the sums of the individual Sobol indices account almost entirely for the variances of the projections.

### 8.3.5 Projections of grounded-ice retreat

Figure 8.10 provides insight into the regions of Antarctica that are most at risk of ungrounding in different RCP scenarios and at different timescales under the weakly non-linear sliding law. Figure 8.10 was obtained as follows. First, we determined the 100 % confidence region for grounded ice, that is, the region of Antarctica where ice is certain to remain grounded, and we coloured it in grey. Thus, there is no risk that the grounding line will retreat to within the grey region. Then, we determined the 95 % confidence region for grounded ice, that is, the region of Antarctica that remains covered everywhere with grounded ice with a probability of more than 95 %, and we coloured the portion of the 95 % confidence region that extends beyond the 100 % confidence region in dark blue. Thus, there is a low risk of (less than) 5 % that the grounding line will retreat to within the dark blue region. We continued this procedure for decreasing values of the confidence level and using different colours as indicated in the legend in Figure 8.10.

We find that ice remains grounded in regions above sea level. By contrast, in all RCP scenarios, the risk of ungrounding is highest in marine sectors of West Antarctica with fast-flowing ice streams, especially in Siple Coast, in the Ronne basin, notably Ellsworth Land, and in the Amundsen Sea sector. In warm RCP scenarios and at longer timescales, we also observe a risk

of grounding-line retreat in the Wilkes marine basin in East Antarctica, where the grounding line could retreat between 100 km (with a risk of 95 %) and 500 km (with a risk of 5 %) from its present-day position. The risk of retreat in Wilkes basin may partially explain the acceleration in sea-level rise that we observed in Figure 8.6 in RCP 8.5. The risk of grounding-line retreat in the Antarctic Peninsula is very limited due to the bedrock topography being above sea level, the marine glaciers being small, and a high increase in precipitation in this region.

In RCP 2.6, we observe that the grounding line is quite stable over the next millennium, with the 100 % confidence region for grounded ice being almost unchanged from the present-day grounded ice region (the 100 % confidence region for grounded ice by 3000 only differs from the present-day grounded ice region by a few tens of kilometres). In RCP 4.5, ice remains grounded in most of the West Antarctic ice sheet over the next centuries, but our results also suggest a risk of retreat of the grounding line in some sectors of West Antarctica on longer timescales. In RCP 6.0, we find that the West Antarctic ice sheet belongs by 3000 to the 66 % confidence region for grounded ice, while in RCP 8.5, it belongs by 3000 only to the 5 % confidence region. This suggests a risk of 33 % that a major collapse of the West Antarctic ice sheet might occur in RCP 6.0 by 3000 and a risk of 95 % that a major collapse of the West Antarctic ice sheet might occur in RCP 8.5 by 3000.

As compared with the nominal projections of a limited retreat of the grounding line in West Antarctica in RCP 6.0 by 3000, we find that the impact of the parametric uncertainty is that a complete collapse of the West Antarctic ice sheet may occur with a risk of 33 % in RCP 6.0 by 3000. Moreover, Figure 8.3(e) suggests that a complete disintegration of the West Antarctic ice sheet is underway by 3000 in RCP 8.5, while in Figure 8.10(l) the West Antarctic ice sheet has already collapsed by 3000.

Additionally, we compared the projections under the weakly non-linear sliding law with projections under the other sliding laws, that is, the viscous sliding law (Figure 8.21) and the strongly non-linear sliding law (Figure 8.22). We find a lower risk of retreat of the grounding line under the viscous sliding law with a slower disintegration of the West Antarctic ice sheet compared to the other sliding laws, especially in the drainage basins of Thwaites and Pine Island Glaciers, which belong to the 50 % confidence region for grounded ice by 3000 in RCP 8.5, while they belong to the 5 % confidence region by 3000 in RCP 8.5 for the other sliding laws. The strongly non-linear sliding law seems to favour a faster and deeper retreat of the grounding line, especially in the marine sectors of East Antarctica and the drainage basins of Thwaites and Pine Island Glaciers. However, Figure 8.10(i) and Figure 8.22(i) suggest that ungrounding may be less significant in Siple Coast under the strongly non-linear sliding law than the weakly non-linear sliding law. Actually, MISI may occur when driving stresses overcome resistive stresses [Waibel et al., 2018]. Driving stresses are primarily determined by the surface slopes, while resistive stresses depend on the basal sliding coefficient and the ice velocity through the sliding exponent. Driving stresses at the grounding line are higher in the Amundsen Sea sector than in Siple Coast due to steeper surface slopes, leading to a greater sensitivity of the grounding line in the former region to non-linearity and a more plastic response.

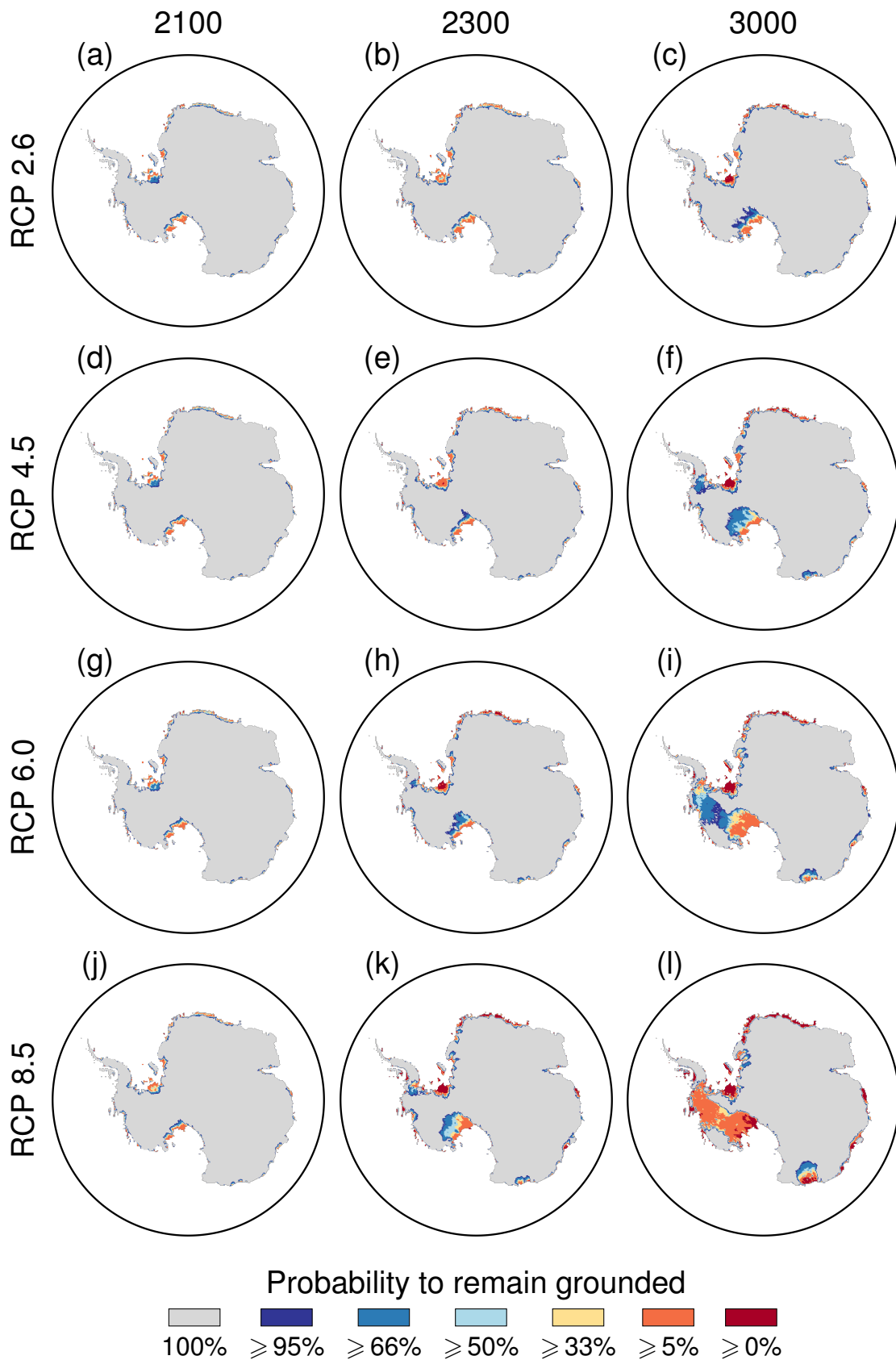


Figure 8.10: Confidence regions for grounded ice under the weakly non-linear sliding law. Confidence regions are shown at (a, d, g, j) 2100, (b, e, h, k) 2300, and (c, f, i, l) 3000.

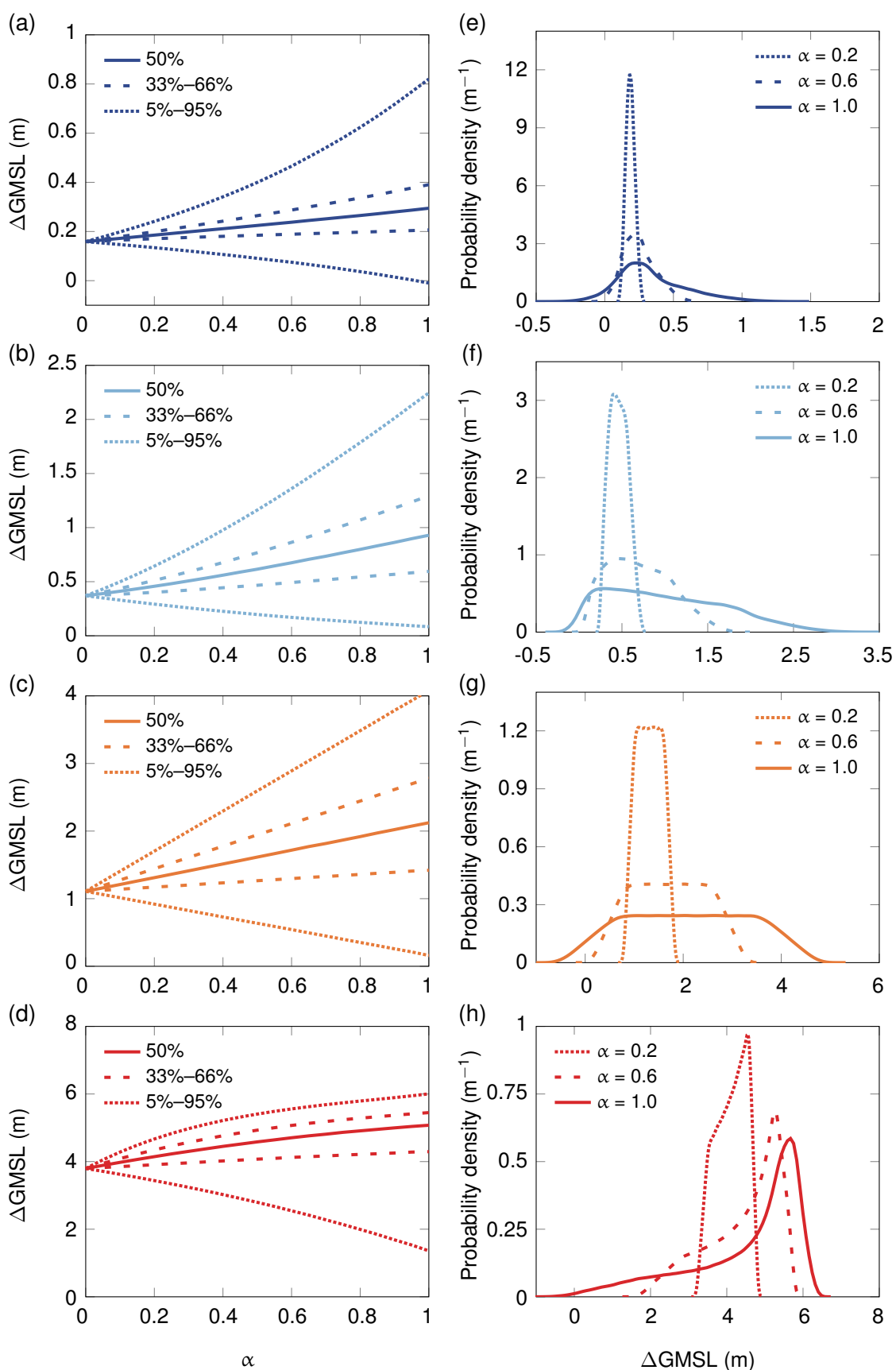


Figure 8.11: Robustness of probabilistic projections with respect to the scaling factor  $\alpha$ . Median projections and their 33–66 % and 5–95 % probability intervals by 3000 under the weakly non-linear sliding law in (a) RCP 2.6, (b) RCP 4.5, (c) RCP 6.0, and (d) RCP 8.5. Probability density functions for  $\alpha = 0.2$  (dotted lines),  $\alpha = 0.6$  (dashed lines), and  $\alpha = 1$  (solid lines) in (e) RCP 2.6, (f) RCP 4.5, (g) RCP 6.0, and (h) RCP 8.5.

### 8.3.6 Influence of the parameter probability density function

So far, we have represented the uncertain parameters  $F_{\text{calv}}$ ,  $F_{\text{melt}}$ ,  $E_{\text{shelf}}$ ,  $\tau_e$ , and  $\tau_w$  by a uniform distribution on a fixed support. For instance, the uncertain parameter  $F_{\text{calv}}$  is represented by a uniform distribution with support  $[F_{\text{calv,min}}, F_{\text{calv,max}}]$ , where  $F_{\text{calv,min}}$  and  $F_{\text{calv,max}}$  are the minimum and maximum values in Table 8.1. We now address the influence of the probabilistic characterisation of the parametric uncertainty on our probabilistic projections by controlling the size of these supports. Hence, we represent the uncertain parameters  $F_{\text{calv}}$ ,  $F_{\text{melt}}$ ,  $E_{\text{shelf}}$ ,  $\tau_e$ , and  $\tau_w$  by a family of uniform probability density functions indexed by a unique scaling factor  $\alpha \in [0, 1]$  that controls the supports of the uniform probability density functions. For instance, the uncertain parameter  $F_{\text{calv}}$  is represented for a given value of  $\alpha$  by a uniform distribution with support  $[F_{\text{calv,nom}} + \alpha(F_{\text{calv,min}} - F_{\text{calv,nom}}), F_{\text{calv,nom}} + \alpha(F_{\text{calv,max}} - F_{\text{calv,nom}})]$ , where  $F_{\text{calv,nom}}$ ,  $F_{\text{calv,min}}$ , and  $F_{\text{calv,max}}$  are the nominal, minimum, and maximum values in Table 8.1. For the other parameters, the supports are defined similarly. The value  $\alpha = 0$  represents the ice-sheet model without parametric uncertainty, that is, the ice-sheet model for the nominal values of the parameters, and the value  $\alpha = 1$  represents the full uncertainty ranges considered so far. We propagated the uncertainty from the parameters to the sea-level rise projections for different values of the scaling factor, reusing the emulator that we had built for  $\alpha = 1$  over the whole parameter space. Hence, the projections to follow for  $\alpha = 0$  based on this emulator are not exactly equal to the nominal projections determined directly from the ice-sheet model.

For the long-term projections, Figures 8.11(a)–(d) show the median and the 33–66 % and 5–95 % probability intervals as a function of the scaling factor in the different RCP scenarios under the weakly non-linear sliding law and Figures 8.11(e)–(h) show the probability density functions for the values  $\alpha = 0.2, 0.6$ , and  $1.0$ . We find that the median projections increase with an increase in the scaling factor and range in RCP 2.6 from 0.16 m to 0.30 m, in RCP 4.5 from 0.37 m to 0.93 m, in RCP 6.0 from 1.11 m to 2.16 m and in RCP 8.5 from 3.80 m to 5.08 m. In addition, the width of the probability intervals increases with increasing uncertainty in the parameters. While the width of the 33–66 % probability interval increases rather linearly with the scaling factor and is rather symmetric about the median, the width of the 5–95 % probability interval increases more non-linearly with an increase in the scaling factor, as illustrated in Figure 8.11(a) in RCP 2.6 and Figure 8.11(d) in RCP 8.5. The probability density functions attribute higher weight to larger values of  $\Delta\text{GMSL}$  under increased parametric uncertainty, with increased weight given to larger values of in particular  $E_{\text{shelf}}$  in RCP 2.6 (Figure 8.4(i)) and  $F_{\text{melt}}$  in RCP 8.5 (Figure 8.5(f)). Figures 8.11(a)–(d) show that the sensitivity of the amount of uncertainty in the projections (probability intervals) to the amount of uncertainty in the parameters (scaling factor) is higher for warmer scenarios, with an upper bound between RCP 6.0 and RCP 8.5 as a consequence of the collapse of the West Antarctic ice sheet.

### 8.3.7 Projections under a more plastic sliding law

We ran the same ensemble of simulations under a more plastic sliding law ( $m = 5$ ). Table 8.4 and Figure 8.12 give for the AIS contribution to sea level the median and the 33–66 % and 5–95 % probability intervals. As compared with less plastic sliding laws ( $m = 1, 2, 3$ ), we find an increase in sea-level rise projections on short-term and medium-term timescales, thus suggesting a more significant and faster response to perturbations under more plastic sliding conditions. On a long-term timescale, the ice-sheet mass loss can be less important under  $m = 5$  than  $m = 3$ ,

as observed in the median projections by 3000 in RCP 4.5 and RCP 8.5.

We find that overall the AIS contribution to sea level is an increasing function of the sliding exponent, with the differences between successive exponents getting smaller as  $m$  increases, as already pointed out by Gillet-Chaulet et al. [2016]; for instance, we observe a greater difference in the projections between  $m = 1$  and  $m = 2$  than between  $m = 3$  and  $m = 5$ . On longer timescales, tipping points and nonlinearities associated with MISI may trigger a slightly different response of the ice sheet depending on the initial conditions, which could explain the smaller ice loss in our results under  $m = 5$  than  $m = 3$ .

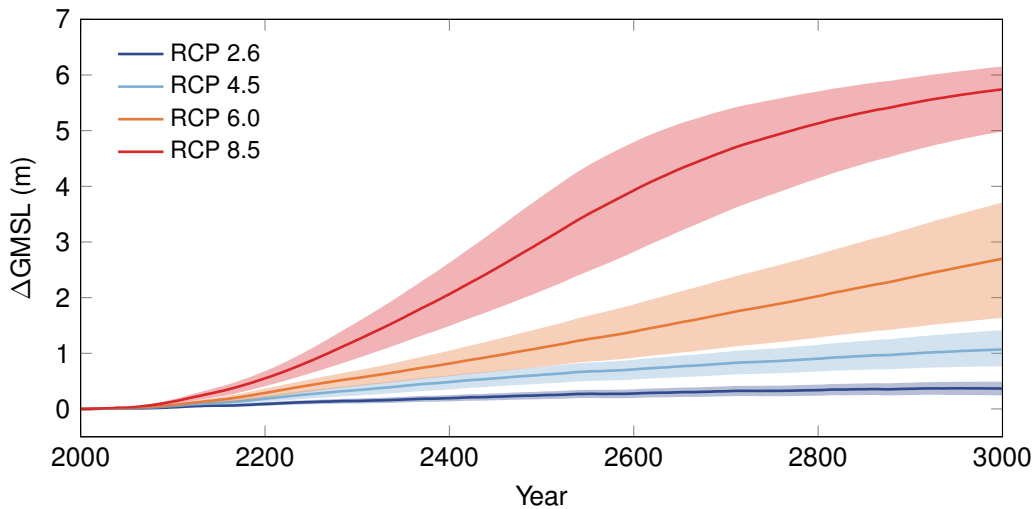


Figure 8.12: Same as Figure 8.6 but under Weertman’s sliding law with exponent  $m = 5$ .

Year	RCP 2.6	RCP 4.5	RCP 6.0	RCP 8.5
2100	0.03 (−0.02, 0.08)	0.05 (−0.01, 0.12)	0.07 (−0.01, 0.15)	0.13 (0.01, 0.25)
2300	0.14 (−0.02, 0.32)	0.34 (0.04, 0.61)	0.56 (0.10, 0.99)	1.24 (0.40, 2.19)
3000	0.37 (−0.07, 0.92)	1.07 (0.17, 2.56)	2.70 (0.41, 5.16)	5.74 (1.92, 7.03)

Table 8.4: Same as Table 8.3 but with sliding exponent  $m = 5$ .  $\Delta$ GMSL projections are the median projections with their 5–95 % probability intervals between parentheses.

### 8.3.8 TGL parameterisation

We ran the same ensemble of simulations under the weakly nonlinear sliding law using, this time, the TGL parameterisation instead of the SGL parameterisation. Under the TGL parameterisation, Table 8.5 and Figure 8.13(a) give for the AIS contribution to sea level the median and the 33–66 % and 5–95 % probability intervals. We find an overall increase in sea-level rise projections compared to our results under the SGL parameterisation. This result was expected as the TGL parameterisation has been shown to increase grounding-line sensitivity to environmental changes [Tsai et al., 2015; Pattyn, 2017]. The probability of exceeding 0.5 m by 2100 is still negligible (probability of less than 1 %) in all RCP scenarios. However, the probability of

exceeding 0.5 m and 1 m by 3000 in RCP 2.6 can reach more than 40 % and 10 %, respectively. For other scenarios, the retreat of the Antarctic ice sheet is much more pronounced and faster than under the SGL parameterisation and the probability to exceed 1.5 m of sea-level rise by 3000 can reach more than 50 % in RCP 4.5, 80 % in RCP 6.0, and 99 % in RCP 8.5.

Figures 8.13(b)–(d) show the confidence regions for grounded ice under the TGL parameterisation in RCP 8.5. As also pointed out by Pattyn [2017], the TGL parameterisation leads to a faster and more significant grounding-line retreat in the marine sectors and an additional mass loss from East Antarctica, especially in the Aurora basin.

Year	RCP 2.6	RCP 4.5	RCP 6.0	RCP 8.5
2100	0.06 (0.00, 0.14)	0.10 (0.02, 0.19)	0.12 (0.02, 0.23)	0.21 (0.05, 0.37)
2300	0.20 (0.02, 0.47)	0.47 (0.10, 0.89)	0.83 (0.18, 1.43)	1.85 (0.59, 3.12)
3000	0.46 (0.00, 1.30)	1.73 (0.22, 2.91)	3.47 (0.76, 5.37)	7.43 (3.85, 10.79)

Table 8.5: Same as Table 8.3 but with the TGL parameterisation.  $\Delta$ GMSL projections are the median projections with their 5–95 % probability intervals between parentheses.

## 8.4 Discussion

### 8.4.1 Comparison of the sea-level rise projections with previous work

Regarding the short-term AIS contribution to sea level, we projected in the RCP 2.6 scenario a median of 0.02–0.03 m under the SGL parameterisation and 5–95 % probability intervals from –0.06 m to 0.10 m. These projections are similar to other estimates based on other mechanisms. Golledge et al. [2015] reported an AIS contribution to sea level between –0.01 m and 0.10 m with the lower and higher bounds corresponding to the absence and presence of sub-grid interpolation of basal melting at the grounding line. DeConto and Pollard [2016] reported an AIS contribution to sea level between –0.11 m and 0.15 m based on a model calibration with a range of Pliocene sea-level targets between 5 and 15 m higher than today. In the same scenario, we found an increased AIS response under the TGL parameterisation with a median AIS contribution to sea level of 0.06 m and a 5–95 % probability interval between 0.00 m and 0.14 m by 2100. These higher projections are similar to the higher projections (0–0.22 m) reported by DeConto and Pollard [2016] for a higher range of Pliocene sea-level targets between 10 and 20 m. In all RCP scenarios, under all sliding laws, and under both grounding-line parameterisations, our results suggested that the AIS contribution to sea level does not exceed 0.5 m by 2100 with a probability of at least 99 %. These results are in agreement with Ritz et al. [2015], who determined an AIS contribution to sea level that lies between 0.05 m and 0.30 m, and Golledge et al. [2015], who found an AIS contribution to sea level that reaches at most 0.38 m in RCP 8.5 with sub-grid interpolation of basal melting at the grounding line. Yet, projections by DeConto and Pollard [2016] and Schlegel et al. [2018], who applied the more sensitive Budd-type friction law [Brondex et al., 2017], can exceed 0.5 m and even 1 m, but these higher projections are under extreme and maybe unrealistic warming conditions.

Regarding the long-term AIS contribution to sea level, our projections under the SGL parameterisation are similar to other estimates by Golledge et al. [2015]. In particular, both studies

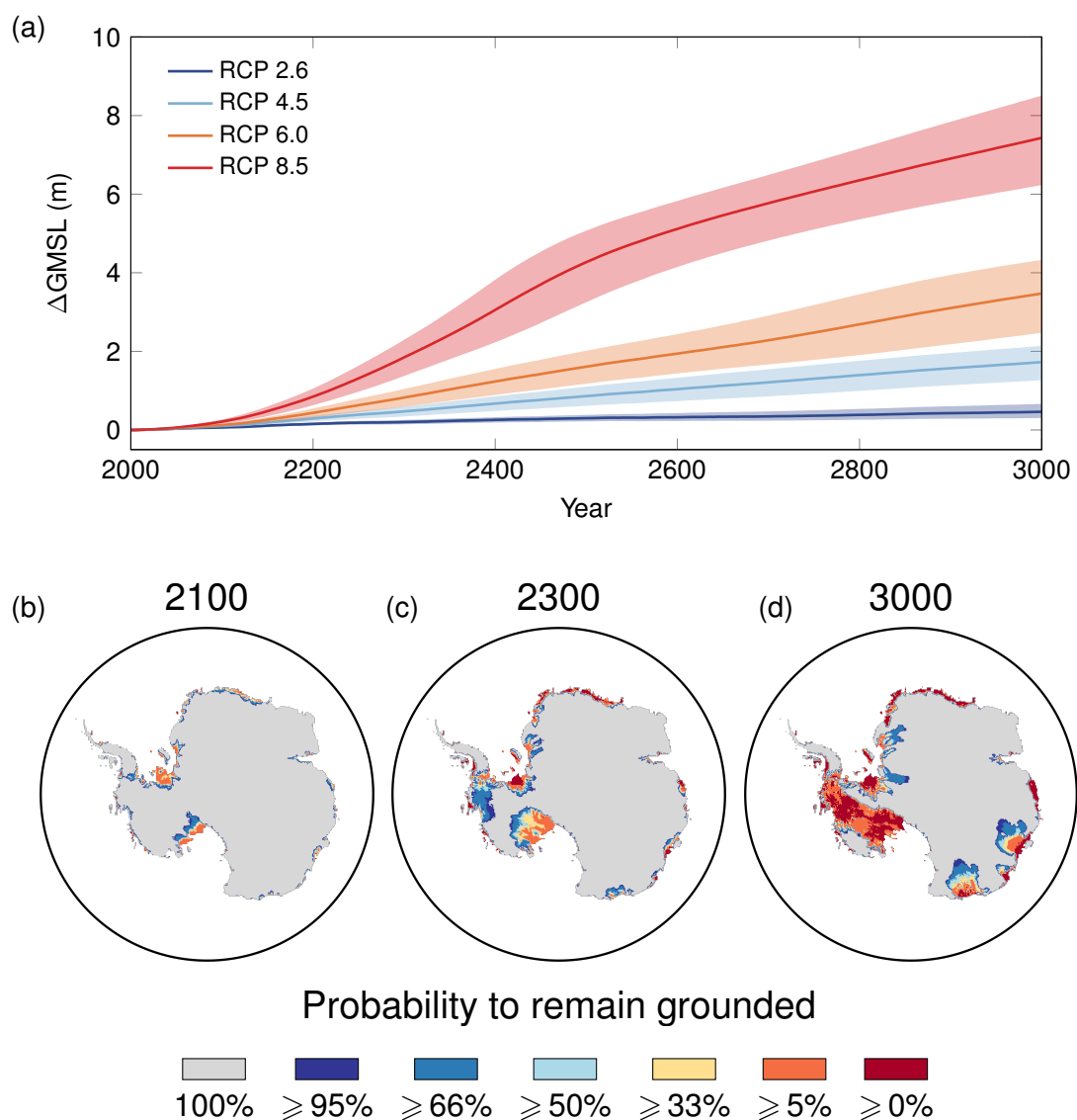


Figure 8.13: (a) Same as Figure 8.6 but under the TGL parameterisation and the weakly nonlinear sliding law. (b, c, d) Confidence regions for grounded ice under the TGL parameterisation and the weakly nonlinear sliding law for the RCP 8.5 scenario. Confidence regions are shown at (b) 2100, (c) 2300, and (d) 3000.

suggest that the AIS contribution to sea level by 3000 in RCP 2.6 is limited to less than 1 m with a probability estimated to be at least 95 % in our study, while an AIS contribution to sea level above 1.5 m by 3000 may arise in all other RCP scenarios. Yet, our long-term projections are generally below projections by DeConto and Pollard [2016] with hydrofracturing and ice-cliff failure mechanisms especially under warmer RCP scenarios, but the discrepancies between the projections of both models are reduced under the TGL parameterisation. In RCP 2.6, our projections by 2500 under the TGL parameterisation range from 0.04 m to 0.73 m, which is similar to projections by DeConto and Pollard [2016], which range respectively from  $-0.23$  m to 0.61 m

and 0.02 m to 0.48 m for the lower and higher ranges of Pliocene of sea-level targets.

#### 8.4.2 Comparison of the impact of parametric uncertainty with previous work

Similarly to [Golledge et al. \[2015, 2017\]](#), our study emphasised the pivotal role played by the emission scenario and sub-shelf melting as critical drivers of the future changes in the AIS mass balance on medium-term and long-term timescales through ice-shelf thinning and subsequent reduced buttressing. As in [Ritz et al. \[2015\]](#), we found that the AIS contribution to sea level is an increasing function of the sliding exponent, thus meaning that more plastic sliding conditions speed up the ice flow and consequently ice loss. Following [Pattyn \[2017\]](#), we highlighted the greater sensitivity of the grounding-line migration under the TGL parameterisation, thus stressing the key role played by physical processes in the vicinity of the grounding line.

#### 8.4.3 Comparison of projections of grounded-ice retreat with previous work

Consistent with our results, [Golledge et al. \[2015\]](#), with a 10-km resolution model, projected that grounding-line retreat is most significant in the Siple Coast region. However, [Ritz et al. \[2015\]](#), based on the probability of MISI onset, as well as [Cornford et al. \[2015\]](#), with a sub-kilometre resolution around the grounding line, projected that grounding-line retreat is most significant in the Amundsen Sea sector. [Schlegel et al. \[2018\]](#) found that grounding-line retreat is most significant in the Amundsen Sea sector under generalised ocean warming experiments for the Antarctic ice sheet, but, after calibrating sub-shelf melt rates with bounds that vary region by region and are assigned values deduced from the literature and model sensitivity studies, they found that the western Ronne basin has the greater sensitivity. These discrepancies between our findings and those of [Cornford et al. \[2015\]](#), [Ritz et al. \[2015\]](#), and [Schlegel et al. \[2018\]](#) may be explained by our ocean model which may overestimate sub-shelf melting underneath the Ross ice shelf and underestimate ocean circulation in the Amundsen Sea and by our initialisation method which may underestimate the basal sliding coefficients for Thwaites and Pine Island Glaciers. Moreover, the lower sensitivity of the Amundsen Sea sector may arise in our simulations from shortcomings in the buttressing parameterisation, our low resolution not capturing properly the bedrock topography, the small pinning points and the flow dynamics in the narrower sectors of the ice sheet, and our representation of calving, which may increase the instability threshold; see, for instance, [Arthern and Williams \[2017\]](#) and [Waibel et al. \[2018\]](#) for more thorough discussions about the instability threshold in the Amundsen Sea sector.

#### 8.4.4 Projections of ice loss and grounding-line retreat under parametric uncertainty

The significance of the contribution of the Antarctic ice sheet to sea level under climate change is primarily controlled by the sensitivity, the response time, and the vulnerability of its marine drainage basins, with the West Antarctic ice sheet more sensitive and vulnerable than the East Antarctic ice sheet. The instability of marine drainage basins and their ability to trigger accelerated ice loss and significant grounding-line retreat is determined by bedrock topography and ice-shelf buttressing which depends on the importance of ice-shelf thinning. Our nominal projections showed that the AIS contribution to sea level by 3000 is rather limited (less than 1

metre) in RCP 2.6, RCP 4.5, and RCP 6.0, while an accelerated ice loss that leads to a contribution of several metres is triggered in RCP 8.5 (Figure 8.3(a)). In addition, the nominal retreat of the grounding line by 3000 is rather limited in RCP 2.6, RCP 4.5, and RCP 6.0 (Figures 8.3(b)–(d)), while a significant retreat of the grounding line is triggered in the Siple Coast, Ronne–Filchner and Amundsen Sea sectors in RCP 8.5 (Figure 8.3(e)).

Our probabilistic results provide insight into the impact of parametric uncertainty on these projections. In RCP 2.6, the projections hold irrespective of parametric uncertainty: the AIS contribution to sea level by 3000 has a 95 % quantile of up to 0.91 m (Table 8.3) and there is a limited risk that the grounding line will retreat beyond our nominal projections (Figure 8.3(b) and Figure 8.10(c)). In RCP 4.5 and RCP 6.0, the projections are more sensitive to parametric uncertainty than in RCP 2.6: the AIS contribution to sea level by 3000 has a 95 % quantile of up to 2.56 m in RCP 4.5 and up to 5.17 m in RCP 6.0 (Table 8.3) and both scenarios entail a risk of triggering a more significant retreat of the grounding line beyond our nominal projections (Figures 8.3(c)–(d)). This risk is present especially in the Amundsen Sea sector and it is less significant in RCP 4.5 than in RCP 6.0, in which a complete disintegration of the West Antarctic ice sheet may be triggered (Figures 8.10(f) and (i)). Finally, in RCP 8.5, our probabilistic results suggest an accelerated ice loss and a significant retreat of the grounding line in West Antarctica, as in our nominal projections: the AIS contribution to sea level by 3000 has an uncertainty range with a 5 % quantile above 0.82 m and a 95 % quantile of up to 7.68 m (Table 8.3) and there is a high risk of triggering a complete disintegration of the West Antarctic ice sheet (Figure 8.10(l)).

In conclusion, the projections hold irrespective of parametric uncertainty in the strongly mitigated RCP 2.6 scenario: accommodating parametric uncertainty in the ice-sheet model leads to projections in agreement with the nominal projections of limited ice loss and limited grounding-line retreat in RCP 2.6. However, the projections are more sensitive to parametric uncertainty for intermediate scenarios such as RCP 4.5 and RCP 6.0: accommodating parametric uncertainty in the ice-sheet model leads to projections in disagreement with the nominal projections and indicates instead some risk of triggering accelerated ice loss and significant grounding-line retreat for intermediate scenarios such as RCP 4.5 and RCP 6.0. Finally, the warm RCP 8.5 scenario triggers the collapse of the West Antarctic ice sheet, almost irrespective of parametric uncertainty.

#### 8.4.5 Structural uncertainty and limitations

A first limitation of our study is associated with the modelling hypotheses inherent to our ice-sheet model. The f.ETISH model is an ice-sheet model that focuses on essential marine ice-sheet mechanisms, similarly to the ice-sheet model by Pollard and DeConto [2012a]. Certain physical processes, especially small-scale processes, may be represented imperfectly, especially with the 20-km resolution adopted for our simulations. This may reduce the ability to simulate important ice streams such as Pine Island and Thwaites Glaciers (only represented by a few grid points), whose stability is controlled by local bedrock features [Waibel et al., 2018]. Hence, grounding-line migration and thresholds for instabilities may not be captured properly even with a parameterisation of the grounding-line flux, especially in low-forcing scenarios and short-term projections. As discussed in Section 8.2.1, the flux condition at the grounding line is also questionable for buttressed ice shelves [Pattyn et al., 2013; Reese et al., 2018a] found around Antarctica and

short transients [Drouet et al., 2013; Pattyn et al., 2013; Pattyn and Durand, 2013]. Yet, we think that using a 20-km resolution and a flux condition at the grounding-line remains an acceptable assumption in large-scale and long-term ice-sheet simulations and large-ensemble simulations. We expect discrepancies between our results and results at a higher spatial resolution or with a higher level of complexity to be limited when compared to the uncertainty in the results due to the uncertainty in the model parameters and forcing. Besides, sub-shelf melting may not be captured properly despite the use of the PICO ocean-model coupler, especially in the Amundsen Sea sector and underneath the Ross ice shelf [Timmermann et al., 2012; Depoorter et al., 2013; Rignot et al., 2013; Moholdt et al., 2014]. A second limitation comes from the hypotheses relevant to our characterisation of uncertainties. We adopted rather large uncertainty ranges for the parameters. As discussed in Section 8.3.6, projections can be strongly affected by extreme conditions. Moreover, we chose the bounds of the uncertainty ranges quite heuristically. A third limitation comes from the fairly simple way in which certain sources of uncertainty were introduced. We assumed a direct influence of the atmospheric forcing on sub-shelf melting through the ocean melt factor. However, as discussed in Section 8.2.2.5, atmospheric forcing affects the Circumpolar Deep Water circulation in ice-shelf cavities and subsequently modifies sub-shelf melting [Pritchard et al., 2012]. Still, the fate of the Southern Ocean and the evolution of sub-shelf melting under global climate change remains unclear [Hellmer et al., 2012; Dinniman et al., 2012; Timmermann and Hellmer, 2013; Hellmer et al., 2017]. Given the importance of sub-shelf melting in driving the future response of the Antarctic ice sheet, there is a clear need to better constrain future sub-shelf melt and incorporate it properly into ice-sheet models. We also introduced uncertainty in calving with a simple multiplier factor that does not take into account the stress regime in the ice shelves. A fourth limitation concerns the correction for the initial drift that adds a bias to the projections. We adopted this correction to make our results insensitive to model initialisation but our corrected results are likely to underestimate the AIS response on a short-term timescale, as our approach does not take into account any current transient changes in the Antarctic ice sheet. Another limitation is related to the construction of our emulator. To avoid overfitting the training data, we tuned the emulator to reproduce the overall trend in the parameters-to-projections relationship but not local variations in the parameter space that may stem from numerical noise and errors.

## 8.5 Conclusion

We studied the multicentennial response of the Antarctic ice sheet under uncertainty using methods from the field of UQ. We investigated uncertainties in atmospheric forcing, basal sliding, grounding-line parameterisation, sub-shelf melting, calving, ice-shelf rheology, and bedrock relaxation. We used emulation-based methods to represent the parameters-to-projection relationship, stochastic sensitivity analysis to assess the significance of each source of uncertainty in inducing uncertainty in the projections, and confidence regions for excursion sets to assess the risk of grounding-line retreat. We found that all investigated sources of uncertainty, except bedrock relaxation time, contribute to the uncertainty in the projections. We showed that the sensitivity of the projections to uncertainties increases and the contribution of the uncertainty in sub-shelf melting to the uncertainty in the projections becomes more and more dominant as atmospheric and oceanic temperatures rise, with a contribution to the uncertainty in sea-level rise projections that goes from 5% to 25% in RCP 2.6 to more than 90% in RCP 8.5. We showed that the significance of the AIS contribution to sea level is controlled by MISI in ma-

rine basins, with the biggest contribution stemming from the more vulnerable West Antarctic ice sheet. We found that, irrespective of parametric uncertainty, the strongly mitigated RCP 2.6 scenario prevents the collapse of the West Antarctic ice sheet, that in both the RCP 4.5 and RCP 6.0 scenarios the occurrence of MISI in marine basins is more sensitive to parametric uncertainty, and that, almost irrespective of parametric uncertainty, RCP 8.5 triggers the collapse of the West Antarctic ice sheet.

## 8.A Polynomial chaos expansion

In this Appendix, we concisely provide further details about how we used PC expansions in our study; we refer the reader to, for instance, [Ghanem et al. \[2017\]](#) and [Le Maître and Knio \[2010\]](#) for more comprehensive treatments of the theory and various applications of PC expansions.

Let us represent the ice-sheet model as an abstract model  $y = g(\mathbf{x})$  where  $\mathbf{x} = (x_1, \dots, x_d)$  is a vector of  $d$  parameters,  $y$  the model response and  $g$  the response function. In our study,  $d = 5$ ,  $x_1 = F_{\text{calv}}$ ,  $x_2 = F_{\text{melt}}$ ,  $x_3 = E_{\text{shelf}}$ ,  $x_4 = \tau_e$ ,  $x_5 = \tau_w$ , and  $y = \Delta\text{GMSL}$  at a given time. In our study, the parameters are uncertain and have a probability density function that we denote by  $p$ .

A polynomial chaos expansion is an approximation of the response function  $g$  with a polynomial  $g^K$  as

$$g(\mathbf{x}) \approx g^K(\mathbf{x}) = \sum_{k=0}^K c_k \psi_k(\mathbf{x}), \quad (8.4)$$

where the  $\psi_k$  are a basis of predefined polynomials of increasing degree and orthonormal with respect to the probability density function of the parameters, by which we understand that

$$\int_{\mathbb{R}^d} \psi_k(\mathbf{x}) \psi_l(\mathbf{x}) p(\mathbf{x}) d\mathbf{x} = \begin{cases} 0 & \text{if } k \neq l \\ 1 & \text{if } k = l \end{cases}, \quad (8.5)$$

and  $K + 1$  is the number of predefined polynomials in the expansion.

In order to fit the PC expansion in Equation (8.4) to the ice-sheet model, we calculate the coefficients using a (weighted) least-squares approach:

$$\mathbf{c} = \arg \min_{\mathbf{d} \in \mathbb{R}^{K+1}} \sum_{i=1}^N w^{(i)} \left( y^{(i)} - \sum_{k=0}^K d_k \psi_k(\mathbf{x}^{(i)}) \right)^2, \quad (8.6)$$

where the ensemble  $\{\mathbf{x}^{(i)}, 1 \leq i \leq N\}$  is a set of  $N$  training points in the parameter space, the ensemble  $\{y^{(i)} = g(\mathbf{x}^{(i)}), 1 \leq i \leq N\}$  is the set of model responses at the training points,  $\mathbf{c} = (c_0, c_1, \dots, c_K)$  collects the PC coefficients, and  $\{w^{(i)}, 1 \leq i \leq N\}$  is the set of weights. We normalise the parameters to accommodate the different orders of magnitude of the parameters and reduce the potential ill-conditioning of the least-squares problem. We generate the set of training points with a maximin Latin hypercube sampling design [[Stein, 1987](#); [Fajraoui et al., 2017](#); [Hadigol and Doostan, 2018](#)], which is a space-filling design that aims at maximising the

smallest distance between neighbouring points, thus ensuring a proper coverage of the parameter space. We consider a PC expansion of degree 3, which corresponds to  $K = 56$  for  $d = 5$ , as we strive to reproduce the overall trend of the response function without overfitting small local variations.

We solve Equation (8.6) by solving the normal equations

$$([G]^T[W][G])\mathbf{c} = [G]^T[W]\mathbf{y}, \quad (8.7)$$

where  $\mathbf{y} = (y^{(1)}, \dots, y^{(N)})$  collects the model responses at the training points,  $[G]$  is the measurement matrix whose entries are given by  $G_{ik} = \psi_k(\mathbf{x}^{(i)})$ , and  $[W]$  is a diagonal weight matrix whose diagonal entries are the weights ( $W_{ii} = w^{(i)}$ ). As we construct the training points by using a Latin hypercube sampling design, the training points  $\mathbf{x}^{(i)}$  have equal weights of  $W_{ii} = w^{(i)} = 1/N$ . We do note that there exist other methods to determine the coefficients in Equation (8.4) including methods involving deterministic quadrature rules [Le Maître and Knio, 2010]. Here, one of our motivations for choosing a least-squares approach is its good ability to handle numerical noise in low-degree expansions [Iskandarani et al., 2016].

We estimate statistical descriptors of the uncertain model response with Monte Carlo simulation in which the PC expansion is used as a computationally efficient substitute for the ice-sheet model. For instance, we estimate the probability density function of the response through kernel density estimation [Scott, 2015], while we approximate the mean  $\mu$  and the variance  $\sigma^2$  of the model response as

$$\mu \approx \mu^{K,\nu} = \frac{1}{\nu} \sum_{i=1}^{\nu} g^K(\mathbf{x}^{(i)}), \quad (8.8)$$

$$\sigma^2 \approx (\sigma^{K,\nu})^2 = \frac{1}{\nu} \sum_{i=1}^{\nu} (g^K(\mathbf{x}^{(i)}) - \mu^{K,\nu})^2, \quad (8.9)$$

where  $\{\mathbf{x}^{(i)}, 1 \leq i \leq \nu\}$  now denotes an ensemble of  $\nu$  independent and identically distributed samples from the probability density function of the parameters. Because the PC expansion is based on orthonormal polynomials with respect to the probability density function of the uncertain parameters and of increasing degree with  $\psi_0 = 1$ , we can evaluate some of the statistical descriptors of the uncertain model response directly from the PC coefficients. For example, the mean  $\mu$  and the variance  $\sigma^2$  of the model response can also be approximated as follows

$$\mu \approx \mu^K = c_0, \quad (8.10)$$

$$\sigma^2 \approx (\sigma^K)^2 = \sum_{k=1}^K c_k^2. \quad (8.11)$$

The accuracy of the PC expansion has to be assessed with respect to the degree of the PC expansion and the number of training points. We validate the accuracy of the PC expansion using cross-validation and convergence tests. We generate a new set of samples in the parameter space and we compare the exact response of the ice-sheet model with the approximate response of the PC expansion. Figures 8.14(a)–(c) show results of such a cross-validation for a PC expansion of degree 3. These figures suggest that the PC expansion represents the overall model response with

sufficient accuracy. Lower accuracy is achieved near the boundaries of the parameter space. We also carry out convergence tests, as illustrated in Figure 8.14(d) in RCP 8.5 and at time 3000. This figure represents the maximum absolute error and the mean-squared error between the exact response of the ice-sheet model and the approximate response of the PC expansion at the training points as a function of the number of training points. We see that for the 500 training points considered in this chapter, reasonable convergence of the PC expansion is achieved.

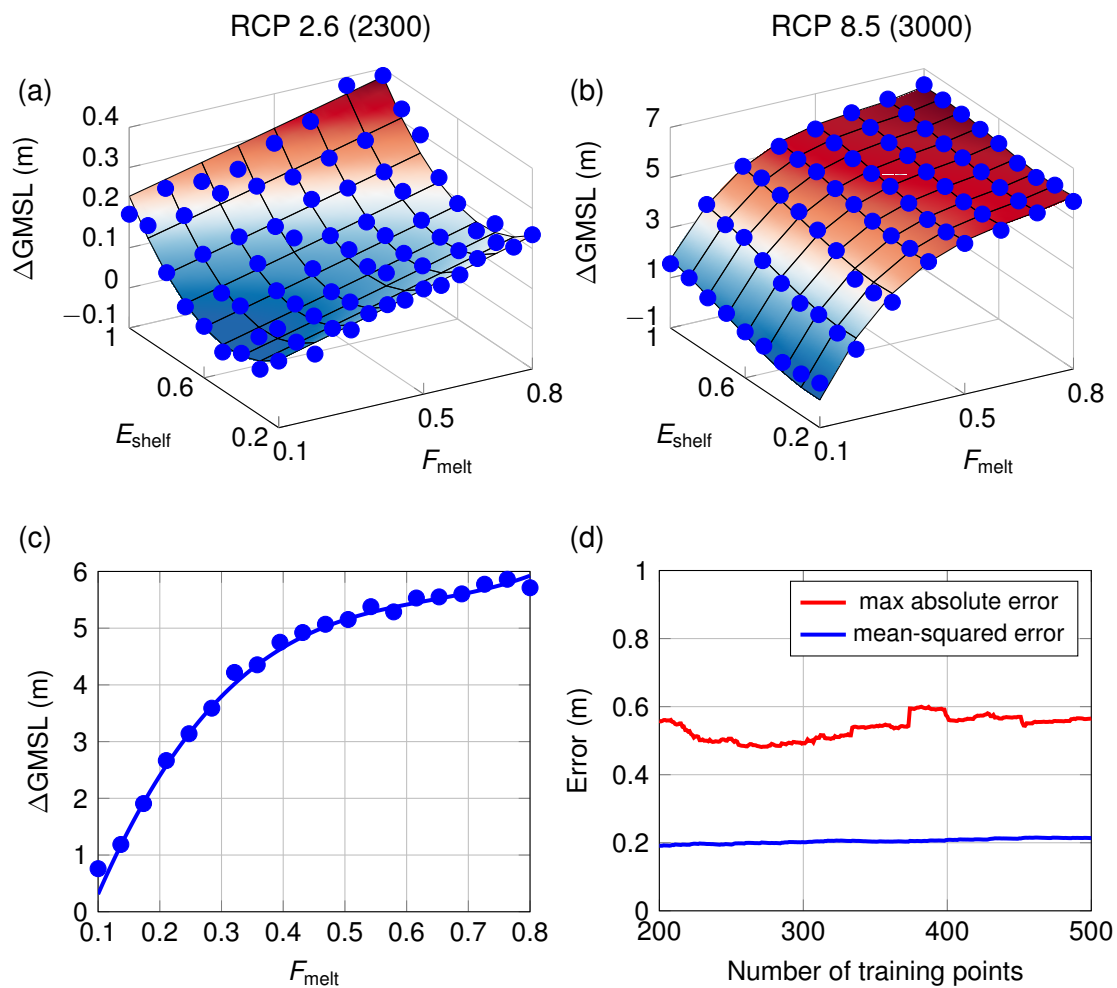


Figure 8.14: Validation tests for the PC expansion. (a) Cross-validation for the PC approximation in Figure 8.16(d) and (b) cross-validation for the PC approximation in Figure 8.16(b). The surface represents the PC approximation of the response of the ice-sheet model and the blue dots are the exact response of the ice-sheet model at the test points. (c) Cross-validation for the PC approximation in Figure 8.5(f) showing the presence of noisy results. (d) Convergence test in RCP 8.5 at time 3000 based on the number of training points used to build the emulator.

## 8.B Sobol sensitivity indices

In this Appendix, we concisely provide further details about how we used stochastic sensitivity analysis; we refer the reader to, for instance, [Ghanem et al. \[2017\]](#) and [Saltelli et al. \[2008\]](#) for more comprehensive treatments of the theory and various applications.

We first assume that the uncertain parameters are statistically independent. Sobol indices are based on the decomposition of the response function  $g$  in terms of the main effects associated with the parameters individually and an interaction effect associated with all parameters together:

$$y = g(\mathbf{x}) = g_0 + \sum_{i=1}^d g_i(x_i) + g_I(\mathbf{x}), \quad (8.12)$$

where  $g_0$  is constant, each  $g_i$  the so-called main effect associated with the corresponding parameter  $x_i$ , and  $g_I$  the so-called interaction effect. The constant, the main effects, and the interaction effect are given by

$$g_0 = \int_{\mathbb{R}^d} g(\mathbf{x})p(\mathbf{x}) d\mathbf{x}, \quad (8.13)$$

$$g_i = \int_{\mathbb{R}^{d-1}} g(\mathbf{x})p_{-i}(\mathbf{x}_{-i}) d\mathbf{x}_{-i} - g_0, \quad 1 \leq i \leq d, \quad (8.14)$$

$$g_I = g - g_0 - \sum_{i=1}^d g_i, \quad (8.15)$$

where  $\mathbf{x}_{-i} = (x_1, \dots, x_{i-1}, x_{i+1}, \dots, x_d)$  denotes the subset of parameters including all the parameters except  $x_i$  and  $p_{-i}$  denotes the probability density function for this subset of parameters. The constant  $g_0$  is the mean value of  $g$ . Using the calculus of variations, it can be shown that the main effect  $g_i$  is such that the function  $g_0 + g_i$  is the least-squares best approximation of  $g$  among all functions that depend only on  $x_i$ . As a consequence of this least-squares best approximation property, the functions  $g_0, g_1, \dots, g_d$ , and  $g_I$  are orthonormal with respect to the probability density function of the uncertain parameters.

As a consequence of the orthonormality of the functions  $g_0, g_1, \dots, g_d$ , and  $g_I$ , the variance  $\sigma^2$  of the model response can be decomposed as

$$\sigma^2 = \left( \sum_{i=1}^d S_i + S_I \right) \sigma^2, \quad (8.16)$$

with

$$S_i = \frac{1}{\sigma^2} \int_{\mathbb{R}} |g_i(x_i)|^2 p_i(x_i) dx_i, \quad 1 \leq i \leq d, \quad (8.17)$$

$$S_I = 1 - \sum_{i=1}^d S_i, \quad (8.18)$$

where  $p_i$  denotes the probability density function of  $x_i$ . Here,  $S_i$ , which takes a value between 0 and 1, is the Sobol index for the  $i$ -th parameter and  $S_I$  is the interaction index. The Sobol index  $S_i$  can be interpreted either as the relative contribution of the uncertainty in the sole  $i$ -th

parameter to the variance of the model response or as the reduction in the variance of the model response that we may expect by learning the exact value of this parameter [Oakley and O'Hagan, 2004]. Sobol indices allow us to rank the uncertain parameters in terms of their contribution to the variance of the model response, thus indicating which parameters are most influential in inducing the uncertainty in the model response.

Here, we substituted the ice-sheet model by a PC expansion based on orthonormal polynomials and estimated the Sobol indices directly from the PC coefficients [Crestaux et al., 2009], that is,

$$S_i \approx S_i^K = \frac{1}{(\sigma^K)^2} \sum_{k \in A_i} c_k^2, \quad (8.19)$$

where  $A_i$  is the set of indices associated with the non-constant polynomials that only depend on  $x_i$ .

## 8.C Confidence regions for grounded ice

In this Appendix, we concisely provide further details about how we defined and computed confidence regions for grounded ice. To distinguish between grounded ice and floating ice at a given time, the f.ETISh model [Pattyn, 2017] evaluates the so-called buoyancy imbalance:

$$\text{BI}(\mathbf{x}) = \rho_w b(\mathbf{x}) + \rho_i h(\mathbf{x}), \quad (8.20)$$

where  $b$  is the bedrock elevation,  $h$  the ice thickness,  $\rho_w$  the water density, and  $\rho_i$  the ice density. The buoyancy imbalance is negative for floating ice, positive for grounded ice, and null at the grounding line. Therefore, the grounded ice domain  $D_g$  is

$$D_g = \{\mathbf{x} : \text{BI}(\mathbf{x}) \geq 0\}. \quad (8.21)$$

In the presence of uncertainties in the model, we define an  $\alpha\%$  confidence region  $D_g(\alpha)$  for the grounded ice domain as a region of Antarctica that has a probability of at least  $\alpha$  of being included in the grounded ice domain, that is,

$$P \{D_g(\alpha) \subseteq D_g\} \geq \alpha. \quad (8.22)$$

We compute the confidence regions using an adaptation of a thresholding algorithm by Bolin and Lindgren [2015]. We seek the confidence regions in a parametric family indexed by a threshold parameter and based on the marginal probability density functions and we determine the threshold parameter so as to achieve the required level of confidence. While Bolin and Lindgren [2015] consider Gaussian random fields, here we work with non-Gaussian random fields, which requires us to evaluate the marginal probability density functions and the probability of inclusion with Monte Carlo simulation.

## 8.D Supplementary figures

Supplementary figures of *Uncertainty quantification of the multi-centennial response of the Antarctic ice sheet to climate change* [Bulthuis et al., 2019a] (<https://doi.org/10.5194/tc-13-1349-2019-supplement>).

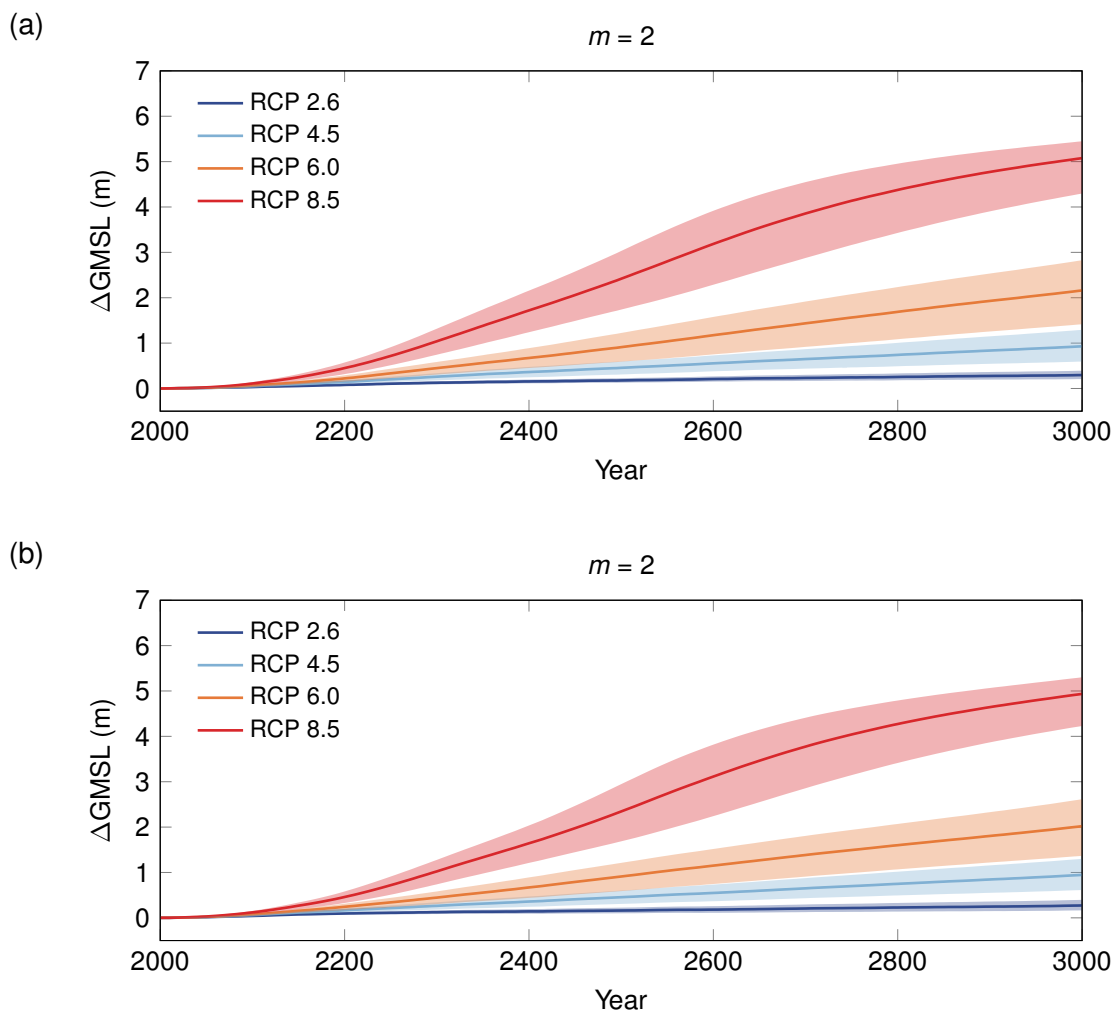


Figure 8.15: Comparison of Antarctic ice-sheet contribution to sea level under Weertman's sliding law with exponent  $m = 2$  as a function of spatial resolution (20 km vs 16 km). (a) Spatial resolution of 20 km and (b) spatial resolution of 16 km. Solid lines are the median projections and the shaded areas are the 33–66% probability intervals that represent the parametric uncertainty in the model.

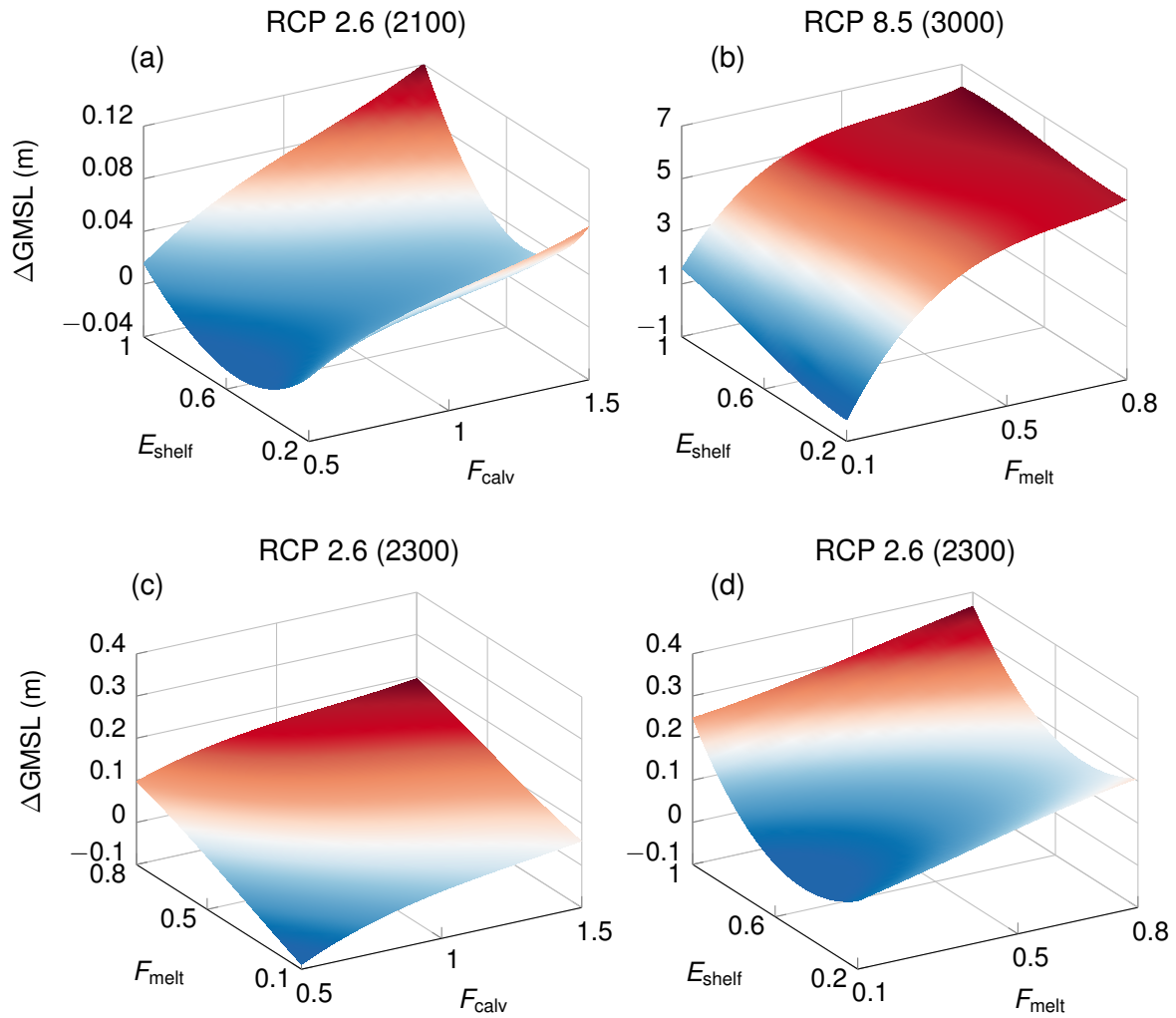


Figure 8.16: Representation of the emulators for pairs of parameters with other parameters fixed at their nominal value. Results are under Weertman's sliding law with exponent  $m = 2$ . Emulators (a) at 2100 in RCP 2.6 for the pair  $(F_{\text{calv}}, E_{\text{shelf}})$ , (b) at 2300 in RCP 8.5 for the pair  $(F_{\text{melt}}, E_{\text{shelf}})$ , (c) at 2300 in RCP 2.6 for the pair  $(F_{\text{calv}}, F_{\text{melt}})$ , and (d) at 3000 in RCP 2.6 for the pair  $(F_{\text{melt}}, E_{\text{shelf}})$ .

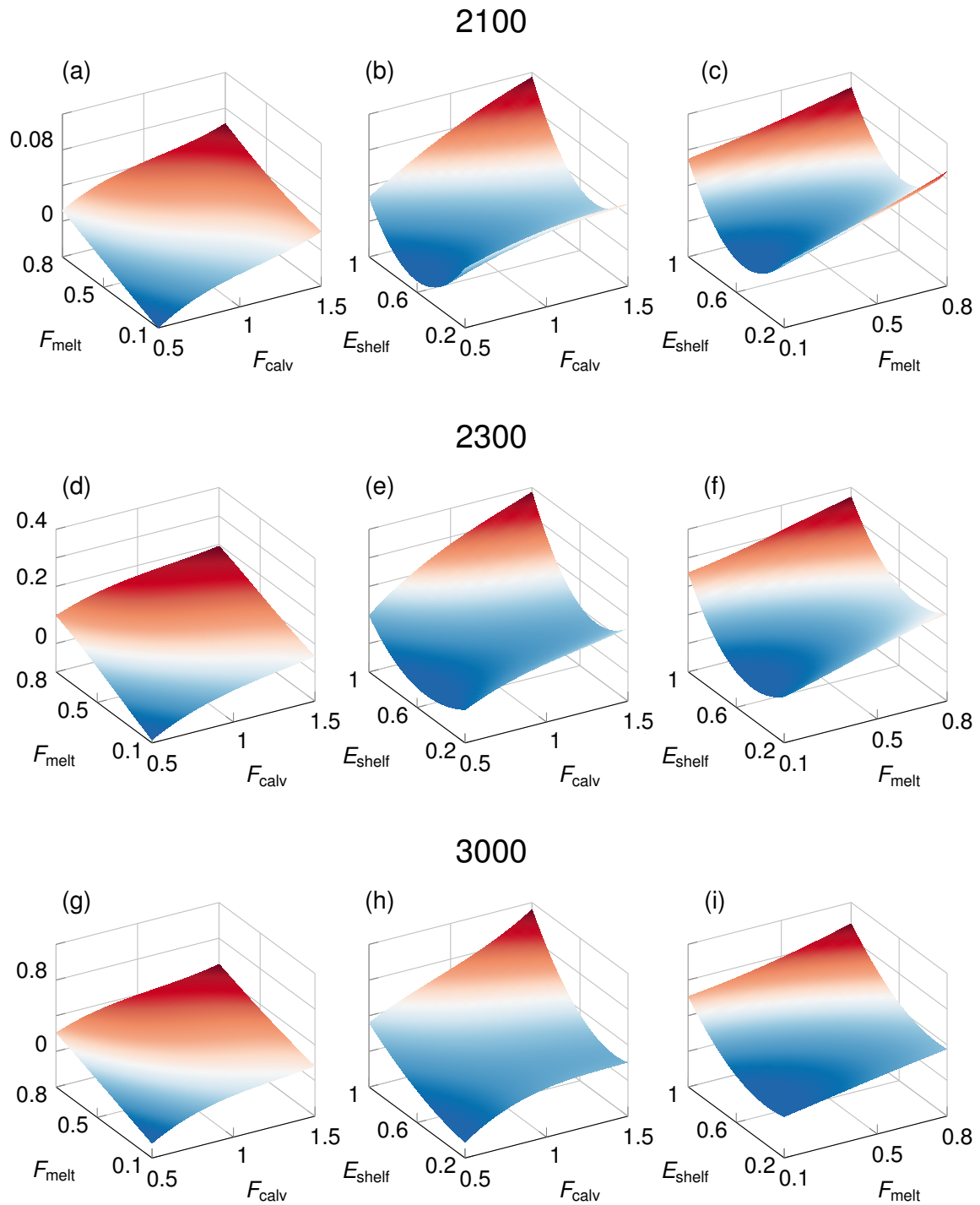


Figure 8.17: Representation of the emulators for pairs of parameters with other parameters fixed at their nominal value. Results are for the RCP 2.6 scenario under Weertman's sliding law with exponent  $m = 2$ . The vertical axis is  $\Delta\text{GMSL}$  (m). Emulators at 2100 (a, b, c), emulators at 2300 (d, e, f), and emulators at 3000 (f, g, i).

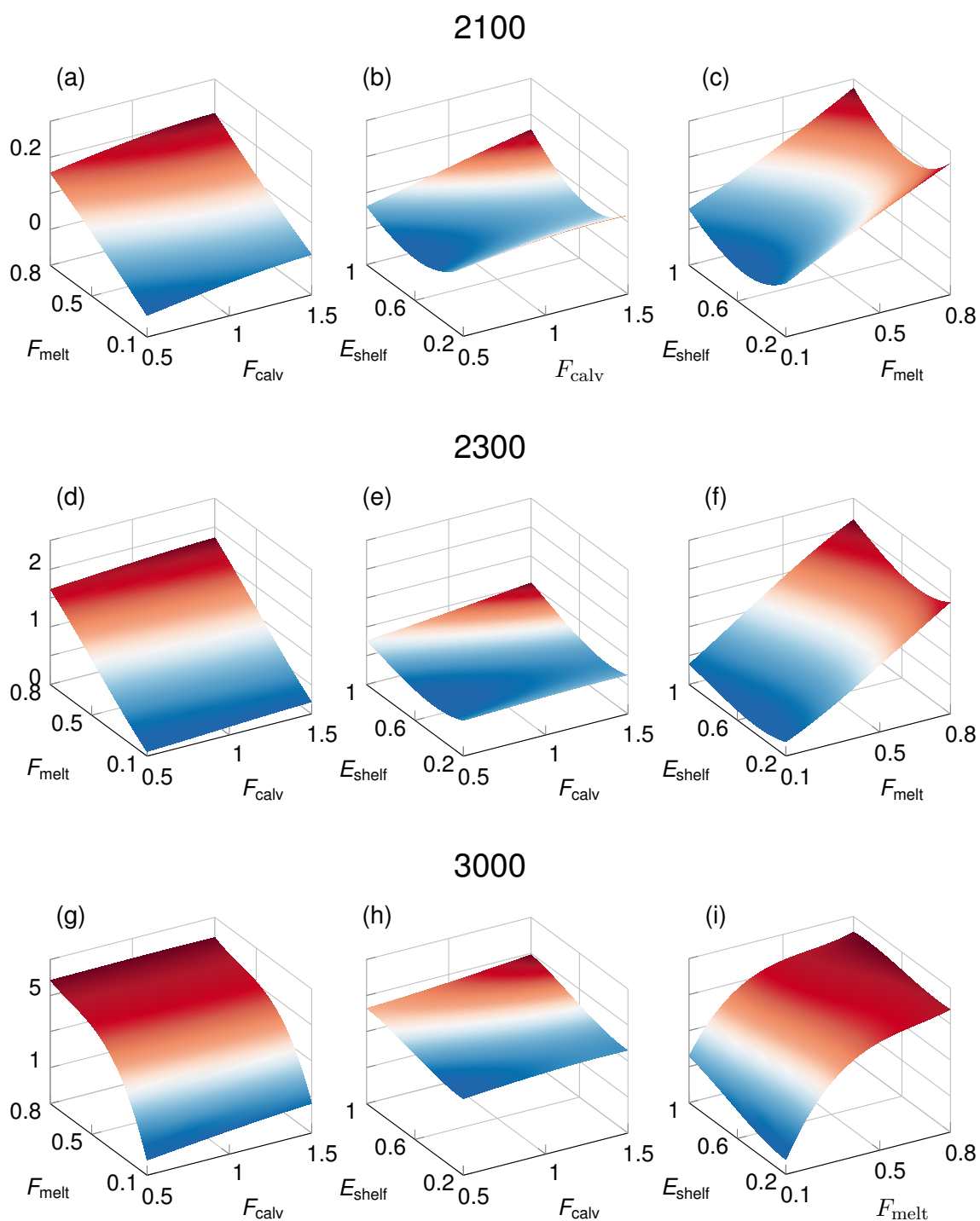


Figure 8.18: Representation of the emulators for pairs of parameters with other parameters fixed at their nominal value. Results are for the RCP 8.5 scenario under Weertman's sliding law with exponent  $m = 2$ . The vertical axis is  $\Delta\text{GMSL}$  (m). Emulators at 2100 (a, b, c), emulators at 2300 (d, e, f), and emulators at 3000 (f, g, i).

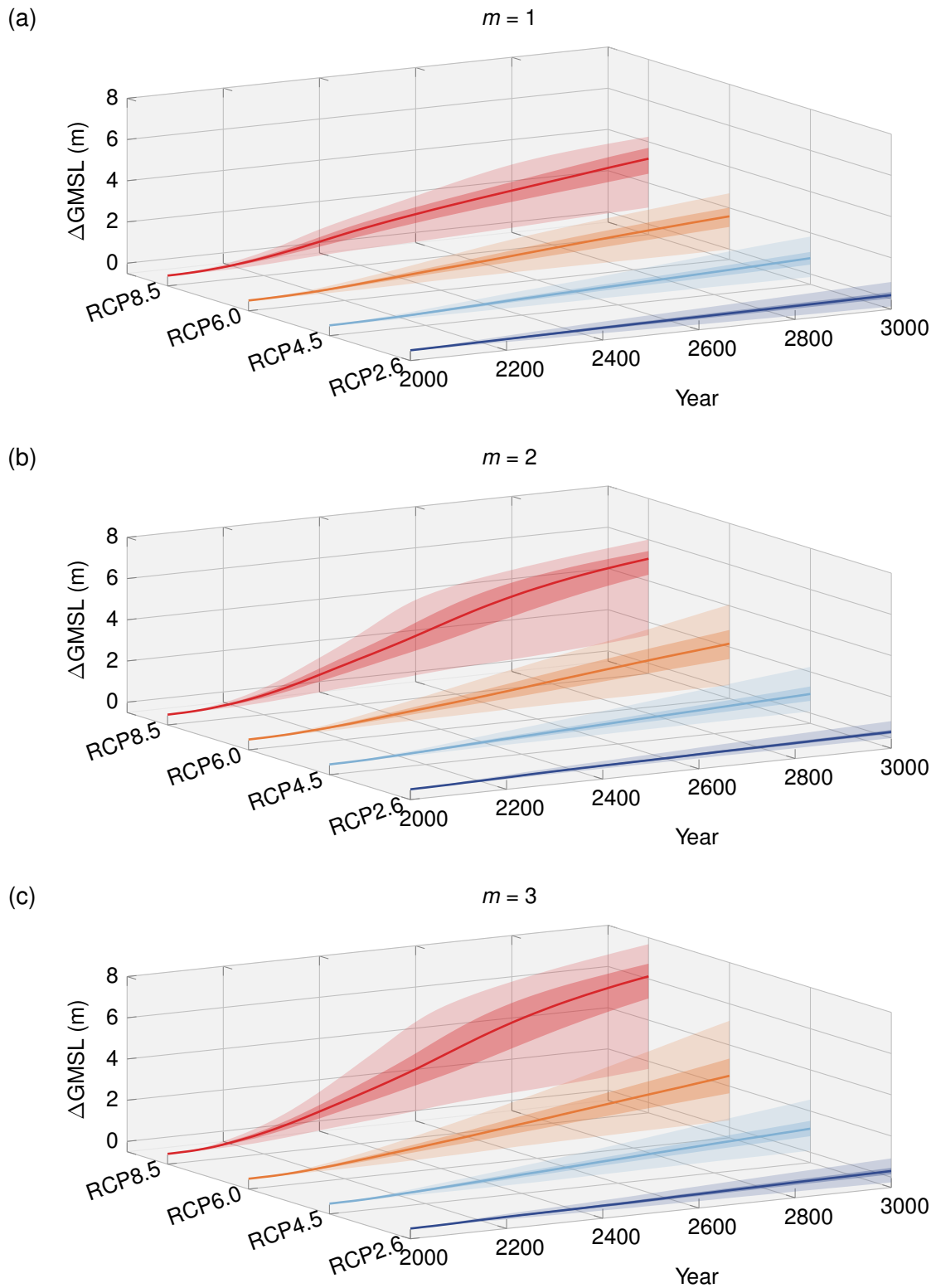


Figure 8.19: Antarctic ice-sheet contribution to global mean sea level relative to 2000. (a) Viscous sliding law, (b) weakly non-linear sliding law, and (c) strongly non-linear sliding law. Solid lines are the median projections and the darker and lighter shaded areas are respectively the 33–66% and 5–95% probability intervals that represent the parametric uncertainty in the model.

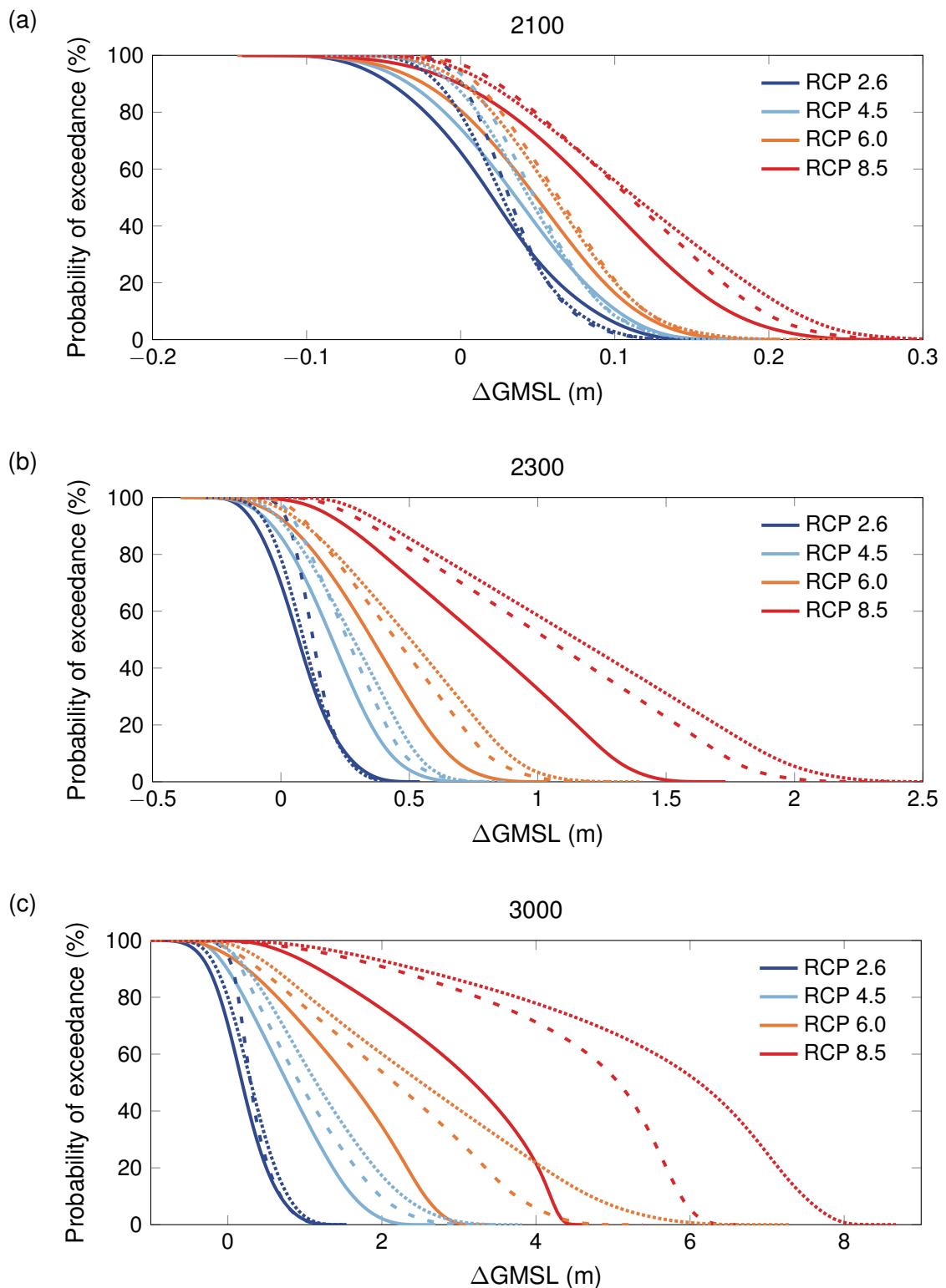


Figure 8.20: Probability of exceeding threshold values for sea-level rise evaluated as the complementary cumulative distribution functions of the probability density functions for sea-level rise projections. Probability of exceedance at 2100, (b) at 2300, and (c) at 3000 under the viscous sliding law (solid lines), the weakly non-linear sliding law (dashed lines), and the strongly non-linear sliding law (dotted lines).

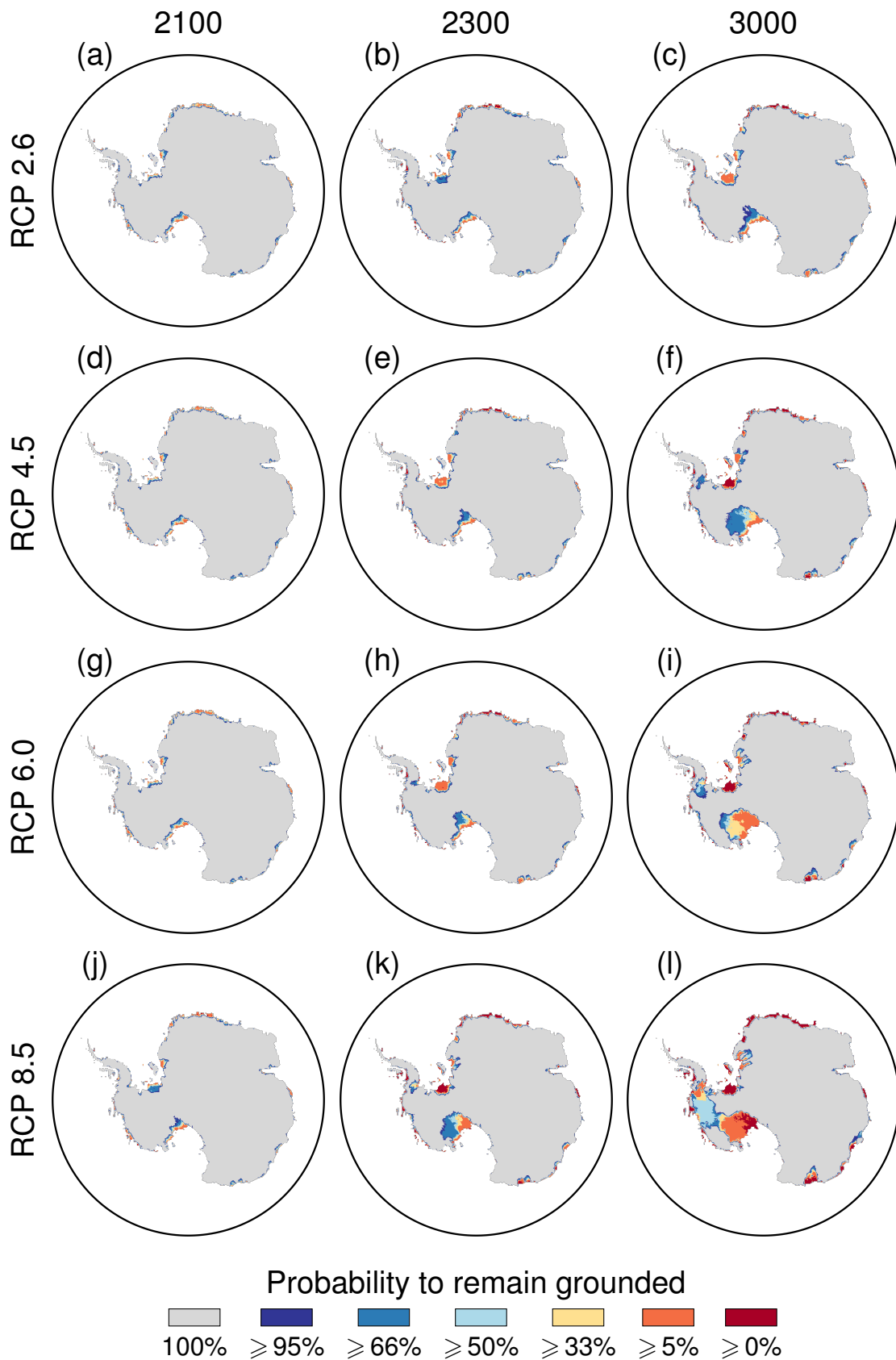


Figure 8.21: Confidence regions for grounded ice under sliding law with exponent  $m = 1$ . Confidence regions are shown at (a, d, g, j) 2100, (b, e, h, k) 2300, and (c, f, i, l) 3000.

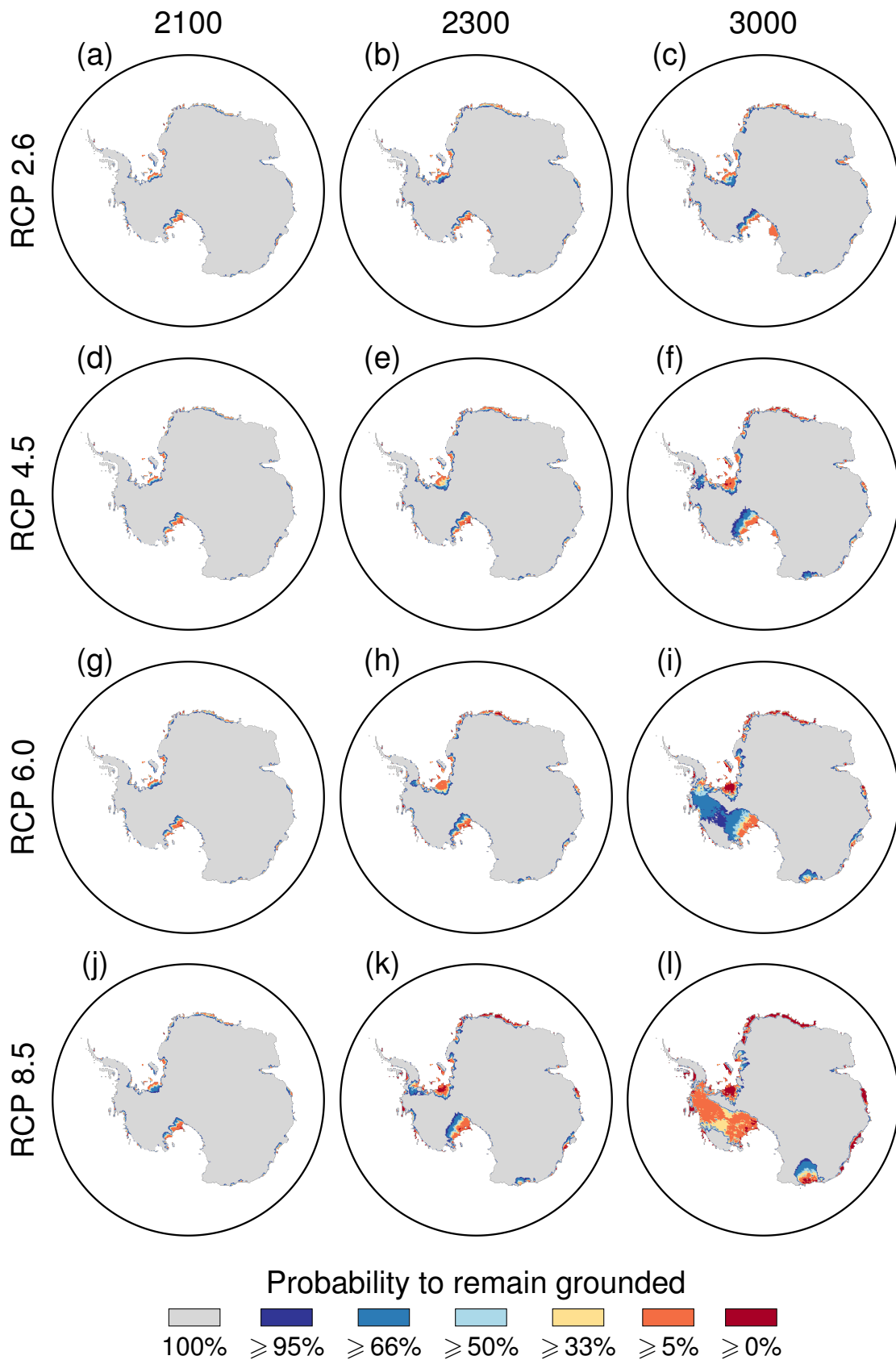


Figure 8.22: Confidence regions for grounded ice under sliding law with exponent  $m = 3$ . Confidence regions are shown at (a, d, g, j) 2100, (b, e, h, k) 2300, and (c, f, i, l) 3000.

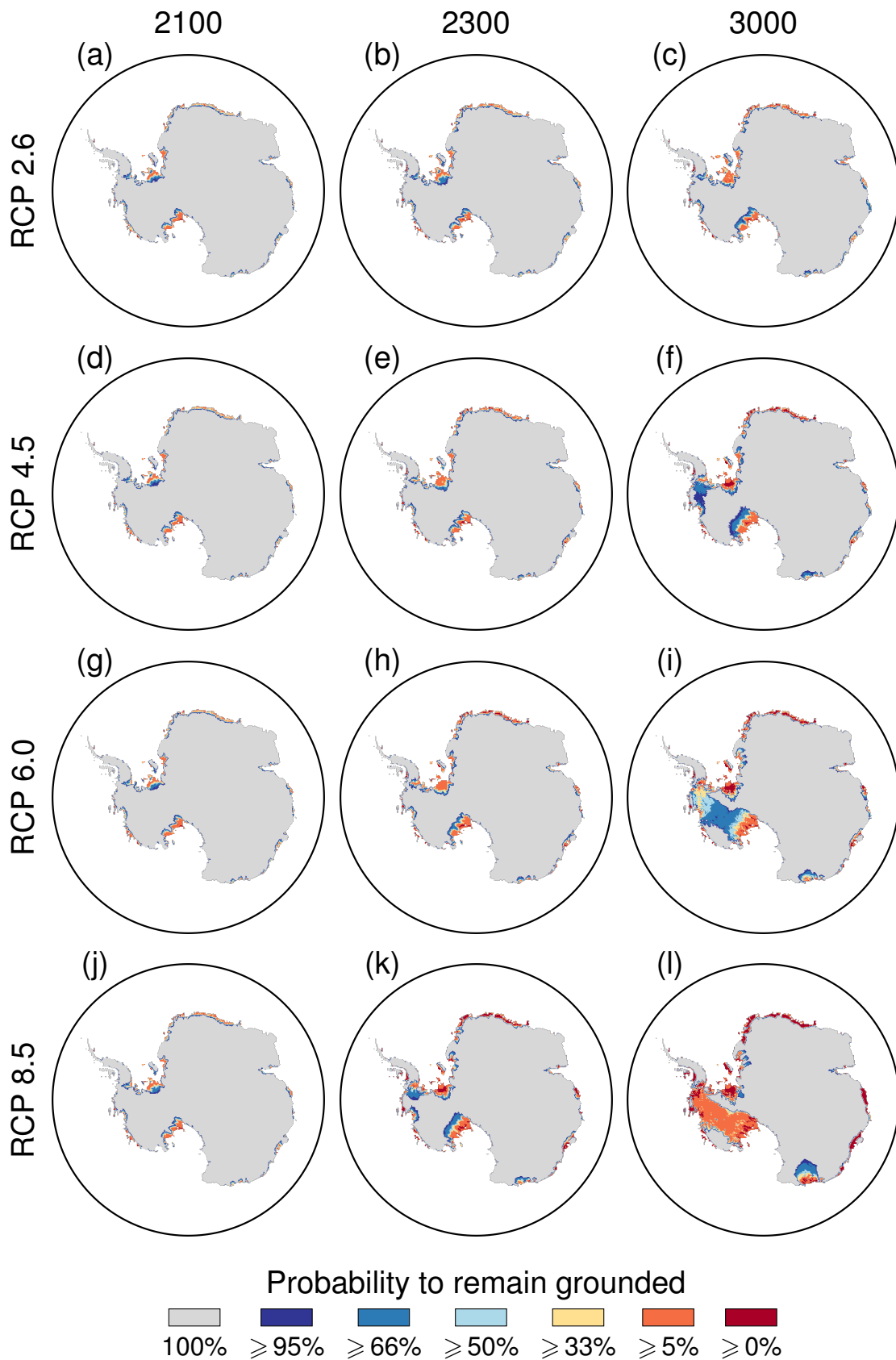


Figure 8.23: Confidence regions for grounded ice under sliding law with exponent  $m = 5$ . Confidence regions are shown at (a, d, g, j) 2100, (b, e, h, k) 2300, and (c, f, i, l) 3000.

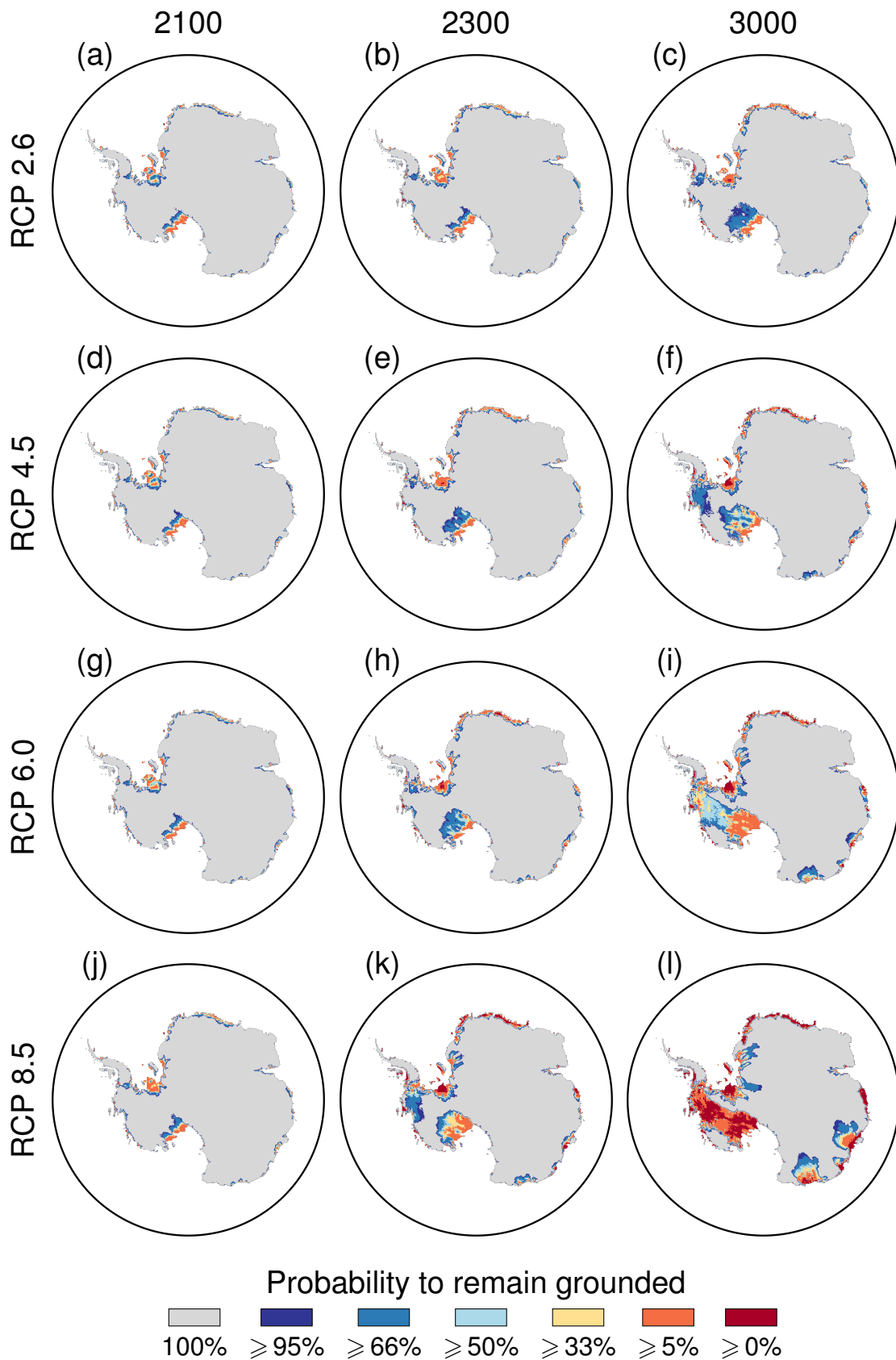


Figure 8.24: Confidence regions for grounded ice under sliding law with exponent  $m = 2$  and Tsai's grounding-line parameterisation. Confidence regions are shown at (a, d, g, j) 2100, (b, e, h, k) 2300, and (c, f, i, l) 3000.



# Multi-model comparison of sea-level rise projections

*In this chapter, we provide a multi-model comparison of the contribution of the Antarctic ice sheet to future sea-level rise for short-term (up to 2100 CE) and medium-term (up to 2300 CE) time horizons under different RCP scenarios. We do not seek to provide new probabilistic projections of sea-level rise by combining results from different models, but we rather seek to provide qualitative insight into the impact of structural uncertainty in ice-sheet models on the response of the Antarctic ice sheet. We also give a comparison with projections from the AR5 IPCC report to provide insight into new advances in the understanding and modelling of the Antarctic ice-sheet dynamics since AR5. Part of the results presented in this chapter are based on a contribution to a multi-model comparison in the publication [Hanna et al., 2020].*

## 9.1 Model description

As a way of assessing the impact of structural uncertainty in inducing uncertainty in sea-level rise projections and to compare the impact of structural uncertainty with the impact of parametric uncertainty, we perform a simple intercomparison exercise of different sea-level rise projections from different sources. In order to provide the largest overview of the impact of structural uncertainty, we consider a wide range of sources, including projections based on expert assessment (K14, Ba19), linear response theory (L14, L19), statistical reanalysis (E19, E19M1C1), minimal ice-sheet models (Ru17), and continental computational ice-sheet models (R15, G15, G19, B19S, B19T, DP16, DP16BC). All these sources serve to define a so-called multi-model ensemble even though some projections are not based directly on computational ice-sheet models. Hereafter, we provide a brief discussion of the different models used in the multi-model ensemble and we refer the reader to the corresponding references for further discussions about these models.

- **Ba19:** Bamber et al. [2019] provided a probabilistic assessment of the AIS contribution to sea-level rise until 2300 based on a scoring and a combination of probabilistic assessments from a group of experts, a method referred to as structured expert judgement or elicitation [Colson and Cooke, 2017, 2018]. Bamber et al. [2019] provided projections

for two atmospheric temperature scenarios: in the first scenario, the atmospheric temperature stabilises in 2100 at 2 °C above preindustrial global mean surface air temperature and in the second scenario, the atmospheric temperature stabilises in 2100 at 5 °C above preindustrial global mean surface air temperature. We consider that the first temperature scenario is representative of the RCP 2.6 scenario and the second temperature scenario is representative of the RCP 8.5 scenario.

- L14: [Levermann et al. \[2014\]](#) used linear response functions to represent the relationship between the ocean forcing (sub-shelf melt rates) and the AIS contribution to sea-level rise for the ice-sheet models involved in the SeaRise intercomparison project [[Bindschadler et al., 2013](#)]. By representing each of the computational ice-sheet models involved in the SeaRise intercomparison project as a linear time-invariant system, the predicted AIS contribution to sea-level rise from each of these models for an arbitrary ocean forcing is expressed as the convolution of the ocean forcing with the linear response function of the corresponding computational model, that is, the AIS contribution to sea-level rise when the ocean forcing is a Dirac delta function. In addition, [Levermann et al. \[2014\]](#) proposed a probabilistic approach to assess the impact of atmospheric and oceanic uncertainty as well as the impact of structural uncertainty in ice-sheet models. [Levermann et al. \[2014\]](#) proposed to estimate sub-shelf melt rates from projections of subsurface Antarctic ocean temperature. These projections of the ocean temperature are expressed as scaled and time-delayed transformations of projections of the global mean atmospheric temperature determined from an ensemble of simulations from a climate emulator. For each RCP scenario, [Levermann et al. \[2014\]](#) determined probabilistic projections of the AIS contribution to sea-level rise by repeatedly and randomly selecting a simulation out of the ensemble of simulations from the climate emulator, a value for each of the parameters involved in the parameterisations of subsurface Antarctic ocean temperature and sub-shelf melting, and a linear response function out of the linear response functions of the SeaRise models.
- L19: [Levermann et al. \[2019\]](#) used a similar approach to [Levermann et al. \[2014\]](#) in which the relationship between sub-shelf melt rates and the AIS contribution to sea-level rise is approximated by means of a linear response function. Probabilistic projections of the AIS contribution to sea-level rise are obtained by using a similar sampling method as in [Levermann et al. \[2014\]](#). The major difference between both studies lies in the ice-sheet models used to project ice-sheet changes, with a larger number of ice-sheet models and generally more accurate ice-sheet models involved in the paper by [Levermann et al. \[2019\]](#).
- Ru17: [Ruckert et al. \[2017\]](#) used the DAIS ice-sheet model [[Shaffer, 2014](#)] to provide a probabilistic assessment of the AIS contribution to sea-level rise for RCP 8.5. The DAIS ice-sheet model is a minimal ice-sheet model that solves for the ice-sheet volume, the volume loss, and the ice-sheet radius. The DAIS ice-sheet model cannot capture regional characteristics of the ice sheet but is able to capture the MISI mechanism. Uncertain parameters are constrained by applying a Bayesian inversion method constrained by paleo and present-day data.
- R15: [Ritz et al. \[2015\]](#) used a probabilistic approach based on estimated probabilities of MISI onset in different marine basins to provide probabilistic projections of the AIS

contribution to sea-level rise until 2200 under the IPCC SRES A1B emission scenario. While results by [Ritz et al. \[2015\]](#) are not provided for the RCP scenarios, we follow [IPCC \[2019\]](#) and we consider these results representative of the RCP 8.5 scenario.

- **G15:** [Golledge et al. \[2015\]](#) provided multi-millennial projections of the AIS contribution to sea-level rise for each RCP scenario using the PISM ice-sheet model [[Winkelmann et al., 2011](#)] with a spatial resolution of 10 km. The PISM ice-sheet model implements a hybrid SIA/SSA reduced-order model of the ice-flow dynamics and a sub-grid parameterisation of the grounding-line position [[Feldmann et al., 2014](#)]. The ice-sheet model is forced with a background change in atmospheric temperature (see [Figure 8.2](#)) and a background change in ocean temperature linked to the change in atmospheric temperature following [Equation \(8.1\)](#), with  $F_{\text{melt}} = 0.25$ . [Golledge et al. \[2015\]](#) did not provide a probabilistic assessment of the AIS contribution to sea-level rise but employed two different grounding-line parameterisations. The first parameterisation considers a sub-grid interpolation of basal melting at the grounding line while the second does not. These two parameterisations provide respectively “high” and “low” projections of sea-level rise.
- **G19:** [Golledge et al. \[2019\]](#) investigated the impact of changing Greenland and Antarctic ice sheets on the Earth climate. They carried out simulations of the Antarctic ice sheet for RCP 2.5, RCP 4.5, and RCP 8.5 using the PISM ice-sheet model [[Winkelmann et al., 2011](#)] with a spatial resolution of 5 km. Simulations are performed with or without melt-water feedback.
- **K14:** [Kopp et al. \[2014\]](#) determined probabilistic projections for the AIS contribution to sea-level rise by combining the projections of AR5 [[Church et al., 2013](#)] and the structured expert elicitation by [Bamber and Aspinall \[2013\]](#).
- **B19S:** Probabilistic projections by [Bulthuis et al. \[2019a\]](#) (see also [Chapter 8](#)) using Weertman’s friction law with exponent  $m = 2$  and Schoof grounding-line flux parameterisation ([Figure 8.6](#) and [Table 8.3](#)).
- **B19T:** Same as **B19S** but using Tsai’s grounding-line flux parameterisation ([Figure 8.13](#) and [Table 8.5](#)).
- **DP16:** [DeConto and Pollard \[2016\]](#) used the PSUICE3-D ice-sheet model [[Pollard and DeConto, 2012b](#)] at a spatial resolution of 10 km to predict the AIS contribution to sea-level rise over the next 500 years in RCP 2.6, RCP 4.5, and RCP 8.5. The implementation of the PSUICE3-D ice-sheet model is similar to the f.ETISh model, with the implementation of a hybrid SIA/SSA reduced-order model and the utilisation of the heuristic rule by [Pollard and DeConto \[2009\]](#) for the migration of the grounding line. However, simulations performed in [DeConto and Pollard \[2016\]](#) account for hydrofracturing and marine ice-cliff instability. [DeConto and Pollard \[2016\]](#) performed an ensemble analysis to quantify the model uncertainty due to poorly known parameter values even though their approach does not fully explore the parameter space to provide a thorough statistical analysis of their projections.
- **DP16BC:** Same as **DP16** but corrected for the ocean-model cool bias in the Amundsen and Bellingshausen Sea sectors (+3 °C adjustment).

- **E19, E19MICI**: [Edwards et al. \[2019\]](#) carried out a probabilistic reanalysis of the results by [DeConto and Pollard \[2016\]](#). They built a Gaussian-process regression emulator of the computational ice-sheet model, which was later used to perform a statistical analysis of sea-level rise projections. The probabilistic reanalysis was carried out without (**E19**) and with the MICI mechanism (**E19MICI**). Projections are calibrated by accepting only values of the parameters that are able to reproduce Antarctic sea-level contributions during the mid-Pliocene, during the last interglacial, and at present.

For the purpose of comparison, we also provide the projections from AR5 [[Church et al., 2013](#)]. The projections from AR5 represent the first assessment of the AIS contribution to sea-level rise. They rely mainly on extrapolation of existing observations [[Little et al., 2013](#)] and a single limited simulation study by [Bindschadler et al. \[2013\]](#).

## 9.2 Multi-model comparison

In this section, we provide a multi-model comparison of sea-level rise projections from the aforementioned models for all RCP scenarios for short-term (up to 2100) and medium-term (up to 2300) time horizons. We also discuss the uncertainty in the projections of each model at years 2100 and 2300. Results by [Golledge et al. \[2015\]](#) and [Golledge et al. \[2019\]](#) do not provide a probabilistic assessment of sea-level rise projections. For these studies, we determined a median AIS contribution to sea-level rise as the mean value for the two sets of simulations (“low” and “high” simulations in [Golledge et al. \[2015\]](#) and simulations with and without meltwater feedback in [Golledge et al. \[2019\]](#)). We determined the quantiles for the projections by [Golledge et al. \[2015\]](#) based on a Gaussian interpretation of the projections with the 5th percentile given by the “low” scenario and the 95th percentile given by the “high” scenario. Similarly, we determined the quantiles for the projections by [Golledge et al. \[2019\]](#) based on a Gaussian interpretation of the projections with the 5th percentile given by the simulation without meltwater feedback and the 95th percentile given by the simulation with meltwater feedback. The uncertainty ranges for [DeConto and Pollard \[2016\]](#) are based on the ensemble analysis provided by the authors even though this approach yields extremely large uncertainty ranges that are sensitive to methodological choices.

### 9.2.1 Short-term sea-level rise projections (2100)

Figure 9.4 shows the median AIS contribution to sea-level rise until 2100 for each model in the multi-model ensemble and each RCP scenario. It should be mentioned that due to their initialisation procedure, projections by [Golledge et al. \[2015\]](#) result in a small contribution to sea-level rise at year 2000. Most models provide projections for RCP 2.6, RCP 4.5, and RCP 8.5, while projections in RCP 6.0 are limited to a few models that do not include MICI. There is clearly a large spread in the results from the different models even though general conclusions can be drawn. In RCP 2.6, all models agree on a limited median contribution to sea-level rise by 2100, with all models that predict a median contribution to sea-level rise by 2100 below 0.2 m and most models that predict a median contribution below 0.1 m. For RCP 4.5 and RCP 8.5, we can distinguish between projections from models that include MICI (**DP16**, **DP16BC**, **E19MICI**) and those that do not. In RCP 8.5, all models that do not include MICI predict a median AIS contribution to sea-level rise between 0.04 and 0.23 m by 2100, while median projections for

models that include MICI exceed 0.66 m. This shows that including processes such as MICI in ice-sheet models can exert a strong influence on the response of the Antarctic ice sheet and lead to considerably higher mass loss. Except for models that include MICI, all models show similar trends regarding the AIS contribution to sea-level rise until 2100. These models predict a median AIS contribution to sea-level rise by 2100 below 0.25 m for all RCP scenarios. These models also suggest a limited impact of the RCP scenario on the projections although an accelerating trend in the mass loss of the Antarctic ice sheet is observed for warmer RCP scenarios, especially for RCP 8.5.

Figure 9.1 and Extended Data Figures 9.5–9.8 show probabilistic projections of the AIS contribution to sea-level rise for each model in the multi-model ensemble at 2100 for all RCP scenarios. The uncertainty in the models is comparable to or can even be larger than the uncertainty in the projections due to structural uncertainty in the multi-model ensemble, especially in RCP 2.6. This suggests that parametric uncertainty and structural uncertainty in ice-sheet models are of similar importance in inducing uncertainty in the projections. Interestingly, we observe that most projections exhibit large tails towards high sea-level contributions, thus meaning that projections of high-end estimates of sea-level contribution (for instance 95 % percentiles) are generally more uncertain than low-end estimates. All models, except for DP16 and E19 in RCP 2.6, also agree on a positive median contribution of the Antarctic ice sheet to sea-level rise by 2100 even though uncertainty ranges do not completely rule out a negative contribution.

Discrepancies in the projections from the different models stem from uncertainty in physical processes and mechanisms driving the ice-sheet dynamics, uncertainty in atmospheric and oceanic interactions and forcings as well as limitations in the mathematical representation of the processes and their numerical implementation in computational ice-sheet models. We discuss below more specifically the projections of some models in the multi-model ensemble in order to provide insight into structural uncertainty in ice-sheet models and the uncertainty in these models.

Projections based on structured expert assessment by Bamber et al. [2019] provide median projections in agreement with projections of other models that do not include MICI. However, the large uncertainty range in the projections, characterised by large upper tails in the probability distribution functions, reflects a large divergence of opinion among experts in assessing the importance and plausibility of different mechanisms in driving the response of the Antarctic ice sheet. In particular, high values for the 95 % percentiles in Bamber et al. [2019] reflect knowledge about the sensitivity of the Antarctic ice sheet to CO<sub>2</sub> forcing during previous warm periods [Cook et al., 2013; Gasson et al., 2016] or the inclusion of new positive feedback processes such as MICI.

Projections by Levermann et al. [2019] only represent the response to basal ice-shelf melt using linear response functions. For this reason, these projections may lead to an overestimation of the mass loss of the Antarctic ice sheet, especially for limited warming scenarios, because projections in Levermann et al. [2019] do not consider mass gain due to, for instance, additional snowfall. On the other hand, these projections may lead to an underestimation of the mass loss of the Antarctic ice sheet because projections based on linear response theory do not allow to capture nonlinearities, feedbacks, or instabilities. The large uncertainty range in the projections

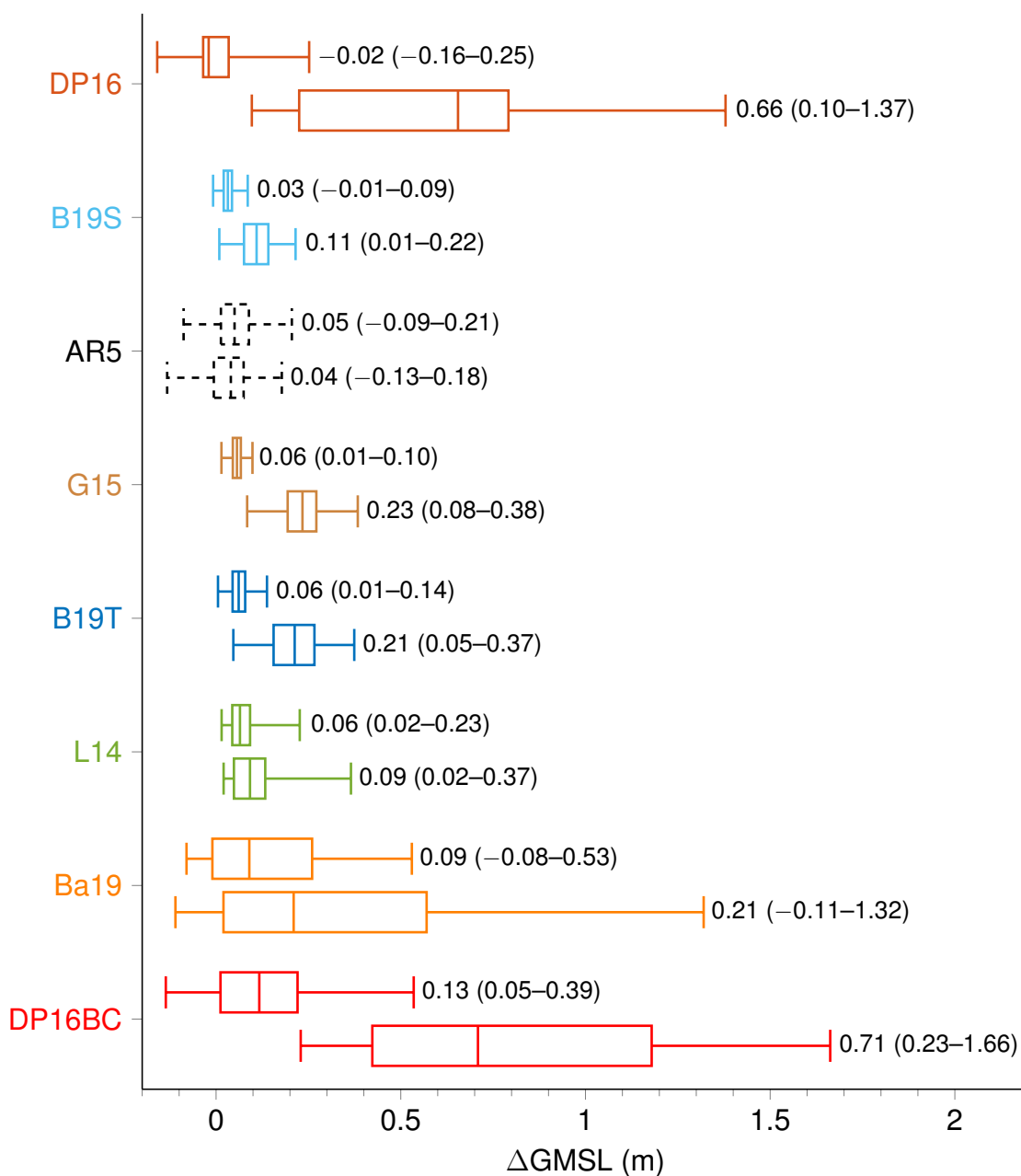


Figure 9.1: Summary figure (adapted from Extended Data Figures 9.5 and 9.8). Projections of AIS contribution to sea-level rise at 2100 in RCP 2.6 (upper line) and in RCP 8.5 (lower line). Boxes and whiskers show the 5th, 33th, 50th, 66th, and 95th percentiles. Dashed boxplots: AR5 projections.

reflects uncertainty in atmospheric and ocean forcings as well as (large) discrepancies between computational ice-sheet models involved in the study. Yet, these projections are based on computational ice-sheet models that do not include the MICI mechanism, thus meaning that the uncertainty range could have been even larger. The large uncertainty range in the projections by

Levermann et al. [2014] can be explained similarly. Projections by Levermann et al. [2014] are however lower than projections by Levermann et al. [2019]. A reason for this difference is that the participating models in Levermann et al. [2019] are more able to reproduce MISI than the participating models in Levermann et al. [2014], which were early versions of continental computational ice-sheet models. For this reason, participating models in Levermann et al. [2019] have a higher sensitivity to basal ice-shelf melt than the participating models in Levermann et al. [2014].

Our projections with Weertman's friction law and Schoof's grounding-line parameterisation [Bulthuis et al., 2019a] are comparable to other projections based on computational ice-sheet models without MICI, for instance, projections by Ritz et al. [2015], Golledge et al. [2015], and Golledge et al. [2019] even though they provide smaller estimates than Ritz et al. [2015] and Golledge et al. [2015]. As discussed in Section 8.4, we attribute these smaller estimates to a weak ocean forcing in the Amundsen Sea sector and insufficient sliding at the base of the Thwaites and Pine Island Glaciers. For these reasons, our projections can be considered as low-end estimates for the AIS contribution to sea-level rise; see also Le Cozannet et al. [2019], where results by Bulthuis et al. [2019a] are used to provide low-end probabilistic sea-level rise projections as a basis for minimum adaptation needs.

Projections by DeConto and Pollard [2016] (DP16 and DP16BC) provide the highest estimates for the AIS contribution to sea-level rise due to the inclusion of MICI and display large uncertainty in the projections. Figure 9.4 suggests that the risk of MICI is limited before 2050 for all RCP scenarios. Projections by DeConto and Pollard [2016] even have a substantial probability of negative contribution until the period 2050–2060. By 2100 and for the strongly mitigated RCP 2.6 scenario, Figure 9.5 suggests that the risk of MICI could be prevented with high certainty only in the absence of strong ocean warming in the Amundsen and Bellingshausen Sea sectors (projections without ocean-bias correction). By 2100 and for the moderate RCP 4.5 scenario, hydrofracturing and marine ice-cliff instability already have the potential to trigger significant Antarctic mass loss, with 95 % percentiles exceeding 0.7 m (Figure 9.6). By 2100 and for the RCP 8.5 scenario, Figure 9.8 suggests that the risk of MICI could not be prevented, with median contributions and 95 % percentiles exceeding 0.66 m and 1.37 m, respectively. Even though the validity of MICI is still debated, projections by DeConto and Pollard [2016] can be considered as high-end estimates for the AIS contribution to sea-level rise and serve as a basis for extreme risk management; see also Le Bars et al. [2017] and Stammer et al. [2019].

Edwards et al. [2019] showed that the MICI hypothesis was not necessary to reproduce the high eustatic sea levels in the past as suggested by DeConto and Pollard [2016]. Without the MICI hypothesis, projections by Edwards et al. [2019], based on the results by DeConto and Pollard [2016], have median contributions and uncertainty ranges consistent with projections based on models that do not include MICI. However, projections by Edwards et al. [2019] with the MICI hypothesis are similar to or even larger than projections by DeConto and Pollard [2016] with ocean-bias correction.

Finally, projections by Kopp et al. [2014] are a bit more peculiar because they rely on projections from AR5 and probably underestimate the response of the Antarctic ice sheet; see discussion below.

The comparison between the projections from the multi-model ensemble (except perhaps for [Kopp et al. \[2014\]](#)) and the projections from AR5 shows significant differences. First, all models predict an increase in the median AIS contribution to sea-level rise as the RCP scenario gets warmer. By contrast, AR5 predicted the median AIS contribution to sea-level rise in RCP 8.5 to be lower than in other scenarios. In AR5, increased atmospheric temperatures lead to a mass gain due to increased snowfall, which is only partially compensated by dynamical changes. Since AR5, dynamical changes due to atmospheric and oceanic forcings have been shown to dominate the response of the Antarctic ice sheet while increased snowfall only partially compensates mass loss due to dynamical changes. Second, all models from the multi-model ensemble agree, with high level of certainty, on a positive contribution of the Antarctic ice to sea-level rise by 2100, especially for warmer RCP scenarios. By contrast, projections in AR5 suggested that a negative contribution to sea-level rise by 2100 would be almost as likely as a positive contribution. Third, projections in AR5 suggested that the contribution of the Antarctic ice sheet to sea-level rise by 2100 would only represent a minor contribution when compared with other contributors such as thermal expansions, glaciers, and the Greenland ice sheet. By contrast, models from the multi-model ensemble suggest that the Antarctic ice sheet might be a more important contributor to sea-level rise over this century than previously thought, with some high-end estimates suggesting that the Antarctic ice sheet might even be the largest contributor by the end of the century.

## 9.2.2 Medium-term sea-level rise projections (2300)

Projections of the AIS contribution to sea-level rise beyond 2100 are characterised by deeper uncertainty than projections by the end of the century, with only a limited number of studies that provide multicentennial projections of the response of the Antarctic ice sheet. In the multi-model ensemble, projections up to 2300 include only three studies based on computational ice-sheet models [[Golledge et al., 2015](#); [DeConto and Pollard, 2016](#); [Bulthuis et al., 2019a](#)], one probabilistic reanalysis of numerical results [[Edwards et al., 2019](#)], one reanalysis of numerical results based on linear response theory [[Levermann et al., 2014](#)], and one study based on a minimal ice-sheet model [[Ruckert et al., 2017](#)].

Figure 9.9 shows the median AIS contribution to sea-level rise until 2300 for each model in the multi-model ensemble and each RCP scenario. Similarly to projections until 2100, one can distinguish between projections that include MICI and those that do not. This time, however, differences in median sea-level rise contributions can amount to several metres, especially for warmer RCP scenarios. Projections suggest that only the RCP 2.6 scenario can prevent a substantial ice loss by 2300 for all models (median contribution of less than 0.5 m for all models but E19MICI). For other scenarios, most models exhibit an increase in mass loss rate beyond 2100, suggesting the possibility of the onset of an instability. For the RCP 8.5 scenario, all models exhibit an acceleration in the rate of mass loss in the next centuries. For this same scenario, all models also agree on a median contribution to sea-level rise above 1 m. While the impact of the RCP scenario on the projections is rather limited by the end of the century, projections beyond 2100 are strongly dependent on the emission scenario. Figure 9.2 and Extended Data Figures 9.10–9.13 show probabilistic projections of the AIS contribution to sea-level rise at 2300 for each model in the multi-model ensemble and each RCP scenario. Except for the RCP 2.6

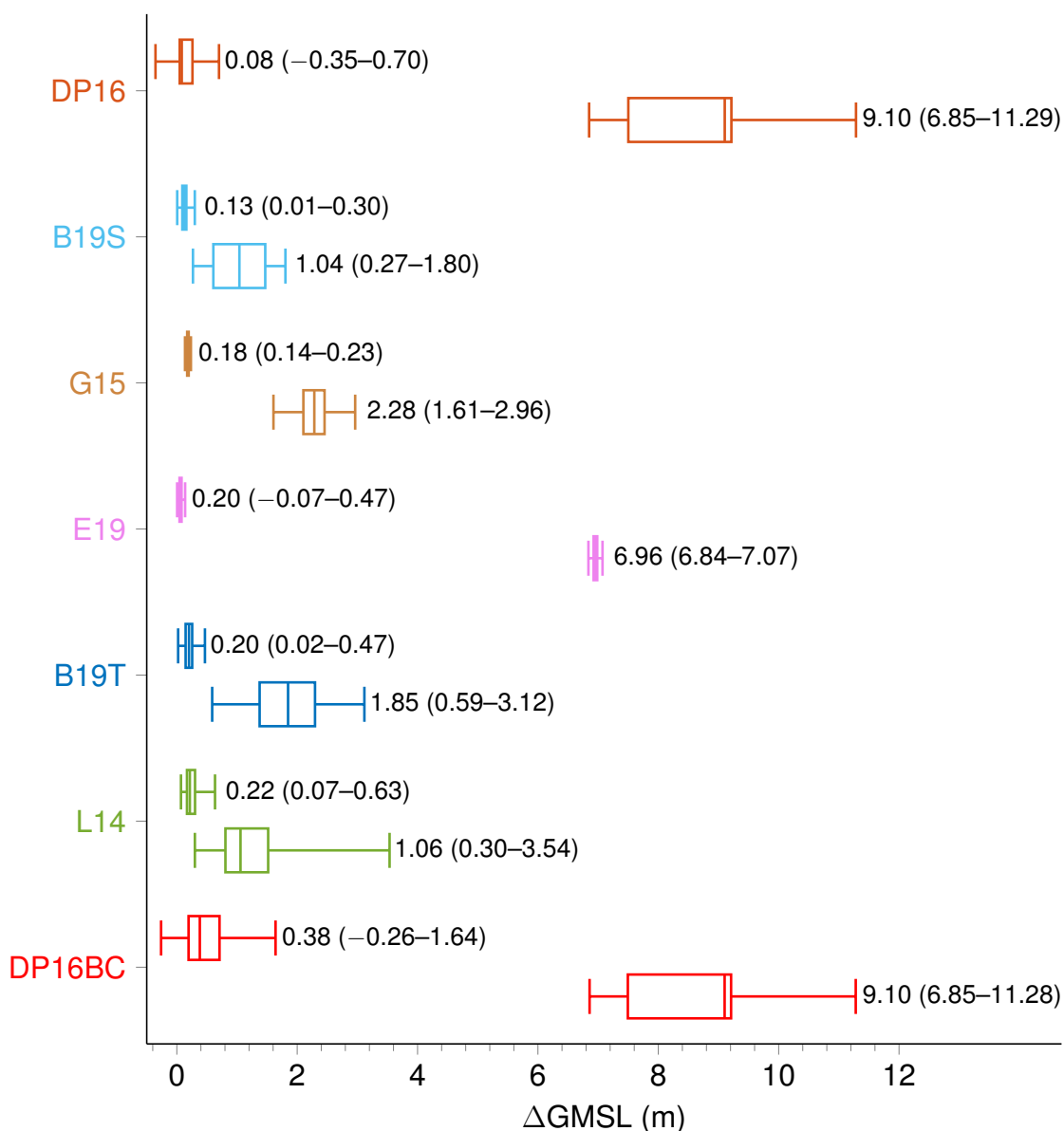


Figure 9.2: Summary figure (adapted from Extended Data Figures 9.10 and 9.13). Projections of AIS contribution to sea-level rise at 2300 in RCP 2.6 (upper line) and in RCP 8.5 (lower line). Boxes and whiskers show the 5th, 33th, 50th, 66th, and 95th percentiles. For comparison, projections of the AIS contribution to sea-level rise at 2300 in AR5 give a contribution of  $-0.03$  m in RCP 2.6 and a contribution that ranges from  $0.02$  m to  $0.19$  m in RCP 8.5.

scenario, uncertainty ranges (5–95 % probability intervals) predict a positive contribution of the Antarctic ice sheet to sea-level rise over the next centuries.

Discrepancies in the projections until 2300 between the different models are qualitatively similar to discrepancies in the projections until 2100. Our projections under Weertman’s fric-

tion law and Schoof's grounding-line parameterisation (B19S) provide in most cases low-end estimates for the AIS contribution to sea-level rise. Projections under Weertman's friction law and Tsai's grounding-line parameterisation (B19T) are generally consistent with projections by [Golledge et al. \[2015\]](#). Projections by [Levermann et al. \[2014\]](#) (L14) are of the same order as B19S, B19T, and G15. Yet, projections based on linear response theory might be questionable on multicentennial timescales because of instabilities in marine basins. Projections by [DeConto and Pollard \[2016\]](#) without ocean-bias correction suggest that the RCP 2.6 scenario can prevent substantial ice loss due to the MICI mechanism in the next centuries. Projections from DP16 also show a substantial probability of a negative contribution by 2300. For other scenarios, projections by [DeConto and Pollard \[2016\]](#) suggest the onset of MICI with high level of certainty and seem to be relatively insensitive to the ocean-bias correction. Without the MICI hypothesis, projections by [Edwards et al. \[2019\]](#), based on the results by [DeConto and Pollard \[2016\]](#), have median contributions and uncertainty ranges consistent with projections based on models that do not include MICI for the RCP 2.6 and RCP 4.5 scenarios. More surprisingly, projections by [Edwards et al. \[2019\]](#) without MICI for the RCP 8.5 scenario show high sea-level rise estimates (6.96 m median contribution) that are more consistent with models with MICI than those without MICI. [Edwards et al. \[2019\]](#) suggested that the computational ice-sheet model used by [DeConto and Pollard \[2016\]](#) might be oversensitive to very large atmospheric temperature changes even in the absence of MICI. Also, the uncertainty range from E19 for the RCP 8.5 scenario seems excessively narrow, thus suggesting deficiency in the sampling method in [DeConto and Pollard \[2016\]](#) or in the ability of the computational ice-sheet model to represent the multicentennial response of the Antarctica under warm atmospheric forcings.

Projections in the AR5 report for the AIS contribution to sea-level rise by 2300 rely only on a small number of available simulations based on coarse-resolution ice-sheet models and do not provide an uncertainty assessment. These projections show a negative contribution to sea-level rise by 2300 in RCP 2.6 ( $-0.03$  m) and RCP 4.5 ( $-0.25$  m to  $-0.03$  m) and a small positive contribution in RCP 8.5 ( $0.02$  m to  $0.19$  m). Thus, conclusions in AR5 indicated that the Antarctic ice sheet would be a minor contributor to sea-level rise until 2300 and could even mitigate the effect of climate warming on sea-level rise. New studies since AR5 definitely rule out these conclusions. New studies show that the Antarctic ice sheet will most certainly lose mass over the next centuries, with a potential contribution of several metres if climate warming is not abated.

Beyond 2300, projections of the AIS contribution to sea-level rise become even further uncertain, with only a few studies providing projections beyond 2300 [[Golledge et al., 2015](#); [DeConto and Pollard, 2016](#); [Bulthuis et al., 2019a](#)]. Regarding the AIS contribution to sea-level rise on a millennial time horizon (by 3000), projections by [Golledge et al. \[2015\]](#) give for the RCP 2.6 scenario a median contribution of  $0.32$  m with a 5–95 % probability interval that ranges from  $0.36$  m to  $0.40$  m and for the RCP 8.5 scenario a median contribution of  $5.70$  m with a 5–95 % probability interval that ranges from  $3.39$  m to  $8.01$  m. By comparison, our projections with Weertman's friction law and Schoof's grounding-line parameterisation give for the RCP 2.6 scenario a median contribution of  $0.30$  m with a 5–95 % probability interval that ranges from  $-0.01$  m to  $0.82$  m and for the RCP 8.5 scenario a median contribution of  $5.08$  m with a 5–95 % probability interval that ranges from  $1.36$  m to  $6.00$  m. In addition, our projections with Weertman's friction law and Tsai's grounding-line parameterisation give for the

RCP 2.6 scenario a median contribution of 0.46 m with a 5–95 % probability interval that ranges from 0.00 m to 1.30 m in RCP 2.6 and for the RCP 8.5 scenario a median contribution of 7.43 m with a 5–95 % probability interval that ranges from 3.85 m to 10.79 m. These limited projections suggests that the RCP 2.6 scenario can prevent substantial ice loss even on a millennial time horizon, while the RCP 8.5 scenario will trigger with high certainty the complete collapse of the West Antarctic ice sheet and a significant retreat of marine basins in East Antarctica over the next millenium.

### 9.2.3 Multi-model projections in the SROCC report

We do not seek to provide (probabilistic) projections of the contribution of the Antarctic ice sheet to sea-level rise by combining projections from different models because we find it unclear how to properly combine these models. We mention however that a similar exercise has been performed in the SROCC report [IPCC, 2019] to provide reassessed projections of sea-level rise by 2100 since AR5 (Table 9.1 and Figure 9.3). The new assessment is based on computational ice-sheet models of the Antarctic ice sheet driven by diverse climate scenarios. In particular, this new assessment combines the projections by Levermann et al. [2014], Golledge et al. [2015], Ritz et al. [2015], Bulthuis et al. [2019a], and Golledge et al. [2019] by using a Monte Carlo technique and by assuming mutual dependence between the different studies. It should be noted that in the SROCC assessment, projections by DeConto and Pollard [2016] have been discarded because the timing and the magnitude of their simulated ice loss have been judged too uncertain to be included in the SROCC projections. Thus, SROCC projections rely on the assumption that MICI will not happen before 2100 and the contribution of the Antarctic ice sheet to sea-level rise might be considerably higher than in Table 9.1, as suggested in DeConto and Pollard [2016], Bamber et al. [2019], and Edwards et al. [2019].

	RCP 2.6	RCP 4.5	RCP 8.5
Thermal expansion	0.14 (0.10–0.18)	0.19 (0.14–0.23)	0.27 (0.21–0.33)
Glaciers	0.10 (0.04–0.16)	0.12 (0.06–0.18)	0.16 (0.09–0.23)
Greenland ice sheet	0.06 (0.04–0.10)	0.08 (0.04–0.13)	0.12 (0.07–0.21)
Land water storage	0.04 (–0.01–0.09)	0.04 (–0.01–0.09)	0.04 (–0.01–0.09)
Antarctic ice sheet	0.04 (0.01–0.11)	0.06 (0.01–0.15)	0.12 (0.03–0.28)
Total	0.43 (0.29–0.59)	0.55 (0.39–0.72)	0.84 (0.61–1.10)

Table 9.1: Median values and “likely” ranges (17–83 % probability intervals) for projections of global mean sea-level rise in metres in 2081–2100 relative to 1986–2005 for three RCP scenarios as estimated in the SROCC report [IPCC, 2019]. Contribution to sea-level rise due to thermal expansion, glaciers, the Greenland ice sheet, and land water storage are identical to AR5 [Church et al., 2013], while the contribution of the Antarctic ice sheet to global sea-level rise has been reassessed based on recent studies since AR5. For comparison, projections of future global mean sea-level rise in the AR5 report are given in Table 1.1.

Time series of the SROCC projections of global mean sea-level rise for the different RCP scenarios (Figure 9.3) show that the median global mean sea-level rise projections in the SROCC

report are similar to the median global mean sea-level rise projections in the AR5 report for the RCP 2.6 and RCP 4.5 scenarios. However, these series indicate a divergence in median global mean sea-level rise projections for the RCP 8.5 scenario during the second half of the century between the SROCC and AR5 projections. This divergence results from an additional contribution from the Antarctic ice sheet to global mean sea-level rise due to dynamical changes which are captured more accurately in recent studies than in AR5. Contrary to the median AR5 projections of the contribution of the Antarctic ice sheet to sea level, the corresponding SROCC projections increase as the RCP scenario gets warmer, thus suggesting that ice loss due to ice-sheet dynamical changes driven by increased atmospheric and ocean forcings are more significant than mass gain due to increased snowfall. Uncertainty ranges between both reports are similar although slightly increased in the SROCC report for RCP 8.5, especially towards high sea-level rise contributions. Uncertainty ranges in the SROCC report also indicate a positive contribution of the Antarctic ice sheet to sea-level rise with a high level of certainty, even for the RCP 2.6 scenario.

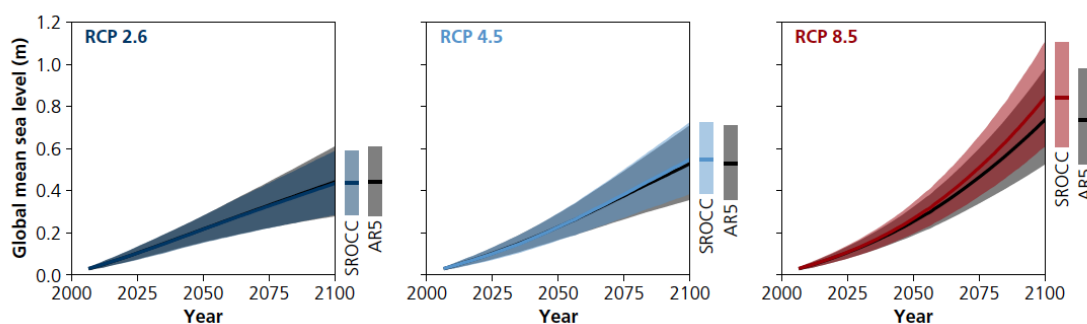


Figure 9.3: Time series of  $\Delta\text{GMSL}$  for RCP 2.6, RCP 4.5, and RCP 8.5 as determined in the SROCC report and, for reference the AR5 report. Results are based on AR5 results for all components except the Antarctic contribution. The shaded region should be considered as the “likely” range (17–83 % probability interval). Credit: IPCC [2019].

The SROCC report also provides reassessed projections of the AIS contribution to sea-level rise beyond 2100 based on the results by [Levermann et al. \[2014\]](#), [Golledge et al. \[2015\]](#), and [Bulthuis et al. \[2019a\]](#) (Table 9.2). As for the SROCC projections by 2100, SROCC projections beyond 2100 do not account for the possibility of the onset of marine ice-cliff instabilities. Given the limited number of studies involved in this assessment and the uncertainty in the dominant processes that could trigger a major retreat of the Antarctic ice sheet, estimates beyond 2100 are considered as highly uncertain. Nonetheless, these projections and studies by [Levermann et al. \[2014\]](#), [Golledge et al. \[2015\]](#), [DeConto and Pollard \[2016\]](#), and [Bulthuis et al. \[2019a\]](#) suggest that a substantial ice loss can only be prevented for strongly mitigated scenarios, like the RCP 2.6 scenario. On the other hand, projections for the RCP 8.5 scenario suggest a high probability of triggering a significant retreat of the Antarctic ice sheet in the coming centuries. Overall, projections by 2300 in the SROCC report are significantly higher than projections in the AR5 report, especially for warm atmospheric scenarios, thus meaning that the response of the Antarctic ice sheet to climate change was heavily underestimated in the AR5 report.

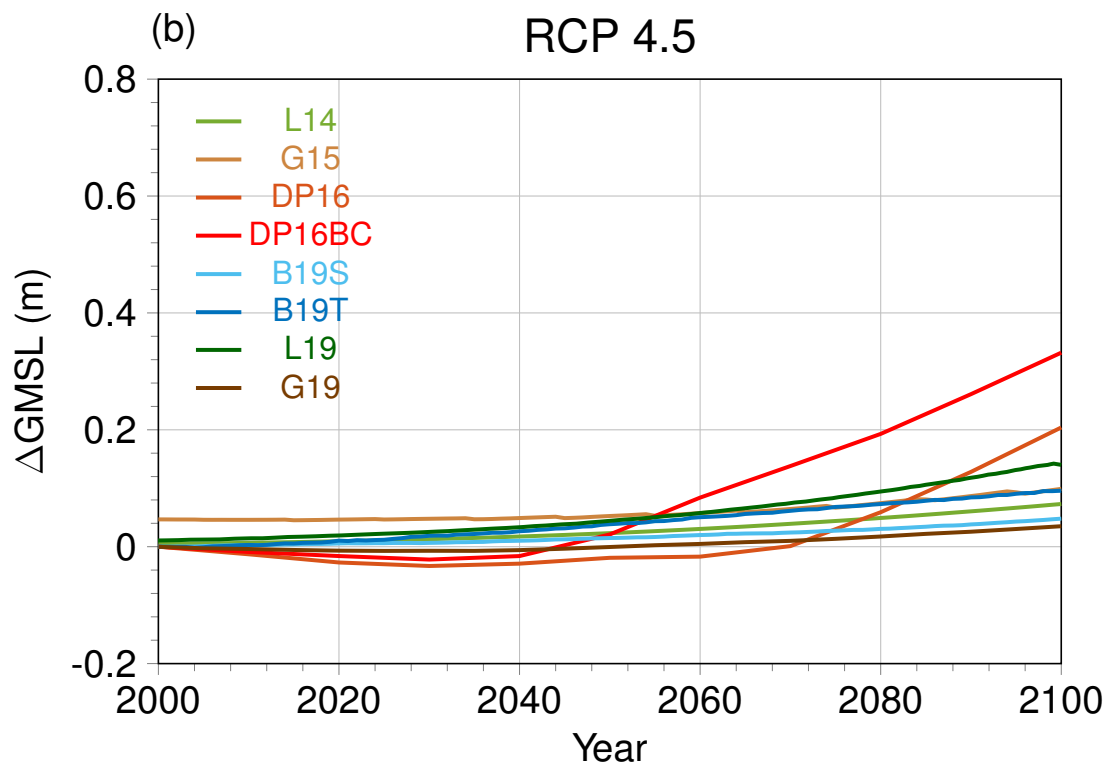
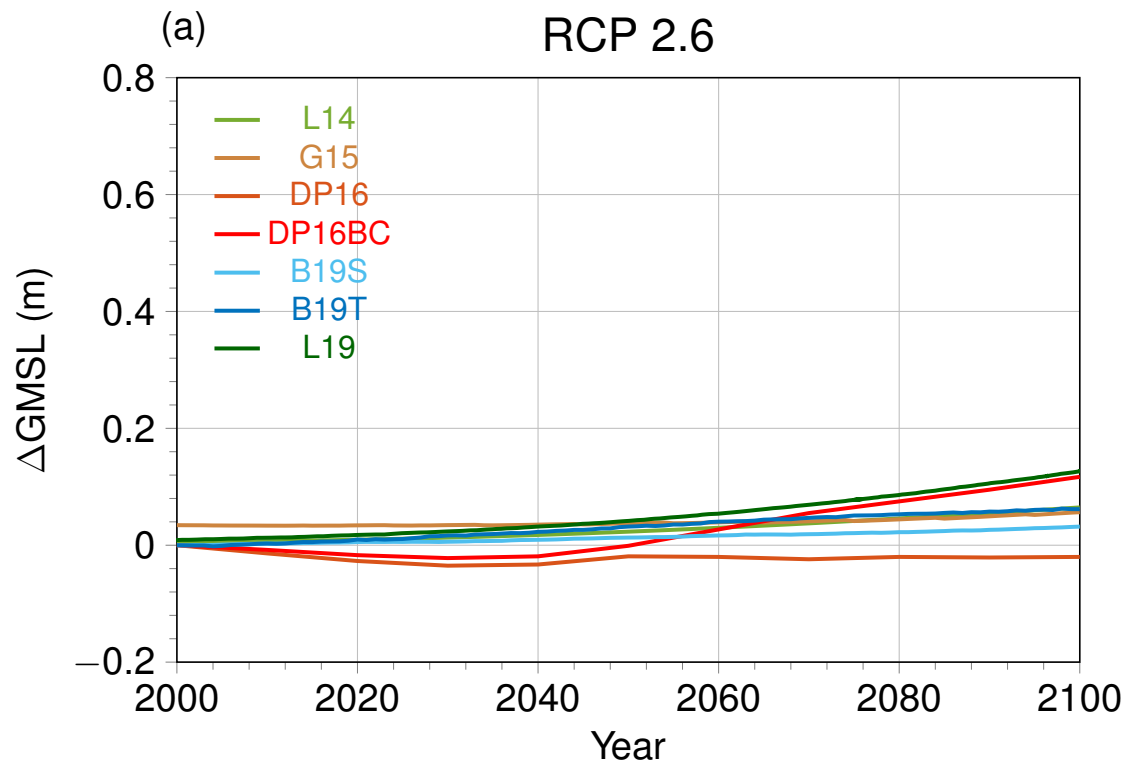
	RCP 2.6	RCP 4.5	RCP 8.5
2100	0.04 (0.01–0.11)	0.06 (0.01–0.16)	0.13 (0.02–0.31)
2200	0.11 (0.04–0.26)	0.24 (0.10–0.48)	0.71 (0.32–1.39)
2300	0.16 (0.07–0.37)	0.46 (0.24–0.88)	1.46 (0.60–2.90)

Table 9.2: Probabilistic projections (in metres) of the AIS contribution to sea level by 2100, 2200, and 2300 for three RCP scenarios as estimated in the SROCC report [IPCC, 2019].  $\Delta$ GMSL projections are the median projections with their 5–95 % probability intervals between parentheses. For comparison, projections of the AIS contribution to sea level rise by 2300 in AR5 [Church et al., 2013] give a contribution of  $-0.03$  m in RCP 2.6, from  $-0.25$  m to  $-0.03$  m in RCP 4.5, and from  $0.02$  m to  $0.19$  m in RCP 8.5.

### 9.3 Chapter summary

In this chapter, we provided a multi-model comparison of the contribution of the Antarctic ice sheet to future sea-level rise for short-term (up to 2100) and medium-term (up to 2300) time horizons under different RCP scenarios. We compared projections from different studies published after the AR5 report. Ice-sheet models used since AR5 are able to capture more accurately dynamical changes in the Antarctic ice sheet. New studies since AR5 indicate that ice-sheet dynamical changes will control the contribution of the Antarctic ice sheet to sea level, while mass gain due to increased snowfall will only play a mitigation effect. Projections from the multi-model ensemble suggest a limited contribution of the Antarctic ice sheet to sea level before 2050 for all RCP scenarios. By 2100, models that do not include MICI agree on a limited AIS contribution to sea-level rise (less than  $0.35$  m for all models without MICI and for all RCP scenarios), while models that include MICI raise concerns about the potential of climate warming to trigger substantial mass loss from the Antarctic ice sheet (more than  $1$  m) by the end of the century. Projections beyond 2100 are much more uncertain and large differences exist between models with MICI and those without MICI. Almost all models agree on a limited median contribution ( $<0.5$  m) by 2300 in RCP 2.6, while median projections by 2300 in RCP 8.5 range from just over  $1$  m to more than  $9$  m.

To summarise, a key finding of studies since AR5 is that substantial mass loss from the Antarctic ice sheet in the next centuries can only be prevented with high certainty for the strongly mitigated RCP 2.6, while substantial mass loss from the Antarctic ice sheet in the next centuries is expected to be triggered with high certainty for the RCP 8.5 scenario. High uncertainty still remains in determining the increase in atmospheric temperature capable of triggering a major retreat of the Antarctic ice sheet.



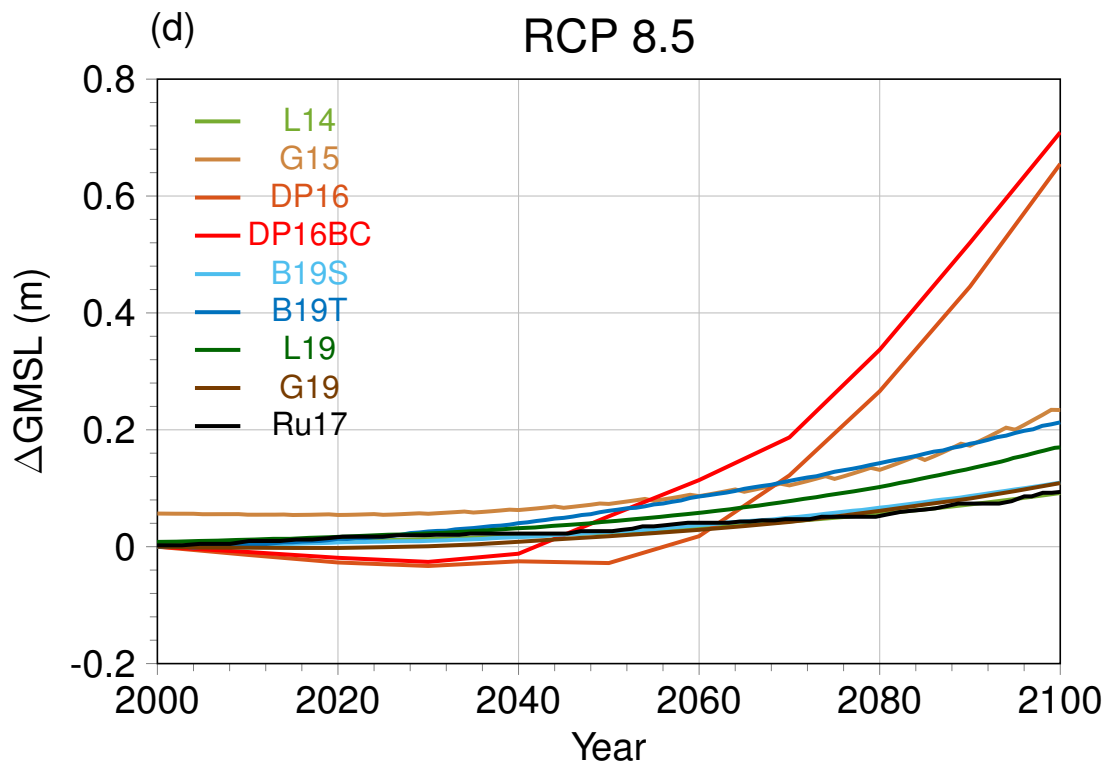
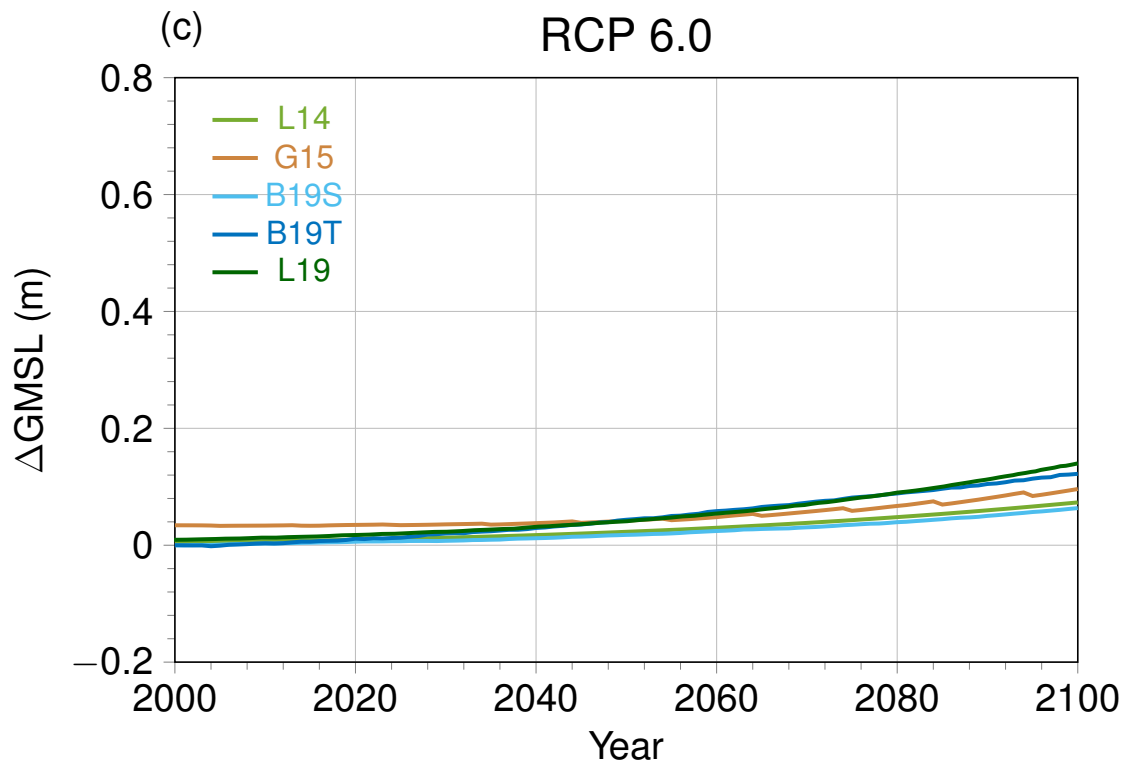


Figure 9.4: Median projections of AIS contribution to sea-level rise until 2100.

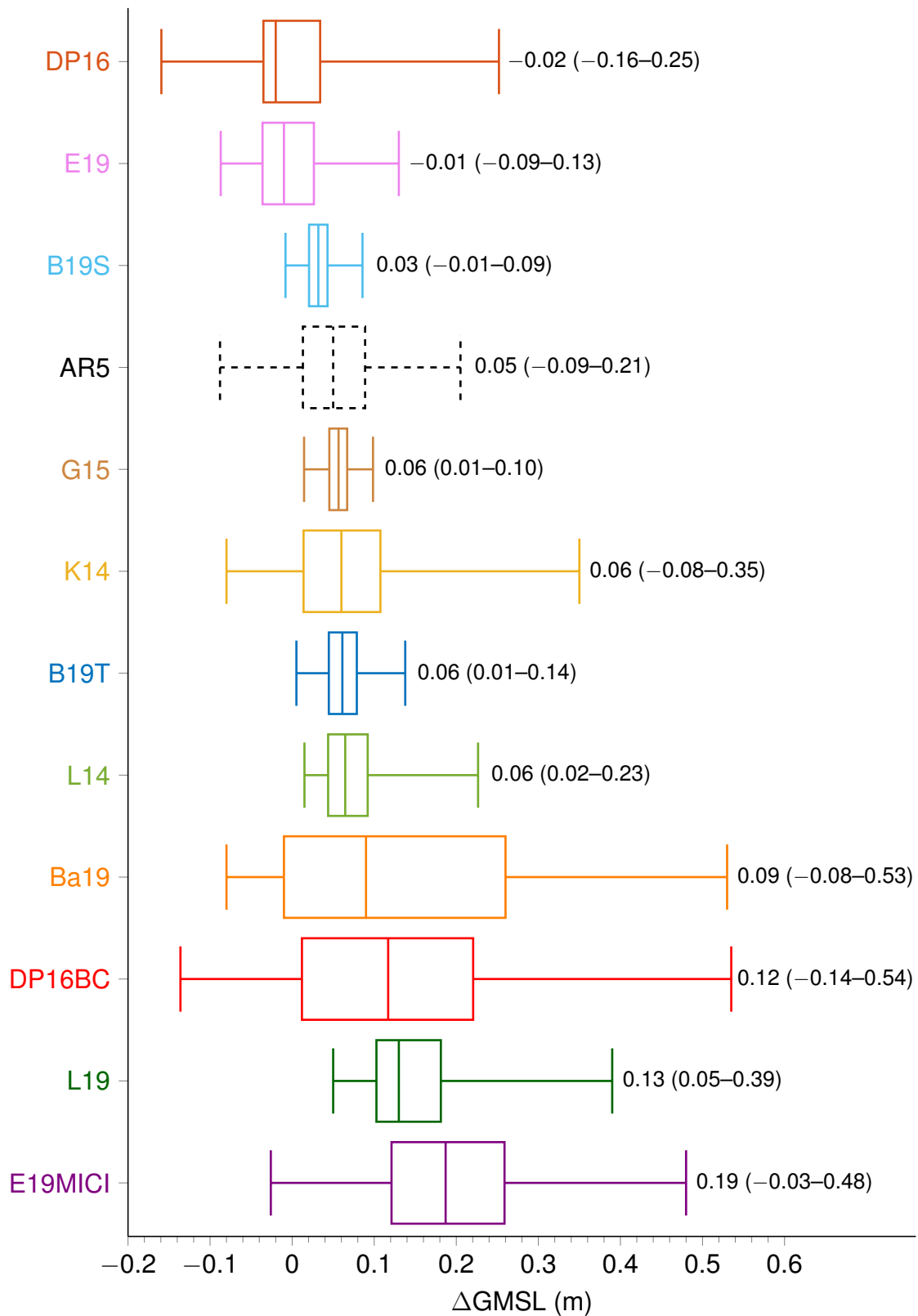


Figure 9.5: Projections of AIS contribution to sea-level rise at 2100 in RCP 2.6. Boxes and whiskers show the 5th, 33th, 50th, 66th, and 95th percentiles. Dashed boxplot: AR5 projections.

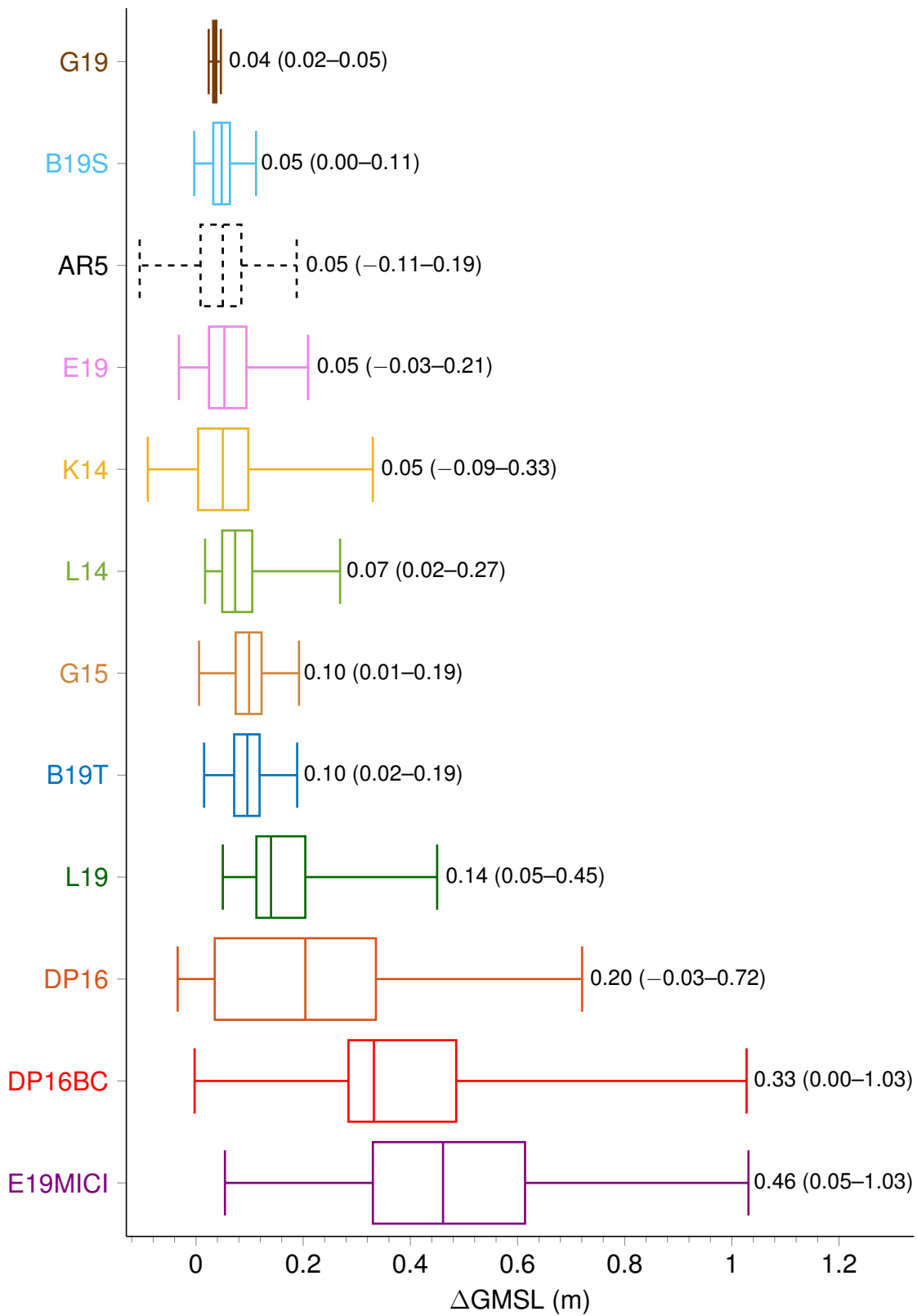


Figure 9.6: Projections of AIS contribution to sea-level rise at 2100 in RCP 4.5. Boxes and whiskers show the 5th, 33th, 50th, 66th, and 95th percentiles. Dashed boxplot: AR5 projections.

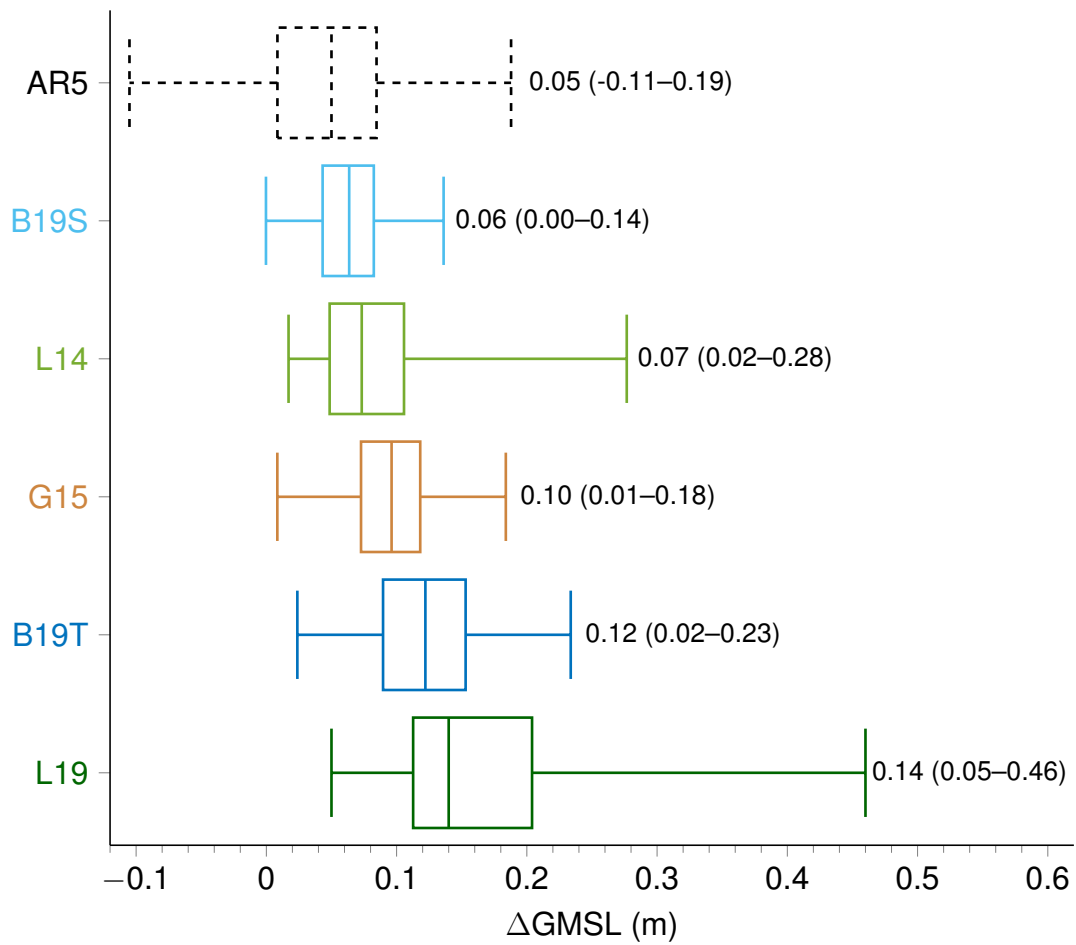


Figure 9.7: Projections of AIS contribution to sea-level rise at 2100 in RCP 6.0. Boxes and whiskers show the 5th, 33th, 50th, 66th, and 95th percentiles. Dashed boxplot: AR5 projections.

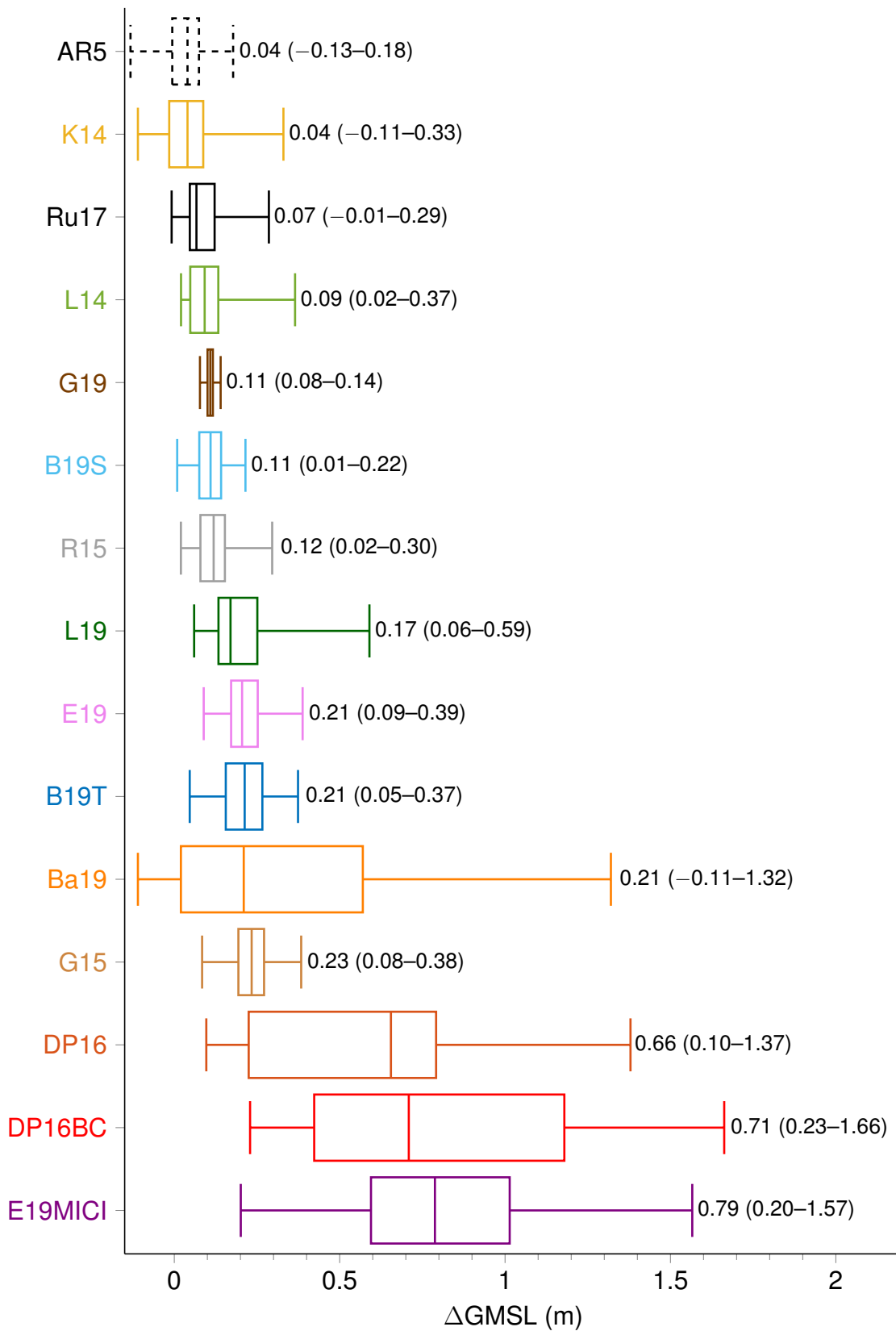
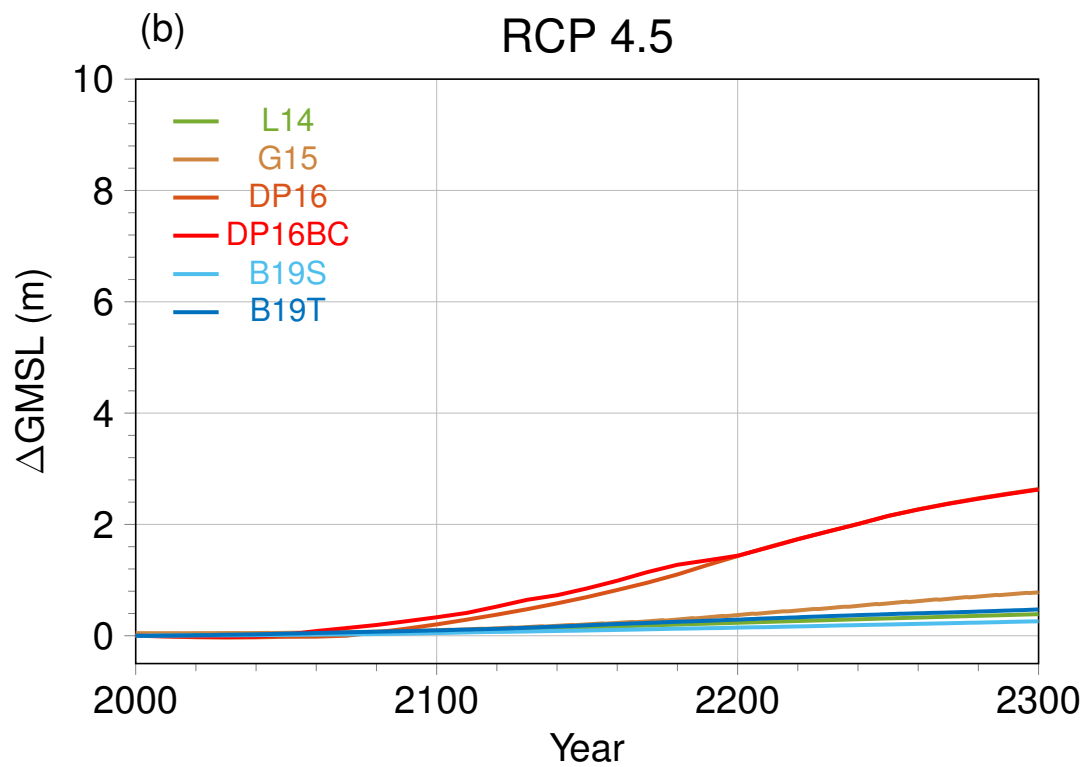
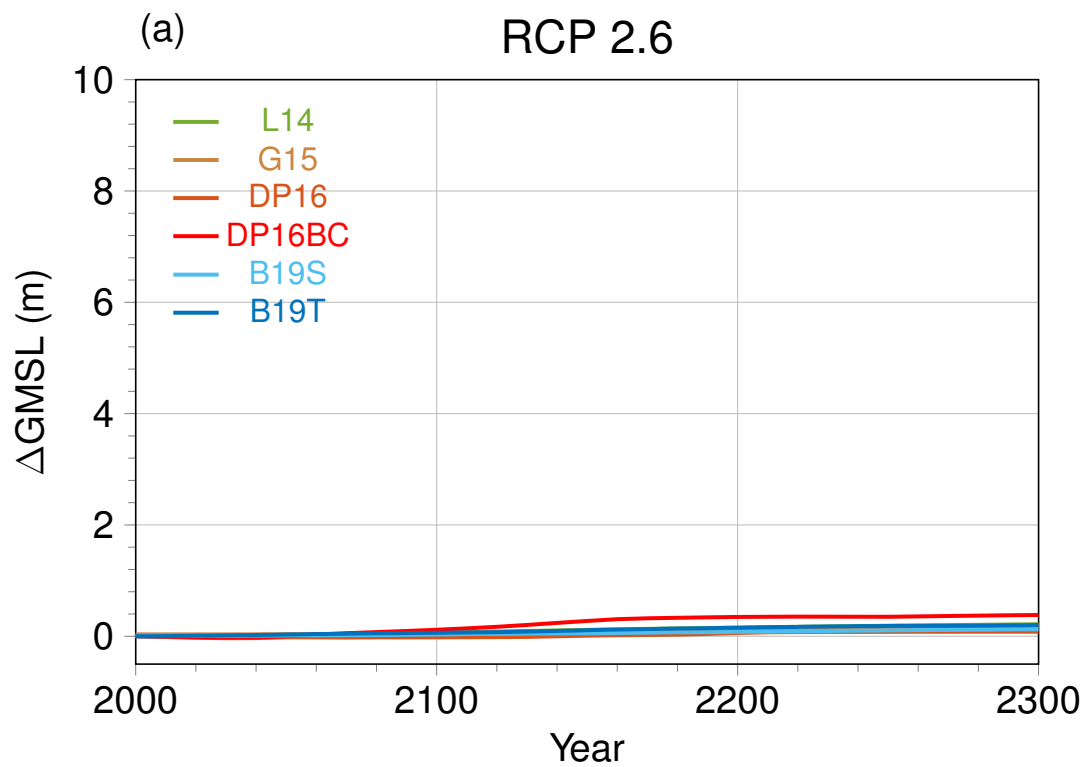


Figure 9.8: Projections of AIS contribution to sea-level rise at 2100 in RCP 8.5. Boxes and whiskers show the 5th, 33th, 50th, 66th, and 95th percentiles. Dashed boxplot: AR5 projections.



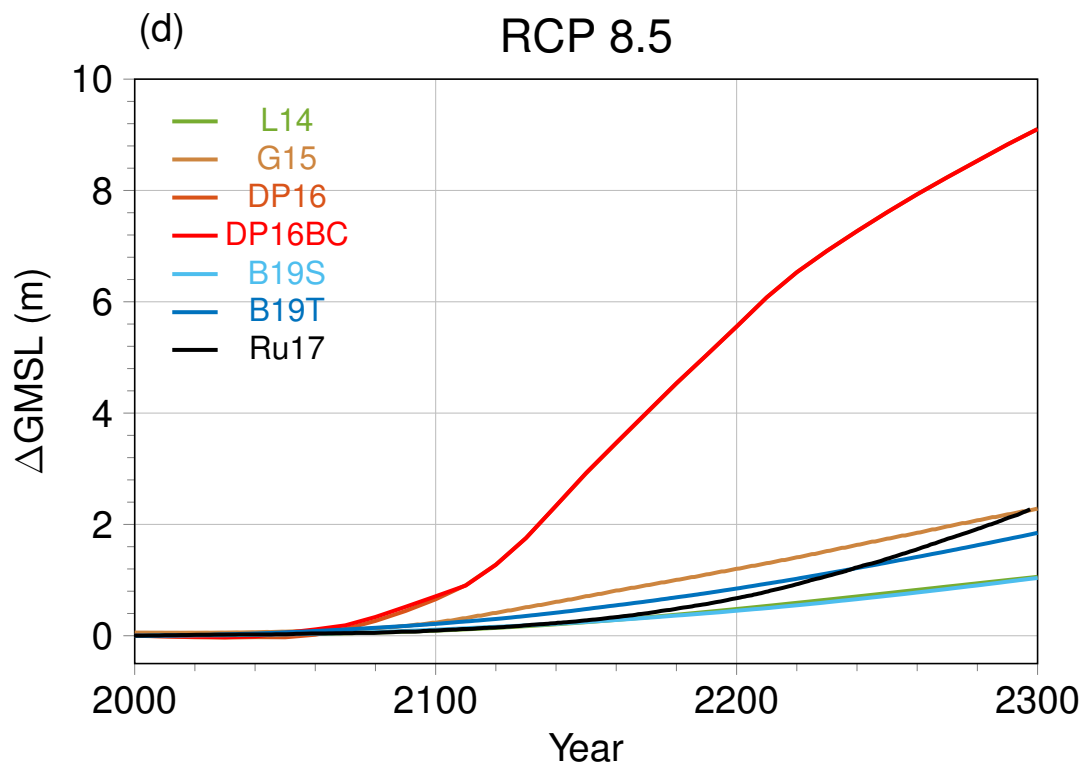
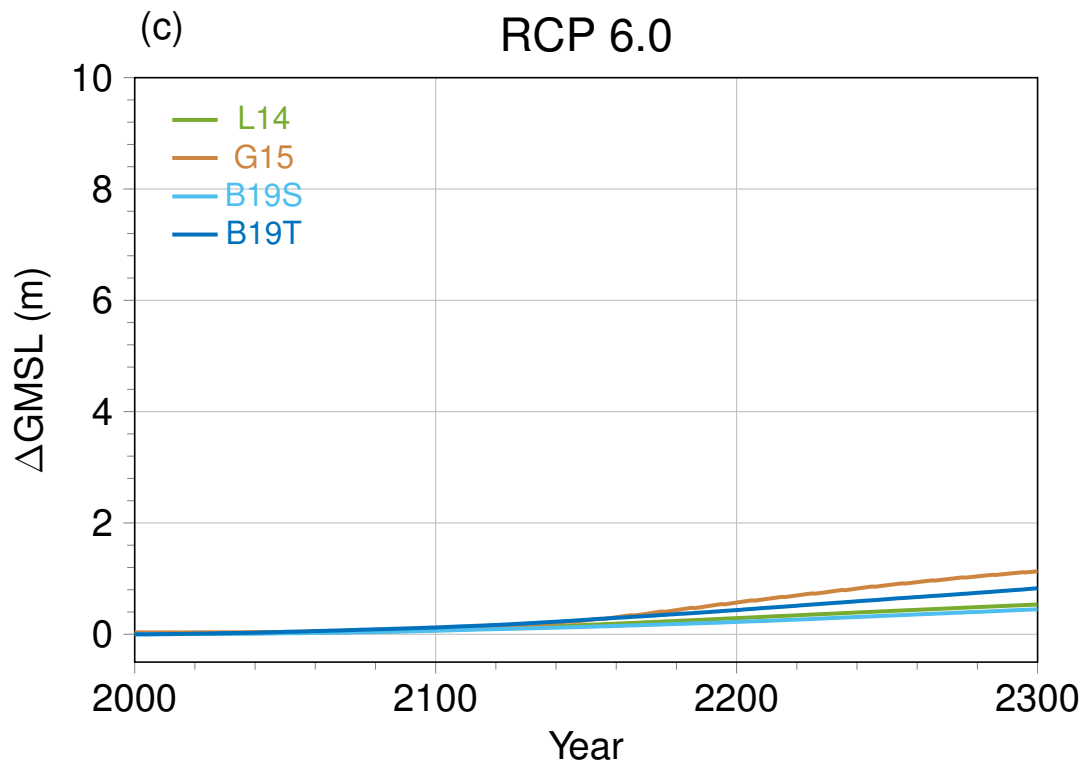


Figure 9.9: Median projections of AIS contribution to sea-level rise until 2300.

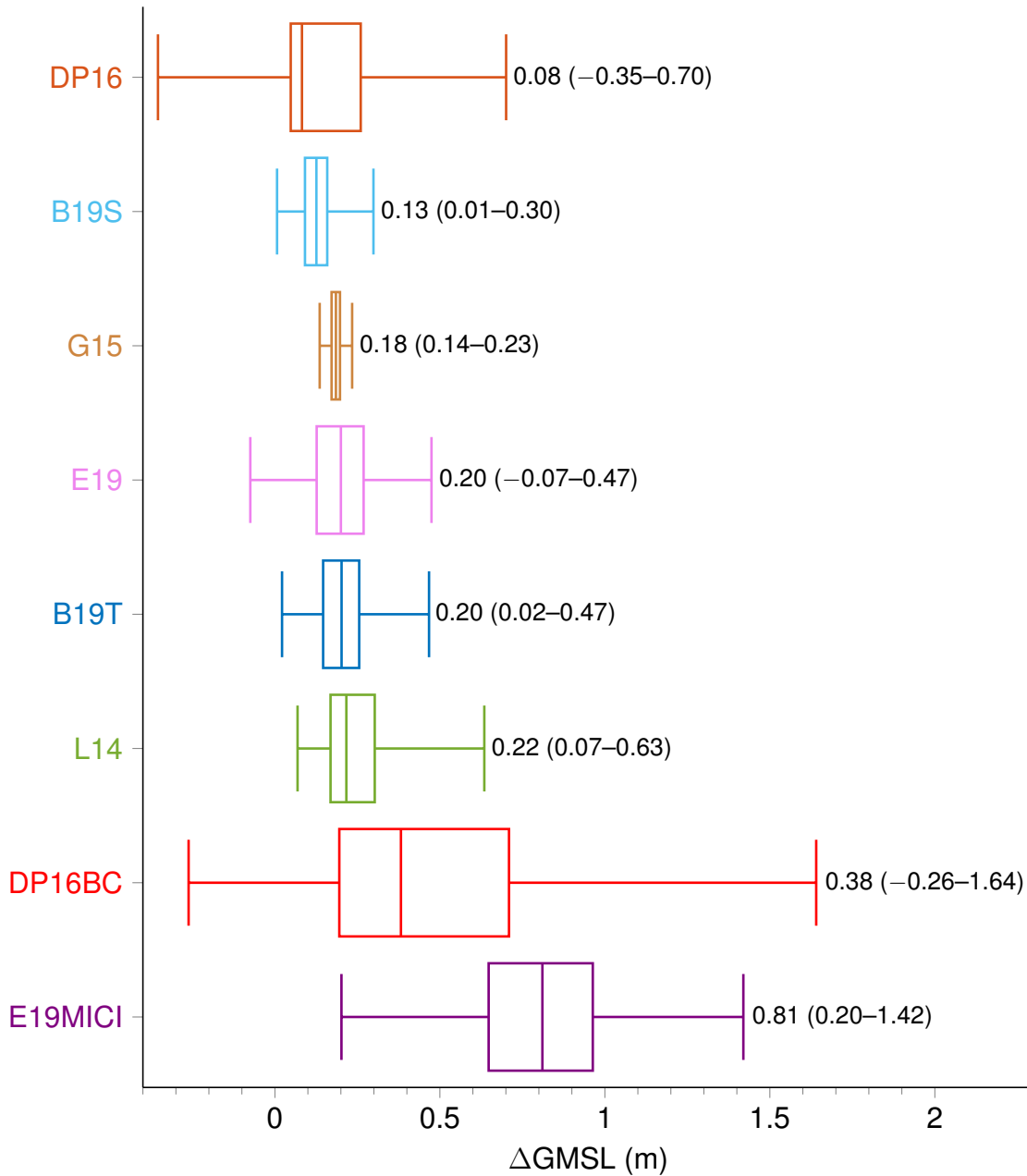


Figure 9.10: Projections of AIS contribution to sea-level rise at 2300 in RCP 2.6. Boxes and whiskers show the 5th, 33th, 50th, 66th, and 95th percentiles. For comparison, projections of the AIS contribution to sea-level rise at 2300 in AR5 give a contribution of  $-0.03$  m.

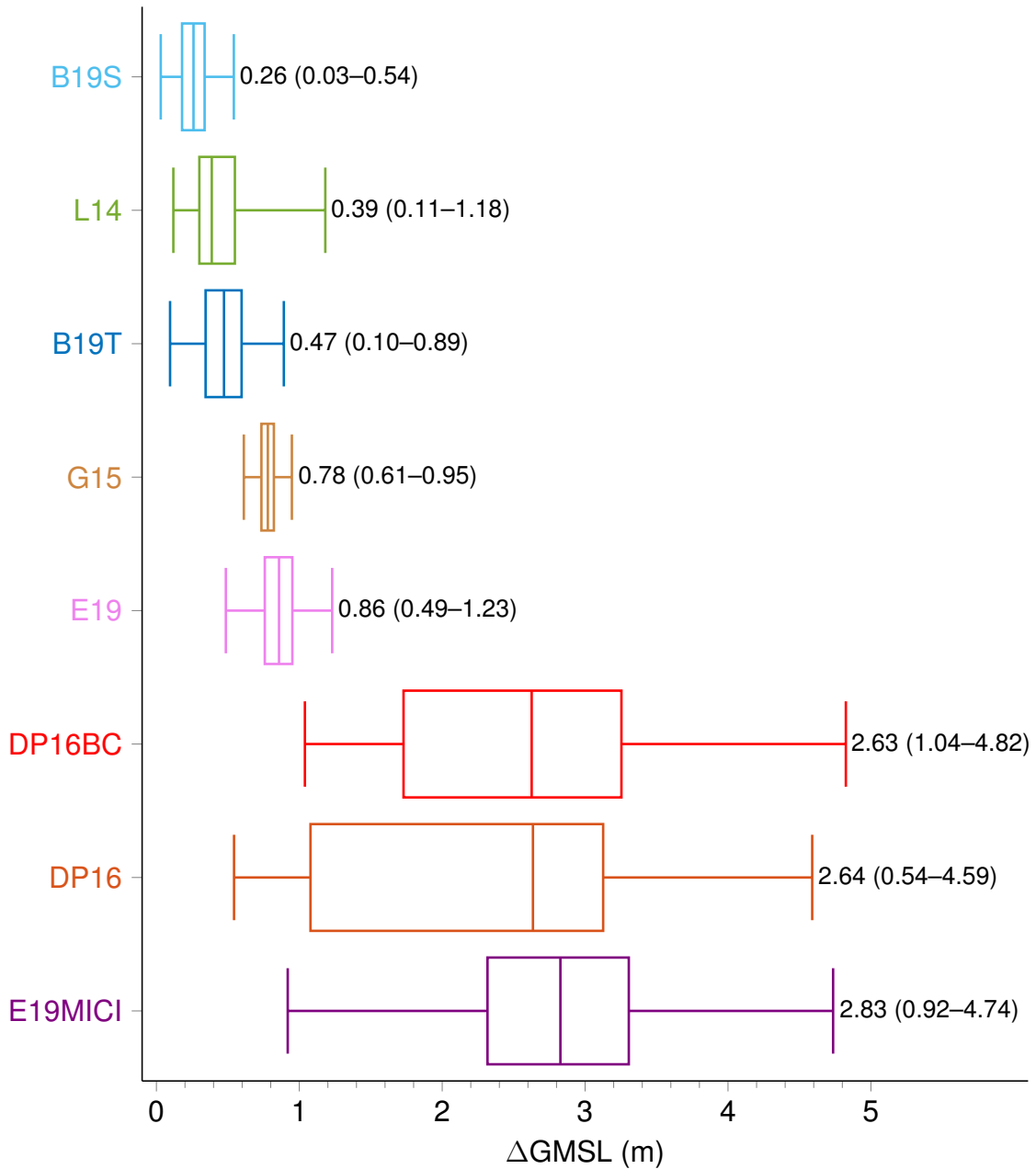


Figure 9.11: Projections of AIS contribution to sea-level rise at 2300 in RCP 4.5. Boxes and whiskers show the 5th, 33th, 50th, 66th, and 95th percentiles. For comparison, projections of the AIS contribution to sea-level rise at 2300 in AR5 range from  $-0.25$  m to  $-0.03$  m.

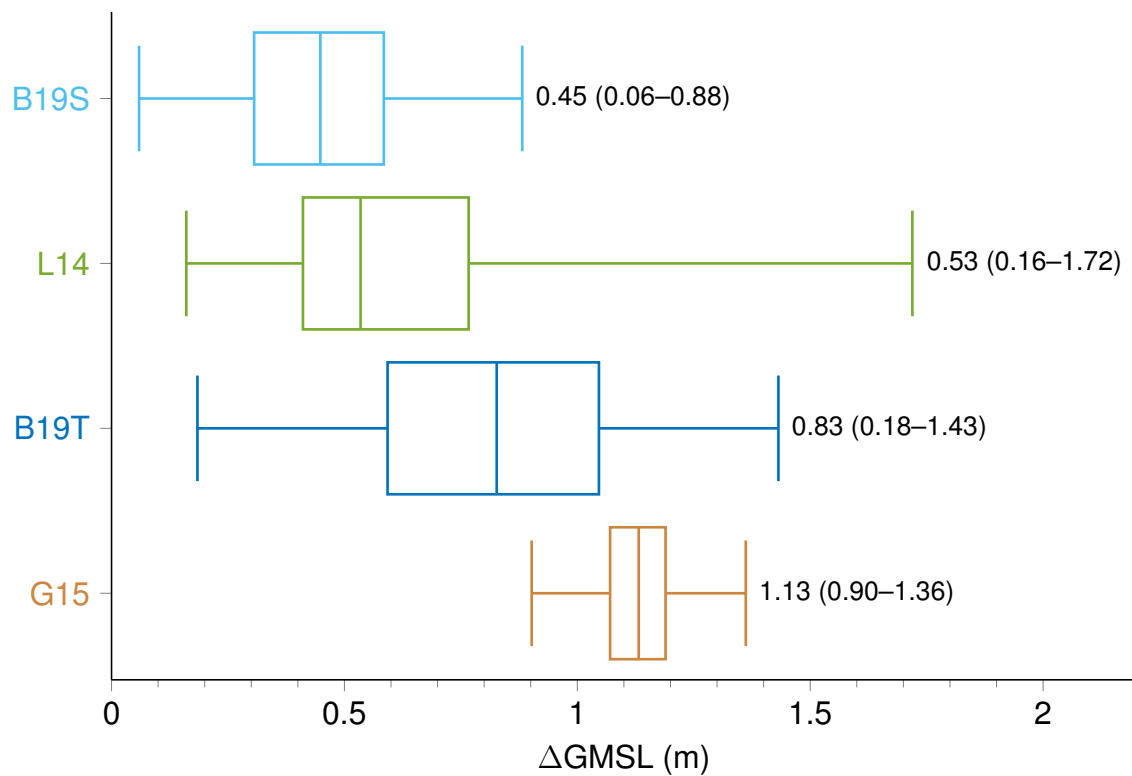


Figure 9.12: Projections of AIS contribution to sea-level rise at 2300 in RCP 6.0. Boxes and whiskers show the 5th, 33th, 50th, 66th, and 95th percentiles.

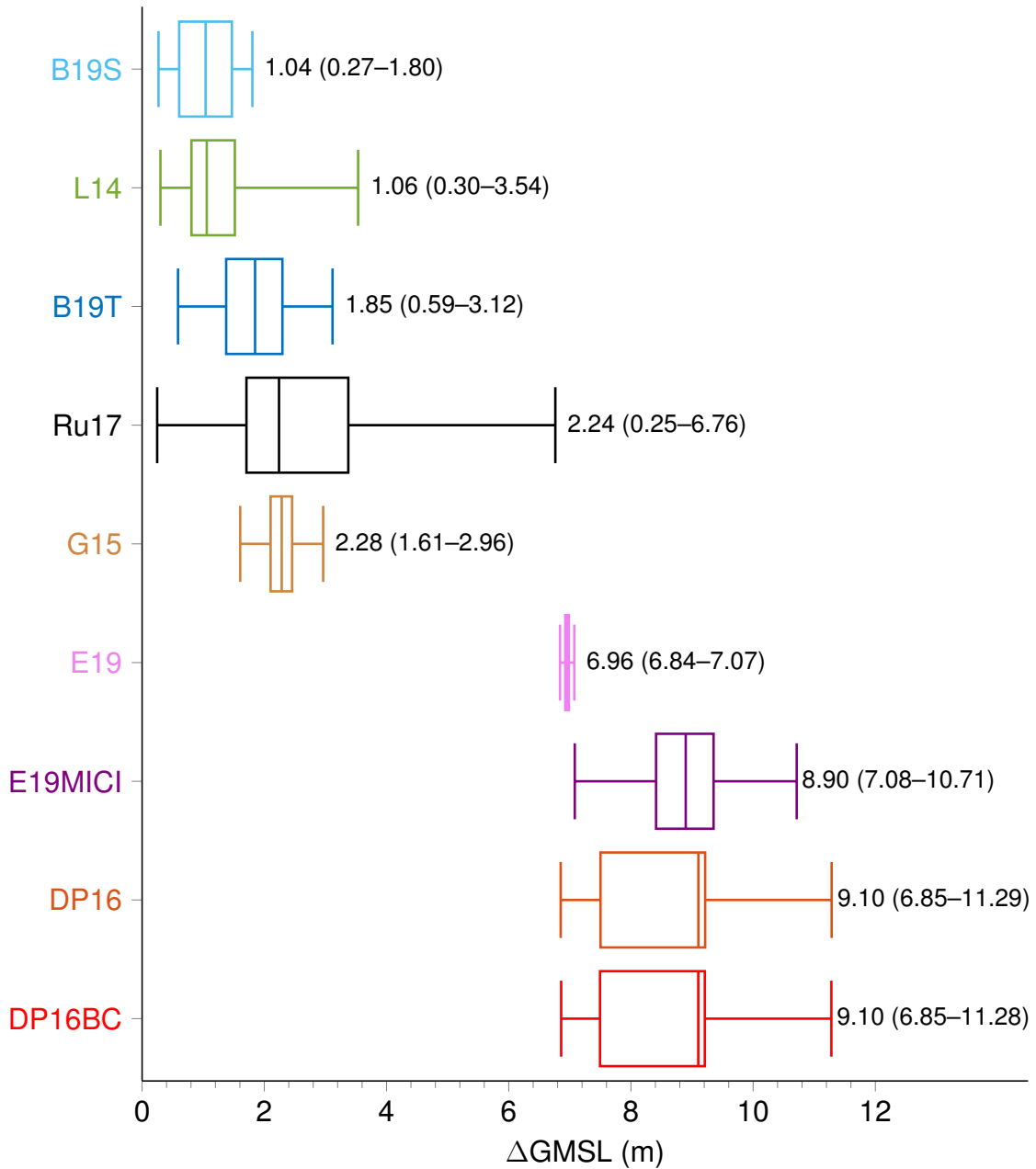


Figure 9.13: Projections of AIS contribution to sea-level rise at 2300 in RCP 8.5. Boxes and whiskers show the 5th, 33th, 50th, 66th, and 95th percentiles. For comparison, projections of the AIS contribution to sea-level rise at 2300 in AR5 range from 0.02 m to 0.19 m.



## **Part III**

# **Conclusion and directions for future work**



# 10

## Conclusion and directions for future work

*“In order to make progress, one must leave the door to the unknown ajar”*

– Richard P. Feynman

### 10.1 Summary and general conclusions

In this dissertation, we contributed to clarifying the role played by uncertainties in the continental response of the Antarctic ice sheet to climate change on multicentennial-to-millennial timescales. On the one hand, we proposed and applied theory and methods from the field of uncertainty quantification to predict with quantified uncertainty the evolution of the Antarctic ice sheet over the next millennium. On the other hand, we contributed to new methods for uncertainty quantification of complex physics-based computational models with a high computational cost. In the following, we summarise and outline the main conclusions and findings of this thesis and we provide directions for future research in the next section.

In Part I (Chapters 2–3) of the thesis, we provided an introduction to the physics of ice sheets and discussed the present state and future state of the Antarctic ice sheet as well as challenges in predicting the future response of the Antarctic ice sheet to climate change. In Chapter 2, we focused the discussion on essential (or fundamental) physical processes controlling the ice-sheet dynamics, including the ice-sheet thermodynamics, the ice-sheet mass balance, glacial isostatic adjustment, basal friction, and the migration of the grounding line. Such essential processes can be modelled mathematically with reduced-order models that take advantage of the small aspect ratio of ice sheets. These reduced-order models lend themselves well to being numerically implemented into efficient large-scale computational models of the Antarctic ice sheet and to being used for uncertainty quantification. A key aspect in the physics of ice sheets is the potential for instability mechanisms, most notably the marine ice-sheet and ice-cliff instabilities, which may trigger collapse of marine sectors in response mostly to ocean and atmospheric forcings. As discussed in Chapter 3, these instability mechanisms are expected to govern the response of the Antarctic ice sheet to climate change, with interactions between the ice sheet and other components of the Earth system expected to play a significant role in providing stabilising or destabilising conditions.

In Part II (Chapters 4–5) of the thesis, we reviewed and developed theory and methods from the field of uncertainty quantification to predict with quantified uncertainty the response of physics-based computational models. Motivated by predicting with quantified uncertainty the AIS contribution to sea-level rise and assessing the impact of parametric uncertainties on this contribution, we reviewed in Chapter 4 nonintrusive methods for the propagation of uncertainty and sensitivity analysis when the quantity of interest is a random variable or vector. Motivated by predicting with quantified uncertainty the retreat of the Antarctic ice sheet, we proposed in Chapter 5 a multifidelity quantile-based method for the estimation of confidence sets for random excursion sets. Within the probabilistic context of the random set theory, we developed the concept of confidence sets that either contain or are contained within an excursion set of the spatial response with a specified probability level. We showed that the identification of a confidence set in a parametric family of candidate sets can be recast as an equivalent problem of quantile estimation of a random variable. Then, we proposed a computationally efficient bifidelity method that exploits a polynomial chaos expansion of the random field or the random variable further away from the quantile to be estimated while the computational model is used closer to the quantile to be estimated. We found this method to be computationally efficient as compared to Monte Carlo reference, while avoiding approximation errors induced by surrogate models. Finally, we also contributed as an additional piece of research to the use of a probabilistic learning method for the estimation of Sobol indices for small datasets, which may provide an interesting alternative to surrogate models when the dataset encapsulates information that the probabilistic learning method can exploit.

Part III (Chapters 6–9) of the thesis was concerned with uncertainty quantification and large-scale and long-term simulations of the Antarctic ice sheet. In Chapter 6, we discussed essential ice-sheet models that are amenable to multicentennial and large-scale simulations and uncertainty quantification with a focus on the f.ETISh ice-sheet model. In Chapter 7, we illustrated and demonstrated the performance of existing and newly developed uncertainty quantification methods on model problems relevant to ice-sheet modelling. We showed that existing UQ methods based on surrogate models can provide an efficient alternative to computational ice-sheet models in providing probabilistic sea-level rise projections as long as the surrogate models are sufficiently accurate and do not tend to overfit the data. We also recommended the use of experimental designs with enough samples to avoid stochastic variations due to the choice of the experimental design. We showed how the concept of confidence sets for random excursion sets developed in Chapter 5 can help predict with quantified uncertainty the retreat of the Antarctic ice sheet. We demonstrated the efficiency of the multifidelity quantile-based method developed in Chapter 5 in estimating confidence sets of the grounded portion of the Antarctic ice sheet when compared with Monte Carlo. We proposed to use confidence sets of the grounded portion of the Antarctic ice sheet to build a visual representation of the uncertainty in the retreat of the Antarctic ice sheet by means of risk assessment maps. Finally, as part of our additional contribution to the computation of Sobol indices in small-data settings, we showed that the recently introduced PLoM algorithm applied to the estimation of sensitivity indices was able to attain converged estimates based on only a small data set of only a few hundred samples, while a usual Monte Carlo method would have required a data set of several thousands of samples.

In Chapter 8, we predicted with quantified uncertainty the multicentennial response of the Antarctic ice sheet to climate change. We investigated the impact of various sources of uncer-

tainty, namely uncertainty in atmospheric forcing, basal sliding, grounding-line flux parameterisation, calving, sub-shelf melting, ice-shelf rheology and bedrock relaxation, on the projections. A key finding of this study is that, in the strongly mitigated RCP 2.6 scenario, the AIS contribution to sea-level rise and the retreat of the Antarctic ice sheet remain limited over the next millenium. By contrast, in the warm RCP 8.5 scenario, the AIS contribution to sea-level rise exceeds several metres over the next millenium and the West Antarctic ice sheet undergoes an irreversible retreat. For both scenarios, we found these conclusions to be robust with respect to the uncertainty in the computational ice-sheet model. These results suggest that the threshold for instability of the West Antarctic ice sheet is associated with atmospheric forcings similar to RCP 4.5 and RCP 6.0. However, we found that the occurrence of MISI for the RCP 4.5 and RCP 6.0 scenarios was sensitive to parametric uncertainty, thus precluding a robust identification of the threshold for instability. Regarding the impact of the different sources of uncertainty, we found that the contribution of the uncertainty in sub-shelf melting to the uncertainty in the projections becomes more and more the dominant source of uncertainty as the scenario gets warmer. However, for the strongly mitigated RCP 2.6 scenario, we found that the contribution of the uncertainty in the ice-shelf rheology and the calving to the uncertainty in the projections was more important than the contribution of the uncertainty in sub-shelf melting.

Finally, in Chapter 9, we provided a multi-model comparison of sea-level projections over the period 2000–2300 as a means of assessing structural uncertainties in ice-sheet models. We found that all models agree on a limited contribution of the Antarctic ice sheet to sea level before 2050 for all RCP scenarios. Beyond 2050, sea-level rise projections show discrepancy between computational ice-sheet models with MICI and without MICI. By 2100, only projections that include MICI are able to produce an AIS contribution to sea level over 1 metre. Projections beyond 2100 are much more uncertain but we found that almost all models agree on a limited median contribution (<0.5 m) by 2300 in RCP 2.6 while substantial mass loss from the Antarctic ice sheet in the next centuries is expected to be triggered with high certainty for the RCP 8.5 scenario. We showed that our projections generally agree with other projections without MICI even though they can be considered as low-end estimates due to weak ocean forcing.

## 10.2 Directions for future research

### 10.2.1 Directions in ice-sheet modelling

In this dissertation, we discussed and applied methods from uncertainty quantification in the context of essential ice-sheet models. We identified limitations in using such models as well as research areas to focus on in order to reduce uncertainties in ice-sheet models and provide more robust projections. We discuss some of them in the following.

Another source of uncertainty in computational ice-sheet models beyond parametric uncertainties stems from the initialisation procedure. Intercomparison projects [Goelzer et al., 2018; Seroussi et al., 2019] have shown large discrepancies in projections between computational models initialised with different methods, with the impact of the initialisation procedure that might be significant for short-term horizons and low-forcing scenarios. For this reason, new improvements in ice-sheet modelling should be directed towards improving initialisation schemes as well as taking into account uncertainties in initialisation schemes. New opportunities for

improved initialisation schemes include data assimilation of time series [Larour et al., 2014], ensemble Kalman filters [Bonan et al., 2014, 2017], and Bayesian inference [Petra et al., 2014; Isaac et al., 2015; Gopalan et al., 2018; Conrad et al., 2018].

Given the significant impact of atmospheric and oceanic forcings and their uncertainties on the dynamics of the Antarctic ice sheet, opportunities in ice-sheet modelling lie in improving ice-sheet coupling with the climate system. From a physical point of view, attention should be directed towards the understanding of key processes that control the variability of the ice-ocean-atmosphere system and the interactions between the components at regional scales and the links with larger spatial scales. In particular, improved representation of the links between atmospheric warming and changes in ocean temperature and circulation and subsequent changes in sub-shelf melting is critical to understand and predict the response of marine basins to climate change. These needs have motivated recent initiatives in ice-sheet modelling such as the ISMIP6 Intercomparison Project [Nowicki et al., 2016], the MISOMIP intercomparison project [Asay-Davis et al., 2016], the cryosphere-ocean project in the E3SM Exascale Earth System Model <sup>1</sup>, and the PARAMOUR project <sup>2</sup>.

As shown in Section 8.3.4, a significant part of the uncertainty in future sea-level rise projections can also be attributed to processes such as calving and ice-shelf rheology, especially for low-forcing scenarios. Thus, additional opportunities in ice-sheet modelling also lie in improved modelling of these processes.

Given the significant role played by the grounding-line dynamics in controlling the response of marine basins to climate change, opportunities in ice-sheet modelling lie in gaining new understanding of the impact of grounding-line flux parameterisations in computational ice-sheet models as well in developing new methods to capture the dynamics of the grounding line more accurately, including methods that allow to account for the bedrock topography more effectively. In parallel, attention should be directed towards the understanding of basal friction at the ice-bedrock interface (choice of the friction law) and the representation of basal friction in computational ice-sheet models. New methods for improved numerical modelling of grounding-line dynamics and basal friction can be built on methods for frictional contact problems in applied mathematics and computational mechanics.

## 10.2.2 Directions in uncertainty quantification

Providing robust projections of the response of the Antarctic ice sheet in the presence of uncertainty requires appropriate probabilistic characterisations of the sources of uncertainty. In this thesis, we focused our attention on the probabilistic characterisation of the quantity of interest while assuming simple probabilistic characterisations of the sources of uncertainty. Further work could be directed towards using physical constraints to constrain the model parameters. New research opportunities could include Bayesian inference using paleoconstraints. Furthermore, we limited this work to investigating a rather limited subset of sources of uncertainty, usually in the form of model parameters constant over the whole ice sheet. However, most pa-

<sup>1</sup><https://e3sm.org/> (last accessed: 7 December 2019)

<sup>2</sup><http://www.climate.be/php/users/klein/PARAMOUR/index.html> (last accessed: 7 December 2019)

parameters or input quantities in a computational ice-sheet model are ideally described as spatially-varying and usually non-homogeneous fields. This raises new issues about the identification of such spatially non-homogeneous fields and uncertainty quantification in high dimension.

In this thesis, we only considered methods based on surrogate models (and to a lesser extent probabilistic learning) as a means to alleviate the computational cost of Monte Carlo methods. Uncertainty quantification provides other methods that might be of interest even when dealing with high-fidelity computational ice-sheet models, for instance, multilevel Monte Carlo [Cliffe et al., 2011; Giles, 2015], multifidelity methods [Peherstorfer et al., 2018], ensemble propagation [Phipps et al., 2017], methods from machine learning. Advanced methods for high-performance computing could also help reduce the computational cost of ice-sheet models.

In Chapter 9, we discussed qualitatively the impact of structural uncertainties in ice-sheet models through a multi-model comparison. As new projections with quantified uncertainty are becoming available, interest should be directed towards providing quantitative multi-model projections of the AIS contribution to sea-level rise. Directions for future research may include methods for model selection and multi-model inference [Burnham and Anderson, 2002; Link and Barker, 2006], methods to quantify structural uncertainty [Strong and Oakley, 2014], and weighted multi-model projections [Knutti et al., 2017].

Finally, future work may also consider the impact of uncertainty and stochastic perturbations on steady states, instabilities, and bifurcations of the Antarctic sheet. This work may build on the theory of nonlinear dynamical systems, which provides a proper mathematical setting for looking at nonlinear structure of system dynamics, and the theory of random dynamical systems; see, for instance, Arnold [1998]. To date only limited studies have been dedicated to investigating the impact of stochastic perturbations on ice-sheet dynamics [Mantelli et al., 2016; Mulder et al., 2018], and significant work remains in applying these methods to realistic ice-sheet models.



**Part IV**  
**Appendices**



## Elements of probability theory

Most of the theory and methods presented and elaborated in this manuscript are based on the theory of probability. In the following, we provide an overview of fundamental elements of the theory of probability, which may help the reader to understand more technical aspects of the manuscript. We refer the reader, for instance, to [Billingsley \[2012\]](#) for a textbook about the foundations of the theory of probability and to [Grigoriu \[2002\]](#) and [Ang and Tang \[2007\]](#) for textbooks about probability concepts in science and engineering.

### A.1 Probability space

A probability space is defined in the following way. First, let  $\Theta$  be the set of all possible outcomes of a random experiment. The set  $\Theta$  is referred to as the sample space and an element of  $\Theta$  is denoted by  $\theta$ . Second, let  $\mathfrak{B}$  denote a  $\sigma$ -algebra on  $\Theta$ , that is,

1.  $\emptyset \in \mathfrak{B}$ ;
2.  $B \in \mathfrak{B} \Rightarrow B^c \in \mathfrak{B}$ ;
3.  $B_1, B_2, \dots \in \mathfrak{B} \Rightarrow \cup_i B_i \in \mathfrak{B}$ .

An element  $B$  in  $\mathfrak{B}$  is called an event. Third, let  $\mathbb{P}$  denote a probability measure on  $(\Theta, \mathfrak{B})$ , that is,  $\mathbb{P}$  is a set function from  $\mathfrak{B}$  into  $[0, 1]$  that satisfies the postulates

1.  $\mathbb{P}(\emptyset) = 0$ ;
2.  $\mathbb{P}(\Theta) = 1$ ;
3.  $B_1, B_2, \dots \in \mathfrak{B}, B_i \cap B_{j \neq i} = \emptyset \Rightarrow \mathbb{P}(\cup_i B_i) = \sum_i \mathbb{P}(B_i)$ .

The triplet  $(\Theta, \mathfrak{B}, \mathbb{P})$  is called a probability space. The probability space is said to be complete if for all  $B$  in  $\mathfrak{B}$  with  $\mathbb{P}(B) = 0$  and for all  $A \subset B$ , one has that  $A$  is in  $\mathfrak{B}$ .

In a probability space, the following properties are satisfied for all  $A$  and  $B$  in  $\mathfrak{B}$ :

$$\mathbb{P}(B) = 1 - \mathbb{P}(B^c), \tag{A.1}$$

$$A \subset B \Rightarrow \mathbb{P}(A) \leq \mathbb{P}(B), \tag{A.2}$$

$$\mathbb{P}(A \cup B) = \mathbb{P}(A) + \mathbb{P}(B) - \mathbb{P}(A \cap B). \tag{A.3}$$

### A.1.1 Conditional probability

Given a probability space  $(\Theta, \mathfrak{B}, \mathbb{P})$ , a new measure of probability can be defined on  $(\Theta, \mathfrak{B})$  assuming that an event  $B$  in  $\mathfrak{B}$  has occurred. This probability measure, denoted by  $\mathbb{P}(\cdot|B)$ , is called the conditional probability on  $B$ . Assuming that  $\mathbb{P}(B) > 0$ , the conditional probability of  $A$  in  $\mathfrak{B}$  given  $B$  is given by

$$\mathbb{P}(A|B) = \frac{\mathbb{P}(A \cap B)}{\mathbb{P}(B)}. \quad (\text{A.4})$$

If  $\mathbb{P}(A|B) = \mathbb{P}(A)$ , then the events  $A$  and  $B$  are said to be (statistically) independent and  $\mathbb{P}(A \cap B)$  can be factorised as  $\mathbb{P}(A) \times \mathbb{P}(B)$ .

## A.2 Random variable

An  $\mathbb{R}$ -valued random variable  $X$  defined on the probability space  $(\Theta, \mathfrak{B}, \mathbb{P})$  is a measurable mapping  $\theta \mapsto X(\theta)$  from  $(\Theta, \mathfrak{B}, \mathbb{P})$  into  $(\mathbb{R}, \mathfrak{D})$ , with  $\mathfrak{D}$  the  $\sigma$ -algebra endowed on  $\mathbb{R}$ , which means that

$$\forall D \in \mathfrak{D}, X^{-1}(D) \in \mathfrak{B}, \quad (\text{A.5})$$

with  $X^{-1}(D) = \{\theta \in \Theta : X(\theta) \in D\}$ .

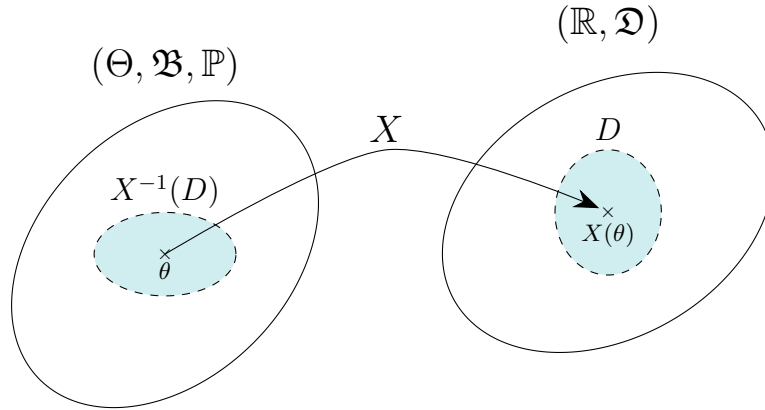


Figure A.1: Schematic representation of an  $\mathbb{R}$ -valued random variable  $X$  from  $(\Theta, \mathfrak{B})$  into  $(\mathbb{R}, \mathfrak{D})$ .

For any  $\theta$  fixed in  $\Theta$ ,  $X(\theta)$  is a deterministic  $\mathbb{R}$ -valued scalar called a realisation of the random variable. The probability distribution  $\mathbb{P}_X$  of  $X$  on  $\mathbb{R}$  is the probability measure,  $D \mapsto \mathbb{P}_X(D) = \mathbb{P}(X^{-1}(D))$  from  $\mathfrak{D}$  into  $[0, 1]$  such that

$$0 \leq \mathbb{P}_X(D) = \int_D \mathbb{P}_X(dx) = \int_{X^{-1}(D)} \mathbb{P}(d\theta) \leq 1, \quad (\text{A.6})$$

$$\mathbb{P}_X(\mathbb{R}) = \int_{\mathbb{R}} \mathbb{P}_X(dx) = \int_{\Theta} \mathbb{P}(d\theta) = 1. \quad (\text{A.7})$$

The cumulative distribution function of  $X$  is the function  $x \mapsto F_X(x)$  with values in  $[0, 1]$  such that

$$F_X(x) = \mathbb{P}(X \leq x) = \mathbb{P}_X(X \leq x) = \int_{-\infty}^x \mathbb{P}_X(dx). \quad (\text{A.8})$$

If  $F_X$  is absolutely continuous in  $\mathbb{R}$ ,  $X$  is said to be a continuous random variable and admits a probability density function  $\rho_X$ , that is, a function from  $\mathbb{R}$  into  $\mathbb{R}^+ = [0, \infty[$ , such that

$$\mathbb{P}_X(D) = \int_D \rho_X(x) dx, \quad (\text{A.9})$$

for any meaningful subset  $D$  of  $\mathbb{R}$ . If the cumulative distribution function  $F_X$  is differentiable on  $\mathbb{R}$ , then

$$\rho_X = \frac{dF_X}{dx}. \quad (\text{A.10})$$

If  $X$  takes only a finite or countable number of values in  $\mathbb{R}$ ,  $X$  is said to be a discrete random variable and admits a probability mass function  $p_X$ , that is, a function from  $\mathbb{R}$  into  $\mathbb{R}^+ = [0, \infty[$ , such that

$$p_X(x) = \mathbb{P}_X(X = x). \quad (\text{A.11})$$

A random variable  $X$  is a  $q$ -order random variable, with  $1 \leq q < \infty$ , if

$$\int_{\Theta} |X(\theta)|^q \mathbb{P}(d\theta) = \int_{\mathbb{R}} |x|^q \mathbb{P}_X(dx) < \infty, \quad (\text{A.12})$$

that is,  $X$  is  $\mathbb{P}_X$ - $q$ -integrable on  $\mathbb{R}$ . For any  $\mathbb{P}_X$ -integrable random variable  $X$  on  $\mathbb{R}$ , the linear operator

$$\mathbb{E}[X] = \int_{\Theta} X(\theta) \mathbb{P}(d\theta) = \int_{\mathbb{R}} x \mathbb{P}_X(dx) \equiv m_X, \quad (\text{A.13})$$

is called the mathematical expectation or simply the mean value of  $X$ . For any  $\mathbb{P}_X$ -square-integrable random variable  $X$  on  $\mathbb{R}$ , the operator

$$\mathbb{V}[X] = \int_{\Theta} (X(\theta) - m_X)^2 \mathbb{P}(d\theta) = \int_{\mathbb{R}} (x - m_X)^2 \mathbb{P}_X(dx) = \mathbb{E}[X^2] - m_X^2 \equiv \sigma_X^2, \quad (\text{A.14})$$

is called the variance of  $X$  and  $\sigma_X$  is its standard deviation. Please note that other statistical descriptors of  $X$  can be deduced from its probability distribution  $\mathbb{P}_X$ , for instance, quantiles, which will be handled in Chapter 5.

### A.3 Random vector

Similarly to an  $\mathbb{R}$ -valued random variable, an  $\mathbb{R}^n$ -valued random vector  $\mathbf{X}$  defined on the probability space  $(\Theta, \mathfrak{B}, \mathbb{P})$  is a measurable mapping  $\theta \mapsto \mathbf{X}(\theta)$  from  $(\Theta, \mathfrak{B}, \mathbb{P})$  into  $(\mathbb{R}^n, \mathfrak{D})$ , with  $\mathfrak{D}$  being here the  $\sigma$ -algebra endowed on  $\mathbb{R}^n$ . The cumulative distribution function of  $\mathbf{X}$  is the function  $\mathbf{x} \mapsto F_{\mathbf{X}}(\mathbf{x})$  with values in  $[0, 1]$  such that

$$F_{\mathbf{X}}(\mathbf{x}) = \mathbb{P}(\mathbf{X} \leq \mathbf{x}) = \int_{\mathbf{x}' \in D_{\mathbf{x}}} \mathbb{P}_{\mathbf{X}}(d\mathbf{x}'), \quad (\text{A.15})$$

with  $D_{\mathbf{x}} = ]-\infty, x_1] \times \dots \times ]-\infty, x_n]$  and  $\mathbb{P}_{\mathbf{X}}$  the probability distribution of  $\mathbf{X}$  on  $\mathbb{R}^n$ . A continuous random vector admits a probability density function  $\rho_{\mathbf{X}}$  such that  $\mathbb{P}_{\mathbf{X}}(D) = \int_D \rho_{\mathbf{X}}(\mathbf{x}) d\mathbf{x}$  for any meaningful  $D$  in  $\mathbb{R}^n$  and its probability density function writes as  $\rho_{\mathbf{X}} =$

$\frac{\partial F_{\mathbf{X}}}{\partial \mathbf{x}}$  if  $F_{\mathbf{X}}$  is differentiable on  $\mathbb{R}^n$ . The marginal probability distribution  $\mathbb{P}_{X_i}$ ,  $1 \leq i \leq n$ , of the random variable  $X_i$  with values in  $\mathbb{R}$  satisfies

$$\mathbb{P}_{X_i}(D_i) = \int_{x_1 \in \mathbb{R}} \cdots \int_{x_i \in D_i} \cdots \int_{x_n \in \mathbb{R}} \mathbb{P}_{\mathbf{X}}(dx_1, \dots, dx_n), \quad (\text{A.16})$$

for any meaningful  $D_i$  in  $\mathbb{R}$ . If the random variables  $X_1, \dots, X_n$  are independent, then the probability  $\mathbb{P}_{\mathbf{X}}$  writes as a product of the marginal probability distributions.

For any  $\mathbb{P}_{\mathbf{X}}$ -integrable random vector  $\mathbf{X}$  on  $\mathbb{R}$ , the mathematical expectation of  $\mathbf{X}$  is defined as

$$\mathbb{E}[\mathbf{X}] = \int_{\mathbb{R}^n} \mathbf{x} \mathbb{P}_{\mathbf{X}}(d\mathbf{x}) \equiv \mathbf{m}_{\mathbf{X}}, \quad (\text{A.17})$$

and for any  $\mathbb{P}_{\mathbf{X}}$ -square-integrable random variable  $X$  on  $\mathbb{R}$ , the covariance matrix  $[C_{\mathbf{X}}]$  is the real symmetric positive-semidefinite matrix

$$[C_{\mathbf{X}}] = \mathbb{E}[\mathbf{X}\mathbf{X}^T] = \int_{\mathbb{R}^n} (\mathbf{x} - \mathbf{m}_{\mathbf{X}})(\mathbf{x} - \mathbf{m}_{\mathbf{X}})^T \mathbb{P}_{\mathbf{X}}(d\mathbf{x}). \quad (\text{A.18})$$

### A.3.1 Gaussian random vector

**Definition A.1.** An  $\mathbb{R}^n$ -valued random vector  $\mathbf{Z}$  is a multivariate Gaussian vector with mean  $\boldsymbol{\mu}$  and covariance matrix  $[\Sigma]$  if every linear combination  $\mathbf{a}^T \mathbf{Z}$ ,  $\mathbf{a} \in \mathbb{R}^n$ , follows a Gaussian probability distribution  $\mathcal{N}(\mathbf{a}^T \boldsymbol{\mu}, \mathbf{a}^T [\Sigma] \mathbf{a})$ . The multivariate Gaussian probability distribution with mean  $\boldsymbol{\mu}$  and covariance matrix  $[\Sigma]$  is denoted by  $\mathcal{N}(\boldsymbol{\mu}, [\Sigma])$ .

## A.4 Random field

A random field is a generalisation of a random vector by allowing the random vector to be of infinite dimension. Let  $D$  be a subset of  $\mathbb{R}^d$ , with  $d \geq 1$ . It is assumed that  $D$  is an uncountable set. A (real-valued) random field  $\{X(\mathbf{s}), \mathbf{s} \in D\}$  defined on the probability space  $(\Theta, \mathfrak{B}, \mathbb{P})$  is a collection of random variables, indexed by  $D$ , with values in  $\mathbb{R}$ . Then for any fixed  $\mathbf{s}$  in  $D$ ,  $X(\mathbf{s})$  is a random variable from  $(\Theta, \mathfrak{B})$  into  $(\mathbb{R}, \mathfrak{D})$ . For any fixed  $\theta$  in  $\Theta$ , the mapping  $\mathbf{s} \mapsto X(\mathbf{s}, \theta)$  is called a realisation or a trajectory of the random field. For any finite subset  $\{\mathbf{s}_1, \dots, \mathbf{s}_t\}$  of  $D$ , the probability distribution of the random vector  $(X(\mathbf{s}_1), \dots, X(\mathbf{s}_t))$  defines the marginal probability distribution of the random field related to the finite subset  $\{\mathbf{s}_1, \dots, \mathbf{s}_t\}$ . The distribution of the random field is characterised by all the finite marginal probability distributions obtained for all finite subsets of  $D$ .

For any  $\mathbb{P}_{\mathbf{X}}$ -integrable random field  $\{X(\mathbf{s}), \mathbf{s} \in D\}$ , the mean function is the mapping

$$\mathbf{x} \mapsto m_{\mathbf{X}}(\mathbf{s}) = \mathbb{E}[X(\mathbf{s})] \quad (\text{A.19})$$

from  $D$  into  $\mathbb{R}$ , and for any  $\mathbb{P}_{\mathbf{X}}$ -square-integrable random field  $\{X(\mathbf{s}), \mathbf{s} \in D\}$ , the covariance function is the mapping

$$(\mathbf{s}, \mathbf{s}') \mapsto C_{\mathbf{X}}(\mathbf{s}, \mathbf{s}') = \mathbb{E}[(X(\mathbf{s}) - \mathbb{E}[X(\mathbf{s})])(X(\mathbf{s}') - \mathbb{E}[X(\mathbf{s}')])] \quad (\text{A.20})$$

from  $D \times D$  into  $\mathbb{R}$ . If  $m_{\mathbf{X}}(\mathbf{s})$  is a constant in  $\mathbb{R}$  and  $C_{\mathbf{X}}(\mathbf{s}, \mathbf{s}')$  only depends on the difference between  $\mathbf{s}$  and  $\mathbf{s}'$ , then the random field is said to be mean-square stationary.

### A.4.1 Gaussian process

**Definition A.2.** A Gaussian process is a random field  $\{Z(\mathbf{s}), \mathbf{s} \in D\}$ ,  $D \subset \mathbb{R}^d$ , such that all finite-dimensional random vector  $\mathbf{Z} = (Z(\mathbf{s}_1), \dots, Z(\mathbf{s}_n))$  is an  $\mathbb{R}^n$ -valued Gaussian random vector. The Gaussian process with mean function  $\mu(\mathbf{s}) = \mathbb{E}[Z(\mathbf{s})]$  and covariance function  $C(\mathbf{s}, \mathbf{s}') = \mathbb{E}[(Z(\mathbf{s}) - \mathbb{E}[Z(\mathbf{s})])(Z(\mathbf{s}') - \mathbb{E}[Z(\mathbf{s}')])]$  is denoted by  $\text{GP}(\mu(\mathbf{s}), C(\mathbf{s}, \mathbf{s}'))$ .

A Gaussian process is completely characterised by its mean function and its covariance function, also called the kernel of the Gaussian process and usually denoted by  $k(\mathbf{s}, \mathbf{s}')$ .



# Bibliography

- Abramowitz, M. and Stegun, I. A. (1970). *Handbook of Mathematical Functions: with Formulas, Graphs, and Mathematical Tables*. New York, NY: Dover Publications, 9th edition.
- Adams, C. M., Hernandez, E., and Cato, J. C. (2004). The economic significance of the Gulf of Mexico related to population, income, employment, minerals, fisheries and shipping. *Ocean Coast. Manage.*, 47(11–12), 565–580, <https://doi.org/10.1016/j.ocecoaman.2004.12.002>.
- Adhikari, S., Ivins, E. R., Larour, E., Seroussi, H., Morlighem, M., and Nowicki, S. (2014). Future Antarctic bed topography and its implications for ice sheet dynamics. *Solid Earth*, 5(1), 569–584, <https://doi.org/10.5194/se-5-569-2014>.
- Adler, R. J. (2008). Some new random field tools for spatial analysis. *Stoch. Environ. Res. Risk Assess.*, 22(6), 809–822, <https://doi.org/10.1007/s00477-008-0242-6>.
- Adler, R. J. and Taylor, J. E. (2007). *Random Fields and Geometry*. New York, NY: Springer, <https://doi.org/10.1007/978-0-387-48116-6>.
- Agosta, C., Amory, C., Kittel, C., Orsi, A., Favier, V., Gallée, H., van den Broeke, M. R., Lenaerts, J. T. M., van Wessem, J. M., van de Berg, W. J., and Fettweis, X. (2019). Estimation of the Antarctic surface mass balance using the regional climate model MAR (1979–2015) and identification of dominant processes. *Cryosphere*, 13(1), 281–296, <https://doi.org/10.5194/tc-13-281-2019>.
- An, M., Wiens, D. A., Zhao, Y., Feng, M., Nyblade, A., Kanao, M., Li, Y., Maggi, A., and Lévêque, J.-J. (2015). Temperature, lithosphere-asthenosphere boundary, and heat flux beneath the Antarctic Plate inferred from seismic velocities. *J. Geophys. Res.: Solid Earth*, 120(12), 8720–8742, <https://doi.org/10.1002/2015jb011917>.
- Ang, A. H.-S. and Tang, W. H. (2007). *Probability Concepts in Engineering: Emphasis on Applications in Civil & Environmental Engineering*. Hoboken, NJ: John Wiley & Sons, 2nd edition.
- Arakawa, A. and Lamb, V. R. (1977). Computational Design of the Basic Dynamical Processes of the UCLA General Circulation Model. In *General Circulation Models of the Atmosphere*, (pp. 173–265). Academic Press, <https://doi.org/10.1016/b978-0-12-460817-7.50009-4>.

- Arnold, B. C., Balakrishnan, N., and Nagaraja, H. N. (1992). *A First Course in Order Statistics*. Philadelphia, PA: SIAM, <https://doi.org/10.1137/1.9780898719062>.
- Arnold, L. (1998). *Random Dynamical Systems*. Berlin, Germany: Springer-Verlag, <https://doi.org/10.1007/978-3-662-12878-7>.
- Arnst, M., Ghanem, R., Phipps, E., and Red-Horse, J. (2012). Measure transformation and efficient quadrature in reduced-dimensional stochastic modeling of coupled problems. *Int. J. Numer. Metho. Eng.*, 92(12), 1044–1080, <https://doi.org/10.1002/nme.4368>.
- Arnst, M. and Ponthot, J.-P. (2014). An overview of nonintrusive characterization, propagation, and sensitivity analysis of uncertainties in computational mechanics. *Int. J. Uncertain. Quantif.*, 4(5), 387–421, <https://doi.org/10.1615/int.j.uncertaintyquantification.2014006990>.
- Arnst, M., Soize, C., and Bulthuis, K. (2019). Computation of Sobol indices in global sensitivity indices from small data sets by probabilistic learning on manifolds. Under review.
- Aronszajn, N. (1950). Theory of reproducing kernels. *T. Am. Math. Soc.*, 68(3), 337–404, <https://doi.org/10.1090/s0002-9947-1950-0051437-7>.
- Arthern, R. J. and Williams, C. R. (2017). The sensitivity of West Antarctica to the submarine melting feedback. *Geophys. Res. Lett.*, 44(5), 2352–2359, <https://doi.org/10.1002/2017gl072514>.
- Asay-Davis, X. S., Cornford, S. L., Durand, G., Galton-Fenzi, B. K., Gladstone, R. M., Gudmundsson, G. H., Hattermann, T., Holland, D. M., Holland, D., Holland, P. R., Martin, D. F., Mathiot, P., Pattyn, F., and Seroussi, H. (2016). Experimental design for three interrelated marine ice sheet and ocean model intercomparison projects: MISMIP v. 3 (MISMIP +), ISOMIP v. 2 (ISOMIP +) and MISOMIP v. 1 (MISOMIP1). *Geosci. Model Dev.*, 9(7), 2471–2497, <https://doi.org/10.5194/gmd-9-2471-2016>.
- Aschwanden, A., Aðalgeirsdóttir, G., and Khroulev, C. (2013). Hindcasting to measure ice sheet model sensitivity to initial states. *Cryosphere*, 7(4), 1083–1093, <https://doi.org/10.5194/tc-7-1083-2013>.
- Aschwanden, A., Fahnestock, M. A., and Truffer, M. (2016). Complex Greenland outlet glacier flow captured. *Nat. Commun.*, 7, 10524, <https://doi.org/10.1038/ncomms10524>.
- Azzimonti, D. (2016). *Contributions to Bayesian set estimation relying on random field priors*. PhD thesis, Universität Bern, Bern, Switzerland.
- Azzimonti, D., Bect, J., Chevalier, C., and Ginsbourger, D. (2016). Quantifying Uncertainties on Excursion Sets Under a Gaussian Random Field Prior. *SIAM/ASA JUQ*, 4(1), 850–874, <https://doi.org/10.1137/141000749>.
- Bakker, A. M. R., Wong, T. E., Ruckert, K. L., and Keller, K. (2017). Sea-level projections representing the deeply uncertain contribution of the West Antarctic ice sheet. *Sci. Rep.*, 7, 3880, <https://doi.org/10.1038/s41598-017-04134-5>.
- Bamber, J. L. and Aspinall, W. P. (2013). An expert judgement assessment of future sea level rise from the ice sheets. *Nat. Clim. Change*, 3(4), 424–427, <https://doi.org/10.1038/nclimate1778>.

- Bamber, J. L., Oppenheimer, M., Kopp, R. E., Aspinall, W. P., and Cooke, R. M. (2019). Ice sheet contributions to future sea-level rise from structured expert judgment. *PNAS*, 116(23), 11195–11200, <https://doi.org/10.1073/pnas.1817205116>.
- Bamber, J. L., Westaway, R. M., Marzeion, B., and Wouters, B. (2018). The land ice contribution to sea level during the satellite era. *Environ. Res. Lett.*, 13(6), 063008, <https://doi.org/10.1088/1748-9326/aac2f0>.
- Baral, D. R., Hutter, K., and Greve, R. (2001). Asymptotic Theories of Large-Scale Motion, Temperature, and Moisture Distribution in Land-Based Polythermal Ice Sheets: A Critical Review and New Developments. *Appl. Mech. Rev.*, 54(3), 215–256, <https://doi.org/10.1115/1.3097296>.
- Barletta, V. R., Bevis, M., Smith, B. E., Wilson, T., Brown, A., Bordoni, A., Willis, M., Khan, S. A., Rovira-Navarro, M., Dalziel, I., Smalley, Jr., R., Kendrick, E., Konfal, S., Caccamise II, D. J., Aster, R. C., Nyblade, A., and Wiens, D. A. (2018). Observed rapid bedrock uplift in Amundsen Sea Embayment promotes ice-sheet stability. *Science*, 360(6395), 1335–1339, <https://doi.org/10.1126/science.aao1447>.
- Bathiany, S., Dijkstra, H., Crucifix, M., Dakos, V., Brovkin, V., Williamson, M. S., Lenton, T. M., and Scheffer, M. (2016). Beyond bifurcation: using complex models to understand and predict abrupt climate change. *Dyn. Stat. Clim. Syst.*, 1(1), dzw004, <https://doi.org/10.1093/climsys/dzw004>.
- Bayarri, M. J., Berger, J. O., Calder, E. S., Dalbey, K., Lunagomez, S., Patra, A. K., Pitman, E. B., Spiller, E. T., and Wolpert, R. L. (2009). Using Statistical and Computer Models to Quantify Volcanic Hazards. *Technometrics*, 51(4), 402–413, <https://doi.org/10.1198/tech.2009.08018>.
- Beckmann, A. and Goosse, H. (2003). A parameterization of ice shelf–ocean interaction for climate models. *Ocean Model.*, 5(2), 157–170, [https://doi.org/10.1016/s1463-5003\(02\)00019-7](https://doi.org/10.1016/s1463-5003(02)00019-7).
- Bell, R. E., Banwell, A. F., Trusel, L. D., and Kingslake, J. (2018). Antarctic surface hydrology and impacts on ice-sheet mass balance. *Nat. Clim. Change*, 8(12), 1044–1052, <https://doi.org/10.1038/s41558-018-0326-3>.
- Bell, R. E., Chu, W., Kingslake, J., Das, I., Tedesco, M., Tinto, K. J., Zappa, C. J., Frezzotti, M., Boghosian, A., and Lee, W. S. (2017). Antarctic ice shelf potentially stabilized by export of meltwater in surface river. *Nature*, 544(7650), 344–348, <https://doi.org/10.1038/nature22048>.
- Bennett, M. R. (2003). Ice streams as the arteries of an ice sheet: their mechanics, stability and significance. *Earth-Sci. Rev.*, 61(3–4), 309–339, [https://doi.org/10.1016/s0012-8252\(02\)00130-7](https://doi.org/10.1016/s0012-8252(02)00130-7).
- Berger, S., Favier, L., Drews, R., Derwael, J.-J., and Pattyn, F. (2016). The control of an uncharted pinning point on the flow of an Antarctic ice shelf. *J. Glaciol.*, 62(231), 37–45, <https://doi.org/10.1017/jog.2016.7>.

- Bernabeu, N. (2015). *Multiphysics modeling of viscoplastic flows : application to volcanic lava flows*. PhD thesis, Université Grenoble Alpes, Grenoble, France.
- Bernales, J., Rogozhina, I., Greve, R., and Thomas, M. (2017). Comparison of hybrid schemes for the combination of shallow approximations in numerical simulations of the Antarctic Ice Sheet. *Cryosphere*, 11(1), 247–265, <https://doi.org/10.5194/tc-11-247-2017>.
- Bernardo, J. M. and Smith, A. F. M. (2000). *Bayesian Theory*. Chichester, United Kingdom: John Wiley & Sons.
- Billingsley, P. (2012). *Probability and Measure*. Hoboken, NJ: John Wiley & Sons, Anniversary edition.
- Bindschadler, R. A., Nowicki, S., Abe-Ouchi, A., Aschwanden, A., Choi, H., Fastook, J., Granzow, G., Greve, R., Gutowski, G., Herzfeld, U., Jackson, C., Johnson, J., Khroulev, C., Levermann, A., Lipscomb, W. H., Martin, M. A., Morlighem, M., Parizek, B. R., Pollard, D., Price, S. F., Ren, D., Saito, F., Sato, T., Seddik, H., Seroussi, H., Takahashi, K., Walker, R., and Wang, W. L. (2013). Ice-sheet model sensitivities to environmental forcing and their use in projecting future sea level (the SeaRISE project). *J. Glaciol.*, 59(214), 195–224, <https://doi.org/10.3189/2013jog12j125>.
- Blatman, G. (2009). *Adaptive sparse polynomial chaos expansions for uncertainty propagation and sensitivity analysis*. PhD thesis, Université Blaise Pascal – Clermont II, Clermont-Ferrand, France.
- Blatman, G. and Sudret, B. (2010). An adaptive algorithm to build up sparse polynomial chaos expansions for stochastic finite element analysis. *Probabilist. Eng. Mech.*, 25(2), 183–197, <https://doi.org/10.1016/j.probengmech.2009.10.003>.
- Blatman, G. and Sudret, B. (2011). Adaptive sparse polynomial chaos expansion based on least angle regression. *J. Comput. Phys.*, 230(6), 2345–2367, <https://doi.org/10.1016/j.jcp.2010.12.021>.
- Blatter, H. (1995). Velocity and stress fields in grounded glaciers: a simple algorithm for including deviatoric stress gradients. *J. Glaciol.*, 41(138), 333–344, <https://doi.org/10.3189/s002214300001621x>.
- Blatter, H., Greve, R., and Abe-Ouchi, A. (2011). Present State and Prospects of Ice Sheet and Glacier Modelling. *Surv. Geophys.*, 32(4–5), 555–583, <https://doi.org/10.1007/s10712-011-9128-0>.
- Bolin, D. (2012). *Models and Methods for Random Fields in Spatial Statistics with Computational Efficiency from Markov Properties*. PhD thesis, Lunds universitet, Lund, Sweden.
- Bolin, D. and Lindgren, F. (2015). Excursion and contour uncertainty regions for latent Gaussian models. *J. Royal Stat. Soc. B*, 77(1), 85–106, <https://doi.org/10.1111/rssb.12055>.
- Bonan, B., Nichols, N. K., Baines, M. J., and Partridge, D. (2017). Data assimilation for moving mesh methods with an application to ice sheet modelling. *Nonlinear Proc. Geoph.*, 24(3), 515–534, <https://doi.org/10.5194/npg-24-515-2017>.

- Bonan, B., Nodet, M., Ritz, C., and Peyaud, V. (2014). An ETKF approach for initial state and parameter estimation in ice sheet modelling. *Nonlinear Proc. Geoph.*, 21(2), 569–582, <https://doi.org/10.5194/npg-21-569-2014>.
- Bourinet, J.-M. (2018). *Reliability analysis and optimal design under uncertainty – Focus on adaptive surrogate-based approaches*. Habilitation thesis, Université Clermont Auvergne, Clermont-Ferrand, France.
- Boutounet, M., Monnier, J., and Vila, J.-P. (2016). Multi-regime shallow free surface laminar flow models for quasi-Newtonian fluids. *Eur. J. Mech. B-Fluid.*, 55(1), 182–206, <https://doi.org/10.1016/j.euromechflu.2015.10.005>.
- Briggs, R., Pollard, D., and Tarasov, L. (2013). A glacial systems model configured for large ensemble analysis of Antarctic deglaciation. *Cryosphere*, 7(6), 1949–1970, <https://doi.org/10.5194/tc-7-1949-2013>.
- Brondex, J., Gagliardini, O., Gillet-Chaulet, F., and Durand, G. (2017). Sensitivity of grounding line dynamics to the choice of the friction law. *J. Glaciol.*, 63(241), 854–866, <https://doi.org/10.1017/jog.2017.51>.
- Brondex, J., Gillet-Chaulet, F., and Gagliardini, O. (2019). Sensitivity of centennial mass loss projections of the Amundsen basin to the friction law. *Cryosphere*, 13(1), 177–195, <https://doi.org/10.5194/tc-13-177-2019>.
- Bronselaer, B., Winton, M., Griffies, S. M., Hurlin, W. J., Rodgers, K. B., Sergienko, O. V., Stouffer, R. J., and Russell, J. L. (2018). Change in future climate due to Antarctic meltwater. *Nature*, 564(7734), 53–58, <https://doi.org/10.1038/s41586-018-0712-z>.
- Brotchie, J. F. and Silvester, R. (1969). On crustal flexure. *J. Geophys. Res.*, 74(22), 5240–5252, <https://doi.org/10.1029/jb074i022p05240>.
- Budd, W. F., Jenssen, D., and Smith, I. N. (1984). A Three-Dimensional Time-Dependent Model of the West Antarctic Ice Sheet. *Ann. Glaciol.*, 5, 29–36, <https://doi.org/10.3189/1984aog5-1-29-36>.
- Bueler, E. and Brown, J. (2009). Shallow shelf approximation as a “sliding law” in a thermomechanically coupled ice sheet model. *J. Geophys. Res.*, 114(F3), F03008, <https://doi.org/10.1029/2008jf001179>.
- Bueler, E. and van Pelt, W. (2015). Mass-conserving subglacial hydrology in the Parallel Ice Sheet Model version 0.6. *Geosci. Model Dev.*, 8(6), 1613–1635, <https://doi.org/10.5194/gmd-8-1613-2015>.
- Bulthuis, K., Arnst, M., Sun, S., and Pattyn, F. (2019a). Uncertainty quantification of the multi-centennial response of the Antarctic ice sheet to climate change. *Cryosphere*, 13(4), 1349–1380, <https://doi.org/10.5194/tc-13-1349-2019>.
- Bulthuis, K., Pattyn, F., and Arnst, M. (2019b). A multifidelity quantile-based approach for confidence sets of random excursion sets with application to ice-sheet dynamics. Under review.

- Burnham, K. P. and Anderson, D. R. (2002). *Model Selection and Multimodel Inference: A Practical Information-Theoretic Approach*. New York, NY: Springer-Verlag, 2nd edition, <https://doi.org/10.1007/b97636>.
- Caffisch, R. E. (1998). Monte Carlo and quasi-Monte Carlo methods. *Acta Numer.*, 7, 1–49, <https://doi.org/10.1017/S0962492900002804>.
- Calonne, N., Montagnat, M., Matzl, M., and Schneebeli, M. (2017). The layered evolution of fabric and microstructure of snow at Point Barnola, Central East Antarctica. *Earth Planet. Sc. Lett.*, 460, 293–301, <https://doi.org/10.1016/j.epsl.2016.11.041>.
- Calvo, N., Durany, J., and Vázquez, C. (2003). Finite elements numerical solution of a coupled profile–velocity–temperature shallow ice sheet approximation model. *J. Comput. Appl. Math.*, 158(1), 31–41, [https://doi.org/10.1016/s0377-0427\(03\)00466-7](https://doi.org/10.1016/s0377-0427(03)00466-7).
- Calvo, N., Durany, J., and Vázquez, C. (2015). Enthalpy balance methods versus temperature models in ice sheets. *Commun. Nonlinear Sci. Numer. Simulat.*, 22(1–3), 526–544, <https://doi.org/10.1016/j.cnsns.2014.08.007>.
- Campos, L. T., Oden, J. T., and Kikuchi, N. (1982). A numerical analysis of a class of contact problems with friction in elastostatics. *Comput. Methods Appl. Mech. Eng.*, 34(1–3), 821–845, [https://doi.org/10.1016/0045-7825\(82\)90090-1](https://doi.org/10.1016/0045-7825(82)90090-1).
- Capatina, A. (2014). *Variational Inequalities and Frictional Contact Problems*. Cham, Switzerland: Springer, <https://doi.org/10.1007/978-3-319-10163-7>.
- Chastaing, G. (2013). *Indices de Sobol généralisés pour variables dépendantes*. PhD thesis, Université de Grenoble, Grenoble, France.
- Chastaing, G., Gamboa, F., and Prieur, C. (2012). Generalized Hoeffding-Sobol decomposition for dependent variables – application to sensitivity analysis. *Electron. J. Stat.*, 6, 2420–2448, <https://doi.org/10.1214/12-ejs749>.
- Chastaing, G., Gamboa, F., and Prieur, C. (2015). Generalized Sobol sensitivity indices for dependent variables: numerical methods. *J. Stat. Comput. Sim.*, 85(7), 1306–1333, <https://doi.org/10.1080/00949655.2014.960415>.
- Chen, B., Haeger, C., Kaban, M. K., and Petrunin, A. G. (2018). Variations of the effective elastic thickness reveal tectonic fragmentation of the Antarctic lithosphere. *Tectonophysics*, 746, 412–424, <https://doi.org/10.1016/j.tecto.2017.06.012>.
- Chilès, J.-P. and Delfiner, P. (2012). *Geostatistics: Modeling Spatial Uncertainty*. Hoboken, NJ: John Wiley & Sons, 2nd edition.
- Christianson, K., Bushuk, M., Dutrieux, P., Parizek, B. R., Joughin, I. R., Alley, R. B., Shean, D. E., Abrahamsen, E. P., Anandkrishnan, S., Heywood, K. J., Kim, T.-W., Lee, S. H., Nicholls, K., Stanton, T., Truffer, M., Webber, B. G. M., Jenkins, A., Jacobs, S., Bindshadler, R., and Holland, D. M. (2016). Sensitivity of Pine Island Glacier to observed ocean forcing. *Geophys. Res. Lett.*, 43(20), 10,817–10,825, <https://doi.org/10.1002/2016gl070500>.

- Church, J. A., Clark, P. U., Cazenave, A., Gregory, J. M., Jevrejeva, S., Levermann, A., Merrifield, M. A., Milne, G. A., Nerem, R. S., P. D. Nunn, A. J. P., Pfeffer, W. T., Stammer, D., and Unnikrishnan, A. S. (2013). Sea level change. In T. Stocker, D. Qin, G.-K. Plattner, M. Tignor, S. K. Allen, J. Boschung, A. Nauels, Y. Xia, V. Bex, and P. M. Midgley (Eds.), *Climate Change 2013: The Physical Science Basis. Contribution of Working Group I to the Fifth Assessment Report of the Intergovernmental Panel on Climate Change*, chapter 13, (pp. 1137–1216). Cambridge, United Kingdom: Cambridge University Press, <https://doi.org/10.1017/CBO9781107415324.026>.
- Cliffe, K. A., Giles, M. B., Scheichl, R., and Teckentrup, A. L. (2011). Multilevel monte carlo methods and applications to elliptic PDEs with random coefficients. *Computing and Visualization in Science*, 14(1), 3–15, <https://doi.org/10.1007/s00791-011-0160-x>.
- Coifman, R. R. and Lafon, S. (2006). Diffusion maps. *Appl. Comput. Harmon. A.*, 21(1), 5–30, <https://doi.org/10.1016/j.acha.2006.04.006>.
- Coifman, R. R., Lafon, S., Lee, A. B., Maggioni, M., Nadler, B., Warner, F., and Zucker, S. W. (2005). Geometric diffusions as a tool for harmonic analysis and structure definition of data: Diffusion maps. *PNAS*, 102(21), 7426–7431, <https://doi.org/10.1073/pnas.0500334102>.
- Collins, M., Knutti, R., Arblaster, J., Dufresne, J.-L., Fichenet, T., Friedlingstein, P., Gao, X., Gutowski, W. J., Johns, T., Krinner, G., Songwe, M., Tebaldi, C., Weaver, A. J., and Wehner, M. (2013). Long-term Climate Change: Projections, Commitments and Irreversibility. In T. F. Stocker, D. Qin, G.-K. Plattner, M. Tignor, S. K. Allen, J. Boschung, A. Nauels, Y. Xia, V. Bex, and P. M. Midgley (Eds.), *Climate Change 2013: The Physical Science Basis. Contribution of Working Group I to the Fifth Assessment Report of the Intergovernmental Panel on Climate Change*, chapter 12, (pp. 1029–1136). Cambridge, United Kingdom: Cambridge University Press, <https://doi.org/10.1017/CBO9781107415324.024>.
- Colson, A. R. and Cooke, R. M. (2017). Cross validation for the classical model of structured expert judgment. *Reliab. Eng. Syst. Safet.*, 163, 109–120, <https://doi.org/10.1016/j.ress.2017.02.003>.
- Colson, A. R. and Cooke, R. M. (2018). Expert Elicitation: Using the Classical Model to Validate Experts' Judgments. *Rev. Env. Econ. Policy*, 12(1), 113–132, <https://doi.org/10.1093/reep/rex022>.
- Conrad, P. R., Davis, A. D., Marzouk, Y. M., Pillai, N. S., and Smith, A. (2018). Parallel Local Approximation MCMC for Expensive Models. *SIAM/ASA JUQ*, 6(1), 339–373, <https://doi.org/10.1137/16m1084080>.
- Cook, C. P., van de Flierdt, T., Williams, T., Hemming, S. R., Iwai, M., Kobayashi, M., Jimenez-Espejo, F. J., Escutia, C., González, J. J., Khim, B.-K., McKay, R. M., Passchier, S., Bohaty, S. M., Riesselman, C. R., Tauxe, L., Sugisaki, S., Galindo, A. L., Patterson, M. O., Sangiorgi, F., Pierce, E. L., Brinkhuis, H., Klaus, A., Fehr, A., Bendle, J. A. P., Bijl, P. K., Carr, S. A., Dunbar, R. B., Flores, J. A., Hayden, T. G., Katsuki, K., Kong, G. S., Nakai, M., Olney, M. P., Pekar, S. F., Pross, J., Röhl, U., Sakai, T., Shrivastava, P. K., Stickle, C. E., Tuo, S., Welsh, K., and Yamane, M. (2013). Dynamic behaviour of the East Antarctic ice sheet during Pliocene warmth. *Nat. Geosci.*, 6(9), 765–769, <https://doi.org/10.1038/ngeo1889>.

- Cornford, S. L., Martin, D. F., Graves, D. T., Ranken, D. F., Le Brocq, A. M., Gladstone, R. M., Payne, A. J., Ng, E. G., and Lipscomb, W. H. (2013). Adaptive mesh, finite volume modeling of marine ice sheets. *J. Comput. Phys.*, 232(1), 529–549, <https://doi.org/10.1016/j.jcp.2012.08.037>.
- Cornford, S. L., Martin, D. F., Lee, V., Payne, A. J., and Ng, E. G. (2016). Adaptive mesh refinement versus subgrid friction interpolation in simulations of Antarctic ice dynamics. *Ann. Glaciol.*, 57(73), 1–9, <https://doi.org/10.1017/aog.2016.13>.
- Cornford, S. L., Martin, D. F., Payne, A. J., Ng, E. G., Le Brocq, A. M., Gladstone, R. M., Edwards, T. L., Shannon, S. R., Agosta, C., van den Broeke, M. R., Hellmer, H. H., Krinner, G., Ligtenberg, S. R. M., Timmermann, R., and Vaughan, D. G. (2015). Century-scale simulations of the response of the West Antarctic Ice Sheet to a warming climate. *Cryosphere*, 9(4), 1579–1600, <https://doi.org/10.5194/tc-9-1579-2015>.
- CReSIS (2019). Center for Remote Sensing of Ice Sheets (CReSIS), Available at [https://www.cresis.ku.edu/content/research/maps?qt-sea\\_level\\_rise\\_maps=4#qt-sea\\_level\\_rise\\_maps](https://www.cresis.ku.edu/content/research/maps?qt-sea_level_rise_maps=4#qt-sea_level_rise_maps), last accessed: 5 November 2019.
- Crestaux, T., Le Maître, O., and Martinez, J.-M. (2009). Polynomial chaos expansion for sensitivity analysis. *Reliab. Eng. Syst. Safe.*, 94(7), 1161–1172, <https://doi.org/10.1016/j.res.2008.10.008>.
- Cuffey, K. M. and Paterson, W. S. B. (2010). *The Physics of Glaciers*. Oxford, United Kingdom: Butterworth-Heinemann, 4th edition.
- Da Veiga, S. (2015). Global sensitivity analysis with dependence measures. *J. Stat. Comput. Sim.*, 85(7), 1283–1305, <https://doi.org/10.1080/00949655.2014.945932>.
- de Boer, B., Dolan, A. M., Bernales, J., Gasson, E., Goelzer, H., Golledge, N. R., Sutter, J., Huybrechts, P., Lohmann, G., Rogozhina, I., Abe-Ouchi, A., Saito, F., and van de Wal, R. S. W. (2015). Simulating the Antarctic ice sheet in the late-Pliocene warm period: PLISMIP-ANT, an ice-sheet model intercomparison project. *Cryosphere*, 9(3), 881–903, <https://doi.org/10.5194/tc-9-881-2015>.
- De Fleurian, B., Werder, M. A., Beyer, S., Brinkerhoff, D. J., Delaney, I., Dow, C. F., Downs, J., Gagliardini, O., Hoffman, M. J., Hooke, R. L., Seguinot, J., and Sommers, A. N. (2018). SHMIP the subglacial hydrology model intercomparison Project. *J. Glaciol.*, 64(248), 897–916, <https://doi.org/10.1017/jog.2018.78>.
- De Lozzo, M. and Marrel, A. (2016). Estimation of the Derivative-Based Global Sensitivity Measures Using a Gaussian Process Metamodel. *SIAM/ASA JUQ*, 4(1), 708–738, <https://doi.org/10.1137/15M1013377>.
- DeConto, R. M. and Pollard, D. (2016). Contribution of Antarctica to past and future sea-level rise. *Nature*, 531(7596), 591–597, <https://doi.org/10.1038/nature17145>.
- Depoorter, M. A., Bamber, J. L., Griggs, J. A., Lenaerts, J. T. M., Ligtenberg, S. R. M., van den Broeke, M. R., and Moholdt, G. (2013). Calving fluxes and basal melt rates of Antarctic ice shelves. *Nature*, 502(7469), 89–92, <https://doi.org/10.1038/nature12567>.

- Dinniman, M. S., Asay-Davis, X. S., Galton-Fenzi, B. K., Holland, P. R., Jenkins, A., and Timmermann, R. (2016). Modeling Ice Shelf/Ocean Interaction in Antarctica: A Review. *Oceanography*, 29(4), 144–153, <https://doi.org/10.5670/oceanog.2016.106>.
- Dinniman, M. S., Klinck, J. M., and Hofmann, E. E. (2012). Sensitivity of Circumpolar Deep Water Transport and Ice Shelf Basal Melt along the West Antarctic Peninsula to Changes in the Winds. *J. Climate*, 25(14), 4799–4816, <https://doi.org/10.1175/jcli-d-11-00307.1>.
- Docquier, D., Perichon, L., and Pattyn, F. (2011). Representing Grounding Line Dynamics in Numerical Ice Sheet Models: Recent Advances and Outlook. *Surv. Geophys.*, 32(4–5), 417–435, <https://doi.org/10.1007/s10712-011-9133-3>.
- Drouet, A. S., Docquier, D., Durand, G., Hindmarsh, R., Pattyn, F., Gagliardini, O., and Zwinger, T. (2013). Grounding line transient response in marine ice sheet models. *Cryosphere*, 7(2), 395–406, <https://doi.org/10.5194/tc-7-395-2013>.
- Dubourg, V. (2011). *Adaptive surrogate models for reliability analysis and reliability-based design optimization*. PhD thesis, Université Blaise Pascal – Clermont Ferrand II, Clermont-Ferrand, France.
- Dubourg, V., Sudret, B., and Bourinet, J.-M. (2011). Reliability-based design optimization using kriging surrogates and subset simulation. *Struct. Multidiscip. O.*, 44(5), 673–690, <https://doi.org/10.1007/s00158-011-0653-8>.
- Dudley, R. M. (2002). *Real Analysis and Probability*. Cambridge, United Kingdom: Cambridge University Press, 2nd edition, <https://doi.org/10.1017/cbo9780511755347>.
- Durand, G., Gagliardini, O., de Fleurian, B., Zwinger, T., and Le Meur, E. (2009). Marine ice sheet dynamics: Hysteresis and neutral equilibrium. *J. Geophys. Res.*, 114(F3), F03009, <https://doi.org/10.1029/2008jf001170>.
- Durand, G. and Pattyn, F. (2015). Reducing uncertainties in projections of Antarctic ice mass loss. *Cryosphere*, 9(6), 2043–2055, <https://doi.org/10.5194/tc-9-2043-2015>.
- Dutrieux, P., De Rydt, J., Jenkins, A., Holland, P. R., Ha, H. K., Lee, S. H., Steig, E. J., Ding, Q., Abrahamsen, E. P., and Schröder, M. (2014). Strong Sensitivity of Pine Island Ice-Shelf Melting to Climatic Variability. *Science*, 343(6167), 174–178, <https://doi.org/10.1126/science.1244341>.
- Edwards, T. L., Brandon, M. A., Durand, G., Edwards, N. R., Golledge, N. R., Holden, P. B., Nias, I. J., Payne, A. J., Ritz, C., and Wernecke, A. (2019). Revisiting Antarctic ice loss due to marine ice-cliff instability. *Nature*, 566(7742), 58–64, <https://doi.org/10.1038/s41586-019-0901-4>.
- Efron, B. and Tibshirani, R. J. (1993). *An Introduction to the Bootstrap*. Dordrecht, Holland: Springer Science+Business Media.
- Elfverson, D., Estep, D. J., Hellman, F., and Målqvist, A. (2014). Uncertainty Quantification for Approximate  $p$ -Quantiles for Physical Models with Stochastic Inputs. *SIAM/ASA JUQ*, 2(1), 826–850, <https://doi.org/10.1137/140967039>.

- Emery, X. (2007). Using the Gibbs sampler for conditional simulation of Gaussian-based random fields. *Comput. Geosci.*, 33(4), 522–537, <https://doi.org/10.1016/j.cageo.2006.08.003>.
- Emery, X., Arroyo, D., and Peláez, M. (2014). Simulating Large Gaussian Random Vectors Subject to Inequality Constraints by Gibbs Sampling. *Math. Geosci.*, 46(3), 265–283, <https://doi.org/10.1007/s11004-013-9495-9>.
- Enss, G. C., Kohler, M., Krzyżak, A., and Platz, R. (2016). Nonparametric Quantile Estimation Based on Surrogate Models. *IEEE T. Inform. Theory*, 62(10), 5727–5739, <https://doi.org/10.1109/tit.2016.2586080>.
- Ernst, O. G., Mugler, A., Starkloff, H.-J., and Ullmann, E. (2012). On the convergence of generalized polynomial chaos expansions. *ESAIM–Math. Model. Num.*, 46(2), 317–339, <https://doi.org/10.1051/m2an/2011045>.
- Fajraoui, N., Marelli, S., and Sudret, B. (2017). Sequential Design of Experiment for Sparse Polynomial Chaos Expansions. *SIAM/ASA JUQ*, 5(1), 1061–1085, <https://doi.org/10.1137/16m1103488>.
- Farinotti, D., Huss, M., Fürst, J. J., Landmann, J., Machguth, H., Maussion, F., and Pandit, A. (2019). A consensus estimate for the ice thickness distribution of all glaciers on Earth. *Nat. Geosci.*, 12(3), 168–173, <https://doi.org/10.1038/s41561-019-0300-3>.
- Favier, L., Durand, G., Cornford, S. L., Gudmundsson, G. H., Gagliardini, O., Gillet-Chaulet, F., Zwinger, T., Payne, A. J., and Le Brocq, A. M. (2014). Retreat of Pine Island Glacier controlled by marine ice-sheet instability. *Nat. Clim. Change*, 4(2), 117–121, <https://doi.org/10.1038/nclimate2094>.
- Favier, L., Gagliardini, O., Durand, G., and Zwinger, T. (2011). A three-dimensional full Stokes model of the grounding line dynamics: effect of a pinning point beneath the ice shelf. *Cryosphere*, 6(1), 101–112, <https://doi.org/10.5194/tc-6-101-2012>.
- Favier, L., Jourdain, N. C., Jenkins, A., Merino, N., Durand, G., Gagliardini, O., Gillet-Chaulet, F., and Mathiot, P. (2019). Assessment of sub-shelf melting parameterisations using the ocean–ice-sheet coupled model NEMO(v3.6)–Elmer/Ice(v8.3). *Geosci. Model Dev.*, 12(6), 2255–2283, <https://doi.org/10.5194/gmd-12-2255-2019>.
- Favier, L. and Pattyn, F. (2015). Antarctic ice rise formation, evolution, and stability. *Geophys. Res. Lett.*, 42(11), 4456–4463, <https://doi.org/10.1002/2015gl064195>.
- Favier, L., Pattyn, F., Berger, S., and Drews, R. (2016). Dynamic influence of pinning points on marine ice-sheet stability: a numerical study in Dronning Maud Land, East Antarctica. *Cryosphere*, 10(6), 2623–2635, <https://doi.org/10.5194/tc-10-2623-2016>.
- Feldman, D. and Tucker, H. G. (1966). Estimation of Non-Unique Quantiles. *Ann. Math. Stat.*, 37(2), 451–457, <https://doi.org/10.1214/aoms/1177699527>.
- Feldmann, J., Albrecht, T., Khroulev, C., Pattyn, F., and Levermann, A. (2014). Resolution-dependent performance of grounding line motion in a shallow model compared with a full-Stokes model according to the MISMIP3d intercomparison. *J. Glaciol.*, 60(220), 353–360, <https://doi.org/10.3189/2014jog13j093>.

- Fernández-Nieto, E. D., Noble, P., and Vila, J.-P. (2010). Shallow Water equations for Non-Newtonian fluids. *J. Non-Newton. Fluid*, 165(13–14), 712–732, <https://doi.org/10.1016/j.jnnfm.2010.03.008>.
- Fisher, R. A. (1912). On an Absolute Criterion for Fitting Frequency Curves. *Messenger Math.*, 41, 155–160.
- Forrester, A. I. J., Sóbester, A., and Keane, A. J. (2008). *Engineering Design via Surrogate Modelling: A Practical Guide*. Chichester, United Kingdom: John Wiley & Sons, <https://doi.org/10.1002/9780470770801>.
- Fowler, A. (2011). *Glaciers and Ice Sheets*, In *Mathematical Geoscience*, chapter 10, (pp. 617–739). Springer-Verlag London: London, United Kingdom, [https://doi.org/10.1007/978-0-85729-721-1\\_10](https://doi.org/10.1007/978-0-85729-721-1_10).
- French, J., Kokoszka, P., Stoev, S., and Hall, L. (2019). Quantifying the risk of heat waves using extreme value theory and spatio-temporal functional data. *Comput. Stat. Data An.*, 131, 176–193, <https://doi.org/10.1016/j.csda.2018.07.004>.
- French, J. P. (2014). Confidence regions for the level curves of spatial data. *Environmetrics*, 25(7), 498–512, <https://doi.org/10.1002/env.2295>.
- French, J. P. and Hoeting, J. A. (2015). Credible regions for exceedance sets of geostatistical data. *Environmetrics*, 27(1), 4–14, <https://doi.org/10.1002/env.2371>.
- French, J. P. and Sain, S. R. (2013). Spatio-temporal exceedance locations and confidence regions. *Ann. Appl. Stat.*, 7(3), 1421–1449, <https://doi.org/10.1214/13-aos631>.
- Fretwell, P., Pritchard, H. D., Vaughan, D. G., Bamber, J. L., Barrand, N. E., Bell, R., Bianchi, C., Bingham, R. G., Blankenship, D. D., Casassa, G., Catania, G., Callens, D., Conway, H., Cook, A. J., Corr, H. F. J., Damaske, D., Damm, V., Ferraccioli, F., Forsberg, R., Fujita, S., Gim, Y., Gogineni, P., Griggs, J. A., Hindmarsh, R. C. A., Holmlund, P., Holt, J. W., Jacobel, R. W., Jenkins, A., Jokar, W., Jordan, T., King, E. C., Kohler, J., Krabill, W., Riger-Kusk, M., Langley, K. A., Leitchenkov, G., Leuschen, C., Luyendyk, B. P., Matsuoka, K., Mouginot, J., Nitsche, F. O., Nogi, Y., Nost, O. A., Popov, S. V., Rignot, E., Rippin, D. M., Rivera, A., Roberts, J., Ross, N., Siegert, M. J., Smith, A. M., Steinhage, D., Studinger, M., Sun, B., Tinto, B. K., Welch, B. C., Wilson, D., Young, D. A., Xiangbin, C., and Zirizzotti, A. (2013). Bedmap2: improved ice bed, surface and thickness datasets for Antarctica. *Cryosphere*, 7(1), 375–393, <https://doi.org/10.5194/tc-7-375-2013>.
- Frieler, K., Clark, P. U., He, F., Buizert, C., Reese, R., Ligtenberg, S. R. M., van den Broeke, M. R., Winkelmann, R., and Levermann, A. (2015). Consistent evidence of increasing Antarctic accumulation with warming. *Nat. Clim. Change*, 5(4), 348–352, <https://doi.org/10.1038/nclimate2574>.
- Fürst, J. J., Durand, G., Gillet-Chaulet, F., Tavard, L., Rankl, M., Braun, M., and Gagliardini, O. (2016). The safety band of Antarctic ice shelves. *Nat. Clim. Change*, 6(5), 479–482, <https://doi.org/10.1038/nclimate2912>.

- Gagliardini, O., Zwinger, T., Gillet-Chaulet, F., Durand, G., Favier, L., de Fleurian, B., Greve, R., Malinen, M., Martín, C., Råback, P., Ruokolainen, J., Sacchetti, M., Schäfer, M., Seddik, H., and Thies, J. (2013). Capabilities and performance of Elmer/Ice, a new-generation ice sheet model. *Geosci. Model Dev.*, 6(4), 1299–1318, <https://doi.org/10.5194/gmd-6-1299-2013>.
- Garcia, E. S., Sandwell, D. T., and Luttrell, K. M. (2015). An iterative spectral solution method for thin elastic plate flexure with variable rigidity. *Geophys. J. Int.*, 200(2), 1012–1028, <https://doi.org/10.1093/gji/ggu449>.
- Gardner, A. S., Moholdt, G., Scambos, T., Fahnestock, M., Ligtenberg, S., van den Broeke, M., and Nilsson, J. (2018). Increased West Antarctic and unchanged East Antarctic ice discharge over the last 7 years. *Cryosphere*, 12(2), 521–547, <https://doi.org/10.5194/tc-12-521-2018>.
- Gasson, E., DeConto, R., and Pollard, D. (2015). Antarctic bedrock topography uncertainty and ice sheet stability. *Geophys. Res. Lett.*, 42(13), 5372–5377, <https://doi.org/10.1002/2015gl064322>.
- Gasson, E., DeConto, R. M., Pollard, D., and Levy, R. H. (2016). Dynamic Antarctic ice sheet during the early to mid-Miocene. *PNAS*, 113(13), 3459–3464, <https://doi.org/10.1073/pnas.1516130113>.
- Gautschi, W. (1982). On generating orthogonal polynomials. *SIAM J. Sci. Stat. Comp.*, 3(3), 289–317, <https://doi.org/10.1137/0903018>.
- Gerbeau, J.-F. and Perthame, B. (2001). Derivation of viscous Saint-Venant system for laminar shallow water; Numerical validation. *Discrete Cont. Dyn.-B*, 1(1), 89–102, <https://doi.org/10.3934/dcdsb.2001.1.89>.
- Gerstner, T. and Griebel, M. (1998). Numerical integration using sparse grids. *Numer. algorithms*, 18(3-4), 209–232, <https://doi.org/10.1023/A:1019129717644>.
- Gerstner, T. and Griebel, M. (2003). Dimension-Adaptive Tensor-Product Quadrature. *Computing*, 71(1), 65–87, <https://doi.org/10.1007/s00607-003-0015-5>.
- Ghanem, R., Higdon, R., and Owhadi, H., Eds. (2017). *Handbook of Uncertainty Quantification*. Cham, Switzerland: Springer, <https://doi.org/10.1007/978-3-319-12385-1>.
- Ghanem, R. and Soize, C. (2018). Probabilistic nonconvex constrained optimization with fixed number of function evaluations. *Int. J. Numer. Meth. Eng.*, 113(4), 719–741, <https://doi.org/10.1002/nme.5632>.
- Ghanem, R. G. and Spanos, P. D. (2003). *Stochastic Finite Elements: A Spectral Approach*. Mineola, NY: Dover Publications, revised edition.
- Giles, M. B. (2015). Multilevel Monte Carlo methods. *Acta Numer.*, 24, 259–328, <https://doi.org/10.1017/s096249291500001x>.
- Gillet-Chaulet, F., Durand, G., Gagliardini, O., Mosbeux, C., Mougnot, J., Rémy, F., and Ritz, C. (2016). Assimilation of surface velocities acquired between 1996 and 2010 to constrain the form of the basal friction law under Pine Island Glacier. *Geophys. Res. Lett.*, 43(19), 10,311–10,321, <https://doi.org/10.1002/2016gl069937>.

- Gladstone, R., Schäfer, M., Zwinger, T., Gong, Y., Strozzi, T., Mottram, R., Boberg, F., and Moore, J. C. (2014). Importance of basal processes in simulations of a surging Svalbard outlet glacier. *Cryosphere*, 8(4), 1393–1405, <https://doi.org/10.5194/tc-8-1393-2014>.
- Gladstone, R. M., Warner, R. C., Galton-Fenzi, B. K., Gagliardini, O., Zwinger, T., and Greve, R. (2017). Marine ice sheet model performance depends on basal sliding physics and sub-shelf melting. *Cryosphere*, 11(1), 319–329, <https://doi.org/10.5194/tc-11-319-2017>.
- Glen, J. W. (1955). The creep of polycrystalline ice. *Proc. R. Soc. Lon. A Mat.*, 228(1175), 519–538, <https://doi.org/10.1098/rspa.1955.0066>.
- Glowinski, R., Lions, J.-L., and Trémolières, R. (1981). *Numerical Analysis of Variational Inequalities*. Amsterdam, The Netherlands: North-Holland.
- Goelzer, H., Nowicki, S., Edwards, T., Beckley, M., Abe-Ouchi, A., Aschwanden, A., Calov, R., Gagliardini, O., Gillet-Chaulet, F., Golledge, N. R., Gregory, J., Greve, R., Humbert, A., Huybrechts, P., Kennedy, J. H., Larour, E., Lipscomb, W. H., Le clec'h, S., Lee, V., Morlighem, M., Pattyn, F., Payne, A. J., Rodehacke, C., Rückamp, M., Saito, F., Schlegel, N., Seroussi, H., Shepherd, A., Sun, S., van de Wal, R., and Ziemen, F. A. (2018). Design and results of the ice sheet model initialisation experiments initMIP-Greenland: an ISMIP6 intercomparison. *Cryosphere*, 12(4), 1433–1460, <https://doi.org/10.5194/tc-12-1433-2018>.
- Goelzer, H., Robinson, A., Seroussi, H., and van de Wal, R. S. (2017). Recent Progress in Greenland Ice Sheet Modelling. *Curr. Clim. Change Rep.*, 3(4), 291–302, <https://doi.org/10.1007/s40641-017-0073-y>.
- Golledge, N. R., Keller, E. D., Gomez, N., Naughten, K. A., Bernales, J., Trusel, L. D., and Edwards, T. L. (2019). Global environmental consequences of twenty-first-century ice-sheet melt. *Nature*, 566(7742), 65–72, <https://doi.org/10.1038/s41586-019-0889-9>.
- Golledge, N. R., Kowalewski, D. E., Naish, T. R., Levy, R. H., Fogwill, C. J., and Gasson, E. G. W. (2015). The multi-millennial Antarctic commitment to future sea-level rise. *Nature*, 526(7573), 421–425, <https://doi.org/10.1038/nature15706>.
- Golledge, N. R., Levy, R. H., McKay, R. M., and Naish, T. R. (2017). East Antarctic ice sheet most vulnerable to Weddell Sea warming. *Geophys. Res. Lett.*, 44(5), 2343–2351, <https://doi.org/10.1002/2016gl072422>.
- Golub, G. H. and Meurant, G. (2010). *Matrices, Moments, and Quadrature with Applications*. Princeton, NJ: Princeton University Press.
- Gomez, N., Mitrovica, J. X., Huybers, P., and Clark, P. U. (2010). Sea level as a stabilizing factor for marine-ice-sheet grounding lines. *Nat. Geosci.*, 3(12), 850–853, <https://doi.org/10.1038/ngeo1012>.
- Gomez, N., Pollard, D., and Holland, D. (2015). Sea-level feedback lowers projections of future Antarctic Ice-Sheet mass loss. *Nat. Commun.*, 6, 8798, <https://doi.org/10.1038/ncomms9798>.
- Gomez, N., Pollard, D., and Mitrovica, J. X. (2013). A 3-D coupled ice sheet – sea level model applied to Antarctica through the last 40 ky. *Earth Planet. Sc. Lett.*, 384, 88–99, <https://doi.org/10.1016/j.epsl.2013.09.042>.

- Goodman, I. R. and Nguyen, H. T. (2002). Fuziness and randomness. In C. Bertoluzza, M.-Á. Gil, and D. A. Ralescu (Eds.), *Statistical Modeling, Analysis and Management of Fuzzy Data*, chapter 1, (pp. 3–21). Berlin, Germany: Springer-Verlag, <https://doi.org/10.1007/978-3-7908-1800-0>.
- Gopalan, G., Hrafinkelsson, B., Aðalgeirsdóttir, G., Jarosch, A. H., and Pálsson, F. (2018). A Bayesian hierarchical model for glacial dynamics based on the shallow ice approximation and its evaluation using analytical solutions. *Cryosphere*, 12(7), 2229–2248, <https://doi.org/10.5194/tc-12-2229-2018>.
- Greene, C. A., Blankenship, D. D., Gwyther, D. E., Silvano, A., and van Wijk, E. (2017). Wind causes Totten Ice Shelf melt and acceleration. *Sci. Adv.*, 3(11), e1701681, <https://doi.org/10.1126/sciadv.1701681>.
- Gretton, A., Bousquet, O., Smola, A., and Schölkopf, B. (2005). Measuring Statistical Dependence with Hilbert-Schmidt Norms. In S. Jain, H. U. Simon, and E. Tomita (Eds.), *Algorithmic Learning Theory* (pp. 63–77). Berlin, Germany: Springer-Verlag. Proceedings of the 16th International Conference, ALT 2005.
- Greve, R. and Blatter, H. (2009a). *Dynamics of Ice Sheets and Glaciers*. Berlin, Germany: Springer-Verlag, <https://doi.org/10.1007/978-3-642-03415-2>.
- Greve, R. and Blatter, H. (2009b). *Glacial Isostasy*, In *Dynamics of Ice Sheets and Glaciers*, chapter 8, (pp. 185–201). Springer-Verlag: Berlin, Germany, <https://doi.org/10.1007/978-3-642-03415-2>.
- Grigoriu, M. (2002). *Stochastic Calculus: Applications in Science and Engineering*. New York, NY: Springer Science+Business Media, <https://doi.org/10.1007/978-0-8176-8228-6>.
- Hadigol, M. and Doostan, A. (2018). Least squares polynomial chaos expansion: A review of sampling strategies. *Comput. Method. Appl. M.*, 332, 382–407, <https://doi.org/10.1016/j.cma.2017.12.019>.
- Hallegatte, S., Green, C., Nicholls, R. J., and Corfee-Morlot, J. (2013). Future flood losses in major coastal cities. *Nat. Clim. Change*, 3(9), 802–806, <https://doi.org/10.1038/nclimate1979>.
- Hanna, E., Pattyn, F., Francisco Navarro, Vincent Favier, H. G., van den Broeke, M. R., Viczaino, M., Pippa L. Whitehouse, C. R., Bulthuis, K., and Smith, B. (2020). Mass balance of the ice sheets and glaciers – progress since AR5 and challenges. *Earth-Sci. Rev.*, <https://doi.org/10.1016/j.earscirev.2019.102976>. In press.
- Haykin, S. O. (2009). *Neural Networks and Learning Machines*. Upper Saddle River, NJ: Pearson Education, 3rd edition.
- Hellmer, H. H., Kauker, F., Timmermann, R., Determann, J., and Rae, J. (2012). Twenty-first-century warming of a large Antarctic ice-shelf cavity by a redirected coastal current. *Nature*, 485(7397), 225–228, <https://doi.org/10.1038/nature11064>.

- Hellmer, H. H., Kauker, F., Timmermann, R., and Hattermann, T. (2017). The Fate of the Southern Weddell Sea Continental Shelf in a Warming Climate. *J. Climate*, 30(12), 4337–4350, <https://doi.org/10.1175/jcli-d-16-0420.1>.
- Hertz, H. (1884). Ueber das Gleichgewicht schwimmender elastischer Platten. *Ann. Phys.*, 258(7), 449–455, <https://doi.org/10.1002/andp.18842580711>.
- Hindmarsh, R. C. A. (1999). On the numerical computation of temperature in an ice sheet. *J. Glaciol.*, 45(151), 568–574, <https://doi.org/10.3189/s0022143000001441>.
- Hoffman, M. J., Perego, M., Price, S. F., Lipscomb, W. H., Zhang, T., Jacobsen, D., Tezaur, I., Salinger, A. G., Tuminaro, R., and Bertagna, L. (2018). MPAS-Albany Land Ice (MALI): a variable-resolution ice sheet model for Earth system modeling using Voronoi grids. *Geosci. Model Dev.*, 11(9), 3747–3780, <https://doi.org/10.5194/gmd-11-3747-2018>.
- Holland, D. M. and Jenkins, A. (1999). Modeling Thermodynamic Ice–Ocean Interactions at the Base of an Ice Shelf. *J. Phys. Oceanogr.*, 29(8), 1787–1800, [https://doi.org/10.1175/1520-0485\(1999\)029<1787:mtioia>2.0.co;2](https://doi.org/10.1175/1520-0485(1999)029<1787:mtioia>2.0.co;2).
- Holland, P. R., Jenkins, A., and Holland, D. M. (2008). The Response of Ice Shelf Basal Melting to Variations in Ocean Temperature. *J. Climate*, 21(11), 2558–2572, <https://doi.org/10.1175/2007jcli1909.1>.
- Homma, T. and Saltelli, A. (1996). Importance measures in global sensitivity analysis of nonlinear models. *Reliab. Eng. Syst. Safe.*, 52(1), 1–17, [https://doi.org/10.1016/0951-8320\(96\)00002-6](https://doi.org/10.1016/0951-8320(96)00002-6).
- Hu, A. and Deser, C. (2013). Uncertainty in future regional sea level rise due to internal climate variability. *Geophys. Res. Lett.*, 40(11), 2768–2772, <https://doi.org/10.1002/grl.50531>.
- Hubbard, B., Luckman, A., Ashmore, D. W., Bevan, S., Kulesa, B., Munneke, P. K., Philippe, M., Jansen, D., Booth, A., Sevestre, H., Tison, J.-L., O’Leary, M., and Rutt, I. (2016). Massive subsurface ice formed by refreezing of ice-shelf melt ponds. *Nat. Commun.*, 7, 11897, <https://doi.org/10.1038/ncomms11897>.
- Hutter, K. (1983). *Theoretical Glaciology: Material Science of Ice and the Mechanics of Glaciers and Ice Sheets*. Dordrecht, Holland: D. Reidel Publishing Company, <https://doi.org/10.1007/978-94-015-1167-4>.
- Huybrechts, P., Abe-Ouchi, A., Marsiat, I., Pattyn, F., Payne, T., Ritz, C., and Rommelaere, V. (1998). Report of the Third EISMINT Workshop on Model Intercomparison. European Science Foundation (Strasbourg).
- Huybrechts, P. and de Wolde, J. (1999). The Dynamic Response of the Greenland and Antarctic Ice Sheets to Multiple-Century Climatic Warming. *J. Climate*, 12(8), 2169–2188, [https://doi.org/10.1175/1520-0442\(1999\)012<2169:TDROTG>2.0.CO;2](https://doi.org/10.1175/1520-0442(1999)012<2169:TDROTG>2.0.CO;2).
- Iooss, B. and Lemaître, P. (2015). A Review on Global Sensitivity Analysis Methods. In G. Dellino and C. Meloni (Eds.), *Uncertainty Management in Simulation-Optimization of Complex Systems: Algorithms and Applications*, chapter 5, (pp. 101–122). New York, NY: Springer Science+Business Media, <https://doi.org/10.1007/978-1-4899-7547-8>.

- IPCC (2018). *Global Warming of 1.5°C. An IPCC Special Report on the impacts of global warming of 1.5°C above pre-industrial levels and related global greenhouse gas emission pathways, in the context of strengthening the global response to the threat of climate change, sustainable development, and efforts to eradicate poverty*. V. Masson-Delmotte, P. Zhai, H. O. Pörtner, D. Roberts, J. Skea, P. R. Shukla, A. Pirani, W. Moufouma-Okia, C. Péan, R. Pidcock, S. Connors, J. B. R. Matthews, Y. Chen, X. Zhou, M. I. Gomis, E. Lonnoy, T. Maycock, M. Tignor, and T. Waterfield (Eds.). Geneva, Switzerland: World Meteorological Organization.
- IPCC (2019). *IPCC Special Report on the Ocean and Cryosphere in a Changing Climate*. H.-O. Pörtner, D. C. Roberts, V. Masson-Delmotte, P. Zhai, M. Tignor, E. Poloczanska, K. Mintenbeck, A. Alegría, M. Nicolai, A. Okem, J. Petzold, B. Rama, and N. M. Weyer (Eds.). In press.
- Isaac, T., Petra, N., Stadler, G., and Ghattas, O. (2015). Scalable and efficient algorithms for the propagation of uncertainty from data through inference to prediction for large-scale problems, with application to flow of the Antarctic ice sheet. *J. Comput. Phys.*, 296, 348–368, <https://doi.org/10.1016/j.jcp.2015.04.047>.
- Iskandarani, M., Wang, S., Srinivasan, A., Thacker, W. C., Winokur, J., and Knio, O. M. (2016). An overview of uncertainty quantification techniques with application to oceanic and oil-spill simulations. *J. Geophys. Res.: Oceans*, 121(4), 2789–2808, <https://doi.org/10.1002/2015jc011366>.
- Ivins, E. R. and James, T. S. (1999). Simple models for late Holocene and present-day Patagonian glacier fluctuations and predictions of a geodetically detectable isostatic response. *Geophys. J. Int.*, 138(3), 601–624, <https://doi.org/10.1046/j.1365-246x.1999.00899.x>.
- Jacobs, S. S., Helmer, H. H., Doake, C. S. M., Jenkins, A., and Frolich, R. M. (1992). Melting of ice shelves and the mass balance of Antarctica. *J. Glaciol.*, 38(130), 375–387, <https://doi.org/10.3189/s0022143000002252>.
- Jacobs, S. S., Jenkins, A., Giulivi, C. F., and Dutrieux, P. (2011). Stronger ocean circulation and increased melting under Pine Island Glacier ice shelf. *Nat. Geosci.*, 4(8), 519–523, <https://doi.org/10.1038/ngeo1188>.
- Janon, A., Klein, T., Lagnoux, A., Nodet, M., and Prieur, C. (2014). Asymptotic normality and efficiency of two Sobol index estimators. *ESAIM: Probab. Stat.*, 18, 342–364, <https://doi.org/10.1051/ps/2013040>.
- Janssens, I. and Huybrechts, P. (2000). The treatment of meltwater retention in mass-balance parameterizations of the Greenland ice sheet. *Ann. Glaciol.*, 31, 133–140, <https://doi.org/10.3189/172756400781819941>.
- Jevrejeva, S., Frederikse, T., Kopp, R. E., Le Cozannet, G., Jackson, L. P., and van de Wal, R. S. W. (2019). Probabilistic Sea Level Projections at the Coast by 2100. *Surv. Geophys.*, 40(6), 1673–1696, <https://doi.org/10.1007/s10712-019-09550-y>.
- Joughin, I., Smith, B. E., and Holland, D. M. (2010). Sensitivity of 21st century sea level to ocean-induced thinning of Pine Island Glacier, Antarctica. *Geophys. Res. Lett.*, 37(20), L20502, <https://doi.org/10.1029/2010gl044819>.

- Joughin, I., Smith, B. E., and Medley, B. (2014). Marine Ice Sheet Collapse Potentially Under Way for the Thwaites Glacier Basin, West Antarctica. *Science*, 344(6185), 735–738, <https://doi.org/10.1126/science.1249055>.
- Joughin, I., Smith, B. E., and Schoof, C. G. (2019). Regularized Coulomb Friction Laws for Ice Sheet Sliding: Application to Pine Island Glacier, Antarctica. *Geophys. Res. Lett.*, 46(9), 4764–4771, <https://doi.org/10.1029/2019gl082526>.
- Joughin, I., Tulaczyk, S., Bamber, J. L., Blankenship, D., Holt, J. W., Scambos, T., and Vaughan, D. G. (2009). Basal conditions for Pine Island and Thwaites Glaciers, West Antarctica, determined using satellite and airborne data. *J. Glaciol.*, 55(190), 245–257, <https://doi.org/10.3189/002214309788608705>.
- Kikuchi, N. and Oden, J. T. (1988). *Contact Problems in Elasticity: A Study of Variational Inequalities and Finite Element Methods*. Philadelphia, PA: SIAM, <https://doi.org/10.1137/1.9781611970845>.
- Kingslake, J., Scherer, R. P., Albrecht, T., Coenen, J., Powell, R. D., Reese, R., Stansell, N. D., Tulaczyk, S., Wearing, M. G., and Whitehouse, P. L. (2018). Extensive retreat and re-advance of the West Antarctic Ice Sheet during the Holocene. *Nature*, 558(7710), 430–434, <https://doi.org/10.1038/s41586-018-0208-x>.
- Kirchner, N., Hutter, K., Jakobsson, M., and Gyllencreutz, R. (2011). Capabilities and limitations of numerical ice sheet models: a discussion for Earth-scientists and modelers. *Quaternary Sci. Rev.*, 30(25–26), 3691–3704, <https://doi.org/10.1016/j.quascirev.2011.09.012>.
- Knutti, R., Furrer, R., Tebaldi, C., Cermak, J., and Meehl, G. A. (2010). Challenges in Combining Projections from Multiple Climate Models. *J. Climate*, 23(10), 2739–2758, <https://doi.org/10.1175/2009jcli3361.1>.
- Knutti, R., Sedláček, J., Sanderson, B. M., Lorenz, R., Fischer, E. M., and Eyring, V. (2017). A climate model projection weighting scheme accounting for performance and interdependence. *Geophys. Res. Lett.*, 44(4), 1909–1918, <https://doi.org/10.1002/2016gl072012>.
- Konrad, H., Sasgen, I., Pollard, D., and Klemann, V. (2015). Potential of the solid-Earth response for limiting long-term West Antarctic Ice Sheet retreat in a warming climate. *Earth Planet. Sc. Lett.*, 432, 254–264, <https://doi.org/10.1016/j.epsl.2015.10.008>.
- Kopp, R. E., DeConto, R. M., Bader, D. A., Hay, C. C., Horton, R. M., Kulp, S., Oppenheimer, M., Pollard, D., and Strauss, B. H. (2017). Evolving Understanding of Antarctic Ice-Sheet Physics and Ambiguity in Probabilistic Sea-Level Projections. *Earth's Future*, 5(12), 1217–1233, <https://doi.org/10.1002/2017ef000663>.
- Kopp, R. E., Horton, R. M., Little, C. M., Mitrovica, J. X., Oppenheimer, M., Rasmussen, D. J., Strauss, B. H., and Tebaldi, C. (2014). Probabilistic 21st and 22nd century sea-level projections at a global network of tide-gauge sites. *Earth's Future*, 2(8), 383–406, <https://doi.org/10.1002/2014ef000239>.
- Krug, J., Weiss, J., Gagliardini, O., and Durand, G. (2014). Combining damage and fracture mechanics to model calving. *Cryosphere*, 8(6), 2101–2117, <https://doi.org/10.5194/tc-8-2101-2014>.

- Krzyżak, A. (2016). Recent Results on Nonparametric Quantile Estimation in a Simulation Model. In S. Matwin and J. Mielniczuk (Eds.), *Challenges in Computational Statistics and Data Mining*, (pp. 225–246). Cham, Switzerland: Springer, <https://doi.org/10.1007/978-3-319-18781-5>.
- Kuipers Munneke, P., Ligtenberg, S. R. M., van den Broeke, M. R., and Vaughan, D. G. (2014). Firm air depletion as a precursor of Antarctic ice-shelf collapse. *J. Glaciol.*, 60(220), 205–214, <https://doi.org/10.3189/2014JoG13J183>.
- Kulp, S. A. and Strauss, B. H. (2019). New elevation data triple estimates of global vulnerability to sea-level rise and coastal flooding. *Nat. Commun.*, 10, 4844, <https://doi.org/10.1038/s41467-019-12808-z>.
- Kummu, M., de Moel, H., Salvucci, G., Viviroli, D., Ward, P. J., and Varis, O. (2016). Over the hills and further away from coast: global geospatial patterns of human and environment over the 20th–21st centuries. *Environ. Res. Lett.*, 11(3), 034010, <https://doi.org/10.1088/1748-9326/11/3/034010>.
- Larour, E., Schiermeier, J., Rignot, E., Seroussi, H., Morlighem, M., and Paden, J. (2012). Sensitivity Analysis of Pine Island Glacier ice flow using ISSM and DAKOTA. *J. Geophys. Res.*, 117(F2), F02009, <https://doi.org/10.1029/2011jf002146>.
- Larour, E., Seroussi, H., Adhikari, S., Ivins, E., Caron, L., Morlighem, M., and Schlegel, N. (2019). Slowdown in Antarctic mass loss from solid Earth and sea-level feedbacks. *Science*, 364(6444), eaav7908, <https://doi.org/10.1126/science.aav7908>.
- Larour, E., Utke, J., Csatho, B., Schenk, A., Seroussi, H., Morlighem, M., Rignot, E., Schlegel, N., and Khazendar, A. (2014). Inferred basal friction and surface mass balance of the North-east Greenland Ice Stream using data assimilation of ICESat (Ice Cloud and land Elevation Satellite) surface altimetry and ISSM (Ice Sheet System Model). *Cryosphere*, 8(6), 2335–2351, <https://doi.org/10.5194/tc-8-2335-2014>.
- Lazeroms, W. M. J., Jenkins, A., Gudmundsson, G. H., and van de Wal, R. S. W. (2018). Modelling present-day basal melt rates for Antarctic ice shelves using a parametrization of buoyant meltwater plumes. *Cryosphere*, 12(1), 49–70, <https://doi.org/10.5194/tc-12-49-2018>.
- Le Bars, D., Drijfhout, S., and de Vries, H. (2017). A high-end sea level rise probabilistic projection including rapid Antarctic ice sheet mass loss. *Environ. Res. Lett.*, 12(4), 044013, <https://doi.org/10.1088/1748-9326/aa6512>.
- Le Brocq, A., Payne, A. J., Siegert, M. J., and Alley, R. B. (2009). A subglacial water-flow model for West Antarctica. *J. Glaciol.*, 55(193), 879–888, <https://doi.org/10.3189/002214309790152564>.
- Le clec’h, S., Charbit, S., Quiquet, A., Fettweis, X., Dumas, C., Kageyama, M., Wyard, C., and Ritz, C. (2019). Assessment of the Greenland ice sheet–atmosphere feedbacks for the next century with a regional atmospheric model coupled to an ice sheet model. *Cryosphere*, 13(1), 373–395, <https://doi.org/10.5194/tc-13-373-2019>.

- Le Cozannet, G., Thiéblemont, R., Rohmer, J., Idier, D., Manceau, J.-C., and Quique, R. (2019). Low-End Probabilistic Sea-Level Projections. *Water*, 11(7), 1507, <https://doi.org/10.3390/w11071507>.
- Le Gratiet, L., Cannamela, C., and Iooss, B. (2014). A Bayesian Approach for Global Sensitivity Analysis of (Multifidelity) Computer Codes. *SIAM/ASA JUQ*, 2(1), 336–363, <https://doi.org/10.1137/130926869>.
- Le Gratiet, L., Marelli, S., and Sudret, B. (2017). Metamodel-Based Sensitivity Analysis: Polynomial Chaos Expansions and Gaussian Processes. In R. Ghanem, R. Higdon, and H. Owhadi (Eds.), *Handbook of Uncertainty Quantification*, chapter 38, (pp. 1289–1325). Cham, Switzerland: Springer, <https://doi.org/10.1007/978-3-319-12385-1>.
- Le Maître, O. P. and Knio, O. M. (2010). *Spectral Methods for Uncertainty Quantification: With Applications to Computational Fluid Dynamics*. Dordrecht, Holland: Springer Science + Business Media, <https://doi.org/10.1007/978-90-481-3520-2>.
- Le Meur, E. and Huybrechts, P. (1996). A comparison of different ways of dealing with isostasy: examples from modelling the Antarctic ice sheet during the last glacial cycle. *Ann. Glaciol.*, 23, 309–317, <https://doi.org/10.3189/s0260305500013586>.
- Lebrun, R. and Dutfoy, A. (2009). Do Rosenblatt and Nataf isoprobabilistic transformations really differ? *Probabilist. Eng. Mech.*, 24(4), 577–584, <https://doi.org/10.1016/j.probenmech.2009.04.006>.
- Lee, C. Y. and Oden, J. T. (1993). Theory and approximation of quasistatic frictional contact problems. *Comput. Methods Appl. Mech. Eng.*, 106(3), 407–429, [https://doi.org/10.1016/0045-7825\(93\)90098-i](https://doi.org/10.1016/0045-7825(93)90098-i).
- Lempert, R. J., Popper, S. W., and Bankes, S. C. (2003). *Shaping the Next One Hundred Years: New Methods for Quantitative, Long-Term Policy Analysis*. Santa Monica, CA: RAND.
- Lenaerts, J. T. M., Medley, B., van den Broeke, M. R., and Wouters, B. (2019). Observing and Modeling Ice Sheet Surface Mass Balance. *Rev. Geophys.*, 57(2), 376–420, <https://doi.org/10.1029/2018rg000622>.
- Lenaerts, J. T. M., Vizcaino, M., Fyke, J., van Kampenhout, L., and van den Broeke, M. R. (2016). Present-day and future Antarctic ice sheet climate and surface mass balance in the Community Earth System Model. *Clim. Dyn.*, 47(5-6), 1367–1381, <https://doi.org/10.1007/s00382-015-2907-4>.
- Lenton, T. M., Held, H., Kriegler, E., Hall, J. W., Lucht, W., Rahmstorf, S., and Schellnhuber, H. J. (2008). Tipping elements in the Earth's climate system. *PNAS*, 105(6), 1786–1793, <https://doi.org/10.1073/pnas.0705414105>.
- Levermann, A., Albrecht, T., Winkelmann, R., Martin, M. A., Haseloff, M., and Joughin, I. (2012). Kinematic first-order calving law implies potential for abrupt ice-shelf retreat. *Cryosphere*, 6(2), 273–286, <https://doi.org/10.5194/tc-6-273-2012>.

- Levermann, A., Winkelmann, R., Albrecht, T., Goelzer, H., Golledge, N. R., Greve, R., Huybrechts, P., Jordan, J., Leguy, G., Martin, D., Morlighem, M., Pattyn, F., Pollard, D., Quiquet, A., Rodehacke, C., Seroussi, H., Sutter, J., Zhang, T., Van Breedam, J., DeConto, R., Dumas, C., Garbe, J., Gudmundsson, G. H., Hoffman, M. J., Humbert, A., Kleiner, T., Lipscomb, W., Meinshausen, M., Ng, E., Perego, M., Price, S. F., Saito, F., Schlegel, N.-J., Sun, S., and van de Wal, R. S. W. (2019). Projecting Antarctica's contribution to future sea level rise from basal ice-shelf melt using linear response functions of 16 ice sheet models (LARMIP-2). *Earth Syst. Dynam. Discuss.*, <https://doi.org/10.5194/esd-2019-23>. Under review.
- Levermann, A., Winkelmann, R., Nowicki, S., Fastook, J. L., Frieler, K., Greve, R., Hellmer, H. H., Martin, M. A., Meinshausen, M., Mengel, M., Payne, A. J., Pollard, D., Sato, T., Timmermann, R., Wang, W. L., and Bindschadler, R. A. (2014). Projecting Antarctic ice discharge using response functions from SeaRISE ice-sheet models. *Earth Syst. Dynam.*, 5(2), 271–293, <https://doi.org/10.5194/esd-5-271-2014>.
- Lewis, E. L. and Perkin, R. G. (1986). Ice pumps and their rates. *J. Geophys. Res.*, 91(C10), 11756–11762, <https://doi.org/10.1029/jc091ic10p11756>.
- Li, J. and Xiu, D. (2010). Evaluation of failure probability via surrogate models. *J. Comput. Phys.*, 229(23), 8966–8980, <https://doi.org/10.1016/j.jcp.2010.08.022>.
- Ligtenberg, S. R. M., van de Berg, W. J., van den Broeke, M. R., Rae, J. G. L., and van Meijgaard, E. (2013). Future surface mass balance of the Antarctic ice sheet and its influence on sea level change, simulated by a regional atmospheric climate model. *Clim. Dynam.*, 41(3–4), 867–884, <https://doi.org/10.1007/s00382-013-1749-1>.
- Lindgren, G. and Rychlik, I. (1995). How Reliable Are Contour Curves? Confidence Sets for Level Contours. *Bernoulli*, 1(4), 301–319, <https://doi.org/10.2307/3318485>.
- Link, W. A. and Barker, R. J. (2006). Model Weights and the Foundations of Multimodel Inference. *Ecology*, 87(10), 2626–2635, [https://doi.org/10.1890/0012-9658\(2006\)87\[2626:MWATFO\]2.0.CO;2](https://doi.org/10.1890/0012-9658(2006)87[2626:MWATFO]2.0.CO;2).
- Lipscomb, W. H., Price, S. F., Hoffman, M. J., Leguy, G. R., Bennett, A. R., Bradley, S. L., Evans, K. J., Fyke, J. G., Kennedy, J. H., Perego, M., Ranken, D. M., Sacks, W. J., Salinger, A. G., Vargo, L. J., and Worley, P. H. (2019). Description and evaluation of the Community Ice Sheet Model (CISM) v2.1. *Geosci. Model Dev.*, 12(1), 387–424, <https://doi.org/10.5194/gmd-12-387-2019>.
- Little, C. M., Urban, N. M., and Oppenheimer, M. (2013). Probabilistic framework for assessing the ice sheet contribution to sea level change. *PNAS*, 110(9), 3264–3269, <https://doi.org/10.1073/pnas.1214457110>.
- Liu, Y., Moore, J. C., Cheng, X., Gladstone, R. M., Bassis, J. N., Liu, H., Wen, J., and Hui, F. (2015). Ocean-driven thinning enhances iceberg calving and retreat of Antarctic ice shelves. *PNAS*, 112(11), 3263–3268, <https://doi.org/10.1073/pnas.1415137112>.
- Luo, X., Lu, Z., and Xu, X. (2014). Non-parametric kernel estimation for the ANOVA decomposition and sensitivity analysis. *Reliab. Eng. Syst. Safe.*, 130, 140–148, <https://doi.org/10.1016/j.ress.2014.06.002>.

- Ma, Y., Gagliardini, O., Ritz, C., Gillet-Chaulet, F., Durand, G., and Montagnat, M. (2010). Enhancement factors for grounded ice and ice shelves inferred from an anisotropic ice-flow model. *J. Glaciol.*, 56(199), 805–812, <https://doi.org/10.3189/002214310794457209>.
- Ma, Y., Genton, M. G., and Parzen, E. (2011). Asymptotic properties of sample quantiles of discrete distributions. *Ann. I. Stat. Math.*, 63(2), 227–243, <https://doi.org/10.1007/s10463-008-0215-z>.
- Ma, Y., Tripathy, C. S., and Bassis, J. N. (2017). Bounds on the calving cliff height of marine terminating glaciers. *Geophys. Res. Lett.*, 44(3), 1369–1375, <https://doi.org/10.1002/2016gl071560>.
- MacAyeal, D. R. (1989). Large-Scale Ice Flow over a Viscous Basal Sediment: Theory and Application to Ice Stream B, Antarctica. *J. Geophys. Res.*, 94(B4), 4071–4087, <https://doi.org/10.1029/jb094ib04p04071>.
- Mantelli, E., Bertagni, M. B., and Ridolfi, L. (2016). Stochastic ice stream dynamics. *PNAS*, 113(32), E4594–E4600, <https://doi.org/10.1073/pnas.1600362113>.
- Marchau, V. A. W. J., Walker, W. E., Bloemen, P. J. T. M., and Popper, S. W., Eds. (2019). *Decision Making under Deep Uncertainty: From Theory to Practice*. Cham, Switzerland: Springer, <https://doi.org/10.1007/978-3-030-05252-2>.
- Maris, M. N. A., de Boer, B., Ligtenberg, S. R. M., Crucifix, M., van de Berg, W. J., and Oerlemans, J. (2014). Modelling the evolution of the Antarctic ice sheet since the last interglacial. *Cryosphere*, 8(4), 1347–1360, <https://doi.org/10.5194/tc-8-1347-2014>.
- Marotzke, J. (2018). Quantifying the irreducible uncertainty in near-term climate projections. *WIREs Clim. Change*, 10(1), e563, <https://doi.org/10.1002/wcc.563>.
- Marrel, A. (2017). *Contributions to the uncertainty management in numerical simulations: Statistical methods for metamodeling and sensitivity analysis*. Habilitation thesis, Université Toulouse III - Paul Sabatier, Toulouse, France.
- Marrel, A., Iooss, B., Laurent, B., and Roustant, O. (2009). Calculations of Sobol indices for the Gaussian process metamodel. *Reliab. Eng. Syst. Safe.*, 94(3), 742–751, <https://doi.org/10.1016/j.res.2008.07.008>.
- Martin, M. A., Winkelmann, R., Haseloff, M., Albrecht, T., Bueler, E., Khroulev, C., and Levermann, A. (2011). The Potsdam Parallel Ice Sheet Model (PISM-PIK) – Part 2: Dynamic equilibrium simulation of the Antarctic ice sheet. *Cryosphere*, 5(3), 727–740, <https://doi.org/10.5194/tc-5-727-2011>.
- Martín-Español, A., Zammit-Mangion, A., Clarke, P. J., Flament, T., Helm, V., King, M. A., Luthcke, S. B., Petrie, E., Rémy, F., Schön, N., Wouters, B., and Bamber, J. L. (2016). Spatial and temporal Antarctic Ice Sheet mass trends, glacio-isostatic adjustment, and surface processes from a joint inversion of satellite altimeter, gravity, and GPS data. *J. Geophys. Res. Earth Surf.*, 121(2), 182–200, <https://doi.org/10.1002/2015jf003550>.

- Martins, J. A. C. and Oden, J. T. (1983). A numerical analysis of a class of problems in elastodynamics with friction. *Comput. Methods Appl. Mech. Eng.*, 40(3), 327–360, [https://doi.org/10.1016/0045-7825\(83\)90105-6](https://doi.org/10.1016/0045-7825(83)90105-6).
- Martos, Y. M., Catalán, M., Jordan, T. A., Golynsky, A., Golynsky, D., Eagles, G., and Vaughan, D. G. (2017). Heat Flux Distribution of Antarctica Unveiled. *Geophys. Res. Lett.*, 44(22), 11,417–11,426, <https://doi.org/10.1002/2017gl075609>.
- Mathew, T. P. A. (2008). *Domain Decomposition Methods for the Numerical Solution of Partial Differential Equations*. Berlin, Germany: Springer-Verlag, <https://doi.org/10.1007/978-3-540-77209-5>.
- Matsuoka, K., Hindmarsh, R. C. A., Moholdt, G., Bentley, M. J., Pritchard, H. D., Brown, J., Conway, H., Drews, R., Durand, G., Goldberg, D., Hattermann, T., Kingslake, J., Lenaerts, J. T., Martín, C., Mulvaney, R., Nicholls, K. W., Pattyn, F., Ross, N., Scambos, T., and Whitehouse, P. L. (2015). Antarctic ice rises and rumples: Their properties and significance for ice-sheet dynamics and evolution. *Earth-Sci. Rev.*, 150, 724–745, <https://doi.org/10.1016/j.earscirev.2015.09.004>.
- McKay, M. D., Beckman, R. J., and Conover, W. J. (1979). A Comparison of Three Methods for Selecting Values of Input Variables in the Analysis of Output from a Computer Code. *Technometrics*, 21(2), 239–245.
- Merkens, J.-L., Reimann, L., Hinkel, J., and Vafeidis, A. T. (2016). Gridded population projections for the coastal zone under the Shared Socioeconomic Pathways. *Global Planet. Change*, 145, 57–66, <https://doi.org/10.1016/j.gloplacha.2016.08.009>.
- Meyer, C. R. and Minchew, B. M. (2018). Temperate ice in the shear margins of the Antarctic Ice Sheet: Controlling processes and preliminary locations. *Earth Planet. Sc. Lett.*, 498, 17–26, <https://doi.org/10.1016/j.epsl.2018.06.028>.
- Milillo, P., Rignot, E., Rizzoli, P., Scheuchl, B., Mouginot, J., Bueso-Bello, J., and Prats-Iraola, P. (2019). Heterogeneous retreat and ice melt of Thwaites Glacier, West Antarctica. *Sci. Adv.*, 5(1), eaau3433, <https://doi.org/10.1126/sciadv.aau3433>.
- Moholdt, G., Padman, L., and Fricker, H. A. (2014). Basal mass budget of Ross and Filchner-Ronne ice shelves, Antarctica, derived from Lagrangian analysis of ICESat altimetry. *J. Geophys. Res. Earth Surf.*, 119(11), 2361–2380, <https://doi.org/10.1002/2014jfr003171>.
- Molchanov, I. (2017). *Theory of Random Sets*. London, UK: Springer-Verlag, 2nd edition, <https://doi.org/10.1007/978-1-4471-7349-6>.
- Morland, L. W. (1987). Unconfined Ice-Shelf Flow. In C. J. van der Veen and J. Oerlemans (Eds.), *Dynamics of the West Antarctic Ice Sheet*, (pp. 99–116). Dordrecht, Holland: D. Reidel Publishing Company, [https://doi.org/10.1007/978-94-009-3745-1\\_6](https://doi.org/10.1007/978-94-009-3745-1_6).
- Morlighem, M., Rignot, E., Binder, T., Blankenship, D., Drews, R., Eagles, G., Eisen, O., Ferraccioli, F., Forsberg, R., Fretwell, P., Goel, V., Greenbaum, J. S., Gudmundsson, H., Guo, J., Helm, V., Hofstede, C., Howat, I., Humbert, A., Jokat, W., Karlsson, N. B., Lee, W. S., Matsuoka, K., Millan, R., Mouginot, J., Paden, J., Pattyn, F., Roberts, J., Rosier,

- S., Ruppel, A., Seroussi, H., Smith, E. C., Steinhage, D., Sun, B., van den Broeke, M. R., van Ommen, T. D., van Wessem, M., and Young, D. A. (2019). Deep glacial troughs and stabilizing ridges unveiled beneath the margins of the Antarctic ice sheet. *Nat. Geosci.*, <https://doi.org/10.1038/s41561-019-0510-8>.
- Morlighem, M., Rignot, E., Seroussi, H., Larour, E., Dhia, H. B., and Aubry, D. (2010). Spatial patterns of basal drag inferred using control methods from a full-Stokes and simpler models for Pine Island Glacier, West Antarctica. *Geophys. Res. Lett.*, 37(14), L14502, <https://doi.org/10.1029/2010gl043853>.
- Morlighem, M., Seroussi, H., Larour, E., and Rignot, E. (2013). Inversion of basal friction in Antarctica using exact and incomplete adjoints of a higher-order model. *J. Geophys. Res. Earth Surf.*, 118(3), 1746–1753, <https://doi.org/10.1002/jgrf.20125>.
- Morokoff, W. J. and Caflisch, R. E. (1995). Quasi-Monte Carlo Integration. *J. Comput. Phys.*, 122(2), 218–230, <https://doi.org/10.1006/jcph.1995.1209>.
- Mouginot, J., Rignot, E., and Scheuchl, B. (2014). Sustained increase in ice discharge from the Amundsen Sea Embayment, West Antarctica, from 1973 to 2013. *Geophys. Res. Lett.*, 41(5), 1576–1584, <https://doi.org/10.1002/2013gl059069>.
- Moustapha, M., Sudret, B., Bourinet, J.-M., and Guillaume, B. (2016). Quantile-based optimization under uncertainties using adaptive Kriging surrogate models. *Struct. Multidiscip. O.*, 54(6), 1403–1421, <https://doi.org/10.1007/s00158-016-1504-4>.
- Mulder, T. E., Baars, S., Wubs, F. W., and Dijkstra, H. A. (2018). Stochastic marine ice sheet variability. *J. Fluid Mech.*, 843, 748–777, <https://doi.org/10.1017/jfm.2018.148>.
- Myhre, G., Shindell, D., Bréon, F.-M., Collins, W., Fuglestedt, J., Huang, J., Koch, D., Lamarque, J.-F., Lee, D., Mendoza, B., Nakajima, T., Robock, A., Stephens, G., Takemura, T., and Zhang, H. (2013). Anthropogenic and Natural Radiative Forcing. In T. F. Stocker, D. Qin, G.-K. Plattner, M. Tignor, S. K. Allen, J. Boschung, A. Nauels, Y. Xi, V. Bex, and P. M. Midgley (Eds.), *Climate Change 2013: The Physical Science Basis. Contribution of Working Group I to the Fifth Assessment Report of the Intergovernmental Panel on Climate Change*, chapter 8, (pp. 659–740). Cambridge, United Kingdom: Cambridge University Press, <https://doi.org/10.1017/CBO9781107415324.018>.
- Nadai (1963). *Theory of flow and fracture of solids*, volume 2. New York, NY: McGraw-Hill Book Company.
- Nakićenović, N., Alcamo, J., Davis, G., de Vries, B., Fenhann, J., Gaffin, S., Gregory, K., Grübler, A., Jung, T. Y., Kram, T., La Rovere, E. L., Michaelis, L., Mori, S., Morita, T., Pepper, W., Pitcher, H., Price, L., Riahi, K., Roehrl, A., Rogner, H.-H., Sankovski, A., Schlesinger, M., Shukla, P., Smith, S., Swart, R., van Rooijen, S., Victor, N., and Dadi, Z. (2000). *Special Report on Emission Scenarios*. Cambridge, United Kingdom: Cambridge University Press.
- Nataf, A. (1962). Détermination des distributions de probabilités dont les marges sont données. *Comptes Rendus de l'Académie des Sciences*, 225, 42–43.

- Naughten, K. A., Meissner, K. J., Galton-Fenzi, B. K., England, M. H., Timmermann, R., and Hellmer, H. H. (2018). Future Projections of Antarctic Ice Shelf Melting Based on CMIP5 Scenarios. *J. Climate*, 31(13), 5243–5261, <https://doi.org/10.1175/jcli-d-17-0854.1>.
- Nelsen, R. B. (2006). *An Introduction to Copulas*. New York, NY: Springer Science+Business Media, 2nd edition, <https://doi.org/10.1007/0-387-28678-0>.
- Neumann, B., Vafeidis, A. T., Zimmermann, J., and Nicholls, R. J. (2015). Future Coastal Population Growth and Exposure to Sea-Level Rise and Coastal Flooding - A Global Assessment. *PLOS ONE*, 10(3), e0118571, <https://doi.org/10.1371/journal.pone.0118571>.
- Nguyen, H. T. and Walker, E. A. (2006). *A First Course in Fuzzy Logic*. Boca Raton, FL: Chapman & Hall/CRC, 3rd edition.
- Niederreiter, H. (1992). *Random Number Generation and Quasi-Monte Carlo Methods*. Philadelphia, PA: SIAM, <https://doi.org/10.1137/1.9781611970081>.
- Nocedal, J. and Wright, S. J. (2006). *Numerical Optimization*. New York, NY: Springer, 2nd edition.
- Nowicki, S., Bindschadler, R. A., Abe-Ouchi, A., Aschwanden, A., Bueler, E., Choi, H., Fastook, J., Granzow, G., Greve, R., Gutowski, G., Herzfeld, U., Jackson, C., Johnson, J., Khroulev, C., Larour, E., Levermann, A., Lipscomb, W. H., Martin, M. A., Morlighem, M., Parizek, B. R., Pollard, D., Price, S. F., Ren, D., Rignot, E., Saito, F., Sato, T., Seddik, H., Seroussi, H., Takahashi, K., Walker, R., and Wang, W. L. (2013). Insights into spatial sensitivities of ice mass response to environmental change from the SeaRISE ice sheet modeling project I: Antarctica. *J. Geophys. Res. Earth Surf.*, 118(2), 1002–1024, <https://doi.org/10.1002/jgrf.20081>.
- Nowicki, S. and Seroussi, H. (2018). Projections of Future Sea Level Contributions from the Greenland and Antarctic Ice Sheets: Challenges Beyond Dynamical Ice Sheet Modeling. *Oceanography*, 31(2), 109–117, <https://doi.org/10.5670/oceanog.2018.216>.
- Nowicki, S. M. J., Payne, A., Larour, E., Seroussi, H., Goelzer, H., Lipscomb, W., Gregory, J., Abe-Ouchi, A., and Shepherd, A. (2016). Ice Sheet Model Intercomparison Project (ISMIP6) contribution to CMIP6. *Geosci. Model Dev.*, 9(12), 4521–4545, <https://doi.org/10.5194/gmd-9-4521-2016>.
- Oakley, J. E. and O'Hagan, A. (2004). Probabilistic sensitivity analysis of complex models: a Bayesian approach. *J. Royal Stat. Soc. B*, 66(3), 751–769, <https://doi.org/10.1111/j.1467-9868.2004.05304.x>.
- Oden, J. T. and Pires, E. B. (1983). Nonlocal and Nonlinear Friction Laws and Variational Principles for Contact Problems in Elasticity. *J. Appl. Mech.*, 50(1), 67–76, <https://doi.org/10.1115/1.3167019>.
- Olbers, D. and Hellmer, H. (2010). A box model of circulation and melting in ice shelf caverns. *Ocean Dynam.*, 60(1), 141–153, <https://doi.org/10.1007/s10236-009-0252-z>.
- Owen, A. B. (2013). Variance Components and Generalized Sobol' Indices. *SIAM/ASA JUQ*, 1(1), 19–41, <https://doi.org/10.1137/120876782>.

- Owen, A. B. (2014). Sobol' Indices and Shapley Value. *SIAM/ASA JUQ*, 2(1), 245–251, <https://doi.org/10.1137/130936233>.
- Palerme, C., Genthon, C., Claud, C., Kay, J. E., Wood, N. B., and L'Ecuyer, T. (2017). Evaluation of current and projected Antarctic precipitation in CMIP5 models. *Clim. Dynam.*, 48(1–2), 225–239, <https://doi.org/10.1007/s00382-016-3071-1>.
- Parizek, B. R., Christianson, K., Alley, R. B., Voytenko, D., Vaňková, I., Dixon, T. H., Walker, R. T., and Holland, D. M. (2019). Ice-cliff failure via retrogressive slumping. *Geology*, 47(5), 449–452, <https://doi.org/10.1130/g45880.1>.
- Parizek, B. R., Christianson, K., Anandakrishnan, S., Alley, R. B., Walker, R. T., Edwards, R. A., Wolfe, D. S., Bertini, G. T., Rinehart, S. K., Bindshadler, R. A., and Nowicki, S. M. J. (2013). Dynamic (in)stability of Thwaites Glacier, West Antarctica. *J. Geophys. Res. Earth Surf.*, 118(2), 638–655, <https://doi.org/10.1002/jgrf.20044>.
- Park, J. W., Gourmelen, N., Shepherd, A., Kim, S. W., Vaughan, D. G., and Wingham, D. J. (2013). Sustained retreat of the Pine Island Glacier. *Geophys. Res. Lett.*, 40(10), 2137–2142, <https://doi.org/10.1002/grl.50379>.
- Parzen, E. (2004). Quantile Probability and Statistical Data Modeling. *Statist. Sci.*, 19(4), 652–662, <https://doi.org/10.1214/088342304000000387>.
- Pattyn, F. (2003). A new three-dimensional higher-order thermomechanical ice sheet model: Basic sensitivity, ice stream development, and ice flow across subglacial lakes. *J. Geophys. Res.*, 108(B8), 2382, <https://doi.org/10.1029/2002jb002329>.
- Pattyn, F. (2010). Antarctic subglacial conditions inferred from a hybrid ice sheet/ice stream model. *Earth Planet. Sc. Lett.*, 295(3–4), 451–461, <https://doi.org/10.1016/j.epsl.2010.04.025>.
- Pattyn, F. (2017). Sea-level response to melting of Antarctic ice shelves on multi-centennial timescales with the fast Elementary Thermomechanical Ice Sheet model (f.ETISH v1.0). *Cryosphere*, 11(4), 1851–1878, <https://doi.org/10.5194/tc-11-1851-2017>.
- Pattyn, F. (2018). The paradigm shift in Antarctic ice sheet modelling. *Nat. Commun.*, 9, 2728, <https://doi.org/10.1038/s41467-018-05003-z>.
- Pattyn, F. and Durand, G. (2013). Why marine ice sheet model predictions may diverge in estimating future sea level rise. *Geophys. Res. Lett.*, 40(16), 4316–4320, <https://doi.org/10.1002/grl.50824>.
- Pattyn, F., Favier, L., Sun, S., and Durand, G. (2017). Progress in Numerical Modeling of Antarctic Ice-Sheet Dynamics. *Curr. Clim. Change Rep.*, 3(3), 174–184, <https://doi.org/10.1007/s40641-017-0069-7>.
- Pattyn, F., Perichon, L., Durand, G., Favier, L., Gagliardini, O., Hindmarsh, R. C. A., Zwinger, T., Albrecht, T., Cornford, S., Docquier, D., Fürst, J. J., Goldberg, D., Gudmundsson, G. H., Humbert, A., Hütten, M., Huybrechts, P., Jouvett, G., Kleiner, T., Larour, E., Martin, D., Morlighem, M., Payne, A. J., Pollard, D., Rückamp, M., Rybak, O., Seroussi, H., Thoma,

- M., and Wilkens, N. (2013). Grounding-line migration in plan-view marine ice-sheet models: results of the ice2sea MISMIP3d intercomparison. *J. Glaciol.*, 59(215), 410–422, <https://doi.org/10.3189/2013jog12j129>.
- Pattyn, F., Ritz, C., Hanna, E., Asay-Davis, X., DeConto, R., Durand, G., Favier, L., Fettweis, X., Goelzer, H., Golledge, N. R., Munneke, P. K., Lenaerts, J. T. M., Nowicki, S., Payne, A. J., Robinson, A., Seroussi, H., Trusel, L. D., and van den Broeke, M. (2018). The Greenland and Antarctic ice sheets under 1.5 °C global warming. *Nat. Clim. Change.*, 8(12), 1053–1061, <https://doi.org/10.1038/s41558-018-0305-8>.
- Pattyn, F., Schoof, C., Perichon, L., Hindmarsh, R. C. A., Bueler, E., de Fleurian, B., Durand, G., Gagliardini, O., Gladstone, R., Goldberg, D., Gudmundsson, G. H., Huybrechts, P., Lee, V., Nick, F. M., Payne, A. J., Pollard, D., Rybak, O., Saito, F., and Vieli, A. (2012). Results of the Marine Ice Sheet Model Intercomparison Project, MISMIP. *Cryosphere*, 6(3), 573–588, <https://doi.org/10.5194/tc-6-573-2012>.
- Peherstorfer, B., Willcox, K., and Gunzburger, M. (2018). Survey of Multifidelity Methods in Uncertainty Propagation, Inference, and Optimization. *SIAM Rev.*, 60(3), 550–591, <https://doi.org/10.1137/16m1082469>.
- Pelle, T., Morlighem, M., and Bondzio, J. H. (2019). Brief communication: PICOP, a new ocean melt parameterization under ice shelves combining PICO and a plume model. *Cryosphere*, 13(3), 1043–1049, <https://doi.org/10.5194/tc-13-1043-2019>.
- Perego, M., Price, S., and Stadler, G. (2014). Optimal initial conditions for coupling ice sheet models to Earth system models. *J. Geophys. Res. Earth Surf.*, 119(9), 1894–1917, <https://doi.org/10.1002/2014jf003181>.
- Petra, N., Martin, J., Stadler, G., and Ghattas, O. (2014). A Computational Framework for Infinite-Dimensional Bayesian Inverse Problems, Part II: Stochastic Newton MCMC with Application to Ice Sheet Flow Inverse Problems. *SIAM J. Sci. Comput.*, 36(4), A1525–A1555, <https://doi.org/10.1137/130934805>.
- Petra, N., Zhu, H., Stadler, G., Hughes, T. J., and Ghattas, O. (2012). An inexact Gauss-Newton method for inversion of basal sliding and rheology parameters in a nonlinear Stokes ice sheet model. *J. Glaciol.*, 58(211), 889–903, <https://doi.org/10.3189/2012jog11j182>.
- Phipps, E., D’Elia, M., Edwards, H. C., Hoemmen, M., Hu, J., and Rajamanickam, S. (2017). Embedded Ensemble Propagation for Improving Performance, Portability, and Scalability of Uncertainty Quantification on Emerging Computational Architectures. *SIAM J. Sci. Comput.*, 39(2), C162–C193, <https://doi.org/10.1137/15m1044679>.
- Picheny, V., Wagner, T., and Ginsbourger, D. (2013). A benchmark of kriging-based infill criteria for noisy optimization. *Struct. Multidiscip. O.*, 48(3), 607–626, <https://doi.org/10.1007/s00158-013-0919-4>.
- Polfeldt, T. (1999). On the quality of contour maps. *Environmetrics*, 10(6), 785–790, [https://doi.org/10.1002/\(SICI\)1099-095X\(199911/12\)10:6<785::AID-ENV399>3.0.CO;2-7](https://doi.org/10.1002/(SICI)1099-095X(199911/12)10:6<785::AID-ENV399>3.0.CO;2-7).

- Pollard, D., Chang, W., Haran, M., Applegate, P., and DeConto, R. (2016). Large ensemble modeling of the last deglacial retreat of the West Antarctic Ice Sheet: comparison of simple and advanced statistical techniques. *Geosci. Model Dev.*, 9(5), 1697–1723, <https://doi.org/10.5194/gmd-9-1697-2016>.
- Pollard, D. and DeConto, R. M. (2009). Modelling West Antarctic ice sheet growth and collapse through the past five million years. *Nature*, 458(7236), 329–332, <https://doi.org/10.1038/nature07809>.
- Pollard, D. and DeConto, R. M. (2012a). Description of a hybrid ice sheet-shelf model, and application to Antarctica. *Geosci. Model Dev.*, 5(5), 1273–1295, <https://doi.org/10.5194/gmd-5-1273-2012>.
- Pollard, D. and DeConto, R. M. (2012b). A simple inverse method for the distribution of basal sliding coefficients under ice sheets, applied to Antarctica. *Cryosphere*, 6(5), 953–971, <https://doi.org/10.5194/tc-6-953-2012>.
- Pollard, D., DeConto, R. M., and Alley, R. B. (2015). Potential Antarctic Ice Sheet retreat driven by hydrofracturing and ice cliff failure. *Earth Planet. Sc. Lett.*, 412, 112–121, <https://doi.org/10.1016/j.epsl.2014.12.035>.
- Pollard, D., Gomez, N., and Deconto, R. M. (2017). Variations of the Antarctic Ice Sheet in a Coupled Ice Sheet-Earth-Sea Level Model: Sensitivity to Viscoelastic Earth Properties. *J. Geophys. Res. Earth Surf.*, 122(11), 2124–2138, <https://doi.org/10.1002/2017jf004371>.
- Popp, A. (2012). *Mortar Methods for Computational Contact Mechanics and General Interface Problems*. PhD thesis, Technische Universität München, Munich, Germany.
- Pritchard, H. D., Ligtenberg, S. R. M., Fricker, H. A., Vaughan, D. G., van den Broeke, M. R., and Padman, L. (2012). Antarctic ice-sheet loss driven by basal melting of ice shelves. *Nature*, 484(7395), 502–505, <https://doi.org/10.1038/nature10968>.
- Purich, A., England, M. H., Cai, W., Sullivan, A., and Durack, P. J. (2018). Impacts of Broad-Scale Surface Freshening of the Southern Ocean in a Coupled Climate Model. *J. Climate*, 31(7), 2613–2632, <https://doi.org/10.1175/jcli-d-17-0092.1>.
- Purucker, M. (2013). Geothermal heat flux data set based on low resolution observations collected by the CHAMP satellite between 2000 and 2010, and produced from the MF-6 model following the technique described in Fox Maule et al. (2005). Available at [https://core2.gsfc.nasa.gov/research/purucker/heatflux\\_updates.html](https://core2.gsfc.nasa.gov/research/purucker/heatflux_updates.html), last accessed: August 2017.
- Quarteroni, A. and Valli, A. (1999). *Domain Decomposition Methods for Partial Differential Equations*. Cambridge, United Kingdom: Clarendon Press.
- Quiquet, A., Dumas, C., Ritz, C., Peyaud, V., and Roche, D. M. (2018). The GRISLI ice sheet model (version 2.0): calibration and validation for multi-millennial changes of the Antarctic ice sheet. *Geosci. Model Dev.*, 11(12), 5003–5025, <https://doi.org/10.5194/gmd-11-5003-2018>.
- Rahman, S. (2016). The  $f$ -Sensitivity Index. *SIAM/ASA JUQ*, 4(1), 130–162, <https://doi.org/10.1137/140997774>.

- Rasmussen, C. E. and Williams, C. K. I. (2006). *Gaussian Processes for Machine Learning*. Cambridge, MA: The MIT Press.
- Reese, R., Albrecht, T., Mengel, M., Asay-Davis, X., and Winkelmann, R. (2018a). Antarctic sub-shelf melt rates via PICO. *Cryosphere*, 12(6), 1969–1985, <https://doi.org/10.5194/tc-12-1969-2018>.
- Reese, R., Winkelmann, R., and Gudmundsson, G. H. (2018b). Grounding-line flux formula applied as a flux condition in numerical simulations fails for buttressed Antarctic ice streams. *Cryosphere*, 12(10), 3229–3242, <https://doi.org/10.5194/tc-12-3229-2018>.
- Rignot, E., Jacobs, S., Mouginot, J., and Scheuchl, B. (2013). Ice-Shelf Melting Around Antarctica. *Science*, 341(6143), 266–270, <https://doi.org/10.1126/science.1235798>.
- Rignot, E., Mouginot, J., Morlighem, M., Seroussi, H., and Scheuchl, B. (2014). Widespread, rapid grounding line retreat of Pine Island, Thwaites, Smith, and Kohler glaciers, West Antarctica, from 1992 to 2011. *Geophys. Res. Lett.*, 41(10), 3502–3509, <https://doi.org/10.1002/2014gl060140>.
- Rignot, E., Mouginot, J., and Scheuchl, B. (2011). Ice Flow of the Antarctic Ice Sheet. *Science*, 333(6048), 1427–1430, <https://doi.org/10.1126/science.1208336>.
- Rignot, E., Mouginot, J., Scheuchl, B., van den Broeke, M., van Wessem, M. J., and Morlighem, M. (2019). Four decades of Antarctic Ice Sheet mass balance from 1979–2017. *PNAS*, 116(4), 1095–1103, <https://doi.org/10.1073/pnas.1812883116>.
- Ritz, C., Edwards, T. L., Durand, G., Payne, A. J., Peyaud, V., and Hindmarsh, R. C. A. (2015). Potential sea-level rise from Antarctic ice-sheet instability constrained by observations. *Nature*, 528(7580), 115–118, <https://doi.org/10.1038/nature16147>.
- Robel, A. A., Seroussi, H., and Roe, G. H. (2019). Marine ice sheet instability amplifies and skews uncertainty in projections of future sea-level rise. *PNAS*, 116(30), 14887–14892, <https://doi.org/10.1073/pnas.1904822116>.
- Robert, C. P. and Casella, G. (2013). *Monte Carlo Statistical Methods*. New York, NY: Springer Science & Business Media, 2nd edition, <https://doi.org/10.1007/978-1-4757-4145-2>.
- Rommelaere, V. and Ritz, C. (1996). A thermomechanical model of ice-shelf flow. *Ann. Glaciol.*, 23, 13–20, <https://doi.org/10.3189/s0260305500013203>.
- Rosenblatt, M. (1952). Remarks on a Multivariate Transformation. *Ann. Math. Stat.*, 23(3), 470–472, <https://doi.org/10.1214/aoms/1177729394>.
- Ruckert, K. L., Shaffer, G., Pollard, D., Guan, Y., Wong, T. E., Forest, C. E., and Keller, K. (2017). Assessing the Impact of Retreat Mechanisms in a Simple Antarctic Ice Sheet Model Using Bayesian Calibration. *PLoS ONE*, 12(1), e0170052, <https://doi.org/10.1371/journal.pone.0170052>.
- Saito, F., Abe-Ouchi, A., Takahashi, K., and Blatter, H. (2016). SeaRISE experiments revisited: potential sources of spread in multi-model projections of the Greenland ice sheet. *Cryosphere*, 10(1), 43–63, <https://doi.org/10.5194/tc-10-43-2016>.

- Saltelli, A. (2002). Making best use of model evaluations to compute sensitivity indices. *Comput. Phys. Commun.*, 145(2), 280–297, [https://doi.org/10.1016/s0010-4655\(02\)00280-1](https://doi.org/10.1016/s0010-4655(02)00280-1).
- Saltelli, A., Ratto, M., Andres, T., Campolongo, F., Cariboni, J., Gatelli, D., Saisana, M., and Tarantola, S. (2008). *Global Sensitivity Analysis: The Primer*. West Sussex, United Kingdom: John Wiley & Sons.
- Santner, T. J., Williams, B. J., and Notz, W. I. (2003). *The Design and Analysis of Computer Experiments*. New York, NY: Springer Science + Business Media, <https://doi.org/10.1007/978-1-4757-3799-8>.
- Scambos, T. A., Bell, R. E., Alley, R. B., Anandakrishnan, S., Bromwich, D. H., Brunt, K., Christianson, K., Creyts, T., Das, S. B., DeConto, R., Dutrieux, P., Fricker, H. A., Holland, D., MacGregor, J., Medley, B., Nicolas, J. P., Pollard, D., Siegfried, M. R., Smith, A. M., Steig, E. J., Trusel, L. D., Vaughan, D. G., and Yager, P. L. (2017). How much, how fast?: A science review and outlook for research on the instability of Antarctica's Thwaites Glacier in the 21st century. *Global Planet. Change*, 153, 16–34, <https://doi.org/10.1016/j.gloplacha.2017.04.008>.
- Schäfer, M., Zwinger, T., Christoffersen, P., Gillet-Chaulet, F., Laakso, K., Pettersson, R., Pohjola, V. A., Strozzi, T., and Moore, J. C. (2012). Sensitivity of basal conditions in an inverse model: Vestfonna ice cap, Nordaustlandet/Svalbard. *Cryosphere*, 6(4), 771–783, <https://doi.org/10.5194/tc-6-771-2012>.
- Schlegel, N.-J., Seroussi, H., Schodlok, M. P., Larour, E. Y., Boening, C., Limonadi, D., Watkins, M. M., Morlighem, M., and van den Broeke, M. R. (2018). Exploration of Antarctic Ice Sheet 100-year contribution to sea level rise and associated model uncertainties using the ISSM framework. *Cryosphere*, 12(11), 3511–3534, <https://doi.org/10.5194/tc-12-3511-2018>.
- Schmidtko, S., Heywood, K. J., Thompson, A. F., and Aoki, S. (2014). Multidecadal warming of Antarctic waters. *Science*, 346(6214), 1227–1231, <https://doi.org/10.1126/science.1256117>.
- Schoof, C. (2005). The effect of cavitation on glacier sliding. *P. Roy. Soc. A-Math. Phys.*, 461(2055), 609–627, <https://doi.org/10.1098/rspa.2004.1350>.
- Schoof, C. (2006). Variational methods for glacier flow over plastic till. *J. Fluid Mech.*, 555, 299–320, <https://doi.org/10.1017/s0022112006009104>.
- Schoof, C. (2007a). Ice sheet grounding line dynamics: Steady states, stability and hysteresis. *J. Geophys. Res.*, 112(F3), F03S28, <https://doi.org/10.1029/2006JF000664>.
- Schoof, C. (2007b). Marine ice-sheet dynamics. Part 1. The case of rapid sliding. *J. Fluid. Mech.*, 573, 27–55, <https://doi.org/10.1017/s0022112006003570>.
- Schoof, C. (2010). Coulomb friction and other sliding laws in a higher order glacier flow. *Math. Mod. Meth. Appl. S.*, 20(1), 157–189, <https://doi.org/10.1142/s0218202510004180>.
- Schoof, C. (2011). Marine ice sheet dynamics. Part 2. A Stokes flow contact problem. *J. Fluid. Mech.*, 679, 122–155, <https://doi.org/10.1017/jfm.2011.129>.

- Schoof, C. (2012). Marine ice sheet stability. *J. Fluid Mech.*, 698, 62–72, <https://doi.org/10.1017/jfm.2012.43>.
- Schoof, C., Davis, A. D., and Popa, T. V. (2017). Boundary layer models for calving marine outlet glaciers. *Cryosphere*, 11(5), 2283–2303, <https://doi.org/10.5194/tc-11-2283-2017>.
- Schoof, C. and Hewitt, I. (2013). Ice-Sheet Dynamics. *Annu. Rev. Fluid Mech.*, 45, 217–239, <https://doi.org/10.1146/annurev-fluid-011212-140632>.
- Scott, D. W. (2015). *Multivariate Density Estimation: : Theory, Practice, and Visualization*. John Wiley & Sons, 2nd edition, <https://doi.org/10.1002/9781118575574>.
- Seroussi, H. (2012). *Modeling ice flow dynamics with advanced multi-model formulations*. PhD thesis, École Centrale Paris, Paris, France.
- Seroussi, H., Nakayama, Y., Larour, E., Menemenlis, D., Morlighem, M., Rignot, E., and Khazendar, A. (2017). Continued retreat of Thwaites Glacier, West Antarctica, controlled by bed topography and ocean circulation. *Geophys. Res. Lett.*, 44(12), 6191–6199, <https://doi.org/10.1002/2017gl072910>.
- Seroussi, H., Nowicki, S., Simon, E., Abe-Ouchi, A., Albrecht, T., Brondex, J., Cornford, S., Dumas, C., Gillet-Chaulet, F., Goelzer, H., Golledge, N. R., Gregory, J. M., Greve, R., Hoffman, M. J., Humbert, A., Huybrechts, P., Kleiner, T., Larour, E., Leguy, G., Lipscomb, W. H., Lowry, D., Mengel, M., Morlighem, M., Pattyn, F., Payne, A. J., Pollard, D., Price, S. F., Quiquet, A., Reerink, T. J., Reese, R., Rodehacke, C. B., Schlegel, N.-J., Shepherd, A., Sun, S., Sutter, J., Van Breedam, J., van de Wal, R. S. W., Winkelmann, R., and Zhang, T. (2019). initMIP-Antarctica: an ice sheet model initialization experiment of ISMIP6. *Cryosphere*, 13(5), 1441–1471, <https://doi.org/10.5194/tc-13-1441-2019>.
- Shaffer, G. (2014). Formulation, calibration and validation of the DAIS model (version 1), a simple Antarctic ice sheet model sensitive to variations of sea level and ocean subsurface temperature. *Geosci. Model Dev.*, 7(4), 1803–1818, <https://doi.org/10.5194/gmd-7-1803-2014>.
- Shapiro, N. M. and Ritzwoller, M. H. (2004). Inferring surface heat flux distributions guided by a global seismic model: particular application to Antarctica. *Earth Planet. Sc. Lett.*, 223(1–2), 213–224, <https://doi.org/10.1016/j.epsl.2004.04.011>.
- Shepherd, A., Ivins, E., Rignot, E., Smith, B., van den Broeke, M., Velicogna, I., Whitehouse, P., Briggs, K., Joughin, I., Krinner, G., Nowicki, S., Payne, T., Scambos, T., Schlegel, N., A. G., Agosta, C., Ahlstrøm, A., Babonis, G., Barletta, V., Blazquez, A., Bonin, J., Csatho, B., Cullather, R., Felikson, D., Fettweis, X., Forsberg, R., Gallee, H., Gardner, A., Gilbert, L., Groh, A., Gunter, B., Hanna, E., Harig, C., Helm, V., Horvath, A., Horwath, M., Khan, S., Kjeldsen, K. K., Konrad, H., Langen, P., Lecavalier, B., Loomis, B., Luthcke, S., McMillan, M., Melini, D., Mernild, S., Mohajerani, Y., Moore, P., Mougnot, J., Moyano, G., Muir, A., Nagler, T., Nield, G., Nilsson, J., Noel, B., Otosaka, I., Pattle, M. E., Peltier, W. R., Pie, N., Rietbroek, R., Rott, H., Sandberg-Sørensen, L., Sasgen, I., Save, H., Scheuchl, B., Schrama, E., Schröder, L., Seo, K.-W., Simonsen, S., Slater, T., Spada, G., Sutterley, T., Talpe, M., Tarasov, L., van de Berg, W. J., van der Wal, W., van Wessem, M., Vishwakarma, B. D.,

- Wiese, D., and Wouters, B. (2018). Mass balance of the Antarctic Ice Sheet from 1992 to 2017. *Nature*, 558(7709), 219–222, <https://doi.org/10.1038/s41586-018-0179-y>.
- Shields, M. D. and Sundar, V. S. (2015). Targeted random sampling: a new approach for efficient reliability estimation for complex systems. *Int. J. Reliab. Safe.*, 9(2–3), 174–190, <https://doi.org/10.1504/IJRS.2015.072718>.
- Shields, M. D., Teferra, K., Hapij, A., and Daddazio, R. P. (2015). Refined Stratified Sampling for efficient Monte Carlo based uncertainty quantification. *Reliab. Eng. Syst. Safe.*, 142, 310–325, <https://doi.org/10.1016/j.res.2015.05.023>.
- Shields, M. D. and Zhang, J. (2016). The generalization of Latin hypercube sampling. *Reliab. Eng. Syst. Safe.*, 148, 96–108, <https://doi.org/10.1016/j.res.2015.12.002>.
- Silvano, A., Rintoul, S. R., and Herraiz-Borreguero, L. (2016). Ocean-Ice Shelf Interaction in East Antarctica. *Oceanography*, 29(4), 130–143, <https://doi.org/10.5670/oceanog.2016.105>.
- Silvano, A., Rintoul, S. R., Peña-Molino, B., Hobbs, W. R., van Wijk, E., Aoki, S., Tamura, T., and Williams, G. D. (2018). Freshening by glacial meltwater enhances melting of ice shelves and reduces formation of Antarctic Bottom Water. *Sci. Adv.*, 4(4), eaap9467, <https://doi.org/10.1126/sciadv.aap9467>.
- Smith, R. (2014). *Uncertainty Quantification: Theory, Implementation, and Applications*. Philadelphia, PA: SIAM.
- Smola, A. J. and Schölkopf, B. (2004). A tutorial on support vector regression. *Stat. Comput.*, 14(3), 199–222, <https://doi.org/10.1023/b:stco.0000035301.49549.88>.
- Smolyak, S. A. (1963). Quadrature and interpolation formulas for tensor products of certain classes of functions. 148(5), 1042–1045.
- Sobol, I. (2001). Global sensitivity indices for nonlinear mathematical models and their Monte Carlo estimates. *Math. Comput. Simul.*, 55(1–3), 271–280, [https://doi.org/10.1016/s0378-4754\(00\)00270-6](https://doi.org/10.1016/s0378-4754(00)00270-6).
- Sobol, I. M. (1993). Sensitivity Estimates for Nonlinear Mathematical Models. *Math. Model. Comput. Exp.*, 1(4), 407–414.
- Soize, C. (2008). Construction of probability distributions in high dimension using the maximum entropy principle: Applications to stochastic processes, random fields and random matrices. *Int. J. Numer. Meth. Eng.*, 76(10), 1583–1611, <https://doi.org/10.1002/nme.2385>.
- Soize, C. (2015). Polynomial Chaos Expansion of a Multimodal Random Vector. *SIAM/ASA JUQ*, 3(1), 34–60, <https://doi.org/10.1137/140968495>.
- Soize, C. (2017). *Uncertainty Quantification: An Accelerated Course with Advanced Applications in Computational Engineering*. Cham, Switzerland: Springer, <https://doi.org/10.1007/978-3-319-54339-0>.
- Soize, C. and Ghanem, R. (2004). Physical Systems with Random Uncertainties: Chaos Representations with Arbitrary Probability Measure. *SIAM J. Sci. Comput.*, 26(2), 395–410, <https://doi.org/10.1137/s1064827503424505>.

- Soize, C. and Ghanem, R. (2016). Data-driven probability concentration and sampling on manifold. *J. Comput. Phys.*, 321, 242–258, <https://doi.org/10.1016/j.jcp.2016.05.044>.
- Soize, C. and Ghanem, R. (2017). Polynomial chaos representation of databases on manifolds. *J. Comput. Phys.*, 335, 201–221, <https://doi.org/10.1016/j.jcp.2017.01.031>.
- Soize, C. and Ghanem, R. (2020). Physics-constrained non-Gaussian probabilistic learning on manifolds. *Int. J. Numer. Meth. Eng.*, 121(1), 110–145, <https://doi.org/10.1002/nme.6202>.
- Soize, C., Ghanem, R., Safta, C., Huan, X., Vane, Z. P., Oefelein, J., Lacaze, G., Najm, H. N., Tang, Q., and Chen, X. (2019). Entropy-based closure for probabilistic learning on manifolds. *J. Comput. Phys.*, 388, 518–533, <https://doi.org/10.1016/j.jcp.2018.12.029>.
- Sommerfeld, M., Sain, S., and Schwartzman, A. (2018). Confidence Regions for Spatial Excursion Sets from Repeated Random Field Observations, With an Application to Climate. *J. Am. Stat. Assoc.*, 113(523), 1327–1340, <https://doi.org/10.1080/01621459.2017.1341838>.
- Souverijns, N., Gossart, A., Demuzere, M., Lenaerts, J. T. M., Medley, B., Gorodetskaya, I. V., Vanden Broucke, S., and van Lipzig, N. P. M. (2019). A New Regional Climate Model for POLAR-CORDEX: Evaluation of a 30-Year Hindcast with COSMO-CLM<sup>2</sup> Over Antarctica. *J. Geophys. Res. Atmos.*, 124(3), 1405–1427, <https://doi.org/10.1029/2018jd028862>.
- Stammer, D., van de Wal, R. S. W., Nicholls, R. J., Church, J. A., Le Cozannet, G., Lowe, J. A., Horton, B. P., White, K., Behar, D., and Hinkel, J. (2019). Framework for High-End Estimates of Sea Level Rise for Stakeholder Applications. *Earth's Future*, 7(8), 923–938, <https://doi.org/10.1029/2019ef001163>.
- Stein, M. (1987). Large Sample Properties of Simulations Using Latin Hypercube Sampling. *Technometrics*, 29(2), 143–151, <https://doi.org/10.2307/1269769>.
- Stocker, T. F., Qin, D., Plattner, G.-K., Tignor, M., Allen, S. K., Boshung, J., Nauels, A., Xia, Y., Bex, V., and Midgley, P. M., Eds. (2013). *Climate Change 2013: The Physical Science Basis. Contribution of Working Group I to the Fifth Assessment Report of the Intergovernmental Panel on Climate Change*. Cambridge, United Kingdom: Cambridge University Press, <https://doi.org/10.1017/cbo9781107415324>.
- Strong, M. and Oakley, J. E. (2014). When Is a Model Good Enough? Deriving the Expected Value of Model Improvement via Specifying Internal Model Discrepancies. *SIAM/ASA JUQ*, 2(1), 106–125, <https://doi.org/10.1137/120889563>.
- Sudret, B. (2008). Global sensitivity analysis using polynomial chaos expansions. *Reliab. Eng. Syst. Safe.*, 93(7), 964–979, <https://doi.org/10.1016/j.res.2007.04.002>.
- Sullivan, T. (2015). *Introduction to Uncertainty Quantification*. Cham, Switzerland: Springer, <https://doi.org/10.1007/978-3-319-23395-6>.
- Sun, S., Cornford, S. L., Liu, Y., and Moore, J. C. (2014). Dynamic response of Antarctic ice shelves to bedrock uncertainty. *Cryosphere*, 8(4), 1561–1576, <https://doi.org/10.5194/tc-8-1561-2014>.

- Sun, S., Cornford, S. L., Moore, J. C., Gladstone, R., and Zhao, L. (2017). Ice shelf fracture parameterization in an ice sheet model. *Cryosphere*, 11(6), 2543–2554, <https://doi.org/10.5194/tc-11-2543-2017>.
- Tarantola, A. (2005). *Inverse Problem Theory and Methods for Model Parameter Estimation*. Philadelphia, PA: SIAM, <https://doi.org/10.1137/1.9780898717921>.
- Tarasov, L. and Peltier, W. R. (2004). A geophysically constrained large ensemble analysis of the deglacial history of the North American ice-sheet complex. *Quaternary Sci. Rev.*, 23(3–4), 359–388, <https://doi.org/10.1016/j.quascirev.2003.08.004>.
- Taylor, K. E., Stouffer, R. J., and Meehl, G. A. (2012). An Overview of CMIP5 and the Experiment Design. *Bull. Am. Meteorol. Soc.*, 93(4), 485–498, <https://doi.org/10.1175/bams-d-11-00094.1>.
- Tezaur, I. K., Perego, M., Salinger, A. G., Tuminaro, R. S., and Price, S. F. (2015a). Albany/FELIX: a parallel, scalable and robust, finite element, first-order Stokes approximation ice sheet solver built for advanced analysis. *Geosci. Model Dev.*, 8(4), 1197–1220, <https://doi.org/10.5194/gmd-8-1197-2015>.
- Tezaur, I. K., Tuminaro, R. S., Perego, M., Salinger, A. G., and Price, S. F. (2015b). On the Scalability of the Albany/FELIX first-order Stokes Approximation ice sheet solver for large-scale simulations of the Greenland and Antarctic ice sheets. *Procedia Comput. Sci.*, 51, 2026–2035, <https://doi.org/10.1016/j.procs.2015.05.467>.
- Thomas, R. H. and Bentley, C. R. (1978). A model for Holocene Retreat of the West Antarctic Ice Sheet. *Quaternary Res.*, 10(2), 150–170, [https://doi.org/10.1016/0033-5894\(78\)90098-4](https://doi.org/10.1016/0033-5894(78)90098-4).
- Timmermann, R. and Hellmer, H. H. (2013). Southern Ocean warming and increased ice shelf basal melting in the twenty-first and twenty-second centuries based on coupled ice-ocean finite-element modelling. *Ocean Dynam.*, 63(9-10), 1011–1026, <https://doi.org/10.1007/s10236-013-0642-0>.
- Timmermann, R., Wang, Q., and Hellmer, H. H. (2012). Ice-shelf basal melting in a global finite-element sea-ice/ice-shelf/ocean model. *Ann. Glaciol.*, 53(60), 303–314, <https://doi.org/10.3189/2012aog60a156>.
- Torre, E., Marelli, S., Embrechts, P., and Sudret, B. (2019). A general framework for data-driven uncertainty quantification under complex input dependencies using vine copulas. *Probabilist. Eng. Mech.*, 55, 1–16, <https://doi.org/10.1016/j.probengmech.2018.08.001>.
- Trusel, L. D., Frey, K. E., Das, S. B., Karnauskas, K. B., Munneke, P. K., van Meijgaard, E., and van den Broeke, M. R. (2015). Divergent trajectories of Antarctic surface melt under two twenty-first-century climate scenarios. *Nat. Geosci.*, 8(12), 927–932, <https://doi.org/10.1038/ngeo2563>.
- Tsai, V. C., Stewart, A. L., and Thompson, A. F. (2015). Marine ice-sheet profiles and stability under Coulomb basal conditions. *J. Glaciol.*, 61(226), 205–215, <https://doi.org/10.3189/2015jog14j221>.

- Tulaczyk, S., Kamb, W. B., and Engelhardt, H. F. (2000a). Basal mechanics of Ice Stream B, West Antarctica: 1. Till mechanics. *J. Geophys. Res.*, 105(B1), 463–481, <https://doi.org/10.1029/1999jb900329>.
- Tulaczyk, S., Kamb, W. B., and Engelhardt, H. F. (2000b). Basal mechanics of Ice Stream B, West Antarctica: 2. Undrained plastic bed model. *Journal of Geophysical Research: Solid Earth*, 105(B1), 483–494, <https://doi.org/10.1029/1999jb900328>.
- Vafeidis, A., Neumann, B., Zimmermann, J., and Nicholls, R. (2011). Migration and global environmental change: Mr9: Analysis of land area and population in the low-elevation coastal zone (lecZ). Available at <http://www.bis.gov.uk/assets/foresight/docs/migration/modelling/11-1169-mr9-land-and-population-in-the-low-elevation-coastal-zone.pdf>, last accessed: 5 November 2019.
- Valdebenito, M. A. and Schuëller, G. I. (2010). A survey on approaches for reliability-based optimization. *Struct. Multidiscip. O.*, 42(5), 645–663, <https://doi.org/10.1007/s00158-010-0518-6>.
- van der Veen, C. J. (2013). *Fundamentals of Glacier Dynamics*. Boca Raton, FL: CRC Press, 2nd edition, <https://doi.org/10.1201/b14059>.
- Van der Wal, W., Whitehouse, P. L., and Schrama, E. J. O. (2015). Effect of GIA models with 3D composite mantle viscosity on GRACE mass balance estimates for Antarctica. *Earth Planet. Sc. Lett.*, 414, 134–143, <https://doi.org/10.1016/j.epsl.2015.01.001>.
- Van Kampenhout, L., Rhoades, A. M., Herrington, A. R., Zarzycki, C. M., Lenaerts, J. T. M., Sacks, W. J., and van den Broeke, M. R. (2019). Regional grid refinement in an Earth system model: impacts on the simulated Greenland surface mass balance. *Cryosphere*, 13(6), 1547–1564, <https://doi.org/10.5194/tc-13-1547-2019>.
- Van Vuuren, D. P., Edmonds, J., Kainuma, M., Riahi, K., Thomson, A., Hibbard, K., Hurtt, G. C., Kram, T., Krey, V., Lamarque, J.-F., Masui, T., Meinshausen, M., Nakicenovic, N., Smith, S. J., and Rose, S. K. (2011). The representative concentration pathways: an overview. *Climatic Change*, 109(1-2), 5–31, <https://doi.org/10.1007/s10584-011-0148-z>.
- Van Wessem, J., Reijmer, C. H., Morlighem, M., Mouginot, J., Rignot, E., Medley, B., Joughin, I., Wouters, B., Depoorter, M. A., Bamber, J. L., Lenaerts, J. T. M., van de Berg, W. J., van den Broeke, M. R., and van Meijgaard, E. (2014). Improved representation of East Antarctic surface mass balance in a regional atmospheric climate model. *J. Glaciol.*, 60(222), 761–770, <https://doi.org/10.3189/2014jog14j051>.
- Van Wessem, J. M., van de Berg, W. J., Noël, B. P. Y., van Meijgaard, E., Amory, C., Birnbaum, G., Jakobs, C. L., Krüger, K., Lenaerts, J. T. M., Lhermitte, S., Ligtenberg, S. R. M., Medley, B., Reijmer, C. H., van Tricht, K., Trusel, L. D., van Ulf, L. H., Wouters, B., Wuite, J., and van den Broeke, M. R. (2018). Modelling the climate and surface mass balance of polar ice sheets using RACMO2 – Part 2: Antarctica (1979–2016). *Cryosphere*, 12(4), 1479–1498, <https://doi.org/10.5194/tc-12-1479-2018>.
- Vapnik, V. N. (2000). *The Nature of Statistical Learning Theory*. New York, NY: Springer Science + Business Media, 2nd edition, <https://doi.org/10.1007/978-1-4757-3264-1>.

- Vaughan, D. G., Comiso, J. C., Allison, I., Carrasco, J., Kaser, G., Kwok, R., Mote, P., Murray, T., Paul, F., Ren, J., Rignot, E., Solomina, O., Steffen, K., and Zhang, T. (2013). Observations: Cryosphere. In T. F. Stocker, D. Qin, G.-K. Plattner, M. Tignor, S. K. Allen, J. Boschung, A. Nauels, Y. Xi, V. Bex, and P. M. Midgley (Eds.), *Climate Change 2013: The Physical Science Basis. Contribution of Working Group I to the Fifth Assessment Report of the Intergovernmental Panel on Climate Change*, chapter 4, (pp. 317–382). Cambridge University Press, <https://doi.org/10.1017/CBO9781107415324.012>.
- Vergori, L. (2010). Flows at small Reynolds and Froude numbers. *Int. J. Eng. Sci.*, 48(11), 1659–1670, <https://doi.org/10.1016/j.ijengsci.2010.07.008>.
- Vizcaino, M. (2014). Ice sheets as interactive components of Earth System Models: progress and challenges. *WIREs Clim. Change*, 5(4), 557–568, <https://doi.org/10.1002/wcc.285>.
- Waibel, M. S., Hulbe, C. L., Jackson, C. S., and Martin, D. F. (2018). Rate of Mass Loss Across the Instability Threshold for Thwaites Glacier Determines Rate of Mass Loss for Entire Basin. *Geophys. Res. Lett.*, 45(2), 809–816, <https://doi.org/10.1002/2017gl076470>.
- Wameling, A. (2003a). Accuracy of geostatistical prediction of yearly precipitation in Lower Saxony. *Environmetrics*, 14(7), 699–709, <https://doi.org/10.1002/env.616>.
- Wameling, A. (2003b). Vertical and Horizontal Spatial Variation of Geostatistical Prediction. In G. M. Foody and P. M. Atkinson (Eds.), *Uncertainty in Remote Sensing and GIS*, chapter 13, (pp. 209–222). John Wiley & Sons, <https://doi.org/10.1002/0470035269.ch13>.
- Wameling, A. and Saborowski, J. (2001). Construction of local confidence intervals for contour lines. In *Proceedings of the IUFRO.11 Conference in Forest Biometry, Modelling and Information Science*: University of Greenwich.
- Wan, X. and Karniadakis, G. E. (2006). Multi-Element Generalized Polynomial Chaos for Arbitrary Probability Measures. *SIAM J. Sci. Comput.*, 28(3), 901–928, <https://doi.org/10.1137/050627630>.
- Weertman, J. (1957). On the Sliding of Glaciers. *J. Glaciol.*, 3(21), 33–38, <https://doi.org/10.3189/s0022143000024709>.
- Weertman, J. (1974). Stability of the Junction of an Ice Sheet and an Ice Shelf. *J. Glaciol.*, 13(67), 3–11, <https://doi.org/10.3189/S0022143000023327>.
- Weis, M., Greve, R., and Hutter, K. (1999). Theory of shallow ice shelves. *Continuum Mech. Therm.*, 11(1), 15–50, <https://doi.org/10.1007/s001610050102>.
- Werder, M. A., Hewitt, I. J., Schoof, C. G., and Flowers, G. E. (2013). Modeling channelized and distributed subglacial drainage in two dimensions. *J. Geophys. Res. Earth Surf.*, 118(4), 2140–2158, <https://doi.org/10.1002/jgrf.20146>.
- Whitehouse, P. L. (2018). Glacial isostatic adjustment modelling: historical perspectives, recent advances, and future directions. *Earth Surf. Dynam.*, 6(2), 401–429, <https://doi.org/10.5194/esurf-6-401-2018>.

- Whitehouse, P. L., Gomez, N., King, M. A., and Wiens, D. A. (2019). Solid Earth change and the evolution of the Antarctic Ice Sheet. *Nat. Commun.*, 10, <https://doi.org/10.1038/s41467-018-08068-y>.
- Wilby, R. L., Nicholls, R. J., Warren, R., Wheatler, H. S., Clarke, D., and Dawson, R. J. (2011). Keeping nuclear and other coastal sites safe from climate change. *P. I. Civil Eng. - Civ. En.*, 164(3), 129–136, <https://doi.org/10.1680/cien.2011.164.3.129>.
- Winkelmann, R., Martin, M. A., Haseloff, M., Albrecht, T., Bueller, E., Khroulev, C., and Levermann, A. (2011). The Potsdam Parallel Ice Sheet Model (PISM-PIK) – Part 1: Model description. *Cryosphere*, 5(3), 715–726, <https://doi.org/10.5194/tc-5-715-2011>.
- Wise, M. G., Dowdeswell, J. A., Jakobsson, M., and Larter, R. D. (2017). Evidence of marine ice-cliff instability in Pine Island Bay from iceberg-keel plough marks. *Nature*, 550(7677), 506–510, <https://doi.org/10.1038/nature24458>.
- Witteveen, J. A. and Bijl, H. (2006). Modeling arbitrary uncertainties using gram-schmidt polynomial chaos. In *44th AIAA aerospace sciences meeting and exhibit* (pp. 896). <https://doi.org/10.2514/6.2006-896>.
- Wohlmuth, B. (2011). Variationally consistent discretization schemes and numerical algorithms for contact problems. *Acta Numer.*, 20, 569–734, <https://doi.org/10.1017/s0962492911000079>.
- Wriggers, P. (2006). *Computational Contact Mechanics*. Berlin, Germany: Springer-Verlag, 2nd edition, <https://doi.org/10.1007/978-3-540-32609-0>.
- Xiu, D. and Karniadakis, G. E. (2002). The Wiener–Askey Polynomial Chaos for Stochastic Differential Equations. *SIAM J. Sci. Comput.*, 24(2), 619–644, <https://doi.org/10.1137/s1064827501387826>.
- Xiu, D., Lucor, D., Su, C.-H., and Karniadakis, G. E. (2002). Stochastic Modeling of Flow-Structure Interactions Using Generalized Polynomial Chaos. *J. Fluid. Eng.*, 124(1), 51–59, <https://doi.org/10.1115/1.1436089>.
- Yu, H., Rignot, E., Seroussi, H., and Morlighem, M. (2018). Retreat of Thwaites Glacier, West Antarctica, over the next 100 years using various ice flow models, ice shelf melt scenarios and basal friction laws. *Cryosphere*, 12(12), 3861–3876, <https://doi.org/10.5194/tc-12-3861-2018>.
- Zwally, H. J., Giovinetto, M. B., Beckley, M. A., and Saba, J. L. (2012). Antarctic and Greenland Drainage Systems.
- Zwally, H. J., Li, J., Robbins, J. W., Saba, J. L., Yi, D., and Brenner, A. C. (2015). Mass gains of the Antarctic ice sheet exceed losses. *J. Glaciol.*, 61(230), 1019–1036, <https://doi.org/10.3189/2015jog15j071>.

# List of Symbols

## Physical variables (Greek letters)

$\tau_b$	Basal shear stress
$\eta$	Ice (effective) viscosity
$\rho$	Ice mass density
$\rho_w$	Sea-water mass density
$\sigma$	Stress tensor
$\sigma^D$	Deviatoric stress tensor

## Physical variables (Latin letters)

$D$	Strain-rate tensor
$v$	Velocity field
$v_b$	Basal sliding velocity
$A$	Rheological coefficient in Glen's flow law
$a_b$	Mass balance at the ice-bedrock interface
$a_s$	Mass balance at the ice-air interface
$a_w$	Mass balance at the ice-ocean interface
$b$	Bedrock elevation
$c_f$	Calving rate
$g$	Gravitational acceleration
$h$	Ice thickness
$n$	Glen's rheological exponent

$p$	Pressure field
$s$	Ice surface elevation
$T$	Temperature field
$T_{oc}$	Ocean temperature at the continental shelf
$T_s$	Surface air temperature
$T_w$	Ocean temperature at the ice-ocean interface

### Mathematical notations

<b>Deterministic matrix:</b>	A deterministic matrix is denoted by an uppercase letter between brackets such as $[A]$
<b>Deterministic variable:</b>	A deterministic variable is denoted by a lowercase letter such as $x$
<b>Deterministic vector:</b>	A deterministic vector is denoted by a boldface, lowercase letter such as in $\boldsymbol{x} = (x_1, \dots, x_n)$
<b>Random variable:</b>	A deterministic variable is denoted by an uppercase letter such as $X$
<b>Random vector:</b>	A random vector is denoted by a boldface, uppercase letter such as in $\boldsymbol{X} = (X_1, \dots, X_n)$
$\mathbb{E}$	Mathematical expectation
$\mathbb{V}$	Variance
$\mathbf{1}$	Indicator function
$\text{Cov}(X, Y)$	Covariance of $X$ and $Y$
$\text{div}_x \boldsymbol{f}$	Gradient of the vector-valued function $\boldsymbol{f}$
$\text{tr}$	Trace operator
$\nabla_x f$	Divergence of the scalar-valued function $f$
$\mathbb{N}$	Set of integers
$\mathbb{R}$	Set of real numbers

# List of publications and talks

## List of manuscripts and publications

Arnst, M., Soize C., and Bulthuis, K. Computation of Sobol indices in global sensitivity analysis from small data sets by probabilistic learning on manifolds. Under review.

Bulthuis K., Pattyn, F., and Arnst, M. A multifidelity quantile-based approach for confidence sets of random excursion sets with application to ice-sheet dynamics. Under review.

Hanna, E., Pattyn, F., Navarro, F., Favier, V., Goelzer, H., van den Broeke, M., Vizcaino, M., Whitehouse, P., Ritz, C., Bulthuis, K., and Smith, B. Mass balance of the ice sheets and glaciers – progress since AR5 and challenges, *Earth-Sci. Rev.*, <https://doi.org/10.1016/j.earscirev.2019.102976>.

Bulthuis K., Arnst, M., Sun, S., and Pattyn, F. (2019). Uncertainty quantification of the multi-centennial response of the Antarctic ice sheet to climate change. *Cryosphere*, 13(4):1349–1380, <https://doi.org/10.5194/tc-13-1349-2019>.

## List of talks

- |                |  |
|----------------|--|
| June 2019      | Bulthuis, K., Pattyn, F., and Arnst, M. <i>Estimation of confidence regions for random excursion sets with application to large-scale ice-sheet simulations</i> , 3rd International Conference on Uncertainty Quantification in Computational Sciences and Engineering (UNCECOMP 2019), Hersonissos, Greece, <a href="http://hdl.handle.net/2268/238637">http://hdl.handle.net/2268/238637</a> . |
| Mars 2019      | Bulthuis, K., Arnst, M., Sun, S., and Pattyn, F. <i>Uncertainty quantification of the multi-centennial response of the Antarctic ice sheet to climate change</i> , SIAM SIAM Conference on Computational and Mathematical Issues in the Geosciences (SIAMGS19), Houston, TX, <a href="http://hdl.handle.net/2268/233442">http://hdl.handle.net/2268/233442</a> .                                 |
| April 2018     | Bulthuis, K., Pattyn, F., Favier, L., and Arnst, M. <i>Stochastic Modeling of Uncertainties in Fast Essential Antarctic Ice Sheet Model</i> , SIAM Conference on Uncertainty Quantification (SIAMUQ18), Garden Grove, CA, <a href="http://hdl.handle.net/2268/222840">http://hdl.handle.net/2268/222840</a> .  |
| April 2017     | Bulthuis, K., Pattyn, F., Favier, L., and Arnst, M. <i>Uncertainty quantification of Antarctic contribution to sea-level rise using the fast Elementary Thermomechanical Ice Sheet (f.ETISh) model</i> , EGU General Assembly, Vienna, Austria, <a href="http://hdl.handle.net/2268/207549">http://hdl.handle.net/2268/207549</a> .  |
| Septembre 2016 | Bulthuis, K., Pattyn, F., Favier, L., and Arnst, M. <i>Instability and abrupt changes in marine ice sheet behaviour</i> , 1st CRITICS Workshop and Summer School on Critical Transitions in Complex Systems, Kulhuse, Denmark, <a href="http://hdl.handle.net/2268/201873">http://hdl.handle.net/2268/201873</a> .   |